frontiers | Research Topics

Internal flow mechanism of modern hydraulic machinery

Edited by
Kan Kan, Zhiqun Daniel Deng, Yongguang Cheng, Pengcheng Guo and Daqing Zhou

Published in
Frontiers in Energy Research

ISSN 1664-8714
ISBN 978-2-83251-326-2
DOI 10.3389/978-2-83251-326-2

About Frontiers

Frontiers is more than just an open access publisher of scholarly articles: it is a pioneering approach to the world of academia, radically improving the way scholarly research is managed. The grand vision of Frontiers is a world where all people have an equal opportunity to seek, share and generate knowledge. Frontiers provides immediate and permanent online open access to all its publications, but this alone is not enough to realize our grand goals.

Frontiers journal series

The Frontiers journal series is a multi-tier and interdisciplinary set of open-access, online journals, promising a paradigm shift from the current review, selection and dissemination processes in academic publishing. All Frontiers journals are driven by researchers for researchers; therefore, they constitute a service to the scholarly community. At the same time, the *Frontiers journal series* operates on a revolutionary invention, the tiered publishing system, initially addressing specific communities of scholars, and gradually climbing up to broader public understanding, thus serving the interests of the lay society, too.

Dedication to quality

Each Frontiers article is a landmark of the highest quality, thanks to genuinely collaborative interactions between authors and review editors, who include some of the world's best academicians. Research must be certified by peers before entering a stream of knowledge that may eventually reach the public - and shape society; therefore, Frontiers only applies the most rigorous and unbiased reviews. Frontiers revolutionizes research publishing by freely delivering the most outstanding research, evaluated with no bias from both the academic and social point of view. By applying the most advanced information technologies, Frontiers is catapulting scholarly publishing into a new generation.

What are Frontiers Research Topics?

Frontiers Research Topics are very popular trademarks of the *Frontiers journals series*: they are collections of at least ten articles, all centered on a particular subject. With their unique mix of varied contributions from Original Research to Review Articles, Frontiers Research Topics unify the most influential researchers, the latest key findings and historical advances in a hot research area.

Find out more on how to host your own Frontiers Research Topic or contribute to one as an author by contacting the Frontiers editorial office: frontiersin.org/about/contact

Internal flow mechanism of modern hydraulic machinery

Topic editors

Kan Kan — College of Energy and Electrical Engineering, China
Zhiqun Daniel Deng — Pacific Northwest National Laboratory (DOE), United States
Yongguang Cheng — Wuhan University, China
Pengcheng Guo — Xi'an University of Technology, China
Daqing Zhou — Hohai University, China

Citation

Kan, K., Deng, Z. D., Cheng, Y., Guo, P., Zhou, D., eds. (2023). *Internal flow mechanism of modern hydraulic machinery*. Lausanne: Frontiers Media SA. doi: 10.3389/978-2-83251-326-2

Table of contents

frontiers | Frontiers in Energy Research

TYPE Editorial
PUBLISHED 03 January 2023
DOI 10.3389/fenrg.2022.1096541

OPEN ACCESS

EDITED AND REVIEWED BY
Ellen B. Stechel,
Arizona State University, United States

*CORRESPONDENCE
Daqing Zhou,
zhoudaqing@hhu.edu.cn

SPECIALTY SECTION
This article was submitted to Process and Energy Systems Engineering, a section of the journal Frontiers in Energy Research

RECEIVED 12 November 2022
ACCEPTED 22 November 2022
PUBLISHED 03 January 2023

CITATION
Kan K, Deng ZD, Cheng Y, Guo P and Zhou D (2023), Editorial: Internal flow mechanism of modern hydraulic machinery.
Front. Energy Res. 10:1096541.
doi: 10.3389/fenrg.2022.1096541

Editorial: Internal flow mechanism of modern hydraulic machinery

Kan Kan[1], Zhiqun Daniel Deng[2], Yongguang Cheng[3], Pengcheng Guo[4] and Daqing Zhou[1]*

[1]College of Energy and Electrical Engineering, Hohai University, Nanjing, China, [2]Energy and Environment Directorate, Pacific Northwest National Laboratory, Richland, WA, United States, [3]State Key Laboratory of Water Resources and Hydropower Engineering Science, Wuhan University, Wuhan, China, [4]State Key Laboratory of Eco-hydraulic in Northwest Arid Region, Xi'an University of Technology, Xi'an, China

KEYWORDS

hydraulic turbine, pump, pump-turbine, flow characteristics, transient process, cavitation, numerical method

Editorial on the Research Topic
Internal flow mechanism of modern hydraulic machinery

Hydraulic machines can be broadly defined as machines that convert the hydraulic energy of the liquid passing through them to the mechanical energy of their specific mechanical components, or *vice versa*. This definition using energy direction leads to two classes of hydraulic machinery: turbines and pumps. In these machines, the external performance characteristics are an indicator of their internal flow state. In their daily operations and in line with the system operational requirements, hydraulic machines may be forced to operate under off-design operating conditions, resulting in flow unsteadiness within the machines' fluid passage channels. Subsequently emerged secondary flow phenomena generally lead to detrimental outcomes such as flow and pressure pulsations, machine structural vibrations, noise, and machine performance degradation. Therefore, it is fundamentally important to improve the understanding of the flow dynamics of the hydraulic machines and their evolution mechanism under different operating circumstances. The improved understanding can increase the machines' operational performance, safety and associated economic benefits. Therefore, the papers included in the current Research Topic focus on the three aspects through both numerical and experimental methods: the general hydrodynamics of hydraulic machinery and its systems, fluid-solid interactions, and acoustic measurement of fluid systems.

A number of studies have been conducted on flow dynamics within pump-turbines and the parameters that influence flow unsteadiness onset and evolution process in hydraulic machinery. In a study by Zeng et al., the vortex distribution and associated energy loss characteristics within a pump-turbine in its S-shaped operating zone have been analyzed. Vortex flow structures that emerged in the S-shaped zone could be classified as leaf channel vortex and flow separation vortex for operating conditions within the runaway and turbine brake operating zones. These vortices grew larger and expanded upstream, blocking multiple channels within the

guide and stay vane flow zones. Hu et al. investigated the five operating conditions in the whole four-quadrant plane of characteristics curves. They found that the flow unsteadiness increases as the machine operates at the point far away from the optimum conditions for both turbine and pump operating modes. The flow impacting on the runner blades in the pump-brake zone led to serious flow instabilities and subsequent runner force pulsations, while the rotating stall and associated pressure pulsations were obvious under hump and the S-shaped region. The highest pressure pulsations were recorded in the vaneless zone and the amplitude increased with guide vane opening. Deng et al. conducted a similar study considering the pump and turbine operating modes under four different guide vane openings (6°, 14°, 18°, and 20°). Vortices that emerged in the vaneless space under pump mode were counterclockwise-rotating flow separations. These vortices eventually blocked the flow passage, leading to massive hydraulic losses and subsequent occurrence of the hump characteristics. As for the turbine mode, most of the recorded vaneless space vortex structures showed a clockwise-rotating tendency, and the associated pressure pulsations constituted an important factor of the pump-turbine's S-shaped characteristics, as they were directly linked to the machine performance degradation, and its operational safety. In addition, Hou et al. studied the clearance flow dynamics in pump-turbines by investigating the clearance flow field between a stationary and a rotating disc using experimental measurements and numerical simulations. The distribution of the circumferential velocity showed two distinct zones in the direction of the clearance height, namely the core region and the double-boundary layer region, with the speed of the core region being 41%–42% of the rotating disc speed. They also found that the pressure and hydraulic thrust can be expressed as the functions of the inlet pressure and runner rotating speed.

Several additional investigations have been conducted on hydraulic pumps. Sun et al. simulated the transient characteristics of a submersible tubular pump during power-off process using a 6-degree-of-freedom model based on the fourth-order multi-point Adams-Moulton formula. They revealed that both the flow rate and impeller rotating speed decreased rapidly and changed the direction under the power failure scenario. The time interval between the zero flow and zero speed was found to be 0.6 s. Large vortices emerged within the pump's flow channels, especially at zero flow, where subsequent pressure pulsations threatened the machine operational safety. The blade passing frequency was found to be the dominant pressure pulsation frequency, the intensity of which increased with the impeller speed. Luo et al. investigated the effect of the shaft transition form on the inflow pattern and overall performance of the pre-shaft tubular pump. However, the three investigated forms of the shaft transition showed a negligible effect on the pump's energy characteristics, where the velocity contours at the outlet of the shaft were symmetrically distributed, providing favorable conditions for the impeller. In addition, recorded pressure pulsations were large at the impeller inlet and were dominated by the blade passing frequency, the amplitude of which increased in the hub-to-shroud direction. Shi et al. investigated the effect of inlet grooves on the tubular pump's flow characteristics and found that the decreasing pump flow led to saddle characteristics emergence under low flow conditions. The wall-mounted grooves at the inlet section were demonstrated to eliminate the wall-bounded vortices and backflows, thus improving the pump's head by 1.61 m. The grooves have also considerably weakened the pump inlet pressure pulsations, which were dominated by the blade passing frequency. Another key parameter, wall roughness, has been investigated by Chen et al. using a slanted axial-flow pump operating under a wide range of flow conditions. While the wall roughness of inlet and outlet pipes did not inflict any remarkable effects on the pump's overall flow state and performance characteristics, the wall roughness within the impeller chambers considerably deteriorated the pump performance, especially under large-flow conditions. A gradual increase in wall roughness could progressively induce flow instabilities and subsequent turbulent kinetic energy in the wall vicinal zones. On the other hand, Yang et al. investigated the flow state's changing mechanism in the impeller and guide vanes of a vertical axial-flow pump under different flow conditions. They found that, as the flow increased, the flow streamline distortion zone size on the impeller blade's surface gradually decreased from $0.8Q_{BEP}$ towards $1.2Q_{BEP}$ (Q_{BEP} is the pump flow rate at its best efficiency point). Under $0.8Q_{BEP}$ condition, flow fields within both the impeller and guide vane zones experienced the highest flow unsteadiness. Under this condition, the impeller's radial force, pressure pulsation coefficient, and the energy losses within the guide vanes were the highest, while decreased with the increasing flow. Mohamed et al. (Shamsuddeen et al. studied the pump energy loss characteristics by considering a double suction multistage centrifugal pump and using baffles to counter the pre-swirl phenomenon in its second stage. They tested three baffle plate designs, the performances of which were analyzed. Compared to the vertical and four-plate baffle configurations, the horizontal baffle configuration exhibited the largest efficiency and head improvements, before it was retested for different angles to finally find its 300° clockwise inclination as the optimum configuration, with 9.08% and 3.87% improvements in terms of pump efficiency and hydraulic head, respectively. Li et al. studied the surface pressure pulsation characteristics in the centrifugal pump's shaft end-sealing membrane using the magnetic fluid as the working medium. The centrifugal pump was tested under several flow conditions, where the pressure pulsation on the surface of the magnetic fluid sealing film displayed a periodic trend. The amplitude of this pressure pulsation was found to decrease as the pump flow increased. They found that the period of its fluctuation was equivalent to the time required for the impeller blade to sweep the volute tongue. Liu et al. proposed a new expression of f_k based on rotation-corrected energy spectrum to be used with the SST k-ω PANS model for simulating rotating flows. The model was first successfully applied to the rotating flow channel case and validated through its

application to centrifugal pump flow simulation. The authors showed that the model can accurately capture the time-averaged flow structure formations and associated velocity distribution within the pump flow field for both full and part-load conditions, thus demonstrating its suitability for simulating rotating flows. Han et al. investigated the vortex ring formation mechanism during nozzle injection. Among other findings, they reported that the simulated thrust considering the presence of the vortex ring was 7.0% higher than when it was ignored.

Multiphase flows in hydraulic machinery were also studied. Both Wang et al. and Cheng et al. investigated the dynamics of the solid-liquid two-phase flows in hydraulic pumps and turbines, respectively. Wang et al. focused on the wear characteristics of the pump blade as a function of solid particle's diameter, solid particle's concentration, and the pump blade material. They reported that, while the common zones of wear concentration were the blade middle zone and trailing zone, the gradual increase in the particle mass concentration led to the correspondingly increasing material loss due to blade wear, while the gray cast iron material (HT200) exhibited the best wear-resistive performance. Cheng et al. studied the effects of the same particle parameters (particle size and concentration), on the tubular turbine's cavitation performance. While the cavitation development areas were commonly located at the blade leading edge's hub-vicinal zone, both particle parameters exhibited an inhibitive effect to the local cavitation development, with the particle concentration increase having the biggest impact. Xin et al. studied the pump turbine under transient conditions by exploring the emergence of flow vortices and associated pressure pulsations in the runner inter-blade channels and the vaneless space, especially under high-speed/low-flow conditions. Using the two-way fluid-solid coupling analysis, they found that structural stresses were built at the runner blade inlet zone, precisely at the connection zones between the blade, the upper crown and lower ring. Maximum deformation was predicted to take place in the middle area of the blade due to the occurred fatigue damages. Chen et al. noted that water hammer-induced vibrations within hydropower plants' long diversion pipelines mostly lead to fluid-structure interaction (FSI) occurrence and studied the same phenomenon in the pipeline embedded in concrete. They used a six-equation model to investigate the interaction between the fluid, the pipe, and the concrete. They reported that, some of the concrete properties, such as the Poisson's ratio and density, negligibly contributed to the FSI response; whereas others, such as the elastic modulus and thickness-to-radius ratio, played important roles.

Finally, (Xu et al.; Xu et al.) studied the modal coherence characteristics for broad band noise determination in flow ducts, as well as the mode identification error characteristics of fan noise. In the first study (Xu et al.), three types of ducted sound source distribution modes were investigated. Study results have shown that the coherence of some modes has little impact on the measurement of incident acoustic waves in the flow duct, while it leads to about 3 dB deviation in the prediction of the reflected modal sound power and has little influence on the spectral shape of reflected acoustic waves. The second study (Xu et al.) investigated the mode identification error characteristics of a fan noise and compared two measuring techniques, the radial rake and axial microphone array. They found that the radial rake method can measure the radial distribution of the modal amplitude, but has large errors in mode identification of low frequencies. Compared to the radial rake method, the axial array method exhibited a better accuracy in mode recognition thus making it fit for real life applications.

In conclusion, the papers in this Research Topic have touched several important aspects of flow structure formation mechanisms and associated phenomena within different hydraulic machinery and systems, where different research methods have been presented and various techniques for system performance improvement have been suggested. In addition, the presented contents stimulate new ideas that can be investigated in future studies. Both the authors and editors hope that this Research Topic sheds light on the current state of knowledge in this field, thus opening the horizon for further research, which would contribute to the improved performance and operational safety of hydraulic machinery and associated economic benefits.

Author contributions

All authors listed have made a substantial, direct, and intellectual contribution to the work and approved it for publication.

Funding

Kan Kan was supported by the National Natural Science Foundation of China (52009033), the Natural Science Foundation of Jiangsu Province (BK20200509), the Postdoctoral Research Foundation of China (2022T150185; 2022M711021). Daqing Zhou was supported by the National Natural Science Foundation of China (51979086).

Conflict of interest

The authors declare that the research was conducted in the absence of any commercial or financial relationships that could be construed as a potential conflict of interest.

Publisher's note

frontiers in Energy Research

ORIGINAL RESEARCH
published: 22 March 2022
doi: 10.3389/fenrg.2022.875638

Numerical and Experimental Study on Mode Identification Error Characteristics of Fan Noise

Kunbo Xu[1]*, *Cunliang Liu*[1], *Fan Tong*[2] and *Weiyang Qiao*[3]

[1]School of Mechanical Engineering, NanJing Institute of Technology, Nanjing, China, [2]Key Laboratory of Aerodynamic Noise Control, China Aerodynamics Research and Development Center, Mianyang, China, [3]School of Power and Energy, Northwestern Polytechnical University, Xi'an, China

The influence of different test methods on the accuracy of mode identification is not clear, and it is necessary to explore the error transfer characteristics in mode decomposition of fan noise. Numerical and experimental research studies are carried out on the advantages and disadvantages of radial rake and axial microphone array and error transmission characteristics in mode decomposition. In the numerical study, the error transmission characteristics of different arrays are investigated by adding random disturbances to the artificial sound field, so as to evaluate the applicability and limitations of the two typical arrays in mode identification based on the error analysis theory. The mode recognition error of the single-stage axial flow fan is investigated experimentally using the designed radial rakes and axial arrays. The results show that although the radial rake can directly measure the radial distribution of the modal amplitude, it has a large error in the mode identification at low frequencies. Compared with the radial rake, axial array will take more priority in practical applications. The accuracy of the axial microphone array in mode recognition strongly depends on the axial spacing of the array measuring sensors. The small deviations in the mode identification when applying the two typical arrays are caused by the different signal-to-noise ratio of the sound pressure signals acquired by the two arrays and their discriminative sensitivities to the duct airflow. Based on the obtained modal identification error characteristics, an effective mode identification method can be proposed to help fan noise reduction design.

Keywords: fan noise, error character, modal decomposition, microphone array, signal-to-noise (S/N) ratio

OPEN ACCESS

Edited by:
Kan Kan,
College of Energy and Electrical Engineering, China

Reviewed by:
Qiang Fu,
Xi'an Aeronautical University, China
Yanhua Wang,
Harbin Engineering University, China
Qiang Gao,
University of Minnesota Twin Cities, United States

***Correspondence:**
Kunbo Xu
xukunbo@njit.edu.cn

Specialty section:
This article was submitted to Process and Energy Systems Engineering, a section of the journal Frontiers in Energy Research

Received: *14 February 2022*
Accepted: *03 March 2022*
Published: *22 March 2022*

Citation:
Xu K, Liu C, Tong F and Qiao W (2022) Numerical and Experimental Study on Mode Identification Error Characteristics of Fan Noise. Front. Energy Res. 10:875638. doi: 10.3389/fenrg.2022.875638

1 INTRODUCTION

The acoustic wave propagates in the form of modal waves in the duct, and the number of cut-on modal waves depends on the duct geometry, sound wave frequency, the airflow velocity, and the acoustic boundary conditions of the duct. Aero-engine noise includes tonal noise (such as rotor self-noise, buzzer, and rotor-static interference noise) and broadband noise (Qiao, 2010). The method of mode decomposition is widely used to investigate the generation mechanism of tonal noise and broadband noise in the flow duct. For radial modal analysis in tonal noise, starting in the 1960s, a number of experimental measurement methods have been developed (Bolleter and Crocker, 1972; Bolleter et al., 1973; Moore, 1979; Holste and Neise, 1997; Enghardt et al., 1999; Lan et al., 2002). These methods have different limitations considering the solvable modal order range, the accuracy of analysis results, and the complexity of method application. Ideally, radial mode decomposition is

achieved by far-field measurements (Farassat et al., 2001), as this is easy to achieve in practical measurements and is not limited by size. However, considering the errors introduced by the analytical model when applied to the real engine geometry and the time-consuming in numerical calculation of the transfer function between the inlet (or outlet) and the far field, nowadays, the radial mode decomposition of the sound field at low frequencies is usually performed by arranging a large number of sensors in the duct (Tapken and Enghardt, 2006), and the radial mode distribution results in the duct are obtained by inversely processing the measured sound pressure data. The German Aerospace Academy (DLR) successfully used this method to measure tonal noise in the ducts of fans (Enghardt et al., 2002), low-pressure compressors (Enghardt et al., 2005), and low-pressure turbines (Enghardt et al., 2001).

There are two types of commonly used microphone arrays: radial rakes and axial arrays. The radial rake can directly measure the distribution of modal waves in the radial direction, and it is easier to realize the modal sound power in terms of numerical solution. Enghardt et al. (2001), Sutliff, (2005), Dahl et al. (2013), and Heidelberg and Hall, (1996) used a rotating rake array to measure the sound field in the flow duct, but when placed upstream, its wake will interfere with the original flow field and pollute the sound field. Joppa, (1987) developed a practical method to measure the sound pressure using an array of equally spaced axial microphones flush-mounted on the duct wall, and the distribution of the fan discrete tonal noise can be obtained by using the axial microphones (Wang et al., 2014; Xu et al., 2018), which can perform circumferential modal analysis of compressor rotational instability (Zhou et al., 2015) and compressor fault diagnosis (Cheng et al., 2019). Zillmann and Tapken, (2009) and Tapken et al. (2009) used a circumferentially rotatable axial array to measure fan noise with very large bypass ratios. Yardley (Yardley, 1974) suggested that the microphones should be installed on the duct wall and pointed out that the mode identification of fan duct noise can be carried out by sound pressure measurement at multiple axial positions, and the duct acoustic performance analysis can be carried out according to the acoustic modal amplitude (Wagih Nashed et al., 2018) and sound field reconstruction (Liu et al., 2018). For both radial rakes and axial arrays, the mode identification is achieved by inverting the coefficient matrix between the sound pressure at the measuring sensors and the radial modal amplitudes. Acoustic mode identification is also closely related to the airflow turbulence in the duct (Kan et al., 2021). Under the measured modal coherence characteristics, the accuracy in acoustic mode identification can be effectively improved. However, the influence of different testing methods on mode identification accuracy is not clear, and the error transmission characteristics of different microphone arrays in mode identification are not analyzed in detail.

Based on the modal decomposition theory, the error transfer characteristics of two typical kinds of arrays in turbomachinery noise measurement is investigated in this study. The influence of different microphone arrays on the accuracy of acoustic mode identification is numerically studied, and the design criteria of the axial microphone array are established. Based on the error characteristics shown in the results, acoustic mode identification of a single-stage axial flow fan is investigated experimentally through the processing of rotating radial rakes and axial arrays. Accordingly, effective measures to reduce the mode identification error are proposed.

2 MEASUREMENT THEORY

2.1 Acoustic Mode Recognition Method

For acoustic propagation in an incompressible circular/annular duct, the acoustic propagation equation in a circular/annular duct can be written as follows:

$$\frac{1}{c^2}\frac{D^2p}{Dt^2}-\frac{\partial^2p}{\partial x^2}-\frac{1}{r}\frac{\partial}{\partial r}\left(r\frac{\partial p}{\partial r}\right)-\frac{1}{r^2}\frac{\partial^2p}{\partial\theta^2}=0 \tag{1}$$

where c is the speed of sound and p is the sound pressure. For the propagation of the sound field in a cylindrical or annular hard-walled duct, a numerical solution can be obtained from the formula (**Eq. 1**), which can be obtained by linear superposition of modal waves for a certain frequency (Qiao, 2010).

$$p(x,r,\varphi,t)=\sum_{m=-\infty}^{\infty}\sum_{n=0}^{\infty}\left(A_{mn}^{+}e^{ik_{mn}^{+}x}+A_{mn}^{-}e^{ik_{mn}^{-}x}\right)\psi_{mn}(r)e^{im\varphi}e^{i\omega t} \tag{2}$$

The axial wavenumber $k_{mn}^{\pm}$ depends on the eigenvalues σ_{mn} of the mode (m,n) and the wavenumber in the free field $k=\omega/c$; the modal wave can cut-on along the duct when axial wavenumber $k_{mn}^{\pm}$ is a real number and is defined as follows:

$$k_{mn}^{\pm}=k\frac{-M_a\pm\alpha_{mn}}{1-M_a^2} \tag{3}$$

$$\alpha_{mn}=\sqrt{1-\left(\frac{\sqrt{1-M_a^2}\sigma_{mn}}{kR}\right)^2} \tag{4}$$

The modal characteristic functions satisfy the following:

$$\frac{1}{\pi R^2}\int_0^{2\pi}e^{i(m-\mu)\varphi}\int_{\eta R}^{R}\psi_{mn}(r)\psi_{\mu\nu}(r)rdrd\varphi=\delta_{m\mu}\delta_{n\nu} \tag{5}$$

In which μ,ν represents mode (μ,ν), and assuming that there are K measuring points in the duct for synchronous acquisition of sound pressure data, the sound pressure at the measuring points can be written as follows:

$$\mathrm{p}=\Phi\mathrm{a} \tag{6}$$

In the formula, $\mathrm{p}\in\mathbb{C}^K$ represents the complex sound pressure vector at the measured frequency ω, $a\in\mathbb{C}^L$ represents the complex modal amplitude $A_{mn}^{\pm}$, in which m represents the modal circumferential order and n represents modal radial order, the size of L depends on the total number of cut-on modes in the flow duct, and the values in the matrix $\Phi\in\mathbb{C}^{K\times L}$ are determined by the measuring point position of the microphone array and the modal order. The cross-spectral matrix of the sound pressure signals at the two measuring points

can be defined as $S_{pp} \triangleq E(pp^H)$, where E represents the expectation. Based on the formula (**Eq. 6**), the cross-spectrum of the two sound pressure measuring points can be written as follows:

$$S_{pp} = \Phi S_{aa} \Phi^H \tag{7}$$

Therefore, the cross-spectrum of the modal amplitudes can be written as follows:

$$S_{aa} = \Phi^{\dagger} S_{pp} \left(\Phi^{\dagger}\right)^H \tag{8}$$

where † represents the pseudo-inverse of the matrix. In actual experimental measurements, the number of measurement points K of the microphone array is usually larger than the size L of the modal amplitude vector, and the coefficient matrix may be singular. When solving the matrix with the singular coefficient matrix and the overdetermined equation, singular value decomposition (SVD) (Nelson and Yoon, 2000; Kim and Nelson, 2004) was used in this study to solve the following:

$$Gp = \hat{a} \Leftrightarrow V \cdot \left[diag \left(\frac{1}{w_j} \right) \right] \cdot U^T p = \hat{a} \tag{9}$$

In the formula, U and V are both transformation matrices and orthogonal matrices, which satisfy $U \cdot U^T = 1$ and $V \cdot V^T = 1$, but W is a diagonal matrix, and the elements are all positive values and values tending to zero (i.e., singular values). Appropriately discarding smaller singular values can improve the accuracy of the algorithm. Its optimal estimate can be obtained by the following:

$$p = \left[G^H G\right]^{-1} G^H \hat{a} = G^{+} \hat{a} \tag{10}$$

The solvability and stability of **Eq. 10** and the error transfer characteristics of the system are closely related to the condition number of the square matrix. The condition number depends on many factors: the number of cut-on modes, frequency, hub-to-shroud ratio, airflow parameters, and the shape of the design array. Therefore, it becomes necessary to evaluate the quality of mode decomposition by condition number analysis.

2.2 Error Analysis Theory

In order to explore the limitations of different array schemes in mode identification measurement, the numerical method is used to study the error characteristics of radial rakes and axial arrays in mode identification. By analyzing the coefficient matrix condition number, the influence of the axial spacing in the array design on the mode identification is studied and the error transfer characteristics of different arrays during mode decomposition are investigated by superimposing random disturbances in the artificial sound field, which thus provides theoretical guidance for mode identification of duct noise.

The accuracy of the calculation results in the mode identification is related to the condition number of the matrix. It determines the upper bound of the error transfer coefficient of the system of **Eq. 10**:

$$\frac{\left\|\tilde{A}_{mn}\right\|}{\left\|A_{mn}\right\|} \leq \kappa(w) \frac{\left\|\tilde{A}_m\right\|}{\left\|A_m\right\|} \tag{11}$$

The tilde character ~ represents the perturbation of the circumferential modal amplitude A_m and radial modal amplitude A_{mn}, respectively, and the circumferential modal amplitude can be calculated by reference (Moore, 1979), in which $A_m = W_m \cdot A_{mn}$ and $A_{mn} = [W_m^H W_m]^{-1} W_m^H A_m = W_m^{+} A_m$. $\|*\|$ represents the Euclidean norm. As shown in the formula (**Eq. 11**), if the condition number is $\kappa(w) = 1$, that is to say, when a small disturbance in the input signal is transmitted to the output signal through the system, the magnitude of the disturbance is basically unchanged. When the input amplitude error is 10%, the maximum error of the output signal amplitude after passing through the system can reach 10%. But when the condition number is greater than 1, the small disturbance in the input signal will be amplified after passing through the system, and its amplification rate depends on the condition number of the coefficient matrix in the system, as shown in the formula (**Eq. 11**). Therefore, the error characteristics of different arrays in mode identification can be qualitatively analyzed by calculating the condition numbers of the coefficient matrices constructed by different microphone arrays, and furthermore, their distribution law can be grasped.

The matrix condition number $\kappa(w)$ can only reflect the upper limit of the overall error of the modal recognition system but cannot reflect the error characteristics of a single internal mode. In order to further study the reliability of mode identification, the formula (**Eq. 11**) is used to derive the relative accuracy expression in mode identification, which is defined as follows:

$$\left\| \left| \tilde{A}_{mn} \right| \right\|_{rel} := \frac{\left\| \left| \tilde{A}_{mn} \right| \right\|}{\left\| |A_{mn}| \right\|} \frac{\left\| |A_m| \right\|}{\left\| \left| \tilde{A}_m \right| \right\|} \tag{12}$$

It is easy to know that the larger the relative accuracy value, the larger the relative error in mode identification.

2.3 Error Analysis Process

Numerical simulation is used to investigate the influence of the measurement error on the final output of the system in the experimental test. Generally speaking, measurement error is divided into systematic error and random error, but only the influence of random measurement error is considered here, and the random error added in the simulation satisfies the Gaussian distribution.

The numerical simulation process is mainly divided into four steps: 1) based on the given radial modal amplitude A_{mn}, the circumferential modal amplitude at different measuring points (x_j, r_l) can be constructed, where j and l are integers and the ranges are 1~ N_x and 1~ N_r, respectively; 2) for the ni^{th} measurement, the perturbation superimposed to circumferential modal amplitude at position (x_j, r_l) is defined as follows:

$$\tilde{A}_m\left(x_j, r_l, [ni]\right) = \sigma_{A_m} a_{jl}[ni] e^{ib_{jl}[ni]2\pi} \tag{13}$$

where σ_{A_m} is the standard deviation of the circumferential modal amplitude, and $a_{jk}[i]$ and $b_{jk}[i]$ are real numbers and their time dependence obeys Gaussian distribution; 3) for each

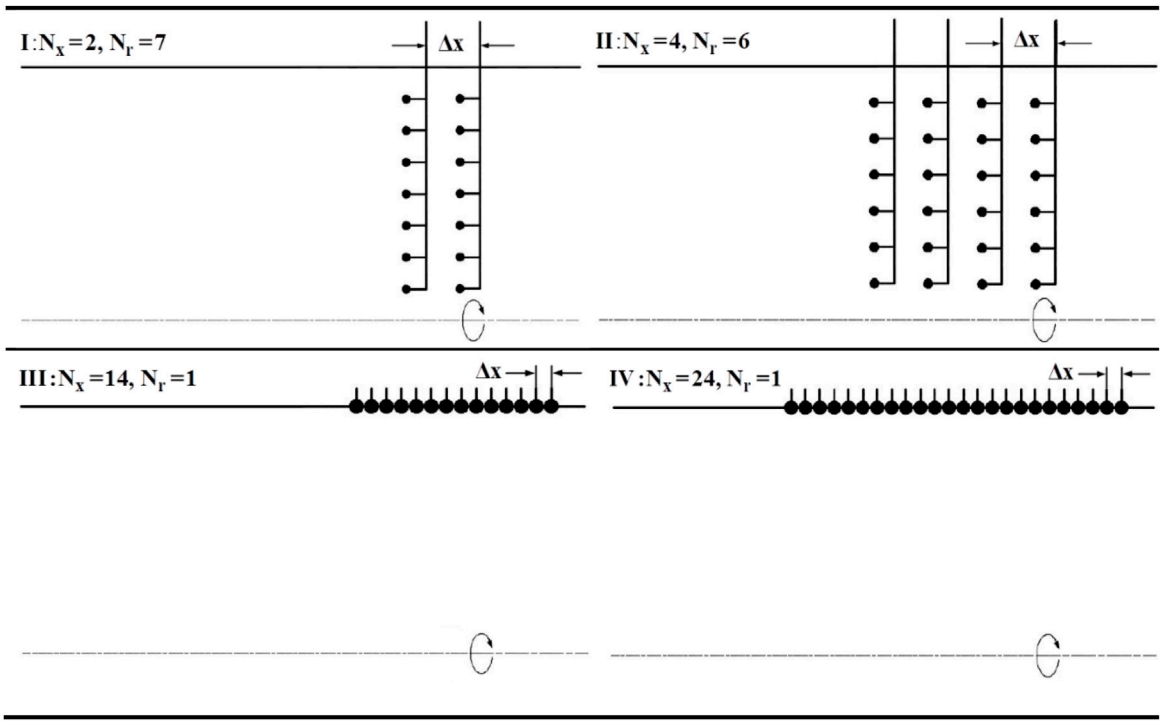

FIGURE 1 | Sensor array schemes A-I to A-VI: N_xN_r = 14 in the left column; N_xN_r = 24 in the right column.

measurement, the radial modal amplitude $A_{mn}[i]$ can be obtained by solving the pseudo-inverse matrix W_m^+; 4) after N_{avg} times averaging, the accuracy of the calculation can be determined by solving the formula (**Eq. 13**) or calculating the standard deviation of each radial mode, which is defined as follows:

$$\sigma_{A_{mn}} = \sqrt{\frac{1}{N_{avg}} \sum_{i=1}^{N_{avg}} \left(A_{mn}[i] - \bar{A}_{mn}\right)^2} \tag{14}$$

The modal amplitude A_{mn}^+ propagating downstream is set as 85 dB, and A_{mn}^- in the upstream direction is set as 75 dB. The average number of times in the calculation is set to 50.

2.4 Array Design Scheme

Radial rakes and axial microphone arrays have been mainly developed for acoustic mode identification of engine noise. Therefore, four array design schemes shown in **Figure 1** are investigated in this section, the array is represented by prefix A, and different schemes are distinguished by Roman numbers. Generally, the experimental measurement section is arranged in the fan inlet section, so the hub ratio of the four arrays is set as $\eta = 0$. The total number of microphones in the A-I and A-III schemes is $N_x \cdot N_r = 14$ and the total number of microphones in the A-II and A-IV schemes is $N_x \cdot N_r = 24$. The details are as follows:

I: Array scheme A-I consists of radial rakes at $N_x = 2$ axial measurement positions. Each radial rake consists of N_r microphones arranged at equal radial spacing, and the radial spacing Δr and radial position r_j are defined as follows:

$$r_j = j\Delta r\ ,\ \ j = (1 \sim N_r),\ \ \Delta r = \frac{R}{N_r + 1} \tag{15}$$

II: The array scheme A-II consists of four radial rakes at N_x = 4 equally spaced axial measurement positions. Each radial rake contains N_r equally distributed sensors, and the radial position and space Δr definitions are the same as those of A-I according to the formula (**Eq. 15**).

III: The array scheme A-III consists of an axial array mounted on the duct wall. There are N_x measuring points arranged at equal intervals in the axial direction. The axial spacing is Δx.

IV: The array scheme A-IV is similar to A-III, in which the microphones are arranged on the duct wall, but the total number of microphones is different.

A-I and A-III consist of the same number of microphones $N_x \cdot N_r = 14$, while A-II and A-IV both have $N_x \cdot N_r = 24$ microphones. A-I and A-II are radial rakes, while A-III and A-IV are axial microphone arrays arranged on the duct wall. Therefore, the only common parameter—Δx—is left. The effect of the array spacing on the matrix condition number and the optimal arrangement will be investigated below.

Considering the number of measuring points N_ϕ in the circumferential direction, it is assumed in the simulation that the arrays are all installed on the rotating measuring section, which can accomplish sound pressure collection with enough circumferential measuring points. In all simulations, it is ensured that there are enough measuring points in the circumferential direction, so that the identification of any circumferential mode can meet the sampling requirements. Based on mathematical principles, the modal

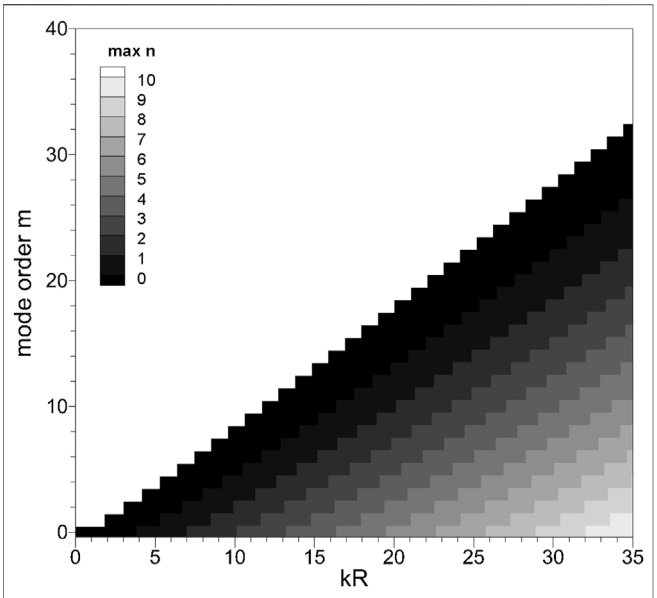

FIGURE 2 | Modal cut-on function up to kR = 35.

amplitudes collected by different radial positions in the radial rakes are different, and they will be distributed in the form of Bessel functions along the radial direction, so the modal decomposition can be achieved by using this fixed phase difference appearing between different measurement sensors. In experimental measurements, the measurement of the duct sound field at the fan inlet section, the wake of one or more sensors in the radial microphone array can interfere with noise sources such as the rotor. This changes the original sound field structure and excites additional noise sources. Especially in smaller diameter test benches, the radial rakes can cause airflow blockage, which will essentially change the working point of the turbomachinery. For axial arrays such as A-III and A-IV, both of these drawbacks can be circumvented.

The frequency range for the numerical study is $0 \le kR \le 35$, where $k = 2\pi f/c$ represents the wavenumber of the sound wave in the free field. The modal cut-on function calculated using **Eq. 3** is shown in **Figure 2**. It can be seen that up to 11 radial modes can be cut on at $kR = 35$, and these modes propagate in the downstream and upstream directions, respectively. It can be seen from the figure that the (0,1) mode is cut on at $kR \approx 3.8$, and then at kR, approximately equal to 6.9, 10.1, and 13.3, more radial modes in the duct begin to cut on. The cut-off frequency difference between different radial modes is approximately equal to kR = 3.2. This rule helps to observe the error characteristics of different array design schemes in mode identification and their sensitivity to radial modal cut-off characteristics in the spectrogram.

3 MODE IDENTIFICATION ERROR SIMULATION

3.1 Mode Identification Relative Accuracy

Figure 3 shows the condition number results of the four array schemes at m = 0 circumferential mode; m = 0 mode is selected for analysis because more radial modes can be cut on at m = 0. The results show that the condition number is very sensitive to the axial spacing of the array as well as the frequency. Comparing the relative accuracy results of the four arrays, it can be found that the corresponding frequencies appearing with poor relative accuracy are roughly the same, while the A-I array is better than the other three arrays initially. It can be found that the poor relative accuracy is caused by insufficient sampling of the phase information of the acoustic wave in the axial direction by the array schemes. Unlike the orthogonality of the radial modal eigenfunctions, the axial wavenumbers are not orthogonal, so frequencies with poor relative accuracy in mode identification appear at the following:

$$\begin{cases} (\alpha_{mn} - \alpha_{m\nu})k\Delta x = s \cdot 2\pi \ (a) \\ (\alpha_{mn} + \alpha_{m\nu})k\Delta x = s \cdot 2\pi \ (b) \end{cases} \tag{16}$$

where s is an integer. In principle, as the frequency increases, the number of combinations (kR and $\Delta x/R$) corresponding to the formula (**Eq. 16**) will also increase. This is because the number of cut-on radial modal waves continues to increase and the modal cut-off factor approaches 1 with increasing frequency. However, the correlation with respect to the formula (**Eq. 16**) of the four arrays is different; it depends on the ratio of the radial measurement points to the number of radial modes N_r/N_{rad}. When the frequency is close to the mode cut-off frequency, the axial wavenumber $k_{mn}^{\pm}$ is approximately equal to 0, at which the wavelength of the mode approaches infinity. For this condition, it is theoretically necessary to arrange microphones far apart in the axial direction to perform modal measurements. For the A-I and A-II schemes, the number of axial measuring points is small, which can cause the condition numbers of A-I and A-II to surge at $kR \approx f_{c,mn}$ as shown in **Figure 3**. After a given threshold value $\max(||\tilde{A}_{mn}||_{rel})$, the optimal axial spacing Δx_{opt} of each array and the corresponding upper limit of the solvable frequency $\max(kR)$ can be calculated. According to the numerical study results, the axial array is more suitable for mode identification of airflow noise in ducts because this type of array can maintain a small coefficient matrix condition number and excellent relative accuracy over a wide frequency range. This characteristic is more pronounced in axial arrays with relatively small axial spacing. For all axial arrays, there is an upper limit of the solvable frequency $\max(kR)$ after a given relative accuracy threshold value, and it can be seen from **Figure 3** that for all microphone arrays, the minimum solution frequency satisfies $\min(kR) \approx 0$, and $||\tilde{A}_{mn}||_{rel}$ is affected by the $n \neq \nu$ modal combination. The upper frequency limit represented by the black long dashed line in **Figure 3** satisfies the law $\Delta x \cdot k = \pi$, which corresponds to the situation in (11(b)) $s = 1$ and $n = \nu = 0$ ($\alpha_{0,0} \equiv 1$ at this time). The lower limit of the axial spacing will decrease with the increase in $N_x N_r/N_{rad}$. When the relative accuracy threshold value is set to $\max(||\tilde{A}_{mn}||_{rel}) = 10$, the optimal spacing of each array and the corresponding upper limit of frequency can be obtained, and the exact values are shown in **Table 1**. It can be seen that the optimal axial spacing continues to decrease with more axial measuring points being applied in the simulation. It should be noted that when the number of axial measuring points is

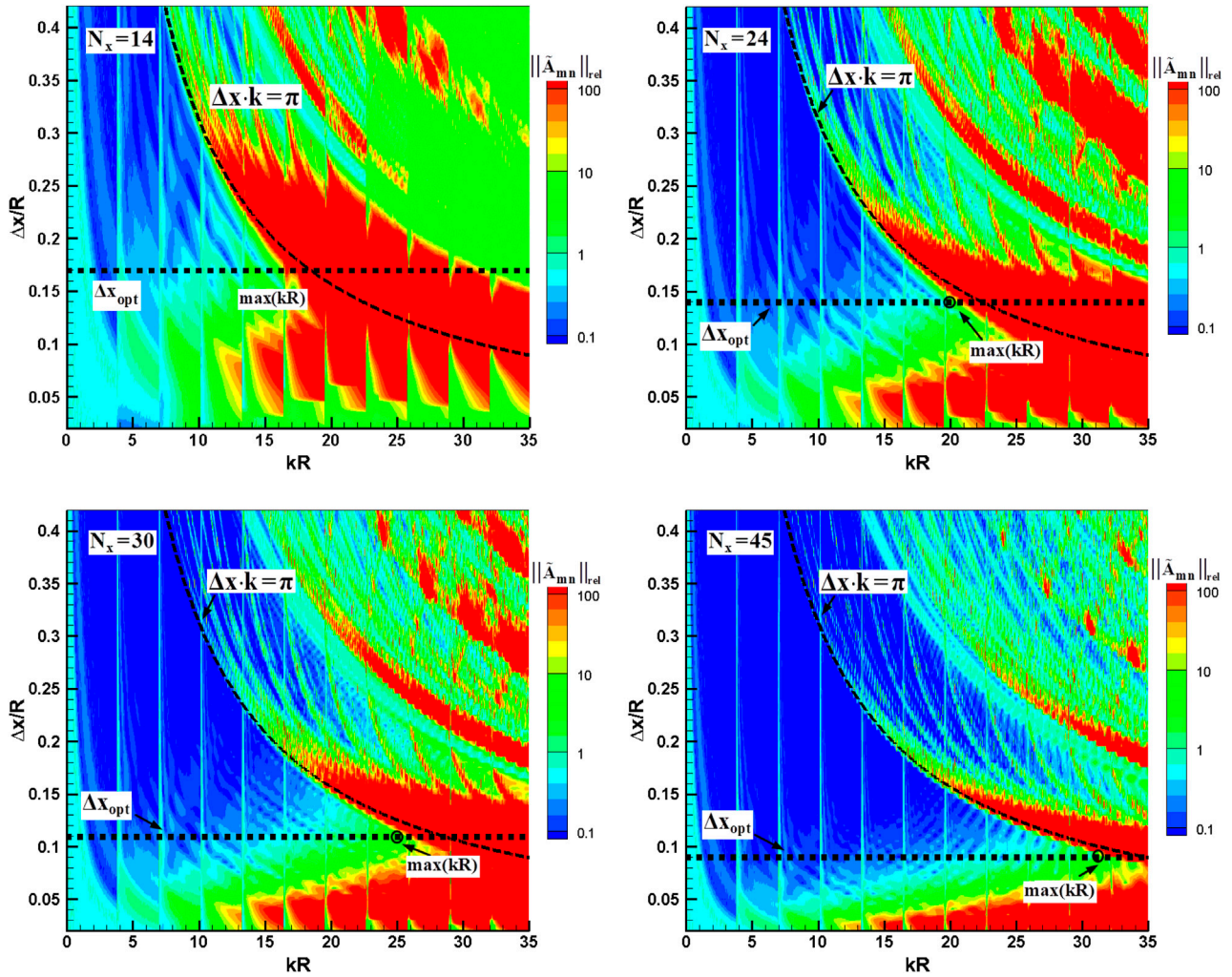

FIGURE 3 | Relative accuracy of the four axial arrays.

TABLE 1 | Optimal axial spacing and upper limit of solvable frequency.

Axial measurement points	14	24	30	45
$\Delta x_{opt}/R$	0.17	0.14	0.11	0.09
max (kR)	16.4	20.0	25.1	31.2

determined, smaller axial spacing between the measuring sensors is not better, especially when the number of axial measuring points is small, such as $N_x = 14$ as shown in **Figure 3**. Moreover, the upper limit of frequency max (kR) that can be solved precisely cannot be obtained simply by $\Delta x \leq \lambda/2$, where $\lambda = c/f$, that is to say, the frequency range of mode identification cannot be determined simply using the Nyquist sampling theorem. In experimental measurements, the frequency range that can be accurately solved in mode identification is much smaller than the range calculated using the Nyquist sampling theorem after a given upper error limit.

Figures 4, **5** present the condition number and relative accuracy results for the four axial arrays at the optimum spacing, respectively. As the frequency increases, the condition number of the axial array presents a monotonically and steadily increasing trend, and the greater the number of axial measuring points in the array, the slower the increasing trend. Different from the spectral characteristics of the condition number, the relative accuracy results show an upward trend of oscillation as the frequency increases. When the threshold values of the condition number and the relative accuracy are given, it can be found by comparing **Figures 4**, **5** that the upper limit of frequency max (kR) determined by the condition number is basically consistent with that determined by the relative accuracy.

3.2 Sensitivity of Relative Accuracy of Mode Identification to Modal Order

The previous section only studied the relationship between the axial spacing Δx and the upper limit of the solution frequency max (kR) during the $m = 0$ mode identification process. When the optimum axial spacing Δx_{opt} is determined, it is necessary to

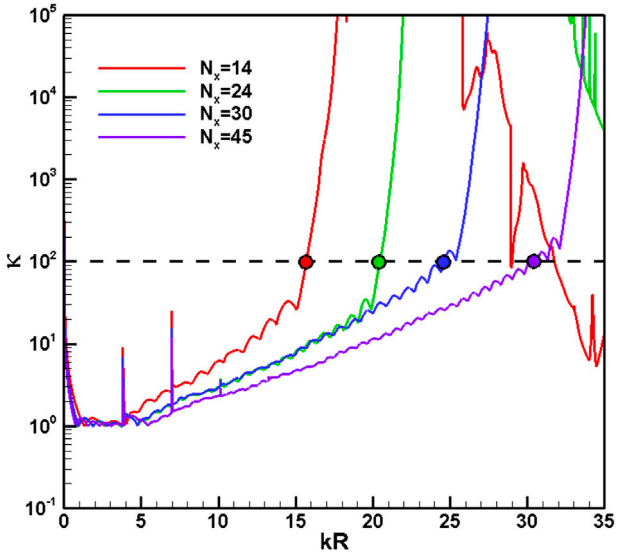

FIGURE 4 | Condition numbers at optimal spacing for the four axial arrays.

investigate the relative accuracy during the mode identification process of each circumferential mode. **Figure 6** shows the solution accuracy results of circumferential modes of different orders after setting the axial spacing of the four arrays to Δx_{opt}, and it is necessary to relate the results of the modal cut-off function shown in **Figure 2** in the comparative analysis. It can be seen that with the increase in the circumferential mode order m, the change trend of the relative accuracy of each circumferential mode is not the same due to the change of the modal cut-off frequency $f_{c,mn}$ and the modal cut-off factor α_{mn}. At high frequencies, the identification operation of the low-order circumferential modes is more likely to become unstable because the eigenvalues σ_{mn} of the low-order circumferential modes are smaller than those of high-order circumferential modes, so that the cut-off factors of the low-order circumferential modes tend to approach 1 more easily, resulting in different modes becoming indistinguishable due to the similar axial wave numbers. This situation will be improved with the increase in axial measuring points. It can also be found in the figure that for any axial array, $m = 0$ mode is always the first to appear as the solution instability phenomenon, which indicates that $m = 0$ mode is the dominant mode restricting the accuracy of the mode identification method and the upper limit of the solvable frequency, which is consistent with the research conclusion in the previous chapter.

4 ARRAY DESIGN METHOD IN MODE DECOMPOSITION

4.1 Standard Deviation in Mode Decomposition

In the turbomachinery noise mode identification experiment, the amplitude of each radial mode is what everyone cares about most. The investigations in the previous chapter can only predict the overall accuracy of each radial mode. In this section, modal standard deviation is used to investigate the accuracy of different microphone arrays in mode identification.

Figure 7 shows the standard deviation σ_{Amn}/σ_{Am} results when $m = 0$ mode is decomposed into each radial mode; the axial spacing of the four arrays is set to $\Delta x = \Delta x_{opt}$. When the flow is uniform in the duct, the modal σ_{Amn} values are the same for mode propagating upstream and downstream. The simulation results of the artificial sound fields show that when the coefficient matrix condition number is within the range $\kappa(w) < 500$ (or relative accuracy $|| \tilde{A}_{mn}||_{rel} < 100$), σ_{Amn}/σ_{Am} is independent of the initial modal amplitude A^0_{mn} in the simulated sound source. Therefore, it can also prove that the law in **Figure 6** can be applied to any modal amplitude $A_0(x_j, r_k)$. The relative standard deviations of the radial modes are very similar, especially for the modes with radial mode order $n = 0$ and $\nu = 1$, and their relative standard deviations are in good agreement. It should be noted that the difference between the relative standard deviations of each radial mode ($n \neq \nu$) is not affected by the new cut-on mode, which makes it possible to measure the individual radial modes more accurately when relative accuracy is poor.

4.2 Guidelines for Microphone Array Design

The previous section presents the upper frequency limit of the four axial arrays for mode identification and the optimal spacing in array scheme design. In general, as the number of measuring points increases, the frequency range that can be accurately solved in mode identification also increases. However, the array design scheme will seriously affect the solution accuracy in the mode identification, so it is necessary to investigate the design criteria of the axial array.

In the process of array design, two main problems need to be solved: (a) when the number of measuring sensors is given, how to quickly determine the distance between the measuring sensors,

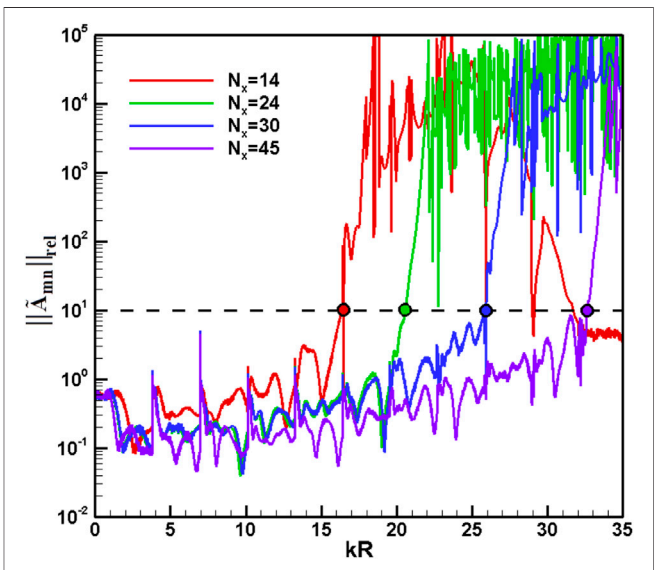

FIGURE 5 | Relative accuracy of the four axial arrays at optimal spacing.

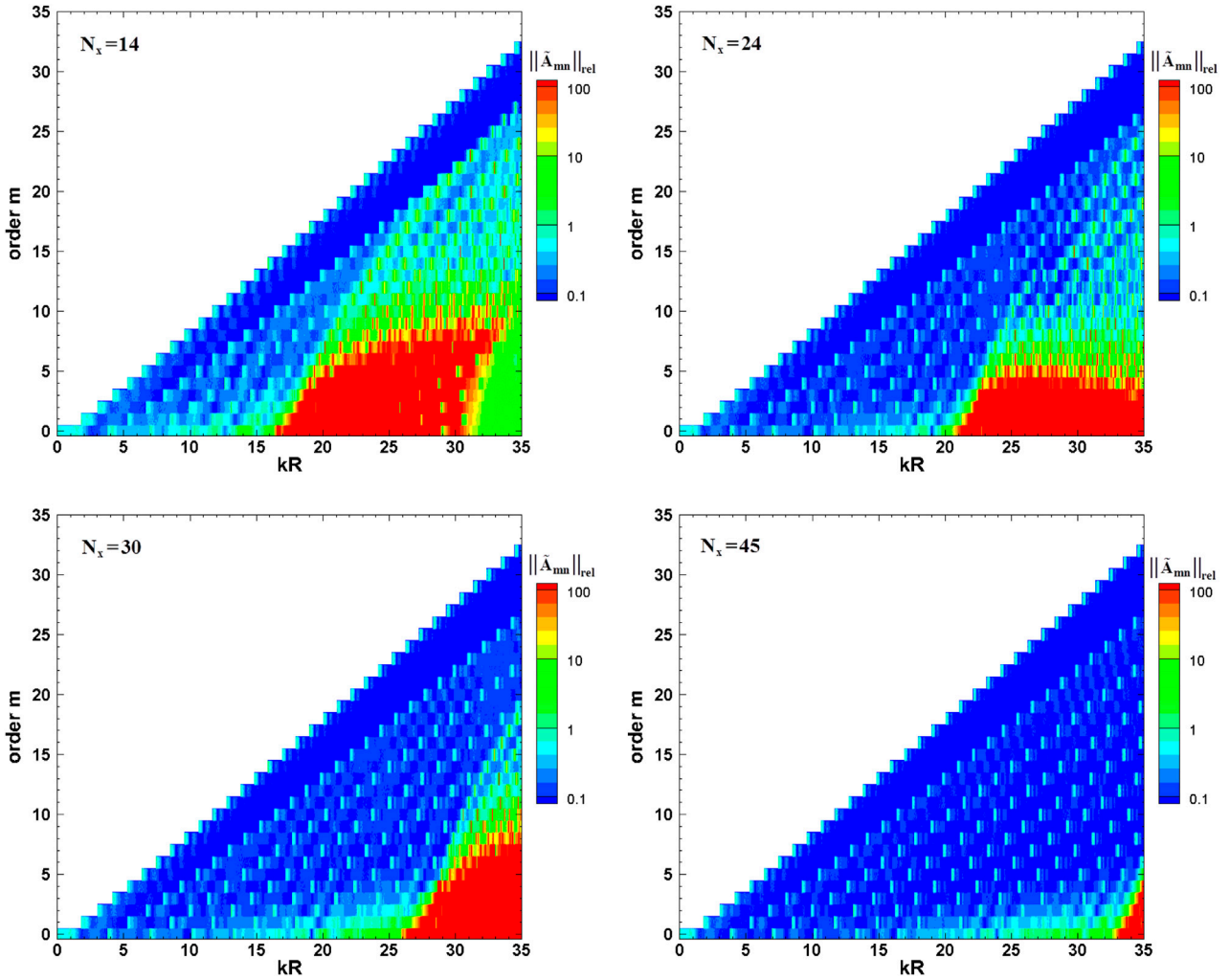

FIGURE 6 | Relative accuracy of the four axial arrays under optimum spacing in different circumferential mode decompositions.

so that the mode identification measurement in a wider frequency range can be realized within a certain error limit; (b) how to quickly determine the number of measuring sensors required by the array design when the frequency of interest is given. For the first problem, it can be achieved by calculating the optimal axial spacing Δx_{opt} and the upper frequency limit $\max(kR)$ under different numbers $N_x N_r$ of measuring sensors in mode identification. **Figure 8** presents the optimal spacing results of the axial arrays at different frequencies, where the frequency range increases from $kR = 8$ to $kR = 56$. In order to describe its distribution law more clearly, two auxiliary curves are given in **Figure 8**, $\Delta x = \pi/k$ and $\Delta x = 0.8\pi/k$, respectively. It can be seen that the optimal spacing satisfies the following:

$$\frac{0.8\pi}{kR} \leq \frac{\Delta x_{opt}}{R} \leq \frac{\pi}{kR} \tag{17}$$

For the second problem, this section investigates the dependence of the frequency upper limit $\max(kR)$ in mode identification on the number $N_x N_r$ of measuring sensors by giving the upper limit of the relative standard deviation $\sigma_{A_{0,0}}/\sigma_{A_m}$. The calculation of relative standard deviations allow the relative accuracy of individual modes to be determined. From the research in the previous section, it can be seen that the m = 0 mode contains most cut-on radial modes. Therefore, this mode is more sensitive to the measurement device, that is to say, the $\sigma_{A_{0,0}}/\sigma_{A_m}$ value can be used to identify the accuracy of the entire mode measurement. For a given σ_{A_m}, the signal-to-noise ratio of the mode can be easily obtained. This section examines two relative standard deviation upper limits: $\sigma_{A_{0,0}}/\sigma_{A_m} = 1$ and $\sigma_{A_{0,0}}/\sigma_{A_m} = 2$. The upper limit selected in this section is actually relatively conservative, because when the relative standard deviation is relatively high, the signal-to-noise ratio in mode identification can be improved using the adaptive resampling method (re-sampling technique). **Figure 9** shows the required measuring sensors for mode identification as the frequency increases under the two upper limit conditions of the relative standard deviation mentioned above, and the cut-on

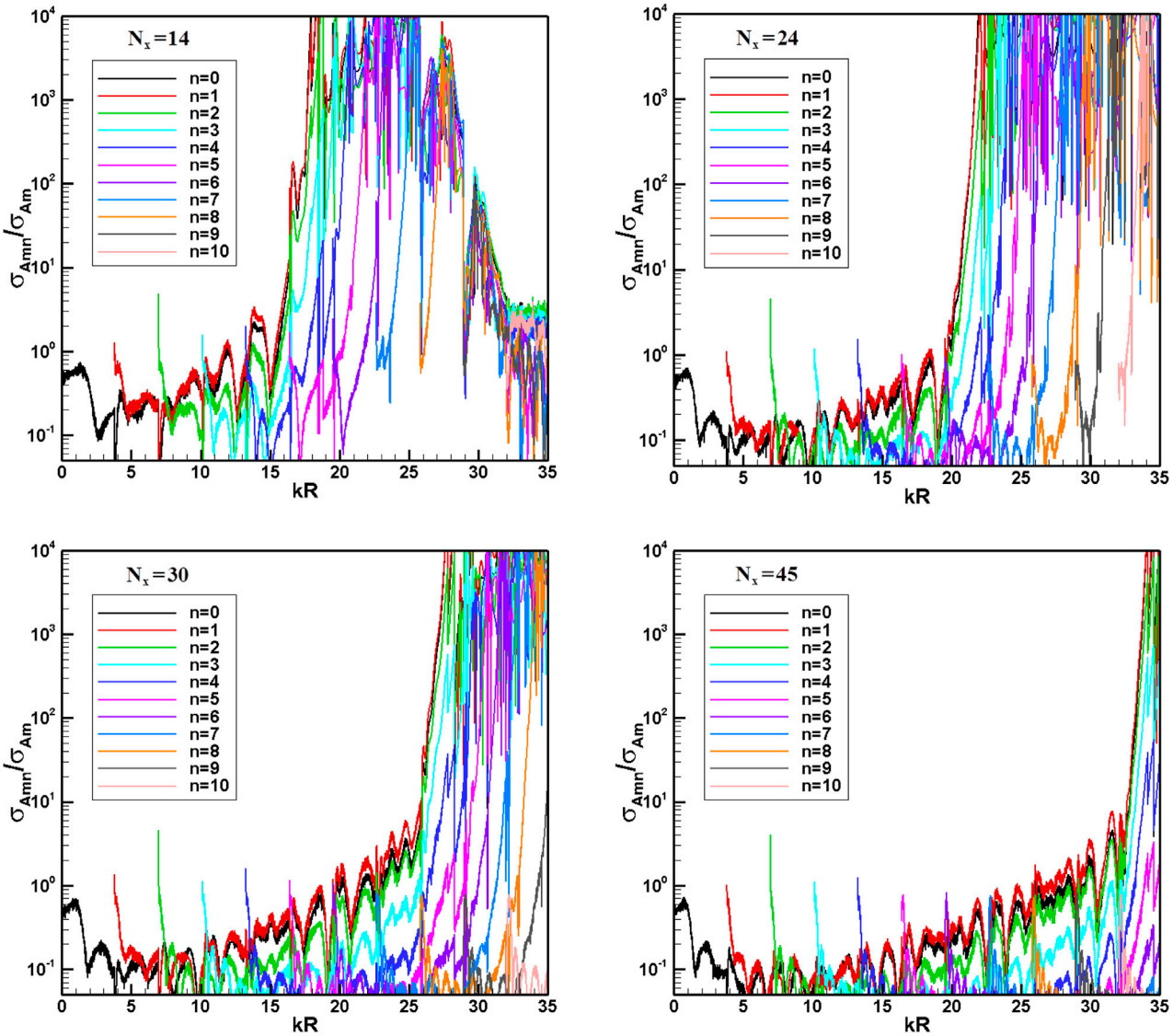

FIGURE 7 | Relative standard deviations $\sigma_{A_{mn}}/\sigma_{A_m}$ in the m = 0 mode decomposition of the four axial arrays with optimal spacing.

frequency of each radial order is marked with a dotted line. It can be clearly seen from the figure that with the increasing number of radial modes, the ratio N_xN_r/N_{rad} of the number of measuring sensors to that of radial modes for mode identification is not fixed, that is to say, the growth rates of the two numbers are different. For example, at $n = 2$, the ratio needs to satisfy $N_xN_r/N_{rad} \geq 1.67$; at $n = 9$, the ratio needs to satisfy $N_xN_r/N_{rad} \geq 4.5$. When given an upper relative standard deviation, it is difficult to determine a parameter that satisfies all modes unless it is set to a large value.

5 EXPERIMENTAL ANALYSIS OF MODE IDENTIFICATION ERROR

Regarding the influence of different microphone arrays on the mode identification accuracy, after numerical investigation of error variation, this section will conduct an experimental measurement based on the axial fan test bench. The main purpose of the research is to conduct an experimental study on the differences in mode identification between axial arrays (Axial Arrays, AA) and radial rakes (Radial Rakes, RR) installed, respectively, in the fan inlet section.

5.1 Acoustic Test Bench

The experimental test scheme of the axial microphone array is shown in **Figure 10**. The acoustic measurement device is installed in the inlet section of the fan, 1.50 m away from the leading edge of the rotor blade tip. The entire acoustic measurement section and the fan inlet are placed in a semi-anechoic chamber. Four rows of microphones were installed on the acoustic measurement section with an axial spacing of 10 cm. Each row consists of 8 flush-mounted microphones with equal angles.

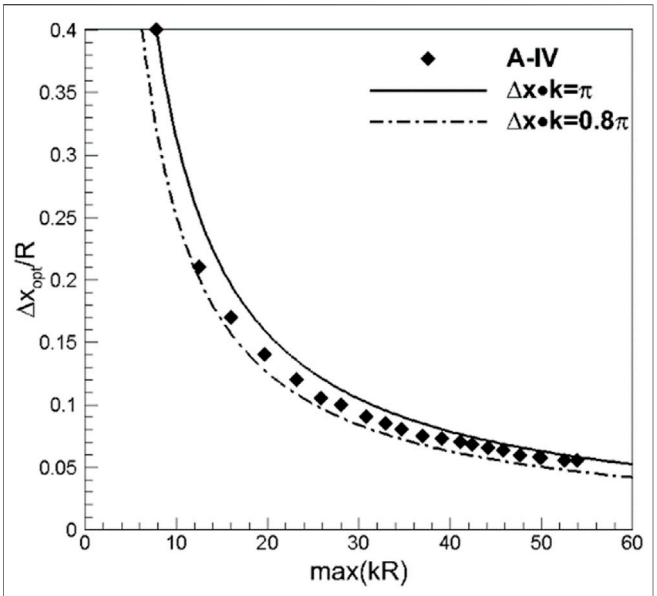

FIGURE 8 | Law of optimal axial spacing applied in array scheme design.

Radial rakes are designed and fabricated in this study in order to compare the influence of different microphone arrays on fan noise measurement. The radial rakes are also installed in the acoustic measurement section at the same location as the axial microphone array, and multi-angle measurement is achieved by installing the radial rakes on the casing that can rotate around the axis. A total of 60 circumferential positions are measured in the experimental test. As shown in **Figure 11**, two radial rakes are installed at the same axial position and separated by 180° in the circumferential direction. **Figure 12** shows the actual photo and three-dimensional design of the radial rakes. Each rake has a total of $N_r = 4$ measuring points in the radial direction.

Applying radial rakes to the mode decomposition test of fan noise needs to pay attention to two issues: (1) since the measuring device penetrates deep into the cross section in the duct, it will inevitably affect the original flow field, and its wake may interfere with the rotor and then generate a new interference mode, which may eventually affect the original fan noise field and (2) the microphone is located inside the flow field, and the measured sound pressure will be affected by the airflow velocity and pressure pulsation, which thereby can reduce the signal-to-noise ratio in acoustic test.

This study adopts two ways to deal with the first issue: on one hand, the outer wall of the pipeline wrapping the signal line is designed to be streamlined, so as to ensure that the radial rake is not a blunt trailing edge structure; on the other hand, the axial position of the radial rake is nearly 2 m away from the rotor leading edge. According to the research of Chong (Chong et al., 2015), the turbulent intensity will decay approximately with a regularity $(x_l - x_0)^{-5}$, where x_l is the observation point and x_0 is the initial position, Therefore, the turbulence intensity 2 m apart will decay to 1/32 of the turbulent intensity at the initial position, which can be approximately ignored. For the second issue, a windshield is installed for each microphone in the experimental measurement to reduce the influence of airflow on the sound pressure test.

5.2 Signal-to-Noise Ratio

In order to analyze the accuracy of sound pressure acquisition data, the concept of signal-to-noise ratio (SNR) is used here, which can be defined as follows (Joseph et al., 2003; Tapken et al., 2008):

$$SNR_p = 20 \times \log\left(P_{RMS}/s_p\right) \tag{18}$$

where P_{RMS} is the root mean square (RMS) result of the complex sound pressure amplitudes (frequency domain results after fast Fourier transform) of all measuring points at a single frequency, but s_p is the random pulsation amplitude of the complex sound pressure amplitudes p. The measured sound pressure time series signal is processed by sub-window truncation, and the truncated data are processed by FFT, respectively, where $p[k]$ represents the complex pressure value calculated from the k'th window truncated data. The component of the sound pressure at the measurement point at this frequency is represented by the mean of multiple Fourier transforms, namely,

$$\bar{p} = \frac{1}{N_{total}} \sum_{k=1}^{N_{total}} p[k] \tag{19}$$

For a single sound pressure measurement point, starting from time i, a single subset consists of N_{win} data, where the mean of $N_{win} \ll N_{total}$ is defined as follows:

$$p_{N_{win}}[i] = \frac{1}{N_{win}} \sum_{j=1}^{N_{win}} p[i-1+j] \tag{20}$$

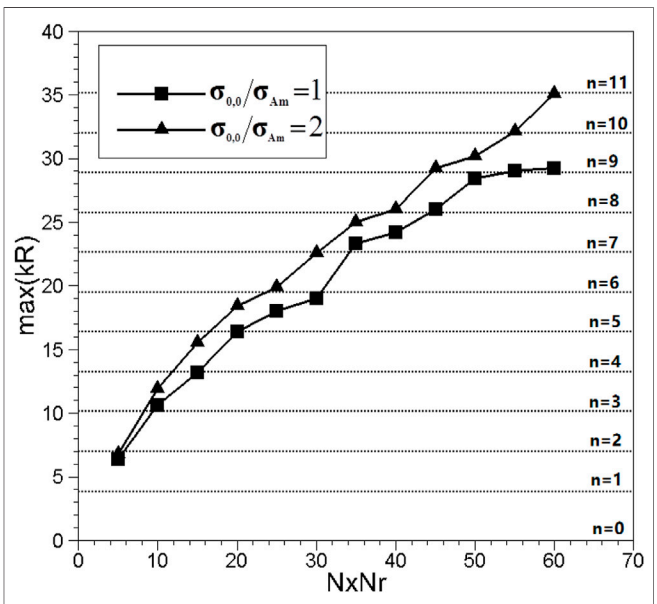

FIGURE 9 | Required sensors under a given threshold value of relative standard deviation.

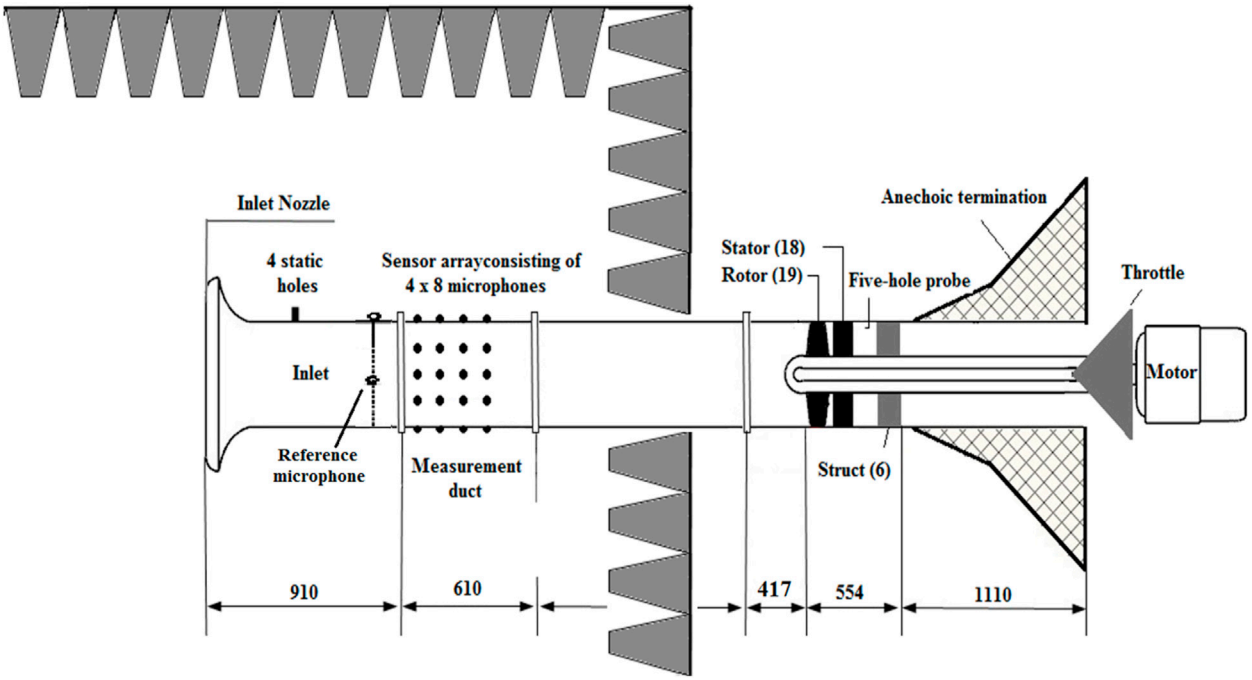

FIGURE 10 | Schematic diagram of the axial microphone array in experimental investigation.

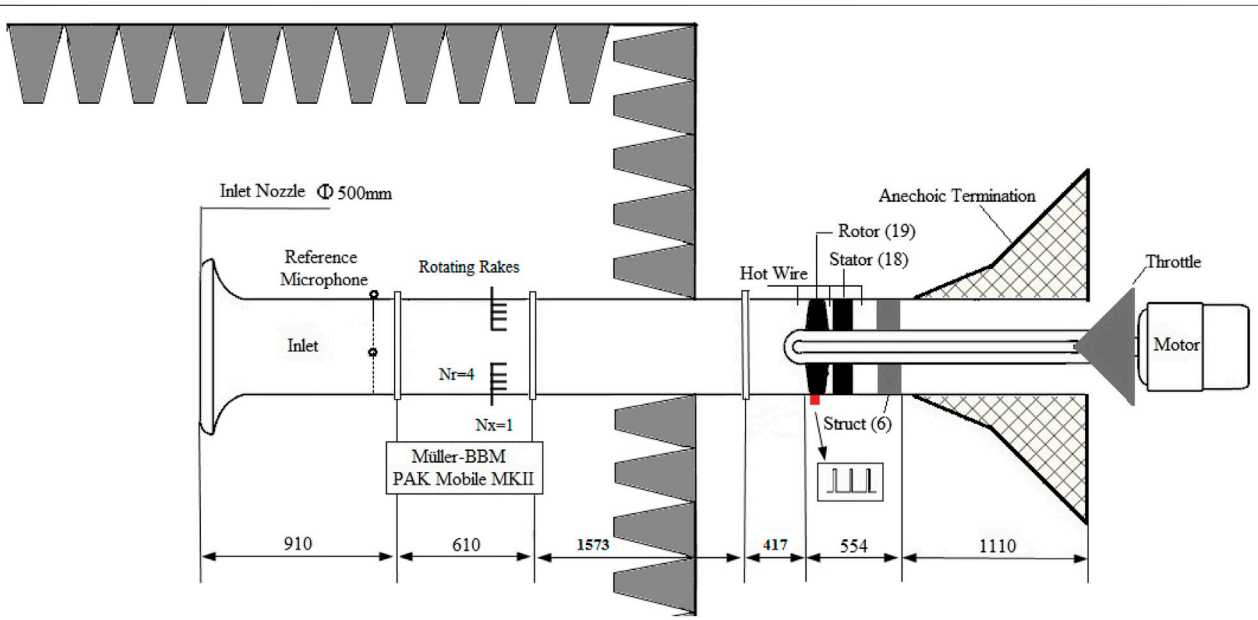

FIGURE 11 | Schematic diagram of rotating radial rakes in experimental investigation.

When repeated $p_{N_{win}}[i]$ such that $i = 1, 2, \ldots, N_{means}$, the s_p of sound pressure is defined as follows:

$$s_p = \sqrt{\frac{1}{N_{means}} \sum_{i=1}^{N_{means}} \left(p_{N_{win}}[i] - \bar{p}\right)^2} \tag{21}$$

It represents the predicted magnitude of random noise superimposed on the valid signal during the measurement.

Figure 13 shows the signal-to-noise ratio results of the sound pressure data measured by the two arrays at different operation conditions. It can be seen that the SNR values at all operation conditions are higher than 10 dB, which indicates that the quality

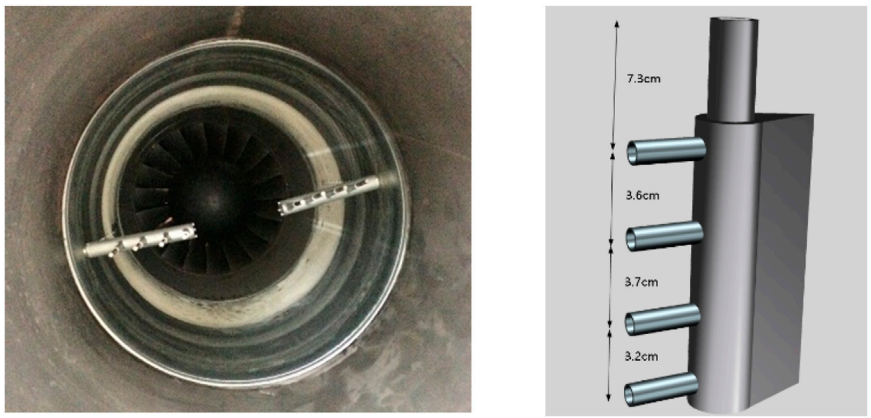

FIGURE 12 | Photo and 3D design drawing of radial rakes.

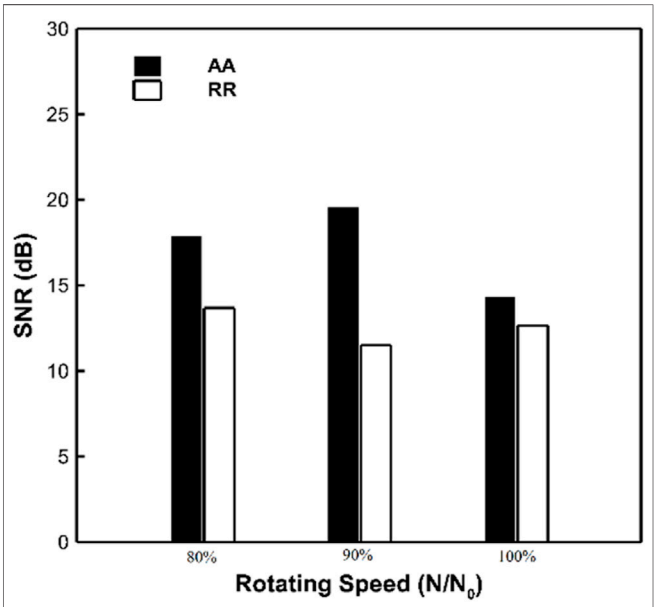

FIGURE 13 | Results of signal-to-noise ratio at different operation conditions.

of the sound pressure data during the entire measurement process is good. The signal-to-noise ratio of the axial array increases as the rotational speed increases because the aerodynamic interference between the rotor and stator becomes stronger with higher rotational speed. However, the signal-to-noise ratio of the radial rakes decreases with increasing rotational speed; this may be because when the air velocity increases, the influence of the air pressure pulsation on the radial rake is also intensified. In order to further investigate this phenomenon, **Figure 14A** presents the RMS and s_p results for radial rakes and axial arrays, respectively. It can be seen that as the rotational speed increases, the RMS of the sound pressure data shows an overall upward trend, although at 80% and 90% design rotational speed, the RMS value of the sound pressure measured by the axial array is lower than that of the radial rake, and the signal-to-noise ratio of the measured signal of the axial array is higher than that of the radial array as shown in **Figure 13** because the random noise of the axial array is smaller. At 100% design speed, although the RMS value of sound pressure has increased, the final signal-to-noise ratio result is smaller than those of the first two operation conditions because of the larger margin increase in random noise at this operation condition. This is the intrinsic reason for the reduction in the SNR of the sound pressure signal at 100% rotational speed in **Figure 13**. **Figure 14B** shows the RMS and s_p difference results of the radial rake array and the axial array, respectively, where the black bar chart represents the RMS difference $RMS^{(RR)} - RMS^{(AA)}$ of all measuring points, and the green histogram represents the amplitude difference of $Sp^{(RR)} - Sp^{(AA)}$. It can be seen that as the fan rotational speed increases, the RMS value of the sound pressure measured by the axial array increases faster than the result of the radial rake. In terms of random noise, the results of radial rake are larger than those of the axial array at the three operation conditions because the microphones of the axial array are all wall-mounted, which are much less affected by airflow velocity or pressure pulsation than the radial rakes exposed to the airflow.

5.3 Mode Decomposition Results

Based on the two measurement devices designed in the above sections, this section conducts experimental measurements on the fan inlet noise. **Figure 15** presents the sound power results for each circumferential mode measured by the axial array (AA) and radial rake (RR) at 1 BPF. **Figure 15A** shows the results of circumferential sound power at 90% design speed condition. It can be seen that the modal sound power calculated by the radial rakes is generally larger than that of the axial arrays, the difference between the dominant mode m = 1 is 3 dB, and the difference between the non-dominant modes is even greater. It can be seen that the results measured by the two arrays are in good agreement on the whole at 100% design speed condition as shown in **Figure 15B**. The difference in the sound power results of the m = 1 dominant mode measured using the two devices is less than

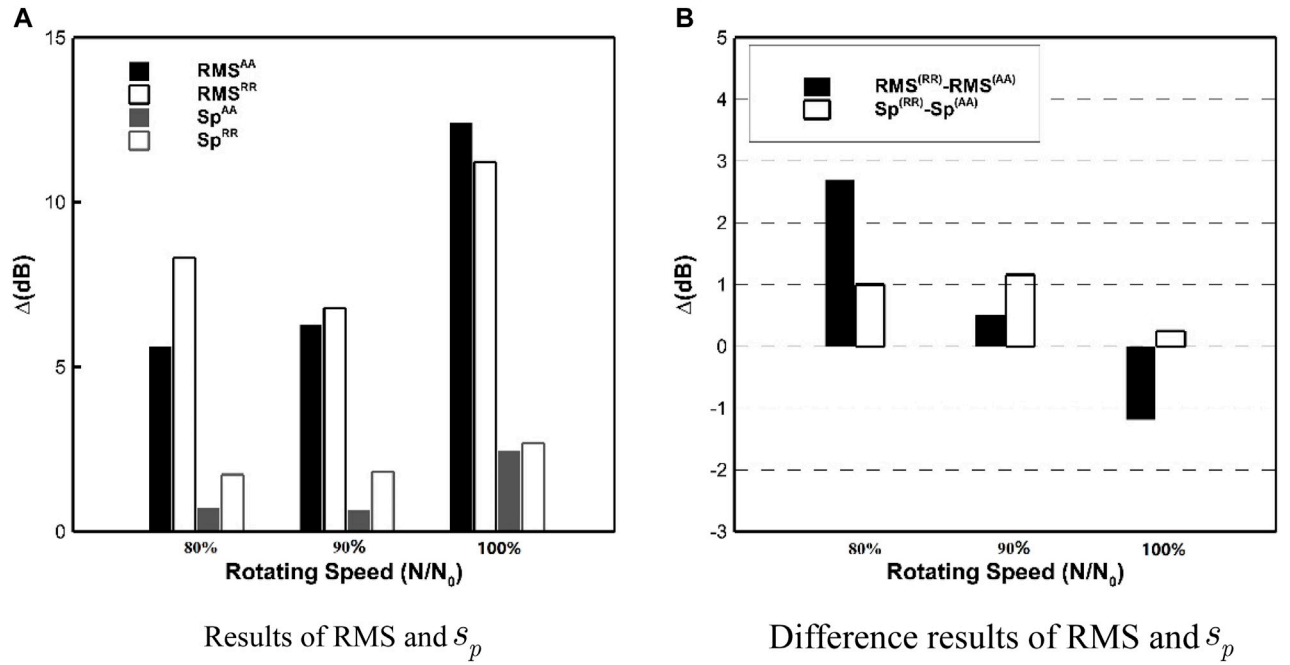

FIGURE 14 | RMS and s_p of sound pressure measurement signals measured by radial rakes and axial arrays. **(A)** Results of RMS and s_p. **(B)** Difference results of RMS and s_p.

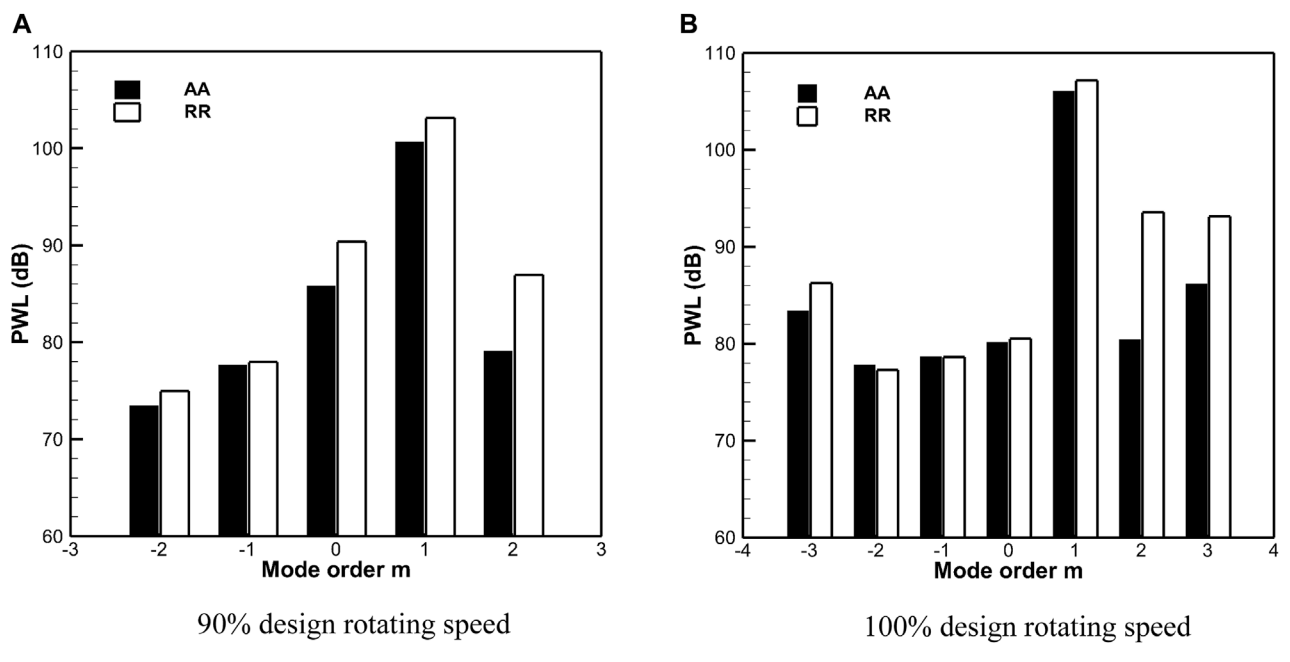

FIGURE 15 | Comparison of modal sound power applying radial rakes and axial microphone arrays. **(A)** 90% design rotating speed. **(B)** 100% design rotating speed.

1 dB, and the test results of the two devices are also in good agreement in the low-order circumferential mode range (m = −2 to m = +1). The sound power results of the high-order circumferential mode measured by different arrays have large deviations, which may be caused by the non-dominant modes being "buried" into random noise in the calculation. Referring to

Figure 13, the SNR of the measured signal at 90% design speed condition is only 11 dB, but the non-dominant mode (m≠1) in **Figure 15A** is at least 13 dB lower than that of the dominant mode, and the difference is greater than the acquisition signal-to-noise ratio of the signal, which makes the estimation results of these non-dominant modes heavily influenced by random noise and eventually unreliable. At 100% design speed condition, although the signal-to-noise ratio of the two arrays is relatively small, the measurement results of the two devices have high consistency. In order to better investigate the influence of random noise during measurement on mode identification, it is necessary to derive the transfer relationship between the mode identification error and the random noise of sound pressure measurement. For the sound pressure measured at a single location, it can be expressed as a superposition of the actual value and random noise, namely,

$$p_l = p_l^0 + \tilde{p}_l \tag{22}$$

In the formula, the random noise amplitude satisfies the Gaussian distribution. If the random noise collected at different measuring points is incoherent, then the expected value of random noise satisfies the following:

$$\langle \tilde{p}_l \rangle = 0 \langle \tilde{p}_l \tilde{p}_{l'}^* \rangle = s_p^2 \delta_{ll'} \tag{23}$$

If it is further assumed that all measuring points and the signal transfer function are the same, then the amplitude of the circumferential mode can be written as follows:

$$A_m = \frac{1}{N_\phi} \sum_{l=0}^{N_\phi - 1} p_l^0 \cdot e^{-iml2\pi / N_\phi} + \frac{1}{N_\phi} \sum_{l=0}^{N_\phi - 1} \tilde{p}_l \cdot e^{-iml2\pi / N_\phi} \tag{24}$$

The first part of **Eq. 19** is denoted as A_m^0 , and the second part is denoted as $\tilde{A}_m$; then the error amplitude of the circumferential mode is equal to the following:

$$\begin{aligned} \langle \tilde{A}_m \tilde{A}_{m'}^* \rangle &= \frac{1}{N_\phi^2} \sum_l \sum_{l'} \langle \tilde{p}_l \tilde{p}_{l'}^* \rangle \cdot e^{-i(ml - m'l')2\pi / N_\phi} \\ &= \frac{s_p^2}{N_\phi^2} \sum_l e^{-i(m-m')l2\pi / N_\phi} = \frac{s_p^2}{N_\phi^2} \delta_{mm'} \end{aligned} \tag{25}$$

Therefore, the standard deviation in mode identification is as follows:

$$s_{A_m} = \frac{s_p}{\sqrt{N_\phi}} \tag{26}$$

That is to say, the standard deviation of mode identification is smaller than the standard deviation of sound pressure measurement, and the two values are proportional. This shows that random noise during measurement will have a linear effect on the accuracy of mode identification.

The modal acoustic powers calculated by the radial rakes in **Figure 15** are generally greater than the results of the axial arrays because the random noise measured by the radial rake is larger than that of the axial array. As shown in **Figure 14**, $Sp^{(RR)} - Sp^{(AA)}$ is a positive value at each operation condition. The physical mechanism of this phenomenon is easy to understand; in experimental measurements, although the microphones on the radial rake are equipped with windshields, the airflow velocity and pressure pulsations in the airflow will still affect the sound pressure data measured by the microphones. In contrast, the microphones arranged on the duct wall are relatively less affected by the airflow velocity or pressure pulsation during the signal acquisition process, that is to say, the two arrays have different sensitivities to the airflow in the duct. In order to analyze the error characteristics of the two microphone arrays in the identification of different radial modes, **Figure 16** shows the (0, 0) and (0, 1) modes measured by the axial array and the radial rakes. At 90% design rotational speed, modal results measured by radial rakes are larger than those identified by the axial arrays, which results in the sound power of the m = 0 mode decomposed by radial rakes being higher than that decomposed by axial arrays as shown in **Figure 15A**. For 100% design rotational speed, the two arrays have high consistency in the identification of the n = 0 radial mode. The main difference is in the identification of the n = 1 radial mode, which may be caused by the low accuracy in mode identification with high cut-on ratios induced by the small angle between the main lobe of modal radiation and the axis.

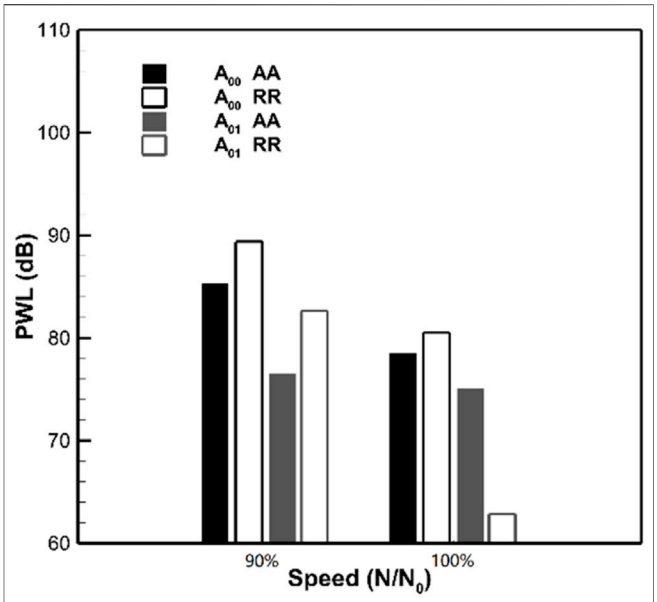

FIGURE 16 | Comparison of results for radial modes n = 0 and n = 1.

Although the mode decomposition results of different radial modes are different, this effect is negligible for circumferential mode recognition, for example, the sound power of the m = 0 mode measured by the two arrays matches very well as shown in **Figure 15B**. The above content mainly focuses on the influence of random noise in sound pressure measurement on modal recognition, but as Taddei et al. (2013) stated, the accuracy of the acoustic model used in mode decomposition is another main factor affecting mode identification. Distortion of the airflow in the duct, other noise sources, errors in the aerodynamic parameters of the airflow, etc. will affect the accuracy of the

mode identification, and the two typical arrays have different sensitivities to the acoustic models used in the mode identification. This study uses an equally spaced axial array and radial rakes to test the fan noise. For non-equidistant or compressed sensing arrays, finding out whether the error transfer characteristics obtained in this study are applicable requires further research. How to use the obtained error characteristics in modal decomposition to design a new test method or a new array scheme needs further research, especially for large ventilation facilities.

6 CONCLUSION

Based on the error analysis theory, the influence of different microphone arrays on the accuracy of acoustic mode identification is studied, and the design criteria for axial microphone arrays are established. Through the processing of rotating radial rakes and axial arrays, the experimental analysis of the acoustic mode identification error applying different arrays is carried out.

Although radial rakes can directly measure the radial distribution of the modal amplitude, this type of array has a large error in the mode identification at low frequencies. As the frequency approaches the cut-on frequency of the mode, the condition number of the coefficient matrix increases by about two orders of magnitude. Compared with the axial arrays, the radial rakes are more suitable for mode identification at high frequencies. At low frequencies, the condition number of the coefficient matrix is less than 10 when applying axial arrays. Therefore, the axial microphone arrays will become more advantageous than the radial rakes in practice. The design criterion of axial microphone array is established: (a) m = 0 mode is the dominant mode that restricts the mode identification accuracy and the upper limit of the frequency that can be solved; (b) the accuracy of the axial microphone array in mode identification strongly depends on the axial spacing of the array measuring points, and when $0.8\pi/kR \le \Delta x/R \le \pi/kR$ is satisfied, the frequency range of the mode identification investigation can be broadened; (c) the upper frequency limit for mode identification cannot be estimated by means of $\Delta x \le \lambda/2$, and when the error threshold value is given in the experimental measurement, the frequency range of mode identification is much smaller than that calculated using the Nyquist sampling theorem; and (d)when given an upper limit of relative standard deviation, it is difficult to determine a $N_x N_r/N_{rad}$ parameter that satisfies all modes unless it is set to a large value.

The experimental test results show that the modal sound power values calculated with axial arrays and radial rakes are in good agreement, especially for the rotor–stator interference mode determination. The small deviations in the mode identification when applying the two typical arrays are caused by the different signal-to-noise ratios of the sound pressure signals acquired by the two arrays and their discriminative sensitivities to the duct airflow.

DATA AVAILABILITY STATEMENT

The raw data supporting the conclusion of this article will be made available by the authors, without undue reservation.

AUTHOR CONTRIBUTIONS

KX is responsible for the whole article, CL is responsible for the experimental investigation and also the data processing, FT is responsible for the error analysis, and WQ is responsible for the article scheme and the idea to investigate the difference of modal sound power when using the two typical arrays.

FUNDING

This work was financially supported by the National Natural Science Foundation of China (Grant No. 12002150), The Ministry of Education of Humanities and Social Science Project (Grant No. 20YJCZH196), the Natural Science Foundation of Jiangsu Province, China (Grant No. BK20201041), the Key Laboratory of Aerodynamic Noise Control of China Aerodynamics Research and Development Center (Grant No. ANCL20190306), and the Scientific Research Fund of High-Level Talents in Nanjing Institute of Technology (Grant No. YKJ201906).

REFERENCES

Bolleter, U., Cohen, R., and Wang, J. (1973). Design Considerations for an In-Duct Soundpower Measuring System. *J. Sound Vibration* 28 (4), 669–685. doi:10.1016/s0022-460x(73)80142-7

Bolleter, U., and Crocker, M. J. (1972). Theory and Measurement of Modal Spectra in Hard-Walled Cylindrical Ducts. *The J. Acoust. Soc. America* 51, 1439–1447. doi:10.1121/1.1912994

Cheng, L., Yang, W. K., and Liang, T. (2019). Failure Diagnosis on Gas Path of Fan/compressor Based on Acoustic Mode[J]. *J. Mech. Eng.* 55 (13), 38–44. doi:10.3901/JME.2019.13.038

Chong, T. P., Vathylakis, A., and Mcewen, A. (2015). "Aeroacoustic and Aerodynamic Performances of an Aerofoil Subjected to Sinusoidal Leading Edges [C]," in 21th AIAA/CEAS Aeroacoustics Conference. Dallas TX. AIAA 2015-2200.

Dahl, M. D., Hixon, R., and Sutliff, D. L. (2013). "Further Development of Rotating Rake Mode Measurement Data Analysis [C]," in 19th AIAA/CEAS Aeroacoustics Conference. AIAA-2013-2246.

Enghardt, L., Tapken, U., Kornow, O., and Kennepohl, F. (2005). "Acoustic Mode Decomposition of Compressor Noise under Consideration of Radial Flow Profiles[C]," in 11th AIAA/CEAS Aeroacoustics Conference, Monterey, United States, 2005–2833.

Enghardt, L., Tapken, U., Neise, W., Kennepohl, F., and Heing, K. (2001). "Turbine Blade/vane Interaction Noise: Acoustic Mode Analysis Using In-Duct Sensor Rakes[C]," in 7th AIAA/CEAS Aeroacoustics Conference. Maastricht, Netherlands, 2001–2153.

Enghardt, L., Tapken, U., Neise, W., Schimming, P., Maier, R., et al. (2002). Active Control of Fan Noise from High-Bypass Aeroengines: Experimental Results[J]. *Aeronaut. J. R. Aeronaut. Soc.* 106, 501–506. doi:10.1017/S0001924000092356

Enghardt, L., Zhang, Y., and Neise, W. "Experimental Verification of a Radial Mode Analysis Technique Using wall-flush Mounted Sensors[C]," in Joint Meeting"Berlin 99" TU-Berlin, March 1999, 137th Regular Meeting of the Acoustical Society of America.

Farassat, F., Nark, D. M., and Thomas, R. H. (2001). "The Detection of Radiated Modes from Ducted Fan Engines[C]," in 7th AIAA/CEAS Aeroacoustics Conference. Maastricht, Netherlands, 2001–2138.

Heidelberg, L., and Hall, D. G. (1996). Inlet Acoustic Mode Measurements Using a Continuously Rotating Rake [J]. *AIAA J. Aircraft.* 32 (4), 761–767. doi:10.2514/3.46788

Holste, F., and Neise, W. (1997). Noise Source Identification in a Propfan Model by Means of Acoustical Near Field Measurements. *J. Sound Vibration* 203 (4), 641–665. doi:10.1006/jsvi.1996.0890

Joppa, P. D. (1987). Acoustic Mode Measurements in the Inlet of a Turbofan Engine. *J. Aircraft* 24 (9), 587–593. doi:10.2514/3.45482

Joseph, P., Morfey, C. L., and Lowis, C. R. (2003). Multi-mode Sound Transmission in Ducts with Flow. *J. Sound Vibration* 264 (3), 523–544. doi:10.1016/s0022-460x(02)01205-1

Kan, K., Yang, Z., and Lyu, P. (2021). Numerical Study of Turbulent Flow Past a Rotating Axial-Flow Pump Based on a Level-Set Immersed Boundary Method [J]. *Renew. Energ.* 168, 960–971. doi:10.1016/j.renene.2020.12.103

Kim, Y., and Nelson, P. A. (2004). Estimation of Acoustic Source Strength within a Cylindrical Duct by Inverse Methods [J]. *J. Sound Vibration* 275 (1-2), 391. doi:10.1016/j.jsv.2003.06.032

Lan, J. H., Premo, J. W., and Sutliff, D. L. (2002). "Inlet Mode Measurements with an Inflow Control Device Microphone Array[C]," in 8th AIAA/CEAS Aeroacoustics Conference, Breckenridge, United States, 2002–2563.

Liu, J., Liu, Y., and Bolton, J. S. (2018). Acoustic Source Reconstruction and Visualization Based on Acoustic Radiation Modes. *J. Sound Vibration* 437, 358–372. doi:10.1016/j.jsv.2018.08.030

Moore, C. J. (1979). Measurement of Radial and Circumferential Modes in Annular and Circular Fan Ducts. *J. Sound Vibration* 62 (2), 235–256. doi:10.1016/0022-460x(79)90024-5

Nelson, P., and Yoon, S. (2000). Estimation of Acoustic Source Strength by Inverse Method: Part I, Conditioning of the Inverse Problem [J]. *J. Sound Vibration* 233 (4), 643–668. doi:10.1006/jsvi.1999.2837

Qiao, W. Y. (2010). *Aero-engine Aeroacoustics [M]*. Beijing: Beijing University of Aeroacoustics & Astronautics Press, 1–8.

Sutliff, D. L. (2005). *Rotating Turbofan Duct Mode Measurement system[R]*. NASA-TM-213828. Cleveland, OH: Glenn Research Center.

Taddei, F., Lucia, M. D., Torzo, D., and Spano, E. (2013). "A Comparison between Radial Rakes of Sensors and Axial Arrays of Microphones for the Experimental Investigation of Tone Noise in LPTs [C]," in 19th AIAA/CEAS Aeroacoustics Conference. Berlin.

Tapken, U., Bauers, R., and Enghardt, L. (2008). "Turbomachinery Exhaust Noise Radiation Experiments-Part 2: In-Duct and Far-Field Mode Analysis [C]," in 14th AIAA/CEAS Aeroacoustics Conference (Vancouver, British Columbia Canada. AIAA-2008-2858.

Tapken, U., and Enghardt, L. (2006). "Optimization of Sensor Arrays for Radial Mode Analysis in Flow Ducts[C]," in 12th AIAA/CEAS Aeroacoustics Conference (Cambridge, MA. UK, 2006–2638.

Tapken, U., Raitor, T., and Enghardt, L. (2009). "Tonal Noise Radiation from an UHBR Fan- Optimized In-Duct Radial Mode Analysis[C]," in 15th AIAA/CEAS Aeroacoustics Conference. AIAA-2009-3288.

Wagih Nashed, M., Elnady, T., and Åbom, M. (2018). Modeling of Duct Acoustics in the High Frequency Range Using Two-Ports. *Appl. Acoust.* 135, 37–47. doi:10.1016/j.apacoust.2018.01.009

Wang, L. F., Qiao, W. Y., and Ji, L. (2014). In-duct Circumferential Acoustic Mode Measurement of Axial fan/Compressor[J]. *J. Aerospace Power* 29 (4), 917–926. doi:10.13224/j.cnki.jasp.2014.04.024

Xu, K. B., Qiao, W. Y., and Huo, S. Y. (2018). Research of Mode Identification and Error Transfer Property on Fan Tonal Noise [J]. *J. Propulsion Technology* 39 (1), 185–195. doi:10.13675/j.cnki.tjjs.2018.01.021

Yardley, P. D. (1974). *Measurement of Noise and Turbulence Generated by Rotating Machinery [D]. PhD Thesis*. Southampton: University of Southampton.

Zhou, D., Wang, X. Y., and Chen, J. (2015). Investigation of Sound Generation by Non-synchronously Vibrating Rotor Blades[J]. *Acta Aeronautica et Astronautica Sinica* 36 (3), 737–748. doi:10.7527/S1000-6893.2015.0029

Zillmann, J., and Tapken, U. (2009). "Tonal Noise Radiation from UHBR Fan-Active Control of Radiation Characteristic [C]," in 15th AIAA/CEAS Aeroacoustics Conference. AIAA-2009-3226.

Conflict of Interest: The authors declare that the research was conducted in the absence of any commercial or financial relationships that could be construed as a potential conflict of interest.

frontiers in Energy Research

ORIGINAL RESEARCH
published: 28 March 2022
doi: 10.3389/fenrg.2022.873749

Numerical and Experimental Investigations of Modal Coherence Characteristics for the Determination of Broadband Noise in Flow Ducts

Kunbo Xu[1]*, *Cunliang Liu*[1], *Fan Tong*[2] and *Weiyang Qiao*[3]

[1]School of Mechanical Engineering, NanJing Institute of Technology, Nanjing, China, [2]Key Laboratory of Aerodynamic Noise Control, China Aerodynamics Research and Development Cen-ter, Mianyang, China, [3]School of Power and Energy, Northwestern Polytechnical University, Xi'an, China

This paper presents a detailed investigation about the modal coherence characteristics of turbomachinery noise. The modal coherence characteristics of ducted noise at high frequencies are investigated by establishing three kinds of ducted sound source distribution models. The results are consistent with the acoustic experimental results of a single-stage axial fan. The results show that acoustic modes of different orders are mutually incoherent, and radial modes within the same circumferential mode have a great degree of coherence. This paper successfully conducted an acoustic measurement on turbomachinery noise by rotating microphone arrays. The acoustic experimental results show that the coherence of some modes has little impact on the measurement of incident acoustic waves in the flow duct, while it leads to about 3 dB deviation in the prediction of the reflected modal sound power and has little influence on the spectral shape of reflected acoustic waves. It was demonstrated that the experimentally measured modal coherence functions give an inner sense of the spatial noise source distribution and enable the investigation of mode scattering within the propagation. Based on the modal coherence characteristics obtained in this paper, more theoretical and methodological studies can be carried out for the turbomachinery broadband noise test.

Keywords: broadband noise, mode amplitude, array, turbomachinery, axial fan

OPEN ACCESS

Edited by:
Kan Kan,
College of Energy and Electrical Engineering, China

Reviewed by:
Guangyao An,
North China Electric Power University, China
Yanhua Wang,
Harbin Engineering University, China

***Correspondence:**
Kunbo Xu
xukunbo@njit.edu.cn

Specialty section:
This article was submitted to Process and Energy Systems Engineering, a section of the journal Frontiers in Energy Research

Received: *11 February 2022*
Accepted: *21 February 2022*
Published: *28 March 2022*

Citation:
Xu K, Liu C, Tong F and Qiao W (2022) Numerical and Experimental Investigations of Modal Coherence Characteristics for the Determination of Broadband Noise in Flow Ducts. Front. Energy Res. 10:873749. doi: 10.3389/fenrg.2022.873749

INTRODUCTION

Ducted broadband noise becomes increasingly important for the noise reduction concept in the modern civil aviation, especially when improved passive absorbers in the engine inlets and bypass sections, modern fan blade configurations, and a cut-off design of the fan rotor and stator become a standard. For the assessment and measurement of broadband noise in a duct, it is of great worth to investigate the multi-mode propagation characteristics and also coherence functions of pairwise modes (Morfey, 1971; Bolleter and Crocker, 1972; Moore, 1979).

Due to the complex mechanism of the broadband noise source inside aero-engines, the acoustic mode identification measurement becomes more difficult than tonal noise. Unlike tonal noise in which the sound energy is mainly concentrated in several dominant modes, the sound energy of turbomachinery turbulent noise is distributed in each cut-on modes. Therefore, in the investigation of turbulent broadband noise, we need to identify all the propagating modes and measure the modal distribution characteristics. Sijtsma and Brouwer (2018) assumed that the sound field of the

turbomachine is dominated by a finite number of acoustic modes and proposed an acoustic mode recognition method based on a non-equally spaced microphone array, the deconvolution algorithm is used in the research to increase the dynamic response range in order to overcome the occurrence of multimodal mutual interference. Compared with the traditional beamforming method, the dynamic response range is increased by 10 dB. In order to evaluate and measure the broadband noise, it is necessary to conduct a detailed study on the propagation characteristics and coherence functions of modes in the flow duct and to analyze the error transfer characteristics in the mode recognition (Xu et al., 2018). Enghardt (Enghardt et al., 2004) considered that the turbulent broadband noise still propagates in the form of statistically averaged modal waves inside the turbine duct and proposed a reference correlation method to identify the broadband acoustic mode. This method uses a measured cross-spectrum vector to obtain the amplitude spectrum of the acoustic mode propagating downstream and upstream in the duct. It should be noted that the method used by Deutsches Zentrum für Luft- und Raumfahrt (DLR) in a lot of applications requires the occupation of several rings of microphones, in which the number of sensors is proportional to the total number of modes propagating within the duct. As the frequency under consideration increases, more microphones are required to accurately decompose the broadband noise accordingly. This needs either an array consisting of a large number of fixed sensors, as employed by Ganz et al. (1998), for example, or an array with a smaller number of microphones rotating around the duct axis (Xu et al., 2017a). Kopiev et al. (2017) used a sparse array of 100 microphones to identify and measure the acoustic mode of a turbofan engine. The experiment was carried out in the anechoic chamber of the Russian State University of Technology. The results show that the sparse microphone array can be used to test the circumferential modal distribution of a new generation turbofan engine (Bu et al., 2020). proposed a compressive sensing technology for radial modal recognition of turbomachines based on the previous circumferential modal recognition research (Yu et al., 2018); when the number of microphones is significantly reduced, the tonal noise modal distribution measured by the compressed sensing technology has good accuracy and can effectively suppress the interference of background noise.

An improved version of the broadband noise measurement method was demonstrated by Jürgens et al. (2011) to expound and prove that the measured modal coherence functions give insight into the spatial noise source distribution. Regarding the coherence characteristics between the duct sound field and internal modes, Dyer (1958) pointed out that the modes generated by a monopole mass source with a random location is statistically uncorrelated, but Michalke et al. (1996) indicated that the sound field generated by the random monopole in the time domain is completely correlated, even in the near field of the sound source, which is completely opposite to the conclusion drawn by Dyer. Michalke et al. (1996) proposed an experimental method to predict the correlation of the sound field with the cross-spectrum signals measured by three microphones (Enghardt et al., 2007), and (Jürgens et al., 2010) used the cross-correlation method to investigate the broadband noise modal coherence function in the duct with no flow. A ducted sound field was artificially constructed by the application of two ring loudspeakers, and the results show that the coherence function results between different modal combinations are completely different (Tapken et al., 2014). Constructing the broadband noise in the duct by arranging several rings of monopole sources on the duct wall, the modes in the artificial sound fields are completely incoherent when 20 rings of monopole sources are arranged; this is consistent with the conclusion of Jürgens et al. (2010). On account of the measured coherence function between broadband noise modes in the flow duct, it is possible to explore the characteristics of broadband noise sources, such as the dominant noise source distribution characteristic and appearance of each sound source (Jürgens et al., 2011) and to further investigate the modal characteristics in the airflow duct with different hub ratios (Jeong et al., 2006). However, in order to achieve noise reduction in the sound source aspect and radiation process, it is worthwhile to investigate the coherence characteristics of acoustic modes in turbomachinery and modal distribution characteristics of broadband noise.

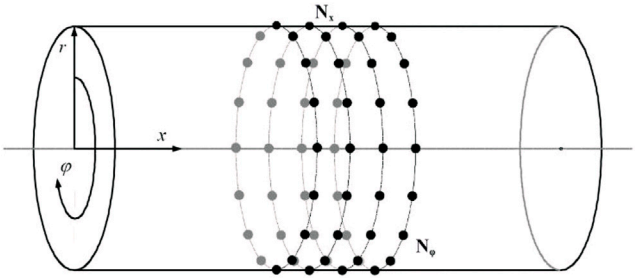

FIGURE 1 | Sensor array with equidistant azimuthal and axial positions in a circular duct.

The purpose of this paper is to deeply investigate the coherence characteristics between the modes of the turbomachinery duct through theoretical analysis, numerical simulation, and experimental testing methods. Based on the obtained modal coherence features, the design of a new modal identification method is guided to meet the noise test requirement of large-sized fans and large bypass ratio engines. This paper provides the modal coherence characteristic measurements of ducted noise in turbomachinery for comparison with models and numerical investigation. The findings should better inform the future cognition of the broadband noise generation mechanism and allow a basis for the broadband noise reduction design in turbomachinery. The paper is organized as follows. The measurement theory is discussed in the *Measurement Theory* section, which includes the modal coherence coefficient, details of synthetic sound fields, and ducted sound source distribution models. The characteristics of the synthetized sound fields are provided in the *Characteristics of the Synthetized Sound Fields* section. In the *Experimental Study on the Acoustic Modal Coherence Characteristics* section, we present the experimental

facility and setup and experimental and theoretical analysis on acoustic modal coherence distribution and broadband modal distribution results. A summary of the findings and future perspectives is provided in the *Conclusion* section.

MEASUREMENT THEORY

Modal Coherence Coefficient

The cross-spectrum of two sound pressure measurement points at a single frequency as shown as **Figure 1** can be expressed as

$$S_{pp'} = < p(x, r, \phi)\, p^{*}(x', r', \phi') > \tag{1}$$

In the formula, the superscripted $*$ represents the complex conjugate. Under the linear assumption, the measured sound pressure p is related to the vector a composed of the modal amplitude $A_{mn}^{\pm}$:

$$a = [a_1\ a_2\ a_3\ \cdots\ a_{K-1}\ a_K]^T \tag{2}$$

In the formula, K represents the length of the modal vector, and its value is equal to twice the number of truncated modes at this frequency; the measured sound pressure signal can be expressed as the product of the coefficient matrix Φ and radial modal amplitude vector a:

$$\mathbf{p} = \mathbf{\Phi} a \tag{3}$$

where$\mathrm{p} \in \mathbb{C}^K$ represents the complex sound pressure vector at the measured frequency; $a \in \mathbb{C}^L$ represents the complex amplitude vector of the mode, the modal amplitude is A_{mn}, and the size of L depends on the total number of cut-on modes in the duct, the value of matrix $\Phi \in \mathbb{C}^{K\times L}$ is determined by the microphone array position and the mode order. The cross-spectrum of two sound pressure signals can be defined as $\mathrm{S}_{pp} \triangleq E(\mathrm{pp}^H)$, where E represents the expectation. According to **Eq. 3**, the cross-spectrum of two sound pressure signals can be written as

$$\mathrm{S}_{pp} = \mathbf{\Phi}\mathbf{S}_{aa}\mathbf{\Phi}^H \tag{4}$$

Therefore, the cross-spectrum of the modal amplitude can be written as

$$\mathrm{S}_{aa} = \mathbf{\Phi}^{\dagger}\mathrm{S}_{pp}\left(\mathbf{\Phi}^{\dagger}\right)^H \tag{5}$$

In the formula, † represents the pseudo-inverse of the matrix. In the actual experimental measurement, the measurement point number K of the microphone array is usually greater than the magnitude of the modal amplitude vector L, and the coefficient matrix may be singular. When solving such a matrix with a singular coefficient matrix and overdetermined equation, singular value decomposition (Nelson and Yoon, 2000; Kim and Nelson, 2004) is used in this paper.

$$\mathrm{G}^{+}\mathrm{p} = \hat{\mathrm{a}} \Leftrightarrow \mathrm{U}\cdot\mathrm{W}\cdot\mathrm{V}^{\mathrm{T}}\mathrm{p} = \hat{\mathrm{a}} \tag{6}$$

In the formula, U and V are both transformation and orthogonal matrices, satisfying $\mathrm{U}\cdot\mathrm{U}^T = 1$ and $\mathrm{V}\cdot\mathrm{V}^T = 1$, but W is a diagonal matrix, consisting of positive elements and singular values. It can improve the accuracy of the algorithm

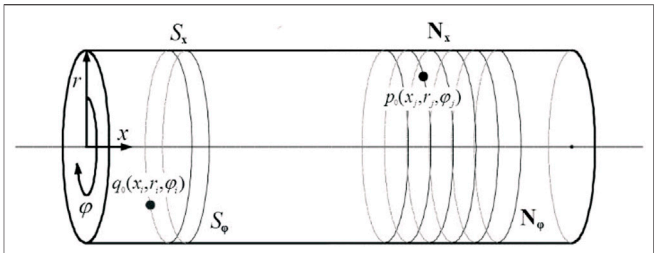

FIGURE 2 | Sound pressure at microphone position of measurement sensor rings.

by discarding smaller singular values appropriately. The best estimate can be obtained by

$$\hat{\mathrm{a}} = \mathrm{V}\cdot\left[\mathrm{diag}\left(\frac{1}{w_j}\right)\right]\cdot\ \mathrm{U}^T \tag{7}$$

The modal amplitude and cross-term between them can be obtained by formula (5), which is defined according to the modal coherence coefficient between the mode (m, n) and (μ, ν):

$$C\ {}^{(\mu,\nu)}_{(m,n)} = \frac{\left|\langle A_{mn}A_{\mu\nu}^{*}\rangle\right|^2}{\langle|A_{mn}|^2\left|A_{\mu\nu}\right|^2\rangle} \tag{8}$$

The coherence characteristics between the cut-on modes in the duct can be obtained. It should be noted that the modal amplitude in formula (8) represents the statistical average of the modal amplitude. The sound power carried by each individual mode can be calculated by

$$PWL_{mn}^{\pm}(\omega) = \frac{\pi\left(r_D^2 - r_H^2\right)}{\rho c}\,\frac{\alpha_{mn}(\omega)\left(1 - M_a^2\right)^2}{\left(1 \mp \alpha_{mn}(\omega)M_a\right)^2}\left|A_{mn}^{\pm}(\omega)\right|^2 \tag{9}$$

with $\alpha_{mn}(\omega) = (1 - (1 - M_a^2)(\sigma_{mn}/(k_{mn}R))^2)^{1/2}$, R is the duct radius, c is the sound speed, ρ is the flow density, and M_a is the Mach number in the axial direction.

Synthetic Sound Fields

A numerical analysis was first performed in the synthetic sound fields. It is assumed that the duct is hard walled and has non-reflecting terminations in the following. The duct radius is 0.25 m. An optionally superposed axial flow is represented as a uniform-profile flow. In this section, M_a is set as 0.10. The sound pressure at position (x_j, r_j, φ_j) is excited by theS_x ring(s) of monopole sources (each ring has S_φ point-like monopole sources) at position (x_i, r_i, φ_i), which are driven with volume velocity, e.g., $q_0(x_i, r_i, \varphi_i)$, cf. **Figure 2**, can be calculated with the appropriate Green's function:

$$p\left(x_i, r_i, \varphi_i \middle| x_j, r_j, \varphi_j\right) = q\sum_{m,n}\chi_{mn}f_{mn}(r_i)f_{mn}\left(r_j\right)e^{im\left(\varphi_j - \varphi_i\right)}e^{ik_{mn}^{+}\left(x_j - x_i\right)} \tag{10}$$

The quantity χ_{mn} is definite for each mode (m, n), which contains the frequency-dependent mode cut-on ratio. Referring to the typical **Eq. 3** of duct mode expansion, the amplitude of mode (m, n) excited by the source is written as

TABLE 1 | Source arrangements used for mode coherence detection.

Condition number	Condition I	Condition II	Condition III	Condition IV
Axial positions	1	1	2	10
Circumferential positions in each ring	1	12	12	12

$$A_{mn}^{\pm}(q, x_i, r_i, \varphi_i) = q\chi_{mn} f_{mn}(r_j) e^{-im\varphi_i} e^{-ik_{mn}^{\pm} x_i} \tag{11}$$

In the following, the modal cross-spectral density is formulated for an array consisting of S_x rings of point-like monopole sources; each ring is equipped with S_φ equidistantly positioned sources. All sources are placed at the outer duct radius $r_i = R$, considering the experimental implementation. If all sources are incoherent and have equal spectral density, the analytical modal cross spectral can be inferred.

$$\langle A_{mn} A_{\mu\nu}^{*} \rangle = \chi_{mn} \chi_{\mu\nu}^{*} \langle qq^{*} \rangle \sum_{j=0}^{N_x} \sum_{l=0}^{N_\varphi - 1} \Gamma_{mn}(x_j, R, \varphi_l) \Gamma_{\mu\nu}^{*}(x_j, R, \varphi_l) \tag{12}$$

Here $\Gamma_{mn}(x, R, \varphi) = f_{mn}(R) e^{-im\varphi} e^{-ik_{mn}^{\pm} x}$, the analytical mode coherence function can be calculated subsequently.

In the actual test, environment reflections can appear upstream or downstream of the sensor array. The impact of the reflections can be integrated into the Green's function with a method of mirrored sources. For simplicity, the reflection coefficient r_c is assumed to be independent of the mode order and also the frequency; here, it is set as 0.2. The effect of mode scattering from an incident mode into another mode with different azimuthal or radial orders is neglected here. The Green's function can be modified subsequently to

$$p(x_j, r_j, \varphi_j) = \frac{\rho c}{4\pi R^2} q_0 \sum_{m,n} \frac{f_{mn}(R)^2}{\alpha_{mn}} e^{im(\varphi_j - \varphi_i)} \left(e^{ik_{mn}^{+}(x_j - x_i)} + r_c e^{ik_{mn}^{-}(x_j - x_i)} \right) \tag{13}$$

In the frame of the numerical study, four substantially different arrangements of point-like monopole sources, denoted by Latin numbers I–IV, are investigated. The detailed information of source configurations is displayed in **Table 1**. The main difference lies in the number of axial sensor rings and also the total number of point-like monopole sources. At each sensor, the position time series of 700 FFT windows are used in the numerical process.

Ducted Sound Source Distribution Models

At high frequency, a large number of modes will be cut on inside the duct according to the Tyler and Sofrin modal theory, which brings great challenges to the experimental test of the modal coherence coefficient. As an alternative strategy, it is necessary to study the modal coherence distribution at a high frequency by pre-assuming the modal amplitude or sound source distribution in the duct. The sound source in the low-speed flow duct is mainly composed of dipole and monopole sound sources. This section will establish three representative sound source models: uniformly distributed monopoles, uniformly distributed dipoles, and equal energy per mode (EEPM) sound source models.

When the incoherent sound sources are uniformly distributed on a certain cross-section in the duct, the non-homogeneous wave equation contains the source term

$$\left(\frac{1}{c^2} \frac{D^2}{Dt^2} - \nabla^2 \right) p = q \tag{14}$$

The source term can be expressed as

$$q = \left(\frac{D}{Dt} \right)^{\nu} \frac{(-\partial)^{\mu}}{\partial x_i \partial x_j \cdots} q_{ij\cdots} \tag{15}$$

in which ν represents the time order of the sound source distribution and μ represents the space order of the sound source distribution. In the follow-up study, the sound source distribution is limited to the axial direction. At this time, the source term can be written as

$$q = \left(\frac{D}{Dt} \right)^{\nu} \left(\frac{-\partial}{\partial x} \right)^{\mu} q_{xx} \tag{16}$$

Considering the single mode generated by a fixed sound source in a semi-infinite duct, Joseph et al. (2003) indicated that the spatial differentiation of the single mode (the second item on the right of **Eq. 16**) is equivalent to

$$\left(\frac{-\partial}{\partial x} \right)^{\mu} \rightarrow (-ik_{mn}^{+})^{\mu} \tag{17}$$

Similarly, the time differential in equation is equivalent to

$$\left(\frac{D}{Dt} \right)^{\nu} \rightarrow \left[-i\omega + U \frac{\partial}{\partial x} \right]^{\nu} = \left[-i\omega \left(\frac{1 - \alpha_{mn} Ma}{1 - Ma^2} \right) \right]^{\nu} \tag{18}$$

Therefore, when the cross-section in the semi-infinite circular duct is uniformly distributed with incoherent sound sources of spatial order μ and time order ν, the modal amplitude value can be expressed in a general form (Joseph and Morfey, 1999):

$$\left| A_{mn}^{(\mu,\nu)} \right|^2 \propto \frac{1}{\alpha_{mn}^2} \left(\frac{Ma - \alpha_{mn}}{1 - Ma^2} \right)^{2\mu} \left(\frac{1 - \alpha_{mn} Ma}{1 - Ma^2} \right)^{2\nu} \tag{19}$$

in which (μ, ν) is used to indicate the sound source type, $(\mu, \nu) = (0, 1)$ corresponds to a monopole sound source, and $(\mu, \nu) = (1, 0)$ corresponds to an axial dipole sound source. There is also a type of sound source distribution in the actual research: EEPM, that is to say, the energy carried by each cut-on mode is the same, that is $\mathrm{PWL}_{mn} = W_0$. The modal amplitude distribution $A_{mn}^{(ee)}$ of EEPM can be expressed as

TABLE 2 | Three sound source models in airflow duct.

Sound source model	Monopole sound source	Dipole sound source	EEPM
(μ, ν, γ)	(0,1,2)	(1,0,2)	(0,1,1)
$C^2_{\mu,\nu,\gamma}$	$(\rho c)^2 \overline{Q_s^2}/2$	$\overline{F_s^2}/2$	$2\rho c W_0/S$

$$\left|A_{mn}^{(ee)}\right|^2 \infty 2\rho c S^{-1} \alpha_{mn}^{-1} W_0 \left(\frac{1-\alpha_{mn}Ma}{1-Ma^2}\right)^2 \tag{20}$$

It can be found that the model formula (20) cannot be unified to formula (19). Therefore, the sound source distribution model is integrated as

$$E\{|A_{mn}|^2\} = C^2_{\mu,\nu,\gamma}\left(\frac{Ma-\alpha_{mn}}{1-Ma^2}\right)^{2\mu}\left(\frac{1-\alpha_{mn}Ma}{1-Ma^2}\right)^{2\nu}\frac{1}{\alpha_{mn}^{\gamma}} \tag{21}$$

in which $E\{|A_m|^2\}$ is the expected value of the square of the modal amplitude, and $C^2_{\mu,\nu,\gamma}$ represents the sound source intensity.

The corresponding values of the three models are shown in **Table 2**; the type of sound source is defined by three Greek letters (μ, ν, γ): $\overline{Q_s^2}$ is the mean value of the squared velocity in the monopole sound source distribution; $\overline{F_s^2}$ is the mean value of the squared force in the dipole sound source distribution; W_0 is the energy carried by each mode in EEPM. The modal amplitudes of the three sound source models can be expressed as

$$E\{|A_{mn}|^2\} = C^2_{012}\left(\frac{1-\alpha_{mn}Ma}{1-Ma^2}\right)^2\frac{1}{\alpha_{mn}^2} \tag{22}$$

$$E\{|A_{mn}|^2\} = C^2_{102}\left(\frac{Ma-\alpha_{mn}}{1-Ma^2}\right)^2\frac{1}{\alpha_{mn}^2} \tag{23}$$

$$E\{|A_{mn}|^2\} = C^2_{011}\left(\frac{1-\alpha_{mn}Ma}{1-Ma^2}\right)^2\frac{1}{\alpha_{mn}} \tag{24}$$

Eq. 22 represents a uniformly distributed incoherent monopole sound source $(\mu, \nu, \gamma) = (0, 1, 2)$, **Eq. 23** represents a uniformly distributed incoherent dipole sound source $(\mu, \nu, \gamma) = (1, 0, 2)$, and **Eq. 24** represents a modal and equal energy distribution sound source $(\mu, \nu, \gamma) = (0, 1, 1)$.

CHARACTERISTICS OF THE SYNTHETIZED SOUND FIELDS

In the frame of the numerical study of modal coherence in a flow duct, four substantially different arrangements of point-like monopole sources displayed in **Table 1** are investigated. On one hand, the analytical coherence functions of pairwise modes theoretically obtained by **Eq. 16** are compared with that inferred from **Eq. 8** in order to assess the characteristics of the simulated sound fields; on the other hand, a comparison of the squared mode amplitudes obtained by **Eq. 11** with that calculated by the cross-correlation mode decomposition method (CC-MDM) (Jürgens et al., 2010; Xu et al., 2015), Reference Correlation Mode Decomposition Method (RC-MDM) (Xu et al., 2017a), Combined Sensor Array (CSA method) (Tapken et al., 2014; Xu et al., 2017b), and also the analytical values inferred from **Eq. 21** is fulfilled to determine the bias. **Figure 3** shows exemplary results in the flow direction for a duct with measurement sensor rings located downstream of the sources rings.

The reflected modes are found to have comparatively little difference compared with the deviation of incident modes, so it is not shown in this paper for simplicity. In the left column of **Figure 3**, the coherence functions of mode pairs (0, 0) and (0, 1), (0, 0) and (1, 0), (1, 0), and (1, 1) are plotted up to 1,400 Hz (corresponding to $kR = 6.47$, $|M_{\max}| = 5$, $N_{\max} = 1$), with the lowest frequency of $f = 397Hz$ $(kR = 1.83)$ delineating the frequency range between purely plane wave propagation, $kR < 1.83$, and higher-order modes $kR \geq 1.83$. Mode pairs are specially chosen to investigate the characteristics of modal coherence with respect to the azimuthal order m and radial order n. Shown on these figures (as a solid line) are the analytical values of the mode coherence, the corresponding terms obtained by the CC-MDM are plotted in dash-dotted form with different symbols. The estimate of the mode coherence functions is completely consistent with the analytical values for all the four conditions.

The sound field within the duct generated by a single monopole source is completely coherent, i.e., all modes are fully coherent, which is consistent with the investigation (Michalke et al., 1996). When a single ring of $S_\varphi = 12$, incoherent monopole sources that have equal spectral density are arranged; the excited sound field is partially coherent as shown in **Figure 3B**, i.e., the modes with a different azimuthal order are incoherent except for pairs $m - \mu = \pm sN_\varphi$ with s being any integer; the radial modes are all coherent not only within each azimuthal mode m but also with the radial modes of azimuthal order μ. Good collapse of the measured coherence between pairwise radial modes are observed in **Figures 3C,D** when more rings of monopole sources are occupied, especially in condition VI in which the statistical coherence between almost all radial modes can be set to zero (referring to (Jeong et al., 2006)). The notable feature of **Figure 3D** is the slow rate of decay observed in the coherence function between (0, 0) and (0, 1) modes. The reason for this behavior is most likely due to the deficiency of the number of source rings and total axial length of source rings. In the right columns of **Figure 3**, the mode sound power determined with CSA method are shown for mode (0, 0) and (0, 1) in comparison with the CC-MDM, RC-MDM methods and with the analytical solutions. Each mode is accurately determined by the CC-MDM, and the values calculated by the CC-MDM are consistent with analytical terms. The results calculated by RC-MDM and CSA methods are relatively consistent, but there appears a 2 dB deviation from the true values, the error of the predicted modal sound power will be higher when the modal sound power is relatively low.

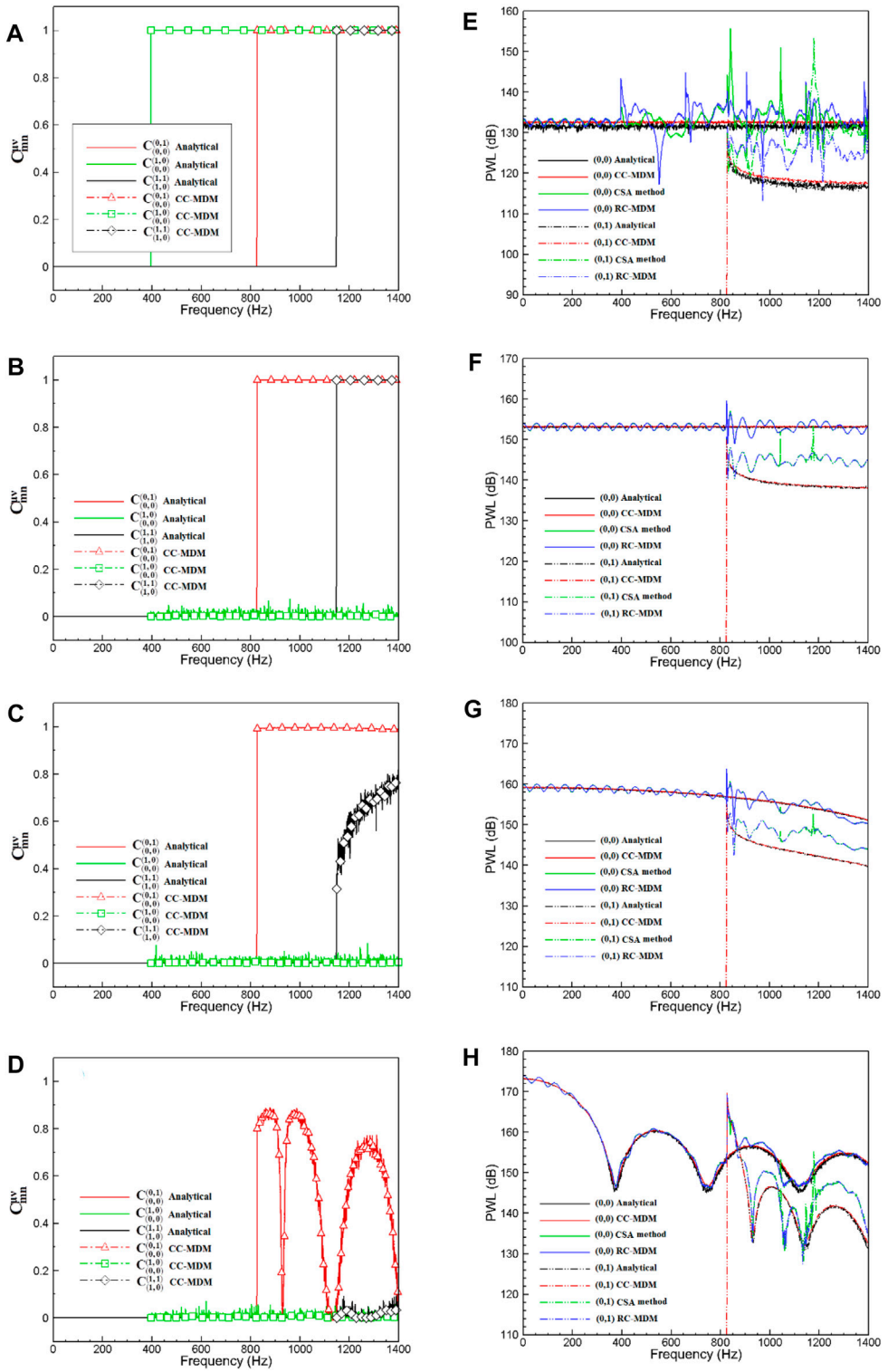

FIGURE 3 | Modal coherence and sound power results of CC-MDM, CSA method, and RC-MDM appended with analytical prediction. Broadband sound fields were synthesized by using different ring numbers of incoherent monopole sources shown in **Table 2**. Diagrams **(A–D)** depict the mode coherence; diagrams **(E–H)** show the modal sound power.

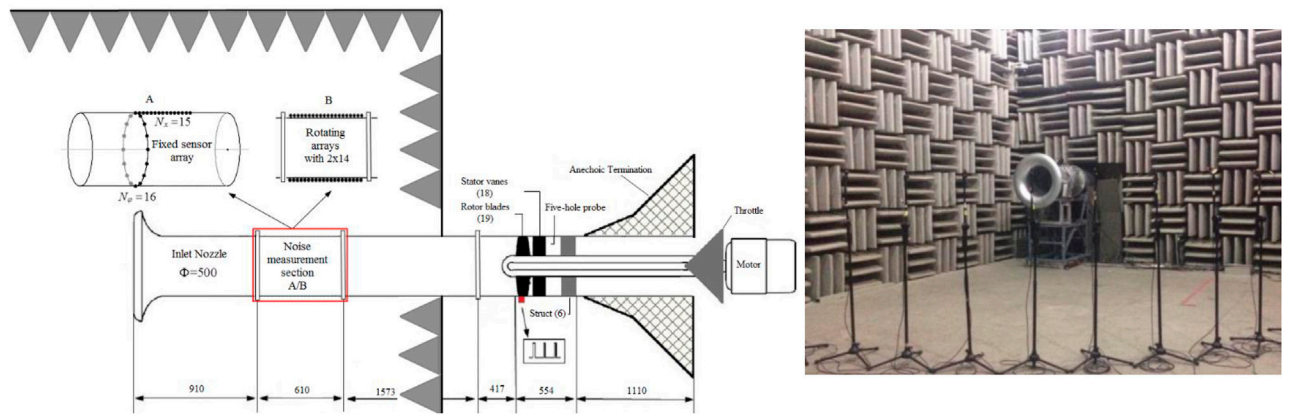

FIGURE 4 | Schematic of the experimental setup with the measurement sensor array located upstream of an axial fan rig with an anechoic termination outlet duct.

In condition I, mode amplitudes above the cut-on frequency of the non-plane wave are determined with large oscillation error since all mode pairs are fully coherent. In conditions II and III, relatively accurate modal sound power results are determined with CSA and RC-MDM methods up to the cut-on frequency of the first higher radial mode order (i.e., f = 826Hz). However, the mode amplitude distribution observed in this figure appear to be systematically oscillatory with 1 dB deviation. Above 826 Hz, the amplitudes of both modes (0, 0) and (0, 1) obtained by the RC-MDM and CSA method are distracted strongly in all source conditions. The underlying precondition of both methods is the assumption that modes with different azimuthal and radial orders are mutually incoherent. However, this is not consistent with the actual modal coherence characteristic referring to the mode coherence results shown alongside. Serious deviation arises as a result of high degree of modal coherence in pairwise mode with respect to a higher radial mode order n.

It should be noted that the resolved mode amplitudes of mode (0, 1) are always higher than the actual value; the potential reason for this phenomenon is that the energy carried by the modal cross-terms is forced to superimpose over the squared mode amplitudes in the process of mode decomposition. In condition IV, a reasonable sound power solution of mode (0, 0) is determined by the CSA method, although a high degree of coherence appears between the radial modes with the azimuthal mode order m = 0. That is to say, internal modal cross-terms have decayed to sufficiently small values in comparison with the dominant mode when more rings of monopole sources are occupied. The peaks observed in the modal sound power are induced by the numerical instability when they are close to the cut-on frequencies of modes. The corresponding axial wave number is nearly zero when the Mach number is very low, i.e., $k_{mn} \doteq 0$ if $M_a \ll 1$; at this typical condition, the only way to decompose this mode is by placing sensors with sufficiently long distance.

In general, broadband modal decomposition appears to be highly sensitive to the mode coherence characteristics, CSA and RC-MDM methods deliver a comparable estimate of the incident modal sound power within the frequency range in which modes are almost mutually incoherent.

EXPERIMENTAL STUDY ON THE ACOUSTIC MODAL COHERENCE CHARACTERISTICS

Experimental Facility and Setup

One important aspect of this paper is to experimentally investigate the modal coherence distribution with respect to an axial fan test rig. A schematic of the experimental set-up is shown in **Figure 4**. It was designed with the intention to capture the most relevant acoustic features of an axial fan. On the inlet side there is a short duct section with a bell mouth nozzle and there are no flow straighteners or screens in the inlet duct. The single-stage axial fan consisting of 19 rotor blades and 18 stator vanes was driven at 3,000 rpm with the help of one motor providing 18.5 kW electric power. The diameter is 0.5 m, and the axial Mach number is 0.1. The outlet duct is equipped with an anechoic termination device; this condition strictly conforms to the international standard ISO 5136 for in-duct sound power determination. The number of stator vanes was designed such that the rotor–stator interaction tone at the blade passing frequency (BPF) is acoustically cut on.

In order to eliminate noise pollution in the experimental measurement, the acoustic environment of the experiment is particularly important. For example, when the standing wave formed by the external enclosed environment radiates into the duct, it will directly affect the experimental measurement of the fan inlet noise and reduce the signal-to-noise ratio of the acoustic signal. The fan inlet and the acoustic measurement section are placed inside the semi-anechoic chamber to reduce the influence of external reflected noise on the fan inlet noise test; perforated acoustic liners are installed on the inner and outer walls of the fan exhaust duct. The phase lock device (shown as a red square in **Figure 4**) used in this paper is a photoelectric sensor. The pulse signal can be used to capture the circumferential angle of the fan blade and also the real-time fan rotating speed; the accuracy can

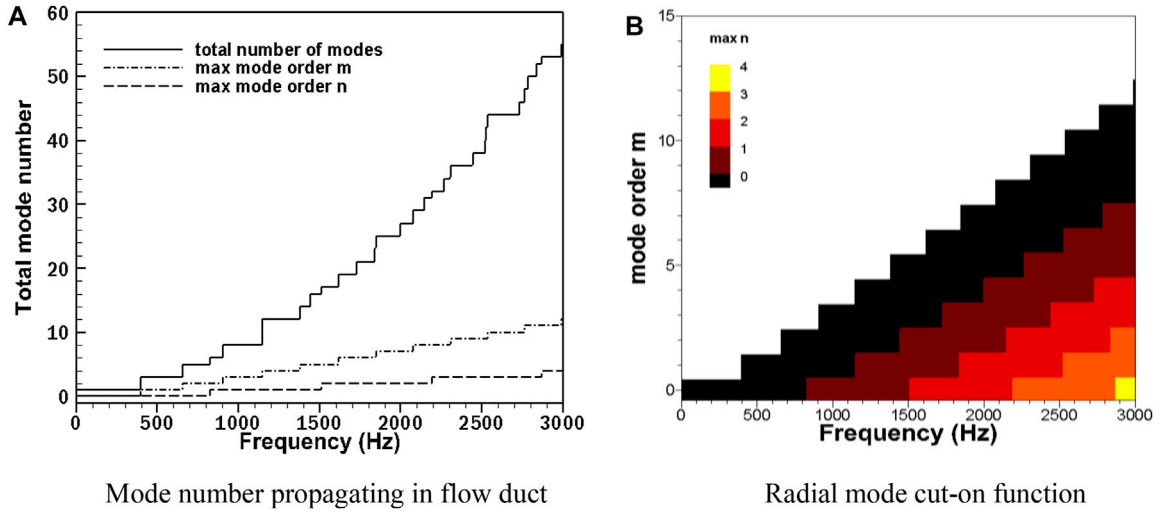

FIGURE 5 | Modal cut-on function of a single-stage axial fan: **(A)** shows the mode number propagating in the flow duct; **(B)** shows the radial mode cut-on function.

be guaranteed to be less than 2°. The sampling frequency is 16,384 Hz, and time series of a length of 60 FFT windows were used here, each window comprising 16,384 data samples. In order to meet the requirements of the designed method, the acoustic measurement section (shown as a red box in **Figure 4**) is divided into two measurement devices: part A and part B. Part A is a combined sensor array that includes a ring of 16 equiangular installed sensors and a row of 15 equidistant microphones. In part B, a rotating measurement system is designed to be driven by a stepper motor; two axial arrays, each consisting of 14 microphones with equal intervals, are installed in the rotating measurement system that can rotate 360° in the circumferential direction in the experiment.

Figure 5 shows the acoustic modal cut-on function of the fan duct. **Figure 5A** shows the total mode number propagating in the flow duct; the solid line, dash-dotted line, and dashed line indicate the total number of cut-on modes, maximum circumferential mode order, and maximum radial mode order, respectively. At 3,000 Hz, a total of 55 modes are able to propagate in the flow duct. Taking into account the forward and backward propagation of the modes, there will be 110 modal waves propagating in the duct, of which the maximum circumferential order is $m = \pm\ 12$ and the maximum radial mode order is $n = 4$. **Figure 5B** shows the radial mode details of each circumferential mode. As the frequency increases, more radial modes will be cut on in the duct. At 3,000 Hz, the circumferential mode $m = 0$ is composed of (0,0), (0,1), (0,2), (0,3), and (0, 4) modes.

Acoustic Modal Coherence Distribution of the Single-Stage Axial Fan

In the turbomachinery, the noise generated by rotor blades is a radially distributed sound source term. It is assumed that the ducted broadband sound field consists of fully incoherent modes, which are the important precondition of the broadband mode decomposition method presented by Enghardt (Enghardt et al., 2004). This assumption has not be verified experimentally so far for turbomachinery noise. Indeed, it is reasonable that specific modes are excited with high degree of coherence if certain conditions with respect to the spatial arrangement of sources are fulfilled; the compactness of the sources and the interference of the in-stationary aerodynamic forces also play an important role on modal coherence.

In the analysis of modal coherence function, the modal combinations are divided into two categories: in the first modal combination, the circumferential orders of modes are different from each other ($m \neq \mu$); the second type satisfies the same circumferential mode order but different radial mode order ($m = \mu$, $n \neq \nu$).

Coherence Coefficient Spectrum of m≠μ Modal Combination

The modal coherence coefficients are measured at four operation conditions: 90%, 92%, 96%, and 100% design speed in the single-stage axial fan noise experiment. It should be noted that, although the microphone in the test is equipped with a windshield, the pressure pulsation of the airflow will inevitably affect the sound pressure measurement. The coherence function between modal complex amplitudes will be affected accordingly; the result will not reach the upper and lower limits, i.e., 1 and 0 defined by the formula eventually. **Figure 6** shows the modal coherence coefficients of the first mode combination, the coherence coefficient is lower than 0.15 from 300 to 1,100 Hz. The test results can show that the modes of different circumferential orders are incoherent from each other, taking into account the influence of airflow pulsation and acoustic test error. At the BPF, the coherence coefficients of $m \neq \mu$ mode combinations rise to the maximum value as shown by the red dashed box; the value reaches to 1 nearly, for example, the peak appearing at 1BPF of 100% design speed condition shown in **Figure 6D**. It indicates that all modes in flow duct are completely coherent. As everyone knows that the tonal noise of

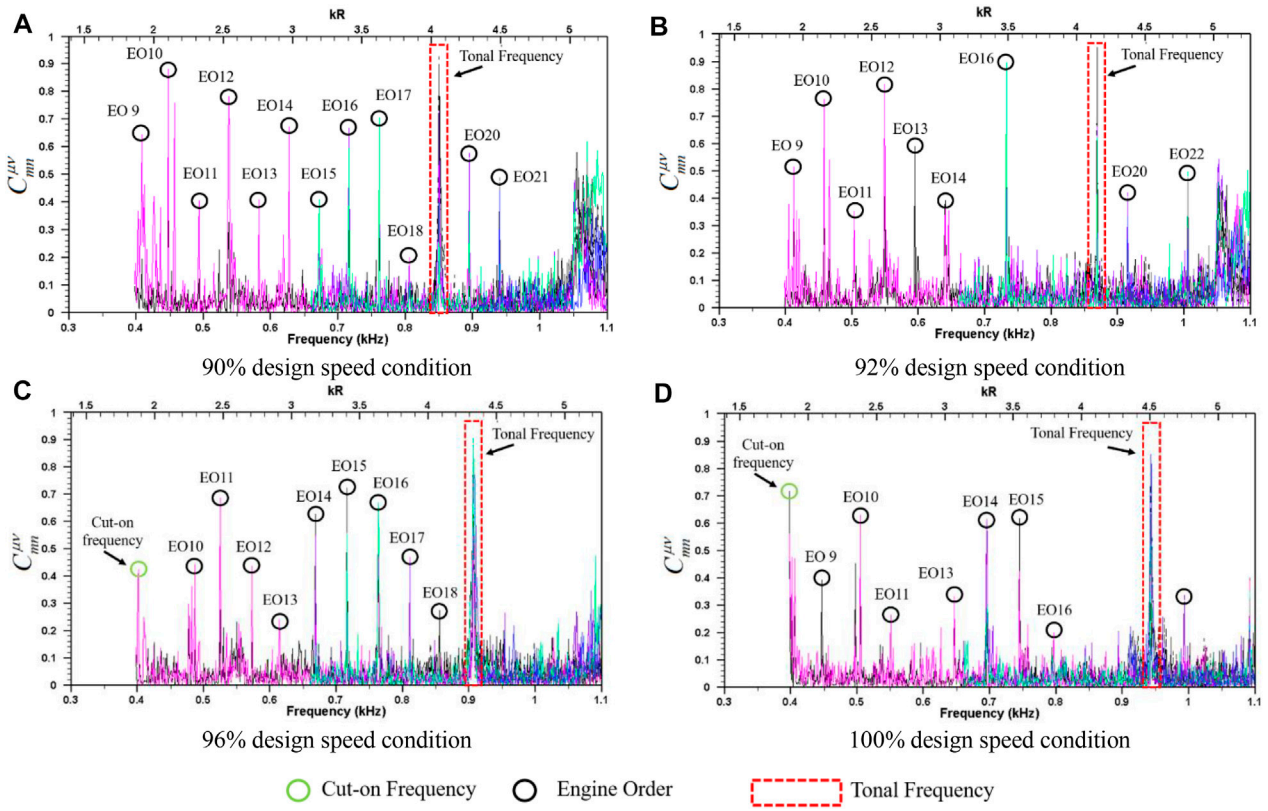

FIGURE 6 | Modal coherence coefficients of fan noise under four operating conditions: **(A–D)** show the modal coherence coefficients of fan noise under 90%, 92%, 96% and 100% design speed condition separately. represents the modal coherence coefficient between and modes.

axial fan is mainly caused by the unsteady aerodynamic force generated by the viscous wake of the upstream blade periodically interfering with the rotor or stator blades. Due to the clear generation mechanism of tonal noise, there is a strong degree of coherence between the internal modes of tonal noise, which is consistent with the coherence coefficient peaks appearing at the tonal noise frequencies in **Figure 6** at different operation conditions.

In addition to the peaks appearing at the tonal noise frequencies, multiple peaks at other frequencies also exist in the experimentally measured coherence coefficient results. The main reasons can be attributed to two categories: (a) when the frequency is close to the mode cut-on frequencies, due to the extreme eigenvalue generated in the process of matrix operation, the instability of numerical calculation leads to unreal complex modal amplitude. The modal coherence coefficients become exaggerated accordingly, which is represented by a green circle in **Figure 6**; (b) there are many peaks at the shaft frequency and its harmonics. For example, in **Figure 6C**, the fundamental shaft frequency (engine order [EO]) is 47.6 Hz; the modal coherence coefficients existing peak at 666, 714, 761.5, and 809 Hz. These frequencies correspond to EO14, EO15, EO16, and EO17, which are marked with black circles in **Figure 6**. The amplitudes of these coherence coefficient peaks are relatively small to that of tonal noise, and the occurrence frequencies are determined regularly. It can be considered to be the mechanical noise generated by the rotating shaft. Therefore, they have limited influence on the acoustic modal coherence characteristics of the flow duct.

Coherence Coefficient Spectrum of m = μ Mode Combination

Figure 7 shows the coherence coefficients of the second type of mode combination. At four operating conditions, the results of C_{00}^{01} show a trend of large oscillations around the value of 0.5, which indicates that fan noise has a high degree of coherence between the radial modes within the same circumferential mode order. The shape of coherence coefficient spectrum is very similar at different operating conditions, which shows that the C_{00}^{01} spectrum is very low sensitive to the tonal noise of flow fan. When the flow parameters of axial fan change, there is almost no obvious variation in the coherence coefficient magnitude and spectrum appearance, showing an approximately constant and regular characteristic.

For turbomachine aerodynamic noise, the hypothesis of the incoherence of internal modes has not been experimentally verified. The experimental results above show that the modes with different circumferential orders are statistically incoherent. As for the specific radial modes with the same circumferential order, the reason for appearing high relevance is closely related to the spatial distribution, compactness of the sound source, and also the individual sound source terms generated by the unsteady aerodynamic force. At low frequencies, a high degree of

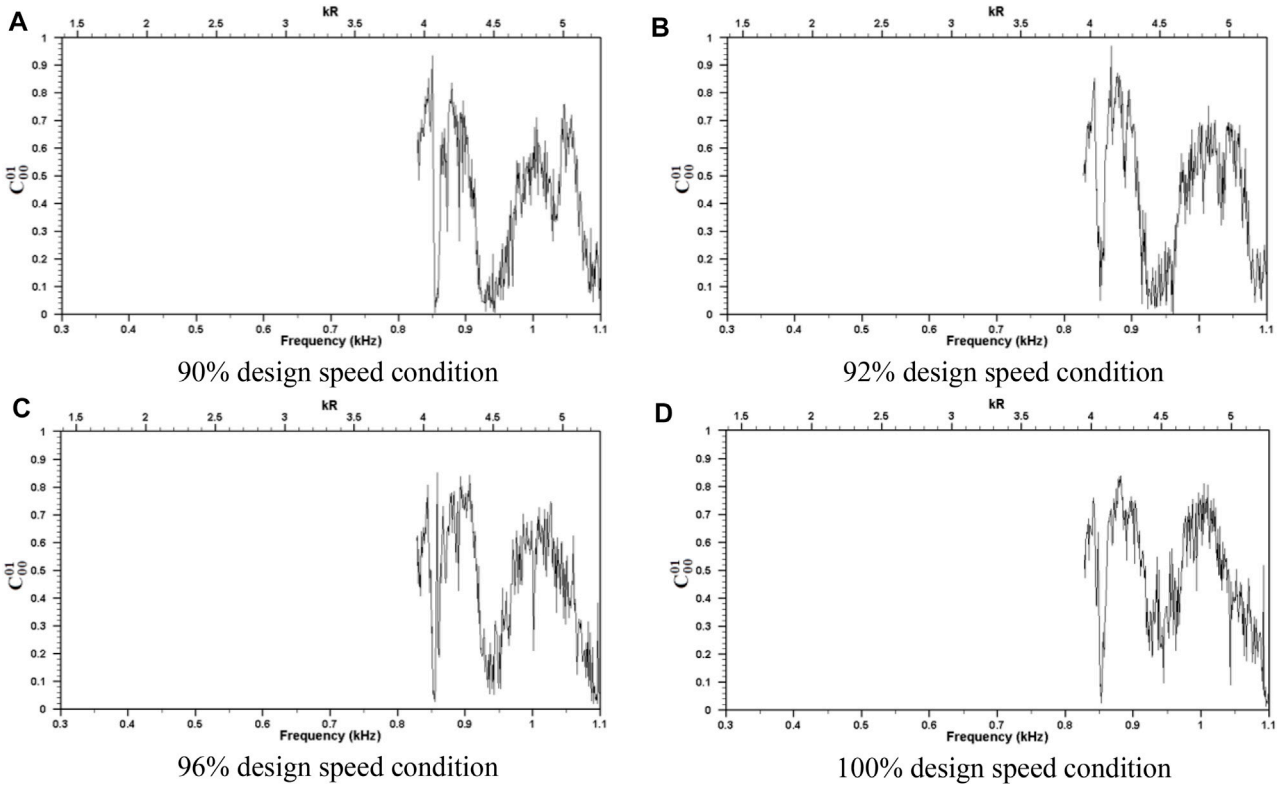

FIGURE 7 | Modal coherence coefficient between mode (0, 0) and mode (0, 1): **(A–D)** show the modal coherence coefficient between mode (0, 0) and mode (0, 1) under 90%, 92%, 96% and 100% design speed condition separately. represents the modal coherence coefficient between and modes.

coherence characteristics appears between the radial modes with the same circumferential order. This may be caused by the self-noise generation mechanism of the blade row, which means that each blade can be regarded as a compact sound source compared to a long sound wavelength at low frequencies. However, it can be expected that the coherence characteristics existing between some modes may change at high frequencies because the characteristic wavelength of the sound wave becomes shorter relative to the blade spanwise length.

Theoretical Analysis on Acoustic Modal Coherence Distribution at High Frequency

The *Characteristics of the Synthetized Sound Fields Section* and *Acoustic Modal Coherence Distribution of the Single-Stage Axial Fan* section investigated the modal coherence distribution between modes in synthetized sound fields and a single-stage axial fan and finally came to important conclusions. As the frequency gradually increases, the number of modes will increase exponentially, and the number of sound pressure measurement points required for experimental measurement will also increase exponentially; this requirement results in a great challenge to the acoustic experiment of turbomachines.

In this section, theoretical analysis methods will be used to further expand the research on the acoustic modal coherence in flow duct at high frequencies in the hope of drawing conclusions over a wider frequency range. The modal amplitude distribution function in the duct can be obtained by using three ducted sound source distribution models proposed in the *Ducted Sound Source Distribution Models* section. Based on the ducted noise propagation model, the sound pressure values at different positions of microphone array measurement can be obtained by complex modal sound pressure superposition; combined with the broadband noise modal coherence analysis method, it can be achieved to further investigate the modal coherence function in a theoretical way. The advantage of this research is that the modal amplitude obtained by the mode decomposition method can be used to verify the reliability of the model based on the preknowledge of the modal amplitude distribution function. The modal coherence is deliberated on the basis of successful verification to make the results more reliable.

The influence of different ducted sound source models on modal coherence is discussed first in theoretical analysis. **Figure 8** shows the modal coherence results of three sound source models at 5,412 Hz, in which the expected values are calculated with a statistical average process. A total of 170 modes are cut on in the flow duct at 5,412 Hz, including the maximum circumferential order $m_{\max} = \pm 22$ and the maximum radial order $n_{\max} = 7$. The microphone array is composed of 20 rings of measuring points; each ring is equipped with 50 equiangular microphones. The coherence coefficients of modes (m, n) and (μ, ν) are expressed as $C_{mn}^{\mu\nu}$; the two modes are distinguished by α_{mn} and $\alpha_{\mu\nu}$, the range of

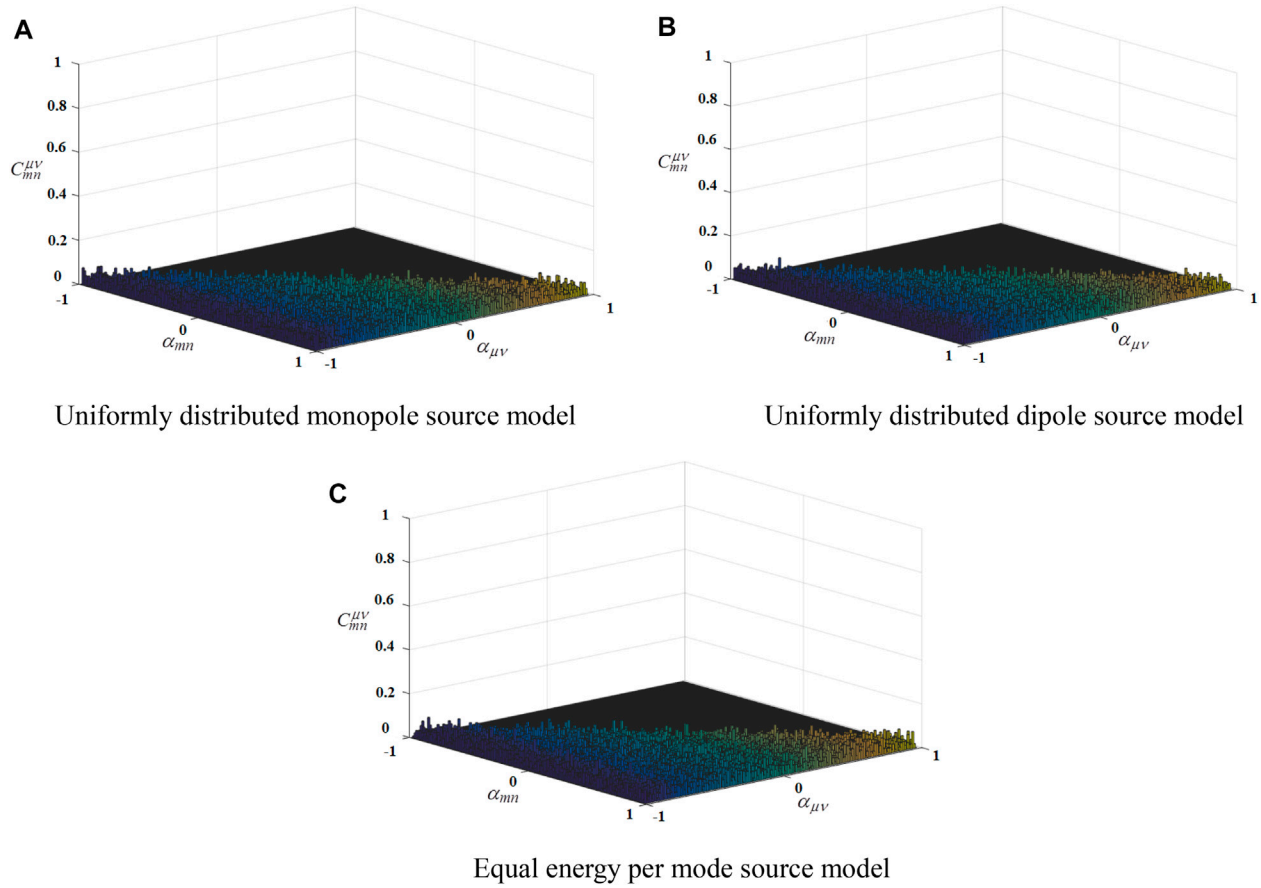

FIGURE 8 | Modal coherence results of three sound source distribution models: **(A)** shows the results of uniformly distributed monopole source model; **(B)** shows the results of uniformly distributed dipole source model; **(C)** shows the results of equal energy per mode source model. represents the modal coherence coefficient between and modes.

which is zero to one, referring to **Eq. 19**. In order to distinguish the forward modes (the modal circumferential order is positive, m > 0) and reverse modes (the modal circumferential order is negative, m < 0), the modal cut-on ratio of reverse modes is set to negative values. Then, all the modes in the duct can be expressed as a single-valued function of the modal cut-on ratio, and the value range becomes −1 to +1. It can be seen in **Figure 8** that the coherence coefficients of all modes are lower than 0.1, that is to say the modes are mutually incoherent. By comparing the modal coherence coefficient results of the three ducted sound source models (monopole source model, dipole source model, EEPM source model), it can be found that the coherence results of the three sound source distribution models are very consistent, which shows that it is not necessary to study all the three sound source distribution models, but only one of them can be used to achieve the purpose of further study on modal coherence coefficients.

Figure 9 shows the modal coherence coefficients of different radial modes within the circumferential mode m = 0, m = 1 and m = 2 at 5,412 Hz. Abscissa n and ν represent different radial mode orders, respectively, and ordinate $C_{mn}^{m\nu}$ represents the coherence coefficients of (m, n) mode and (m, ν) mode. According to formula (19), the main diagonal element in **Figure 9** corresponds to the autocorrelation coefficient of the mode. The numerical result of the main diagonal is close to 1, which is consistent with the theory. The coherence coefficients between different radial modes are all less than 0.1, which indicates that the different radial modes are mutually incoherent. Compared with the experimental results of acoustic modes in the *Coherence Coefficient Spectrum of m = μ Mode Combination* section, the modal coherence coefficient becomes more concise in this section; this is because the sound field in the theoretical study is artificially generated by the ducted sound source models, and there is no aerodynamic self-noise in theoretical analysis. The results further illustrate that high degree of coherence appearing between individual modes is due to the fact that the fan rotor blades and stator vanes are radial compact sound sources.

In this section, three kinds of ducted sound source distribution models are established, and the modal coherence characteristics at high frequencies are investigated theoretically for the first time by using the artificially constructed ducted sound fields. The results show

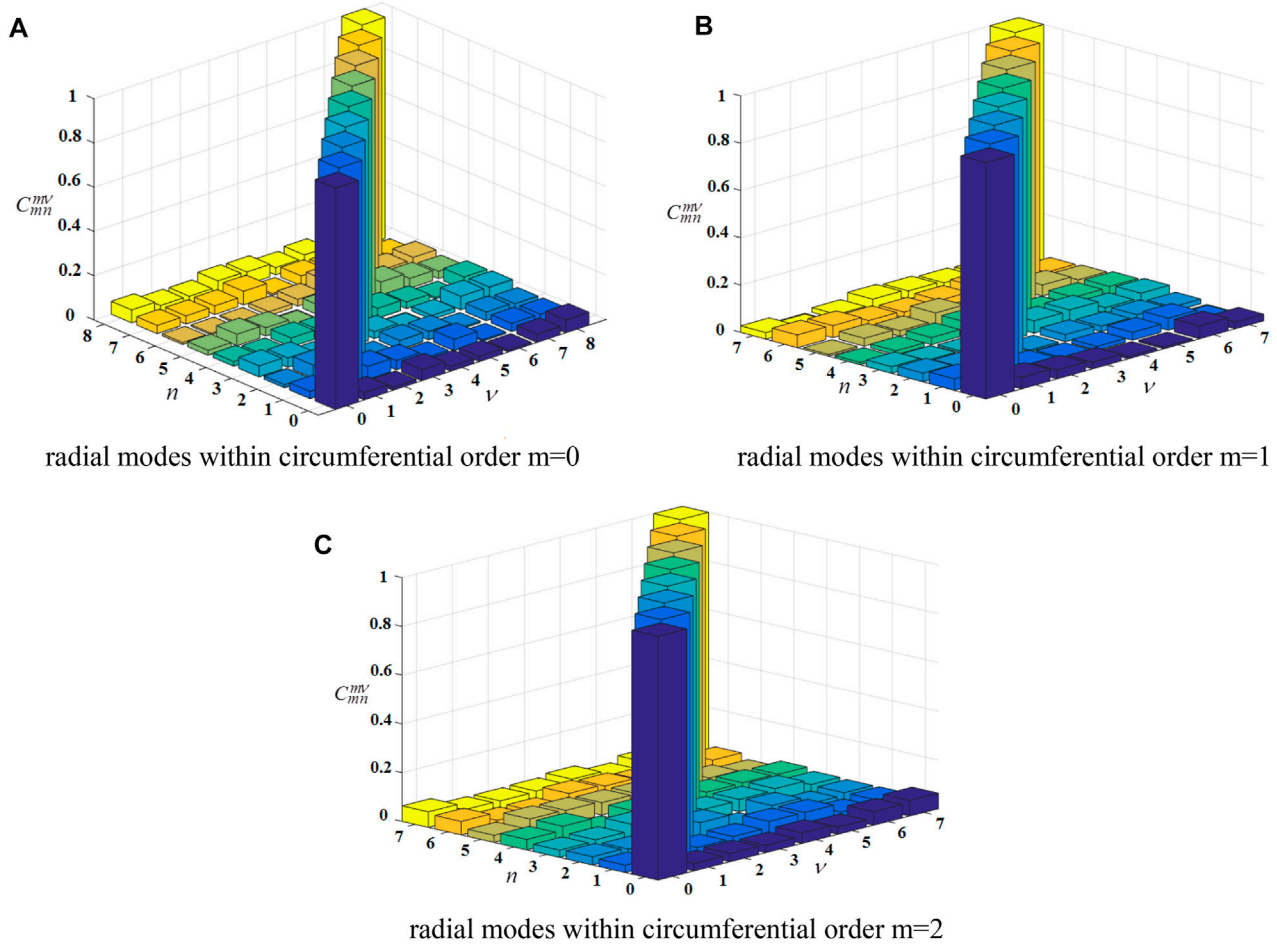

FIGURE 9 | Modal coherence results between radial modes with same circumferential order: **(A–C)** show the radial modes within circumferential order m=0, m=1, m=2 separately. represents the modal coherence coefficient between and modes.

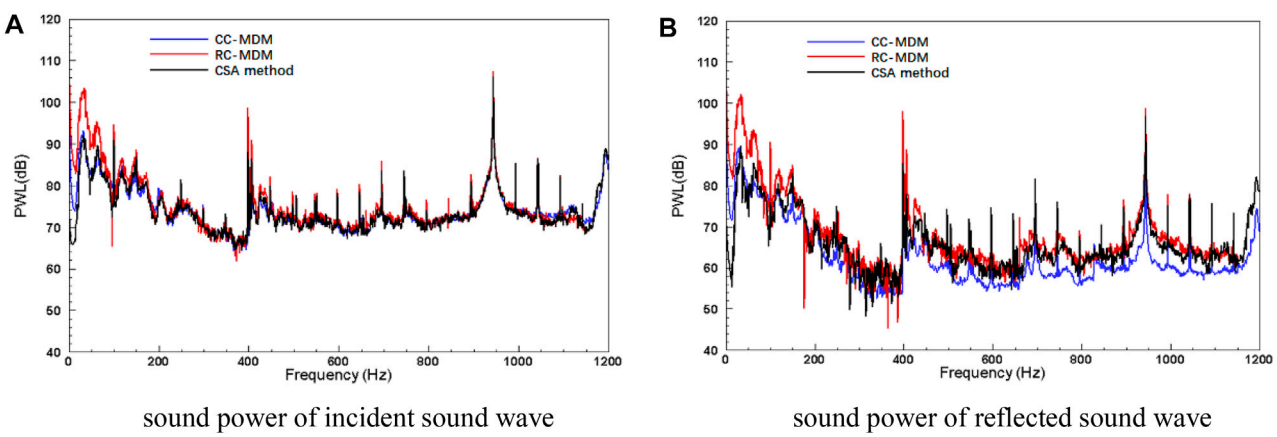

FIGURE 10 | Comparison of sound power results calculated by different mode decomposition methods: **(A)** shows the sound power of incident sound wave; **(B)** shows the sound power of reflected sound wave. Blue line, red line and black line represents the results applying CC-MDM, RC-MDM and CSA method separately.

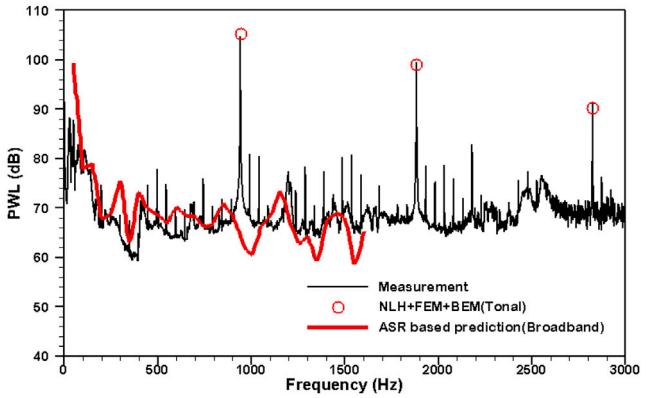

FIGURE 11 | Broadband mode decomposition with rotating sensor arrays.

that all the modes are incoherent at different frequencies, and the modal coherence characteristics are independent of the sound source distribution models. The coherence characteristics of the three ducted sound source models are approximately the same. At high frequencies, the radial modes within the same circumferential mode are incoherent to each other.

Broadband Modal Distribution Results

Different modal identification methods (RC-MDM, CSA method) make relevant assumptions and simplifications about the modal coherence; the influence of this simplified treatment on the sound power and modal amplitude distribution of turbomachinery ducted noise field, which we are most concerned about, needs to be further studied. **Figure 10** shows the sound power results of incident and reflected sound waves calculated by different modal decomposition methods. The red and blue lines represent the computed sound power results calculated by the RC-MDM and CC-MDM, respectively, and the black line represents the sound power results computed by the CSA method. A series of simplifications of complex modal amplitude cross-terms are carried out in CSA and RC-MDM methods. It can be seen from **Figure 10** that the shape of sound power spectral calculated by the three methods are consistent with each other, both in the incident and reflected sound waves.

The cross-terms $C_{mn}^{\mu\nu}$ of modal complex amplitudes are retained completely in the CC-MDM, which make its calculation results more reliable. However, the need to compute the modal cross-terms makes the calculating process more time-consuming compared with RC-MDM and CSA methods, and this method requires much more sensors to synchronously measure the sound pressure in the experiment. The latter feature becomes unaffordable at higher frequencies because the required measuring points multiply exponentially with increased frequency. RC-MDM and CSA methods have attracted more and more attention due to their stronger practicability. The acoustic sound power of the incident sound wave is nearly 10 dB higher than that of the reflected sound wave. In the sound power spectra of the incident sound wave, the maximum deviation of three methods is only 1 dB. In the sound power spectrum of reflected acoustic waves, although the spectrum trend of the three methods is similar, there are significant differences in the magnitude of sound levels. The calculated results of the RC-MDM (red line) and CSA (black line) are in good agreement. However, there is a deviation of nearly 3 dB compared with the outcome of the CC-MDM. This is because the time-averaged modal cross-terms in RC-MDM and CSA methods are forced to be suppressed. In the calculation process of broadband mode identification, the energy of the modal cross-term is artificially imposed into the square-term of the modal amplitudes. This results in reflected sound waves predicted by the RC-MDM and CSA methods being 3 dB higher than the CC-MDM. Based on the successful application of a fixed sensor array, **Figure 10** shows that the modal coherence characteristic has little influence on the prediction of incident sound waves. In order to further investigate the inner mechanism of modal coherence, the rotating sensor arrays shown as part B in **Figure 4** were used in turbomachinery broadband noise measurement.

Under the framework of Sino-European cooperation, the NUMECA is the name of an internationally renowned computational fluid dynamics business company, conducted a numerical acoustic simulation on the single-stage axial fan duct device used in this research. As shown in **Figure 11**, the broadband mode decomposition result calculated by the RC-MDM with rotating sensor arrays is marked as a black solid line; the thick red line is the predicted broadband noise result calculated by NUMECA, using the adaptive spectral reconstruction method. The red circle symbol indicates the predicted tonal noise result. The results of the broadband noise spectrum are in good agreement in the frequency range (50–1,600 Hz), and the overall magnitude is around 68 dB. The broadband noise spectral characteristics are also very consistent at a special frequency, for example, the leap in sound power spectra at 400 Hz. In the tonal noise part, less than 1 dB deviation appears at 1BPF, and less than 0.5 dB arises at 2BPF. At 3BPF, the deviation increases to 1.5 dB. In general, fan noise measurements based on RC-MDM method using the rotating microphone array can be added to the aircraft turbomachinery noise database as standard data, which can provide evaluation and verification criteria for other broadband noise measurement methods or numerical simulation algorithms.

Figure 12 shows the sound power distribution of the incident and reflected modes of fan broadband noise identified by the rotating microphone array. The abscissa is set as the circumferential mode order m, ranging from −12 to +12, and the ordinate is set as the frequency, ranging from 0 to 3,000 Hz. In order to display the sound power results of incident and reflected sound waves more clearly, the legend range of incident sound waves is set to 40–80 dB, while the value of reflected sound waves is set to 35–75 dB, 5 dB lower than incident waves. When the fan operating speed is 3,000 rpm, the 1BPF and 2BPF tones are clearly visible in

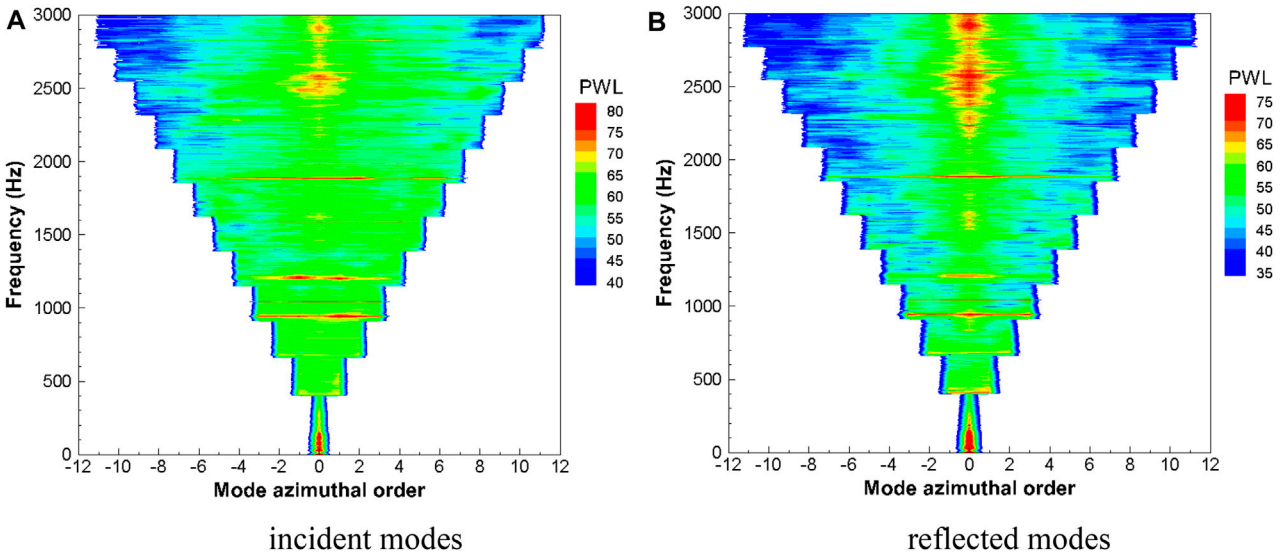

FIGURE 12 | Broadband modal sound power distribution: **(A)** shows the modal sound power distribution map of incident modes; **(B)** shows the modal sound power distribution map of reflected modes.

the incident sound waves; the sound power is mainly concentrated in the −6~+6 circumferential modes. The 1BPF and 2BPF tonal tones can still be seen in the reflected sound waves, but different from the incident sound wave, the dominant mode in the reflected sound wave is not the rotor–stator interference modes but the plane sound wave. In the whole frequency range of reflected sound waves, the modal acoustic power is mainly concentrated in the −2~+2 circumferential modes, and is approximately distributed symmetrically with the m = 0 mode as the center. This paper uses an equally spaced axial array to test the fan noise. For large ventilation facilities, this kind of device is often difficult to meet. How to use the obtained modal coherence characteristics to design a new test method needs further research, and the correlation between error characteristics in mode identification and microphone array design aspects also requires further study.

CONCLUSION

In this paper, the modal coherence characteristics of turbomachinery noise are studied in detail for the first time. The distribution characteristics of complex acoustic pressure in the flow duct are studied by constructing the ducted sound fields artificially, establishing three kinds of ducted sound source distribution models and an acoustic testing of a single-stage axial fan.

The simulation results of artificially constructed ducted sound fields show that the broadband noise power calculated by the RC-MDM, CSA, and CC-MDM are in good agreement. Due to the simplified processing of acoustic modal coherence characteristics, the RC-MDM and CSA methods are extremely sensitive to the phase variation precision of modal wave propagation in the axial direction. Therefore, it is necessary to design microphone arrays with sufficient axial measurement positions for accurately measuring the phase variation resulting from acoustic modal wave axial propagation. The modal coherence characteristics of ducted noise at high frequencies are investigated by establishing three kinds of ducted sound source distribution models. The results are consistent with the acoustic experimental results of a single-stage axial fan. The results show that the acoustic modes of different orders are mutually incoherent, and the radial modes within the same circumferential mode have a great degree of coherence.

It was demonstrated that the experimentally measured mode coherence functions give an inner sense of the spatial noise source distribution and enable the investigation of mode scattering within the propagation. In order to further study the influence of the distribution characteristics of modal coherence on the mode identification of turbomachinery noise, this paper successfully conducted acoustic measurement on turbomachinery noise by rotating microphone arrays. The acoustic experimental results show that the coherence of some modes has little impact on the measurement of incident acoustic waves in the flow duct, while it leads to about 3dB deviation in the prediction of reflected modal sound power and has little influence on the spectral shape of reflected acoustic waves. The acoustic modal distribution results show that the incident mode waves are mainly concentrated in the m = -6 to m = +6 modes; the reflected acoustic waves are concentrated in the m = −2 to m = +2 mode and are approximately distributed symmetrically around the m = 0 mode. In conclusion, although some internal modes of turbomachinery-ducted noise have strong coherence characteristics, the influence of such characteristics on the

acoustic measurement of turbomachinery-ducted noise can be ignored. Based on the modal coherence characteristics obtained in this paper, more theoretical and methodological studies can be carried out for the turbomachinery broadband noise test.

DATA AVAILABILITY STATEMENT

The raw data supporting the conclusion of this article will be made available by the authors, without undue reservation.

AUTHOR CONTRIBUTIONS

KX is responsible for the whole project. CL is responsible for the experiment and the data processing. FT is responsible for the numerical investigation and also the experimental plan design. WQ designs the structure of the thesis and propose suggestions.

FUNDING

This work was financially supported by National Natural Science Foundation of China (Grant No.12002150), also supported by The Ministry of education of Humanities and Social Science project (Grant No. 20YJCZH196), also supported by Natural Science Foundation of Jiangsu Province, China (Grant No. BK20201041), also supported by Key Laboratory of Aerodynamic Noise Control of China Aerodynamics Research and Development Center (Grant No. ANCL20190306), also supported by Scientific Research Fund of high-level talents in Nanjing Institute of Technology (Grant No. YKJ201906).

REFERENCES

Bolleter, U., and Crocker, M. J. (1972). Theory and Measurement of Modal Spectra in Hard-Walled Cylindrical Ducts. *The J. Acoust. Soc. America.* 51, 1439–1447. doi:10.1121/1.1912994

Bu, H., Huang, X., and Zhang, X. (2020). A Compressive-Sensing-Based Method for Radial Mode Analysis of Aeroengine Fan Noise. *J. Sound Vibration.* 464, 114930. doi:10.1016/j.jsv.2019.114930

Dyer, I. (1958). Measurement of Noise Sources in Ducts. *J. Acoust. Soc. America.* 30, 833–841. doi:10.1121/1.1909783

Enghardt, L., Holewa, A., and Tapken, U. "Comparison of Different Analysis Techniques to Decompose a Broadband Ducted Sound Field in its Mode Constituents [C]," in 13th AIAA/CEAS Aeroacoustics Conference, AIAA-2007-3520.

Enghardt, L., Lowis, C., and Neuhaus, L. (2004). "Broadband Sound Power Determination in Flow Ducts [C]," in 10th AIAA/CEAS aeroacoustic conference, AIAA-2004-2940. Manchester, UK.

Ganz, U. W., Joppa, P. D., Patten, T. J., and Scharpf, D. F. (1998). *Boeing 18-inch Fan Rig Broadband Noise Test.* Seattle: NASA. Technical Report CR-1998-208704.

Jeong, W., Lee, S., and Joseph, P. (2006). A wall-mounted Source Array for the Excitation of Incoherent Broadband Sound fields with Prescribed Modal Distributions in Ducts [J]. *J. Sound Vibration.* 290 (1), 490–499. doi:10.1016/j.jsv.2004.12.025

Joseph, P., Morfey, C. L., and Lowis, C. R. (2003). Multi-mode Sound Transmission in Ducts with Flow. *J. Sound Vibration.* 264 (3), 523–544. doi:10.1016/s0022-460x(02)01205-1

Joseph, P., and Morfey, C. L. (1999). Multimode Radiation from an Unflanged, Semi-infinite Circular Duct. *J. Acoust. Soc. America* 105 (5), 2590–2600. doi:10.1121/1.426875

Jürgens, W., Pardowitz, B., and Enghardt, L. (2011). "Separation of Broadband Noise Sources in Aeroengine Ducts with Respect to Modal Decomposition," in 17th AIAA/CEAS aeroacoustic conference. AIAA-2011-2879. Portland, USA.

Jürgens, W., Tapken, U., Pardowitz, B., Kausche, P., Bennett, G. J., and Enghardt, L. "Technique to Analyse Characteristics of Turbomachinery Broadband Noise Sources [C]," in 16th AIAA/CEAS Aeroacoustics Conference, AIAA-2010-3979.

Kim, Y., and Nelson, P. A. (2004). Estimation of Acoustic Source Strength within a Cylindrical Duct by Inverse Methods [J]. *J. Sound Vibration.* 275 (1-2), 391. doi:10.1016/j.jsv.2003.06.032

Kopiev, V. F., Bersenev, Y. V., Viskova, T. A., Burdakov, R. V., Palchikovskiy, V. V., Belyaev, I. V., et al. (2017). Azimuthal Modes Measurement in an Intake Duct for a Turbofan Engine. *Proced. Eng.* 176, 273–277. doi:10.1016/j.proeng.2017.02.319

Michalke, A., Arnold, F., and Holste, F. (1996). On the Coherence of the Sound Field in a Circular Duct with Uniform Mean Flow. *J. Sound Vibration.* 190 (2), 261–271. doi:10.1006/jsvi.1996.0061

Moore, C. J. (1979). Measurement of Radial and Circumferential Modes in Annular and Circular Fan Ducts. *J. Sound Vibration.* 62 (2), 235–256. doi:10.1016/0022-460x(79)90024-5

Morfey, C. L. (1971). Sound Transmission and Generation in Ducts with Flow. *J. Sound Vibration.* 14 (1), 37–55. doi:10.1016/0022-460x(71)90506-2

Nelson, P., and Yoon, S. (2000). Estimation of Acoustic Source Strength by Inverse Method: Part I, Conditioning of the Inverse Problem [J]. *J. Sound Vibration.* 233 (4), 643–668. doi:10.1006/jsvi.1999.2837

Sijtsma, P., and Brouwer, H. (2018). Deconvolution of Azimuthal Mode Detection Measurements. *J. Sound Vibration.* 422, 1–14. doi:10.1016/j.jsv.2018.02.029

Tapken, U., Gutsche, D., and Enghardt, L. (2014). "Radial Mode Analysis of Broadband Noise in Flow Ducts Using a Combined Axial and Azimuthal Sensors Array [C]," in 20th AIAA/CEAS Aeroacoustics Conference. Atanta, GA. AIAA-2014-3318

Xu, K. B., Qiao, W. Y., and Huo, S. Y. (2017a). Experimental of Fan Broadband Noise Determination Based on Rotating Axial Arrays. *J. Acta Aeronautica Astronautica Sinica* 38 (11), 121–132. doi:10.7527/S1000-6893.2017.121132

Xu, K. B., Qiao, W. Y., and Chang, X. Y. (2017b). Fan Broadband Noise Based on Combined Sensor Array Method. *J. Acta Aeronautica Astronautica Sinica.* 38 (12), 121324. doi:10.7527/S1000-6893.2017.121324

Xu, K. B., Qiao, W. Y., and Huo, S. Y. (2018). Research of Mode Identification and Error Transfer Property on Fan Tonal Noise [J]. *J. Propulsion Technology.* 39 (1), 185–195. doi:10.13675/j.cnki.tjjs.2018.01.021

Xu, K. B., Qiao, W. Y., and Wang, L. F. (2015). Experimental Research of Broadband Sound Power Determination in Axial Fan [J]. *Acta Aeronautica et Astronautica Sinica.* 36 (9), 2939–2946. doi:10.7527/S1000-6893.2015.0080

Yu, W., Ma, Z., Lau, A. S. H., and Huang, X. (2018). Analysis and Experiment of the Compressive Sensing Approach for Duct Mode Detection. *AIAA J.* 56 (2), 648–657. doi:10.2514/1.j056347

Conflict of Interest: The authors declare that the research was conducted in the absence of any commercial or financial relationships that could be construed as a potential conflict of interest.

Publisher's Note: All claims expressed in this article are solely those of the authors and do not necessarily represent those of their affiliated organizations, or those of the publisher, the editors and the reviewers. Any product that may be evaluated in this article, or claim that may be made by its manufacturer, is not guaranteed or endorsed by the publisher.

frontiers | Frontiers in Energy Research

ORIGINAL RESEARCH
published: 19 April 2022
doi: 10.3389/fenrg.2022.894258

A PANS Method Based on Rotation-Corrected Energy Spectrum for Efficient Simulation of Rotating Flow

Benqing Liu[1,2], *Wei Yang*[1,2]* *and Zhuqing Liu*[1,2]

[1]College of Water Resources and Civil Engineering, China Agricultural University, Beijing, China, [2]Beijing Engineering Research Centre of Safety and Energy Saving Technology for Water Supply System, Beijing, China

A partially averaged Navier–Stokes method with a new expression of f_k based on the rotation-corrected energy spectrum is proposed. It is coupled with the shear-stress transport turbulence model to simulate two typical rotating flows: rotating channel flow and flow in a centrifugal pump impeller. The results of two traditional energy spectrum-based f_k expressions (ES1 and ES2) and DNS/experimental results are used for comparison. The results show that the f_k distribution predicted based on the rotation-corrected energy spectrum is more reasonable. In the region with enhanced turbulence, more turbulence scales exist, such as the pressure side in the rotating channel flow, where the f_k value is low and more turbulence scales are resolved. While in the region with suppressed turbulence, fewer turbulence scales exist, such as the suction side, where the f_k value is relatively high. The model with a new f_k expression can produce better results since it can give a more reasonable f_k distribution. At the same time, the new model is more efficient since it shows better calculation performance with the same mesh scale and low cost with comparable calculation performance.

Keywords: PANS, energy spectrum, turbulence model, rotating flow, centrifugal pump

OPEN ACCESS

Edited by:
Kan Kan,
College of Energy and Electrical Engineering, China

Reviewed by:
Tianyi Li,
University of Minnesota Twin Cities, United States
Leilei Ji,
Jiangsu University, China

***Correspondence:**
Wei Yang
wyang@cau.edu.cn

Specialty section:
This article was submitted to Process and Energy Systems Engineering, a section of the journal Frontiers in Energy Research

Received: *11 March 2022*
Accepted: *21 March 2022*
Published: *19 April 2022*

Citation:
Liu B, Yang W and Liu Z (2022) A PANS Method Based on Rotation-Corrected Energy Spectrum for Efficient Simulation of Rotating Flow. Front. Energy Res. 10:894258. doi: 10.3389/fenrg.2022.894258

INTRODUCTION

Rotating machinery, such as pumps and turbines, is widely used in engineering practice (Thangam et al., 1999), and their internal flow has large curvature and high rotation speed characteristics. These flow characteristics that play an important role in the performance need to be investigated in-depth (Huang X. et al., 2019), and the relationship between the external characteristics of the centrifugal pump and the internal flow state needs further study (Lin et al., 2022). For internal flow investigation, the computational fluid dynamics (CFD) method plays an efficient and reliable role in the simulation of complex flows (Zhang et al., 2020). In CFD, the Navier–Stokes equation is a mathematical expression that can adequately describe the motion of fluids. The direct numerical simulation (DNS) method concerns the direct application of this equation; thus, it can solve all turbulent flow fields. Nevertheless, according to Kolmogorov's theory (Pope, 2000), when the DNS method is used, the length scale $\eta = (\nu^3/\varepsilon)^{1/4}$ and time scale $\tau_\eta = (\nu/\varepsilon)^{1/2}$ are very small, where ν is the kinematic viscosity and ε is the dispassion of turbulent kinetic energy. Consequently, the DNS method cannot be used to simulate the internal flow of rotating machinery with a high Reynolds number because of the unacceptable simulation cost. The large-eddy simulation (LES) method is used to resolve large vortices directly and model the small ones (Pope, 2000). Various studies have demonstrated that to

simulate complex flows with multiple walls, LES requires meshes with an extremely high amount of elements, which leads to a very high number of calculations, making LES not suitable for engineering calculations. Currently, the Reynolds-averaged Navier–Stokes (RANS) method is widely used for its high performance-to-cost ratio (Pope, 2000). However, in the modeling process, the RANS method omits some key information, such as turbulence pulsation; thus, it is associated with some deficiencies when it comes to the simulation of flow with rotation and curvature characteristics. As a result, the balance between calculational accuracy and simulation cost is the main challenge for the turbulence models. In this aspect, hybrid models such as the partially averaged Navier–Stokes (PANS) model have shown their advantages.

Girimaji et al. (2003) proposed the PANS method, which is based on the ratio of the modeled to resolved turbulent kinetic energy, through which the conversion from DNS to RANS can be achieved. In the PANS method, the control parameters for bridging DNS and RANS are f_k and f_ε (Girimaji, 2006; Girimaji et al., 2006) which are the modeled-to-total ratio of the turbulent kinetic energy and its dissipation, respectively. At high Reynolds number flows, there is little dissipation in the resolved scales; thus, it is reasonable that f_ε is set to unity (Girimaji et al., 2006; Lakshmipathy and Girimaji, 2010). When f_k equals unity, the PANS model degrades to a RANS model, while when f_k equals 0, it indicates a DNS simulation. For flows with a high Reynolds number, a reasonable f_k distribution is a key factor for the PANS method. Based on different theories, several scholars have proposed different expressions of f_k. For example, Abdol-Hamid and Girimaji (2004) introduced an original two-stage procedure to calculate f_k, while Song and Park (2009) and Foroutan and Yavuzkurt (2014) deduced two different f_k formulations based on different energy spectra. Hu et al. (2014) proposed a modified f_k expression for unsteady cavitating flows, where f_k varies as a function of water density and mixture density. In a simulation of the flow around a Clark-Y hydrofoil, their modified model can accurately predict the cavity evolution, vortex shedding frequency, and lift force fluctuation. More recently, Wang et al. (2020) proposed a novel Omega-driven dynamic model, where control parameter f_k is automatically adjusted by the rigid vorticity ratio, and the results on three typical flows demonstrated that their model can improve the prediction accuracy.

At present, there is no general expression of parameter f_k, and it is based on specific flow characteristics. According to the definition of f_k, its expression based on the energy spectrum is more reasonable, and studies have indicated that the expression of the energy spectrum in a rotating flow differs from that in an ordinary (non-rotating) flow. Zeman (1994) investigated the spectral energy transfer in rotating homogeneous turbulence and found that the wavenumber $\kappa_\Omega = (\Omega^3/\varepsilon)^{1/2}$ determines the turbulence length scale and affects the spectral transfer and energy spectrum form in rotating flows, where κ_Ω is the Zeman number, and Ω denotes the rotation speed. Baroud et al. (2002) measured a rotating annulus and revealed that the energy cascade in rotating flow is $E(\kappa) \sim \kappa^{-2}$ rather than the expected one, which is $E(\kappa) \sim \kappa^{-5/3}$. By simulating a helical shell model, Rathor et al. (2020) confirmed that with the decreasing Rossby number, which corresponds to an increasing level of rotation, the compensated spectrum to the left of the Zeman scale (Zeman, 1994) departs from the plateau with an additional scaling factor that asymptotes to $E(\kappa) \sim \kappa^{-2}$. Canuto and Dubovikov (1997); Zhou (1995) obtained the same result through theoretical derivation. Thangam et al. (1999) proposed a model that combines an eddy viscosity model with the rotation-corrected energy spectrum. Their new model can reproduce the rotating effect of rotating homogeneous shear and rotating channel flows, which confirms the rationality of the rotation-corrected energy spectrum.

Since there is no f_k expression based on the rotation-corrected energy spectrum yet for the efficient simulation of the complex flow with rotation effect in the rotating machinery, in this paper, a new f_k expression based on the rotation-corrected energy spectrum is deduced and coupled with the PANS model. The PANS model with the new f_k expression is verified in the rotating channel flow. Then it is applied to flow simulation of a centrifugal pump impeller with complex flows of rotating stall and flow separation for further validation.

GOVERNING EQUATIONS

The PANS model

In the following analysis, the SST PANS model (Luo et al., 2014; Ranjan and Dewan, 2015; Pereira et al., 2015; Ranjan and Dewan, 2016; Pereira et al., 2018; Qian et al., 2020) is used. The transport equations of the SST PANS model are as follows:

$$\frac{\partial k_u}{\partial t} + u_j\frac{\partial k_u}{\partial x_j} = \widetilde{P_{ku}} - \beta^* k_u\omega_u + \frac{\partial}{\partial x_j}\left((\nu + \sigma_{ku}\nu_u)\frac{\partial k_u}{\partial x_j}\right), \tag{1}$$

$$\frac{\partial \omega_u}{\partial t} + u_j\frac{\partial \omega_u}{\partial x_j} = \frac{\gamma}{\nu_u}\widetilde{P_{ku}} - \frac{\gamma}{\nu_u}\beta^*\left(1 - \frac{1}{f_\omega}\right)k_u\omega_u - \frac{\beta\omega_u^2}{f_\omega} + 2(1 - F_{1u})\sigma_{\omega 2}\frac{1}{\omega_u}\frac{\partial k_u}{\partial x_j}\frac{\partial \omega_u}{\partial x_j}\frac{f_\omega}{f_k} + \frac{\partial}{\partial x_j}\left((\nu + \sigma_{\omega u}\nu_u)\frac{\partial \omega_u}{\partial x_j}\right), \tag{2}$$

$$\nu_u = \frac{a_1 k_u}{\max(a_1\omega_u, F_{2u}S)}, \tag{3}$$

where u is the partially averaged velocity; partial averaging corresponds to filtering a portion of the fluctuating scales (Girimaji, 2006), and throughout the study, the words filtering and averaging will be used synonymously. k_u is the unresolved turbulent kinetic energy, ω_u is the unresolved specific dissipation rate, f_ω is the modeled-to-total ratio of the specific turbulence dissipation and $f_\omega = 1/f_k$, υ is the kinematic viscosity, ν_u is the unresolved eddy viscosity, S is the invariant measure of the strain rate, $\tilde{P}_{ku} = \min(P_{ku}, 10\beta^* k_u\omega_u)$ is the production term, $P_{ku} = \nu_u\frac{\partial u_i}{\partial x_j}\left(\frac{\partial u_i}{\partial x_j} + \frac{\partial u_j}{\partial x_i}\right)$, and a_1, β, β^*, $\sigma_{\omega 2}$, and γ are constant coefficients. Moreover, σ_{ku} and $\sigma_{\omega u}$ are Prandtl numbers, and their specific forms are as follows:

$$\sigma_{ku} = \sigma_k \frac{f_\omega}{f_k}, \sigma_{\omega u} = \sigma_\omega \frac{f_\omega}{f_k}. \tag{4}$$

In addition, F_{1u} and F_{2u} are two blending functions for the SST PANS model, which are defined as follows:

$$F_{1u} = \tanh\left[\left(\min\left[\max\left(\frac{\sqrt{k_u}}{\beta^* \omega_u y}, \frac{500\nu}{y^2\omega_u}\right), \frac{4\sigma_{\omega 2u} k_u}{CD_{k\omega} y^2}\right]\right)^4\right], \tag{5}$$

$$F_{2u} = \tanh\left[\left(\max\left(\frac{2\sqrt{k_u}}{\beta^* \omega_u y}; \frac{500\nu}{y^2\omega_u}\right)\right)^2\right], \tag{6}$$

$$CD_{k\omega} = \max\left(\frac{2\rho\sigma_{\omega 2u}}{\omega_u}\frac{\partial k_u}{\partial x_i}\frac{\partial \omega_u}{\partial x_i}, 10^{-10}\right), \tag{7}$$

where y denotes the distance to the next surface.

f_k Expressions Based on the Energy Spectrum

According to the Kolmogorov hypothesis (Pope, 2000), the energy spectrum without rotation is $E(\kappa) = \alpha\varepsilon^{2/3}\kappa^{-5/3}$, where $E(\kappa)$ is the energy spectrum, α is the Kolmogorov constant, ε is the dispassion of turbulent kinetic energy, and κ is the wavenumber. Several researchers derived different f_k equations (Song and Park, 2009; Foroutan and Yavuzkurt, 2014; Qian et al., 2020) based on the Kolmogorov hypothesis. The f_k expression deduced by Song and Park (2009) can be seen as follows:

$$f_k = \frac{k_u}{k_t} = \frac{\int_{\kappa_\Delta}^{\kappa_\eta} E(\kappa)d\kappa}{\int_{\kappa_l}^{\kappa_\eta} E(\kappa)d\kappa} = \frac{\kappa_\eta^{-2/3} - \kappa_\Delta^{-2/3}}{\kappa_\eta^{-2/3} - \kappa_l^{-2/3}} \approx \left(\frac{\Delta}{\eta}\right)^{2/3}\left(1 - \left(\frac{\Delta}{\eta}\right)^{2/3}\right)\left(\frac{\Delta}{l_{turb}}\right)^{2/3}. \tag{8}$$

Eq. 8 is named PANS-ES1. It is similar to that proposed by Song and Park (2009), and l_{turb}, η, and Δ denote the turbulent length scale for RANS, Kolmogorov length scale (length scale for DNS), and grid size, respectively. The corresponding coupled model with SST k-ω PANS is called SST k-ω PANS-ES1 hereafter.

$$l_{turb} = \frac{k_T^{3/2}}{\varepsilon}, \eta = \left(\frac{\nu^3}{\varepsilon}\right)^{1/4}, \Delta = (\Delta x \Delta y \Delta z)^{1/3}, \tag{9}$$

where k_T is the total turbulent kinetic energy, which is equal to $k_r + k_u$. In addition, k_r is the resolved turbulent kinetic energy, $k_r = 0.5(U_i - \bar{U})^2$, where U_i is the instantaneous velocity and $\bar{U}$ is the time-averaged velocity.

Different from Song et al., Foroutan and Yavuzkurt (2014) adopted a von Kármán-like spectrum (Schiestel and Dejoan, 2005) and derived another f_k formulation, (**Eq. 10**), which here is referred to as PANS-ES2, and the corresponding coupled model with SST k-ω PANS is called SST k-ω PANS-ES2 hereafter.

$$f_k = 1 - \left[\frac{(l_{turb}/\Delta)^{2/3}}{0.23 + (l_{turb}/\Delta)^{2/3}}\right]^{4.5} \tag{10}$$

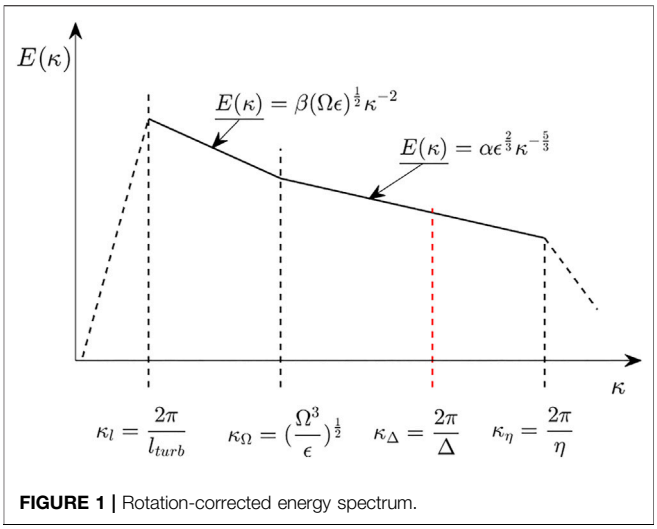

FIGURE 1 | Rotation-corrected energy spectrum.

For the rotation-corrected energy spectrum, the energy spectrum between κ_l and κ_η is divided into two parts by the Zeman number κ_Ω (Zeman, 1994), which is defined as $(\Omega^3/\varepsilon)^{1/2}$, where Ω denotes the rotation speed. More specifically, when $\kappa_c < \kappa_\Omega$, $E(\kappa) = \beta(\Omega\varepsilon)^{1/2}\kappa^{-2}$, while when $\kappa_c > \kappa_\Omega$, $E(\kappa) = \alpha\varepsilon^{2/3}\kappa^{-5/3}$ (**Figure 1**).

From the definition of f_k, $f_k = k_u/k_t$ (different from k_T in **Eq. 9**), it is assumed that for PANS simulation, the grid spacing is located between the turbulent length scale (l_{turb}) and the Kolmogorov length scale (η) (Song and Park, 2009). Therefore, the total turbulent kinetic energy k_t can be obtained as follows:

$$k_t = \int_0^\infty E(\kappa)d\kappa = \int_{\kappa_l}^{\kappa_\Omega} E(\kappa)d\kappa + \int_{\kappa_\Omega}^{\kappa_\eta} E(\kappa)d\kappa = \int_{\kappa_l}^{\kappa_\Omega} \beta\varepsilon^{1/2}\Omega^{1/2}\kappa^{-2}d\kappa + \int_{\kappa_\Omega}^{\kappa_\eta} \alpha\varepsilon^{2/3}\kappa^{-5/3}d\kappa = \left(\frac{3}{2}\alpha - \beta\right)\varepsilon\Omega^{-1} + \frac{1}{2\pi}\beta\varepsilon^{1/2}\Omega^{1/2}l_{turb} - \left(\frac{1}{2\pi}\right)^{\frac{2}{3}}\frac{3}{2}\alpha\varepsilon^{2/3}\eta^{\frac{2}{3}}. \tag{11}$$

For the small turbulent length scale (large wavenumber, $\kappa_\Delta \sim \kappa_\eta$), the turbulent kinetic energy cannot be resolved directly; thus, if $\kappa_\Delta < \kappa_\Omega$,

$$k_u = \int_{\kappa_\Delta}^\infty E(\kappa)d\kappa = \int_{\kappa_\Delta}^{\kappa_\Omega} E(\kappa)d\kappa + \int_{\kappa_\Omega}^{\kappa_\eta} E(\kappa)d\kappa = \int_{\kappa_\Delta}^{\kappa_\Omega} \beta\varepsilon^{1/2}\Omega^{1/2}\kappa^{-2}d\kappa + \int_{\kappa_l}^{\kappa_\eta} \alpha\varepsilon^{2/3}\kappa^{-5/3}d\kappa = \left(\frac{3}{2}\alpha - \beta\right)\varepsilon\Omega^{-1} + \frac{1}{2\pi}\beta\varepsilon^{1/2}\Omega^{1/2}\Delta - \left(\frac{1}{2\pi}\right)^{\frac{2}{3}}\frac{3}{2}\alpha\varepsilon^{2/3}\eta^{\frac{2}{3}}, \tag{12}$$

and if $\kappa_\Delta > \kappa_\Omega$,

$$k_u = \int_{\kappa_\Delta}^\infty E(\kappa)d\kappa = \int_{\kappa_\Delta}^{\kappa_\eta} E(\kappa)d\kappa = \int_{\kappa_\Delta}^{\kappa_\eta} \alpha\varepsilon^{2/3}\kappa^{-5/3}d\kappa = \left(\frac{1}{2\pi}\right)^{\frac{2}{3}}\frac{3}{2}\alpha\varepsilon^{2/3}\left(\Delta^{\frac{2}{3}} - \eta^{\frac{2}{3}}\right). \tag{13}$$

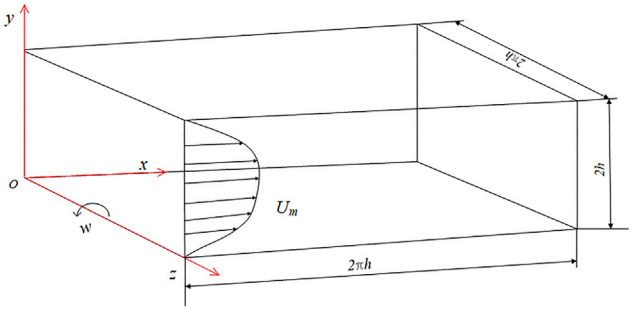

FIGURE 2 | Simulation domain of rotating channel flow.

Based on the study proposed by Thangam et al. (1999), it was assumed that $\alpha = \beta = 1.8$. Consequently, the final f_k form for the rotation-corrected energy spectrum is as follows:

$$f_k = \frac{k_u}{k_t} = \begin{cases} \dfrac{0.9\varepsilon\Omega^{-1} + 0.286(\varepsilon\Omega)^{1/2}\Delta - 0.793(\varepsilon\eta)^{2/3}}{0.9\varepsilon\Omega^{-1} + 0.286(\varepsilon\Omega)^{1/2} l_{turb} - 0.793(\varepsilon\eta)^{2/3}} & (\kappa_c \le \kappa_\Omega) \\ \dfrac{0.793\varepsilon^{2/3}\left(\Delta^{2/3} - \eta^{2/3}\right)}{0.9\varepsilon\Omega^{-1} + 0.286(\varepsilon\Omega)^{1/2} l_{turb} - 0.793(\varepsilon\eta)^{2/3}} & (\kappa_c > \kappa_\Omega) \end{cases} \quad (14)$$

It should be noted that when $\kappa_\Delta = \kappa_\Omega$, the above two equations are equivalent. Here, the f_k equation based on the rotation-corrected energy spectrum is referred to as PANS-RCES, and the corresponding coupled model with SST k-ω PANS is called SST k-ω PANS-RCES hereafter. In all PANS simulations, the dispassion of turbulent kinetic energy, ε, is calculated by $\varepsilon = \beta k\omega$, where β is a constant coefficient.

VERIFICATION AND APPLICATION

Verification in Rotating Channel Flow

In rotating channel flows, the channel rotates in the spanwise direction with a constant angular velocity and is significantly affected by rotating flow characteristics, such as typical asymmetric distribution, streaks near the pressure side, and Taylor–Götler (TG) vortices (Grundestam et al., 2008), which is suitable for verifying the new f_k expression based on the rotation-corrected energy spectrum. In the present study, rotating channel flows with a Reynolds number of 7,000 and rotation numbers of 0.3 and 0.6 are simulated. The Reynolds number is defined as $\mathrm{Re} = U_m h/\nu$, where h is the half channel height and ν denotes the kinematic viscosity. In addition, rotation number Ro is defined as $Ro = 2\omega h/U_m$, where ω denotes the angular velocity of the rotation and $U_m = 1/2h \int_0^{2h} U(y)dy$ is the bulk velocity along the x coordinate. The simulation domain is exhibited in **Figure 2**, where $2\pi h \times 2h \times 2\pi h$ are the dimensions along with the x (streamwise), y (normal), and z (spanwise) directions, respectively. The positive x coordinate is the inflow direction.

Subsequently, the SST k-ω PANS-ES1, SST k-ω PANS-ES2, and SST k-ω PANS-RCES models are used to simulate the rotating channel flow. The new turbulence models are compiled in OpenFOAM, and the simulation results are compared with the DNS data (Yang et al., 2012). For all PANS simulations, the PISO algorithm is applied to pressure–velocity coupling. A "Gauss linear" scheme with second-order accuracy is chosen for both the gradient term and the divergence term. A second-order implicit backward scheme is used for the time scheme.

The simulation results of the velocity and Reynolds stress analyzed in this study were time-, spanwise-, and streamwise-averaged:

$$\bar{\phi} = \frac{1}{L_x L_z T} \int_0^{L_x} \int_0^{L_z} \int_0^{T} \phi dx dz dt, \quad (15)$$

where ϕ is a transient physical quantity, L_x and L_z are the streamwise and spanwise lengths, respectively, and T is the duration for time averaging. The half-height of the channel, h, is set as the reference scale for the length. Furthermore, the plane $y/h = 0$ is at the position of the pressure side, and $y/h = 2$ is at the position of the suction side.

Grid Convergence Study

A grid convergence study is performed for rotating channel flow to investigate grid dependence. The details of grid information and a part of the corresponding simulation results are shown in **Table 1**. The mesh elements vary in the y-direction (Kamble et al., 2019) as shown in **Table 1**. In the present grid convergence study, two rotation numbers of rotating channel flow are selected. Four meshes coupled with three different f_k expressions, 12 cases for each rotation number in total, are simulated. In **Table 1**, only the results of $Ro = 0.6$ calculated by SST k-ω PANS-RCES are shown, which are similar to results obtained by the other two f_k expressions. The same time step is used in all calculations, and the maximum Courant–Friedrichs–Lewy (CFL) number is all less than unity in the calculation process. For the y^+ on the pressure surface (PS) and suction surface (SS) of the four meshes in the table, the y^+ of the four meshes is all around unity, and the maximum is no more than 2, especially for the three grids except mesh1, the y^+ is all below unity. By comparing the y^+ of the PS and the SS (the first layer height of the PS and SS meshes are the same), it can be found that under the same grid, the y^+ of the pressure surface is larger than that of the suction surface.

The magnitude and distribution of f_k are key parameters that can determine the calculation accuracy of PANS models. **Figure 3** plots the time-space-averaged results of the three f_k expressions in rotating channel flow. Four different meshes and two different rotation numbers are used in the simulation, and the legend is the same for both figures. For the same f_k expressions, the figures show that the magnitude of f_k decreases with the increase of grid points. By comparing the f_k distributions obtained using the three different expressions, the SST k-ω PANS-RCES result is much smaller than the results of SST k-ω PANS-ES1 and SST k-ω

TABLE 1 | Parameters of grid convergence for rotating channel flow at *Ro* = 0.6.

Mesh	Mesh size (N_x, N_y, N_z)	Averaged y^+ (PS)	Averaged y^+ (SS)	Max CFL
Mesh1	48 × 32 × 128	1.672	1.196	0.488
Mesh2	48 × 64 × 128	0.849	0.560	0.628
Mesh3	48 × 96 × 128	0.573	0.382	0.777
Mesh4	48 × 128 × 128	0.428	0.282	1.143

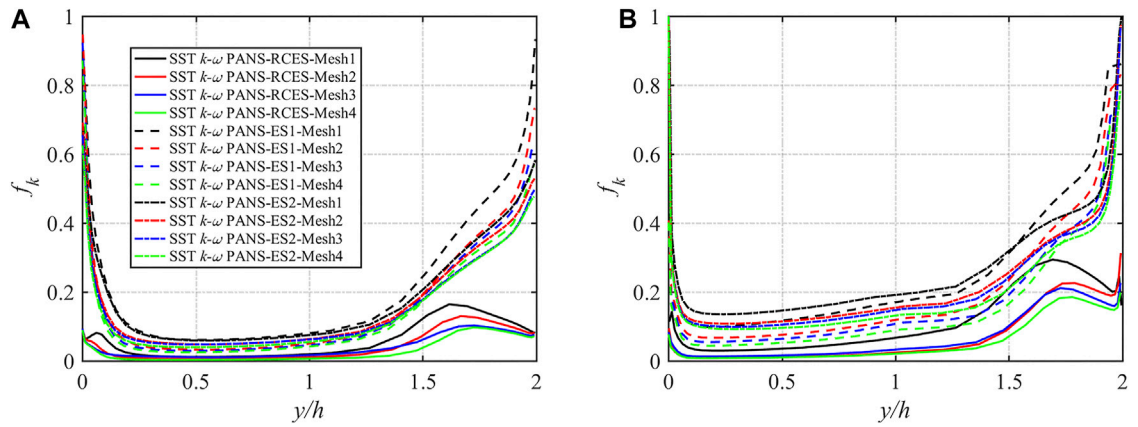

FIGURE 3 | f_k distribution in rotating channel flow under different meshes: **(A)** *Ro* = 0.3 and **(B)** *Ro* = 0.6.

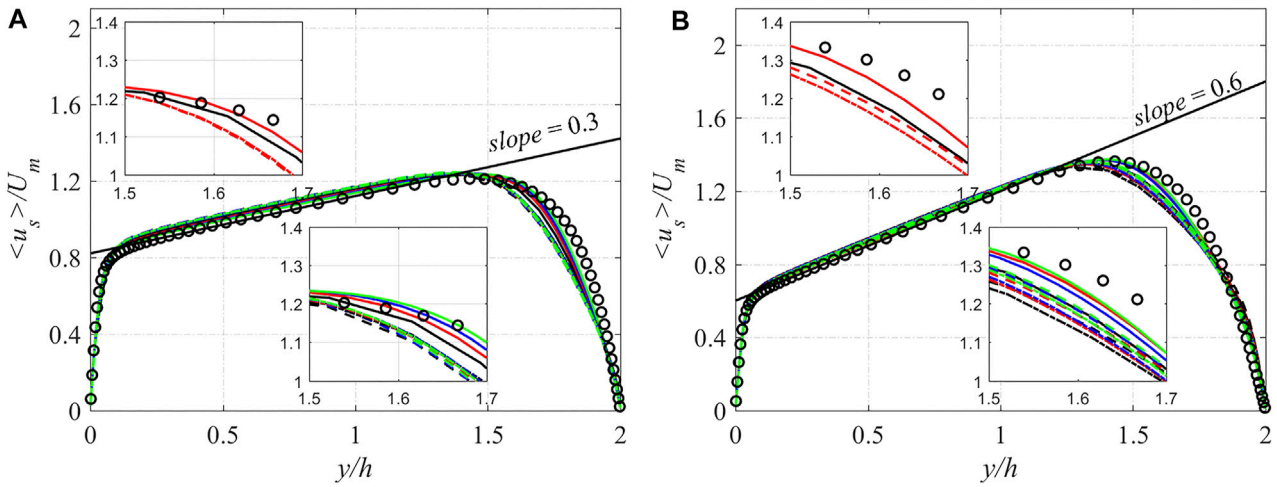

FIGURE 4 | Mean streamwise velocity profiles in rotating channel flow: **(A)** *Ro* = 0.3 and **(B)** *Ro* = 0.6.

PANS-ES2, and the distribution pattern is also different. For all the three different f_k expressions, the f_k value is smaller in the region far from the wall than that in the region near the walls. However, the f_k profiles near the pressure and suction surface of the SST *k-ω* PANS-RCES are different from the ones of the other two f_k expressions. The f_k value based on the rotation-corrected energy spectrum near the walls is generally lower than those of the other two f_k expressions under both rotation numbers as shown in **Figure 3**, which may contribute to the better simulation performance near the walls.

Due to the Coriolis effect, the mean streamwise velocity profiles are increasingly asymmetric with an increasing rotation rate, and their slope is equal to the rotation number at the main flow region of the channel (Kristoffersen and Andersson, 1993; Huang et al., 2017). The mean streamwise velocities obtained by the different f_k equations coupled with

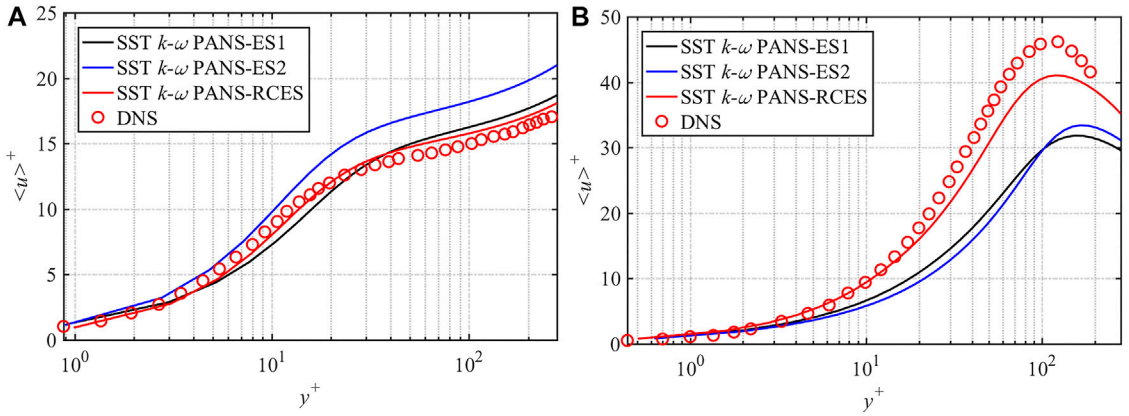

FIGURE 5 | Comparison of mean streamwise velocity distribution in the near-wall area at *Ro* = 0.3: **(A)** pressure side and **(B)** suction side.

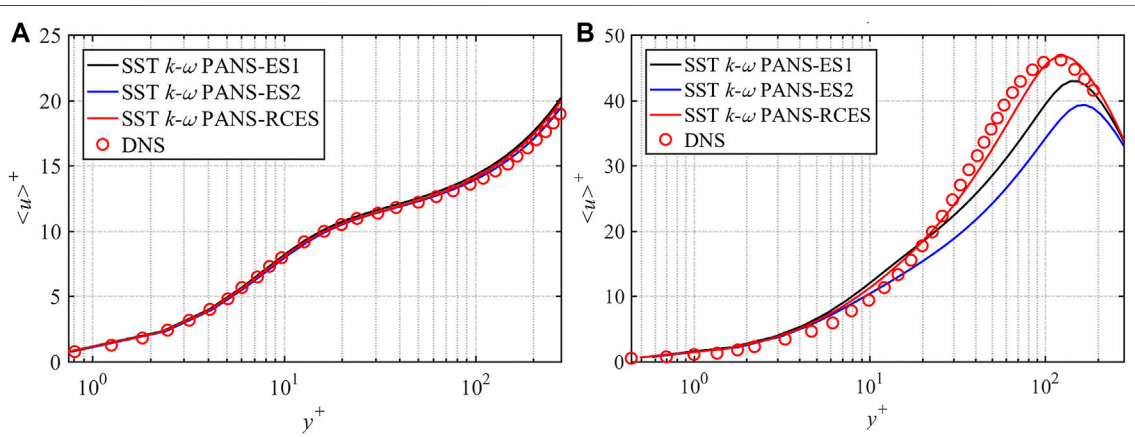

FIGURE 6 | Comparison of mean streamwise velocity distribution in the near-wall area at *Ro* = 0.6: **(A)** pressure side and **(B)** suction side.

four meshes at *Ro* = 0.3 and 0.6 are presented in **Figure 4**, and the legend is the same as in **Figure 3**. It can be observed that reasonable results are obtained with different f_k expressions for all four meshes, and the slope of the mean streamwise velocity profiles is equal to the rotation number. For the same f_k expression, with the increase of mesh points, the numerical simulation results gradually approach the DNS results, and it converges when the number of mesh points increases to mesh3 at *Ro* = 0.3, and it happens at mesh2 when *Ro* = 0.6. For both two rotation numbers with four meshes, the results obtained by SST *k-ω* PANS-RCES are better than those obtained by SST *k-ω* PANS-ES1 and SST *k-ω* PANS-ES2. Especially, even with fewer meshes (mesh1, black solid lines), the SST *k-ω* PANS-RCES shows better performance than the other two PANS models with more mesh points (mesh2, red dotted, and dashed lines).

Near-Wall Velocity and Turbulence Statistics

The profiles of mean streamwise velocity in the near-wall area at both rotation numbers are shown in **Figure 5** and **Figure 6**. According to the grid convergence study, results of *Ro* = 0.3 with mesh3 and results of *Ro* = 0.6 with mesh2 are discussed in this section. When *Ro* = 0.3, the results of SST *k-ω* PANS-RCES and SST *k-ω* PANS-ES1 are close to each other and consistent with DNS results, while the results of SST *k-ω* PANS-ES2 show some deviations. As for the velocity near the pressure side of *Ro* = 0.6, the results of the three models are relatively consistent. On the suction side, it can be observed more clearly that the SST *k-ω* PANS-RCES model has a more obvious advantage in predicting the near-wall velocity distribution under both rotation numbers, which is due to the more reasonable distribution of f_k near the suction side shown in **Figure 3**.

The profiles of root-mean-square (RMS) velocity and Reynolds shear stress under the two rotation numbers are exhibited in **Figures 7**, **8**, respectively. v_{rms} is the RMS velocity in the normal direction. Since the results of the streamwise and the normal RMS velocity are similar, they are not presented here. The RMS velocity and Reynolds shear stress are normalized by U_m and U_m^2, respectively. It was found that the RMS velocity and the Reynolds shear stress are higher on

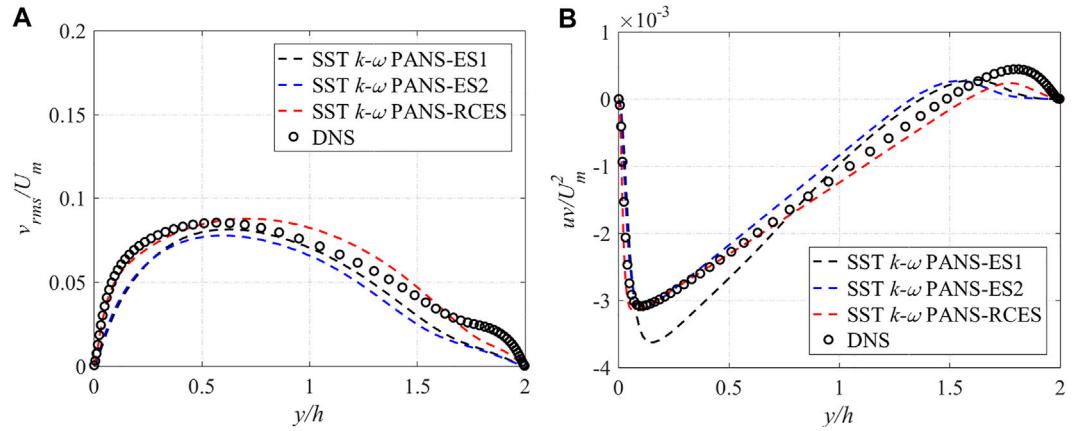

FIGURE 7 | Comparison of turbulence statistics at *Ro* = 0.3 **(A)** normal RMS velocity **(B)** Reynolds shear stress.

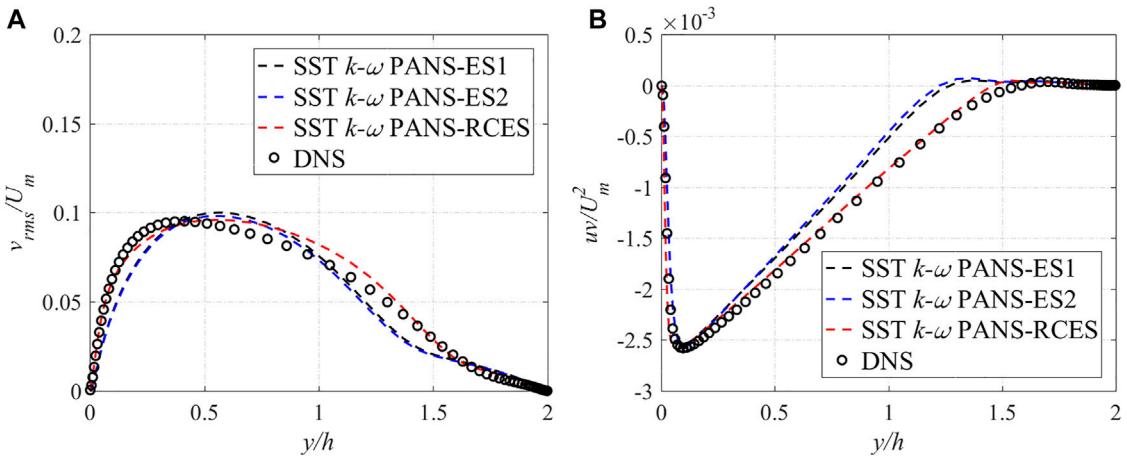

FIGURE 8 | Comparison of turbulence statistics at *Ro* =0.6 **(A)** normal RMS velocity **(B)** Reynolds shear stress.

the pressure side and decrease from the pressure side toward the suction side. This suggests that the rotating effect strengthens the turbulence intensity at the pressure side and suppresses it at the suction side, which has also been confirmed by Kristoffersen and Andersson (1993). As for the normal RMS velocity at $Ro = 0.3$, at the near-wall area ($y/h = 0$–0.5 and $y/h = 1.5$–2), the result of the SST k-ω PANS-RCES model agrees well with the DNS results, while the other two models show some deviations in all regions. As for the Reynolds shear stress near the pressure surface (near $y/h = 0$–0.5) where the turbulence is enhanced, SST k-ω PANS-ES1 and SST k-ω PANS-RCES models show more convincible results than that of SST k-ω PANS-ES2 model. Near the suction side, only the SST k-ω PANS-RCES model can accurately predict the correct profile of Reynolds shear stress, which may be due to the decreased tendency of f_k at the near suction surface shown in **Figure 3**. Whether it is near the pressure side or the suction side, the SST k-ω PANS-ES2 model fails to predict the correct results.

When $Ro = 0.6$, the v_{rms} results demonstrate that the SST k-ω PANS-RCES model performance is consistent with the DNS results. Especially in near-wall areas, the SST k-ω PANS-RCES model results agree well with the DNS data. As for the Reynolds shear stress, both the SST k-ω PANS-ES1 and SST k-ω PANS-ES2 model results exhibit some deviation at the mainstream region ($y/h = 0.5$–1.5), while the SST k-ω PANS-RCES model can accurately predict the correct profile in the whole area.

TG Vortices

Johnston et al. (1973) were the first to experimentally observe the TG vortices, and later, in a DNS study, Kristoffersen and Andersson (1993) observed the TG vortices as well. TG vortices are induced by the unstable flow near the pressure surface, and when the Reynolds number increases, their presence generates complex flow structures. Hence, the TG vortex is an important large-scale structure and a prominent physical phenomenon in rotating channel flows. To isolate the TG vortex, the fluctuation velocity is defined as follows:

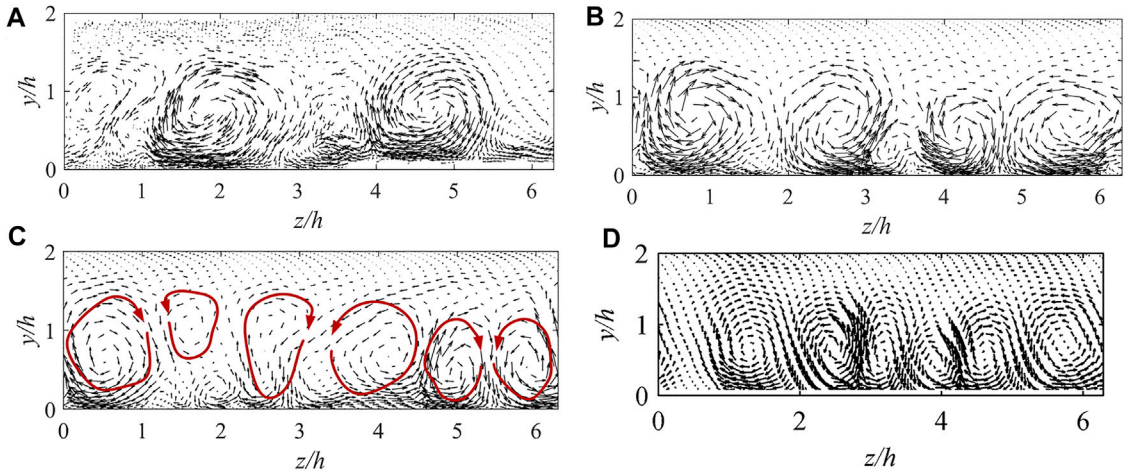

FIGURE 9 | Comparison of Taylor–Götler vortices at *Ro* = 0.3: **(A)** SST *k-ω* PANS-ES1, **(B)** SST *k-ω* PANS-ES2, **(C)** SST *k-ω* PANS-RCES, and **(D)** DNS.

TABLE 2 | Time cost of different f_k expression for rotating channel flow at *Ro* = 0.6.

Case	Mesh	f_k expression	Time steps	Tc (s)
Case 1	Mesh1	RCES	5,000	1,053
Case 2	Mesh2	ES1	5,000	1,956
Case 3	Mesh2	ES2	5,000	2,005
Case 4	Mesh2	RCES	5,000	2,004

$$u_i' = u_i - \frac{1}{L_x L_z T}\int_0^{L_x}\int_0^{L_z}\int_0^{T}\bar{u}_i dx dz dt. \quad (16)$$

That is, the fluctuation velocity is the difference between the instantaneous velocity and the time-, streamwise-, and spanwise-averaged velocities. The TG fluctuation is defined as the streamwise average of the fluctuation velocity:

$$u_i^{TG} = \frac{1}{L_x}\int_0^{L_x} u_i' dx. \quad (17)$$

When the rotation number increases, the TG vortex becomes unstable. According to the DNS results of this example (Yang et al., 2010), the TG vortex becomes unstable and difficult to capture at *Ro* = 0.6; thus, in this section, the TG vortices at *Ro* = 0.3 with mesh3 are analyzed (**Figure 9**).

As can be observed in **Figure 9**, SST *k-ω* PANS-ES1 can predict only a pair of apparent vortices (z/h = 2 and z/h = 5), whereas SST *k-ω* PANS-ES2 predicts two pairs of vortices, and the vortex boundaries are very clear. Nevertheless, they are significantly different from the three pairs of TG vortices predicted by DNS. Only the SST *k-ω* PANS-RCES can capture all three pairs of vortices as DNS does. The vortex distribution on the right side of the flow channel is more apparent, while that on the left side is more ambiguous. By comparing the results, some discrepancies among the PANS results could be observed. Overall, the SST *k-ω* PANS-RCES results are better than those of SST *k-ω* PANS-ES1 and SST *k-ω* PANS-ES2, which further indicates that the SST *k-ω* PANS-RCES model based on the rotation-corrected energy spectrum is more suitable for predicting rotating flows.

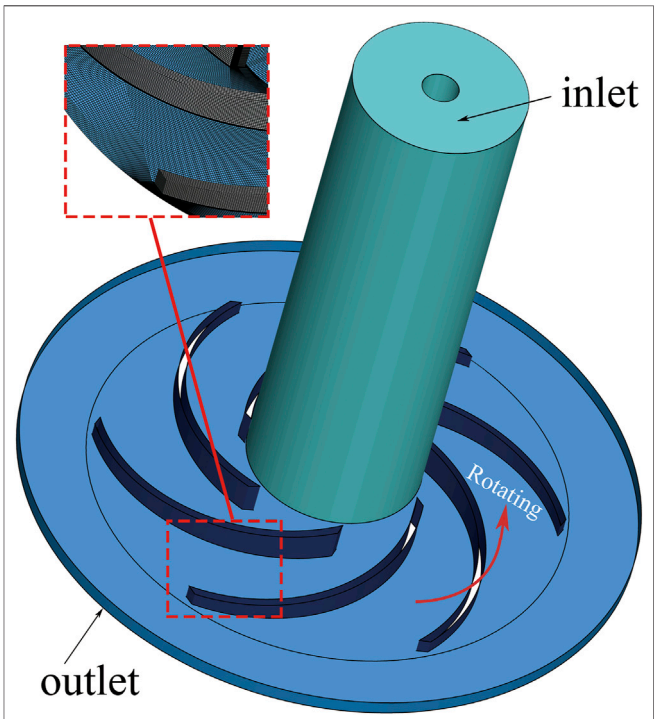

FIGURE 10 | Computational domain of the centrifugal pump impeller.

Simulation Cost

For turbulence models, the balance of the simulation accuracy and cost is always the main target. According to the grid convergence study in **Section 3.1.1**, SST *k-ω* PANS-RCES with mesh1 can obtain similar results to the calculation accuracy of SST *k-ω* PANS-ES1 and SST *k-ω* PANS-ES2 with mesh2. For a better comparison of simulation cost, the time consumption (Tc)

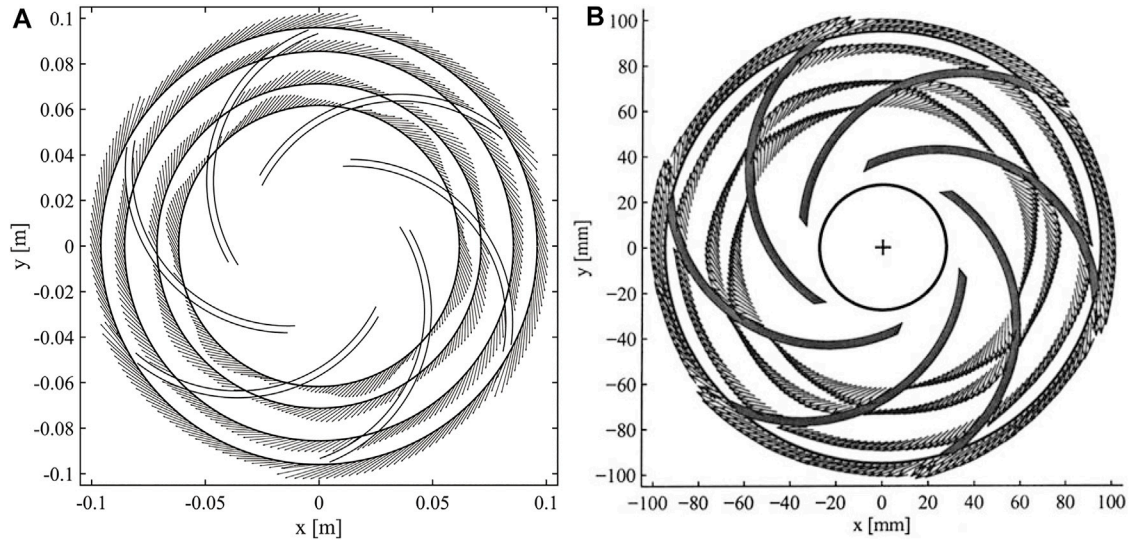

FIGURE 11 | Velocity vector distributions at different radial positions under the design-load condition: **(A)** PANS and **(B)** LDV.

of four cases with two meshes at $Ro = 0.6$ is shown in **Table 2**. The statistical time consumption is 5,000 time steps after all calculations are stabilized. The Intel Xeon(R) Gold 5120 CPU with 2.2 GHz and 28 cores is installed in the simulation workstation. From **Table 2**, for the first three cases, it can be seen that the expression of RCES takes the shortest time to calculate the 5,000 time steps. In other words, for similar calculation accuracy, the newly developed f_k expression can save more calculation resources than the other expressions. For the last three cases with the same meshes, the time consumption is almost the same. Combined with the simulation performance, it can be found that the PANS model with the new f_k expression balances the simulation accuracy and the simulation cost commendably for rotating channel flow.

Application in a Centrifugal Pump

The flow in a centrifugal pump is another typical rotating flow type. The large curvature and multiwall characteristics of the pump structure make the accurate prediction of the internal flow very difficult. In this study, a low specific speed centrifugal pump is used to verify the applicability of the new f_k expression based on the rotation-corrected energy spectrum. The pump has a rotating speed of 725 r/min, inlet diameter of D_1 = 71 mm, and outlet radius of R_2 = 95 mm, and the Reynolds number based on the inlet diameter D_1 and the rated flow rate Q_0 was approximately 5.5×10^4. The calculation domain is illustrated in **Figure 10**, and the grid points are approximately 2.78 million, which is determined based on previous simulations of this flow case (Byskov et al., 2003; Huang et al., 2015). In addition, the flow rate at the design condition was 3.06 L/s, and at the stall

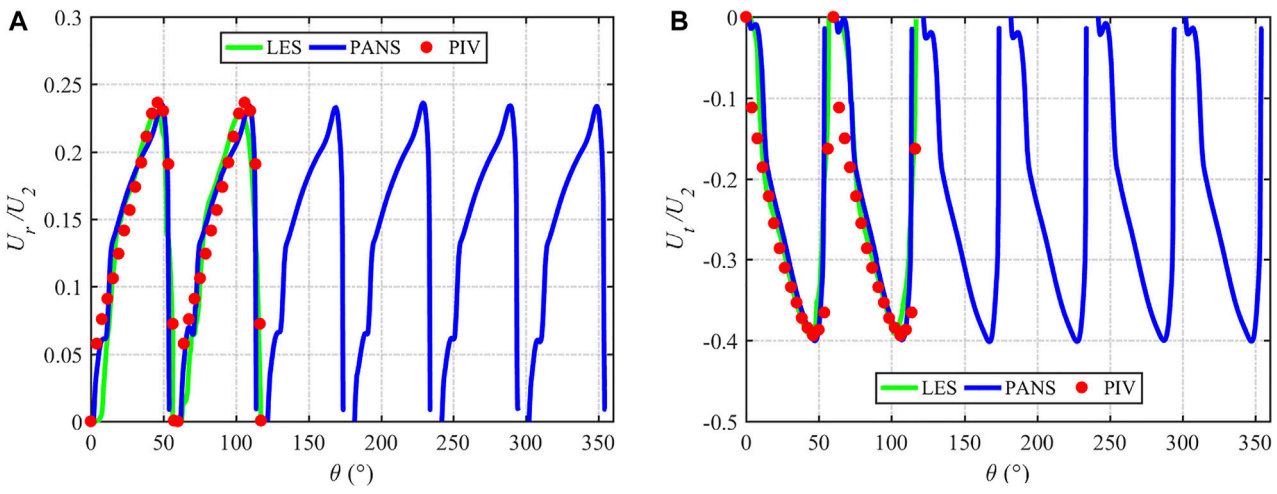

FIGURE 12 | Comparison of time-averaged velocity at $Q = 1.0Q_0$ flow condition: **(A)** $0.5R_2$ radial velocity and **(B)** $0.5R_2$ tangential velocity.

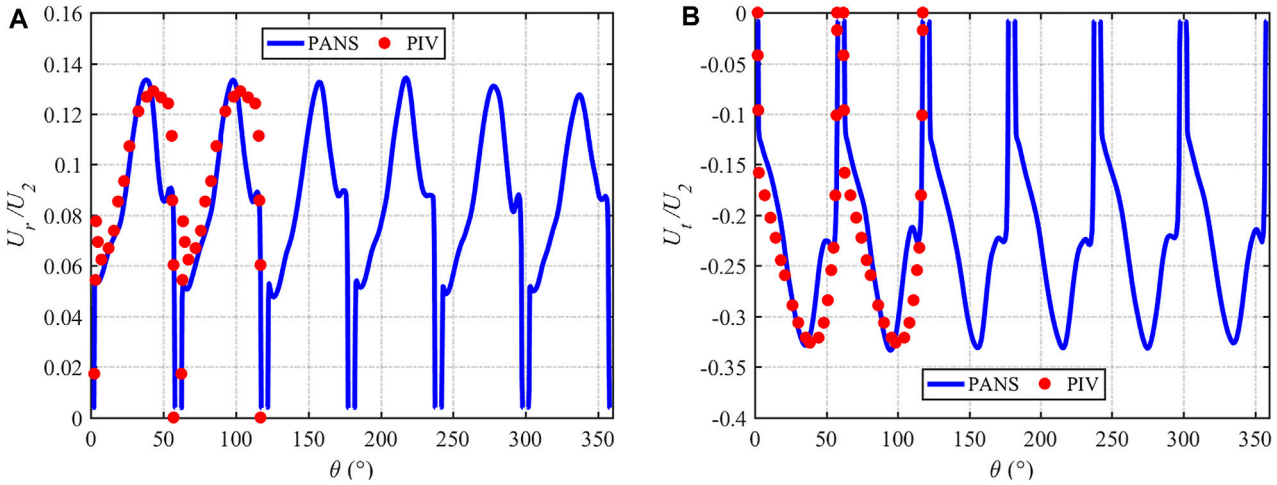

FIGURE 13 | Comparison of time-averaged velocity at $Q = 1.0Q_0$ flow condition: **(A)** $0.75R_2$ radial velocity and **(B)** $0.75R_2$ tangential velocity.

condition, it was 0.76 L/s. The corresponding experimental and simulation results are found in the studies by Pedersen et al. (2003) and Byskov et al. (2003).

Under the design conditions, the streamlines are smooth. Nevertheless, under part-load conditions, a stall happens in the impeller. More specifically, under stall conditions, a stall vortex is generated and blocks the channel. Therefore, the flow becomes more unstable, and the requirements for the turbulence model become higher (Pedersen et al., 2003; Zhou et al., 2014; Tao et al., 2014; Yao et al., 2016; Huang X.-b. et al., 2019). In this study, both the design-load condition, $1.0Q_0$, and the part-load condition, $0.25Q_0$, are used to verify the accuracy of the SST k-ω PANS-RCES (abbreviated as PANS hereafter) model. The mass flow rate is used as the inlet boundary condition, a pressure outlet boundary condition is used at the outlet, and a no-slip condition is set at the walls.

The $Q = 1.0Q_0$ flow condition results of the velocity vector distributions in the impeller mid-height at the different radial positions of $r/R_2 = \{0.65, 0.75, 0.90, 1.01\}$ obtained by PANS and laser Doppler velocimetry (LDV) (Pedersen, 2000) are depicted in **Figure 11**. Under the design-load condition, the velocity vectors in the six flow channels are the same. The main feature is that the velocity at the suction surface (SS) of blades is large at 0.65 R_2 and 0.75 R_2, and the velocity at the pressure surface (PS) is small. The velocity distribution at 0.90 R_2 is more uniform. At 1.01 R_2, the velocity of the pressure surface is slightly greater than the velocity of the suction surface. This may be due to the secondary flow of the low specific speed centrifugal pump that causes the jet-wake flow at the exit to occur (Brun and Kurz, 2005; Zhang et al., 2019). The results of PANS and LDV show that PANS can capture the above phenomenon well. A more detailed comparison of the velocity distribution at 0.5 R_2 and 0.75 R_2 is shown in **Figures 12**,

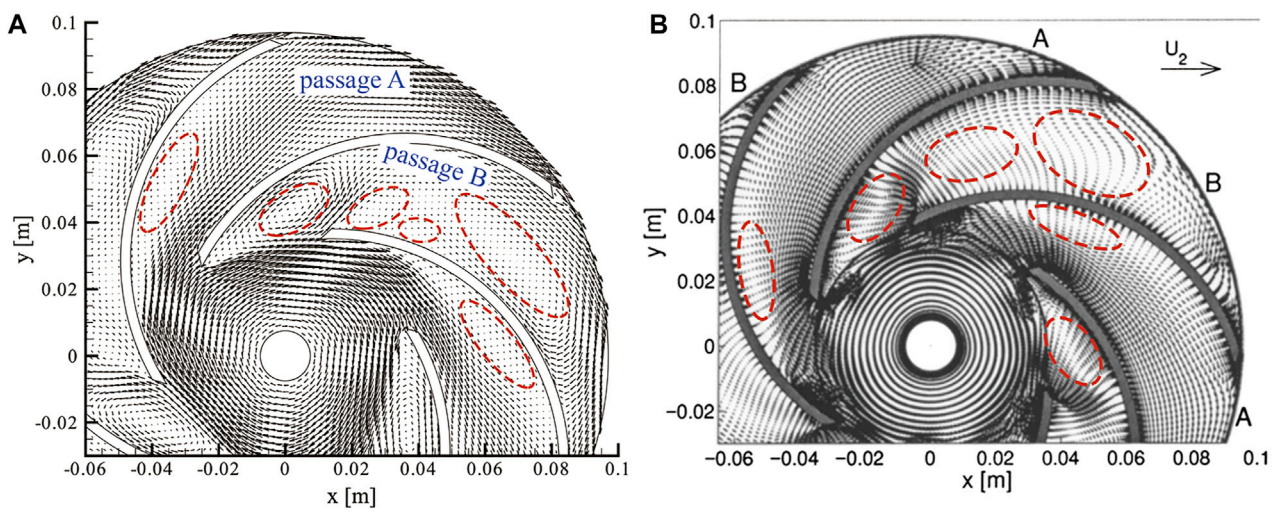

FIGURE 14 | Velocity vector distributions in the impeller mid-height under $0.25Q_0$ flow condition: **(A)** PANS and **(B)** LES.

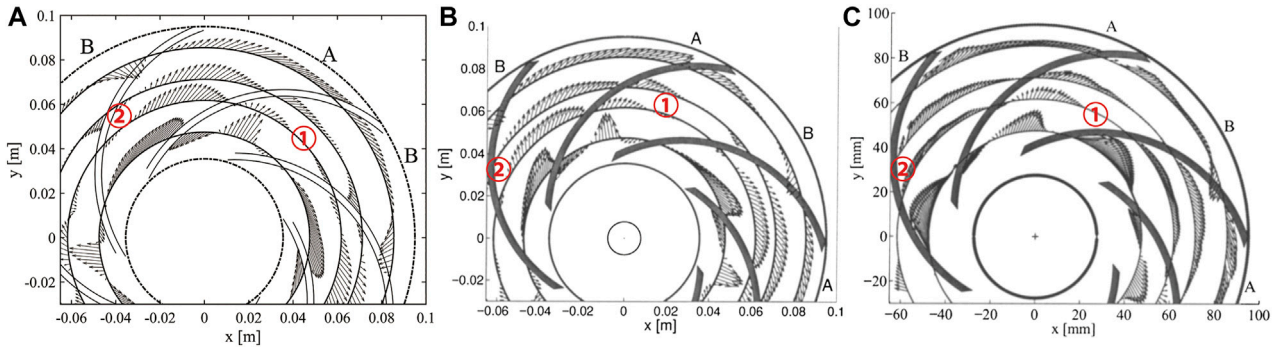

FIGURE 15 | Velocity vector distributions in the impeller mid-height at different radial positions: **(A)** PANS, **(B)** LES, and **(C)** LDV.

13. From the figures, it is more obvious that the results of PANS are consistent with those of LES and PIV results, indicating that the velocity distribution can be well predicted in both near-wall and mainstream regions, and the newly developed f_k expression RCES can accurately predict the flow field in the design-load condition.

The velocity vector in the impeller mid-height under the part-load condition is shown in **Figure 14**. Under this working condition, the velocity vector of adjacent flow passages is different, which can be marked as non-stall Passage A and stall Passage B, respectively. It can be seen from **Figure 14** that only one vortex appears on the suction surface in the non-stall Passage A. A smaller vortex appears at the inlet of the stall passage, and a larger one appears near the exit of the passage. The results of PANS are consistent with those of LES. **Figure 15** shows the velocity vector results of r/R_2 = {0.50, 0.65, 0.75, 0.90}. For stall passage, backflow occurs on the suction surface at the inlet, which is an important factor to generate stall vortices. The results of PANS and LES can accurately predict this result. For other flow direction positions, PANS also shows good prediction accuracy.

CONCLUSION

1) An SST k-ω PANS model with a new expression of f_k based on the rotation-corrected energy spectrum is proposed in this study. The new model is verified in the rotating channel flow at two different rotation numbers, and then it is applied to a centrifugal pump impeller for further validation.
2) It was found that the f_k distribution of the new model is reasonably distributed in the rotating channel flow. In the near-wall area, the reasonable reduction of f_k allows the new model to have better performance in near-wall flow calculation. In the region near the pressure side with turbulence enhanced, the f_k value turns out to be small, and it increases toward the suction side since the turbulence is suppressed. The f_k distribution shows that it corresponds to the flow characteristics well, and the simulation results, including mean velocity, RMS velocities, and TG vortexes, agree well with the DNS data. From the calculation cost results, it was found that the new model shows a better performance than the other two PANS models with the same mesh points, and it shows comparable performance even with fewer mesh points.
3) The application of the new model in a centrifugal pump impeller shows that it can accurately capture the time-averaged flow fields including stall vortices under part-load conditions and velocity vector distributions under both design-load and part-load conditions. In addition, the new PANS model can predict the tangential and radial velocities well under both flow conditions, showing that the new model is appropriate for the simulation of flows with rotation effects.

DATA AVAILABILITY STATEMENT

The original contributions presented in the study are included in the article/Supplementary Material; further inquiries can be directed to the corresponding author.

AUTHOR CONTRIBUTIONS

This is a joint work and the authors were in charge of their expertise and capability: BL worked on investigation, analysis, writing, and revision; WY and ZL worked on methodology and revision.

FUNDING

The authors would like to acknowledge the financial support received from the National Natural Science Foundation of China (grant number 52179093).

ACKNOWLEDGMENTS

The authors would like to acknowledge ZL and Yaojun Li for their valuable advice to this study.

REFERENCES

Abdol-Hamid, K., and Girimaji, S. S. (2004). *A Two-Stage Procedure toward the Efficient Implementation of Pans and Other Hybrid Turbulence Models*. Hampton, Virginia: Technical Memorandum NASA Langley Research Center.

Baroud, C. N., Plapp, B. B., She, Z.-S., and Swinney, H. L. (2002). Anomalous Self-Similarity in a Turbulent Rapidly Rotating Fluid. *Phys. Rev. Lett.* 88 (11), 114501. doi:10.1103/PhysRevLett.88.114501

Brun, K., and Kurz, R. (2005). Analysis of Secondary Flows in Centrifugal Impellers. *Int. J. Rotating Machinery* 2005, 45–52. doi:10.1155/IJRM.2005.45

Byskov, R. K., Jacobsen, C. B., and Pedersen, N. (2003). Flow in a Centrifugal Pump Impeller at Design and Off-Design Conditions-Part II: Large Eddy Simulations. *J. Fluids Eng.* 125 (1), 73–83. doi:10.1115/1.1524586

Canuto, V. M., and Dubovikov, M. S. (1997). A Dynamical Model for Turbulence. V. The Effect of Rotation. *Phys. Fluids* 9 (7), 2132–2140. doi:10.1063/1.869332

Foroutan, H., and Yavuzkurt, S. (2014). A Partially-Averaged Navier-Stokes Model for the Simulation of Turbulent Swirling Flow with Vortex Breakdown. *Int. J. Heat Fluid Flow* 50, 402–416. doi:10.1016/j.ijheatfluidflow.2014.10.005

Girimaji, S. S., Jeong, E., and Srinivasan, R. (2006). Partially Averaged Navier-Stokes Method for Turbulence: Fixed Point Analysis and Comparison with Unsteady Partially Averaged Navier-Stokes. *J. Appl. Mech.* 73, 422–429. doi:10.1115/1.2173677

Girimaji, S. S. (2006). Partially-Averaged Navier-Stokes Model for Turbulence: A Reynolds-Averaged Navier-Stokes to Direct Numerical Simulation Bridging Method. *J. Appl. Mech.* 73 (5), 413–421. doi:10.1115/1.2151207

Girimaji, S. S., Srinivasan, R., and Jeong, E. (2003). "PANS Turbulence Model for Seamless Transition between RANS and LES Fixed-point Analysis and Preliminary Results," in *4th ASME_JSME Joint Fluids Engineering Conference* (Honolulu, Hawaii, USA. doi:10.1115/fedsm2003-45336

Grundestam, O., Wallin, S., and Johansson, A. V. (2008). Direct Numerical Simulations of Rotating Turbulent Channel Flow. *J. Fluid Mech.* 598 (598), 177–199. doi:10.1017/s0022112007000122

Hu, C., Wang, G., Chen, G., and Huang, B. (2014). A Modified PANS Model for Computations of Unsteady Turbulence Cavitating Flows. *Sci. China Phys. Mech. Astron.* 57 (10), 1967–1976. doi:10.1007/s11433-014-5538-6

Huang, X.-b., Liu, Z.-q., Li, Y.-j., Yang, W., and Guo, Q. (2019). Study of the Internal Characteristics of the Stall in a Centrifugal Pump with a Cubic Nonlinear SGS Model. *J. Hydrodyn.* 31 (4), 788–799. doi:10.1007/s42241-018-0170-y

Huang, X., Liu, Z., and Yang, W. (2015). Comparative Study of SGS Models for Simulating the Flow in a Centrifugal-Pump Impeller Using Single Passage. *Eng. Comput.* 32 (7), 2120–2135. doi:10.1108/EC-09-2014-0193

Huang, X., Yang, W., Li, Y., Qiu, B., Guo, Q., and Zhuqing, L. (2019). Review on the Sensitization of Turbulence Models to Rotation/curvature and the Application to Rotating Machinery. *Appl. Maths. Comput.* 341, 46–69. doi:10.1016/j.amc.2018.08.027

Johnston, J. P., Halleen, R. M., and Lezius, D. K. (1973). Effects of Spanwise Rotation on the Structure of Two-Dimensional Fully Developed Turbulent Channel Flow. *J. Fluid Mech.* 56, 533–557. doi:10.1017/S0022112073002077

Kamble, C., Girimaji, S. S., and Chen, H.-C. (2020). Partially Averaged Navier-Stokes Formulation of a Two-Layer Turbulence Model. *AIAA J.* 58 (1), 174–183. doi:10.2514/1.J058742

Kristoffersen, R., and Andersson, H. I. (1993). Direct Simulations of low-Reynolds-number Turbulent Flow in a Rotating Channel. *J. Fluid Mech.* 256, 163–197. doi:10.1017/s0022112093002757

Lakshmipathy, S., and Girimaji, S. S. (2010). Partially Averaged Navier-Stokes (PANS) Method for Turbulence Simulations: Flow Past a Circular Cylinder. *J. Fluids Eng.* 132 (12). doi:10.1115/1.4003154

Lin, P., Yang, T., Xu, W., and Zhu, Z. (2022). Influence of Different Offset Angles of Inlet Guide Vanes on Flow Characteristics of Centrifugal Pump. *Front. Energ. Res.* 10, 818244. doi:10.3389/fenrg.2022.818244

Luo, D., Yan, C., Liu, H., and Zhao, R. (2014). Comparative Assessment of PANS and DES for Simulation of Flow Past a Circular cylinder. *J. Wind Eng. Ind. Aerodynamics* 134, 65–77. doi:10.1016/j.jweia.2014.08.014

Pedersen, N. (2000). *Experimental Investigation of Flow Structures in a Centrifugal Pump Impeller Using Particle Image Velocimetry*. USA: Technical University of Denmark. [Ph.D thesis]. dissertation.

Pedersen, N., Larsen, P. S., and Jacobsen, C. B. (2003). Flow in a Centrifugal Pump Impeller at Design and Off-Design Conditions-Part I: Particle Image Velocimetry (PIV) and Laser Doppler Velocimetry (LDV) Measurements. *J. Fluids Eng.* 125 (1), 61–72. doi:10.1115/1.1524585

Pereira, F. S., Vaz, G., Eça, L., and Girimaji, S. S. (2018). Simulation of the Flow Around a Circular cylinder at Re =3900 with Partially-Averaged Navier-Stokes Equations. *Int. J. Heat Fluid Flow* 69, 234–246. doi:10.1016/j.ijheatfluidflow.2017.11.001

Pereira, S. F., Vaz, G., and Eca, L. (2015). "An Assessment of Scale-Resolving Simulation Models for the Flow Around a Circular cylinder," in *Turbulence, Heat and Mass Transfer* (Sarajevo: Begell House), 8. doi:10.1615/ichmt.2015.thmt-15.540

Pope, S. B. (2000). *Turbulent Flows*. Cambridge,UK: Cambridge University Press.

Qian, Y., Wang, T., Yuan, Y., and Zhang, Y. (202011814). Comparative Study on Wind Turbine Wakes Using a Modified Partially-Averaged Navier-Stokes Method and Large Eddy Simulation. *Energy* 206, 118147. doi:10.1016/j.energy.2020.118147

Ranjan, P., and Dewan, A. (2016). Effect of Side Ratio on Fluid Flow and Heat Transfer from Rectangular Cylinders Using the PANS Method. *Int. J. Heat Fluid Flow* 61 (B), 309–322. doi:10.1016/j.ijheatfluidflow.2016.05.004

Ranjan, P., and Dewan, A. (2015). Partially Averaged Navier Stokes Simulation of Turbulent Heat Transfer from a Square cylinder. *Int. J. Heat Mass Transfer* 89, 251–266. doi:10.1016/j.ijheatmasstransfer.2015.05.029

Rathor, S. K., Sharma, M. K., Ray, S. S., and Chakraborty, S. (2020). Bridging Inertial and Dissipation Range Statistics in Rotating Turbulence. *Phys. Fluids* 32 (9), 095104. doi:10.1063/5.0016495

Schiestel, R., and Dejoan, A. (2005). Towards a New Partially Integrated Transport Model for Coarse Grid and Unsteady Turbulent Flow Simulations. *Theoret. Comput. Fluid Dyn.* 18 (6), 443–468. doi:10.1007/s00162-004-0155-z

Song, C.-S., and Park, S.-O. (2009). Numerical Simulation of Flow Past a Square cylinder Using Partially-Averaged Navier-Stokes Model. *J. Wind Eng. Ind. Aerodynamics* 97, 37–47. doi:10.1016/j.jweia.2008.11.004

Tao, R., Xiao, R., Yang, W., and Wang, F. (2014). A Comparative Assessment of Spalart-Shur Rotation/Curvature Correction in RANS Simulations in a Centrifugal Pump Impeller. *Math. Probl. Eng.* 2014, 1–9. doi:10.1155/2014/342905

Thangam, S., Wang, X.-H., and Zhou, Y. (1999). Development of a Turbulence Model Based on the Energy Spectrum for Flows Involving Rotation. *Phys. Fluids* 11 (8), 2225–2234. doi:10.1063/1.870084

Wang, C.-y., Wang, F.-j., Wang, B.-h., Tang, Y., and Zhao, H.-r. (2020). A Novel Omega-driven Dynamic PANS Model. *J. Hydrodyn.* 32, 710–716. doi:10.1007/s42241-020-0052-y

Xianbei, H., Zhuqing, L., Wei, Y., Yaojun, L., and Zixuan, Y. (2017). A Cubic Nonlinear Subgrid-Scale Model for Large Eddy Simulation. *J. Fluids Eng.* 139 (4), 41101. doi:10.1115/1.4035217

Yang, Z., Cui, G., Xu, C., Shao, L., and Zhang, Z. (2010). The Effect of the Taylor-Görtler Vortex on Reynolds Stress Transport in the Rotating Turbulent Channel Flow. *Sci. China Phys. Mech. Astron.* 53 (4), 725–734. doi:10.1007/s11433-010-0168-0

Yang, Z., Cui, G., Xu, C., and Zhang, Z. (2012). Large Eddy Simulation of Rotating Turbulent Channel Flow with a New Dynamic Global-Coefficient Nonlinear Subgrid Stress Model. *J. Turbulence* 13 (48), N48–N20. doi:10.1080/14685248.2012.726996

Yao, Z.-F., Yang, Z.-J., and Wang, F.-J. (2016). Evaluation of Near-wall Solution Approaches for Large-Eddy Simulations of Flow in a Centrifugal Pump Impeller. *Eng. Appl. Comput. Fluid Mech.* 10 (1), 452–465. doi:10.1080/19942060.2016.1189362

Zeman, O. (1994). A Note on the Spectra and Decay of Rotating Homogeneous Turbulence. *Phys. Fluids* 6 (10), 3221–3223. doi:10.1063/1.868053

Zhang, N., Liu, X., Gao, B., and Xia, B. (2019). DDES Analysis of the Unsteady Wake Flow and its Evolution of a Centrifugal Pump. *Renew. Energ.* 141, 570–582. doi:10.1016/j.renene.2019.04.023

Zhang, X., Xia, G., Cong, T., Peng, M., and Wang, Z. (2020). Uncertainty Analysis on K-ε Turbulence Model in the Prediction of Subcooled Boiling in Vertical Pipes. *Front. Energ. Res.* 8, 584531. doi:10.3389/fenrg.2020.584531

Zhou, P. J., Wang, F. J., Yang, Z. J., and Mou, J. G. (2014). Investigation of Rotating Stall for a Centrifugal Pump Impeller Using Various SGS Models. *J. Hydrodyn.* 29 (2), 235–242. doi:10.1016/S1001-6058(16)60733-3

Zhou, Y. (1995). A Phenomenological Treatment of Rotating Turbulence. *Phys. Fluids* 7 (8), 2092–2094. doi:10.1063/1.868457

Conflict of Interest: The authors declare that the research was conducted in the absence of any commercial or financial relationships that could be construed as a potential conflict of interest.

Publisher's Note: All claims expressed in this article are solely those of the authors and do not necessarily represent those of their affiliated organizations, or those of the publisher, the editors, and the reviewers. Any product that may be evaluated in this article, or claim that may be made by its manufacturer, is not guaranteed or endorsed by the publisher.

frontiers | Frontiers in Energy Research

ORIGINAL RESEARCH
published: 25 April 2022
doi: 10.3389/fenrg.2022.904201

Influence of Solid–Liquid Two-Phase Flow on Cavitation of Tubular Turbine Blades Under Combined Conditions

Chuang Cheng[1], Zhenggui Li[1], Fubing He[2], Siyuan Wu[3], Chuchu Zeng[4], Kui Zhang[5] and Jing Zheng[6]*

[1]Key Laboratory of Fluid and Power Machinery, Ministry of Education, Xihua University, Chengdu, China, [2]Guoneng Dadu River Basin Hydropower Development Co., Ltd., Leshan, China, [3]China Three Gorges Construction Engineering (Group) Co., Ltd., Chengdu, China, [4]Dongyuan Branch of Shenzhen Water Planning and Design Institute Co., Ltd., Changsha, China, [5]China Gezhouba Group Electromechanical Construction Co., Ltd., Chengdu, China, [6]Sichuan Water Conservancy Vocational College, Chengdu, China

The influence of sediment media on the blade pressure and cavitation of a tubular turbine was investigated in this study. The Zwart–Geber–Belamri cavitation model and the shear stress transport *k–w* turbulence model were applied to numerically simulate and experimentally validate the full flow path of the tubular turbine under combined conditions for sediment particle sizes of 0.01 and 0.05 mm and concentrations of 1%, 1.5%, and 2%. The results show that the pressure of the blade increases with the sediment concentration. Cavitation mainly occurs between the blade shroud and the leading edge. The higher the sediment concentration, the lower the vapor volume fraction at the same sediment particle size. The presence of sediments inhibits further cavitation development, and the inhibition effect is significant. At the same concentration, the larger the particle size of the sediment, the lower the vapor volume fraction. Thus, the increase in the particle size inhibits cavitation, but the inhibition effect is not significant.

Keywords: tubular turbine, cooperative condition, cavitation, solid-liquid two-phase flow, sediment concentration

OPEN ACCESS

Edited by:
Kan Kan,
College of Energy and Electrical Engineering, China

Reviewed by:
Qiang Gao,
University of Minnesota Twin Cities, United States
Wenwu Zhang,
China Agricultural University, China

****Correspondence:***
Zhenggui Li
lzhgui@mail.xhu.edu.cn

Specialty section:
This article was submitted to Process and Energy Systems Engineering, a section of the journal Frontiers in Energy Research

Received: *25 March 2022*
Accepted: *06 April 2022*
Published: *25 April 2022*

Citation:
Cheng C, Li Z, He F, Wu S, Zeng C, Zhang K and Zheng J (2022) Influence of Solid–Liquid Two-Phase Flow on Cavitation of Tubular Turbine Blades Under Combined Conditions. Front. Energy Res. 10:904201. doi: 10.3389/fenrg.2022.904201

INTRODUCTION

China has made ecological civilization construction with Chinese characteristics a vital part of the socialist cause, encouraged ecological civilization promotion, fully implemented the new resource concept, and promoted the economical and efficient use of resources (Li et al., 2022). Hydropower development is economically valuable because it is clean, renewable, and efficient compared to traditional sources of thermal power generation (Wu and Zhu, 2021). Tubular turbines have broad application prospects in developing low-head hydraulic resources (Shu-tang, 2000).

During turbine operations, the fluid exhibits a strong nonlinear motion, that is, turbulent motion, under the influence of the complex turbine structure and three-dimensional transient nonconstant operating conditions. Turbulence is a critical factor that causes pulsations in the physical quantities of the flow field (Li D. et al., 2021; Wangxu et al., 2021). When sediment particles carrying tiny air nuclei enter the rotor area, the existence of a negative pressure fluctuation peak facilitates the rapid expansion and growth of bubbles, which contract and break under the action of the fluid (Xu-na et al., 2019). In addition, the collapse of these bubbles near the solid surface generates microjets and high-pressure waves that directly impact the solid surface and cause deformation. The deformation continues to increase because of the continuous collapse of the bubbles until the surface material breaks down, owing to fatigue and cavitation (Li et al., 2021b). When cavitation occurs, the collapse

of the cavitation bubbles changes the amplitude of the pressure fluctuation frequency (Li et al., 2021; Li et al., 2022), increasing the instability of the tubular turbine unit and generating vibration and noise (Fu et al., 2021; Sun, 2022).

In recent years, many scholars have investigated the influence of the sediment inside the turbine on cavitation performance. Lu (1991) investigated the collapse of cavitation bubbles in a solid–liquid two-phase flow and found that the solid particles in the liquid reduced the collapse rate of the bubbles. They observed that the higher the concentration of solids, the more pronounced the effect, which could reduce the destructive capacity of the bubbles. Liao (2012) argued that vortices in fluids are the source of cavitation; large particles in a vortex cannot be pulled into the vortex, and tiny particles cannot be ejected from the vortex. Therefore, appropriate particle size is an induced condition for cavitation. Particle-borne air nuclei facilitate early cavitation initiation, sometimes accompanied by pulsating pressure generation and exacerbating cavitation damage. Zeng and He (2020) simplified sediment particles into spherical shapes and simulated the interaction between cavitation bubbles and sediment particles near the wall. They concluded that the initial bubbles, which were adversely affected by the particles during the growth phase, were mushroom-shaped during the collapse, and bubbles less affected by the particles were pear-shaped. Zhang and Wei (2014) analyzed the distribution patterns of the sediment medium in a hydraulic turbine and the influence of the pressure field. They found that sand-containing water flow resulted in increased pressure load on the surface of turbine runner blades. Dong and Sun (2021) experimentally investigated the mechanism of the effect of different sand contents on the cavitation of high-speed water flow. They concluded that the cavitation factor increased with increasing sediment content at the median particle size (d = 1.09 mm), promoting cavitation. Wang et al. (2019) conducted numerical simulations of a Francis turbine at different sediment concentrations and found that in a high-speed rotating runner, solid particles collided forcefully at the walls because of inertial and centrifugal forces. These forces tended to induce cavitation inside the runner, increasing the head loss in the runner and aggravating blade wear. Teran et al. (2018) combined numerical simulations and experimental tests to investigate the interactions between cavitation bubbles and particles collapsing near the solid wall of a Francis turbine. They found that the initial positions of the solid particles and bubbles could significantly influence the particle velocity, inhibiting or accelerating the damage caused by the cavitation bubble collapses. Liang et al. (1997) investigated the vibration of a vacuolar cloud in a dilute solid–liquid two-phase flow and found that the main frequency of the vibration decreased when solid particles were in the bubble cloud. In addition, the solid particles significantly decreased the high-frequency part. In summary, the sediments inside the turbine induce internal wear and tear, whereas the generated air bubbles cause fatigue damage to the runner. In some cases, both phenomena work synergistically to cause more severe damage than each would cause separately. Although many scholars investigated cavitation under a solid–liquid two-phase flow and established systematic theoretical systems, most studies focused on Francis turbines. The study of cavitation under a solid–liquid two-phase flow in a tubular turbine is crucial, as this research area has not been studied extensively. In this study, the effects of different sediment concentrations and particle sizes on the cavitation characteristics of turbine rotor blades in the inlet flow of a tubular turbine were investigated, considering the combined conditions of a light bulb tubular turbine as a premise (Li et al., 2021a).

TURBULENCE MODELS AND CONTROL EQUATIONS

In terms of turbulence model selection, the k–ε model can simulate complex flows and has the advantages of being efficient and stable (Li W. et al., 2021). The k–ω model replaces the dissipation rate, ε, in the equation with the specific dissipation rate, ω, and is more stable in the viscous sublayer (Deyou et al., 2021). The shear stress transport k–ω equation combines the advantages of both equations and modifies the turbulent viscosity equation to obtain a more accurate simulation (Li et al., 2021). Because fluid compressibility slightly influences the flow field, the fluid domain is used as an incompressible fluid in constant-condition calculations for tubular turbines. No heat exchange between the phases in the fluid is considered. Under adiabatic no-slip conditions, the solid phase is equal in size and contains uniform spherical particles, and the phase change effect is negligible. The volume fraction α_m and density ρ_m of the mixed phase are expressed as follows:

$$\alpha_m = \alpha_l + \alpha_s + \alpha_v \tag{1}$$

$$\rho_m = 1 \Big/ \left(\frac{y_v}{\rho_v} + \frac{y_s}{\rho_s} + \frac{y_l}{\rho_l} \right) \tag{2}$$

where α_l, α_s, α_v are the liquid-, solid-, and gas-phase volume fractions, respectively, and y_l, y_s, y_v are the liquid-, solid-, and gas-phase mass fractions, respectively. The mass fraction, y, satisfies the following condition expressed by **Eq. 3**.

$$y_l + y_s + y_v = 1 \tag{3}$$

The continuity equation is a concrete expression of the law of matter indestructibility in fluid mechanics and is expressed by **Eq. 4**:

$$\frac{\partial \rho}{\partial t} + \nabla \cdot \left(\rho \cdot \vec{v} \right) = 0 \tag{4}$$

where ρ is the fluid density, and $\vec{v}$ is the velocity vector.

In hydrodynamic machinery, the entire process of a fluid passing through the flow components obeys the law of conservation of momentum, expressed as follows:

$$\frac{\partial}{\partial t}\left(\rho \vec{v} \right) + \nabla \cdot \left(\rho \vec{v} \vec{v} \right) = -\nabla \cdot p + \nabla \cdot \left(\vec{\tau} \right) + \rho \vec{g} + \vec{F} \tag{5}$$

TABLE 1 | Technical parameters of crossflow turbines.

Parameter	Value
Runner diameter	7.27 m
Synchronous speed	68.18 r/min
Rated output of individual machines	26.8 MW
Rated discharge	378 m^3/s
Maximum head	12 m
Minimum head	2.6 m
Rated head	7.8 m
Number of blades	4
Number of guide vanes	16

where p is the static pressure, and $\rho\vec{g}$ and $\vec{F}$ are the gravitational force and external force, respectively. The shear stress tensor for shear $\vec{\tau}$ is defined as follows:

$$\vec{\tau} = \mu\left[\left(\nabla\vec{v} + \nabla\vec{v}^T\right) - \frac{2}{3}\nabla\vec{v}I\right] \tag{6}$$

where μ is the dynamic viscosity, and I is the unit tensor. The second term on the right-hand side represents the volume expansion effect.

MODEL AND ITS BASIC PARAMETERS

In this study, a tubular turbine unit in the upper reaches of the Yellow River was selected. Its basic design parameters are listed in **Table 1**.

The cavitation performance curve between the cavitation coefficient and turbine efficiency was obtained by determining the different draft tube pressure conditions. When the turbine efficiency decreases by 1%, cavitation of the blades occurs at this pressure, and the draft tube outlet pressure becomes the critical cavitation pressure (Fubing, 2021).

The turbine cavitation coefficient is expressed as follows:

$$\sigma_p = \frac{\frac{P_0}{\rho g} - \frac{P_c}{\rho g} - H_s}{H} \tag{7}$$

where P_0 is the draft tube outlet pressure, P_c is the saturated vapor pressure of water, ρ is the density of water, g is the acceleration owing to gravity, H_s is the turbine suction height, and H is the working head of the turbine.

Ansys ICEM was used to simulate the hybrid meshing of the overall model. Hexahedral structural meshes were used for the inlet section, bulb body, and draft tube, and tetrahedral structural meshes were used for the complex guide vane and runner sections (Li et al., 2021). The entire flow channel mesh is depicted in **Figure 1**.

The minimum pressure on the blade surface significantly influences the cavitation performance of the runner during cavitation calculations (Hui et al., 2016). Therefore, the relationship between the overall grid number of the turbine, minimum pressure on the blade surface, and cavitation coefficient of the turbine under combined conditions was analyzed to minimize the influence of the grid number on calculation accuracy (**Figure 2**). The cavitation coefficient increased with an increasing number of grid nodes, with a maximum difference of 0.0031 (**Figure 2**). In contrast, the minimum pressure on the blade surface decreased with an increasing number of nodes, with a maximum difference of 8,000 Pa (**Figure 2**). When the number of grids in the entire fluid domain increased from 5.16 million to 8.84 million, the minimum pressure decreased by 3,000 Pa, and the cavitation coefficient increased by only 0.0001, satisfying the calculation accuracy requirements. Therefore, 8846777 grids and 1973260 nodes were adopted for the calculations.

This study focused on a solid–liquid two-phase flow, and Ansys CFX was used for numerical simulations. The nonhomogeneous phase model was selected for the multiphase flow, and the particle model was used for interphase transport, which is mainly applicable when a phase is continuous, and the other phase is dispersed or polydispersed. The inlet boundary condition was set as the mass flow, the outlet was set as the average static pressure outlet, and the solid boundary surface was a nonslip wall surface. The rotor speed was set to 68.18 r/min, and the calculation area reflected the effect of gravitational acceleration on the sediments. The guide vane opening and impeller opening were 10° and −34.5°, respectively, for the combined conditions (Li, 2014). The rated flow rate, Q, was 375.2 m^3/s, the sediment density was 2,650 kg/m^3, the sediment particle sizes were 0.01 and 0.05 mm. Sediment concentrations of 1%, 1.5%, and 2% were selected as discrete phases based on the actual measured data obtained at the upper Yellow River. The drag force during momentum exchange was considered. The high-accuracy solution mode was selected, and the convergence target root mean square was 1×10^{-4}.

TEST VERIFICATION

Tests were conducted in a hydropower station at the upper reaches of the Yellow River based on hydrological sediment observation data in May 2019 to obtain an average sediment

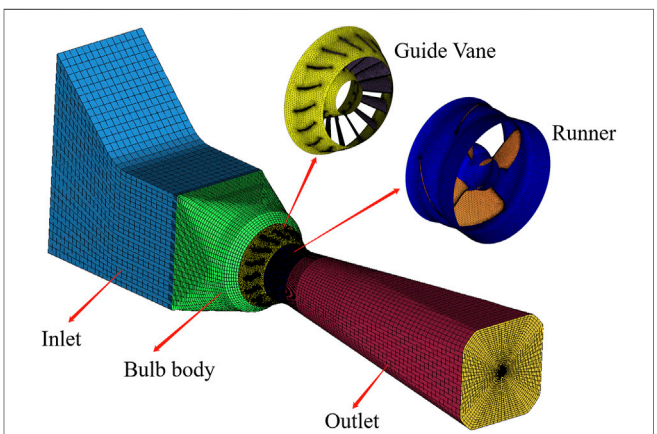

FIGURE 1 | Overall grid of fluid domain of tubular turbine.

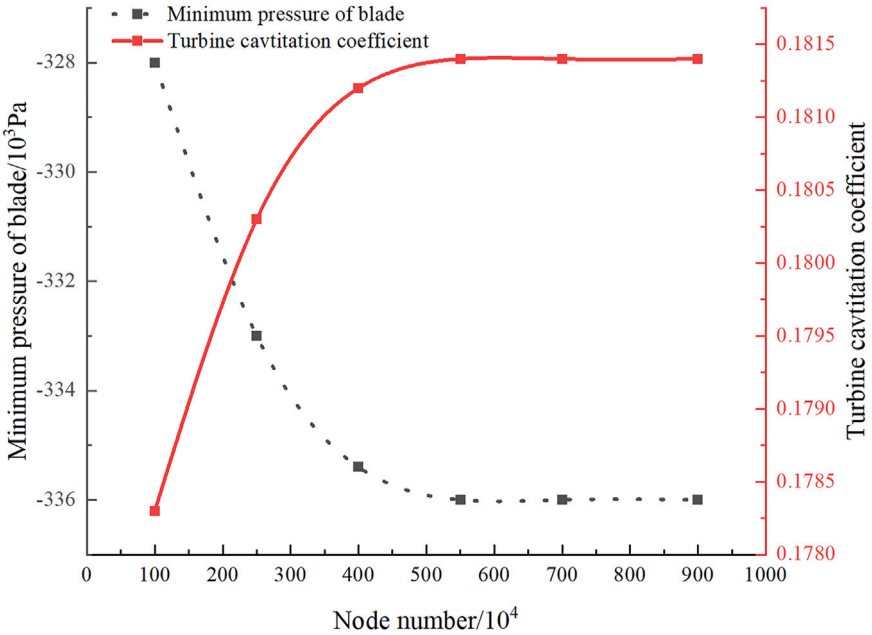

FIGURE 2 | Grid independence verification.

FIGURE 3 | Crossflow hydropower station at upper Yellow River.

TABLE 2 | Experimental monitoring data at different sediment particle concentrations.

Sediment particle size/mm	Sediment volume fraction/%	Test head/m	Monitoring efficiency/%
0.05	1	7.85	89.9
	1.5	8.24	87.4
	2	8.21	83.7

particle size of approximately 0.05 mm. The tests were conducted at sediment concentrations of 1%, 1.5%, and 2% of the water flow using unit #1 as the test verification unit. The unit paddle and guide vane openings were adjusted to 10° and 34.5°, respectively, and a water head of approximately 8 m was selected. Actual experimental tests were performed to collect data, including the

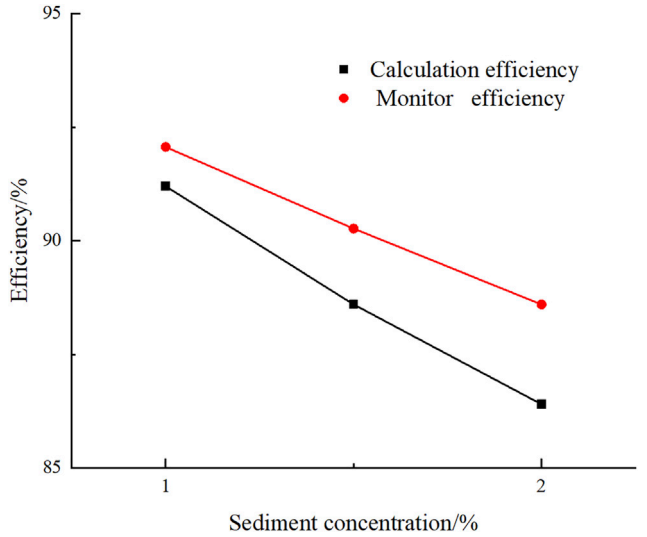

FIGURE 4 | Comparison of efficiency at different sediment concentrations for 0.05 mm particle size.

turbine efficiency at different concentrations. Because the sediment content and incoming water flow in the river were different, the measurements were performed at different times.

Water flows with sediment concentrations of 1%, 1.5%, and 2% at a particle size of 0.05 mm were intercepted for observation. The turbine efficiency data were received in the central control room of the power station (**Figure 3**).

Table 2 lists the experimental monitoring efficiency values for different sediment concentrations with a particle size of 0.05 mm, and **Figure 4** shows the corresponding efficiency comparison graph. The efficiency of the test monitoring results was higher than the calculated efficiency, and the efficiency decreased as the sediment concentration increased. Overall, the difference between the efficiency calculated through numerical simulations and the efficiency obtained experimentally was slight. The most significant difference in efficiency was observed for the 2% sediment concentration, with a difference of only 1.1%, indicating that the simulation results are accurate.

Figure 5 shows the blade cavitation for the 0.05 mm particle size and 2% concentration for the test performed after maintenance. A part of the damaged area appeared at the back of the blade at the junction between the water inlet edge and the rim. The surface metal was flaked off, and tiny pockmarks, pinhole pits, and cracks appeared, indicating cavitation damage. The cavitation location determined from the test was consistent with that predicted through simulations, demonstrating the accuracy of the simulation model.

CALCULATION RESULTS AND ANALYSIS

Figure 6 shows the relationship between the efficiency and the cavitation coefficient of the turbine. A single sediment on the blade drag force could be neglected. However, an increase in the sediment content impeded the water flow on the blade. The higher the drag force impact on the blade, the lower the efficiency of the turbine. The curve also showed that the lower the sediment concentration, the higher the turbine efficiency (**Figure 6**). The comparison shows that the turbine efficiency was slightly higher at the sediment particle size of 0.05 mm than at 0.01 mm. Moreover, the larger the sediment concentration, the more significant this phenomenon. At cavitation coefficients σ_p of 2.35–1.96, the overall efficiency tended to be stable, indicating that cavitation did not occur, and the turbine operated stably. As the outlet pressure decreased, the cavitation coefficient approached 1.96–1.84, and the turbine efficiency decreased. When the cavitation coefficient decreased to 1.84, the turbine efficiency decreased by 1%, suggesting that critical cavitation occurred on the blades at an outlet pressure of 0.6 atm (approximately 60.795 kPa). The outlet pressure continued to decrease, the cavitation coefficient decreased from 1.84 to 1.71, and the overall efficiency decreased. However, the slope of the curve gradually decreased; at this time, the blade had numerous cavitation bubbles, and blade cavitation intensified. After the cavitation coefficient decreased to 1.45, the turbine efficiency decreased sharply, and the cavitation bubble occupied the entire blade and flow channel, obstructing the water flow. If this condition occurs for an extended period, the

FIGURE 5 | Blade cavitation of tubular turbine (Shengyang, 2020).

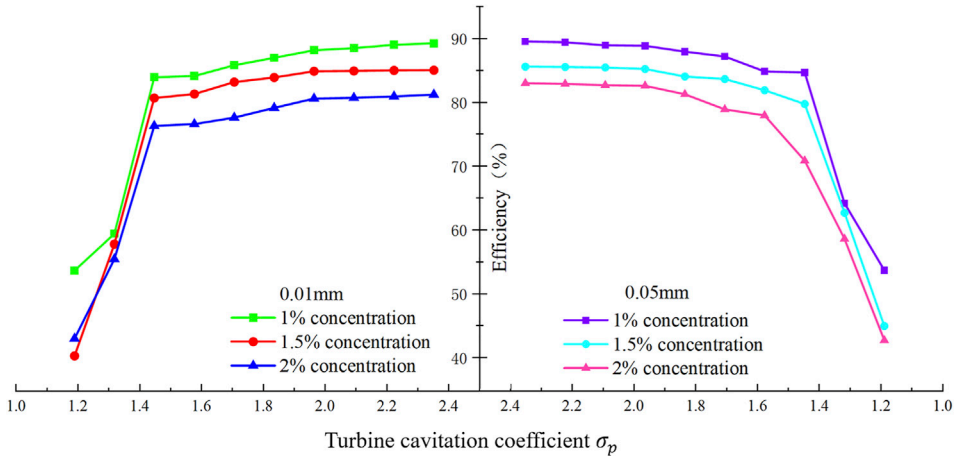

FIGURE 6 | Relationship between efficiency and cavitation coefficient of hydraulic turbine.

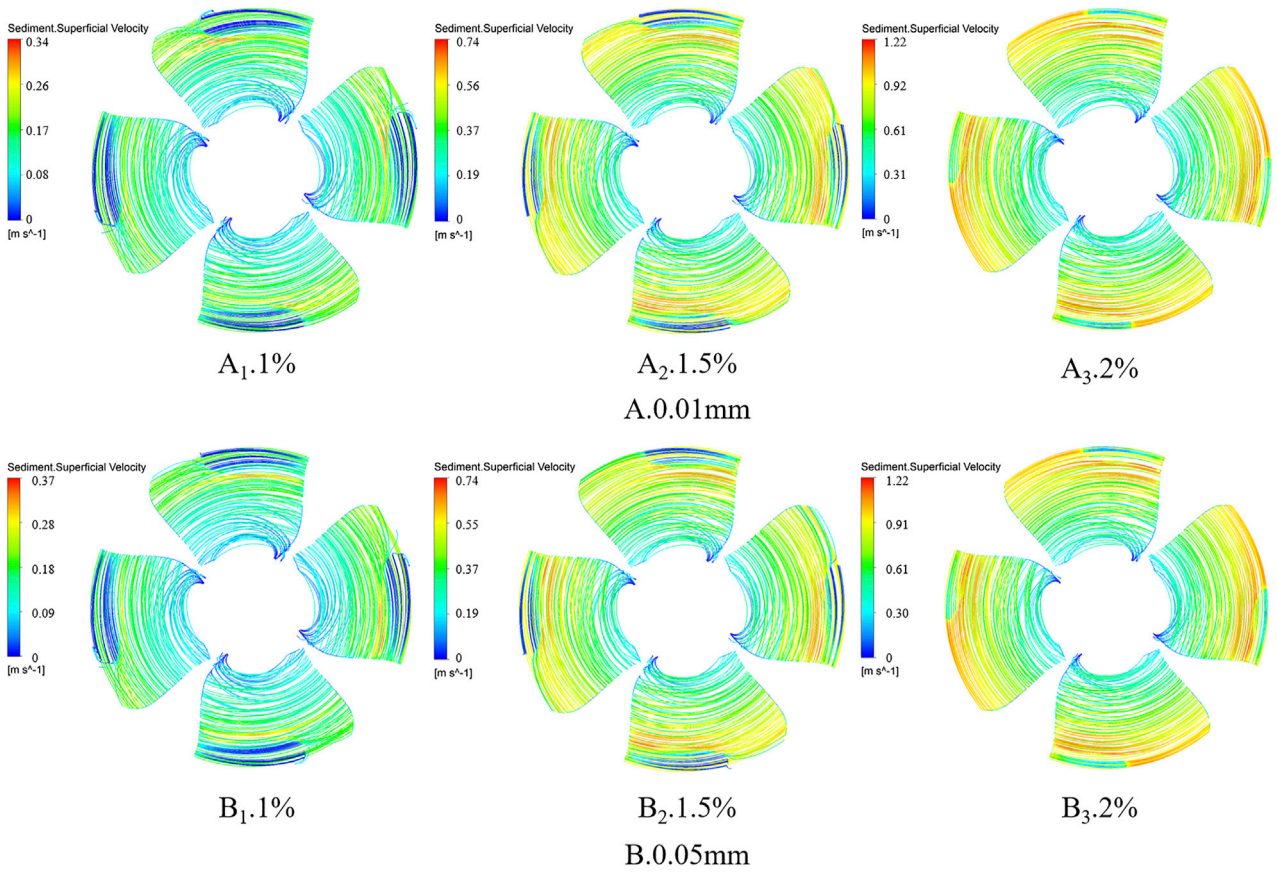

FIGURE 7 | Distribution of streamlines on suction side of blade for different sediment particle sizes and concentrations [**(A, B)** are 0.01 and 0.05 mm particle sizes, respectively; 1, 2, and 3 correspond to 1%, 1.5%, and 2% concentrations, respectively, same as in **Figures 8**, **9**)].

unit may generate vibration and noise, damaging the blade. Therefore, a critical cavitation factor, σ_p, of 1.84 was adopted to evaluate the effect of solid–liquid two-phase flow on the cavitation characteristics of the blade.

Effects of Concentration and Particle Size on Sediment Velocity on Blades

During the flow of water with sediments inside the turbine, the centrifugal force of the rotating blades caused the sediment

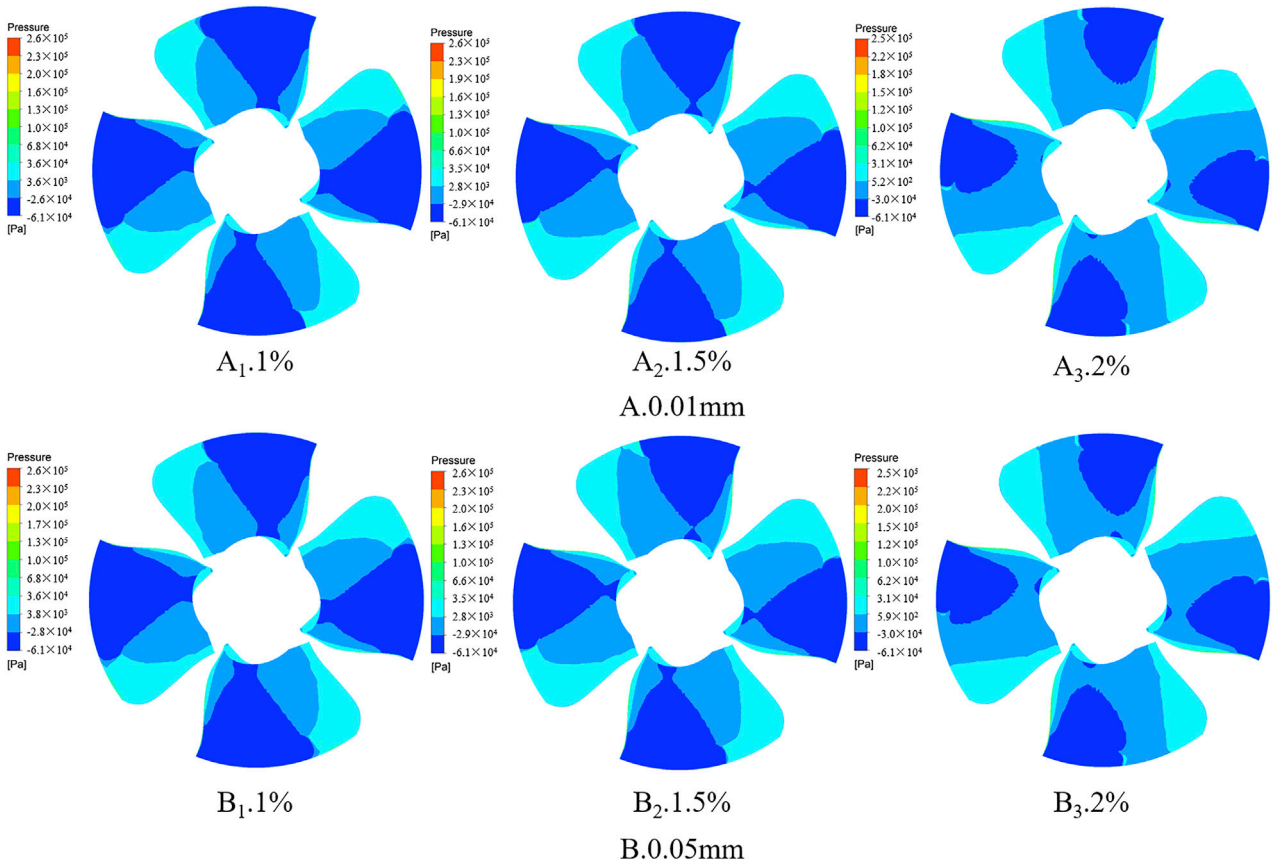

FIGURE 8 | Pressure distribution on suction side of blade for different sediment particle sizes and concentrations. **(A)** and **(B)** are 0.01 and 0.05 mm particle sizes, respectively; 1, 2, and 3 correspond to 1%, 1.5%, and 2% concentrations, respectively.

particles to gradually gather at the shroud. Here, the sediment was affected by the cavitation bubble blockage, and the sediment flow velocity decreased during this process. This is expressed in the flow line, which is the low-speed area at the shroud, as shown by the dark blue flow line in **Figure 7**. The sediment velocity of the large particles was lower than that of the small particles because when the sediment particle size was large, the inertial force increased, and the water flow was increasing affected by the sediment particles. At the same inlet concentration, the larger the particle size, the lower the velocity. The difference in flow distribution and absolute velocity between the different particle sizes gradually reduced, and the overall flow velocity tended to be smooth as the sediment concentration and velocity increased for both particle sizes. Thus, the vapor volume fraction might gradually decrease with increasing sediment concentration. Therefore, further verification is required.

Effects of Concentration and Particle Size on Blade Pressure

Figure 8 shows the pressure distribution on the suction side of the blade. The negative-pressure area gradually decreased from the shroud to the hub. At a sediment concentration of 1%, the negative pressure area for both particle sizes was 23.9 m^2, confirming that cavitation occurred here. Cavitation was most severe near the shroud (A_1 and B_1 in **Figure 8**). The width of the negative-pressure area decreased at a concentration of 1.5%, decreasing the pressure area to 20.6 m^2 for the sediment particle size of 0.01 mm (A_2 in **Figure 8**) and approximately 20.1 m^2 for the 0.05 mm sediment (B_2 in **Figure 8**). When the sediment concentration reached 2%, the negative-pressure area near the hub decreased sharply, and the total area of the negative-pressure region for both particle sizes was 13.3 m^2. As the sediment concentration increased, the negative-pressure area decreased. Thus, more sediments hit the blade surface as the concentration increased, increasing the overall pressure on the blade.

The maximum pressures corresponding to the 1%, 1.5%, and 2% concentrations were 2.61×10^5, 2.57×10^5, and 2.46×10^5 Pa for the 0.01 mm sediment particle size and 2.62×10^5, 2.57×10^5, and 2.46×10^5 Pa for the 0.05 mm particle size. The maximum sediment pressure decreased with increasing concentration, probably because of the increase in sediment distribution and the mutual pressure transfer between sediment particles. This resulted in a smoothening of the overall pressure and no pressure

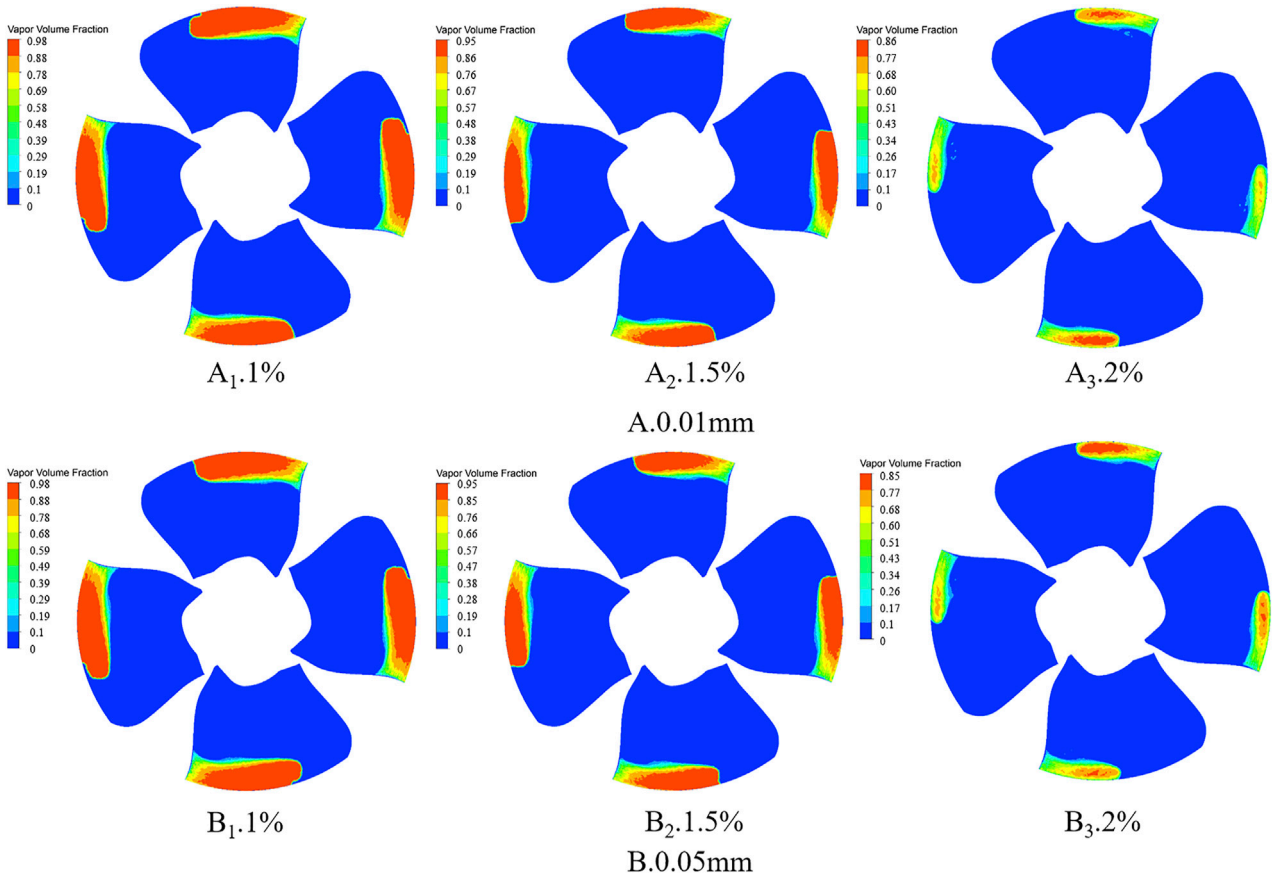

FIGURE 9 | Vapor volume distribution on suction side of blade for different sediment particle sizes and concentrations. **(A)** and **(B)** are 0.01 and 0.05 mm particle sizes, respectively; 1, 2, and 3 correspond to 1%, 1.5%, and 2% concentrations, respectively.

peaks, owing to the dispersed distribution of some sediments. The effect of particle size on the magnitude and pressure distribution of the blade pressure was negligible. The results showed that an increase in the sediment content decreased the area of the negative-pressure zone and inhibited cavitation evolution.

Effects of Concentration and Particle Size on Blade Cavitation

As the low-pressure areas of the tubular turbines appeared at the suction side of the runner and were mainly concentrated near the shroud, cavitation mainly occurred at the shroud of the suction side of the blades. For the sediment flow with the runner operating, the cavitation bubble from the center started to collapse outwards when the cavitation bubble just contacted the blade or sediment particles, and the boundary quickly contracted. Here, the pressure gradient of the cavitation bubble edge decreased sharply. The center of the cavitation bubble generated a significant pressure gradient, causing the water to flow towards the blade boundary and sediment particles, forming two microjet flows. Therefore, when sediments were present, a part of the energy generated through the collapse of the cavitation bubbles was transported by the sediment particles. Thus, the higher the sediment content, the lower the bubble distribution on the blade (**Figure 9**). Extensive cavitation occurred at the shroud, and the bubble distribution was concentrated. A comparison with the pressure distribution graph indicated a significant distribution of bubbles in the area of least pressure at the shroud. The most severe cavitation occurred when the sediment concentration was 1%; at 0.01 mm, the maximum vapor volume fraction was 97.85%, and at 0.05 mm, it was 97.7%. The least significant cavitation was observed at a sediment concentration of 2%; the maximum vapor volume fractions at 0.01 and 0.05 mm were 85.59 and 85.24%, respectively. The calculated cavitation areas were 14.9, 11.3, and 7.39 m^2 at sediment concentrations of 1%, 1.5%, and 2%, respectively, for the 0.01 mm particle size. For the 0.05 mm particle size, the cavitation areas were 12.61, 10.69, and 7.58 m^2 at sediment concentrations of 1%, 1.5%, and 2%, respectively. At the same sediment particle size, the sediment concentration increased with decreasing vapor volume, indicating that the sediments significantly inhibited further cavitation development. At the same concentration, the larger the particle size of the sediment, the lower the volume fraction of vapor, indicating that an increase in the particle size had a constraining effect on cavitation. However, the inhibiting effect

of the concentration was less significant than that of the particle size.

DISCUSSION

Although the effect of sediment concentration and sediment particle size on the distribution of cavitation bubbles has been analysed in this paper, the size and strength of cavitation bubbles has not been investigated. Much research has been done by some scholars and experts on the occurrence and development of cavitation bubbles, GAO Q (Gao et al., 2021a; Gao et al., 2021b; Gao et al., 2021c) performed numerical simulations using coupled level set and volume of fluid (CLSVOF) method to resolve air-water interface directly and studied the statistics of bubble size distributions; Wang et al. (2021) conducted simulations on the bubbles in the ventilated cavitation and studied the bubble distribution under the effects of breakup and coalescence.

Due to experimental constraints, this paper has some shortcomings below:

1). In the actual operation of hydropower stations, the distribution of sediment particle size and concentration within the sand-bearing water stream is more complex, so the tests carried out in this paper differ to a small extent from the boundary conditions set by the numerical simulation, which is also reflected in the efficiency diagrams derived from the tests.
2). This paper only considers the distribution and size of cavitation under sand-bearing water flow conditions, but lacks the study of other dimensions such as bubble generation, breakage, intensity and size. Although some effects of solid and liquid phases on each other can be obtained, the analysis of the development and evolution of cavitation bubbles is lacking.

We anticipate using a model turbine in future work to test this in order to bring the flow of water with different sediment concentrations and particle sizes within a controlled range and to increase the reliability of the test results. In addition, the solid-water interface will be studied in more detail and the development and evolution of cavitation bubbles will be considered, exploring the specific influence of sediment particles on the size and distribution of cavitation bubbles at the microscopic level.

CONCLUSION

In this study, a three-dimensional flow-field numerical study of the blade flow and cavitation performance of a tubular turbine was conducted for different sediment particle sizes and concentrations. The blade cavitation and bubble distribution behavior under different working conditions were analyzed. The following conclusions were drawn.

1) The negative-pressure area of the blade decreased with increasing sediment concentration. For the 0.01 mm particle size, the negative-pressure areas were 23.9, 20.6, and 13.3 m^2 at 1%, 1.5%, and 2% sediment concentrations, respectively. For the 0.05 mm condition, the negative-pressure areas were 23.9, 20.1, and 13.3 m^2 at 1%, 1.5%, and 2% concentrations, respectively. The larger the concentration of sediments on the blade, the smaller the negative-pressure area. In addition, the maximum pressure decreased with increasing sediment concentration. Apart from the cavitation area, sediment concentration was the main factor influencing the area of the negative-pressure zone on the blade.
2) The vapor area on the blade decreased with increasing sediment concentration. For the 0.01 mm particle size, the vapor areas were 14.9, 11.3, and 7.39 m^2 at 1%, 1.5%, and 2% sediment concentrations, respectively. For the 0.05 mm size, the vapor areas were 12.61, 10.69, and 7.58 m^2 at 1%, 1.5%, and 2% sediment concentrations, respectively. The higher the sediment concentration, the lower the volume fraction of vapor. The presence of sediments inhibited further development of cavitation, and the inhibition effect was significant. The inhibition effect of the particle size on cavitation became less significant as the concentration increased.

DATA AVAILABILITY STATEMENT

The original contributions presented in the study are included in the article/Supplementary Material, further inquiries can be directed to the corresponding author.

AUTHOR CONTRIBUTIONS

The CC wrote and improved the paper; ZL provided guidance and advice on writing the paper; FH, SW, and CZ provided guidance on the analysis of the study, KZ provided guidance on the test apparatus, and JZ provided guidance on the tests.

FUNDING

This work was supported by the National Natural Science Foundation of China (Grant No. 52079118), Central leading local (scientific and technological innovation base construction) project XZ202201YD0017C, National Key Research and Development Program (2018YFE0128500).

REFERENCES

Deyou, L., Liang, Y., Xunyu, Y., Hongjie, W., Qian, S., and Xianzhu, W. (2021). Runner Cone Optimization to Reduce Vortex Rope-Induced Pressure Fluctuations in a Francis Turbine. *Sci. China Technol. Sci.* 64, 1953–1970. doi:10.1007/s11431-021-1867-2

Dong, Z-Y., and Sun, J-Y. (2021). Experimental Study of Effects of Sediment Concentration on Cavitation Erosion in High Velocity Flows. *J. Hydroelectric Eng.* 40 (10), 10–18. doi:10.11660/slfdxb.20211002

Fu, X., Zuo, Z., Chang, H., Li, D., Wang, H., and Wei, X. (2021). Mechanism of Low Frequency High Amplitude Pressure Fluctuation in a Pump-Turbine during the Load Rejection Process. *J. Hydraulic Res.* 59 (2), 280–297. doi:10.1080/00221686.2020.1780488

Fubing, H. (2021). *Study on Cavitation Characteristics and Flow Field of Tubular under Different Clearances [D]*. Chengdu: Xi Hua University.

Gao, Q., Deane, G. B., Liu, H., and Shen, L. (2021a). A Robust and Accurate Technique for Lagrangian Tracking of Bubbles and Detecting Fragmentation and Coalescence. *Int. J. Multiphase Flow* 135, 103523. doi:10.1016/j.ijmultiphaseflow.2020.103523

Gao, Q., Deane, G. B., and Shen, L. (2021b). Bubble Production by Air Filament and Cavity Breakup in Plunging Breaking Wave Crests. *J. Fluid Mech.* 929, 890. doi:10.1017/jfm.2021.890

Gao, Q., Shen, L., and Deane, G. B. (2021c). A Numerical Simulation Framework for Bubbly Flow and Sound Generation in Laboratory-Scale Breaking Waves. *JASA Express Lett.* 1 (10), 100801. doi:10.1121/10.0006584

Hui, R., Weili, L., Xingqi, L., Yaping, Z., Hongzhe, Q., and Zhongjie, Y. (2016). Effects of Low Pressure Meridional Position on Cavitation Performance for High-Head Pump-Turbine. *Trans. Chin. Soc. Agric. Eng.* 32 (16), 73–81. doi:10.11975/j.issn.1002-6819.2016.16.011

Li, D., Song, Y., Lin, S., Wang, H., Qin, Y., and Wei, X. (2021). Effect Mechanism of Cavitation on the Hump Characteristic of a Pump-Turbine. *Renew. Energ.* 167, 369–383. doi:10.1016/j.renene.2020.11.095

Li, W., Li, Z., Qin, Z., Yan, S., Wang, Z., and Peng, S. (2022). Influence of the Solution pH on the Design of a Hydro-Mechanical Magneto-Hydraulic Sealing Device. *Eng. Fail. Anal.* 135, 106091. doi:10.1016/j.engfailanal.2022.106091

Li, W., Li, Z., Wang, Z., Wu, F., Xu, L., and Peng, S. (2021). Turbulence Intensity Characteristics of a Magnetoliquid Seal Interface in a Liquid Environment. *Coatings* 11 (11), 1333. doi:10.3390/coatings11111333

Li, Z-G. (2014). *Research on Co-associated Relation and Performance of Bulb Tubular Turbine [D]*. Lanzhou: Lanzhou University of Technology.

Li, Z., Cheng, C., and Yan, S. (2021a). Theoretical Analysis of Entropy Generation at the Blade Interface of a Tubular Turbine under Cooperative Conditions. *Front. Energ. Res.* 9, 788416. doi:10.3389/fenrg.2021.788416

Li, Z., Li, W., Li, W., Wang, Q., Xiang, R., Cheng, J., et al. (2021b). Effects of Medium Fluid Cavitation on Fluctuation Characteristics of Magnetic Fluid Seal Interface in Agricultural Centrifugal Pump. *Int. J. Agric. Biol. Eng.* 14 (6), 85–92. doi:10.25165/j.ijabe.20211406.6718

Liang, Z., Jiang, J., and Cheng, L-J. (1997). A Study on the Oscillation of the Cloud of Bubbles in a Dilute Solid-Liquid Two-Phase Flow. *J. Huazhong Univ. Sci. Tech.* 1997 (09), 45–48.

Liao, T-T. (2012). Research on the Size of Sediment Passing through the Turbine Effects on Cavitation and Cavitation Erosion for the Blade of Three Gorges Hydropower Plant. *China Rural Water and Hydropower* 2012 (02), 121–123+126.

Lu, L. (1991). Bubble Collapse in Solid-Liquid Two-Phase Fluid [J]. *Acta Mechanica Sinica* 1991 (01), 8–16.

Shengyang, P. (2020). *Application of Vortex Dynamics in Solid-Liquid Two Phase Flow of Tubular Turbine [D]*. Chengdu: Xihua University.

Shu-tang, T. (2000). *Tubular Turbine Generator Set and its Selection Method [M]*. Beijing: China Electric Power Press.

Sun, J. (2022). "Study on the Influence of Operating Head on Cavitation Performance of an Ultra-low Head Two-Blade Tubular Turbine [J/OL]," in Proceedings of the CSEE, 1–12.

Teran, L. A., Rodríguez, S. A., Lain, S., and Jung, S. (2018). Interaction of Particles with a Cavitation Bubble Near a Solid Wall. *Phys. Fluids* 30, 123304. doi:10.1063/1.5063472

Wang, L., Li, B-Y., and Zhao, W-G. (2019). Dynamics and Wear Analysis of Hydraulic Turbines in Solid-Liquid Two-Phase Flow. *Open Phys.* 17 (1), 790–796. doi:10.1515/phys-2019-0082

Wang, Z., Liu, H., Gao, Q., Wang, Z., Wang, Y., Wang, G., et al. (2021). Numerical Investigation of Ventilated Cavitating Flow in the Wake of a Circular Cylinder. *Phys. Rev. Fluids* 6 (6), 064303. doi:10.1103/physrevfluids.6.064303

Wangxu, L., Zhenggui, L., Wanquan, D., Lei, J., Yilong, Q., and Huiyu, C. (2021). Particle Image Velocimetry Flowmeter for Natural Gas Applications. *Flow Meas. Instrumentation* 82, 102072. doi:10.1016/j.flowmeasinst.2021.102072

Wu, L., and Zhu, Q. (2021). Impacts of the Carbon Emission Trading System on China's Carbon Emission Peak: A New Data-Driven Approach. *Nat. Hazards* 107 (3), 2487–2515. doi:10.1007/s11069-020-04469-9

Xu-na, G., Yuan, J., Jiang, F., and Ma, X. (2019). Molecular Dynamics Simulation of Hydraulic Mechanical Cavitation. *J. Eng. Therm. Energ. Power* 34 (08), 43–49. doi:10.16146/j.cnki.rndlgc.2019.08.007

Zeng, Q-F., and He, Z-B. (2020). "Numerical Simulation of the Interaction between Cavitation Bubbles and Sediment Particles in the Hydroturbine," in Proceedings of the 31st National Symposium on Hydrodynamics (Volume II), Xiamen, Fujian, China, October 30–November 3, 2020, 65–73.

Zhang, G., and Wei, X-Z. (2014). Numerical Analysis for Effects of Concentration and Diameter of Sediment on Solid-Liquid Two-Phase Flow in Hydraulic Turbine Runner. *Trans. Chin. Soc. Agric. Eng.* 30 (23), 94–100. doi:10.3969/j.issn.1002-6819.2014.23.013

Conflict of Interest: FH is employed by Guoneng Dadu River Basin Hydropower Development Co., Ltd. SW is employed by China Three Gorges Construction Engineering (Group) Co., Ltd. CZ is employed by Dongyuan Branch of Shenzhen Water Planning and Design Institute Co., Ltd. KZ is employed by China Gezhouba Group Electromechanical Construction Co., Ltd.

The remaining authors declare that the research was conducted in the absence of any commercial or financial relationships that could be construed as a potential conflict of interest.

Publisher's Note: All claims expressed in this article are solely those of the authors and do not necessarily represent those of their affiliated organizations, or those of the publisher, the editors and the reviewers. Any product that may be evaluated in this article, or claim that may be made by its manufacturer, is not guaranteed or endorsed by the publisher.

frontiers | Frontiers in Energy Research

ORIGINAL RESEARCH
published: 09 May 2022
doi: 10.3389/fenrg.2022.904202

Vortex Distribution and Energy Loss in S-Shaped Region of Pump Turbine

Hongji Zeng[1], Zhenggui Li[1], Deyou Li[2], Hao Chen[3] and Zhihong Li[4]*

[1]Key Laboratory of Fluid and Power Machinery, Xihua University, Chengdu, China, [2]School of Energy Science and Power Engineering, Harbin Institute of Technology, Harbin, China, [3]China Three Gorges Construction Engineering Group Co., Ltd., Chengdu, China, [4]China Gezhouba Group Electromechanical Construction Co., Ltd., Chengdu, China

Research on the S-shaped region of pump turbines requires a detailed understanding of the vortex distribution law and energy losses under various working conditions. In this study, numerical simulations of a pump turbine model were conducted, and the results were consistent with the experimental results. The $|\omega|$-criterion in the vortex analysis method was combined with the Q-criterion to reveal vortex distribution in the S-shaped region for each working condition along the Q_{11}-n_{11} curve for all the conditions. Under the runaway and turbine break conditions, the flow field vortices were mainly the leaf channel vortex and separation vortex. Under zero-flow-rate and reverse-pump conditions, the vortices developed towards the stay-guide vanes, obstructing the flow path. Combined with the entropy production rate distribution, vorticity is closely related to energy loss. Compared to the rotation, the vorticity generated by the strong shear effect is significant.

Keywords: pump turbine, S-shaped region, vortex analysis method, vortex distribution, entropy production rate

OPEN ACCESS

Edited by:
Kan Kan,
College of Energy and Electrical Engineering, China

Reviewed by:
Tianyi Li,
University of Minnesota Twin Cities, United States
Dan Zi,
China Agricultural University, China

****Correspondence:***
Zhenggui Li
lzhgui@mail.xhu.edu.cn

Specialty section:
This article was submitted to Process and Energy Systems Engineering, a section of the journal Frontiers in Energy Research

Received: *25 March 2022*
Accepted: *12 April 2022*
Published: *09 May 2022*

Citation:
Zeng H, Li Z, Li D, Chen H and Li Z (2022) Vortex Distribution and Energy Loss in S-Shaped Region of Pump Turbine. Front. Energy Res. 10:904202. doi: 10.3389/fenrg.2022.904202

INTRODUCTION

Climate change is a global issue, and the increasing emission of greenhouse gases, particularly carbon dioxide, is a threat to humankind. Consequently, countries are reducing their greenhouse gas emissions through a global compact. In September 2020, China announced at the United Nations General Assembly its goal to achieve carbon peaking by 2030 and carbon neutrality by 2060 (Caide, 2021; Peng 2021; Li et al., 2022). In response to its national policy, China has accelerated the construction of pumped-storage power plants. As the core of a pumped-storage power plant, the pump turbine needs to switch back and forth between different operating conditions during operations and is likely to enter the "S" characteristic instability region (Chen 2018). When operating in this area, the internal fluid of the pump turbine exhibits a strong nonlinear turbulent motion (Wangxu et al., 2021), and the turbulent motion is a critical factor for determining pulsating physical quantities, such as flow-field pressure and velocity. Under the combined action of complex boundary conditions of the pump turbine and the three-dimensional transient turbulent motion of the internal fluid, the flow and speed in the unit change significantly, accompanied by a strong pressure pulsation and significant energy loss.

Pejovic et al. (1976) first published relevant findings on the S-shaped region of pump turbines in 1976. Kinoue et al. (2019) investigated the start-up process of a low-specific-speed pump turbine and found that when it was close to the S-shaped region, more vortices appeared in the channel. Cavazzini et al. (2016) examined the load-shedding process of a pump turbine under a large guide vane opening and analyzed the causes of impeller rotation stall under turbine brake conditions. Singh et al. (2015) conducted a velocity triangle analysis at an impeller inlet, determined the velocity and pressure distribution, and comprehensively evaluated the changes in the internal flow pattern in the S-shaped region. However, in the operation process under various working conditions of the

S-shaped region of pump turbines, the variations in the flow pattern and energy of the internal flow field are difficult to observe. With the development of the vortex motion theory, entropy generation theory, and computational fluid dynamics (CFD), several relevant studies have been conducted using these new techniques.

Liu et al. (2016), Liu et al. (2019) developed vortex identification methods based on the Omega and Liutex systems. Peng (2020) applied the $|\omega|$-criterion, Q-criterion, and regularized helicity in the vortex analysis method to investigate the internal vortex under the solid–liquid two-phase flow of a tubular turbine. Peng (2020) found that the sediment significantly influences the size, position, and rotation direction of the vortex. Li et al. (2021a) reported that cavitation generates a degree of large-scale vortices in the hump area of a pump turbine. Zhang et al. (2018a) applied a new omega vortex identification method to examine an S-shaped region and verified its effectiveness. Fu et al. (2021) investigated the load-shedding process of a pump turbine and found that the leading causes of flow-field pressure fluctuation are the water hammer, reflux, and water-retaining ring. Ni et al. (2018) assessed the instantaneous vortex structure in a nuclear reactor coolant pump using the Q-criterion and found that the vortex structure in the impeller was critical. Kye et al. (2018) used a large eddy simulation model and found that the dynamic and static interferences between the centrifugal pump impeller and volute generate extremely strong vorticity at the casing tongue. Zhang N. et al. (2019) performed unsteady computations for a centrifugal pump using a delayed detached-eddy simulation model. They found that the vorticity in the volute was large, and the distribution of turbulent kinetic energy was similar to that of vorticity. Li et al. (2016) applied the Q-criterion in the hump area of a pump turbine. They demonstrated that the vortex originated from blade surface friction, and the hump characteristics were related to the blade suction surface pressure, friction, and vortex motion. Ji et al. (2016) applied the Q-criterion to analyze cavitation in Francis turbines and revealed the potential interaction mechanism between cavitation and vortices. However, the vortex analysis method has been applied to vorticity and vortex distribution studies. The entropy production theory needs to be introduced to evaluate energy characteristics.

Qin et al. (2017) conducted experimental tests and CFD simulations and proved that the hydraulic loss during the load rejection process of pump turbines is related to vortex distribution. Yuan et al. (2021) confirmed that a significant shearing effect is a sufficient condition for intense irreversible losses compared to the rotation effect. Lu et al. (2019) analyzed a pump turbine based on the entropy production theory and found that the total entropy production of the runner and draft tube is significantly higher than that of the guide vane and volute. Ren et al. (2021) evaluated a centrifugal pump using the entropy production theory and Q-criterion and found that the volute and impeller are the core areas where internal energy loss occurred in the centrifugal pump. The vortex analysis method and entropy production theory have been rarely used in studies on the S-shaped region of pump turbines, and the relationship between vortex distribution and energy loss is unclear.

The internal vortex dynamics characteristics of the S-shaped region of pump turbines under different working conditions were investigated using a vortex analysis method. The internal flow law was established, and a quantitative study on the internal energy conversion and loss of pump turbines was conducted using the entropy production theory to establish the relationship between vortex and energy loss. This study serves as a reference for further research on pump turbines.

CALCULATION METHOD AND THEORY

Vortex Analysis Method

Vortex motion is prevalent in fluids that cause vibration and fatigue in hydraulic turbines (Zhang et al., 2018b), and vortices are often difficult to observe in complex turbulent flows within fluid machinery. Therefore, with the development of CFD and vortex dynamics, vortex analysis methods that do not depend on the selection of coordinates and rotational variations have gradually been developed.

Vorticity can be regarded as twice the angular velocity of a fluid microcluster rotating rigidly around its center, derived from the flow-field velocity gradient. The vorticity of a flow field can be quantified using the $|\omega|$-criterion, mathematically expressed as follows:

$$\omega = \nabla \times v \tag{1}$$

where v is the velocity vector of the fluid mass, and ω is the vorticity of the fluid mass.

The Q-criterion can be expressed as follows:

$$Q = \frac{1}{2}\left[|\Omega|^2 - |S|^2\right] \tag{2}$$

$$\Omega = \frac{1}{2}\left[\nabla v - (\nabla v)^T\right] \tag{3}$$

$$S = \frac{1}{2}\left[\nabla v + (\nabla v)^T\right] \tag{4}$$

$$\nabla v = S + \Omega \tag{5}$$

where S and Ω are the symmetry and antisymmetry tensors, respectively, S is the strain, Ω is the rotation, and ∇v is the velocity gradient. When $Q > 0$, rotation is dominant, but when $Q < 0$, the shear strain is dominant.

Entropy Production Theory

According to the second law of thermodynamics, a fluid system is always accompanied by increased entropy (Li et al., 2017). The relationship between the entropy production rate and energy dissipation is expressed as follows.

$$\dot{S}_D^{\cdots} = \frac{\dot{Q}}{T} \tag{6}$$

where $\dot{Q}$ represents the energy dissipation rate.

Therefore, the entropy production rate can characterize the energy loss. When the fluid flow inside the pump turbine is turbulent, the entropy production rate is influenced by the time-averaged and pulsating velocities, expressed as follows:

TABLE 1 | Parameters of model.

Parameter	Value
Runner inlet diameter, D_1	477.5 mm
Runner outlet diameter, D_2	240 mm
Number of runner blades, Z_1	9
Number of stay vanes, Z_2	20
Number of guide vanes, Z_3	20

$$\dot{S}_D^{\cdots} = \dot{S}_{\dot{D}}^{\cdots} + \dot{S}_{\bar{D}}^{\cdots} \tag{7}$$

$$\dot{S}_{\dot{D}}^{\cdots} = \frac{\mu_{eff}}{T}\left\{2\left[\left(\frac{\partial u_1'}{\partial x_1}\right)^2 + \left(\frac{\partial u_2'}{\partial x_2}\right)^2 + \left(\frac{\partial u_3'}{\partial x_3}\right)^2\right] + \left(\frac{\partial u_2'}{\partial x_1} + \frac{\partial u_1'}{\partial x_2}\right)^2 + \left(\frac{\partial u_3'}{\partial x_1} + \frac{\partial u_1'}{\partial x_3}\right) + \left(\frac{\partial u_2'}{\partial x_3} + \frac{\partial u_3'}{\partial x_2}\right)^2\right\}^2 \tag{8}$$

$$\dot{S}_{\bar{D}}^{\cdots} = \frac{2\mu}{T}\left[\left(\frac{\partial \overline{u_1}}{\partial x_1}\right)^2 + \left(\frac{\partial \overline{u_2}}{\partial x_2}\right)^2 + \left(\frac{\partial \overline{u_3}}{\partial x_3}\right)^2\right] + \frac{\mu}{T}\left[\left(\frac{\partial \overline{u_2}}{\partial x_1} + \frac{\partial \overline{u_1}}{\partial x_2}\right)^2 + \left(\frac{\partial \overline{u_3}}{\partial x_1} + \frac{\partial \overline{u_1}}{\partial x_3}\right) + \left(\frac{\partial \overline{u_2}}{\partial x_3} + \frac{\partial \overline{u_3}}{\partial x_2}\right)^2\right]^2 \tag{9}$$

$$\mu_{eff} = \mu + \mu_t \tag{10}$$

where $\dot{S}_D^{\cdots}$ is the entropy production rate, $\dot{S}_{\dot{D}}^{\cdots}$ is the entropy production rate due to pulsating velocity, and $\dot{S}_{\bar{D}}^{\cdots}$ is the entropy production rate due to the time-averaged velocity. μ_{eff} is fluid effective dynamic viscosit. μ_t is turbulent power viscosity.

For the k–ω turbulence model, the entropy production rate of the pulsating velocity can be calculated using **Eq. 10**.

$$\dot{S}_{\dot{D}}^{\cdots} = \beta\frac{\rho\omega k}{T} \tag{11}$$

Where $\beta = 0.09$. ω is turbulent vortex viscous frequency. k is turbulent kinetic energy.

NUMERICAL MODEL AND CALCULATION SETUP

Computational Domain

In this study, a pump turbine model machine was used for calculations. The overflow components included the volute, stay vane, guide vane, runner blade, and draft tube. The geometric parameters of the model are listed in **Table 1**.

Turbulence Model

Fluid motion follows the continuity equation and momentum equation, the continuity equation that the net mass flow into the control body and the control body due to density changes in the mass added per unit of time is equal, the momentum equation that a system is not subject to external forces or the sum of the external forces is zero, expressed by **Eqs 12–15**:

$$\frac{\partial \rho}{\partial t} + \frac{\partial(\rho u)}{\partial t} + \frac{\partial(\rho v)}{\partial y} + \frac{\partial(\rho \omega)}{\partial z} = 0 \tag{12}$$

$$\frac{\partial(\rho u)}{\partial t} + \nabla\cdot(\rho u V) = \rho f_x + \frac{\partial \tau_{xx}}{\partial x} + \frac{\partial \tau_{yx}}{\partial y} + \frac{\partial \tau_{zx}}{\partial z} - \frac{\partial P}{\partial x} \tag{13}$$

$$\frac{\partial(\rho v)}{\partial t} + \nabla\cdot(\rho v V) = \rho f_y + \frac{\partial \tau_{yy}}{\partial y} + \frac{\partial \tau_{xy}}{\partial x} + \frac{\partial \tau_{zy}}{\partial z} - \frac{\partial P}{\partial y} \tag{14}$$

$$\frac{\partial(\rho \omega)}{\partial t} + \nabla\cdot(\rho \omega V) = \rho f_z + \frac{\partial \tau_{zz}}{\partial z} + \frac{\partial \tau_{xz}}{\partial x} + \frac{\partial \tau_{yz}}{\partial y} - \frac{\partial P}{\partial y} \tag{15}$$

In computational fluid dynamics, the shear stress transport SST k–ω model is an optimization model of the k–ω and k–ε models, expressed by **Eqs 16**, **17**:

$$\frac{\partial}{\partial t}(\rho k) + \frac{\partial}{\partial_{x_i}}(\rho k u_i) = \frac{\partial}{\partial_{x_j}}\left(\Gamma_k \frac{\partial k}{\partial x_j}\right) + G_k - Y_k + S_k \tag{16}$$

$$\frac{\partial}{\partial t}(\rho \omega) + \frac{\partial}{\partial_{x_i}}(\rho \omega u_i) = \frac{\partial}{\partial_{x_j}}\left(\Gamma_\omega \frac{\partial \omega}{\partial x_j}\right) + G_\omega - Y_\omega + D_\omega + S_\omega \tag{17}$$

where ρ is the fluid density, k is the turbulent kinetic energy, ω is the turbulent dissipation rate, and Γ_k and Γ_ω are the effective diffusion terms of k and ω, respectively. G_k and G_ω are generative terms, Y_k and Y_ω are diffusion terms, D_ω represents the orthogonal divergence terms, and S_k and S_ω are custom terms.

The SST k–ω model considers the transfer of principal shear stress in the near-wall inverse pressure gradient boundary layer (Li et al., 2021b). It precisely predicts the inverse pressure gradient and flow separation, while the entropy production is closely related to the viscous force in the boundary layer. Therefore, the SST k–ω model was adopted for the calculations.

Grid Information and Grid Irrelevance Verification

The entire model was meshed using ICEM Surf. Because the grid quality significantly impacts the calculation accuracy and considering that the structured grid simulation results are highly accurate (Li Z. et al., 2021; Li et al., 2021d), all parts of the computing domain were meshed to form a structured grid. **Table 2** lists the grid details for the six sets of grids in the model. Taking the normal turbine working condition as the calculation working condition point, we obtained the relative values of the calculated head, test head, and pump turbine efficiency as the independent verification standard (**Figure 1**).

The y^+ values for all six grid sets were lower than 11.6 (**Table 2**), and the velocity field in the wall region could be obtained directly using the SST k–ω model (Li 2017). The head and efficiency were in the grid number exceeding 4.7 million close to the test data and tended to stabilize, considering the calculation accuracy (**Figure 1**). Finally, the sixth grid set was selected as the grid model for the calculations. The grid division is depicted in **Figure 2**.

Boundary Conditions

Ansys Fluent was used to perform a constant numerical simulation of the entire fluid domain. The inlet boundary condition was set as the mass flow inlet, and the draft tube

TABLE 2 | Grid information.

Number	Volute	Stay-guide vanes	Runner	Draft tube	Total	y^+
1	256,720	427,692	543,010	150,870	1,378,922	3.1
2	294,782	665,932	975,825	212,680	2,149,219	3.3
3	594,112	830,122	1,437,975	376,480	3,500,849	2.4
4	634,782	1,217,522	2,392,875	476,490	4,721,669	1.9
5	691,204	1,780,168	2,398,032	712,680	5,582,084	1.8
6	691,204	2,089,988	3,398,032	959,130	7,158,354	1.6

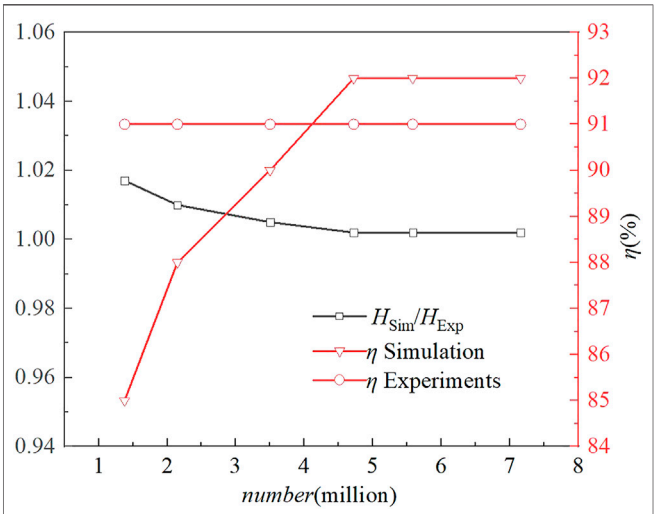

FIGURE 1 | Validation of grid independence.

outlet was the pressure outlet. The solid wall surface had a no-slip boundary condition. In addition, the flow field applied SIMPLEC pressure–velocity coupling, the rotation was set to a frame motion, and the convergence residual was set to 10^{-4}. The energy characteristics were analyzed for all cases without considering cavitation.

TEST VERIFICATION

The reliability of the numerical simulations was verified experimentally using a model pump turbine. A schematic of the testbed is shown in **Figure 3**. The test bench adopted a circular closed two-way operating system, and the experimental accuracy and operational stability satisfied relevant requirements.

In the numerical simulations, a minimum flow was selected to replace the zero flow because it is impossible to select the flow as zero under the zero-flow-rate condition; otherwise, the flow cannot be calculated. The specific operating point data are listed in **Table 3**, where n_{11} and Q_{11} are the unit speed and unit flow rate, respectively. n_{11} and Q_{11} are transformed using **Eqs 18**, **19**, respectively:

$$n_{11} = \frac{nD}{\sqrt{H}} \tag{18}$$

$$Q_{11} = \frac{Q}{D^2\sqrt{H}} \tag{19}$$

where n is the rotational speed, Q is the flow rate, D is the nominal diameter of the runner, and H is the water head.

The Q_{11}-n_{11} curve of the pump turbine depicts the inverse "S" shape of the guide vane opening line; hence, this area is called the S-shaped region of the pump turbine. The "S" property of the pump turbine is unique, and its existence can create difficulties in grid connection in the unit and fail to achieve no-load stability after load shedding. The test data for the turbine operating conditions were presented as the Q_{11}-n_{11} curve and compared with the CFD results for verification (**Figure 4**).

The most significant difference between the numerical simulation and test results near the runaway condition is attributed to the high speed and flow mismatch under this condition (**Figure 4**). However, the maximum error was still lower than 3%, and the numerical simulation and test results were consistent and satisfied the accuracy requirements (Liu 2013).

ANALYSIS OF VORTEX IN S-SHAPED REGION

The physical quantity that characterizes the angular velocity of rotation of a fluid microelement is vorticity, which originates from the velocity gradient of the flow field (Norizan et al., 2018; Tajul 2018). The $|\omega|$-criterion uses the modulus of vorticity as the criterion for vortex. However, because vorticity originates from the velocity gradient of a flow field, it cannot distinguish between the rotation and shear motion, although it can intuitively show the difference in velocity gradient. When the vorticity modulus is very high, it becomes inconsistent with the existence of a vortex. Therefore, the Q-criterion was introduced to identify vortices (Zhang Y.-n. et al., 2019). **Figure 5** shows the vorticity distribution of the stay-guide vanes and runner for each operating condition in the S-shaped region. **Figure 6** shows the Q-criterion discrimination results of the stay-guide vanes and runner for each operating condition in the S-shaped region.

The velocity gradient of the internal flow field of the turbine condition was mainly induced by the impact of the incoming flow on the runner (**Figures 5**, **6**). Therefore, the vorticity modulus was very low, and the vortices were small-scale vortices.

The vorticity under the runaway condition was significantly increased compared with OP1. Not only did vorticity exceeding 600 s^{-1} occur on each blade pressure surface, but

FIGURE 2 | Grids of different parts.

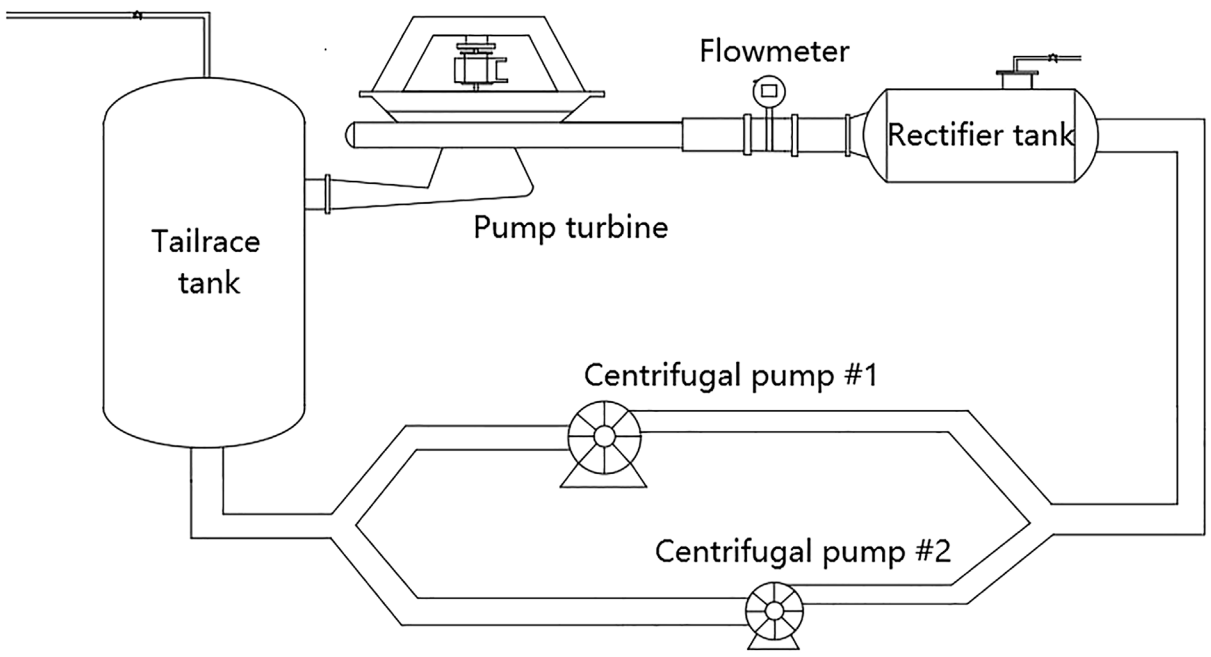

FIGURE 3 | Pump turbine test bench.

TABLE 3 | Calculated working points.

Working condition	n_{11}	Q_{11}
Turbine condition, OP1	37.02	0.69
Runaway condition, OP2	50.01	0.31
Turbine break condition, OP3	47.46	0.12
Zero-flow-rate condition, OP4	45.05	−0.02
Reverse pump condition, OP5	47.46	−0.11

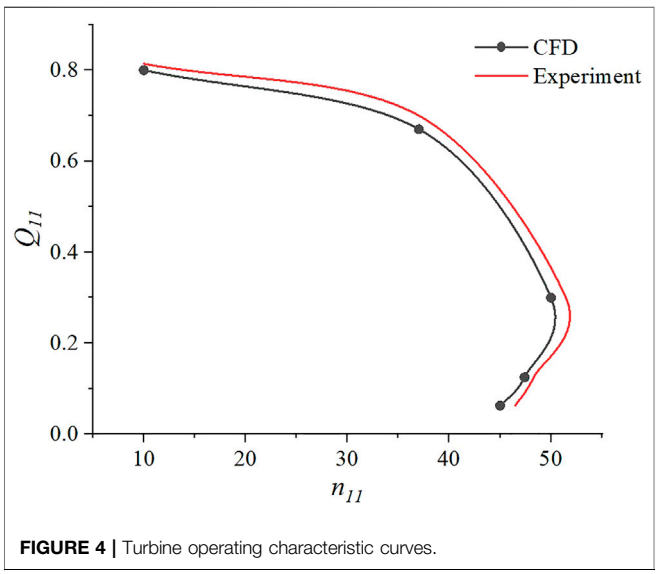

FIGURE 4 | Turbine operating characteristic curves.

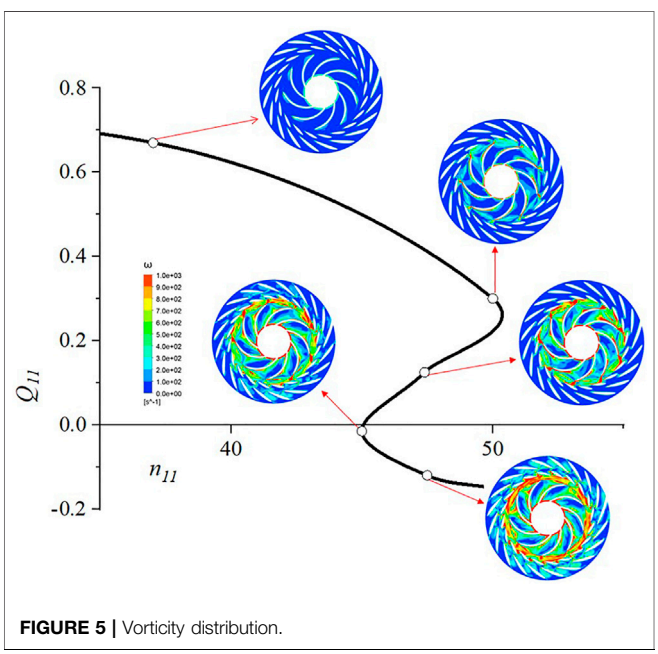

FIGURE 5 | Vorticity distribution.

the vorticity in the vaneless space also increased. A significant velocity gradient existed at the entrance of each runner flow channel, obstructing the normal passage of water and blocking

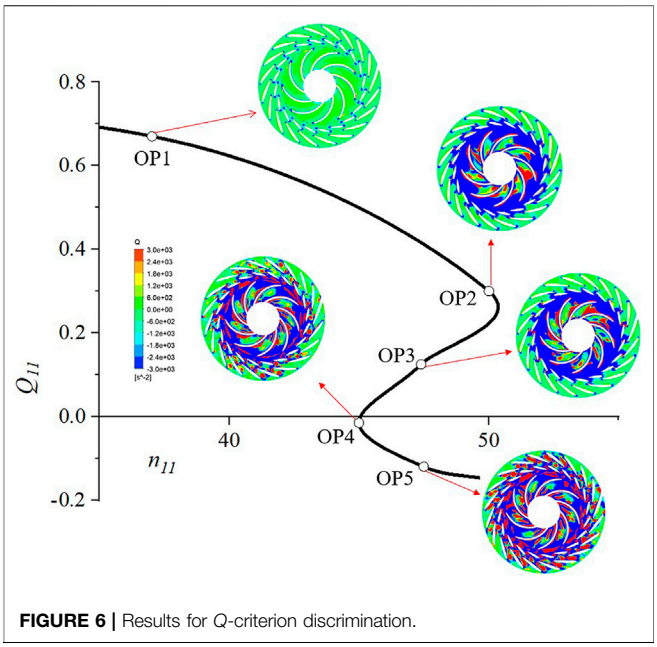

FIGURE 6 | Results for *Q*-criterion discrimination.

the flow channel. The *Q*-criterion discrimination results for the runaway condition indicated that the blade pressure surface exhibited a larger-scale vortex because the runaway condition had a high speed and low flow rate, and flow separation occurred on the blade wall. However, the *Q* value of the vaneless space was lower than zero. Based on the *Q*-criterion definition and velocity gradient equation, the vorticities in these areas were dominated by shear strain. Under the turbine brake condition, its speed slightly decreased compared with OP2, but the flow decreased rapidly; therefore, the flow separation and the rotating stall of the runner were intense. The unit exhibited significant instability, and the scales of the passage and separation vortices increased.

Under the zero-flow-rate condition, numerous vortices started to appear in the stay-guide vane flow paths. These vortices, formed by the secondary and cross flows, prevented water from flowing smoothly into the runner area. This obstruction indicated that the vortex propagated towards the stay-vane and guide-vane flow channels. Under the reverse pump condition, the vorticity inside the pump turbine was very large. In many areas, it exceeded 900 s^{-1}. Numerous vortices were distributed in the circumferential direction in the vaneless space. The stress on the blade became complex, and the flow channel of the stay-guide vanes was almost wholly occupied by vortices. These phenomena mainly occurred because the rotation direction of the blade was inconsistent with the incoming flow direction. Therefore, the water could not smoothly enter the volute and flow out, generating strong exciting forces in the mainstream area. In engineering practice, the unit should prevent reaching this working condition as much as possible.

In summary, the vorticity increased in all the areas for all the conditions. The OP1, OP2, and OP3 vortices were mainly distributed on the blade pressure surface, and the velocity

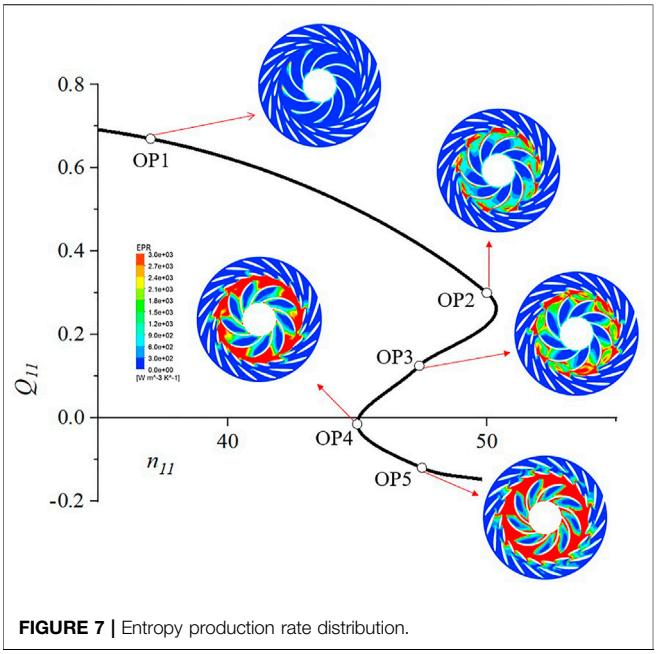

FIGURE 7 | Entropy production rate distribution.

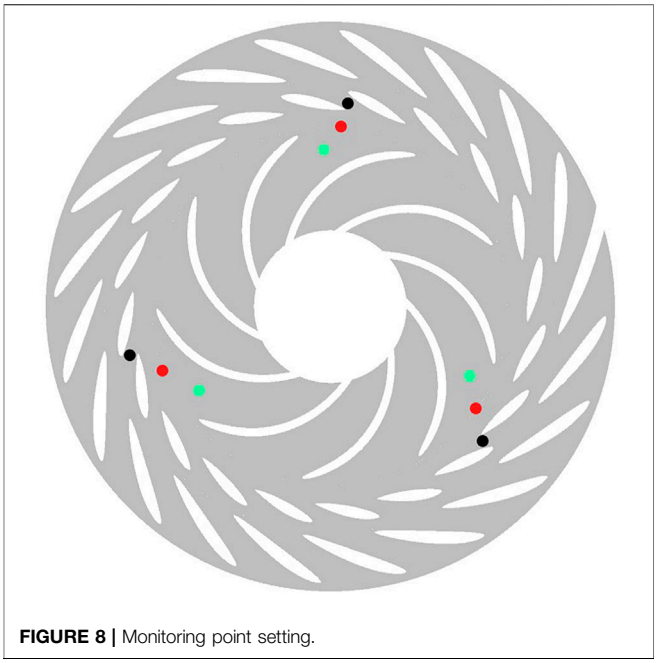

FIGURE 8 | Monitoring point setting.

gradient in the vaneless space was mainly generated by shear strain. The OP4 and OP5 vortices propagated towards the stay-guide vane flow paths, and the flow patterns in the entire mainstream area were highly turbulent.

ANALYSIS OF ENTROPY PRODUCTION RATE IN S-SHAPED REGION

According to the second law of thermodynamics, entropy always increases in fluid systems (Gong et al., 2013). Yao (2018) found that the high entropy production rate in the main flow area of a pump turbine is mainly caused by flow separation, impact, and circulation. The entropy production rate can characterize the energy loss. The entropy production rate distribution was plotted to determine the energy loss of each working condition in the S-shaped region (**Figure 7**).

The entropy production rate of the turbine condition was low and lower than 1,000 $Wm^{-3}K^{-1}$ in most areas (**Figure 7**). Under the runaway condition, the entropy production rate in the vaneless space increased, the energy loss was significant, and the overall distribution of the entropy production rate exhibited periodicity and symmetry. At this time, the energy loss of the pump turbine was mainly generated by the rotating stall and rotor–stator interaction. The entropy production rate distribution of the turbine break condition was similar to that of the runaway condition; however, the flow rate of the turbine break condition was halved, and the internal flow pattern of the turbine break condition was more turbulent than that of the runaway condition. Thus, the mechanical energy loss propagated towards the middle of the runner channel, the maximum entropy production rate exceeded 8,000 $Wm^{-3}K^{-1}$, and the efficiency of the unit decreased.

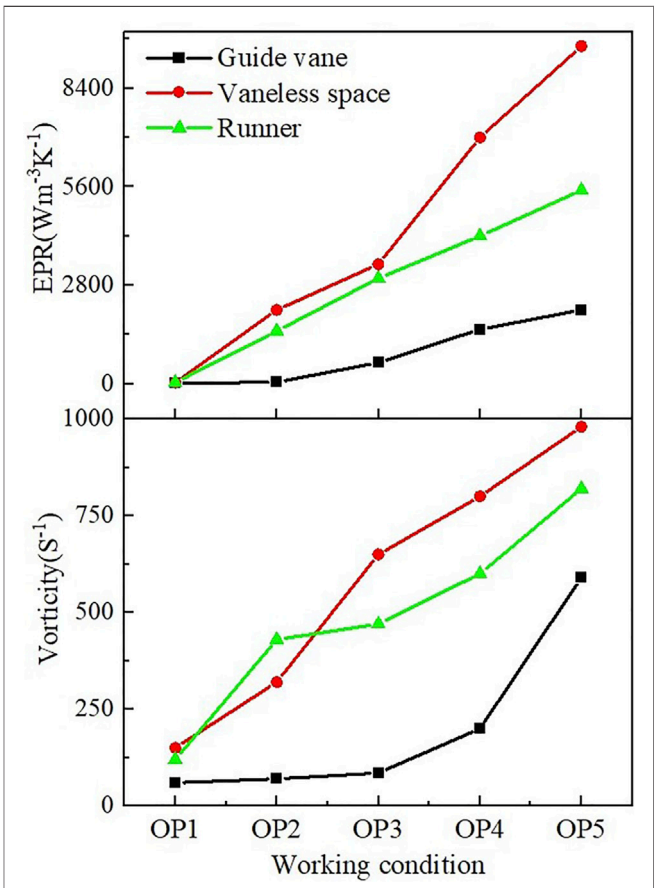

FIGURE 9 | Variations in vorticity and entropy production rate.

Under the zero-flow-rate condition, the entropy production rate of the blade pressure surface and vaneless space continued to increase compared to the turbine condition, owing to the low flow rate. However, the energy loss of the blade suction surface was still minimal. Entropy production rates exceeding 5,000 $Wm^{-3}K^{-1}$ were observed for the stay-guide vane channel, indicating that the energy loss spread outward. The reverse pump condition had a comparable speed but in the opposite direction of fluid flow of the turbine break condition. The mismatch between the incoming flow and blade rotation direction increased the energy loss. At this time, the vortices blocked the flow channel, forming a high-speed water-blocking ring, and a significant amount of mechanical energy inside the unit was transformed into internal energy.

RELATIONSHIP BETWEEN VORTEX DISTRIBUTION AND ENERGY LOSS

Although vortices are caused by shear, no rotational flow occurs when the shear stress direction is parallel, which explains why intense vorticity exists in laminar boundary flow but without vortex structures (Yuan 2020). Because the vorticity and entropy production rates were distributed periodically, the relationship between the energy loss and adverse flow was investigated. Three monitoring points were selected from the guide vane channel, vaneless space, and runner channel, and their vorticities and entropy production rates were quantitatively analyzed and averaged. **Figure 8** shows the locations of the monitoring points, and **Figure 9** shows the variations in the average vorticity and average entropy production rate.

As can be seen from **Figure 9**, OP1 has small vorticity everywhere. The average vorticity of the guide vane flow channel in OP2, OP3 is almost no increase, this is because although the high speed flow rate is small, but the bad flow mainly occurs in the runner and vaneless space, the guide vane flow channel does not appear larger velocity gradient. And in OP4, OP5 vorticity increased more, when the blade rotation direction and the direction of incoming flow does not match, vorticity is mainly caused by the guide vane flow channel vortex. The maximum average vorticity is 590 s^{-1}. The vorticity of the runner flow channel is mainly due to the velocity gradient generated by the flow separation. The vorticity increases more in the vaneless space, and the average vorticity is close to 1000 s^{-1} at OP5, which is also the location of the largest velocity gradient in the whole mainstream area. This indicates that the rotor-stator interaction effects have the greatest impact on the vorticity inside the pump turbine (Li et al., 2021e).

The growth rate of the average EPR is similar to that of the vorticity, which also indicates that the vorticity and energy loss have a strong correlation. At OP5, the average EPR in the vaneless space is close to 10,000 $Wm^{-3}K^{-1}$, and at this time, the strong rotor-stator interaction effects cause strong vibration, and the mechanical energy is converted into internal energy in a large amount.

The vorticity and entropy production rate in each working condition not only increase in a similar pattern, but also correspond to high entropy production rate in places with high vorticity, which are all near the vaneless space, showing a good match. Vorticity is strongly correlated with energy loss. The runaway and turbine break conditions had more shear strains in the vaneless space dominating the flow. Under both conditions, the rotor–stator interaction in the vaneless space was intense, and the strong shear effect generated larger vorticity than the rotation. Under the zero-flow-rate and reverse-pump conditions, the vaneless space still had the largest vorticity and entropy production rate. Although there are many vortices and large energy loss in the stay-guide vanes channel, the vorticity caused by shear strain reaches 980 s^{-1} in reverse-pump conditions, while the vorticity caused by rotation is only 590 s^{-1}. Therefore, the vorticity caused by the strong shear effect was more significant than that caused by the rotation.

CONCLUSION

The aim of this study was to investigate the characteristics of vortex distribution and its relationship with energy losses in the S-shaped region of a pump turbine. The following conclusions are drawn.

1) The $|\omega|$-criterion can be used to derive the vorticity distribution in a flow field based on the vortex analysis of each working condition of the S-shaped region. However, the $|\omega|$-criterion cannot distinguish between rotation and shear motion, whereas the Q-criterion can effectively solve this problem.
2) Under all the conditions, the vorticity and entropy production rate increased, and the passage and separation vortices were densely distributed gradually. Under the zero-flow-rate and reverse pump conditions, vortices propagated towards the stay-guide vanes, significantly blocking the flow channel and obstructing the smooth flow of water.
3) The vorticity and entropy production rates in the vaneless space were the highest. The vorticity and energy loss were strongly correlated, and the vorticity induced by the strong shear effect was more significant than that induced by the rotation.

DATA AVAILABILITY STATEMENT

The raw data supporting the conclusion of this article will be made available by the authors, without undue reservation.

AUTHOR CONTRIBUTIONS

HZ completed the main writing of the paper, ZEL revised the paper, DL provided writing opinions, HC provided experimental guidance, and ZIL provided software guidance.

FUNDING

The work was supported by the National Natural Science Foundation of China (Grant No. 52079118), Central leading local (scientific and technological innovation base construction) project XZ202201YD0017C, National Key Research and Development Program (2018YFE0128500).

REFERENCES

Caide, P. (2021). Contribute to the Realization of the Goal of "Carbon Peak and Carbon Neutrality" Speed up the Development of Pumped Storage Power Plants[J]. *Hydropower and Pumped Storage* 7 (06), 4–6. doi:10.3969/j.issn.2096-093X.2021.06.002

Cavazzini, G., Giovanna, Covi, A., Pavesi, G., and Ardizzon, G. (20162016). Analysis of the Unstable Behavior of a Pump-Turbine in Turbine Mode: Fluid-Dynamical and Spectral Characterization of the S-Shape Characteristic. *J. Fluids Eng. Trans. ASME* 138 (2). doi:10.1115/1.4031368

Chen, Q. F. (2018). *Entropy Production Rate Analysis in S Zone for a Pump-turbine [D]*. Beijing: Tsinghua University.

Fu, X., Zuo, Z., Chang, H., Li, D., Wang, H., and Wei, X. (2021). Mechanism of Low Frequency High Amplitude Pressure Fluctuation in a Pump-Turbine during the Load Rejection Process. *J. Hydraulic Res.* 59 (2), 280–297. doi:10.1080/00221686.2020.1780488

Gong, R., Wang, H., Chen, L., Li, D., Zhang, H., and Wei, X. (20132013). Application of Entropy Production Theory to Hydro-Turbine Hydraulic Analysis. *Sci. China Technol. Sci.* 56 (07), 1636–1643. doi:10.1007/s11431-013-5229-y

Ji, B., Wang, J., and Luo, X. (20162016). Numerical Simulation of Cavitation Surge and Vortical Flows in a Diffuser with Swirling Flow[J]. *J. Mech. Sci. Technol.* 30 (6). doi:10.1007/s12206-016-0511-0

Kinoue, Y., Shiomi, N., and Sakaguchi, M. (2019). A Pump System with Wave Powered Impulse Turbine[J]. *IOP Conf. Ser. Earth Environ. Sci.* 240 (5). doi:10.1088/1755-1315/240/5/052009

Kye, B., Park, K., and Choi, H. (2018). Flow Characteristics in a Volute-type Centrifugal Pump Using Large Eddy Simulation[J]. *Int. J. Heat Fluid Flow* 72, 52–60. doi:10.1016/j.ijheatfluidflow.2018.04.016

Li, D., Chang, H., Zuo, Z., Wang, H., and Liu, S. (2021b). Aerodynamic Characteristics and Mechanisms for Bionic Airfoils with Different Spacings. *Phys. Fluids* 33 (66), 064101. doi:10.1063/5.0049704

Li, D., Song, Y., Lin, S., Wang, H., Qin, Y., and Wei, X. (2021a). Effect Mechanism of Cavitation on the Hump Characteristic of a Pump-Turbine. *Renew. Energ.* 167, 369–383. doi:10.1016/j.renene.2020.11.095

Li, D. Y., Gong, R. Z., and Wang, H. J. (2016). Analysis of Vorticity Dynamics for Hump Characteristics of a Pump Turbine Model[J]. *J. Mech. Sci. Technol.* 30 (8). doi:10.1007/s12206-016-0725-1

Li, D. Y. (2017). *Investigation on Flow Mechanism and Transient Characteristics in Hump Region of a pump-turbine[D]*. Harbin: Harbin Institute of Technology.

Li, D. Y., Wang, H. J., and Qin, Y. L. (2017). Entropy Production Analysis of Hysteresis Characteristic of a Pump-Turbine Model[J]. *Energ. Convers. Manage.* 149, 175–191. doi:10.1016/j.enconman.2017.07.024

Li, W., Li, Z., Qin, Z., Yan, S., Wang, Z., and Peng, S. (2022). Influence of the Solution pH on the Design of a Hydro-Mechanical Magneto-Hydraulic Sealing Device. *Eng. Fail. Anal.* 135, 106091. doi:10.1016/j.engfailanal.2022.106091

Li, W., Li, Z., Wang, Z., Wu, F., Xu, L., and Peng, S. (2021d). Turbulence Intensity Characteristics of a Magnetoliquid Seal Interface in a Liquid Environment. *Coatings* 11 (11), 1333. doi:10.3390/coatings11111333

Li, Y. B., Wang, Z. K., and Wang, Z. J. (2021e). Numerical Evaluation of Unsteady Flow in a Centrifugal Pump by Omega Vortex Identification Method[J]. *JOURNAL ENGINEERING THERMOPHYSICS* 42 (12), 3187–3194.

Li, Z., Li, W. X., Li, W., Wang, Q., Xiang, R., Cheng, J., et al. (2021c). Effects of Medium Fluid Cavitation on Fluctuation Characteristics of Magnetic Fluid Seal Interface in Agricultural Centrifugal Pump. *Int. J. Agric. Biol. Eng.* 14 (6), 85–92. doi:10.25165/j.ijabe.20211406.6718

Liu, C. Q., Gao, Y. S., and Dong, X. R. (2019). Third Generation of Vortex Identification Methods: Omega and Liutex/Rortex Based Systems[J]. *J. Hydrodynamics* 31 (2). doi:10.1007/s42241-019-0022-4

Liu, C. Q., Wang, Y. Q., and Yang, Y. (2016). New omega Vortex Identification Method[J]. *Sci. China(Physics,Mechanics Astronomy)* 59 (08), 62–70. doi:10.1007/s11433-016-0022-6

Liu, D. X. (2013). *Internal Flow Instability Analysis in Misalignment Guide Vanes of Francis Pump Turbine at Low Specific speed[D]*. Lanzhou: Lanzhou University of Technology.

Lu, J. L., Wang, L. K., and Liao, W. L. (2019). Entropy Production Analysis for Vortex Rope of a Turbine Model[J]. *SHUILI XUEBAO* 50 (02), 233–241. doi:10.13243/j.cnki.slxb.20180762

Ni, D., Yang, M. G., and Gao, B. (2018). Experimental and Numerical Investigation on the Pressure Pulsation and Instantaneous Flow Structure in a Nuclear Reactor Coolant Pump. *Nucl. Eng. Des.* 337, 261–270. doi:10.1016/j.nucengdes.2018.07.014

Norizan, T. A., RedaReda, E., and Harun, Z. (2018). Enhancement of Vorticity Reduction by Floor Splitter in Pump Sump to Improve Pump Efficiency. *Sustainable Energ. Tech. Assessments* 26, 28–36. doi:10.1016/j.seta.2017.06.001

Pejovic, S., Krsmanovic, L., and Jemcov, R. (1976). *Unstable Operation of High-Head Reversible pump-turbines[J]*. Leningrad: IAHR 8th Symposium.

Peng, S. Y. (2020). *Numerical Simulation of Solid-Liquid Two-phase Flow of Tubular Turbine Based on Vortex Analysis[D]*. Chengdu: Xihua University.

Qin, D. Q., Li, D. Y., and Zhang, G. H. (2017). Energy Analysis in a Pump-Turbine during the Load Rejection Process[J]. *J. Fluids Eng.* 140 (10). doi:10.1115/1.4040038

Ren, Y., Zhu, Z. C., and Wu, D. H. (2021). Flow Loss Characteristics of a Centrifugal Pump Based on Entropy Production[J]. *J. Harbin Eng. Univ.* 42 (02), 266–272. doi:10.11990/jheu.201906053

Singh, P. M., Chen, C., and Choi, Y.-D. (2015). Hydrodynamic Performance of a Pump-Turbine Model in the "S" Characteristic Region by CFD Analysis. *J. Korean Soc. Mar. Eng.* 39 (10), 1017–1022. doi:10.5916/jkosme.2015.39.10.1017

Wangxu, L., Zhenggui, L., Wanquan, D., Lei, J., Yilong, Q., and Huiyu, C. (2021). Particle Image Velocimetry Flowmeter for Natural Gas Applications. *Flow Meas. Instrumentation* 82, 102072. doi:10.1016/j.flowmeasinst.2021.102072

Yao, Q. W. (2018). *Mechanism Study on S-Shaped Characteristics and Hysteresis Effect of a pump-turbine[D]*. Harbin: Harbin Institute of Technology.

Yuan, Z. Y., Zhang, Y. X., and Wang, C. (2021). Study on Characteristics of Vortex Structures and Irreversible Losses in the Centrifugal Pump. *Proc. Inst. Mech. Eng. A: J. Power Energ.* 235 (5), 1080–1093. doi:10.1177/0957650920983061

Zhang, N., Liu, X. K., and Gao, B. (2019a). DDES Analysis of the Unsteady Wake Flow and its Evolution of a Centrifugal Pump. *Renew. Energ.* 141, 570–582. doi:10.1016/j.renene.2019.04.023

Zhang, Y.-n., Wang, X.-y., Zhang, Y.-n., and Liu, C. (2019b). Comparisons and Analyses of Vortex Identification between Omega Method and Q Criterion. *J. Hydrodyn* 31 (2), 224–230. doi:10.1007/s42241-019-0025-1

Zhang, Y. N., Liu, K. H., and Li, J. W. (2018a). Analysis of the Vortices in the Inner Flow of Reversible Pump Turbine with the New omega Vortex Identification Method[J]. *J. Hydrodynamics* 30 (3). doi:10.1007/s42241-018-0046-1

Zhang, Y. N., Liu, K. H., and Xian, H. Z. (2018b). A Review of Methods for Vortex Identification in Hydroturbines[J]. *Renew. Sustain. Energ. Rev.* 81. doi:10.1016/j.rser.2017.05.058

Conflict of Interest: HC was employed by the company China Three Gorges Construction Engineering Group Co., Ltd., China, ZIL was employed by the company China Gezhouba Group Electromechanical Construction Co., Ltd., China.

The remaining authors declare that the research was conducted in the absence of any commercial or financial relationships that could be construed as a potential conflict of interest.

frontiers | Frontiers in Energy Research

ORIGINAL RESEARCH
published: 10 May 2022
doi: 10.3389/fenrg.2022.880293

Distribution Features of Flow Patterns and Pressure Pulsations of Pump-Turbine in Five Operating Modes on the Four-Quadrant Plane

Dongliang Hu[1], Yongguang Cheng[1], Pengcheng Zhang[1], Xi Wang[2], Jinghuan Ding[3] and Xiaoxi Zhang[4]*

[1]State Key Laboratory of Water Resources and Hydropower Engineering Science, Wuhan University, Wuhan, China, [2]Anhui Jinzhai Pumped Storage Company Ltd., Lu'an, China, [3]Pumped-Storage Power Institute of Technology and Economy, State Grid Xinyuan Company Ltd., Beijing, China, [4]School of Environmental Science and Engineering, Xiamen University of Technology, Xiamen, China

To meet the demand of the power grid for flexible regulation, pump turbines have to frequently and fleetly stop, start, and transition between different modes, causing many instability problems. To solve the problems, understanding the complex flow and pressure pulsation features in different working conditions is the prerequisite. In this study, the flow patterns, pressure pulsations, cavitation characteristics, and runner forces of a prototype pump-turbine working under the five operating modes were displayed and analyzed based on computational fluid dynamics simulations. It is shown that when working points are near the pump and turbine design working points, the flow is smooth, with small pressure pulsation and without cavitation; however, when working points deviate from the optimal ones, flow patterns become worse and cavitation appears. In the pump-brake mode, the flow hits the runner blades violently, causing obvious pressure and runner force fluctuations. In the hump region, the flow has a strong impact on the guide vanes, and the rotating stall vortices are apparent in the vane area. In the S-shaped region, pressure pulsations are the highest with prominent rotor–stator interaction and rotating stall. Under similar working conditions, a larger guide-vane opening corresponds to a larger pressure pulsation amplitude. On the spatial distribution, the largest pressure pulsations happen in the vaneless space.

Keywords: pump-turbine, operating modes, cavitation, pressure pulsations, runner forces, CFD simulation

OPEN ACCESS

Edited by:
Umberto Desideri, University of Pisa, Italy

Reviewed by:
Zhigang Zuo, Tsinghua University, China
Desheng Zhang, Jiangsu University, China

****Correspondence:***
Yongguang Cheng
ygcheng@whu.edu.cn

Specialty section:
This article was submitted to Process and Energy Systems Engineering, a section of the journal Frontiers in Energy Research

Received: *21 February 2022*
Accepted: *08 April 2022*
Published: *10 May 2022*

Citation:
Hu D, Cheng Y, Zhang P, Wang X, Ding J and Zhang X (2022) Distribution Features of Flow Patterns and Pressure Pulsations of Pump-Turbine in Five Operating Modes on the Four-Quadrant Plane. Front. Energy Res. 10:880293. doi: 10.3389/fenrg.2022.880293

1 INTRODUCTION

Driven by the "Emission Peak and Carbon Neutrality" goal, the excellent "regulator" function of pumped storage becomes more and more prominent in the new energy-dominated modern energy system. As the core equipment of pumped storage power stations, pump turbines directly affect the safe, stable, and flexible operation of the power stations. To meet the demand of the power grid for flexible regulation, pump turbines have to frequently and fleetly stop, start, and transition between different modes, causing many instability problems. To solve the problems, understanding the complex flow and pressure characteristics in different working conditions is the prerequisite. The full characteristic curves of pump turbines are usually expressed on the four-quadrant pump-turbine characteristics, on which the five operating modes are defined: Pump, pump-brake, turbine, turbine-

brake, and reverse pump. In these modes, the pump-turbine operates in the positive or negative rotation direction and positive or negative flow direction. The flow patterns, pressure pulsations, cavitation characteristics, and runner forces in different operating modes are quite different and not well understood. Most of the existing studies focused on the narrow normal operating regions and the two special operating regions, namely, the hump and S-shaped regions. Also, there are no systematic and comprehensive descriptions of the flow characteristics in the whole region. The descriptions of the changes and distributions of characteristics across the five operating modes on the four-quadrant characteristics plane are of great reference values to runner design and pressure pulsation study for transient processes, during which the working point fleetly slides across different modes or regions.

In recent years, three-dimensional (3D) computational fluid dynamics (CFD) has become an important means to study flow patterns and pressure pulsations of pump turbines and can accurately predict pressure pulsation characteristics (Yan et al., 2013), cavitation characteristics (Celebioglu et al., 2017), the S-shaped characteristics (Liu et al., 2013), and the hump characteristics (Ran et al., 2011) and has played an important role in finding general laws and revealing underlying mechanism. There have been many studies on the formation mechanism and flow characteristics of the two highly unstable regions (Zuo et al., 2016), the S-shaped region and the hump region.

For the studies on the S-shaped region, Ji and Lai (2011) claimed that the high-speed and high-pressure water retaining ring at the runner inlet is the cause of unit start-up difficulty at low heat in the S-shaped region. Widmer et al. (2011) pointed out that the stable stall vortex and rotating stall vortex structures in the vaneless space block the flow, causing the local pressure to rise in the area near the vortex structure and leading to the S-shaped characteristics. Xiao R. et al. (2012) and Xiao Y. X. et al. (2012) pointed out that pre-opening guide vanes are an effective method to improve stability in the S-shaped region, however, with limitations. Zhang et al. (2011) claimed that the pressure pulsations in the vaneless space reach the largest when the working point is in the S-shaped region. Zhang et al. (2019) further pointed out that the pressure pulsation amplitude near the runaway working point is the largest. After sorting out the distribution characteristics of pressure pulsations on the

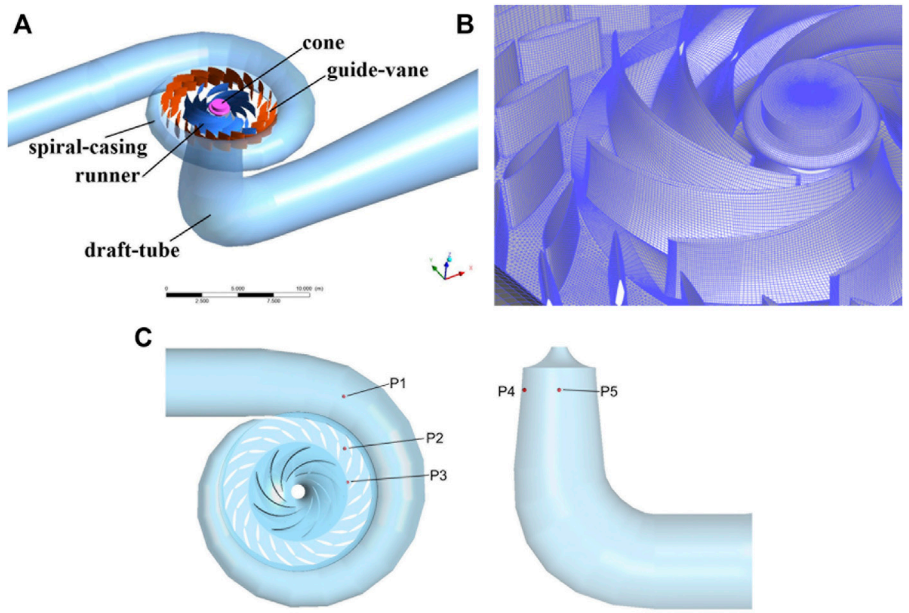

FIGURE 1 | CFD computational model of the pump-turbine and schematic layout of monitoring points for pressure pulsations. **(A)** Computational domains. **(B)** Meshes in the runner and guide-vane areas. **(C)** The layout of monitoring points for pressure pulsations.

TABLE 1 | Basic parameters of the pump turbine.

Parameter	Value	Parameter	Value
Specific speed n_q (m, m³/s)	189.8	Runner inlet diameter D_1 (m)	5.26
Rated rotational speed n_r (rpm)	250	Runner outlet diameter D_2 (m)	3.57
Rated discharge Q_r (m³/s)	174	Number of blades Z_b	9
Rated output P_r (MW)	306	Number of guide-vanes n_{gv}	20
Rated head H_r (m)	195	Suction head H_s (m)	−57

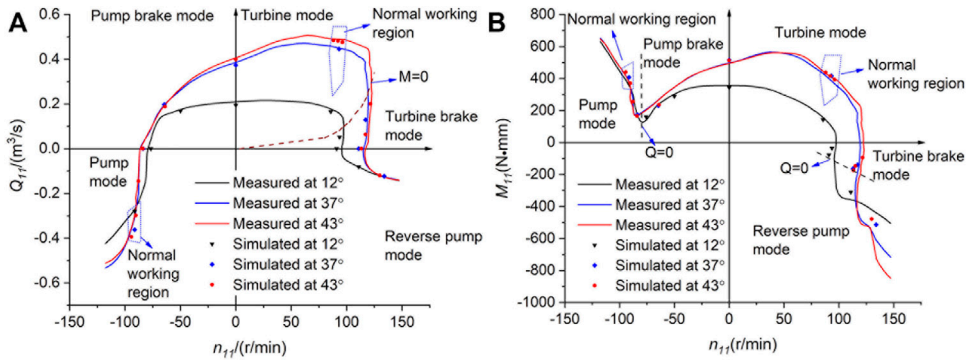

FIGURE 2 | Comparison between CFD simulation and model test. **(A)** n_{11}-Q_{11} characteristic curves. **(B)** n_{11}-M_{11} characteristic curves.

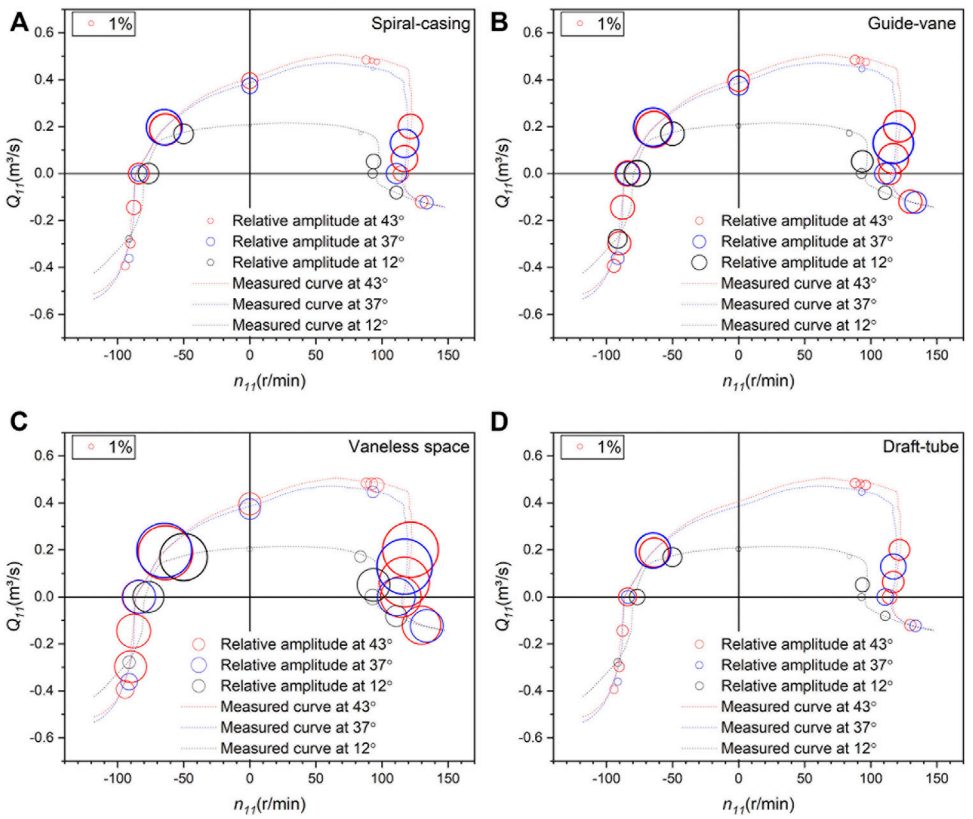

FIGURE 3 | Distributions of $\Delta H'$ on the 4-quadrant characteristic plane at different locations. **(A)** Spiral-casing. **(B)** Guide-vane. **(C)** Vaneless space. **(D)** Draft-tube.

operating characteristic plane, it is equally important to analyze their causes, such as rotor–stator interaction, rotating vortex rope, rotating stall, and cavitation (Goyal and Gandhi, 2018). Hasmatuchi et al. (2011) claimed that when the working point deviates from the optimal one under the turbine mode, the pressure pulsation increases due to interference between the rotating stall and the flow channel after entering the turbine-brake zone, and the rotational speed of the rotating stall zone is about 70% of the rotational speed of the runner. Jun-Won et al. (2021) further pointed out that the frequency of rotating stall in the S-shaped region is 0.6 times the rotation frequency of the runner. Shang (2020) claimed that the effect of cavitation on the S-shaped characteristics is mainly reflected in the vortex structure in the vaneless space, and the changes in vortex structure and cavitation cavity volume have an effect on the pressure pulsation characteristics. Wang (2020) pointed out that when the cavitation coefficient decreases, the cavitation phenomenon arises and develops continuously, and when cavitation is more serious,

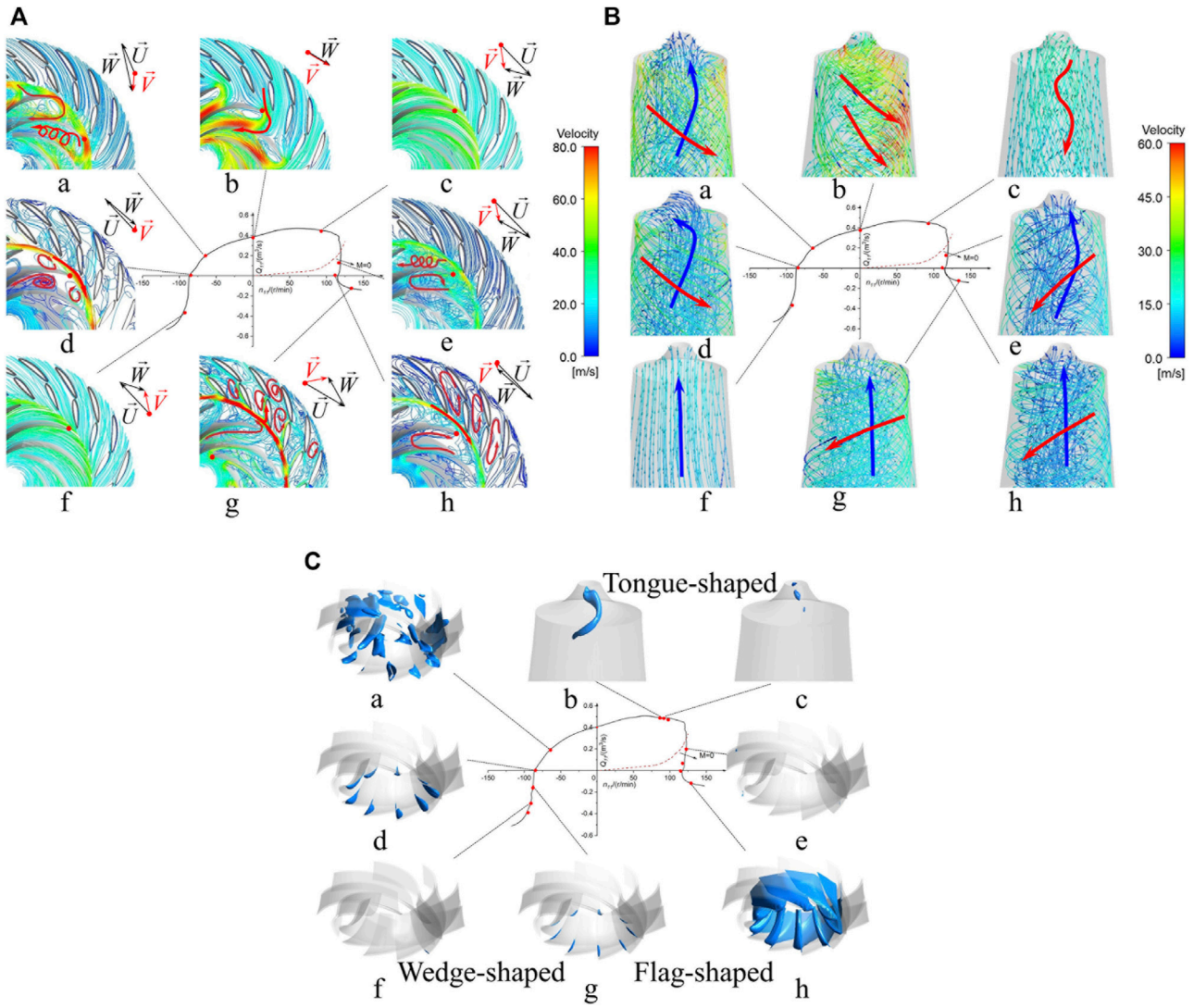

FIGURE 4 | Flow patterns and cavitation patterns for different working points. **(A)** Flow patterns in guide-vanes and runner at opening 37°. **(B)** Flow patterns in the draft tube at opening 37°. **(C)** Cavitation patterns at opening 43°(WVVF = 0.1).

the backflow vortex in the blade channel obstructs the flow, resulting in insufficient discharge capacity.

For the studies on the hump region in the pump operating mode, Wang and Guo (2018) claimed that the internal flow patterns of the pump-turbine become worse with the decrease of discharge. LI et al. (2017) pointed out that the main cause of the hump characteristic is that the vortex and flow separation in the guide-vane space block the flow channels. Li and Wang (2015) claimed that the hydraulic loss in the runner is also one of the main causes of the hump characteristics' formation. It has also been found that the generation of the hump characteristics is also related to cavitation near the suction surface of the runner blade leading edge (Li et al., 2021), which reduces the head of the pump-turbine (Liu et al., 2012); the reduction of the cavitation coefficient has a significant effect on the hump characteristic curve (Ješe et al., 2014) and runner forces (Zhu et al., 2021).

For studies on pressure pulsations in pump turbines, Wang et al. (2013) claimed that the more distant the working point deviates from the optimal one, the greater the pressure pulsation amplitude, and the blade passing frequency is dominant in the vaneless space. Also, Wu et al. (2021) pointed out that when the discharge decreases to zero, the amplitude of pressure pulsation in the vaneless space increases with the guide-vane opening, and the blade passing frequency caused by rotor–stator interaction dominates at each monitoring point. In addition to rotor–stator interaction, the rotating stall is also an important cause of pressure pulsations in the hump region. Zhang C. Z. et al. (2017) claimed that the rotating stall usually occurs at part load in the pump mode, which can cause severe pressure pulsations. Ješe and Fortes-Patella (2016) claimed that the frequency of rotating stall changes with discharge. Xia et al. (2015) pointed

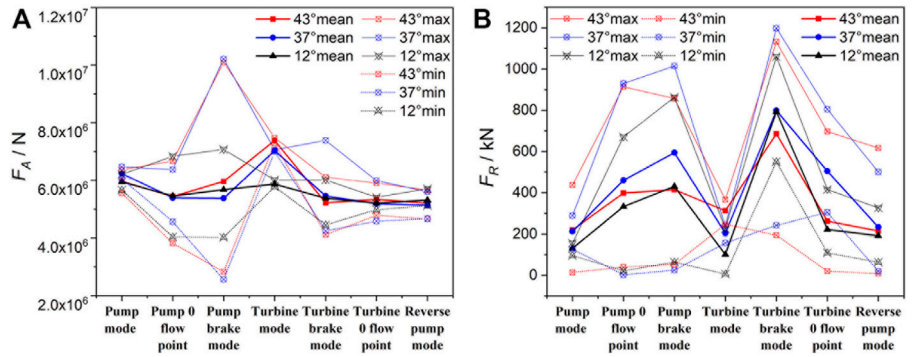

FIGURE 5 | Variation of runner forces under different working conditions. **(A)** Axial force (F_A). **(B)** Radial force (F_R).

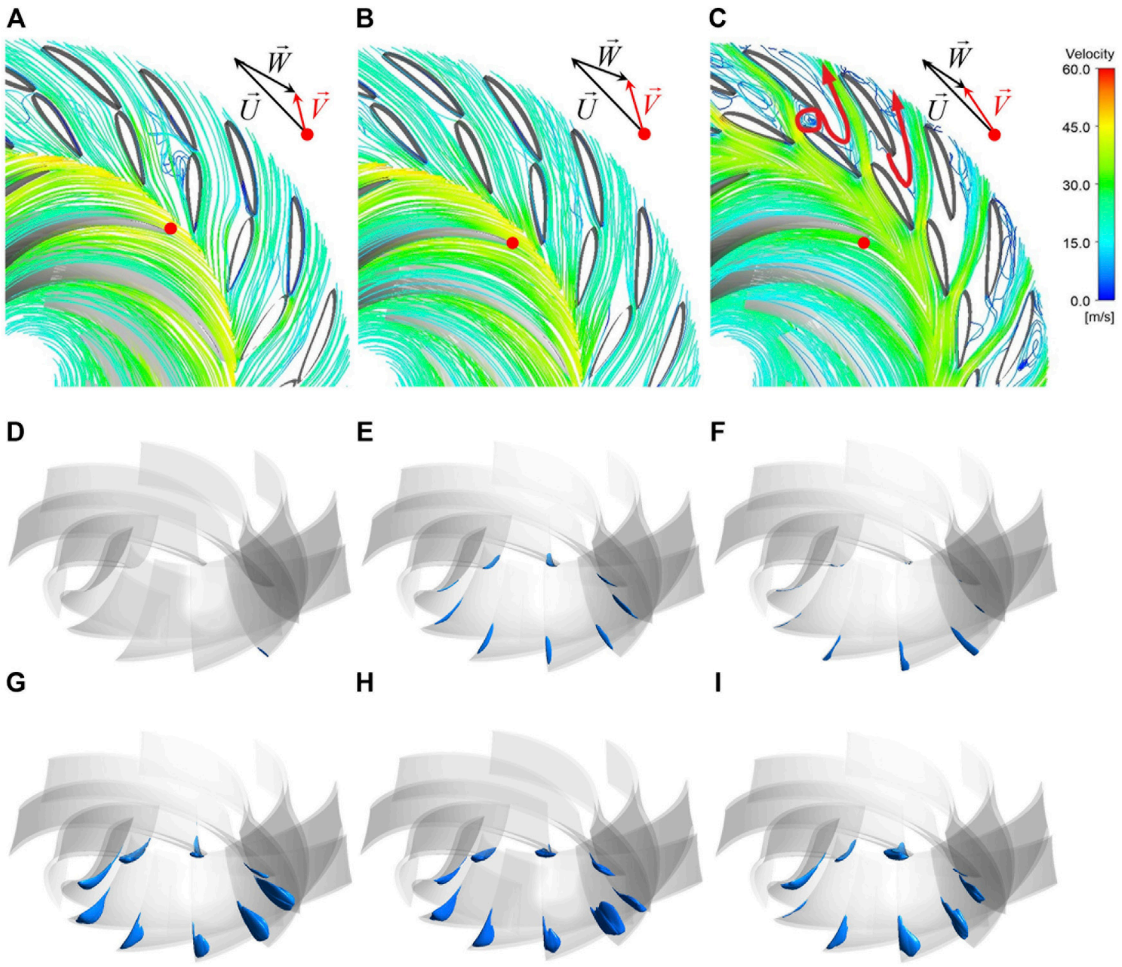

FIGURE 6 | Flow patterns **(A–C)** and cavitation cavity patterns **(D–I)** of different working points within pump mode at different openings (WWF = 0.1). **(A)** 43° (Q = 150 m^3/s). **(B)** 37°. **(C)** 12°. **(D)** 43° (Q = 120 m^3/s). **(E)** 43° (Q = 60 m^3/s). **(F)** 12° (Q = 110 m^3/s). **(G)** 43° (Q = 0 m^3/s). **(H)** 37° (Q = 0 m^3/s). **(I)** 12° (Q = 0 m^3/s).

out that the rotating stall occurs in the guide-vane areas under the pump mode and occurs in the runner under the pump-brake mode. Also, in order to study the causes and distribution characteristics of pressure pulsations under different modes, Zhang (2015) analyzed several working points in the four-quadrant plane and proposed that the low-frequency pulsation is mainly caused by the asymmetrically distributed pressures rotating at a speed slower than the runner rotational speed; the

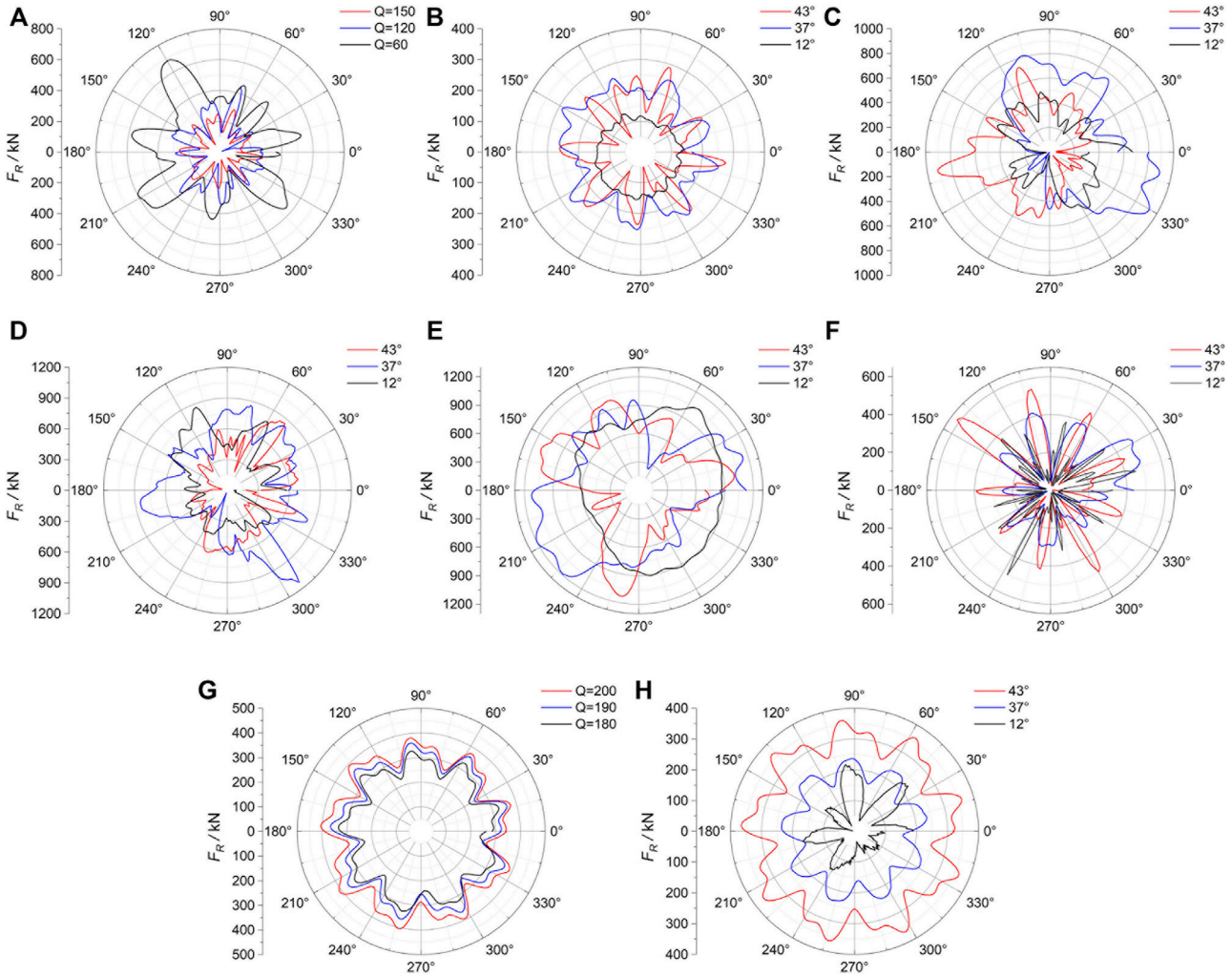

FIGURE 7 | Comparisons of radial force variations for different working points within different modes. **(A)** Radial forces under pump mode at opening 43°. **(B)** Radial forces under pump mode at three openings. **(C)** Radial forces at the pump 0-discharge point at three openings. **(D)** Radial forces under the pump-brake mode at three openings. **(E)** Radial forces under the turbine-brake mode at three openings. **(F)** Radial forces under the reverse pump mode at three openings. **(G)** Radial forces at different flow points under turbine mode at opening 43°. **(H)** Radial forces under turbine mode at three openings.

high-frequency pulsation is caused by the rotor–stator interaction; the low-amplitude pulsation occurs in the smooth-flow region; the high-amplitude pulsation occurs in the pump-brake mode, reverse pump mode, and S-shaped region.

In summary, the current research on the flow characteristics of pump-turbine has achieved rich results, but there were still shortcomings or missing aspects. Most of the existing research focused on the local working operation region, and there were only few panoramic descriptions of the characteristic distributions in the full operating zones (Zhang, 2015), and the cavitation and runner force characteristics were ignored in these works. This study aimed to display and interpret the distribution characteristics of flow patterns, pressure pulsations, cavitation characteristics, and runner forces in each operating condition, based on CFD simulations of a prototype pump-turbine. Also, we hope the resulting laws and mechanisms can provide a reference for related research and runner design. The following section introduces the numerical simulation conditions, including the computational model and mesh, solution settings, selection of simulated working points, and monitoring point arrangement. **Section 3** shows the results and analysis, first giving the overall distribution characteristics of flow and pressure pulsation characteristics in the four-quadrant characteristics plane and then analyzing the flow and pressure pulsation characteristics and their formation mechanism in detail under each mode.

2 NUMERICAL SIMULATION CONDITIONS

2.1 Geometry and Mesh

CFD simulations of a prototype pump-turbine of a pumped storage power station in China were conducted. The computational model is composed of the spiral-casing,

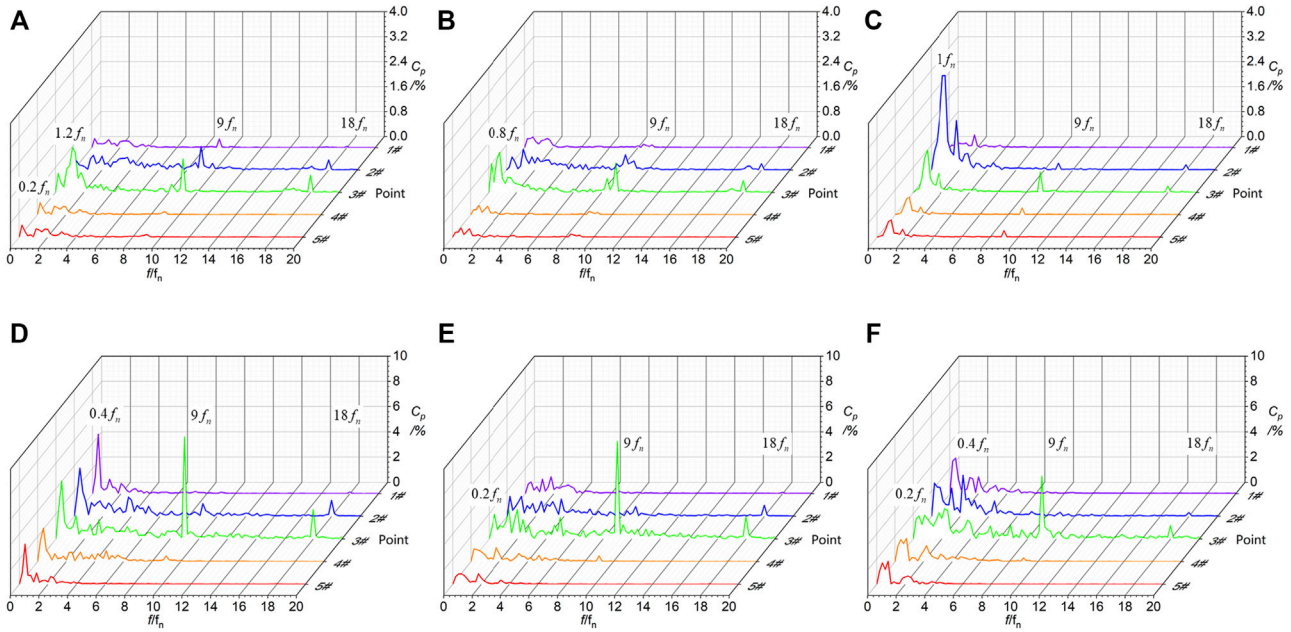

FIGURE 8 | Frequency spectrums of pressure pulsations within pump mode at the three openings. **(A)** 43°. **(B)** 37°. **(C)** 12°. **(D)** 43° ($Q = 0$ m^3/s). **(E)** 37° ($Q = 0$ m^3/s). **(F)** 12° ($Q = 0$ m^3/s).

guide-vane, runner, cone, and draft tube. To avoid boundary conditions' effect on the results, two extending pipes were added to the spiral-casing inlet and the draft-tube outlet, respectively. The overall computational model and the meshes for the guide-vane and runner areas are shown in **Figure 1**. The relevant parameters of the pump-turbine are shown in **Table 1**.

All the meshes were generated separately by using software ANSYS ICEM 19.0. Unstructured wedge mesh was used in the guide-vane domain, while structured hexahedral mesh was used in all the other domains. For the prototype pump-turbine with large dimensions in this study, the turbulence flow in the flow passage is well developed with the maximum Reynolds number of 7×10^6 and the viscous sublayer thickness blew 1 mm, which is very smaller than the flow domain, it is almost impossible to meet $y^+ \sim 1$. To balance the accuracy of the simulation and the computational resources, we used the y^+-insensitive wall treatment options to focus on the flow mechanism of the turbulent core, ignoring the near-wall model approach and ensuring that the y^+ values near the wall are greater than 30 so that the wall function approach can be used in the simulation (Liu et al., 2019). Grid independence verification adopted six stepwise levels, from 3.53 to 4.1, 4.5, 5.8, 6.4, and 8.61 million, respectively. In the rated working point, when the number is more than 4.5 million, the power variation range was small enough to 0.3%. Therefore, balancing simulation accuracy and time, we chose the mesh with a total of 5.8 million cells and a minimum mesh quality of 0.24 for the following simulations.

2.2 Numerical Model and Boundary Conditions

The simulations were conducted by using ANSYS FLUENT. The shear stress transport (SST) $k-\omega$ turbulence model and Zwart-Gerber-Belamri (ZGB) cavitation model were selected. The SST $k-\omega$ model takes full account of the influence of the flow on the vortex viscosity and is particularly suitable for hydraulic machinery with many guide vanes and blades (Wang, 2016). The ZGB cavitation model can capture the cavity more clearly and the calculation process converges more easily. The combination of the SST $k-\omega$ turbulence model and the ZGB cavitation model has been shown to provide a more accurate simulation of pump-turbine flow and cavitation patterns (Li et al., 2019; Li et al., 2020).

For boundary conditions, the inlet and outlet of the turbine computational model were set as mass flow inlet and pressure outlet, respectively; the solid wall surfaces were set as the no-slip boundary condition, and the intersections of different mesh parts were treated as inner interfaces.

2.3 Solution Settings and Timestep

In the simulations, the single-phase flow simulation was performed first, and after the parameters approach stable then the ZGB cavitation model was opened. This means that the results of the single-phase flow simulation were used as the initial conditions of the two-phase flow transient simulations. The saturated vapor pressure is 3,540 Pa and the SIMPLEC scheme was used in the pressure-velocity coupling; the timestep was set to 0.001 s, which is corresponding to 1.5° of runner rotation at the rated speed; the convergence residual target

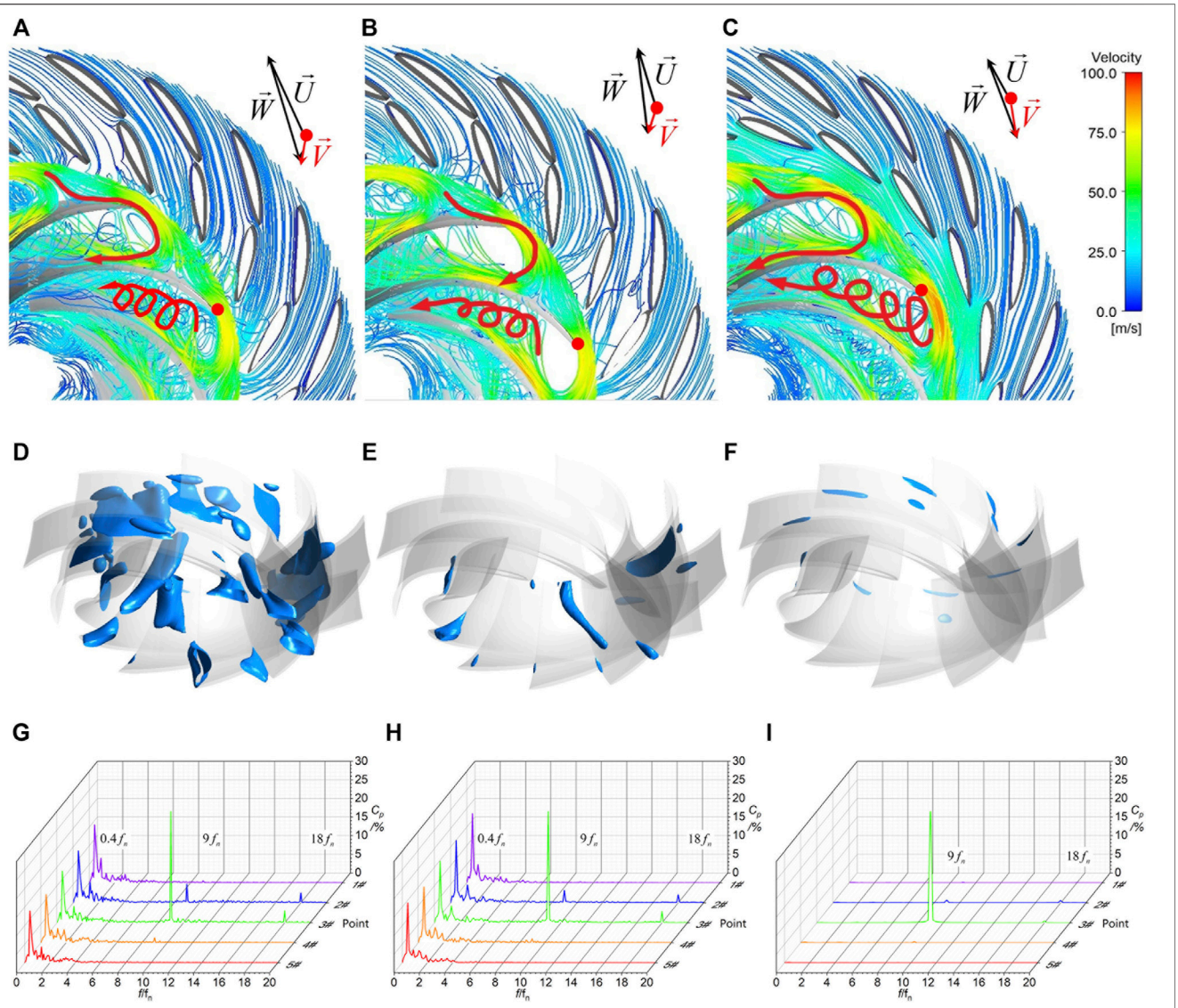

FIGURE 9 | Flow patterns **(A–C)**, cavitation cavity patterns **(D–F),** and frequency spectrums of pressure pulsations **(G–I)** at different working points within the pump-brake mode at different openings (WVVF = 0.1). **(A)** Flow patterns at 43°. **(B)** Flow patterns at 37°. **(C)** Flow patterns at 12°. **(D)** Cavitation cavity patterns at 43°. **(E)** Cavitation cavity patterns at 37°. **(F)** Cavitation cavity patterns at 12°. **(G)** Frequency spectrums at 43°. **(H)** Frequency spectrums at 37°. **(I)** Frequency spectrums at 12°.

values for continuity, velocities, k, ω and vf-phase-2 were set to 1×10^{-4}.

2.4 Selection of Simulated Working Points and Comparison With Measured Curves

A total of 29 working points on the 4-quadrant characteristic plane were specially selected for the simulations. They are at 37° (the rated guide-vane opening), 43° (slightly greater than the rated opening), and 12° (near the no-load opening), with the 0-speed point, 0-discharge point, normal working points, and the points deviated far from the design working points covered. The simulated results are drawn on the n_{11}-Q_{11} (unit speed against unit discharge) and n_{11}-M_{11} (unit speed against unit torque) characteristic planes, and compared with the model test measured curves provided by the manufacturer ($n_{11} = \frac{nD_1}{\sqrt{H}}$, $Q_{11} = \frac{Q}{D_1^2\sqrt{H}}$, $M_{11} = \frac{M}{D_1^3 H}$, where n is the rotational speed, D_1 is the runner inlet diameter, H is the working head, Q is the discharge, and M is the torque). As can be seen from **Figure 2**, although there are some deviations at some working points, the results of the numerical simulation and model test are generally in good agreement, which validates the accuracy and reliability of our three-dimensional numerical simulation method.

2.5 Layout of Monitoring Points for Pressure Pulsations

To obtain the pressure pulsation characteristics, some monitoring points were arranged as shown in **Figure 1C**, where 1# point was located in the spiral-casing, 2# point was located in the guide-

vane channel, 3# was located in the vaneless space, and 4# and 5# were located at the draft-tube inlet. All the monitoring points were located in the middle section of the flow channel.

3 RESULTS AND ANALYSIS

For uniformity of description, in the following sections, the classification of blade inlet and outlet, as well as the blade suction and pressure surfaces, is based on the normal operating conditions of the turbine mode. The directions of runner rotation and the water spiral are both described in the overhead view. Also, the axial forces are positive in the upward direction.

3.1 Overall Distributions of Characteristics in the Four-Quadrant Characteristic Plane

3.1.1 Pressure Pulsations

To better illustrate the pressure pulsation distribution patterns across different operating modes and at different monitoring points in a normalized standard, the pressure coefficient C_p and the relative amplitude of the pressure pulsation $\Delta H'$ were introduced.

$$C_p = \frac{p_i - \bar{p}}{\rho g H} \times 100\%,\ \Delta H' = \frac{\Delta H}{H} = \frac{P_{imax} - P_{imin}}{\rho g H} \times 100\%,$$

where C_p is the dimensionless pressure pulsation coefficient, %; $\Delta H'$ is the relative amplitude of pressure pulsation, %; p_i is the monitoring point pressure, Pa; $\bar{p}$ is the mean pressure values over some time, Pa; H is the working head, m; P_{imax} and P_{imin} are the maximum and minimum pressures at the monitoring points, respectively, Pa. And for the pressure fluctuation analysis, we selected at least five runner rotation cycles to ensure accuracy. The relative amplitudes of pressure pulsations $\Delta H'$ at each working point in the spiral-casing (P1), guide-vanes (P2), vaneless space (P3), and draft-tube (P5) are shown in **Figure 3**, in which the areas of circles represent their relative amplitude values of pressure pulsations.

It can be seen that the distribution laws of pressure pulsations across the four-quadrant characteristic plane at each location of the pump-turbine under different opening degrees are similar, with the relative amplitude of pressure pulsation ($\Delta H'$) being small in the normal working regions in both pump and turbine modes (about 8% in the vaneless space and 4% in the draft-tube), being larger outsides the normal working regions, and being the largest in the pump-brake and turbine-brake regions (about 80% in the vaneless and 30% in the draft-tube). In general, under similar operating conditions, the pressure pulsations increase with the opening degree; at the same working point, the pressure pulsations are different in different locations, with the largest in the vaneless space, the moderate in the guide-vane, and the smaller in the spiral-casing and draft-tube inlet.

3.1.2 Flow Patterns

Pressure pulsations of the pump-turbine are closely related to flow patterns, and worse flow patterns can lead to severe pressure pulsations. We present an overview of the general flow patterns in each operating condition by taking the rated opening of 37° as an example. **Figures 4A,B** show the flow patterns in the guide vane and runner, and in the draft tube, respectively. The velocity triangle (U is the peripheral velocity, W is the relative velocity, and V is the absolute velocity) in **Figure 4A** corresponds to the location of the red dot.

In both the normal working regions of the pump (**Figure 4Af**) and turbine (**Figure 4Ac**) modes, the streamlines are smooth; in the pump mode, the water flows upwards in the draft tube (**Figure 4Bf**), and in the turbine mode, the water flows smoothly downwards but with a slight spiral in the center of the draft-tube due to the vortex rope (**Figure 4Bc**).

When the working condition deviates from the normal working regions, the flow inside the turbine is turbulent. At the pump 0-discharge point (**Figure 4Ad**) there are a large number of backflows and vortices inside the runner, with a circumferential flow water ring in the vaneless space. Also, at the turbine 0-discharge point (**Figure 4Ah**), vortices generate inside the guide vane and backflow occurs in the runner channels. Under the reverse pump mode (**Figure 4Ag**), the water flows upwards along the suction surface of the runner blades, then hits the guide vanes, and then, partly flows into the vane channels in the direction of the guide-vane surface, and the other flows forward to the next vane channel; thus, the vortex inside the guide-vane is obvious. In the pump-brake mode (**Figure 4Aa**), the flow enters the runner and impacts strongly with the pressure surface of the blades, and the water flows in a spiral manner in the runner channels. Under the turbine-brake mode (**Figure 4Ae**) the flow in the runner is extremely turbulent and forms a spatial spiral transverse flow at the runner inlet, creating backflow and vortices along the pressure surface of the blades. As for the flow patterns in the draft tube, in all these off-design conditions, the water spirally flows downwards near the wall and flows upwards in the center of the draft tube. The flows in the pump 0-discharge point (**Figure 4Bd**, pump-brake mode (**Figure 4Ba**), and 0-speed point (**Figure 4Bb**) are counterclockwise (overhead view) spiral near the wall, and in the turbine-brake mode (**Figure 4Be**), the turbine 0-discharge point (**Figure 4Bh**) and reverse pump mode (**Figure 4Bg**) are clockwise spiral.

3.1.3 Cavitation

When the unit is operating at a large opening of 43°, cavitation of various shapes and sizes is generated at most working points, therefore, we take this opening as an example to show the cavitation distribution patterns across modes, as shown in **Figure 4C**, in which the water vapor volume fraction (WVVF) is selected as 0.1. The cavitation volume is small at high discharge pump points (**Figure 4Cf**) and the wedge-shaped cavitation occurs near the shroud side of the suction surface of the trailing edges of some runner blades. As the discharge decreases, cavitation deepens and occurs at every runner blade (**Figure 4Cg**). And cavitation deepens further at the pump 0-discharge point (**Figure 4Cd**). Under the pump-brake mode (**Figure 4Ca**) the internal cavitation of the runner is extremely serious, with a large area of cavitation inside the blade channels. Under the high discharge turbine conditions (**Figures 4Cb,c**), cavitation occurs inside the rotating vortex rope in the draft tube in the form of a helical tongue, with the volume of cavitation

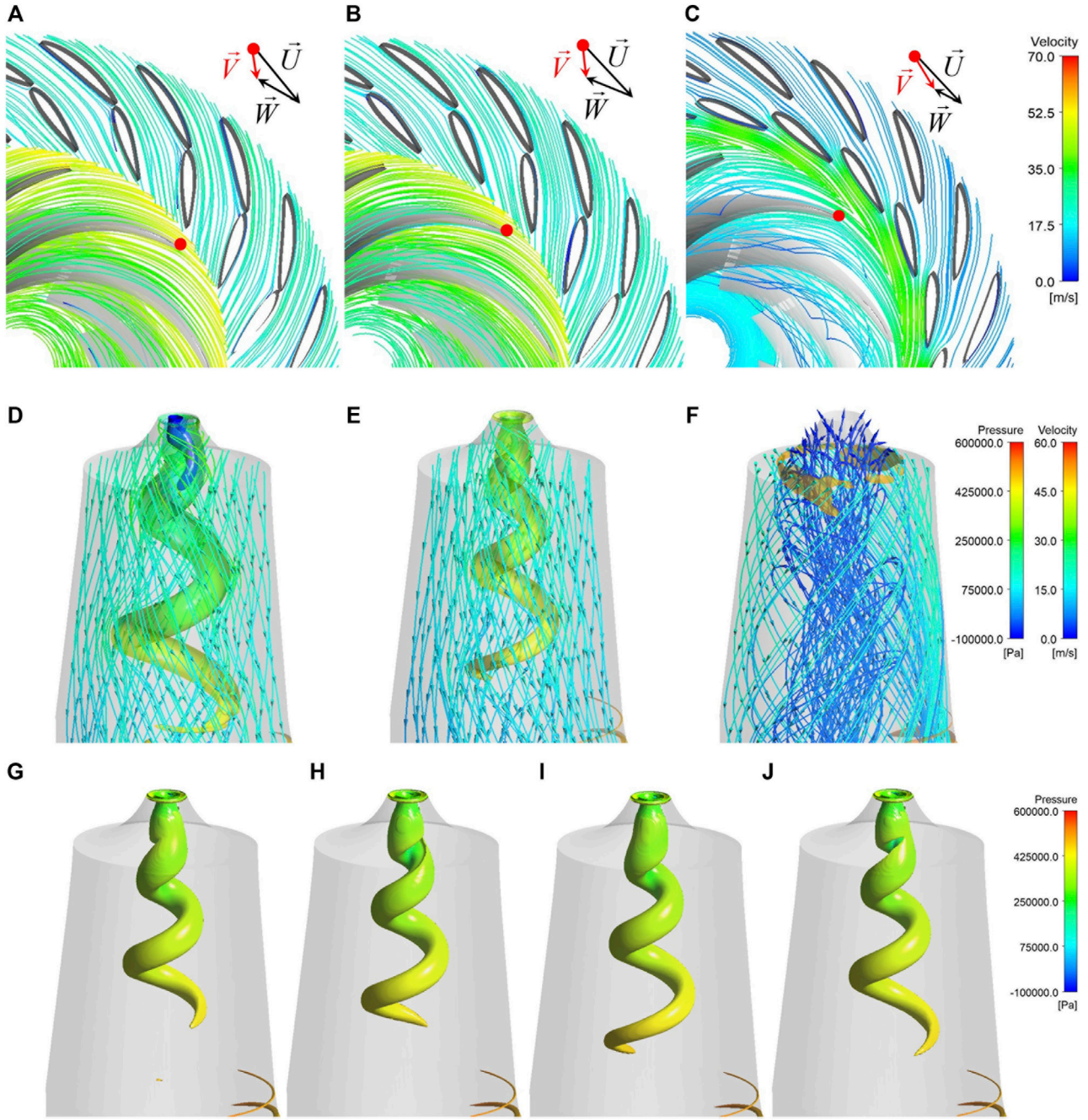

FIGURE 10 | Flow patterns, cavitation cavity patterns, and vortex rope of different working points within the turbine mode at three openings (Swirling Strength = 0.01, WVVF = 0.01). **(A)** Flow patterns at 43° (Q = 190 m^3/s). **(B)** Flow patterns at 37°. **(C)** Flow patterns at 12°. **(D)** Flow patterns in the draft tube at 43°(Q = 190 m^3/s). **(E)** Flow patterns in the draft tube at 37°. **(F)** Flow patterns in the draft tube at 12°. **(G)** Vortex rope at t = 18 s in opening 37°. **(H)** Vortex rope at t = 18.08 s in opening 37°. **(I)** Vortex rope at t = 18.16 s in opening 37°. **(J)** Vortex rope at t = 18.24 s in opening 37°.

decreasing as the discharge decreases. Under the turbine-brake mode (**Figure 4Ce**) the volume of a cavitation becomes small, and the cavitation occurs mainly on the leading edges of the runner blades. Under the reverse pump mode (**Figure 4Ch**), there is a large area of flag-shaped cavitation in the rear half of the pressure surface of the runner blades.

3.1.4 Runner Force Fluctuations

Figure 5A gives the mean, maximum, and minimum axial forces of the pump-turbine at each working point at different openings. Here the axial force represents the force of the main flow channel. In the normal working regions of the turbine mode and pump mode, the mean axial force is the largest but the fluctuation of the

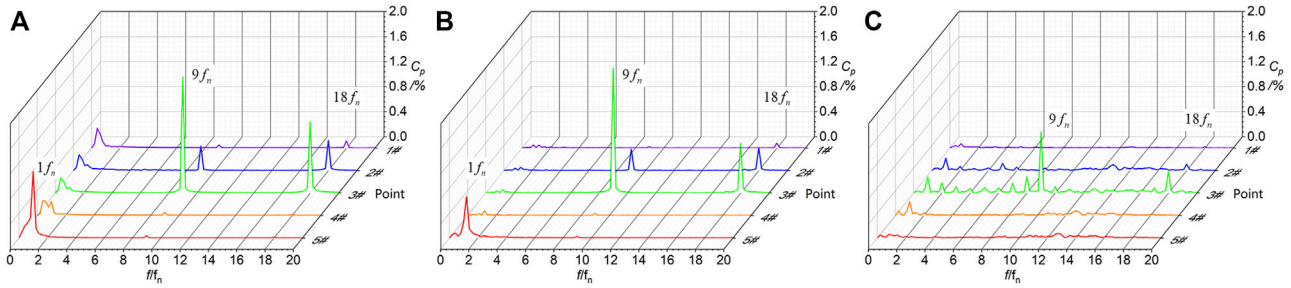

FIGURE 11 | Frequency spectrums of pressure pulsations within turbine mode at three openings. **(A)** 43°. **(B)** 37°. **(C)** 12°.

axial force is the smallest. On the contrary, in the off-design regions, the mean axial force is small, but the fluctuation is large, especially in the pump-brake and turbine-brake modes. In the pump-brake mode, the axial force fluctuation is the largest, with an amplitude of over 1×10^7 N in operation, which may result in unit lifting.

The radial force (the resultant force of x and y directions) variation is slightly different from the axial force, as shown in **Figure 5B**. The average value and fluctuation of radial force in the normal working regions of the turbine mode and pump mode are both small, which reflects the smooth operation of the unit. But under the pump-brake and turbine-brake modes, the average value of radial force reaches the extreme values of about 1000 kN, and the difference between the maximum and minimum values is also large. The serious radial force fluctuations may cause strong vibrations in the runner shaft system. The radial force fluctuations are also high under the remaining unfavorable operating conditions such as the pump 0-discharge and turbine 0-discharge points, and the reverse pump mode.

In general, as the opening decreases, the axial and radial force fluctuations are reduced under most operating modes.

In the following sections, we will discuss the mechanism and correlations of flow characteristics and give a more detailed description of the flow characteristics in each operating mode.

3.2 Mechanism of Flow Characteristics in the Four-Quadrant Characteristic Plane

3.2.1 Pump Mode

When the pump-turbine is operating in the pump mode, the rotation direction of the runner is counterclockwise, pumping water upstream. When it operates near the design working point, there is no obvious flow impact and separation inside the blade channels (**Figure 6A**). As the discharge decreases, the angle between the absolute velocity V and the peripheral velocity U reduces and the flow hits the guide vane significantly, which makes the flow more turbulent in the guide-vane channels. And when the discharge is low, the water flowing out of the runner forms a circumferential flow of high-speed water ring, impeding the flow into the guide vanes, and the flow separation is serious in the guide-vane area. The internal flow patterns of the runner are similarly smooth in the normal working regions of the pump mode at different openings (**Figures 6A–C**). But at the small opening of 12°, the water entering the guide-vane area continues flowing in the direction of the pressure surface of the guide vane, forming a vortex and serious separation in the vane channels (**Figure 6C**).

Under the pump mode, the wedge-shaped cavitation caused by flow separation occurs at the trailing edge of the runner blades and the location is near the shroud side of the suction surface, as shown in **Figure 6**. The degree of cavitation deepens and the volume of cavitation increases as the discharge decreases, corresponding to the deterioration of the flow pattern, no cavitation occurs at the 43° high discharge working point and 37° working point calculated in this study but occurs at the small opening 12°. When the discharge is further reduced to 0, more pronounced cavitation occurs at the three openings and the area of occurrence is unchanged (**Figures 6G–I**).

Runner forces are closely related to flow patterns, the radial force in the better operating conditions has a pronounced periodicity, as shown in **Figures 7A,B** (the graph shows the variation of the radial forces on the whole runner over one cycle of runner rotation). In small-discharge and small-opening conditions the periodicity is damaged due to the turbulent flow. As the discharge decreases the radial force increases, at the pump 0-discharge point (**Figure 7C**), the periodicity of radial forces is severely damaged, and the fluctuations are violent, the largest radial force can reach 900 kN.

The frequency spectrums of pressure pulsations at different openings under the pump mode are similar, as shown in **Figure 8**. Under this mode, because of the upward flow direction, rotor-stator interaction has less effect on the draft-tube area $9f_n$and $18f_n$ is not evident at the draft-tube monitoring points (f_n is the rotational frequency of the runner). Meanwhile, with the decrease in the opening, flow separation in the guide-vane area is more serious, and the low-frequency component is dominant at most monitoring points. At the opening of 12°, the $1f_n$ components of each monitoring point stand out and the highest amplitude of this frequency appears in the guide-vane area, which is related to the internal vortex structure in the guide vanes at this opening, which can be seen in **Figure 6C**. When the discharge is reduced to 0 (**Figures 8D–F**), due to the backflows and vortices inside the turbine, the

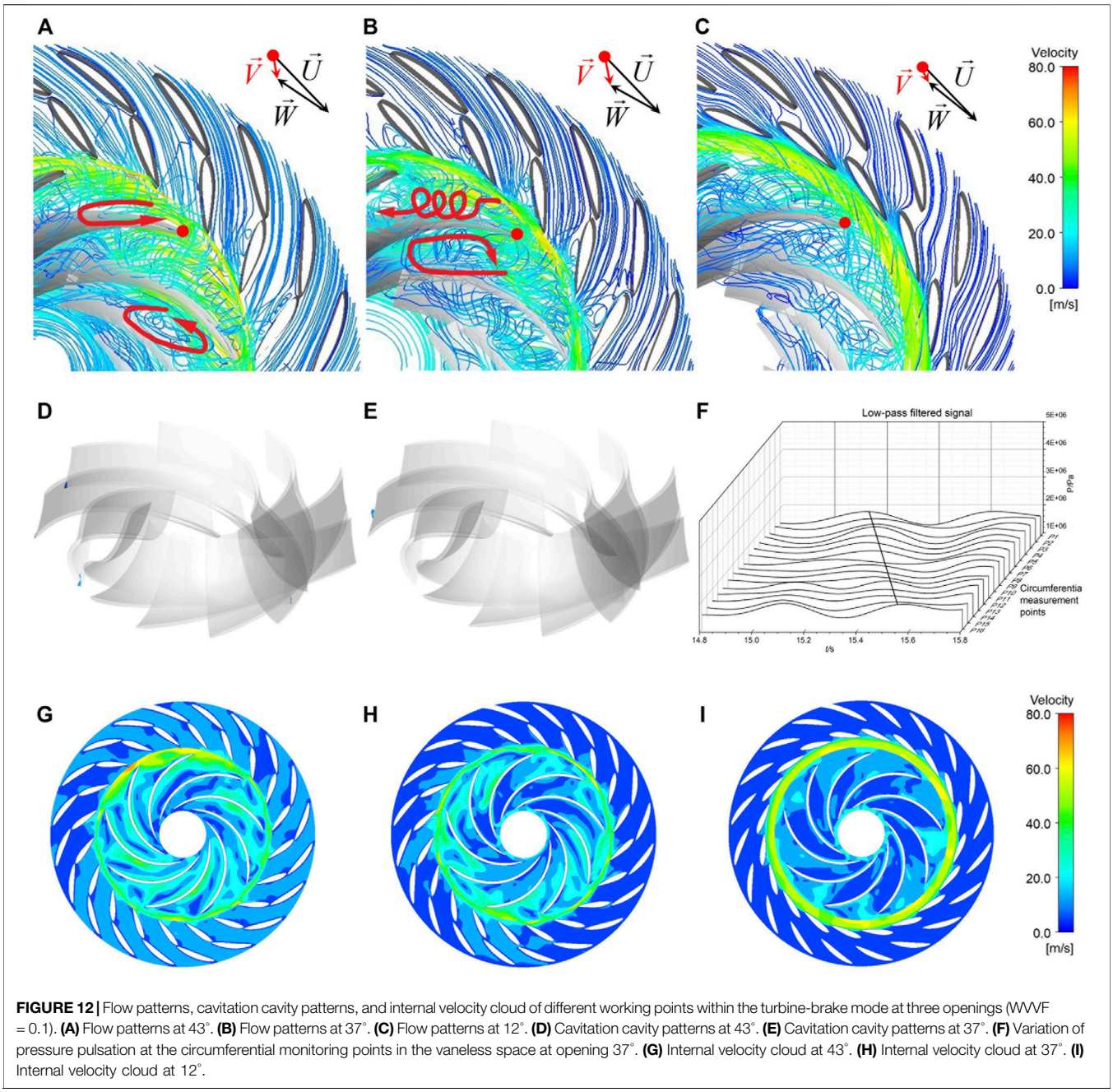

FIGURE 12 | Flow patterns, cavitation cavity patterns, and internal velocity cloud of different working points within the turbine-brake mode at three openings (WVF = 0.1). **(A)** Flow patterns at 43°. **(B)** Flow patterns at 37°. **(C)** Flow patterns at 12°. **(D)** Cavitation cavity patterns at 43°. **(E)** Cavitation cavity patterns at 37°. **(F)** Variation of pressure pulsation at the circumferential monitoring points in the vaneless space at opening 37°. **(G)** Internal velocity cloud at 43°. **(H)** Internal velocity cloud at 37°. **(I)** Internal velocity cloud at 12°.

pulsation amplitude is much higher than the corresponding amplitude of the same opening degree at high-discharge pump conditions (about 1% in the normal pump mode and 5% in the 0-discharge points), and low-frequency components like $0.2f_n$ and $0.4f_n$ are dominant.

3.2.2 Pump-Brake Mode

Under the pump-brake mode, the runner keeps rotating in the pump direction, but the water flows direction changes to the turbine direction. The flow in the vaneless area is turbulent, as shown in **Figures 9A–C**, when the water enters the runner, it first strongly hits the inlet of the pressure surface of the runner, then flows to the adjacent blade channel, and hits the next blade again and continues to flow downwards along the blade surface. The water flows down spirally in the blade channels because of the violent impact between the water and the blades, causing serious flow separation.

Due to the serious flow separation and backflow vortex, local pressure decreases, and the cavitation is serious under this mode, as shown in **Figures 9D–F**. A large area of cavitation appears in the runner channels at the large opening of 43° (**Figure 9D**), and the cavitation area decreases as the opening decreases. The

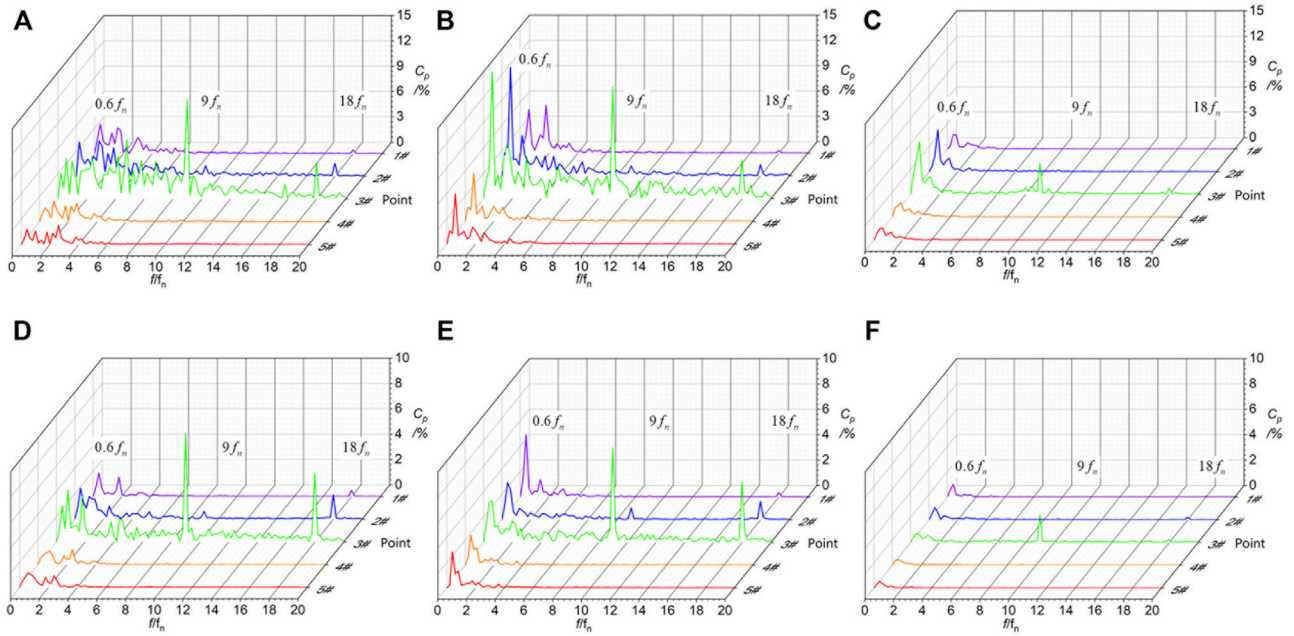

FIGURE 13 | Frequency spectrums of pressure pulsations within the turbine-brake mode at three openings. **(A)** 43°. **(B)** 37°. **(C)** 12°. **(D)** 43° (Q = 0 m^3/s). **(E)** 37° (Q = 0 m^3/s). **(F)** 12° (Q = 0 m^3/s).

turbulent flow patterns and the severe cavitation cavity cause the radial force of the runner to change dramatically and irregularly in one cycle under this mode (**Figure 7D**), and the radial force also increases significantly compared to that of the pump mode (the largest radial force under this mode can reach to 1000 kN), resulting in significant vibration of the unit's shaft system.

The amplitude of the pressure pulsations at each monitoring point under the pump-brake mode is extremely high (**Figures 9G–I**), except the main frequency at the monitoring point in the vaneless space is still $9f_n$ (corresponding amplitude is about 20%), the main frequencies of other points are $0.4f_n$ at 43° and 37°. By setting up circumferential pressure pulsation monitoring points in the vaneless space to obtain the circumferential variation of the pressure pulsation after low-pass filtering, we found that there was no low-frequency pressure signal propagating along the circumferential. So, we confirmed that this frequency is not related to the rotating stall. Through the analysis of the flow pattern at each monitoring point, the low-frequency components under this mode should be related to the structure of the vortex and backflow at the guide vane area and draft-tube inlet. Under the opening of 12°, the guide vane opening is small and the discharge is low, we can see that the flow pattern in the guide vane area is smooth and there is no obvious backflow and vortex (**Figure 9C**), so this frequency $0.4f_n$ is not found.

3.2.3 Turbine Mode

The turbine mode is the normal operating condition of the pump turbine, and the runner rotation direction is clockwise. When the working point is near the optimal one (**Figures 10A–C**), the direction of the relative velocity W of the water flow in the runner follows the direction of the blades, the internal flow patterns are smooth and the impact on the runner blades is weak after the water enters the runner. At the small opening of 12° (**Figure 10C**), the water continues to flow forward in the direction of the guide vanes for some distance before entering the runner, and the flow velocity is higher in the vaneless space, with the streamline slightly turbulent near the pressure surface of the runner blades.

In this mode, the pressure inside the rotating vortex rope in the draft tube reduces to the saturated vapor pressure, resulting in a tongue-like spiral cavity inside the rotating vortex rope (**Figure 10D**). The volume of the cavitation cavity decreases as the discharge decreases; therefore, the cavity disappears for working points at 37° and 12° openings.

Due to the smooth flow without distinct impact on the runner inlet in this mode, the radial force distribution in the radar chart is regularly periodical, with the number of peaks in one cycle of runner rotation equal to the number of blades (**Figures 7G,H**). As the discharge decreases, the radial force also decreases. But at the small opening of 12°, the radial forces lose periodicity and fluctuate widely because of the turbulent flow.

As shown in **Figure 11**, at the large openings 43° and 37° (**Figures 11A,B**), the pressure pulsations between the guide vanes and in the vaneless space have distinct $9f_n$ and $18f_n$ characteristics, which are caused by rotor–stator interaction (corresponding amplitude is about 1%). In the draft tube, the dominant pulsation is the low-frequency component $1f_n$, of which the amplitude is much higher than those of the same frequency component in other areas. This means that the $1f_n$ component is originated in the draft tube. This frequency is found at 43°, 37°, but

not 12° opening. It is independent of cavitation, because cavitation occurs only at 43°, but not at the other two openings. As can be seen from **Figures 10D,E**, a rotating vortex rope developing from the cone to the draft tube generates at both 43° and 37° openings, but not at 12° (**Figure 10F**). Furthermore, we take the 37° as an example (**Figures 10G–J**), the pattern of the vortex rope in the draft tube also varies according to a rotational period of 0.24 s, corresponding to the rotational period of the runner and frequency $1f_n$. Therefore, it is concluded that the frequency $1f_n$ should be related to the vortex rope in the draft tube.

3.2.4 Turbine-Brake Mode

Under the turbine-brake mode, the water flowing out of the guide-vane area first hits the blade suction surface, then partly flows forward, partly flows back, and enters the adjacent blade channel, leading to a high-speed and high-pressure transverse flow water ring formed in the vaneless space. The water in the runner flows spirally forward, forming strong flow separation and vortex structure (**Figures 12A–C**). Cavitation with a small cavity occurs on the pressure surfaces close to the leading edges of the runner blades (**Figures 12D,E**). The unbalanced flow patterns in the blade channels induce strongly and irregularly fluctuating radial forces (**Figure 7E**), similar to that of the pump-brake mode. These two brake modes are the most unfavorable operation conditions of the unit.

The turbulent flow patterns not only affect the runner forces but also causes strong pressure pulsations (**Figure 13**), which are significantly higher than those under the normal operating

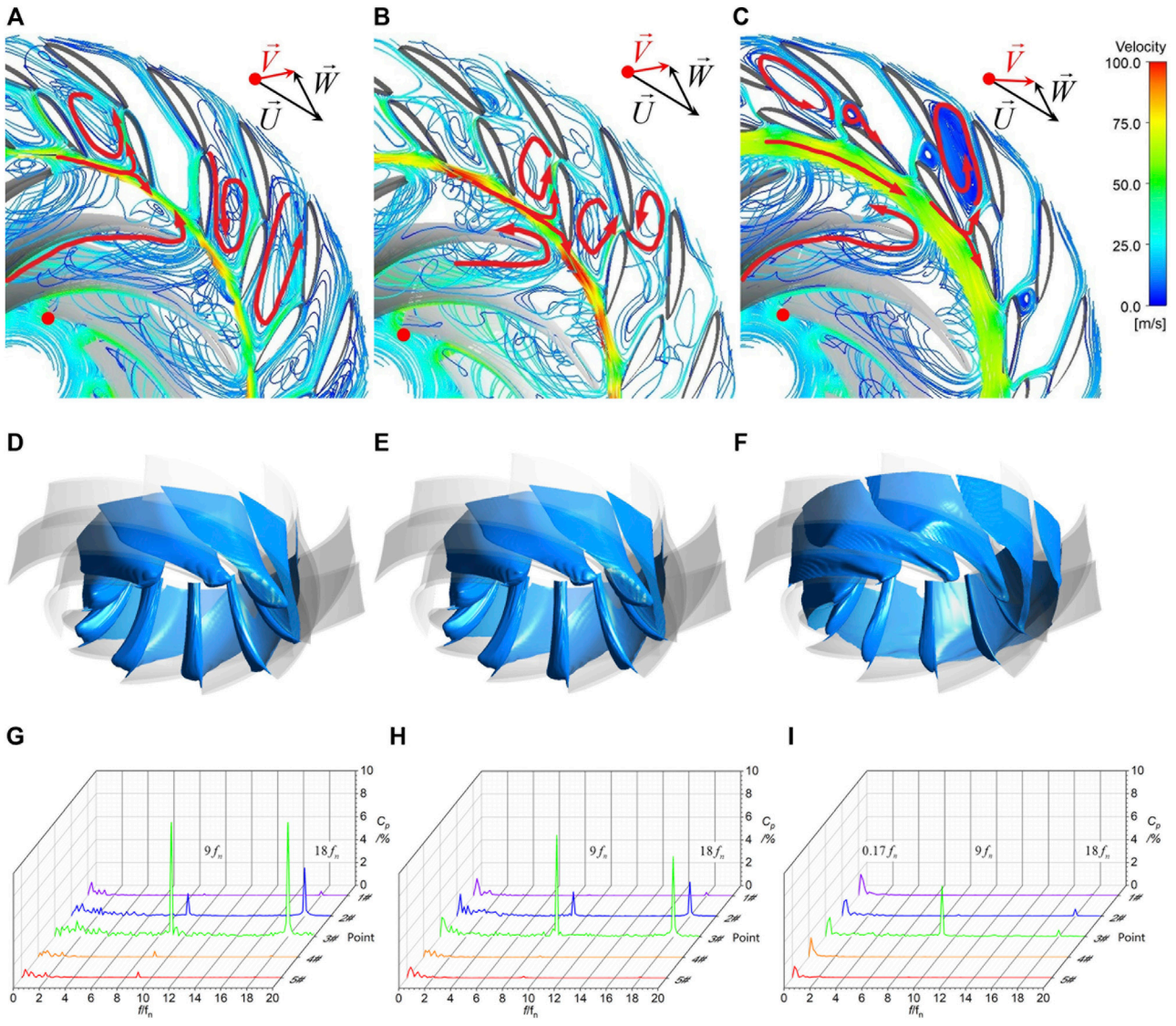

FIGURE 14 | Flow patterns, cavitation cavity patterns, and frequency spectrums of pressure pulsations of different working points within reverse pump mode at different openings (WVF = 0.1). **(A)** Flow patterns at 43°. **(B)** Flow patterns at 37°. **(C)** Flow patterns at 12°. **(D)** Cavitation cavity patterns at 43°. **(E)** Cavitation cavity patterns at 37°. **(F)** Cavitation cavity patterns at 12°. **(G)** Frequency spectrums at 43°. **(H)** Frequency spectrums at 37°. **(I)** Frequency spectrums at 12°.

regions. In the vaneless space, the pressure pulsations have not only strong $9f_n$ signals, but also obvious $0.6f_n$ signals. The pulsations with the frequency of $0.6f_n$ is the highest component in the vaneless and guide-vane areas for 37° and 12° openings (corresponding amplitude is about 10% at opening 37°). This low-frequency component is caused by the developing rotating stall (Zhang Y. et al., 2017), the stall vortex clusters form in several channels of the runner, blocking the runners (**Figures 12G–I**). And it is only as the discharge continues to decrease that the rotating stall develops fully, appearing in the guide vane region. This frequency can also be seen in the low-pass filtered plot of the variation in pressure pulsations at the circumferential monitoring points (Hasmatuchi et al., 2011) (**Figure 12F**). The pressure fluctuation propagates at a low frequency in those circumferential monitoring points (P1-P16), and its propagation period, which is calculated to be about 0.4 s, is corresponding to $0.6f_n$. Therefore, it can be concluded that the $0.6f_n$ under the turbine-brake mode is caused by the rotating stall in the runner.

As the discharge continues to decrease (**Figures 13D–F**), the frequency spectrums of pressure pulsations at the turbine 0-discharge point is similar to that under the turbine-brake mode, but the amplitude of the same frequency decreases and the main frequency of each opening degree in the vaneless space is $9f_n$, indicating that the rotor-stator interaction is dominant at the 0-discharge point.

3.2.5 Reverse Pump Mode

When the pump-turbine enters the reverse pump mode, the runner keeps rotating in the turbine direction, but as the speed continues to rise, the strong centrifugal force draws the water from the draft tube into the runner, pumping water upstream. The flow in the draft tube is turbulent, with the water in the center of the draft tube flowing upward but the water near the wall spiraling downward. After the water is sucked into the runner, the flow first hits the suction surface of the blades, then climbs up along the suction surface. The strong impact on the blades forms flow separations and a large number of vortex structures in the blade channels, and the streamline of each channel is similar. A high-velocity flow ring forms in the vaneless space, preventing the flow from entering the guide-vane area. Because of the small discharge, a large number of vortices generate inside the vane channels. The water entering the guide-vane area first hits the guide-vane blades, then partly flows into the vane channel along the direction of the guide-vane surface, and partly flows forward to the next vane channel. Serious flow separations and vortex structures are forming in the vane channels (**Figures 14A–C**).

Due to the severe flow separation inside the runner, cavitation is extremely serious under this mode. A large flag-shaped cavity forms in the rear half of the pressure surface of every blade (**Figures 14D–F**). The cavitation is uniformly distributed in each runner channel, with a similar distribution at each opening. As shown in **Figure 7F**, radial forces still have peaks in line with the number of blades under the reverse pump mode, but the fluctuation of radial force is large.

The frequency spectrums of pressure pulsations are shown in **Figures 14G–I**, in the vaneless space, the main frequency is still $9f_n$, and the corresponding amplitude decreases with the reduction of opening degree (about 8% at opening 43° and 4% at opening 12°). The $9f_n$ and $18f_n$ components are also prominent in the guide-vane area, indicating that rotor-stator interaction is in effect along the direction of the flow. But at an opening of 12° (**Figure 14I**), because of the smaller opening of the guide-vane and the obstruction of the flow, there is less influence of rotor-stator interaction in the guide-vane, and the corresponding amplitude of frequency $9f_n$ is extremely small. The remaining monitoring points have a predominance of low-frequency components, with the main frequency of $0.17f_n$, at opening 12°, which combined with the flow analysis indicates that this frequency should be related to the flow separation vortex structure in the guide-vane area.

4 CONCLUSION

To understand the distribution characteristics of flow patterns, pressure pulsations, cavitation characteristics, and runner forces of pump-turbine in all five operating modes, we conducted CFD simulations for a prototype pump-turbine and analyzed 29 typical working points at three typical openings. The main conclusions are as follows.

1) Near the design working points, the streamline is smooth, pressure and runner force fluctuations are small, and cavitation is not obvious. However, when the working points deviate from the optimal one, flow patterns are getting worse, leading to violent pressure and runner force fluctuations.
2) Operation in the pump-brake mode is the most unfavorable, with turbulent flow patterns, complex vortex structures, serious cavitation, and prominent low-frequency pressure pulsations. The flow hits the runner blades violently, causing extremely large runner force fluctuations and may lead to severe vibration of the unit. While in the hump region of the pump mode, the flow hits the guide vanes, causing an apparent rotating stall in the vane area. Also, in the S-shaped region, the operation is also unstable with high-pressure pulsation caused by rotor-stator interaction and developing rotating stall.
3) Pressure pulsations reach the largest in the pump-brake and turbine-brake modes, with amplitudes more than 10 times those in the normal working regions. Under similar operating conditions, the pressure pulsations increase with the opening degree; at the same working point, the pressure pulsations are greatest in the vaneless space, followed by in the guide-vane areas, and further smaller in the spiral-casing and draft-tube inlet.
4) When operating at large openings, the pump-turbine has cavitation of various sizes and forms under most operating modes. Under the turbine high-discharge point, tongue-shaped cavitation occurs in the draft tube. Under all other

modes, cavitation occurs inside the runner. The cavitation is serious in the pump-brake mode and reverse pump mode, especially in the latter, with large flag-shaped cavities filling most of the runner channels.

The resulting laws and mechanism of the flow characteristics in each operating mode can provide a reference for related research and runner design, and pump turbines should avoid long-term operation in pump-brake and turbine-brake modes. In future studies, we should pay more attention to the sources of pressure pulsations at different frequencies under unfavorable operating modes and the corresponding improvement measures.

DATA AVAILABILITY STATEMENT

The original contributions presented in the study are included in the article/Supplementary Material, further inquiries can be directed to the corresponding author.

AUTHOR CONTRIBUTIONS

DH: data curation and writing—original draft preparation and editing; YC: writing—original draft preparation and investigation; PZ: formal analysis and validation; XW: writing—review and editing; JD: writing—review and editing; and XZ: assistance with analysis.

FUNDING

This work was supported by the National Natural Science Foundation of China (NSFC) (Grant Nos. 51839008 and 51909226).

ACKNOWLEDGMENTS

The numerical simulations were conducted on the supercomputing system in the Supercomputing Center of Wuhan University.

REFERENCES

Celebioglu, K., Altintas, B., Aradag, S., and Tascioglu, Y. (2017). Numerical Research of Cavitation on Francis Turbine Runners. *Int. J. Hydrogen Energ.* 42 (28), 17771–17781. doi:10.1016/j.ijhydene.2017.03.180

Goyal, R., and Gandhi, B. K. (2018). Review of Hydrodynamics Instabilities in Francis Turbine during Off-Design and Transient Operations. *Renew. Energ.* 116. 697. doi:10.1016/j.renene.2017.10.012

Hasmatuchi, V., Farhat, M., Roth, S., Botero, F., and Avellan, F. (2011). Experimental Evidence of Rotating Stall in a Pump-Turbine at Off-Design Conditions in Generating Mode. *J. Fluids Eng.* 133 (5), 1–8. doi:10.1115/1.4004088

Ješe, U., Fortes-Patella, R., and Antheaume, S. (2014). "High Head Pump-Turbine: Pumping Mode Numerical Simulations with a Cavitation Model for Off-Design Conditions," in *27th IAHR Symposium on Hydraulic Machinery and Systems (IAHR)* 22, 1–11. doi:10.1088/1755-1315/22/3/032048

Ješe, U., and Fortes-Patella, R. (2016). Unsteady Numerical Analysis of the Rotating Stall in Pump- Turbine Geometry. *IOP Conf. Ser. Earth Environ. Sci.* 49, 042005. doi:10.1088/1755-1315/49/4/042005

Ji, X. Y., and Lai, X. (2011). Numerical Simulation of the S-Shaped Characteristics of the Pump-Turbine. *Chin. J. Hydrodynamics* 26 (03), 318–326. doi:10.3969/j.issn1000-4874.2010.03.008

Jun-Won, S., Hyeon-Mo, Y., Jin-Hyuk, K., Won-Gu, J., Jungwan, P., and Young-Seok, C. (2021). Unstable S-Shaped Characteristics of a Pump-Turbine Unit in a Lab-Scale Model. *Renew. Energ.* 171. 1395. doi:10.1016/j.renene.2021.03.013

Li, D.-y., and Wang, H.-j. (2015). Fluid Flow Analysis of Drooping Phenomena in Pump Mode for a Given Guide Vane Setting of a Pump-Turbine Model. *JZUS-A* 16, 851–863. doi:10.1631/jzus.A1500087

Li, D., Song, Y., Lin, S., Wang, H., Qin, Y., and Wei, X. (2021). Effect Mechanism of Cavitation on the Hump Characteristic of a Pump-Turbine. *Renew. Energ.* 167, 369–383. doi:10.1016/j.renene.2020.11.095

Li, Q. F., Chen, X. Y., Meng, Q., Cai, T., Zhou, F., and Wei, X. Z. (2020). Analysis of Correlation Characteristics of Pump-Turbine under Different Cavitation Numbers. *Trans. Chin. Soc. Agric. Machinery* 51 (01), 130–138.

Li, Q. F., Wang, Y. K., Liu, C., and Han, W. (2017). Study on Unsteady Internal Flow Characteristics in Hump Zone of Mixed Flow Pump Turbine. *J. Gansu Sci.* 29 (04), 54–58.

Li, Y. X., Zhou, D. Q., and Yu, A. (2019). Research of Swirl Cavity Flow Performance in the Draft Tube of Pump Turbine. *Renew. Energ. Resour.* 37 (02), 303–309. doi:10.13941/j.cnki.21-1469/tk.2019.02.023

Liu, J., Liu, S., Wu, Y., Jiao, L., Wang, L., and Sun, Y. (2012). Numerical Investigation of the Hump Characteristic of a Pump-Turbine Based on an Improved Cavitation Model. *Comput. Fluids* 68, 105–111. doi:10.1016/j.compfluid.2012.08.001

Liu, K., Yang, F., Yang, Z., Zhu, Y., and Cheng, Y. (2019). Runner Lifting-Up during Load Rejection Transients of a Kaplan Turbine: Flow Mechanism and Solution. *Energies* 12 (24), 4781. doi:10.3390/en12244781

Liu, Z. Q., Sun, H., Xiao, R. F., and Liu, W. C. (2013). S-shaped Characteristics of Pump-Turbine and Improvement on its Performance. *J. Hydroelectric Eng.* 32 (02), 257–260+270.

Ran, H. J., Zhang, Y., Luo, X. W., and Xu, H. Y. (2011). Numerical Simulation of the Positive-Slope Performance Curve of a Reversible Hydro-Turbine in Pumping Mode. *J. Hydroelectric Eng.* 30 (03), 175–179.

Shang, C. Y. (2020). Cavitation Effect On the S-Shaped Characteristics Of Pump-Turbine. *Master Master's Thesis*. Harbin: Harbin Institute of Technology.

Wang, C. H., and Guo, Z. W. (2018). *An Investigation of the Hump Characteristic of a Prototype Pump-Turbine at Pump Modes*. China Rural Water and Hydropower. 7, 178–183.

Wang, F. J. (2016). Research Progress of Computational Model for Rotating Turbulent Flow in Fluid Machinery. *Trans. Chin. Soc. Agric. Machinery* 47 (02), 1–14.

Wang, L. Q., Liu, Y. Y., Liu, W. J., Qin, D. Q., and Jiao, L. (2013). Pressure Fluctuation Characteristics of Pump-Turbine at Pump Mode. *J. Drainage Irrigation Machinery Eng.* 31 (01), 7–10+35.

Wang, Z. P. (2020). Study On Cavitation Performance Of the "s" Characteristics Of the Pump-Turbine. *Master Master's Thesis*. Xi'an: Xi'an University of Technology.

Widmer, C., Staubli, T., and Ledergerber, N. (2011). Unstable Characteristics and Rotating Stall in Turbine Brake Operation of Pump-Turbines. *J. Fluids Eng.* 133 (4). doi:10.1115/1.4003874

Wu, Y. J., Yang, Z. B., and Tian, D. Y. (2021). Influence of Guide Vane Opening on External Characteristics and Stability of Pump Turbine at Zero Flow Condition. *Water Resour. Power* 39 (06), 158–160+157.

Xia, L. S., Cheng, Y. G., Cai, F., and Zhang, X. X. (2015). Numerical Analysis of Flow Characteristics of a Model Pump-Turbine in Four Operating Quadrants. *J. Hydraulic Eng.* 46 (07), 859–868.

Xiao, R., Sun, H., Liu, W. C., and Wang, F. J. (2012a). Analysis of S Characteristics and its Pressure Pulsation of Pump-Turbine under Pre-opening Guide Vanes. *Jme* 48 (08), 174–179. doi:10.3901/jme.2012.08.174

Xiao, Y. X., Sun, D. G., Wang, Z. W., Zhang, J., and Peng, G. Y. (2012b). Numerical Analysis of Unsteady Flow Behaviour and Pressure Pulsation in Pump Turbine with Misaligned Guide Vanes. *IOP Conf. Ser. Earth Environ. Sci.* 15 (3), 032043. doi:10.1088/1755-1315/15/3/032043

Yan, J. P., Seidel, U., and Koutnik, J. (2013). "Numerical Simulation of Hydrodynamics in a Pump-Turbine at Off-Design Operating Conditions in Turbine Mode," in *26th Iahr Symposium on Hydraulic Machinery and Systems, Pts 1-7*. Editors Y. Wu, Z. Wang, S. Liu, S. Yuan, X. Luo, and F. Wang.

Zhang, C. Z., Xia, L. S., Diao, W., and Zhou, J. Y. (2017a). Pressure Fluctuations Characteristics and Rotating Stall Propagation Mechanism of a Pump-Turbine in Pump Mode. *J. Hydraulic Eng.* 48 (07), 837–845.

Zhang, F., Fan, Y. L., Zhu, B. S., Xu, Y. L., and Liu, W. J. (2019). S-shape Region Pressure Pulsation Measurement of Model Reversible Pump-Turbine. *Fluid Machinery* 47 (06), 6–11+28.

Zhang, L. J., Wang, Z. W., and Chang, J. S. (2011). Flow of Pump-Turbine on S-Shaped Region of Complete Characteristics. *Trans. Chin. Soc. Agric. Machinery* 42 (01), 39–43+73.

Zhang, X. X. (2015). *Three-Dimensional Transient Flow in Pumped-Storage Plant: Simulation and Analysis by Coupling One-Dimensional Water Conveyance System with Three-Dimensional Pump-Turbine.Doctor Doctoral Thesis*. Wuhan: Wuhan University.

Zhang, Y., Zhang, Y., and Wu, Y. (2017b). A Review of Rotating Stall in Reversible Pump Turbine. *Proc. Inst. Mech. Eng. C: J. Mech. Eng. Sci.* 231 (7), 1181–1204. doi:10.1177/0954406216640579

Zhu, D., Xiao, R., and Liu, W. (2021). Influence of Leading-Edge Cavitation on Impeller Blade Axial Force in the Pump Mode of Reversible Pump-Turbine. *Renew. Energ.* 163, 939–949. doi:10.1016/j.renene.2020.09.002

Zuo, Z., Fan, H., Liu, S., and Wu, Y. (2016). S-Shaped Characteristics on the Performance Curves of Pump-Turbines in Turbine Mode - A Review. *Renew. Sustain. Energ. Rev.* 60, 836–851. doi:10.1016/j.rser.2015.12.312

Conflict of Interest: XW was employed by Anhui Jinzhai Pumped Storage Company Ltd.; JD was employed by Pumped-Storage Power Institute of Technology and Economy, State Grid Xinyuan Company Ltd.

The remaining authors declare that the research was conducted in the absence of any commercial or financial relationships that could be construed as a potential conflict of interest.

frontiers | Frontiers in Energy Research

ORIGINAL RESEARCH
published: 27 May 2022
doi: 10.3389/fenrg.2022.900050

Dynamic Characteristics and Effect on Thrust of Jet Tail Vortex Ring for Pump Jet Propulsion

Wei Han[1], Zhixiong Li[1], Rennian Li[1], Huimin Feng[1], Lingbo Nan[1,2]*, Jun Xu[1] and Mingzhen Xiao[1]*

[1]College of Energy and Power Engineering, Lanzhou University of Technology, Lanzhou, China, [2]College of Water Resources and Architectural Engineering, Northwest A&F University, Yangling, China

When a pump is propelled by a propeller, the nozzle flooding of the jet wake area will produce a turbulent quasi-sequence structure and have a certain impact on the outflow field structure and thrust characteristics of the water jet propulsion pump. In this paper, a method that combined numerical simulation with vortex dynamics is adopted, which analyzes the dynamic characteristics and influence on the thrust characteristics of the water jet propulsion pump. A large eddy simulation turbulence model and a dimensionless water jet propulsion pump velocity coefficient were used to reveal flow structure and relation, with the pump operation parameters of the wake vortex ring. The thrust with a trailing vortex ring is 7.0% higher than that without a trailing vortex ring. Vortex dynamics and mathematical statistics are combined to quantitatively analyze the dynamic characteristics of the jet tail vortex ring. Finally, the formation time of the vortex ring is obtained in exponential relation with dimensionless transmission velocity and vorticity coefficient, which has nonlinear relation with vortex intensity coefficient and helicity coefficient. BP Neural Network combined with the LM algorithm is used to establish the mathematical relationship between the thrust and the physical characteristic parameters of the vortex ring.

Keywords: pump jet, wake vortex ring, dynamic characteristics, thrust, neural networks

OPEN ACCESS

Edited by:
Kan Kan,
College of Energy and Electrical Engineering, China

Reviewed by:
Qiang Gao,
University of Minnesota Twin Cities, United States
Fan Zhang,
Jiangsu University, China
Qiaorui Si,
Jiangsu University, China

****Correspondence:***
Zhixiong Li
lzxbm@outlook.com
Lingbo Nan
lingbonan19951118@126.com

Specialty section:
This article was submitted to Process and Energy Systems Engineering, a section of the journal Frontiers in Energy Research

Received: *19 March 2022*
Accepted: *06 April 2022*
Published: *27 May 2022*

Citation:
Han W, Li Z, Li R, Feng H, Nan L, Xu J and Xiao M (2022) Dynamic Characteristics and Effect on Thrust of Jet Tail Vortex Ring for Pump Jet Propulsion. Front. Energy Res. 10:900050. doi: 10.3389/fenrg.2022.900050

1 INTRODUCTION

Jet flow is a movement phenomenon in which the fluid flows into another working medium and shoots out from the nozzle or slit. The difference between jet flow and pipe flow is that pipe flow is surrounded by a solid container, while jet flow is uncontained except for the water jet. Most jets are surrounded by fluid (June 1995; HE et al., 2001). In the spraying process of the nozzle of the water jet propulsion pump, both the working fluid and the environmental fluid are water, that is, the jet is a submerged jet. In the whole process of jet movement, vortex pairs and merge with each other due to the shear action of the jet boundary, which exchanges momentum and mass with the surrounding fluid. The vortex makes the surrounding medium flow with the jet, which increases the flow rate and enlarges the cross-section.

At present, domestic and foreign researchers all mainly focus on numerical simulation, experimental research, and theoretical analysis to study jet flow. Yanling Li (Li, 2004) used 3D numerical simulation to study the flow characteristics and vortex structure of the multi-level submerged jet. She not only described the energy dissipation mechanism of the multi-level submerged jet from two aspects of theoretical analysis and numerical simulation but also observed

the whole dissipation process by experimental study. Experimental results showed that the multi-level submerged jet was technically feasible and had the characteristics of significant energy dissipation and a stable flow state. For the quasi-sequence structure generated by the jet, Brown (Brown, 1935) carried out experiments with the jet in the form of a slit. The eddy current structure was observed to change alternately on both sides of a plane jet by the flow display method. The effect of forced jet force on eddy current was studied. The basic law of vortex motion in the jet is obtained by experiment. However, there was no good mathematical model for the observed vortex rate. Davies et al. (Davies et al., 1963) focused on the study of organized motion in turbulent free-shear flow. During the study, a series of vortices were observed to generate continuously near the jet outlet. Experiments showed that there were also significant differences between the time average scalar field and the instantaneous scalar field. The former showed a strong Gaussian distribution, while the latter showed a strong high-order distribution. Becker and Massaro (Becker and Massaro, 1968) focused on the study of flow visualization and observed annular vortices at the initial stage of turbulent jet flow. They considered that the thickness of the boundary layer at the jet outlet was the controlling factor of the disturbance growth. Experiments showed that the turbulent integral time scale becomes inversely proportional to the local tangent in the coordinate system of maximum energy convection in turbulent motion. Mungal et al. (Mungal and Hollingsworth, 1989) studied the vortex structure of relevant jets at a high Reynolds number. He mainly discussed the mechanism of entrainment of ambient fluid by jet. LYDIA. RUIZ et al. (Ruiz et al., 2011), departments of Mechanical Engineering, California Institute of Technology, United States, showed that coherent vortex structures could be generated in the near wake of self-propelled aircraft. The structure could improve the efficiency of propulsion by controlling the local pressure field and entrainment motion. Vortex formation was used to control the near-wake characteristics, which can greatly improve the propulsion efficiency. This was more than 50% better than the performance of the steady jet mode. Compared with stable jet propulsion, Yang Xiang et al. (Xiang et al., 2018) showed that pulsed jet propulsion can show higher efficiency by forming unstable vortex rings. This means that energy can be better transferred and stored in eddy currents to produce propulsion. The mode of effective propulsion in the process of vortex ring energy evolution was illustrated. They pointed out that increasing the energy contribution to the eddy can further enhance propulsive performance. Mark A. Grosenbaugh (Wang, 2020) and researchers studied laminar vortex rings under the influence of background flow using numerical simulation methods. They explained that long, continuous jets maximize thrust for a given amount of energy expend.

Although many scholars have studied the problem of flood jets, they mainly focus on practical applications, and rarely study the flow characteristics of flood jets; especially under the conditions of various vortex topologies, flood jets have unstable flow characteristics. By simulating the vortex ring structure generated in the submerged jet wake, this paper analyzes the hydrodynamics of the whole water jet propulsion device combined with the submerged jet at the tail of the water jet propulsion pump. The influence of the wake vortex ring on the thrust characteristics of the water jet propulsion unit is explained.

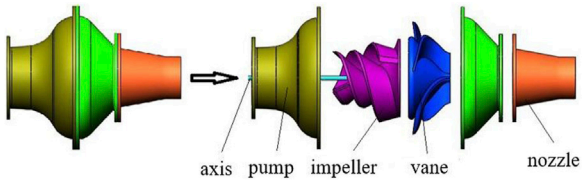

FIGURE 1 | Computational domain model diagram of flow through components of water jet propulsion pump.

In this paper, the spiral mixed-flow water jet propulsion pump is selected as the main power component of the vortex ring. The trailing vortex ring generated by the jet is taken as the study object. Based on the experimental verification of thrust characteristics, the CFD method was used to simulate the submerged jet flow process of the water jet propulsion pump. The induction mechanism of the jet tail vortex ring and its response to thrust characteristics were observed. This provides a reference for further research and application of the submerged jet sequence structure.

2 NUMERICAL SIMULATION OF JET WAKE VORTEX RING OF WATER JET PROPULSION

2.1 Three-Dimensional Modeling of Flow-Through Components of Water Jet Propulsion Pump

In this paper, the spiral mixed flow water jet propulsion pump with the specific speed of $n_s = 278$ is used as the power component. The design flow is $Q = 13.788m^3/h$. The head is $H = 1.3$m. The rotation 9speed is $n = 1500r/$min.

3d drawing software is used for geometric modeling of the water jet propulsion pump. As the core power components of the water jet propulsion pump, the impeller transfers mechanical energy to the fluid through blade rotation. It can increase the static and dynamic pressure energy. This is mainly for energy conversion. Guide vane is the axial length and radical short distribution. Its main function is to eliminate the circumferential component of the fluid flowing through the impeller and convert part of the kinetic energy into pressure energy. In order to ensure uniform flow, the inlet extension section is usually added at the inlet end of the impeller and the length is usually four times the inlet diameter of the impeller. The computational domain model of the flow-through components of the whole water jet propulsion pump is shown in **Figure 1**. The main geometric dimensions are presented in **Table 1**.

2.2 Numerical Simulation of Jet Flow on the Propulsion Pump

2.2.1 Mesh Generation

In this paper, the flow area diagram and water area diagram of each component of the water jet propulsion pumps are divided into grids. It is difficult to divide the impeller and guide the vane of the water jet propulsion pump by using structured mesh because they both

TABLE 1 | Geometric parameters of flow passage parts of water jet pump.

	Parameter	Numerical Value	—	Parameter	Numerical Value
Main geometric parameters of impeller	Impeller inlet diameter	50	Main geometric parameters of guide vane	Inlet diameter of outflow line	108
	Impeller outlet diameter	90		Inlet diameter of inner streamline	80.7
	Impeller Outlet Width	20		Outlet diameter of outer streamline	62
	Blade outlet angle	15		Inner streamline outlet diameter	32
	Wrap angle of impeller blade	360		Axial length of guide vane	53
	Number of impeller blades	2		Entrance angle	35
Main geometric parameters of nozzle	Nozzle inlet radius	31		Exit angle	90
	Nozzle exit radius	16		Shroud angle of guide vane	70
	Nozzle length	60		Number of guide vanes	5
Main geometric parameters of three dimensional water area	The waters are long	720	—	—	—
	Wide water area	240	—	—	—
	High water area	240	—	—	—

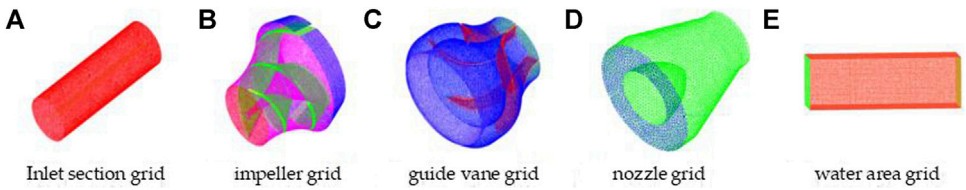

FIGURE 2 | Water area grid division diagram of water jet propulsion pump.

contain curved surfaces with large curvature changes. In order to facilitate the encryption of some local areas, the impeller and guide vane of a water jet propulsion pump is divided into unstructured grids in this paper. In order to capture the development and evolution process of jet tail vortex rings in water jet propulsion, the reasons for a large number of unstructured grids are considered. It divides the inlet end, nozzle, and water body of the water jet propulsion pump with regular shapes into the structured grid with high grid quality and easier access to the actual model. The grid division results of each component are shown in **Figure 2**.

The grid of each part is combined to obtain the overall and water area grid of the water jet propulsion pump, as shown in **Figure 3**.

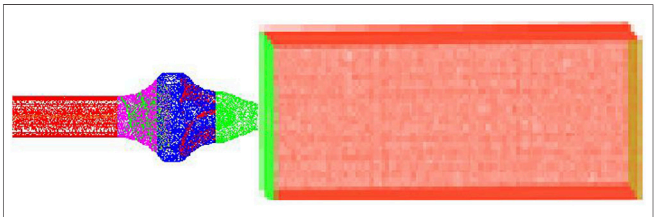

FIGURE 3 | Overall water area grid diagram of water jet propulsion pump.

2.2.2 Grid Independence Test

In this paper, large eddy simulation (LES) is used in the design conditions. Six groups of computing models with different mesh numbers are selected for steady numerical simulation. Head is used as a test criterion for grid independence. Based on ensuring that the mesh quality of impeller and guide vane reaches 0.35 or above, and the mesh quality of inlet section, nozzle, and water area reaches 0.8 or above. By adjusting the grid-scale and the number of grid nodes, the number of grids is obtained as 194,7033, 407,3634, 595,5588,777,8075, 891,2579, and 1202,7317, respectively. The relationship between the grid number and the head is plotted as shown in **Figure 4**. From **Figure 4**, it can be seen that the relative errors among the grids of six different sizes are small and all within 0.3%.

When the solution accuracy and computational resources are both considered, the number of grids is 7.7780750 million and above, and the different rate of the pump head is small. Therefore, we finally selected the grid number 7.778,075 million for numerical simulation.

2.3 Numerical Calculation Method of the Jet Wake Vortex Ring in Water Jet Propulsion

2.3.1 Turbulence Model

In this paper, the three-dimensional unsteady large eddy simulation is used to study the water jet submerged jet. It is obtained the detailed flow

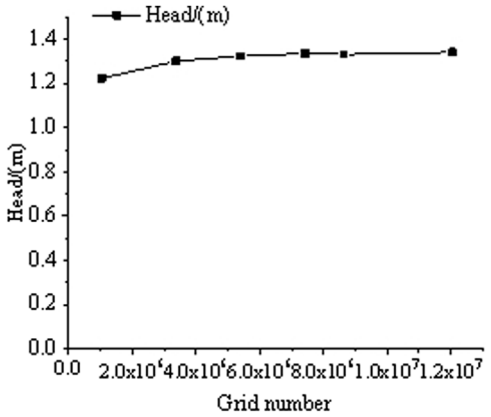

FIGURE 4 | Grid independence check.

field information in the wake region of the submerged jet under different working conditions and the three-dimensional evolution characteristics of the large-scale vortex structure formed near the region.

Large-eddy simulation (LES) is used to filter transient and Navier-Stokes equations in the spatial domain. The small-scale vortices that are smaller than the width of the filter or the scale of the computational grid can be filtered out by the filtering process. It forms the governing equation of large vortices. The small-scale vortex is described by simulation (Wang, 2020).

2.3.2 Control the Numerical Solution of Equations

The numerical solution of the governing equation is obtained by distillation of the algebraic equation. At the same time, the approximate solution of the actual flow field can be obtained by this process. At present, the main flow field solution methods include the coupling solution method and separation solution method. These two methods are divided according to the analytic order and adjustment of unknowns. The coupling methods can deal with the relationship between density, energy, and momentum in the flow field. The core idea of the separation method is to revise and reiterate the repeated pressure until the solution converges. It has been widely used in the numerical solution of the flow field.

In the process of numerical calculation, the SIMPLC algorithm modified pressure and velocity to a certain extent. This accelerates the convergence rate and establishes algebraic modified equations of pressure and velocity. Therefore, the finite volume method is used in this paper to discretize the flow field equations of water jet propulsion. In order to achieve high convergence accuracy, SIMPLC algorithm is used to solve the flow field in this paper.

2.3.3 Vorticity Distribution in Jet Wake Area of Water Jet Propulsion

As shown in **Figure 5**, it can be seen from the distribution of the entire vortex cloud map that the distribution of eddy intensity on the upper and lower sides is basically the same, and the vorticity vector direction is opposite. At the same time, the vorticity on the upper and lower sides of the axis has relatively obvious symmetrical distribution characteristics, which is because the axis is the core area of the jet, which can generate higher vorticity, that is, the shear effect and mixing between the nozzle jet and the tailwater area action leads to the forward transmission and dissipation of energy.

In the region near the nozzle, the vorticity value is relatively large, which is due to the high initial kinetic energy and strong clustering of the jet in the initial stage of the convergent nozzle. With the continuous development of the jet, the jet beam expands continuously along the radial direction, the jet fluid continuously interacts with the surrounding water body, and the energy dissipates gradually. At the same time, vorticity values generally show a downward trend, and the edge of the vorticity concentration area slowly generates smaller-scale vortices. The vorticity distribution in the whole wake area directly reflects the vorticity evolution characteristics of the submerged jet of the three-dimensional nozzle.

2.3.4 Pressure Distribution in the Wake of Water Jet Propulsion

As shown in **Figure 6**, there is a low-pressure area in the region near the nozzle outlet, which is caused by the weak interaction between the nozzle outlet and the surrounding fluid due to the low velocity of the nozzle outlet. Along the axis of the jet flow direction, the vortex street phenomenon is evenly distributed on both sides of the whole jet wake area, and the pressure values of the upper and lower vortices are both the same. At the same time, the pressure distribution between two adjacent vortex pairs presents a positive and negative distribution, and the absolute value of pressure is the same. As the flow continues, the symmetry between the upper and lower vortices is gradually destroyed due to the dissipation of energy.

As the flow continues, due to the strong shear effect between the jet and the wake, a pair of small vortices with symmetrical distribution near the nozzle is formed at the beginning of the nozzle injection, and the pressure values of the small vortices on both sides are the same. When the vortices flow downstream along the flow direction, they gradually merge with the vortices of different scales formed in front of them. In the far-field region near the nozzle exit, the symmetry of the large and small vortices gradually disappears with the dissipation of energy, and the vortices of each scale are distributed irregularly.

2.3.5 Velocity Streamline Distribution in the Wake of Water Jet Propulsion

As shown in **Figure 7**, when the water in the nozzle is ejected, it is not an imaginary direct-current jet, but will be squeezed by the surrounding water and rolled back to form a vortex ring structure. After the jet fluid accelerates fluid through the tapered nozzle, it first forms a DC liquid in the area near the nozzle, and then with the process of spraying, the ejected water gradually begins to suck up the water in the surrounding environment, making the main jet the flow on both sides of the flow area exists in the form of vortex rings, which increases the entrainment effect of environmental fluid (i.e., the volume of the whole wake area).

The main jet area continuously entrains the surrounding fluid and moves forward, causing the surrounding fluid to bend along the jet direction, thus the streamline distribution in the main jet area is no longer stable, the water flow is gradually dispersed, and

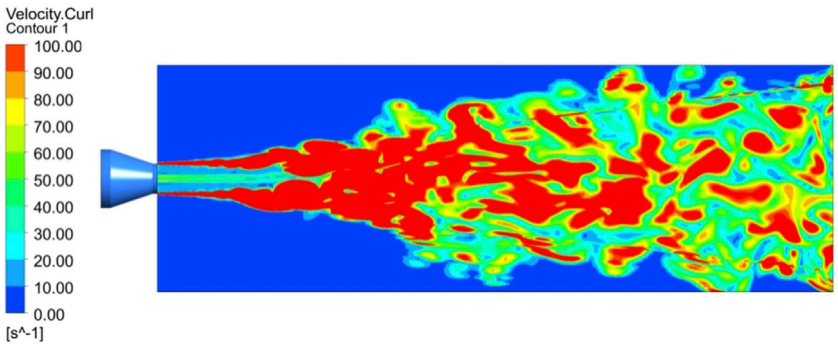

FIGURE 5 | Distribution of vorticity in the wake of water jet propulsion.

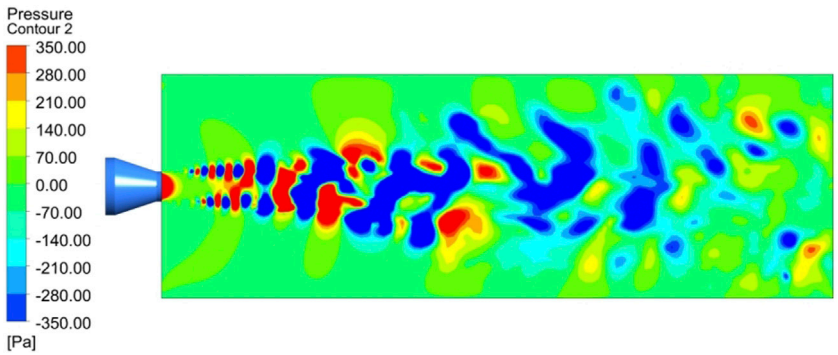

FIGURE 6 | Pressure distribution in the wake of water jet propulsion.

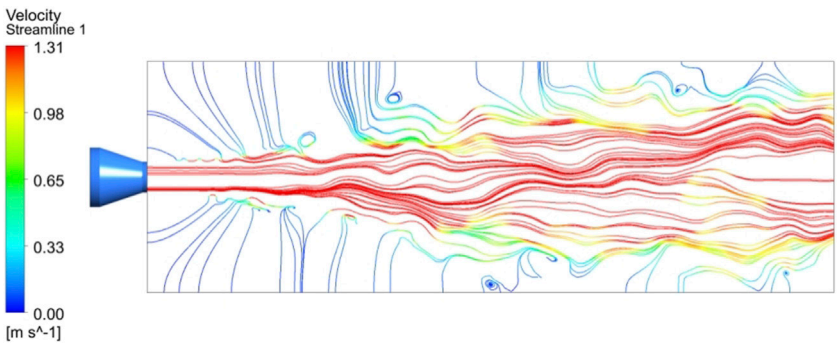

FIGURE 7 | Velocity streamline distribution in the wake area of water jet propulsion.

vortices of various scales continue to propagate backward along the diffusion surface. As the injection proceeds, the entrainment continues. On the upper side of the nozzle main jet area, the vortex distribution is anticlockwise, while on the lower side, the vortex distribution is clockwise. The difference in the direction of vortex distribution is caused by the different entrainment directions of jet flow on the surrounding fluid.

2.4 Thrust Verification of Jet Wake Vortex Ring Simulation for Water Jet Propulsion

Like other underwater bio-jet modes, the thrust generated during the jet propulsion pump can be obtained according to the momentum conservation law and the momentum theorem. Suppose that the outflow velocity of the nozzle of the water jet propulsion pump at time t is u. The nozzle outlet radius is r.

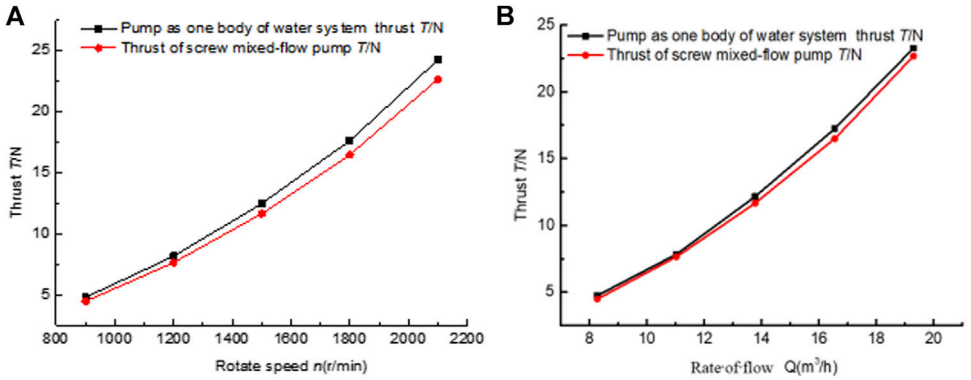

FIGURE 8 | Characteristic curve of water jet propulsion pump. **(A)** N-T characteristic curve of water jet propulsion pump. **(B)** Q-T characteristic curve of water jet propulsion pump.

Without considering the fluid loss at the nozzle outlet, the injection thrust T can be expressed as:

$$T = \frac{dm}{dt}u = \frac{d\left(\rho\pi r^2 L\right)}{dt} = \rho\pi r^2 u^2 \tag{1}$$

In **Eq. 1**, m refers to the mass of ejected water (kg). L is the length of ejected water flow (m). It can be seen that jet thrust is mainly related to jet velocity. The flow velocity in the water area is mainly provided by nozzle outlet velocity and water-induced velocity.

Figure 8A,B respectively show the changeable curve of the relationship between the thrust generated by the helical mixed-flow jet propulsion pump and the average thrust generated by the pump-water integrated system with the impeller speed and inlet flow rate. According to the characteristic curves of impeller speed and average propulsion force in **Figure 8A**, the thrust of the spiral mixed-flow pump and the pump-water integrated system both increase gradually with the change of rotational speed at a given design speed of 1500 r/min. The variation rate of the pump-water system is larger than the spiral mixed-flow pump. The main reason for this situation is that in the spiral mixed flow pump, the pump thrust only needs to be provided by the reaction force generated by the water flowing out of the nozzle due to Newton's third law. In the pump-water integrated system, the thrust generated by the pump-jet thruster is in addition to the above reaction force. As the jet fluid pulls in the surrounding fluid, causing the fluid to accelerate, the water allows the eddy currents to increase part of the thrust of the propulsion. This part of the thrust can compensate for some of the drag in the propulsion system compared to the spiral mixed flow pump. By calculation, the propulsion force produced by the pump-water integrated system is about 6%–7% higher than that produced by the simple spiral mixed flow pump.

It can be seen from the characteristic curve of inlet flow rate and average propulsion force in **Figure 8B** that the thrust of the spiral mixed-flow pump and the pump-water integrated system have basically the same change trend with inlet flow rate. The reason for the slightly higher thrust in the pump-water integrated system is that the entrainment of environmental fluid in the wake area of the nozzle area becomes more significant with the increase of inlet flow. This causes fluid acceleration in the wake area. It is calculated that the propulsive force produced by the pump-water integrated system is about 9% higher than that produced by the spiral mixed-flow pump. Therefore, under the given conditions, accelerating the impeller speed to provide unstable flow and adopting a larger inlet flow rate will greatly enhance the propulsion effect. This also explains that in the jet propulsion process, the contribution of vortex propulsion is enhanced by entrainment of ambient fluid and downstream acceleration of near wake vortex. It reduces the systematic resistance of the entire jet propulsion process.

3 DYNAMIC CHARACTERISTICS OF A JET TAIL VORTEX RING IN WATER JET PROPULSION

3.1 Mathematical Model of Jet Wake Vortex Ring

The vortex ring is a flow structure with axisymmetric characteristics in the cylindrical coordinate system (r, z, θ), $V_\theta = 0$, $\partial/\partial\theta = 0$. In general, the main models of vortex rings are nucleolus linear vortex rings without core, uniform vortex core, and thin core models. Among them, nucleolus linear vortex ring and uniform vortex core are vortex ring models under ideal conditions (Yang, 2013).

Norbury (Norbury, 1973) classified vortex rings according to the dimensionless vortex core radius α. Among them, when $\alpha \to \sqrt{2}$ corresponds to spherical vortex ring and in the range of $0 < \alpha < \sqrt{2}$, the vortex ring belongs to thin core vortex ring. Thin nuclear vortex rings have similar physical characteristics. Fraenkel (Fraenkel, 1972) established a motion mechanics model for thin core vortex rings:

$$E = \frac{1}{2}\rho R\Gamma^2\left(In\frac{8}{\varepsilon} - \frac{7}{4}\right) \tag{2}$$

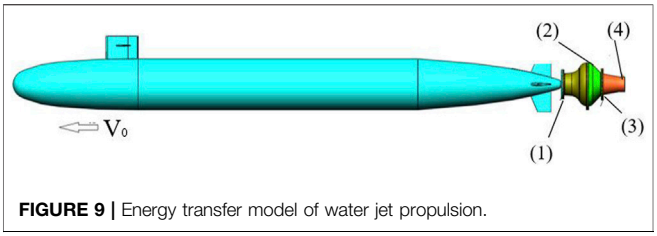

FIGURE 9 | Energy transfer model of water jet propulsion.

$$I = \rho\pi\Gamma R^2 \tag{3}$$

$$U = \frac{\Gamma}{4\pi R}\left(In\frac{8}{\varepsilon} - \frac{1}{4}\right) \tag{4}$$

Where, E, I, Γ, U respectively refer to the energy, momentum, circularity, and transmission speed of the vortex ring. R is the radius of the vortex ring. ε is the radius of the dimensionless vortex core. $\varepsilon = \frac{a}{R}$, a is the radius of the vortex core.

Sullivan (Sullivan et al., 2008) researched the model of thin core vortex rings through the experimental study of piston devices. The changes in the physical characteristics of the vortex ring can be calculated by the growth state of the vortex ring as follows:

$$R = \left(\frac{3\Omega_P}{4\pi\gamma}\right)^{1/3} = \left(\frac{3R_0^2 L}{4\gamma}\right)^{1/3} \tag{5}$$

$$\Gamma = \frac{R_0^2 L V_P}{R^2} = \frac{R_0^2 L^2}{R^2 T} \tag{6}$$

$$V = \frac{\Gamma}{4\pi R}\left(In\frac{8R}{a} - 0.558\right) = \frac{\gamma V_P}{3\pi}\left(In\frac{8R}{a} - 0.558\right) \tag{7}$$

$$a = \sqrt{4\nu T} \tag{8}$$

In the equation, L is the stroke of the piston, R_0 is the radius of the piston, V_P is the speed of the piston, and T is the pushing time of the piston.

3.2 Energy Transfer Model of Water Jet Propulsion

The basic principle of water jet propulsion is similar to that of aero engines. It uses the momentum difference between the inlet and outlet of the propulsion system to generate thrust and propel the ship. In the water jet propulsion system, there is an energy transfer model, as shown in **Figure 9**.

The Bernoulli equation between the pump inlet flow surface and the nozzle is:

$$Z_1 + \frac{P_{1,S}}{\rho g} + \alpha_1\frac{v_1^2}{2g} + \Delta h_1 + H_{13} = Z_2 + \frac{P_{S,4}}{\rho g} + \alpha_2\frac{u^2}{2g} + \Delta h_{3-4} \tag{9}$$

Where Z is the height of the cross-section relative to the free flow surface m; P_s is static pressure Pa;

H_{13} is the total pressure difference of the inlet and outlet section of the pump, that is, the head is m;

Δh_1 is the pump inlet loss head m. Δh_{3-4} is the nozzle loss head m;

α_1, α_2 is the kinetic energy correction coefficient, usually expressed as:

$$\alpha_i = \frac{\int_A \frac{u^2}{2g}\rho g u dA}{\frac{v^2}{2g}\rho g u A} = \frac{\int_A u^3 dA}{v^3 A} \tag{10}$$

It is assumed that the static pressure of the pump inlet surface and the nozzle is equal to the local atmospheric pressure, and the height of the flow section is equal to the height of the free flow surface. It expresses the inlet passage and nozzle loss head as a percentage of $v_0^2/2g$. Then **Eq. 9** can be simplified as:

$$H_{13} = \alpha_2\frac{u^2}{2g} - \alpha^2\frac{v_0^2}{2g} + \zeta\frac{v_0^2}{2g} \tag{11}$$

$$\xi = k_1 + k_2 \tag{12}$$

Where v_0 is the speed, m/s;

k_1 is the inlet passage loss coefficient, equal to the ratio of Δh_1 to $v_0^2/2g$;

k_2 is the nozzle loss coefficient, equal to the ratio of Δh_{3-4} to $v_0^2/2g$;

ξ is the pipeline loss coefficient, equal to the sum of the above two loss coefficients;

α partner flow coefficient. The wake coefficient reflects the difference between actual inlet velocity and ship speed. The wake coefficient is usually the actual measured value. The design is usually 0.85–0.95 (Jin, 1986).

$$a = \frac{v_1}{v_0} \tag{13}$$

The head provided by the water jet pump is mainly used to increase the kinetic energy of the working fluid after overcoming line losses. Part of the increased velocity of the working fluid was converted to a useful head. The other part is to overcome the jet loss.

$$\frac{u^2 - \alpha^2 v_0^2}{2g} = \frac{\Delta v \cdot v_0}{g} + \left[\frac{(\Delta v^2)}{2g} - \frac{(1-\alpha)\Delta v \cdot v_0}{g}\right] \tag{14}$$

Where: Δv is the speed difference between pump inlet and nozzle, equal to $u - v_1$;

The first term on the right is the useful head. The second item is the jet head.

3.3 Physical Characteristic Parameters of Jet Wake Vortex Ring in Water Jet Propulsion

At present, domestic and foreign scholars' research on jet propulsion mode focuses on self-propelled aircraft and underwater organisms, mainly involving theoretical research, experimental research, and irregular calculation of flow field in CFD numerical simulation. In the research process of the vortex ring, Saffman (Saffman, 1978), Norbury (Amick and Fraenkel, 1988), and Fabris (Fabris and Liepmann, 1997) have studied that the vortex ring has an obvious vortex structure. However, determining which parameters affect the formation and physical characteristics of vortex rings is a difficult problem in vortex ring research. The theoretical analysis, numerical simulation, and experimental study of water jets advance the vortex under submerged jet conditions are lack of systematic

knowledge system. In order to fully understand the instability mechanism of the water jet propulsion submerged jet, the physical characteristics of the water jet propulsion jet tail vortex ring are discussed on the basis of previous research.

3.3.1 Formation Time of Trailing Vortex Ring

The formation process of a jet tail vortex ring in water jet propulsion is the process of continuous ejection of fluid in a nozzle and continuous entraining of the surrounding fluid. It is found that when the water behind the nozzle is a static flow field, the main parameter affecting the structure of the vortex ring is the vortex ring formation time t^*.

$$t^* = \frac{L}{D} = \frac{u \times t}{D} \tag{15}$$

In **Eq. 15**, L is the length of the fluid ejected by the jet, D is the diameter of the nozzle outlet. u refers to the speed at which water flows out of the nozzle. t is the time of water's movement.

Water jet propulsion mode mainly includes short pulse jet and long pulse jet. The fundamental difference between the two jets lies in the time of vortex ring formation. Generally, $t^* = 4$ is taken as the formation time of the critical vortex ring. When the formation time of the vortex ring is less than 4, the jet wake region presents a single vortex ring shape. This injection mode is called short pulse injection. When the vortex ring formation time is greater than 4, the wake region shows that the vortex ring structure will be elongated behind the jet. That is, a series of small vortex rings will appear in the wake of the main vortex ring. It is called the jet mode of the long pulse jet.

By monitoring the velocity of the water jet at different times, it is found that the jet of spiral mixed flow water jet propulsion pump belongs to the long pulse jet. This jet carries more water downstream from the surrounding waters than the DC liquid. This increases the additional pressure on the nozzle and enhances the effect of jet propulsion.

3.3.2 Kinematic Parameters of Wake Vortex Ring

Kinematic parameters of the wake vortex ring mainly refer to the transmission speed of the vortex ring induced by water at different times. It also refers to the induced velocity sum of water area as v_w. In order to reflect the variation rule of vortex ring transmission velocity under different vortex ring formation time of water jet propulsion pump more clearly, the dimensionless transmission velocity of vortex ring v^* is introduced:

$$v^* = \frac{v_w}{\overline{v_w}} \tag{16}$$

The change of dimensionless transmission speed of vortex rings under different formation times is shown in **Figure 10**.

As can be seen from the figure above, the dimensionless transmission speed of the vortex ring changes exponentially with the formation time. Combined with mathematical statistical analysis, the dimensionless transmission speed and vortex ring formation time can be expressed as follows:

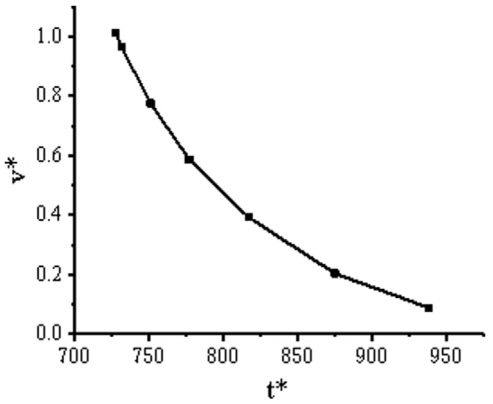

FIGURE 10 | Dimensionless transmission speeds at different formation times.

$$v^* = 173.58 \times e^{\frac{-t^*}{95.86}} + 0.95 \tag{17}$$

3.3.3 Dynamic Parameters of Wake Vortex Ring

In order to study the structure, evolution, and interaction of vortex rings in water jet propulsion, this section analyzes the trailing vortex rings generated under design conditions of water jet propulsion pumps based on vorticity, vortex strength, and helicity of the vortex dynamic diagnosis method. The vortex dynamics method can accurately capture the variation of vortex ring structure and strength in the wake region of jet propulsion.

The curl of the transmission velocity v_w of the vortex ring is called vorticity Ω. Vorticity is one of the most common physical quantities used to describe vortex motion. Its units are denoted as s^{-1}, i.e.:

$$\Omega = \nabla \times v_w \tag{18}$$

Vortex intensity S is introduced into the quantitative analysis of jet tail vortex rings. It describes the intensity of a turbulent vortex. The calculation formula is as follows:

$$S = \sqrt{2 w_{ij} w_{ij}} \tag{19}$$

Where w_{ij} is the average speed of the rotation tensor. Unit of vortex intensity is denoted as $s^{-1} \cdot m^3$.

Helicity is an important parameter used to measure the topological structure of the turbulent vorticity field. The helicity in the three-dimensional flow field of water jet propulsion is defined as:

$$H = \int_V v_w \Omega dV \tag{20}$$

It is called the helicity density by the product, and the units of helicity are m/s^2.

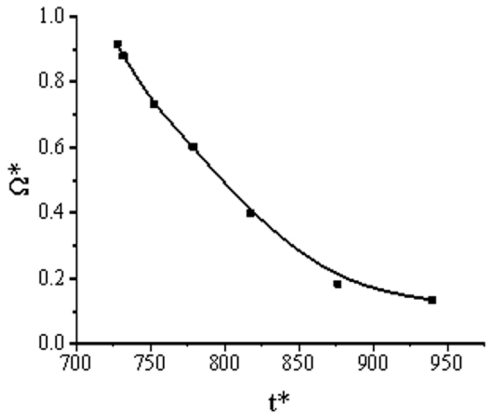

FIGURE 11 | Variations of vorticity coefficients under different formation times.

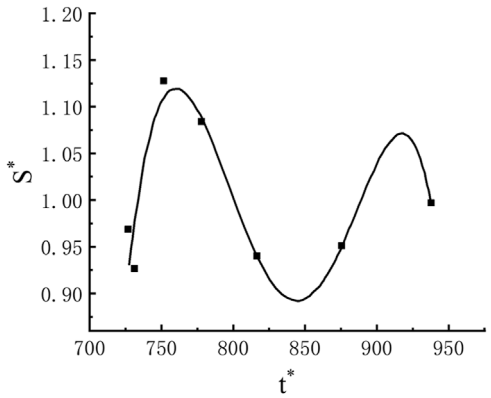

FIGURE 12 | Changes of vortex intensity coefficients at different formation times.

As for the kinematic parameters of trailing vortex rings, the mathematical models of each parameter and the formation time of vortex rings are established at the level of vortex dynamics. It reintroduces the dimensionless vorticity coefficient Ω^*, vortex intensity coefficient S^* and helicity coefficient H^* of the vortex ring. The expressions are shown in **Eqs 21** and **22**, and **23** respectively:

$$\Omega^* = \frac{\Omega}{\overline{\Omega}} \tag{21}$$

$$S^* = \frac{S}{\overline{S}} \tag{22}$$

$$H^* = \frac{H}{\overline{H}} \tag{23}$$

The monitoring of each dynamic parameter at different times in the design condition is calculated. The variation of the formation time of different vortex rings with each dimensionless parameter is shown in **Figures 11–13**.

As can be seen from **Figure 11**, the formation time of the vortex ring changes exponentially with the vorticity coefficient.

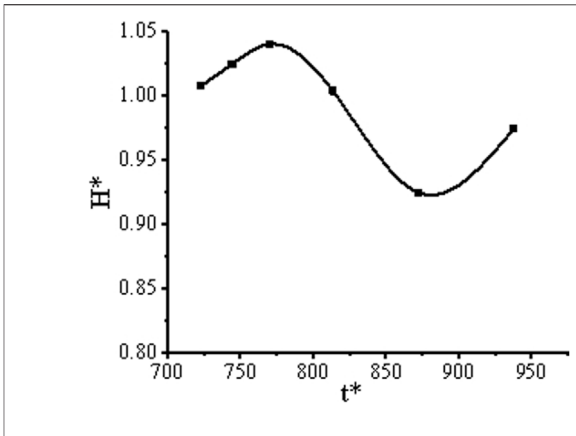

FIGURE 13 | Changes of helicity coefficient under different formation time.

The dimensionless vorticity coefficient and vortex ring formation time can be expressed as:

$$\Omega^* = 64.08 \times e^{\frac{-t^*}{103.6}} + 0.97 \tag{24}$$

It can be seen from **Figure 12** that the formation time of the vortex ring and vortex strength coefficient are non-linear. The function expression of the vortex strength coefficient and vortex ring formation time obtained by the mathematical statistical method is:

$$S^* = -3.09t^* + 0.015t^{*2} - 0.67 \times 10^{-5}t^{*3} + 2.13 \times 10^{-8}t^{*4} - 6.34 \times 10^{-12}t^{*5} - 0.019 \tag{25}$$

It can be seen from **Figure 13** that the formation time of the vortex ring and the helicity coefficient are non-linear. The function expression of the helicity coefficient and vortex ring formation time obtained by the mathematical statistical method is:

$$H^* = -1.17t^* + 0.002t^{*2} - 1.93 \times 10^{-6}t^{*3} + 6.14 \times 10^{-10}t^{*4} + 226.33 \tag{26}$$

Through the numerical simulation and eddy dynamic analysis of the jet propulsion jet vortex ring, it is learned that a coherent vortex structure is generated in the wake area of the water wake of the water jet propulsion nozzle tail, that is, the "jet tail vortex ring". The main factor affecting the formation of the tail vortex ring is the time of vortex ring formation. The long-pulse jet mode has a vortex ring generated throughout the jet process. The formation of the water jet tail vortex ring is mainly due to the influence of the spray water flow by the control of the coiling action of the surrounding water body, and the vortex ring of different scales is rolled up in the near-wake of the water body through the winding action. The near-wake area of the water at the tail of the pump nozzle has the characteristics of the rapid growth of the shear layer and the winding up of the large-scale coherent vortex ring at a fixed time-frequency, and when

the radial component of the velocity vector increases, the level of environmental fluid entrainment is significantly increased. The nonlinear variation relationship between the formation time of the vortex ring and the dimensionless characteristic parameters was obtained by combining vortex dynamics and mathematical statistics.

4 MATHEMATICAL MODEL OF JET WAKE VORTEX RING ON THRUST FORCE OF THE PUMP

4.1 The Process of Establishing a Mathematical Model

To analyze the nonlinear mathematical relationship between the trailing vortex ring generated in the jet propulsion process and the thrust characteristics. Based on the mathematical model between the physical characteristic parameters of the wake vortex ring and the thrust, the physical characteristic parameters of the wake vortex ring under the design condition of the water jet propulsion pump were established to monitor. Finally, the mathematical model of thrust with each parameter is obtained.

Considering that the mathematical relationship between the pump-water integrated thrust and the physical characteristic parameters of the wake vortex ring is not clear, this paper uses MATLAB programming to introduce a method based on the Levenberg-Marquardt (hereinafter referred to as "LM") training algorithm and Back Propagation Neural Network (hereinafter referred to as "BP Neural Network") combination. It can quickly realize the modeling of the nonlinear system between the thrust of the pump water body and the physical characteristic parameters of the vortex ring.

In this paper, the physical characteristic parameters of jet tail vortex ring of water jet propulsion include vortex ring transmission speed, vorticity, vortex intensity, and helicity, and the propulsion performance parameter is thrust. Therefore, it determines the number of neurons in the BP Neural Network input layer to be four. The number of neurons in the output layer was determined to be one.

According to the empirical formula, the number of hidden layer neurons was determined as three. The structure of BP Neural Networks is shown in **Figure 14**.

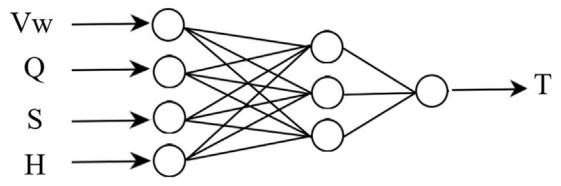

FIGURE 14 | Structure diagram of BP Neural Network.

4.2 Determination of Mathematical Model

This paper constructs the BP Neural Network with four inputs and one output. The above determination of the BP Neural Network structure shows that the input layer consists of four neurons. It is used to complete the input of four physical characteristic parameters of a jet tail vortex ring in water jet propulsion. The hidden layer consists of three neurons. It is used to complete the spatial weighting of input signals and improve the ability of complex mapping between input and output of nonlinear systems. The output layer consists of one neuron. It is used to complete the thrust output of the pump-water integrated system.

It is assumed that the signal transmitted from the input layer to the hidden layer is x_1、 x_2、 x_3, and the calculation formulas are shown in **Equation 27** and **28**, and **Eq. 29**. Where $w_{11} \sim w_{13}$ represents three weights corresponding to vortex ring transmission speed v_w. $w_{21} \sim w_{23}$ represents the three weights corresponding to vorticity Ω. $w_{31} \sim w_{33}$ represents the three weights corresponding to vorticity S. $w_{41} \sim w_{43}$ represents the three weights corresponding to helicity H. b_1、 b_2、 b_3 represents the bias of the hidden layer respectively. The output signals of the hidden layer are denoted as y_1、 y_2、 y_3. The calculation is shown in **Eqs 30** and **31**, and **32** respectively.

$$x_1 = w_{11}v_w + w_{21}\Omega + w_{31}S + w_{41}H + b_1 \tag{27}$$

$$x_2 = w_{12}v_w + w_{22}\Omega + w_{32}S + w_{42}H + b_{12} \tag{28}$$

$$x_3 = w_{13}v_w + w_{23}\Omega + w_{33}S + w_{43}H + b_3 \tag{29}$$

$$y_1 = tan\,sig\,(x_1) = \frac{2}{1 + e^{-2x_1}} - 1 \tag{30}$$

$$y_2 = tan\,sig\,(x_2) = \frac{2}{1 + e^{-2x_2}} - 1 \tag{31}$$

$$y_3 = tan\,sig\,(x_3) = \frac{2}{1 + e^{-2x_3}} - 1 \tag{32}$$

The signal transmitted from the hidden layer to the output layer is denoted as s. The calculation is shown in **Eq. 33**. $w_{i1}^{'}$ represents the weight from the hidden layer to the output layer. $b^{'}$ represents the offset of the output layer.

$$S = \sum_{i=1}^{3} y_1 w_{i1}^{'} + b' \tag{33}$$

The output signal of the output layer is denoted as T, which represents the thrust of the water-jet propulsion pump-water integrated system. The calculation is shown in **Eq. 34**. a and b represent the coefficients of the linear transfer function purelin.

$$T = a\left(\sum_{i=1}^{3} y_1 w_{i1}^{'} + b'\right) + b \tag{34}$$

The weights and biases read after the neural network training are substituted into **Eq. 35**.

$$T = a\left(\frac{5.4}{1 + e^{-2x_2}} + \frac{0.012}{1 + e^{-2x_2}} + \frac{0.012}{1 + e^{-2x_3}} - 3\right) + b \tag{35}$$

Therefore, by combining BP neural network and LM algorithms, the physical characteristic parameters of the jet wake vortex ring of water jet propulsion are established. It is combined with the thrust to create mathematical modeling.

5 CONCLUSION

The submerged shear jet exists widely in the field of nature and engineering technology. The dynamic response of the jet vortex ring in the process of formation, enrolling, and mixing has a great impact on practical engineering applications. In the study of the submerged jet in the nozzle, the evolution of various scale vortex systems, especially symmetrically distributed vortex systems, in the submerged jet section is investigated by numerical simulation. Meanwhile, the interaction between vortex patterns in the water section is analyzed. This paper systematically reveals the vortex ring mechanism during nozzle injection.

The nonlinear mathematical relationship between the time of vortex ring formation and each dimensionless physical characteristic parameter is established, and the hydrodynamic theory is applied to compare the thrust characteristics generated by the pump-water system and bare pump under the same working conditions. The thrust generated is about 7% higher than in the case of the bare pump.

The combination of BP Neural Network and LM algorithm is used to realize the mathematical modeling of each parameter of thrust and jet wake vortex ring.

In future studies, it is necessary to study the jet flow under different nozzle shapes, injection angles, and nozzle outlet diameters, to fully reveal the flow mechanism and influencing factors of the jet tail vortex ring. The vortex systems with different scales generated by the jet propulsion are studied, and the vortex systems with different contributions are classified.

DATA AVAILABILITY STATEMENT

The original contributions presented in the study are included in the article/Supplementary Material, further inquiries can be directed to the corresponding authors.

AUTHOR CONTRIBUTIONS

WH: Conceptualization, Methodology. ZL:Writing- Reviewing and Editing. RL: Supervision Funding acquisition. HF: Formal Analysis. LN: Writing- Original draft preparation and Editing. JX: Resources. MX: Visualization.

FUNDING

This study was supported by the National Natural Science Foundation of China (Grant Nos. 52179086, 51669012) and the Central leading local science and technology development projects "Development and industrialization of Bohai bay shallow water multiphase flow meter".

REFERENCES

Amick, C. J., and Fraenkel, L. E. (1988). The Uniqueness of a Family of Steady Vortex Rings. *Arch. Ration. Mech. Anal.* 100 (3), 207–241. doi:10.1007/bf00251515

Becker, H. A., and Massaro, T. A. (1968). Vortex Evolution in a Round Jet. *J. Fluid Mech.* 31 (3), 435–448. doi:10.1017/s0022112068000248

Brown, G. B. (1935). On Vortex Motion in Gaseous Jets and the Origin of Their Sensitivity to Sound. *Proc. Phys. Soc.* 47 (7), 703–732. doi:10.1088/0959-5309/47/4/314

Davies, P. O. A. L., Fisher, M. J., and Barratt, M. J. (1963). The Characteristics of the Turbulence in the Mixing Region of a Round Jet. *J. Fluid Mech.* 15 (3), 337–367. doi:10.1017/s0022112063000306

Fabris, D., and Liepmann, D. (1997). Vortex Ring Structure at Late Stages of Formation. *Phys. Fluids* 9 (9), 2801–2803. doi:10.1063/1.869391

Fraenkel, L. E. (1972). Examples of Steady Vortex Rings of Small Cross-Section in an Ideal Fluid. *J. Fluid Mech.* 51, 119–135. doi:10.1017/s0022112072001107

He, F., Xie, J., and Pengfei, H. (2001). Numerical Simulation of Free Jet and Impact Jet Using S-A Model. *J. Propuls. Technol.* 22 (1), 43.

Jin, P. (1986). *Marine Water Jet Propulsion*. Beijing, China: National Defense Industry Press.

Jun, P. (1995). *Theoretical Basis and Application of Jet*. Beijing, China: Aerospace Press.

Li, Y. (2004). *Study on Energy Dissipation of Multi-Jet and Multi-Layer Horizontal Submerged Jet*. Sichuan: Sichuan University.

Mungal, M. G., and Hollingsworth, D. K. (1989). Organized Motion in a Very High Reynolds Number Jet. *Phys. Fluids A Fluid Dyn.* 1 (10), 1615–1623. doi:10.1063/1.857527

Norbury, J. (1973). A Family of Steady Vortex Rings. *J. Fluid Mech.* 57, 417–431. doi:10.1017/s0022112073001266

Ruiz, L. A., Whittlesey, R. W., and Dabiri, J. O. (2011). Vortex-enhanced Propulsion. *J. Fluid Mech.* 668, 5–32. doi:10.1017/s0022112010004908

Saffman, P. G. (1978). The Number of Waves on Unstable Vortex Rings. *J. Fluid Mech.* 84 (4), 625–639. doi:10.1017/s0022112078000385

Sullivan, I. S., Niemela, J. J., Hershberger, R. E., Bolster, D., and Donnelly, R. J. (2008). Dynamics of Thin Vortex Rings. *J. Fluid Mech.* 609, 319–347. doi:10.1017/s0022112008002292

Wang, F. (2020). *Flow Analysis Method of Water Pump and Pumping Station*. Beijing, China: China Water Resources and Hydropower Press.

Xiang, Y., Qin, S., and Liu, H. (2018). Patterns for Efficient Propulsion during the Energy Evolution of Vortex Rings. *Eur. J. Mechanics- B/Fluids* 71, 47–58. doi:10.1016/j.euromechflu.2018.03.014

Yang, X. (2013). *Research on Vortex Ring Evolution and its Physical Characteristics*. Shanghai: Shanghai Jiaotong University.

Conflict of Interest: The authors declare that the research was conducted in the absence of any commercial or financial relationships that could be construed as a potential conflict of interest.

Publisher's Note: All claims expressed in this article are solely those of the authors and do not necessarily represent those of their affiliated organizations, or those of the publisher, the editors and the reviewers. Any product that may be evaluated in this article, or claim that may be made by its manufacturer, is not guaranteed or endorsed by the publisher.

frontiers | Frontiers in Energy Research

ORIGINAL RESEARCH
published: 17 June 2022
doi: 10.3389/fenrg.2022.894796

Analysis of Transient Characteristics of Submersible Tubular Pump During Runaway Transition

Zhuangzhuang Sun[1], Jie Yu[1], Fangping Tang[1], Hengjun Ge[2] and Haixia Yuan[2]*

[1]College of Hydraulic Science and Engineering, Yangzhou University, Yangzhou, China, [2]Yangzhou Survey Design Research Institute, Yangzhou, China

In order to study the transient characteristics of the submersible tubular pump in the process of power failure, the 6DOF model was used to carry out three unsteady numerical values for the whole flow channel of the pump. The results show that the calculation results of the 6DOF model based on the fourth-order multi-point Adams–Moulton formula are in better agreement with the experimental results than the first-order format to predict the impeller motion. When the unit is powered off, the speed and flow of the pump device decrease rapidly with time. At the maximum head 3.41 m, when the unit enters the runaway condition, the speed is about −1.88 times the initial speed and the flow rate is about −1.98 times the initial flow. The axial force and radial force of the impeller increase alternately, and compared with the normal operating condition, the radial force is significantly increased. In the process of the pump device changing from forward flow to reverse flow, the internal flow state of the pump device is relatively chaotic, and there are a large number of vortices in the flow channel, which is easy to cause structural vibration. Before reaching the runaway state, a large number of vortices also appear inside the impeller and guide vane, causing flow blockage, especially when the flow rate is zero. At the same time, the reverse flow impact causes the local pressure on the blade surface to increase, which threatens the stability of the blade structure. The pressure at the impeller inlet, impeller outlet, and guide vane outlet monitoring points is the largest near zero flow, and the smallest during runaway. The main frequency of the pressure pulsation in the pump device is the blade pass frequency (f_{BRF}) and its harmonics ($2f_{BRF}$, $3f_{BRF}$, $5f_{BRF}$, etc.), and the pressure pulsation intensity increases with the increase of the impeller speed. The results of this study provide a theoretical reference for the operation of the submersible tubular pump to ensure the safety and stability of the pumping station.

Keywords: submersible tubular pump device, numerical simulation, power-off, 6DOF model, transient process

OPEN ACCESS

Edited by:
Daqing Zhou,
Hohai University, China

Reviewed by:
Huixiang Chen,
Hohai University, China
Tang Xuelin,
China Agricultural University, China

****Correspondence:***
Fangping Tang
tangfp@yzu.edu.cn

Specialty section:
This article was submitted to Process and Energy Systems Engineering, a section of the journal Frontiers in Energy Research

Received: *12 March 2022*
Accepted: *04 May 2022*
Published: *17 June 2022*

Citation:
Sun Z, Yu J, Tang F, Ge H and Yuan H (2022) Analysis of Transient Characteristics of Submersible Tubular Pump During Runaway Transition. Front. Energy Res. 10:894796. doi: 10.3389/fenrg.2022.894796

INTRODUCTION

The submersible tubular pump device is an electromechanical integrated pump device that combines the pump and the submersible motor closely. Compared with the pump device using the conventional motor, it has the advantages of compact structure and convenient installation and is widely used in low-lift pumping stations such as inter-basin water transfer, agricultural irrigation, and urban drainage (Yang, 2013). With the development of submersible motor, the impeller diameter is also increasing, which puts forward new requirements for its safe and stable

operation. It is generally believed that the hydraulic causes of vibration, noise, and rupture of flow passage components of the unit mainly include water excitation, blade cavitation, inlet swirl, and rotating stall. In the event of power failure, the change of working parameters of the pump device usually follows this series of complex physical flow, which will cause great damage to the pumping station unit (Chang, 2005; Xu, 2008).

At present, the research on the transient characteristics of hydraulic machinery units generally adopts the external characteristics based on the single element theory (Suter, 1966; Yang and Chen, 2003; Dorfler, 2010) or the internal characteristics (Liu and Chang, 2008; Guo et al., 2015; Zeng et al., 2015) based on one-dimensional theory to predict the changes of pressure, speed, torque, and other parameters in the transient process, but it is difficult to capture the transient characteristics of the internal flow field of the pump device. A test is the most direct method to study the transient characteristics of submersible tubular pump. However, due to the limitations of cost, environment, and technical level of operators, it is not easy to complete. With the development of computational fluid dynamics (CFD) technology, the CFD method has become a trend to study the three-dimensional transient characteristics in the transition process of hydraulic machinery. In recent years, many scholars have used the method of CFD to study the transition process of hydraulic machinery and have also achieved good results. Avdyushenko et al. (2013) proposed a three-dimensional unsteady turbulent flow calculation method for transient process simulation of hydraulic turbines. The three-dimensional numerical simulation of Reynolds-averaged Navier–Stokes equations was combined with the one-dimensional equation of elastic hydraulic shock propagation. The numerical results are in good agreement with the experimental results. Zhou and Liu (2015) used the VOF model to simulate the startup process of vertical axial flow pump and studied the change process of air sac in a siphon outlet pipe during the startup process. Li et al. (2015) carried out the unsteady numerical simulation of the transient flow in the two stages of pump startup and valve opening in a double suction centrifugal pump closed system based on the SAS-SST (*scale adaptive simulation-shear stress transport*) turbulence model. Li (2012) studied the influence of three different startup accelerations on the startup process of the oblique flow pump and obtained the variation laws of the instantaneous head and flow rate under different accelerations. Li et al. (2010) studied the startup process of centrifugal pump in detail. The vortex dynamics method was used to diagnose the transient flow field distribution during the startup process. The peak value of BVF (*boundary vortex flux*) and the BVF region with negative contribution were obtained, which provided reference for blade design. Zhang et al. (2014a) used a one-dimensional and three-dimensional coupling method to simulate the load rejection process of Francis turbine.

There are also many research studies on the calculation of hydraulic machinery power failure process. On the basis of solving the torque balance, Kan et al. (2020) and Kan et al. (2021) used the VOF (*volume of fluid*) model to establish the numerical calculation method of the power-off process of the S-shaped axially extended tubular pump device. The research shows that the CFD calculation results with the VOF model are closer to the experimental results. During the power-off process, the internal flow pattern of the pump device is complex, and there are a large number of vortex structures. Luo et al. (2017) used Fortran to carry out secondary development of ANSYS CFX to study the transient characteristics of tubular turbine during power failure. It was found that the relative flow angle at the inlet of the turbine decreased during flight, and the de-flow occurred on the surface of the blade, which was prone to cavitation, and the eccentric vortex band in the draft tube induced low frequency pressure pulsation. Xia (Zhang et al., 2014b) used the three-dimensional numerical simulation method to calculate the runaway process of a tubular prototype turbine considering the influence of gravity factors. It was found that the fracture of the wake vortex band led to the complex flow structure, causing severe tail water pressure changes, and the low frequency and high amplitude pressure pulsation was easy to cause the vibration of the unit. Zhou et al. (2016) established a three-dimensional turbulent numerical calculation method for the runaway process of a model axial flow turbine through the secondary development function of Fluent UDF and analyzed the relationship between the maximum runaway speed and the blade opening. Gou et al. (2018) used the three-dimensional coupled turbulence calculation method combined with the VOF two-phase flow model and single-phase flow model to study the transition process of power failure and runaway in the pumped storage pump station. It was found that a large number of eddy currents in the runner formed a strong clockwise spiral vortex band in the draft tube, which was the main reason for the low frequency pressure fluctuation of the unit under runaway condition. Jin et al. (2013) carried out numerical simulation on the inclined axial flow pump device, and the flow rate and velocity under the runaway condition are close to the experimental results. When the pump device is powered off, the water flow changes from positive to reverse, the impeller changes from positive to reverse, and the movement of the impeller is complicated. However, the current research mostly uses the first-order display format to predict the impeller motion in the power-off process, and the calculation accuracy is low (Menter et al., 2003).

There are few literature studies on the transient characteristics of the power failure process of the submersible tubular pump device. Based on the above deficiencies, the three-dimensional numerical simulation of the power failure process of submersible tubular pump is carried out by the ANSYS Fluent platform. At the same time, a 6DOF model based on the fourth-order multi-point Adams–Moulton formula is proposed to analyze the variation law of performance parameters and the evolution process of the internal flow field of the unit during the power failure process, in order to provide a theoretical reference for the safe and stable operation of the submersible tubular pump.

RESEARCH OBJECT

Based on a large submersible tubular pumping station, the main design parameters of the submersible tubular pump device are

TABLE 1 | Characteristic parameters of the pumping station.

Parameters	Value
Diameter of the impeller	2.4 m
Number of impeller blades	3
Number of guide vanes	5
Rotating speed	169 r/min
Design net head	2.44 m
Design flow rate	20.56 m^3/s
Maximum net head	3.41 m
Total unit moment of inertia	805 kg m^2

shown in **Table 1**. The GL-2008-03 hydraulic model is selected for the pump impeller. The hydraulic model is the research result of the research on several key technologies and application of large-scale tubular pump key technologies in the South-to-North Water Transfer Project, which is a major project of the National Science and Technology Support Program of the Eleventh Five-Year Plan. The main structure of the submersible tubular pump device is shown in **Figure 1**. The inlet runner is the water flow channel connecting the suction pool and the pump suction port, and the outlet runner is the water flow channel connecting the water pump outlet and the water outlet pool.

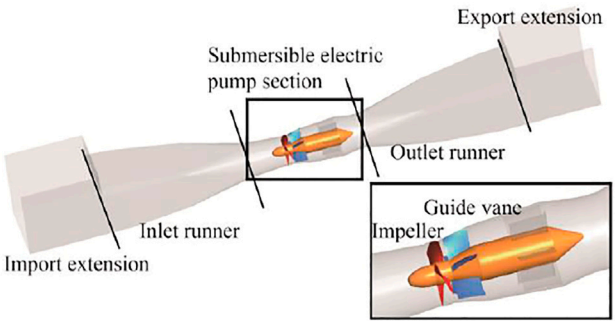

FIGURE 1 | Three-dimensional model of the submersible tubular pump device.

NUMERICAL CALCULATION METHOD

Turbulence Model

The numerical calculation is carried out based on ANSYS Fluent. The control equation is the incompressible Reynolds time-averaged equation:

$$\frac{\partial \overline{u_i}}{\partial t} + \overline{u_j}\frac{\partial \overline{u_i}}{\partial x_j} = -\frac{1}{\rho}\frac{\partial \bar{p}}{\partial x_i} + \frac{\mu_t}{\rho}\frac{\partial^2 \overline{u_i}}{\partial x_j \partial x_j} - \frac{\partial \overline{u_i' u_j'}}{\partial x_j}, \tag{1}$$

where ρ is the density, u is the velocity, p is the pressure, and the subscripts i, j denote the directions of the Cartesian coordinates.

The turbulence model is the SST k–ω model. The SST k–ω model is modified by the standard k–ω model and the k–ε model. The model takes into account the near-wall performance of the k–ω model and the far-field accuracy of the k–ε model and can accurately predict the internal flow characteristics of the pump (Kent, 1954). The transport equations of turbulent kinetic energy k and specific dissipation rate ω in the SST model can be expressed as follows:

$$\frac{\partial \rho k}{\partial t} + \frac{\partial}{\partial x_j}\left(\rho u_j k\right) = P_k - \beta^* \rho k\omega + \frac{\partial}{\partial x_j}\left[\left(\mu + \frac{\mu_t}{\sigma_k}\right)\frac{\partial k}{\partial x_j}\right] + P_{kb}, \tag{2}$$

$$\frac{\partial \rho \omega}{\partial t} + \frac{\partial}{\partial x_j}\left(\rho u_j \omega\right) = \alpha' \frac{\omega}{k} P_k - \rho\beta\omega^2 + \frac{\partial}{\partial x_j}\left[\left(\mu + \frac{\mu_t}{\sigma_\omega}\right)\frac{\partial \omega}{\partial x_j}\right] + P_{\omega b}, \tag{3}$$

The turbulent viscosity μ_t of the SST model is defined as

$$\mu_t = \frac{\rho \alpha_1 k}{\max\left(\alpha_1 \omega, SF_2\right)}, \tag{4}$$

where P_k is the production rate of turbulence, α', β, β^*, σ_k, α_1, and σ_ω are model constants, S is a module of the strain rate tensor, and F_1 and F_2 are mixed functions. SST k–ω model mixing function construction and constant value can be found in the study by Langtry and Menter (2009).

In unsteady calculations, by differencing the equations, the governing fluid dynamics equations can be solved for each time step. From the fluid domain calculations, the forces and moments acting on the reservoir are calculated by integrating the pressure on the surface.

Six-DOF Model

Knowing the forces and moments on the object, the motion of the object is calculated by the 6DOF model. The power-off process of the submersible tubular pump device is a process in which the impeller loses power and passively rotates under the action of water flow. 6DOF is used to simulate the movement of the impeller. The 6DOF model was first applied for the study of external ballistics and was established (Fowler et al., 1920) in the early 20th century, but it was not until the 1950s that R.H. Kent (Kent, 1954) from BRL (*Ballistic Research Laboratory*) and A.S. Galbraith also from BRL redefined rigid body trajectory systematically by the vector method, and the A.S. Galbraith study was not published. The 6DOF model simplifies the motion of the rigid body to the translation and rotation around the centroid and predicts the motion of the rigid body by numerically integrating the Newton–Euler motion equation. In the numerical solution process of Fluent, the force and moment acting on the rigid body are calculated according to the integral of surface pressure (Snyder et al., 2003). For the translational motion of the center of gravity, the control equation is solved in the inertial coordinate system:

$$\dot{\vec{v}} = \frac{1}{m}\sum \vec{f}, \tag{5}$$

where $\vec{v}$ is the velocity vector of the rigid body moving along the center, $\vec{f}$ is the force at the centroid, and m is the mass of the rigid body.

The rotational motion is more easily calculated in the body coordinate to avoid the change of inertial characteristics in the motion process:

$$\frac{d\vec{\omega}_B}{dt} = L^{-1}\left(\sum \vec{M}_B - \vec{\omega}_B \times L\vec{\omega}_B\right), \tag{6}$$

where $\vec{\omega}_B$ is the angular velocity vector, L is the inertia tensor, and $\vec{M}_B$ is the moment acting on the rigid body.

During the power-off process of the tubular pump, the motion of the impeller is mainly the rotational motion around the axis, and the translational motion is very small. During the power failure process of the tubular pump, the motion of the impeller is mainly the rotational motion around the axis, and the translational motion and rotational motion in other directions are very small. For the axial rotational motion, it can be calculated as follows:

$$\frac{d\vec{\omega}_B}{dt} = L^{-1}\sum \vec{M}_B. \tag{7}$$

In case 1, the first-order display format adapted from the study by Kan et al. (2020) was used to solve the above differential equations, and the rotational speed $\vec{\omega}_B$ at time step $k+1$ is determined as follows:

$$\vec{\omega}_B^{k+1} = \vec{\omega}_B^{k} + L^{-1}\sum \vec{M}_B \Delta t, \tag{8}$$

where Δt is the time step during calculation.

There is a large numerical error in the calculation of the first-order display format, and this error will accumulate, which makes the calculation result quite different from the actual result. Therefore, the fourth-order multi-point Adams–Moulton formula is used for numerical integration to determine the speed in case 2, which is an important classical algorithm for solving the initial value problem of differential equations and widely used in aviation and other fields. The algorithm is as follows:

$$\vec{\omega}_B^{k+1} = \vec{\omega}_B^{k} + \frac{\Delta t}{24}\left(9\frac{d\vec{\omega}_B^{k+1}}{dt} + 19\frac{d\vec{\omega}_B^{k}}{dt} - 5\frac{d\vec{\omega}_B^{k-1}}{dt} + \frac{d\vec{\omega}_B^{k-2}}{dt}\right). \tag{9}$$

Boundary Conditions and Numerical Methods

The system reference pressure is set to 1 atmospheric pressure, and the pressure inlet and pressure outlet conditions are adopted. The inlet relative pressure is set to 0 Pa, and the outlet relative pressure is the pressure corresponding to different head conditions. The impeller is the rotating domain, the axis z is the rotating axis, the initial speed of the impeller is 169 r/min, and the rest is the stationary domain. The inlet and outlet channels of the submersible tubular pump device, the wheel hub, the shell, and the guide vane of the impeller are applied without slip conditions, and the wall function is used in the near-wall area to adapt to the turbulence model. The dynamic mesh progressive transient calculation is adopted. The motion of the impeller is predicted by the 6DOF model, and the whole impeller domain is set as the motion domain. Similar to the sliding mesh method, the data transmission is realized through the interface before and after the impeller, and the deformation of the mesh is not involved in the movement of the impeller. The calculation time is the time when the impeller passes through 10 circles, and the impeller passes through 2° at each time step. The last circle is retained as the initial condition for the calculation of the power failure process of the pump device.

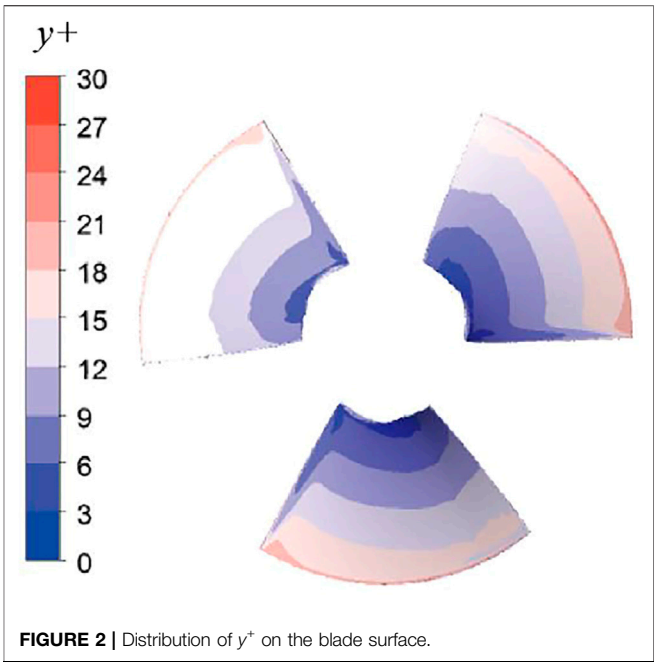

FIGURE 2 | Distribution of y^+ on the blade surface.

The runaway speed is usually checked according to the maximum head in the design of pump station, so the maximum head condition is selected for numerical calculation. The initial calculation state of the power-off process is H_0 = 3.41 m, Q_0 = 18.7 m^3/s, n_0 = 169 r/min, M_0 = 45.2 kN m. The calculation time step of the power-off process is 0.001 s, even if the rotation angle of the impeller reaching the maximum speed within each time step does not exceed 2°, which meets the requirements of the rotor–stator interaction (RSI) (Choi and Moin, 1994; Naidu et al., 2019). To ensure convergence, iteration is 60 steps in each time step. The finite volume method is used to discretize the equations, the gradient discrete method in the equations is least squares cell-based, the pressure term is in the PRESTO format, and the convection term, turbulent kinetic energy, and dissipation rate are in the third-order Runge–Kutta format. The PISO algorithm, a non-iterative algorithm for solving coupled velocity and pressure, is used to solve the flow field equations simultaneously, and the interface is used to transfer information between different regions.

Meshing and Irrelevance Analysis

The block grid division strategy is adopted, in which the impeller and guide vane regions are divided by a hexahedral structured grid by Turbogrid. The block grid division strategy is adopted. Except for the bulb break, which is divided by unstructured grids, the rest of the calculation area is divided by structured grids. The grid parameter y^+ is a dimensionless quantity (Fernholz and

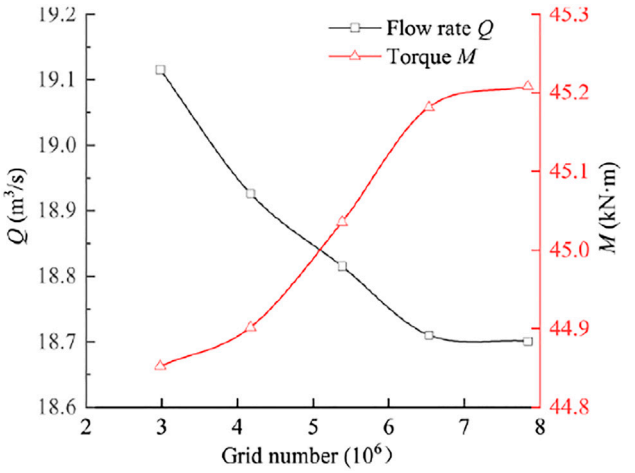

FIGURE 3 | Grid independency test.

Finley, 1980) describing the distance from the first layer of grid to the wall, defined as

$$y^+ = \frac{\Delta y \rho u^*}{\mu} = \frac{\Delta y}{\nu}\sqrt{\frac{\tau_w}{\rho}}, \tag{10}$$

where Δy is the height from the first layer of mesh to the wall, u^* is the friction velocity near the wall, μ is the fluid viscosity, ν is the fluid kinematic viscosity, and τ_w is the wall shear stress.

Maintaining the same topological structure, the global maximum grid size is used to control the grid density of each computational domain, and the local grid of each computational domain is specially encrypted to ensure the quality of the grid. In this study, in the impeller and other main flow components, y^+ is within 30, and y^+ on the blade surface is shown in **Figure 2**, which basically meets the requirements of SST k–ω turbulence model for near-wall grid quality. Moreover, the orthogonality of most of the grid elements of the impeller and guide vane is above 0.9, and the element volume ratio is less than 20. When the head is 3.41 m, the whole flow channel is calculated, and the grid independence is detected with the flow and torque calculation results as the indexes. The calculation results are shown in **Figure 3**. When the grid is increased to more than 6.53 million, the flow and torque change tends to be stable. Using the grid convergence method GCI (*Grid Convergence Index*) recommended by Roache (2003), based on Richardson extrapolation theory, when the grid number is 6.53 million, the uncertainty of flow and torque is 2.1% and 1.3%, respectively, which meets the grid independence requirements. Considering the calculation time and calculation accuracy, the final calculation grid number is determined to be 6.53 million. The grid of the main components is shown in **Figure 4**.

Figure 5 shows the comparison of energy characteristics between the numerical calculation and the experiment results under different flow conditions. It can be seen from the figure that affected by the solution accuracy, the Q–H curve obtained by numerical calculation is lower than the experimental result, which is mainly because the frozen rotor method is used in the steady simulation, and the relative position of the runner and the guide vane is fixed, which is different from the actual situation. However, in the entire calculation range, the numerical simulation results are basically consistent with the external characteristic relationship curve obtained from the experimental results. There is a certain deviation in the head under small flow conditions. This is mainly because the small flow conditions are close to the saddle area and the internal flow is more complicated, but the overall results are in good agreement, so the numerical simulation results can be considered to be highly reliable.

RESULTS AND DISCUSSION

Comparison of the Two Methods

Figure 6 shows the relative values of the external characteristic parameters of the submersible tubular pump device during the power-off process: n/n_0, Q/Q_0, and M/M_0 change with time. The entire power-off process can be divided into four stages: pump mode, braking mode, turbine mode, and runaway mode. At t = 0~0.35 s, the pump works normally. The unit is powered off when t = 0.35 s, and the impeller and water flow still move in the original direction due to inertia. Due to the loss of power, the values of various parameters dropped rapidly. Compared with case 1, case 2 enters the braking mode earlier, and the braking condition lasts longer. When entering the hydraulic mode, the slope of the curve of case 1 is larger, that is, each parameter decreases faster than that of case 2 with time, so that the duration of the entire turbine mode is about 2s shorter than that of case 2. When the runaway condition is reached, the reverse speed and flow reach the maximum, the torque is zero, and the maximum runaway flow and maximum runaway speed of case 1 are higher than those of case 2.

During the runaway test, the head is provided by the auxiliary pump, and the speed and flow rate are measured when the model pump device reverses and the output torque is zero under different heads. Runaway characteristics can be expressed by the unit speed $n'_{1,R}$ and unit flow rate $n'_{1,Q}$, calculated as follows:

$$n'_{1,R} = \frac{n_R D}{\sqrt{H}}, \tag{11}$$

$$n'_{1,Q} = \frac{Q_R D}{D^2\sqrt{H}}, \tag{12}$$

where n_R and Q_R are the rotation speed and flow rate of the model pump device. The unit speed and unit flow rate of the model pump device are obtained from the test, and the rotation speed and flow rate of the prototype pump device in the runaway state under different head conditions can be obtained by conversion. **Figure 7** shows the comparison of the calculation runaway rotation speeds and flow rates under different head conditions with the model test results. Under different heads, the runaway speeds calculated by case 1 and case 2 are larger than the test results, and case 2 is closer to the test results. This may be because the calculation ignores the friction torque of the radial bearing

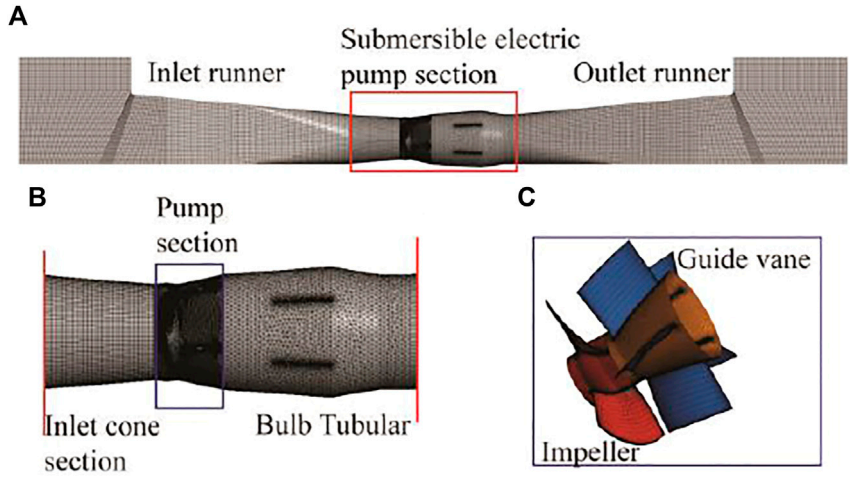

FIGURE 4 | Three-dimensional model of the submersible tubular pump device: **(A)** pump unit; **(B)** submersible electric pump section; **(C)** pump section.

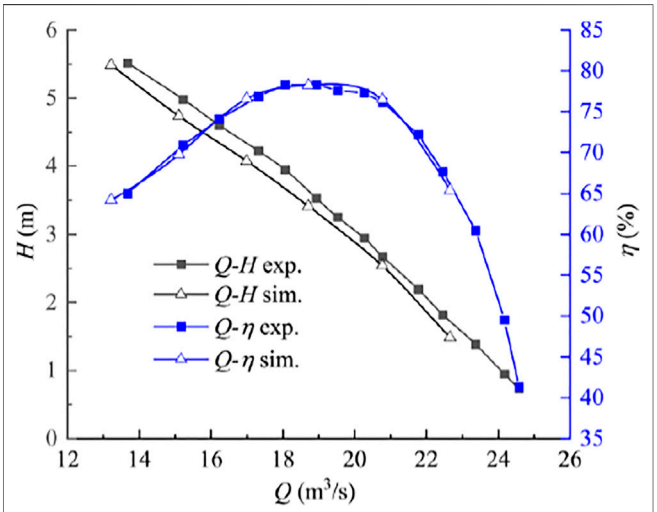

FIGURE 5 | Comparison of the head and efficiency under different flow conditions.

and the rotor wind resistance torque, and there is a certain deviation when the model is converted to the prototype itself. In general, the 6DOF model solved with the fourth-order multi-point Adams–Moulton formula has high accuracy in predicting the power failure process of the submersible tubular pump device. In case 2, t = 0~2.5 s belongs to the pump condition; at this stage, the pump rotates in the forward direction and the water flow is in the forward direction. When t = 2.5 s, the fluid in the device is close to the transient static water body, i.e., Q/Q_0 =0. Until t = 3.1 s, the speed is zero. When t = 16.3 s, the reverse speed and flow reach the maximum, the torque is zero, the speed is about −1.88 times the initial speed, and the flow is about −1.98 times the initial flow. Compared with other pump device types, because the device is a similar straight pipe, the parameters of the unit drop faster when a power failure occurs, which is more harmful.

Analysis of Impeller Force

In the process of power failure, the water flow changes from forward flow to reverse flow. The changes in working conditions

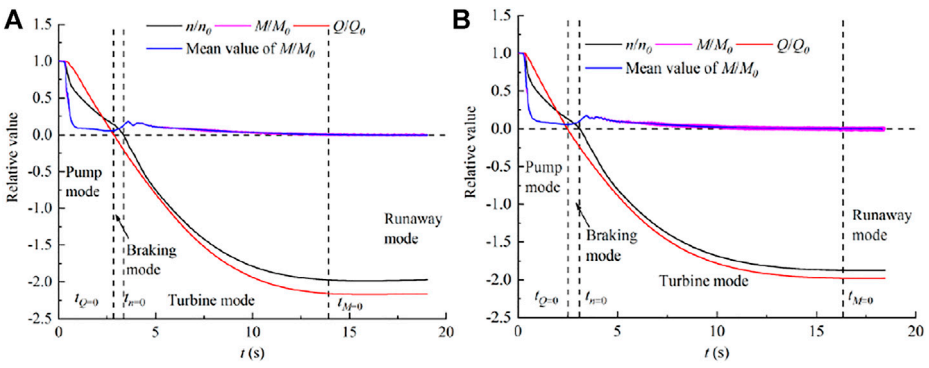

FIGURE 6 | Relative values of dynamic parameter variations with time. **(A)** Case 1. **(B)** Case 2.

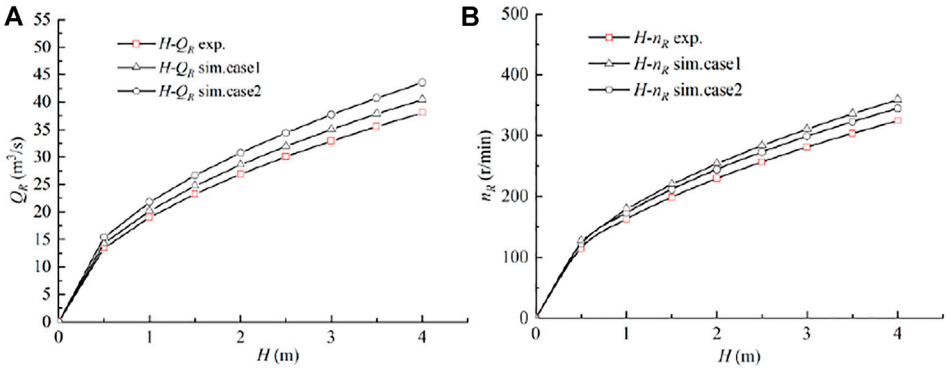

FIGURE 7 | Comparison of the runaway rotation speeds **(A)** and flow rates **(B)** under different heads.

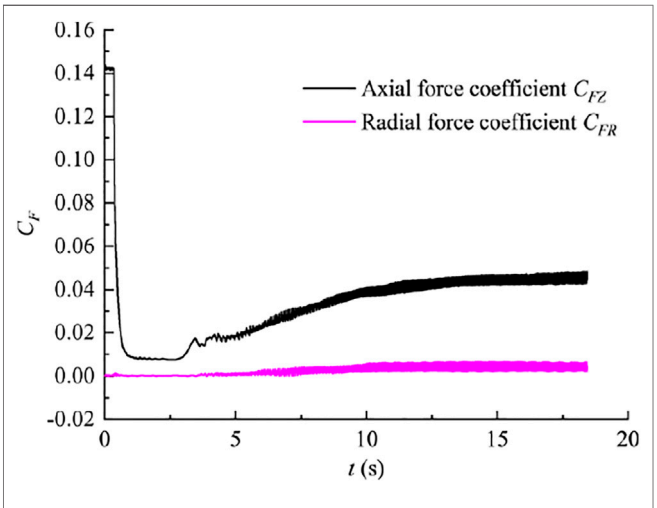

FIGURE 8 | Force coefficient variations with time.

aggravate the asymmetry and unevenness of the flow field distribution in the pump. The uneven force on the pump body is likely to cause vibration and noise. Decompose the impeller force in the power-off process into two directions: axial force F_Z and radial force F_R. Define the dimensionless coefficient C_F as

$$C_F = \frac{2F}{\rho U_t^2 A}, \tag{13}$$

where U_t is the circumferential velocity at the top of the impeller blade and A is the surface area of the blade. **Figure 8** shows the variation curves of the impeller axial force coefficient C_{FZ} and the radial force coefficient C_{FR} calculated. As the working conditions of the unit change, the alternation of axial force and radial force gradually increases. The axial force of the unit presents a trend of gradual increase after a rapid decline over time, and the axial force varies greatly. The initial operating condition has the largest axial force coefficient, about 0.142, and the smallest axial force coefficient during the process is about 0.008, reaching a runaway operating condition of about 0.045. The radial force gradually increases with time, the average radial force coefficient increases from 0 to 0.004, and the radial force increases significantly.

Internal Flow Field Analysis

Figure 9 is a longitudinal section pressure distribution and velocity streamline diagram of the submersible tubular pump device at the characteristic time. In the figure, the inlet of the left runner is the low-pressure side and the outlet of the right runner is the high-pressure side. When the unit is working normally, as shown in **Figure 9A**, the water flow is affected by the work done by the impeller and is from the low-pressure side to the high-pressure side. The streamline on the inlet side is straight, and the outlet side has multiple low-speed vortices propagating downstream due to the influence of the residual circulation of the guide vane outlet. When the unit is powered off, the functional power of the impeller drops rapidly. Under the action of the inlet and outlet pressure difference, part of the water flow starts to flow from the high-pressure side to the low-pressure side, and the vortex is formed by the collision of two water flows. When $Q = 0$, as shown in **Figure 9B**, the inside of the device is approximately still fluid, and a large range of vortices still remain from the streamline. There are also large vortices inside the bulb body, the motor of the submersible tubular pump device is located in the bulb body, and the generation of the vortex easily threatens the stability of the bulb body structure. When $n = 0$, as shown in **Figure 9C**, the reverse flow increases and the internal flow in the inlet channel is reformed, while the flow reformation of the outlet flow channel is relatively lagging, and there is still a certain vortex. Then, the unit enters the working condition of the turbine, and the increase of the reverse flow improves the flow pattern of the outlet flow channel, but at the same time, the accelerated rotation of the blades forms a vortex in the inlet flow channel. As shown in **Figure 9D**, in the runaway condition where the reverse flow rate and reverse rotation speed reach the maximum, the flow line in the outlet flow channel is smooth, and the inlet flow channel has a vortex similar to the draft tube of a hydraulic turbine propagating downstream.

Figure 10 shows the velocity streamline of the middle flow surface of the pump section at the characteristic time. When the

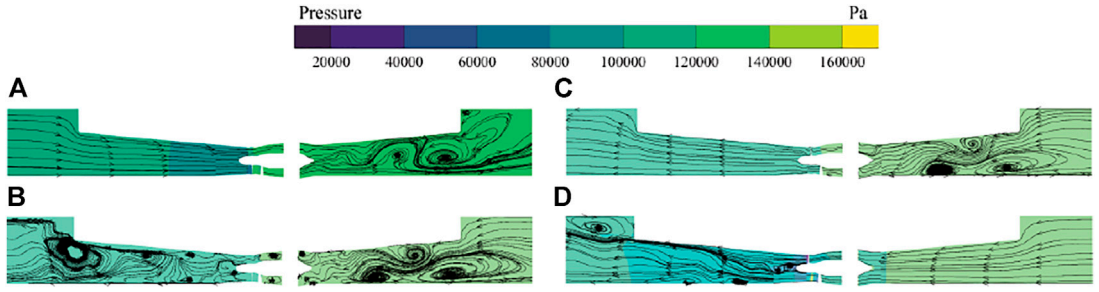

FIGURE 9 | Streamline distribution and static pressure contours in the horizontal plane of the pump: **(A)** t = 0 s; **(B)** t =2.5 s; **(C)** t = 3.1 s; **(D)** t = 16.3 s.

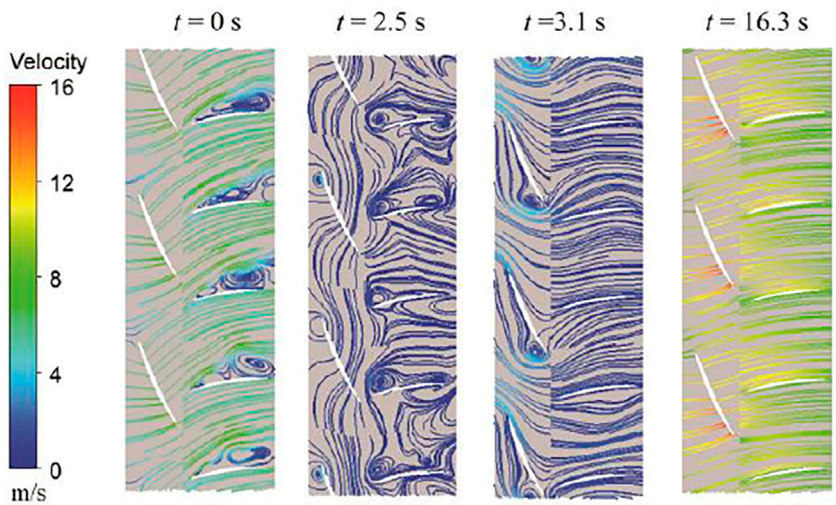

FIGURE 10 | Distribution of velocity streamlines at medium span.

pump is working normally, due to the deviation of the pump operating conditions from the design conditions, the vortex formed by flow separation is on the back of guide vane. When the forward flow rate is zero, the flow pattern in the middle flow surface is relatively chaotic. The water flow in the impeller is mainly in the circumferential direction, affected by the rotation of the impeller. There are also many vortices in the guide vane area, causing flow blockage. When the rotation speed is zero, the reverse flow of water flow improves the flow state in the guide vane, but due to the too large angle of attack of the water flow relative to the impeller, the flow separation occurs at the trailing edge of the blade. When the runaway condition is reached, the flow state of the intermediate flow surface is relatively good, and there is no obvious vortex.

With the development of the power-off process of the pump device, the flow state of the pump inlet and outlet changes. **Figure 11** shows the distribution of the velocity flow angle (the angle between the cross-sectional velocity and the circumferential velocity) at the impeller inlet, the impeller outlet, and the guide vane outlet at different times. When the pump is working normally (t = 0 s), the liquid flow angle at the inlet of the impeller is all around 90°, the water flow is approximately vertical inflow, and the liquid flow angle at the outlet of the impeller is greater than 90° due to the rotation of the impeller, and there is a backflow near the hub. The outlet of the guide vane is affected by the recovery circulation of the guide vane, which is similar to the vertical outflow, and there is also a de-flow at the hub. When the flow rate is 0 (t = 2.5 s), the velocity flow angle at about 3/4 of each section is negative, indicating that the water flow is reverse flow, and the negative liquid flow angle is distributed on the hub and rim side. With the development of time, the reverse flow is strengthened, and the outlet of the guide vane becomes the inlet of the water flow. When the rotation speed is 0, except for the recirculation area formed by the impact of the water flow on the shroud side of the guide vane outlet, the liquid flow angles of the impeller inlet and outlet sections are all negative values, and the flow is completely reverse flow. When t>2.5 s, the reverse rotation speed gradually increases with time, and the impeller's intervention effect on the water flow is enhanced, which makes the inlet and outlet flow angles of the impeller tend to increase. The outlet of the guide vane is mainly affected by the reverse flow, and the recirculation area at the wheel rim gradually decreases.

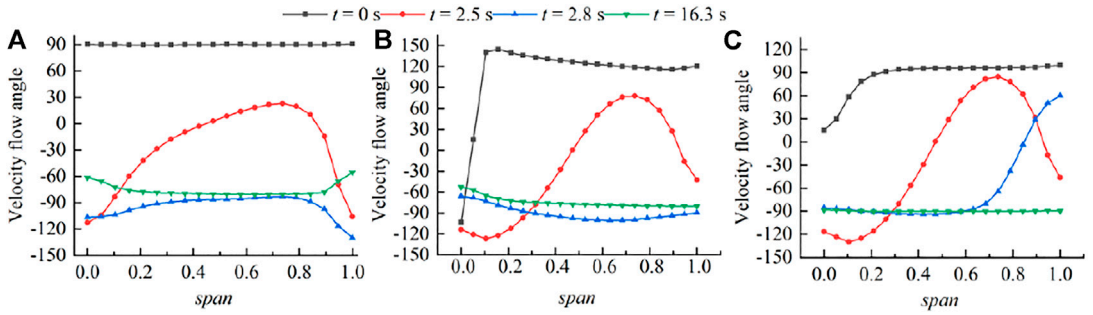

FIGURE 11 | Distribution of the velocity flow angle at different times: **(A)** impeller inlet; **(B)** impeller outlet; **(C)** guide vane outlet.

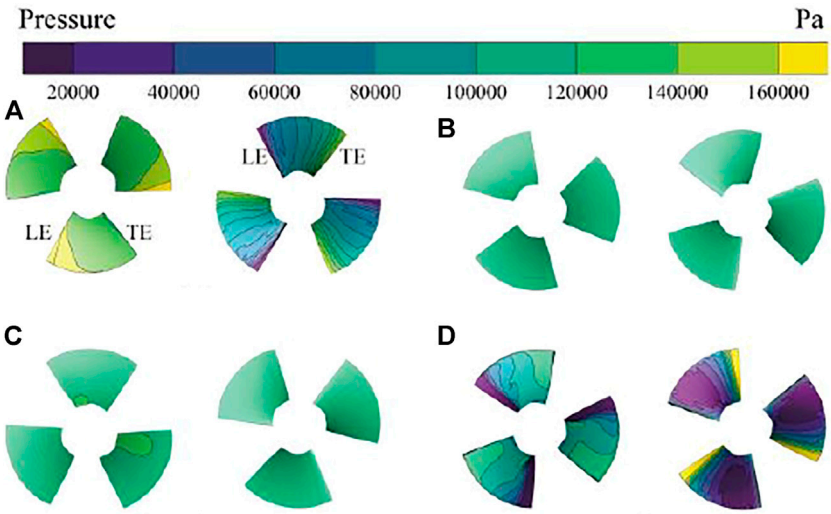

FIGURE 12 | Pressure contours on blade pressure and suction surfaces at different times: **(A)** t = 0 s; **(B)** t =2.5 s; **(C)** t = 3.1 s; **(D)** t = 16.3 s. (The left side is the pressure side, and the right side is the suction side.).

Figure 12 is a cloud diagram of the blade surface pressure distribution at a characteristic time. When the pump is working normally, the pump pressure surface pressure is greater than that on the suction surface as shown in **Figure 12A**. The pressure distribution on the blade surface from the leading edge to the trailing edge shows a good gradient, the pressure on the pressure side shows a decreasing trend, while the suction side shows an increasing trend. As the positive flow rate decreases, part of the kinetic energy is converted into pressure energy. When the flow rate is zero, as shown in **Figure 12B**, there is no axial movement of water flow in the impeller, the pressure on the blade surface is uniformly distributed, and the pressure on the blade pressure surface and the suction surface pressure are almost equal. With the end of the pump condition, the reverse flow shock first causes the pressure in the local area of the blade pressure surface to increase, as shown in **Figure 12C**, which affects the stability of the blade structure. When the runaway condition is reached, as shown in **Figure 12D**, the angle of attack of the water flow relative to the blade airfoil is close to zero-lift, and there are a wide range of low-pressure areas on the suction surface of the blade.

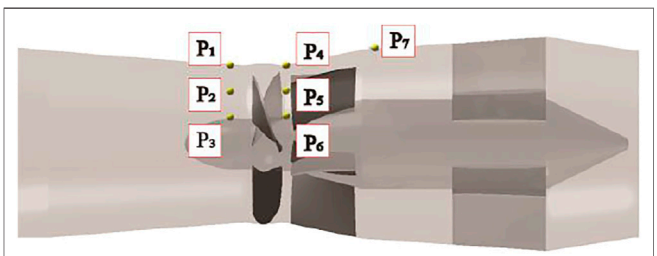

FIGURE 13 | Pressure pulsation monitoring points.

Pressure Pulsation Analysis

In order to study the internal pressure pulsation of the pump unit during a power-off, monitoring points are set at the impeller inlet, impeller outlet, and guide vane outlet. The locations of the monitoring points are shown in **Figure 13**. **Figure 14** shows the variation of pressure at the monitoring points with time. When the unit is working normally, the pressure surface and the

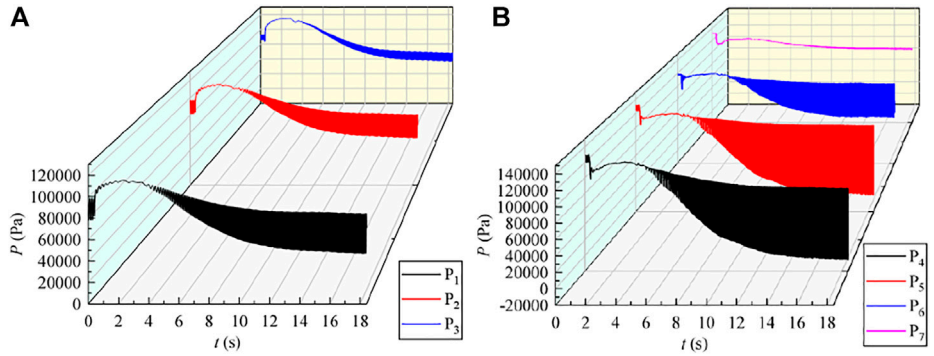

FIGURE 14 | Time domain of the pressure fluctuation: **(A)** monitoring points P_1–P_3; **(B)** monitoring points P_4–P_7.

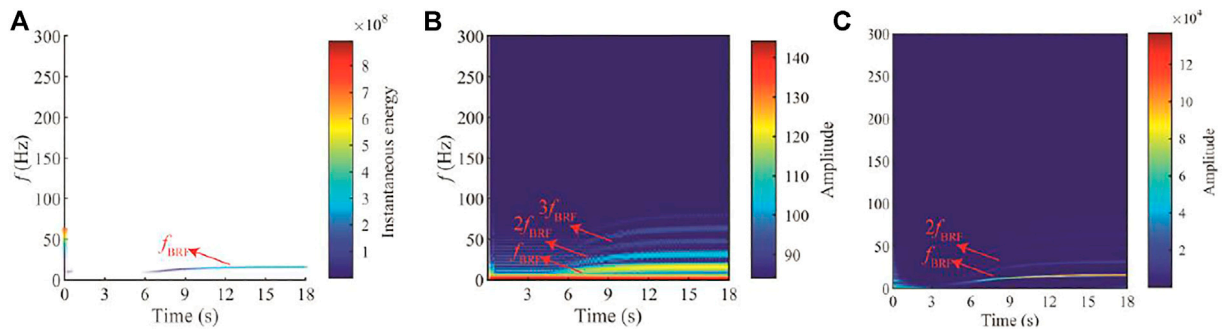

FIGURE 15 | Spectrum analysis at monitoring point 1: **(A)** HHT; **(B)** STFT; **(C)** CWT.

suction surface have a large pressure gradient, which makes the pressure at the monitoring point in front of the impeller change regularly. When the unit is powered off, the speed of the water pump drops sharply, the forward flow velocity of the water flow decreases rapidly, causing the pressure at monitoring points P_1–P_3 before the impeller to rise until the forward flow is zero, and the average pressure in front of the impeller reaches the maximum value. Then, the reverse flow in the device increases, making the pressure in front of the impeller drop. As the pump enters the runaway condition, the reverse flow is the largest, and the average pressure at the monitoring point in front of the impeller reaches the minimum. The change of pressure at the monitoring points P_4–P_7 is the same as that at the monitoring point before the impeller when the unit is working normally. When the unit is powered off, the head of the impeller drops rapidly, the pressure of the water flowing through the impeller decreases rapidly, and the pressure at the monitoring points P_4–P_7 drops rapidly. The subsequent changes are similar to those of the monitoring points before the impeller. When the forward flow is the smallest, the average pressure reaches its maximum value and then continues to decrease. In the runaway condition, the average pressure reaches its minimum value. At the same time, the pressure fluctuations at the monitoring points are related to the speed of the impeller. The greater the speed, the greater the pressure fluctuation. At the same time, the pressure fluctuations before and after the impeller gradually decrease from the shroud to the hub. Compared with that at the monitoring points P_1–P_6, the pressure alternating at the monitoring point P_7 at the outlet of the guide vane is smaller due to the distance from the impeller.

For further analysis of pressure pulsation, HHT (*Hilbert–Huang transform*) was used to process the pressure value. HHT is a new type of adaptive signal time–frequency processing method, which is different from STFT (*short-time Fourier transform*) and CWT (*continuous wavelet transform*). It does not require any basis function and is suitable for the analysis and processing of non-linear and non-stationary signals (Huang and Wu, 2008). The main content of HHT includes two parts: modal decomposition and Hilbert transform. Modal decomposition originally adopted EMD (*empirical mode decomposition*) (Huang et al., 1998; Wu and Huang, 2009), which was proposed by Huang. EMD is often referred to as a screening process. This screening process can decompose the complex signal into a finite number of IMFs (intrinsic mode functions), and each of the decomposed IMF components contains local characteristic signals of different time scales of the original signal. But when EMD decomposes the signal, there will be modal confusion, end effect, and curve problems. Therefore, VMD (variational mode decomposition) is used for modal decomposition in this paper (Dragomiretskiy and Zosso, 2014). VMD is an adaptive signal processing method; by iteratively searching for the optimal solution of variational

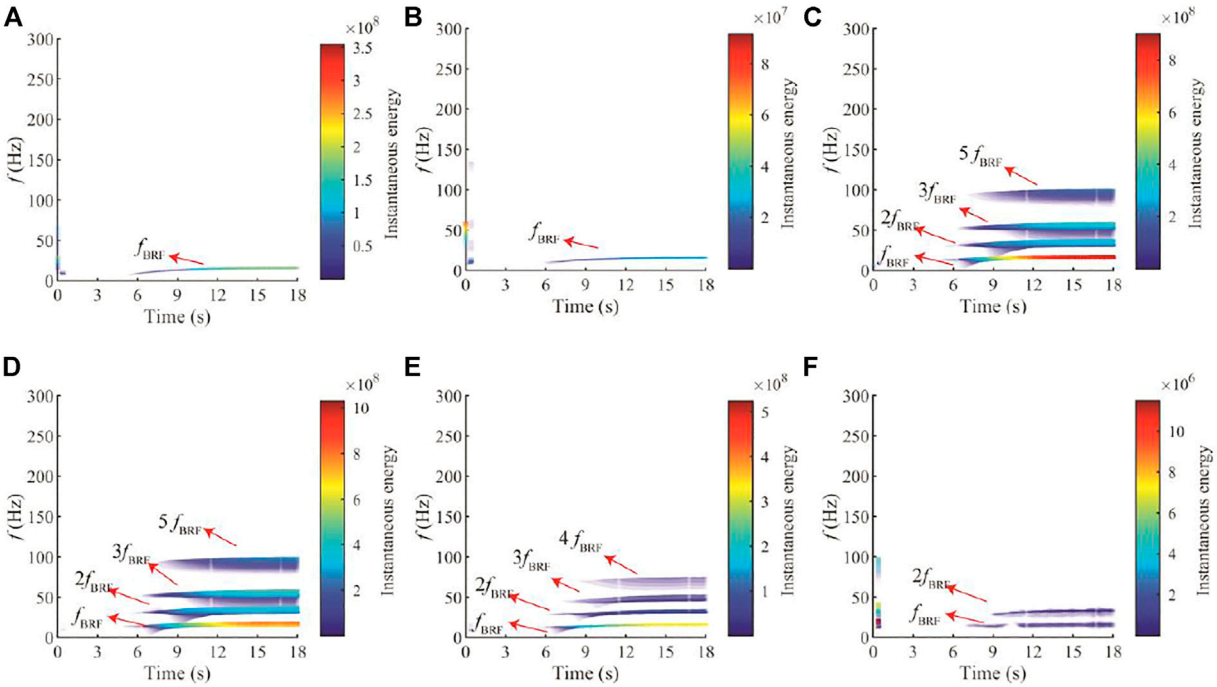

FIGURE 16 | Hilbert spectrum of monitoring points: **(A)** P2; **(B)** P3; **(C)** P4; **(D)** P5; **(E)** P6; **(F)** P7.

mode and constantly updating each mode function and central frequency, several mode functions with a certain broadband are obtained. To remove edge effects, the algorithm extends the signal by mirroring half its length on either side. The second part is HT (*Hilbert transform*); the Hilbert transform of each IMF is obtained on the basis of VMD. **Figure 14** shows the frequency spectrum of monitoring point P1 obtained by using HHT, STFT (window: kaiser), and CWT (wavename: Morlet). **Figure 15** shows the frequency spectrum of monitoring point 1 obtained by using HHT, STFT (window: kaiser), and CWT (wavename: Morlet). The blade rotation frequency is defined as $f_{BRF} = 3n/60$. Compared with CWT and STFT, the time-spectrum frequency distribution obtained by HHT is more concentrated, all near the leaf frequency, avoiding the harmonic frequency (2 f_{BRF}, 3 f_{BRF}, etc.) components caused by the basis function of CWT and STFT.

Figure 16 shows the Hilbert spectrum obtained after HHT transformation. The blade rotation frequency is defined as $f_{BRF} = 3n/60$. The rotation speed of the impeller is the amount that changes with time, so the rotation frequency also changes with time. The instantaneous energy from the shroud to the hub shows a decreasing trend, which is consistent with the pressure fluctuation trend analyzed above. The main instantaneous energy of the monitoring points P_1–P_3 appears after about 6s, the frequency is concentrated around f_{BRF}, and the instantaneous energy gradually increases with time. The main instantaneous energy of the monitoring points P_4–P_6 also appears after 6 s, and the maximum instantaneous frequency is also concentrated around f_{BRF}. With the increase of flow and speed, high frequency components appear at monitoring points. The frequency component of monitoring points 4 and 5 is 2 f_{BRF}, 3 f_{BRF}, and 5 f_{BRF}, the guide vanes are 5, and 5 f_{BRF} are the frequencies due to static and dynamic interference. However, the frequency component of monitoring point P6 is 2 f_{BRF}, 3 f_{BRF}, and 4 f_{BRF}, and monitoring point 6 pressure is less affected by dynamic and static interference. The outlet of the guide vane has high pulsation energy when the pump is working normally, but when the power failure occurs, the monitoring point P7 pressure pulsation is weakened, and the main frequency is around 1 f_{BRF} and 2 f_{BRF}.

CONCLUSION

Using a 6DOF model based on the fourth-order multi-point Adams–Moulton formula, this paper realizes the numerical simulation of the submersible tubular pump device during the power-off process and obtains the transient characteristics and internal flow characteristics of the unit's operating parameter changes. It provides theoretical guidance for the stable operation of the pumping station, which has great engineering significance. The specific conclusions are as follows:

1. The 6DOF model based on the fourth-order multi-point Adams–Moulton formula has high accuracy for predicting the movement of the impeller during power failure. The results obtained using the fourth-order multi-point Adams–Moulton formula are more closer to the experimental values than the commonly used first-order display format.
2. In the process of power failure of the submersible tubular pump device, the flow of the pump device first changes from

positive flow to reverse flow, and then the speed changes from positive to reverse. The interval from zero flow to zero speed is about 0.6 s. When the maximum head is 3.41 m, the speed is about −1.88 times the initial speed and the flow is about −1.98 times the initial flow.

3. The alternation of the axial force and radial force of the impeller gradually increases. The time-averaged axial force presents a trend of rapidly decreasing with time and then gradually increasing, while the radial force gradually increases with time, and the radial force coefficient increases significantly compared with the initial state.
4. In the process of power failure, there are a lot of vortices inside the device, especially when the flow is 0. There are also large vortices near the bulb body, and the generation of the vortex easily threatens the stability of the bulb body structure. There are also a large number of vortices in the impeller and guide vane. The impact of the reverse flow first causes the local pressure on the blade surface to increase, which threatens the stability of the blade structure.
5. The monitoring points at the inlet of the impeller show a trend of rising first and then falling with time. The monitoring points at the outlet of the impeller and the guide vane decrease rapidly when the power is turned off and then also show a trend of first rising and then falling with time. The pressure of each monitoring point is the highest near zero flow, and the pressure is the smallest at runaway. The main frequency of the pressure pulsation in the pump device is the blade pass frequency (f_{BRF}) and its harmonics, and the pressure pulsation intensity increases with the increase of the impeller speed.

DATA AVAILABILITY STATEMENT

The raw data supporting the conclusion of this article will be made available by the authors, without undue reservation.

AUTHOR CONTRIBUTIONS

ZS curated the data and wrote the original draft. FT performed formal analysis. JY reviewed and edited the paper. HG and HY were involved in project administration.

FUNDING

This project was funded by the Priority Academic Program Development (PAPD) of Jiangsu Higher Education Institutions.

REFERENCES

Avdyushenko, A. Y., Cherny, S. G., Chirkov, D. V., Skorospelov, V. A., and Turuk, P. A. (2013). etcNumerical Simulation of Transient Processes in Hydroturbines. *Thermophys. Aeromech.* 20 (5), 577–593. doi:10.1134/s0869864313050059

Chang, J. (2005). *Transition Process of Hydraulic Mechanical Device*. Higher Education Press.

Choi, H., and Moin, P. (1994). Effects of the Computational Time Step on Numerical Solutions of Turbulent Flow. *J. Comput. Phys.* 113 (1), 1–4. doi:10.1006/jcph.1994.1112

Dorfler, P. K. (2010). Improved Suter Transform for Pump-Turbine Characteristics. *Int. J. Fluid Mach. Syst.* 3 (4), 332–341. doi:10.5293/ijfms.2010.3.4.332

Dragomiretskiy, K., and Zosso, D. (2014). "Variational Mode Decomposition," in IEEE Transactions on signal Processing, February 1, 2014 (IEEE) 62, 531–544. doi:10.1109/TSP.2013.2288675

Fernholz, H. H., and Finley, P. J. (1980). *A Critical Commentary on Mean Flow Data for Two-Dimensional Compressible Turbulent Boundary Layers*. Aerodynamics.

Fowler, R. H., Gallop, E., and Lock, C. (1920). The Aerodynamics of a Spinning Shell. *Proc. R. Soc. Lond.* 98, 63. doi:10.1098/rspa.1920.0063

Gou, D., Guo, P., and Luo, X. (2018). 3-D Combined Simulation of Power-Off Runaway Transient Process of Pumped Storage Power Station under Pump Condition. *J. Hydrodynamics* 33 (1), 28–39. doi:10.16076/j.cnki.cjhd.2018.01.004

Guo, W., Zeng, W., and Yang, J. (2015). Runaway Instability of Pump-Turbines in S-Shaped Regions Considering Water Compressibility. *J. Fluids Eng. Trans. ASME* 137 (5), 051401. doi:10.1115/1.4029313

Huang, N. E., Shen, Z., Long, S. R., Wu, M. C., Shih, H. H., Zheng, Q., et al. (1998). The Empirical Mode Decomposition and the Hilbert Spectrum for Nonlinear and Non-stationary Time Series Analysis. *Proc. R. Soc. Lond. A* 454, 903–995. doi:10.1098/rspa.1998.0193

Huang, N. E., and Wu, Z. (2008). A Review on Hilbert-Huang Transform: Method and its Applications to Geophysical Studies. *Rev. Geophys.* 46 (2), 228. doi:10.1029/2007rg000228

Jin, G., Pan, Z., and Meng, J. (2013). Study of the Runaway Character of Slanted Axial-Flow Pump. *Chin. J. Hydrodynamics* 5, 591–596. doi:10.3969/j.issn1000-4874.2013.05.012

Kan, K., Chen, H., Zheng, Y., Zhou, D., Binama, M., and Dai, J. (2021). Transient Characteristics during Power-O*ff* Process in a Shaft Extension Tubular Pump by Using a Suitable Numerical Model. *Renew. Energy* 164, 109–121. doi:10.1016/j.renene.2020.09.001

Kan, K., Zheng, Y., Chen, H., Zhou, D., Dai, J., Binama, M., et al. (2020). etcNumerical Simulation of Transient Flow in a Shaft Extension Tubular Pump Unit during Runaway Process Caused by Power Failure. *Renew. Energy* 154, 1153–1164. doi:10.1016/j.renene.2020.03.057

Kent, R. (1954). *Notes on a Theory of Spinning Shell of Charge*. Army Ballistic Research Lab Aberdeen Proving Ground MD.

Langtry, R. B., and Menter, F. R. (2009). Correlation-based Transition Modeling for Unstructured Parallelized Computational Fluid Dynamics Codes. *Aiaa J.* 47 (12), 2894–2906. doi:10.2514/1.42362

Li, W. (2012). Experimental Study on Transient Unsteady Internal Flow Characteristics of Inclined Flow Pump during Startup. Jiangsu University. Thesis.

Li, Y., Zhu, Q., Liu, Z., and Yang, w. (2015). Numerical Simulation on Transient Characteristics of Double-Suction Centrifugal Pump System during Opening Valve Processes. *Trans. Chin. Soc. Agric. Mach.* 46 (12), 74–81. doi:10.1115/1.4002056

Li, Z., Wang, L., and Dai, W. (2010). Diagnosis of a Centrifugal Pump during Starting Period Based on Vorticity Dynamics. *J. Eng. Thermophys.* 31 (1), 48–51.

Liu, Y., and Chang, J. (2008). Numerical Method Based on Internal Character for Load Rejection Transient Caculation of a Bulb Turbine Installation. *J. China Agric. Univ.* 13 (001), 89–93. doi:10.11841/j.issn.1007-4333.2008.01.021

Luo, X., Li, W., Feng, J., and Zhu, G. (2017). Simulation of Runaway Transient Characteristics of Tubular Turbine Based on CFX Secondary Development. *Trans. Chin. Soc. Agric. Eng.* 13, 97–103. doi:10.11975/j.issn.1002-6819.2017.13.013

Menter, F. R., Kuntz, M., and Langtry, R. (2003). Ten Years of Industrial Experience with the Sst Turbulence Model. *Heat Mass Transf.* 4, 2814.

Naidu, A., Oumer, A. N., and Azizuddin, A. A. (2019). Computational Fluid Dynamic (CFD) of Vertical-axis Wind Turbine: Mesh and Time-step Sensitivity Study[J]. *J. Mech. Eng. Sci.* 13 (3), 5604–5624. doi:10.15282/jmes.13.3.2019.24.0450

Roache, P. J. (2003). Conservatism of the Grid Convergence Index in Finite Volume Computations on Steady-State Fluid Flow and Heat Transfer. *J. Fluids Eng.* 125 (4), 731–732. doi:10.1115/1.1588692

Snyder, D., Koutsavdis, E., and Anttonen, J. (2003). "Transonic Store Separation Using Unstructured Cfd with Dynamic Meshing," in 33rd AIAA fluid dynamics conference and exhibit, 23 June 2003 - 26 June 2003 (Orlando, Florida: AIAA), 3919. doi:10.2514/6.2003-3919

Suter, P. (1966). Representation of Pump Characteristics for Calculation of Water Hammer. *Sulzer Tech. Rev.* 4 (66), 45–48.

Wu, Z., and Huang, N. E. (2009). Ensemble Empirical Mode Decomposition: a Noise-Assisted Data Analysis Method. *Adv. Adapt. Data Anal.* 01 (01), 1–41. doi:10.1142/s1793536909000047

Xu, H. (2008). *Tubular Pumping Station*. China Water&Power Press.

Yang, F. (2013). Research on Hydrodynamic Characteristics of Low-Lift Pump Device and Key Technologies of Multi-Objective Optimization. Yangzhou university. Thesis.

Yang, L., and Chen, N. (2003). Analysis of Relation between Characteristics of Pump-Turbine Runner and Transition of Pumped-Storage Power Station. *J. Tsinghua Univ. Sci. Technol.* 043 (010), 1424–1427. doi:10.16511/j.cnki.qhdxxb.2003.10.034

Zeng, W., Yang, J., and Cheng, Y. (2015). Construction of Pump-Turbine Characteristics at Any Specific Speed by Domain-Partitioned Transformation. *J. Fluids Eng.* 137 (3), 031103. doi:10.1115/1.4028607

Zhang, M. Y., Cheng, Y., Chen, F., Lu, T. L., Dong, Z. F., Pei, X. F., et al. (2014). 3D Cfd Simulation of the Runaway Transients of Bulb Turbine. *Sichuan Da Xue Xue Bao Yi Xue Ban.* 45 (5), 254–257. doi:10.15961/j.jsuese.2014.05.036

Zhang, X. X., Cheng, Y. G., Yang, J. D., Xia, L. S., and Lai, X. (2014). Simulation of the Load Rejection Transient Process of a Francis Turbine by Using a 1-D-3-D Coupling Approach. *J. Hydrodyn.* 26 (5), 715–724. doi:10.1016/s1001-6058(14)60080-9

Zhou, D., Guo, Y., and Jiang, D. (2016). Numerical Simulation of Runaway Transients of Kaplan Turbine Model Based on Blade Regulation. *Adv. Sci. Technol. Water Resour.* 36 (4), 13–19. doi:10.3880/j.issn.1006-7647.2016.04.003

Zhou, D., and Liu, Y. (2015). Numerical Simulation of Axial Pump Unit Startup Process Using Vof Model. *J. Drainage Irrigation Mach. Eng.* 34 (4), 307–312. doi:10.3389/fenrg.2021.706975

Conflict of Interest: The authors declare that the research was conducted in the absence of any commercial or financial relationships that could be construed as a potential conflict of interest.

Publisher's Note: All claims expressed in this article are solely those of the authors and do not necessarily represent those of their affiliated organizations, or those of the publisher, the editors, and the reviewers. Any product that may be evaluated in this article, or claim that may be made by its manufacturer, is not guaranteed or endorsed by the publisher.

frontiers | Frontiers in Energy Research

ORIGINAL RESEARCH
published: 21 June 2022
doi: 10.3389/fenrg.2022.893385

Experimental Study on the Influence of Particle Diameter, Mass Concentration, and Impeller Material on the Wear Performance of Solid–Liquid Two-Phase Centrifugal Pump Blade

*Yanping Wang[1], Weiqin Li[1], Tielin He[1], Hao Liu[2], Chuanfeng Han[1] and Zucao Zhu[1]**

[1]Key Laboratory of Fluid Transmission Technology of Zhejiang Province, Zhejiang Sci -Tech University, Hangzhou, China, [2]Zhejiang Province Institute of Metrology, Hangzhou, China

OPEN ACCESS

Edited by:
Kan Kan,
College of Energy and Electrical Engineering, China

Reviewed by:
Weihua Cai,
Northeast Electric Power University, China
Kumaran Kadirgama,
Universiti Malaysia Pahang, Malaysia

***Correspondence:**
Zucao Zhu
zhuzuchao@zstu.edu.cn

Specialty section:
This article was submitted to Process and Energy Systems Engineering, a section of the journal Frontiers in Energy Research

Received: 10 March 2022
Accepted: 26 April 2022
Published: 21 June 2022

Citation:
Wang Y, Li W, He T, Liu H, Han C and Zhu Z (2022) Experimental Study on the Influence of Particle Diameter, Mass Concentration, and Impeller Material on the Wear Performance of Solid–Liquid Two-Phase Centrifugal Pump Blade. Front. Energy Res. 10:893385. doi: 10.3389/fenrg.2022.893385

A centrifugal pump is an important solid–liquid mixture conveying machinery, which is widely used in mineral mining, water conservancy engineering, and other fields. Solid particles will wear the impeller of the centrifugal pump in the process of transportation, resulting in lower service life of the impeller, especially in the transportation of a high concentration of solid particles. Many scholars use numerical simulation to study the wear of centrifugal pumps, but few efforts have been made in the wear experiment. In this study, the effect of three factors, namely, diameter of solid particles, mass concentration of particles, and material of impellers on the wear of a solid–liquid two-phase centrifugal pump was studied by the wear experiment. The solid particles are SiO_2 with irregular shapes, and the diameter ranges are 0.125–0.212 mm, 0.212–0.425 mm, and 0.425–0.710 mm. The mass concentration of solid particles is 15%, 20%, and 30%. The material of impellers is carbon structural steel (Q235), gray cast iron (HT200), and low-alloy high-strength steel (16 Mn). The amount of wear is determined by measuring the thickness of the impeller material before and after wear experiments. The wear morphology of the impeller was observed by using a digital microscope. The results showed that the wear mainly concentrated on the middle and trailing edges of the blade. Impellers of different materials suffer different wear forms, among which the impeller made of HT200 has the best erosion resistance. The increase of solid mass concentration will aggravate the wear of the impeller. The change of particle diameters also has a great influence on impeller wear.

Keywords: solid–liquid two-phase fluid, numerical simulation, particle diameters, mass concentration, erosion wear, morphology characterization

INTRODUCTION

Erosion wear of centrifugal pumps widely exists in the transportation, aerospace, chemical, mining, environmental protection, and other industries. Erosion wear generally refers to the hard sand with a certain kinetic energy that repeatedly impacts and cuts the surface of flow-through parts of the hydraulic machinery and results in mass loss, which is a very important cause of equipment failure or damage. The erosion wear results in the decrease of centrifugal pump efficiency, which will cause direct economic loss and energy waste.

Many scholars have studied erosion wear caused by solid–liquid two-phase flow. Tarodiya et al. (Tarodiya and Gandhi, 2019) carried out experiments on two kinds of sand mud of equal size at two pump speeds and two flows and examined the SCANNING electron microscopy (SEM) images of wear samples, and the results showed that the wear at the volute tongue was caused by both cutting and deformation. Bozzini et al. (2003) simulated the particle's motion trajectory and collision velocity in the pipeline and deduced the erosion model parameters based on the experiment. Azimian et al. (Azimian and Bart, 2015) conducted experiments on the centrifugal rotary wear equipment and found that the size of erosion pits increases with the increase in sediment concentration. Walker et al. (Walker and Bodkin, 2000) summarized the influence of solid particle size, solid–liquid two-phase fluid concentration, and the rotation speed of the pump on wear and explained the wear rule. Amaro et al. (2020) studied the effect of different impact angles, impact distances, and particle sizes on the impact fatigue life. Peng et al. (Guangjie et al., 2013) studied the relationship between blade surface wear rate and sediment concentration and obtained the distribution rule of the blade surface wear rate. Islam et al. (Islam and Farhat, 2014) carried out an erosion test on APL-X42 steel to study its erosion wear performance under different erosion angles. Feng et al. (2020) tested and analyzed WC-CO cemented carbide and found that the anti-erosion performance of cemented carbide decreased with the increase in WC grain size and Co content. Liu et al. (2004) studied the erosion wear of the centrifugal mud pump and the abrasion resistance of a new kind of anti-erosive wear material (Al_2O_3) through experiments. The results showed that wear of the pressure surface is more serious than that of the suction surface. Compared with cast iron (FC20) and AISI 1316L stainless steel, Al_2O_3 had excellent anti-wear performance. Walker et al. (Walker and Robbie, 2013) measured the wear resistance of natural rubber, eutectic, and hypereutectic white cast iron under the conditions of erosion wear and compared the results with the wear of the materials in a centrifugal slurry pump in a factory. In laboratory experiments, the wear rate of hypereutectic white cast iron is higher than that of eutectic white cast iron, and the wear rate of natural rubber is much lower than that of eutectic white cast iron. The aforementioned laboratory results are the opposite of the field trial results. Walker believed that the aforementioned difference is largely due to particle impact energy or impingement angle and particle shape or size. Xiong et al. (2013) carried out experimental studies on erosion wear of Ti(C, N)-Mo2C-Co cermet in artificial seawater containing SiO_2 solid particles. The results showed that the adhesive phase began to wear at first and gradually expanded and fractured. Nguyen (Nguyen et al., 2014) conducted slurry erosion tests on SUS-304 stainless steel. The results showed that the corrosion rate is high at the beginning and gradually decreases as the test time goes on. Arabnejad et al. (2015) studied the impact of particle hardness on the erosion of stainless steel at low impact velocity and found that the erosion rate increased with the increase of particle hardness. Shah and Jain (Shah and Jain, 2008) used computational fluid dynamics (CFD) and studied the relationship between erosion rate and flow velocity, slurry concentration, proppant (solid particle) size, and density. The results showed that the slurry flow rate was the most important factor affecting erosion, and the slurry concentration and fluid viscosity had a greater influence on the erosion rate. Shen et al. (2016) used computational fluid dynamics (CFD) to study the wear of the screw centrifugal pump when the transmission medium is solid–liquid two-phase flow with large-size particles. The research results showed that the volume fraction of the solid phase has a greater impact on the trajectory when transporting large particles, while for small particles, it has little effect. Prasanna et al. (2018) successfully sprayed Stellite-6, 10% Al_2O_3+90%CoCrTaY, and 25%Cr_3C_2-20(Ni-Cr)+75%NiCrAlY on three kinds of turbine alloys: Ti-6Al-4V, Co-based superalloy (Super Co 605), and Fe-based special steel (MDN121). The microstructure and mechanical properties of the coating were characterized. The research results showed that the relative corrosion resistance of various coatings can be arranged in the following order: Stellite-6> Cr_3C_2-20(Ni-Cr)+75% NiCrAlY > Al_2O_3+90%CoCrTaY. Iwai et al. (Iwai and Nambu, 1997) conducted tests on 13 kinds of materials, including polymers, metals, and ceramics, and found that among these materials, rubber had the best wear resistance and polyurethane had the worst. Bansal et al. (2020) used different influencing factors, namely, average erodent particle size, slurry concentration, impact angle, and impact velocity to test the anti-erosion performance of coated and uncoated SS410 steel and analyzed the effect of the thickness of the hydrophobic coating on the anti-erosion performance. The results showed that the PTFE coating with the smallest thickness had the lowest corrosion rate compared with similar coatings. Medvedovski et al. (Medvedovski and Antonov, 2020) tested the iron boride coatings and carbon steel commonly used in industry and observed the erosion surface using a scanning electron microscope. All test results showed that the performance of iron boride coatings is better than that of carbon steel. The erosion mechanism of carbon steel is determined by plastic deformation and ploughing, and the erosion mechanism of iron boride coatings is related to microcracks such as in many advanced ceramics. Singh et al. (2019) studied the erosion performance of ceramic-reinforced WC–10Co4Cr cermet coatings under different parameters. The microstructure analysis showed that there were interlocked lamellae splats, pores, and unmelted particles on the sprayed surface, and it

has good anti-erosion performance in a weakly acidic environment. Grant et al. (Grant and Tabakoff, 1975) verified the erosion wear prediction model that was established on the basis of considering the aerodynamic resistance of solid particles, rebound dynamics of wall surface, and material removal process. The predicted erosion wear amount and erosion wear location of blades are almost consistent with those of the tested. Dong et al. (Xing et al., 2009) analyzed the position and process of pump wear through simulation and experiment and found that the impact of pulverized coal with a certain diameter, shape, impact velocity, and invasion angle on the flowing parts would produce pits on the surface of the flowing parts. Lai et al. (2019) combined the rebound model and erosion model proposed by Grant and Tabakoff to study the erosion wear problem of solid particles in a solid–liquid two-phase centrifugal pump. The results showed that the maximum erosion rate occurred at the impeller hub, and the most serious erosion area of the blade was located at the leading edge between 55° and 60° curvature angle. Liu et al. (Liu and Zhu, 2011) analyzed the wear characteristics of the impeller of the centrifugal sewage pump and proposed measures to reduce the wear of the impeller. The research results can provide theoretical reference for the optimal design of the centrifugal sewage pump. Ojala et al. (2016) revealed the behavior differences of different materials under mud erosion conditions. The wear surface analysis shows that relative wear properties of steel increase with the increase of abrasive size, while the relative wear properties of elastomer decrease with the increase of abrasive size. Marshall et al. (Marshall, 2009) reviewed the forces and torques applied to particles by fluid motion, particle–particle collision, and van der Waals forces. The effects of different parameters on the normal collision and adhesion of two particles are studied in detail. Ovchinnikov et al. (2019) proposed a calculation method for the maximum metal consumption loss of the impeller of a single-stage centrifugal pump, and the results show that this method can effectively reduce the residual deformation risk of the pump shaft. Oka et al. (2005) proposed an equation that can predict the impact wear of solid particles, which is applicable to any impact condition and any type of material. Through erosion experiments on several materials, the results show that the erosion damage is related to the initial hardness, plastic deformation characteristics, or brittleness of materials. Boon et al. (Ng et al., 2008) conducted a numerical simulation on dense solid–liquid two-phase flow and found that particle friction is an important factor in establishing the constitutive equation of dense particle flow. Aslfattahi et al. (2020) used nanomaterials (MXene) with the chemical formula Ti3C2 together with silicone oil for the first time to improve the thermophysical properties of Mxene-based silicone oil. Das et al. (2021) and Rubbi et al. (2021) reviewed the applications of ionic liquids and ionic fluids in different solar systems and the latest progress of nanoparticles in solar systems. Samylingam et al. (2020) synthesized nanomaterials (MXene) with the chemical formula Ti3C2 by the wet chemistry method, suspended its suspension in pure oil palm oil (OPO), and prepared a new type of heat transfer fluid. Kadirgama et al. (2021) used nanomaterials (MXene) and ethylene glycol (EG) as the base liquid to prepare a homogeneous mixture of nanofluids with good optical properties, which might enable high optical performance applications in the solar system.

Most of the abovementioned research studies are based on the condition of large particles and low concentration, but a few research studies on the wear of high-concentration fine particles on the centrifugal pump are carried out experimentally. However, the collision frequency of dense fine particles with a wall surface is much higher than that of large particles, resulting in different wear characteristics. In order to enrich the wear research of centrifugal pumps under the condition of dense fine particles, the wear tests of the solid–liquid two-phase centrifugal pump impeller under different high mass concentrations, fine particle diameters, and impeller materials were carried out in this study.

EXPERIMENTAL APPARATUS AND METHOD

Figure 1 shows the schematic diagram of the wear experimental system, while parameters of the main components related to the experimental system are shown in **Table 1**. The pressure sensor and electromagnetic flow sensor are used to monitor the centrifugal pump operation during the test. The running time is 72 h per test, and the rotation speed r = 1450 rpm. The valve is adjusted to ensure that the inlet flow reaches the rated flow of 16 m3/h. The impellers of the tested pump were made of three materials, namely, carbon structural steel (Q235), gray cast iron (HT200), and low-alloy high-strength steel (16 Mn). The major properties of the three materials are shown in **Table 2**. Considering economy, universality, and no pollution, SiO_2 particles were chosen as solid components with 2650 kg/m^3 density and 475 MPa Brinell hardness, and the particle diameter ranges are 0.125–0.212 mm, 0.212–0.425 mm, and 0.425–0.710 mm, as shown in **Figure 2**.

An ultrasonic thickness gage (**Figure 3A**) was used to measure the thickness of the blade. The wear loss of the blade is expressed by the variation of blade thickness at the measuring position before and after the wear experiment, namely, $\Delta = T_1 - T_2$, where Δ is the thickness variation; T_1 is the thickness of the blade at the measuring position before the experiment; T_2 is the thickness of the blade at the measuring position after the experiment. For every measuring position, measurements are taken three times and their average value is calculated. The measurement uncertainty of the thickness is estimated as ±0.27%. A digital microscope (**Figure 3B**) was used to observe the wear morphology of the blade surface. The observation sites were the head and tail of the pressure surface of impellers of different materials.

As shown in **Figure 4**, the blades of the experiment impeller (**Figure 4A**) are numbered 1 to 5, the seventeen measuring points are evenly arranged on the pressure surface of each blade, and the longitudinal distance of each measuring point is 5 mm; the transverse distance is 10 mm (**Figure 4B**).

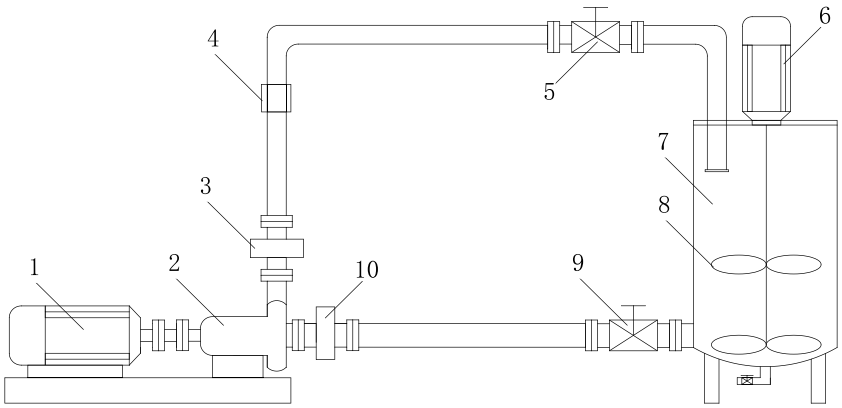

FIGURE 1 | Schematic diagram of the experimental system. 1- Electrical machinery, 2- Test prototype pump, 3- Outlet pressure sensor, 4- Electromagnetic flowmeter, 5- Outlet valve, 6- Agitator motor, 7-Agitator tank, 8- Agitator, 9-Inlet valve, 10-Inlet pressure sensor.

TABLE 1 | Main component parameters of the experimental system.

Component	Type	Specification	Precision
Electrical machinery	YTL2-112M-3	3.0 kW, 1450 rpm	\
Test prototype pump	1PN/4-3 kW	16 m^3/h, 13 m	\
Pressure sensor	SCYG310	–150–150 kPa	±0.5%
Electromagnetic flowmeter	LDG-SUP	2.26–22.6 m^3/h	±0.5%
Ultrasonic thickness gage	PX-7DL	0.15–25.40 mm	0.001 mm
Digital microscope	VHX-2000	0.1X~5000X	—

TABLE 2 | Basic properties of metal impeller materials.

Materials	Density/g·cm^{-3}	Hardness HB/MPa	Tensile strength/MPa
Q235	7.85	150–165	370–500
16 Mn	7.85	150–170	490–675
HT200	7.2	163–255	≥200

FIGURE 2 | Particle morphology.

RESULTS AND DISCUSSION

Many scholars (Walker and Bodkin, 2000; Liu et al., 2004; Guangjie et al., 2013) have found that the wear of the impeller pressure surface is much more serious than that of the suction surface. This is because the density of particles is higher than that of water, and they tend to gather at the pressure surface end under the action of centrifugal force. Therefore, this work mainly analyzes the wear of impeller pressure surface by measuring point data, wear morphology, and electron microscope observation.

Influence of Mass Concentration on Impeller Erosion Wear

This section analyzes the influence of mass concentration on impeller erosion wear. The experiment was conducted under mass concentrations of solid 15, 20, and 30%, the material of impellers is Q235, and the solid particle diameter is 0.125–0.212 mm.

Figure 5 shows the mean value of blade thickness at the measuring point corresponding to different mass concentrations. It can be seen that the wear loss increases with the increase in concentration, but there is no linear relationship, which is consistent with the numerical simulation results of Lai (Lai et al., 2019) and Noon (Liu and Zhu, 2011).

Figures 6, **7** show the surface condition of the impeller after the wear experiment. The parts in the red circle are the parts with obvious wear (same in the following). It can be seen that the middle and tail sections of the pressure surface are the most severely worn parts. This is because the rotating movement of the impeller produces centrifugal force, which induces the particles to move along the pressure surface to the volute, and in this process, the particles have a cutting effect on the pressure surface. As the mass concentration increases, the wear on the pressure surface of the impeller gradually increases, especially at the tail of the blade; at the same time, the wear area expands.

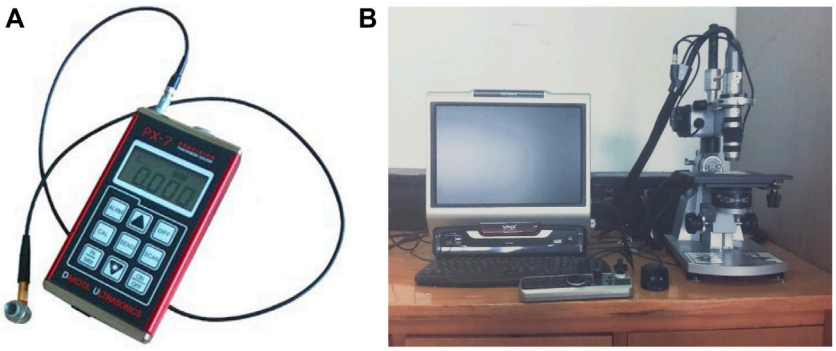

FIGURE 3 | (A) Ultrasonic thickness gauge; **(B)** Digital microscope.

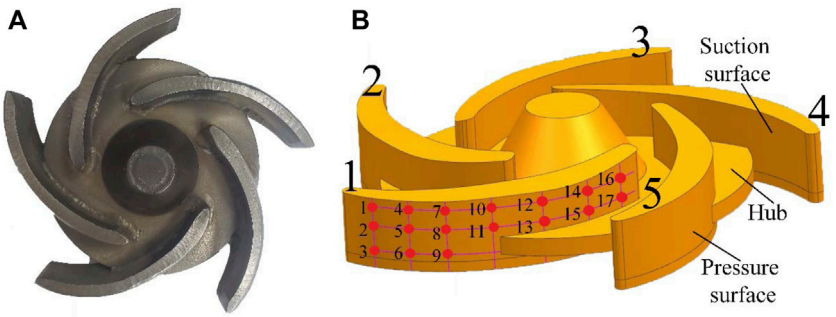

FIGURE 4 | (A) Experiment impeller; **(B)** Measuring point on the impeller model.

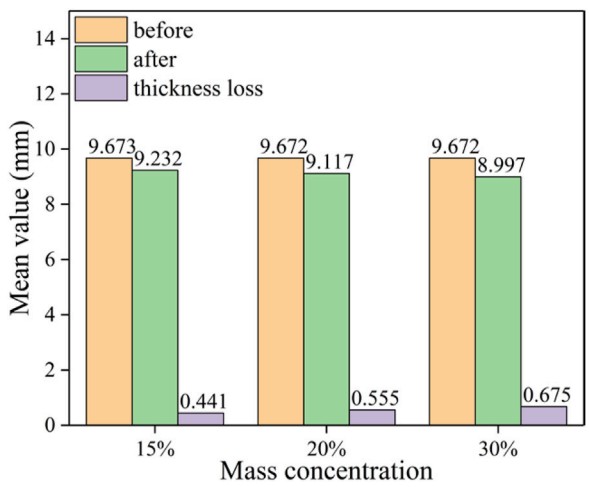

FIGURE 5 | Mean thickness of the blade at the measuring point related with different mass concentrations.

Figure 8 shows that the thickness variation at the measuring point is related to the different mass concentration. The wear is more serious at the middle and trailing edge of the blade; this is because the solid particles are affected by the vortex flow in the middle and tail section of the impeller passage, resulting in the impact of solid particles on the pressure surface. Therefore, the wear on this area will be affected by the combined impact damage and cutting damage, which could lead to the wear increase.

In **Figure 8A**, from point 1 to point 11 of the No. 1 blade, the wear loss fluctuates around 0.4 mm. Along the axial direction of the impeller, the wear of the middle area of the blade (the position of points 2, 5, 8, and 11) is more serious than that of both ends of the blades (the position of points 1, 4, 7, 3, 6, and 9).

It can be seen from **Figure 8B** that the wear of the trailing edge of the blade is more serious. Along the axial direction of the impeller, the upper edge of the blade (the position of points 1, 4, 7, 10, 12, 14, and 16) is more worn. At some measuring points (the positions of point 16 of the No. 2 blade and point 17 of the No. 4 blade), the thickness variation is negative. The main reason is that the area is close to the head of the blade, and impact wear is more serious than sliding wear, so it is more likely to produce an "extrusion lip".

Figure 8C shows that thickness variation at the position of the measuring point when the mass concentration is 30%, which expresses that the wear of the trailing edge of the blade is more serious. Along the axial direction of the impeller, the wear in the middle of the blade (the position of points 2, 5, 8, and 11) is more serious than that of both ends. From point 1 to point 14, the wear loss of each blade is greatly different, while from point 14 to point 17, the wear loss of each blade is nearly similar.

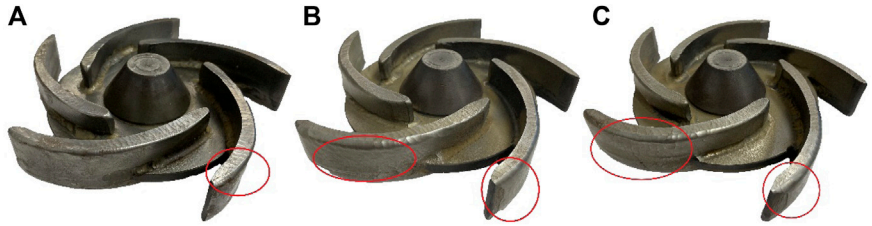

FIGURE 6 | Blade wear under different mass concentration. **(A)** 15%, **(B)** 20%, and **(C)** 30%.

FIGURE 7 | Pressure surface wear under different mass concentration. **(A)** 15%, **(B)** 20%, and **(C)** 30%.

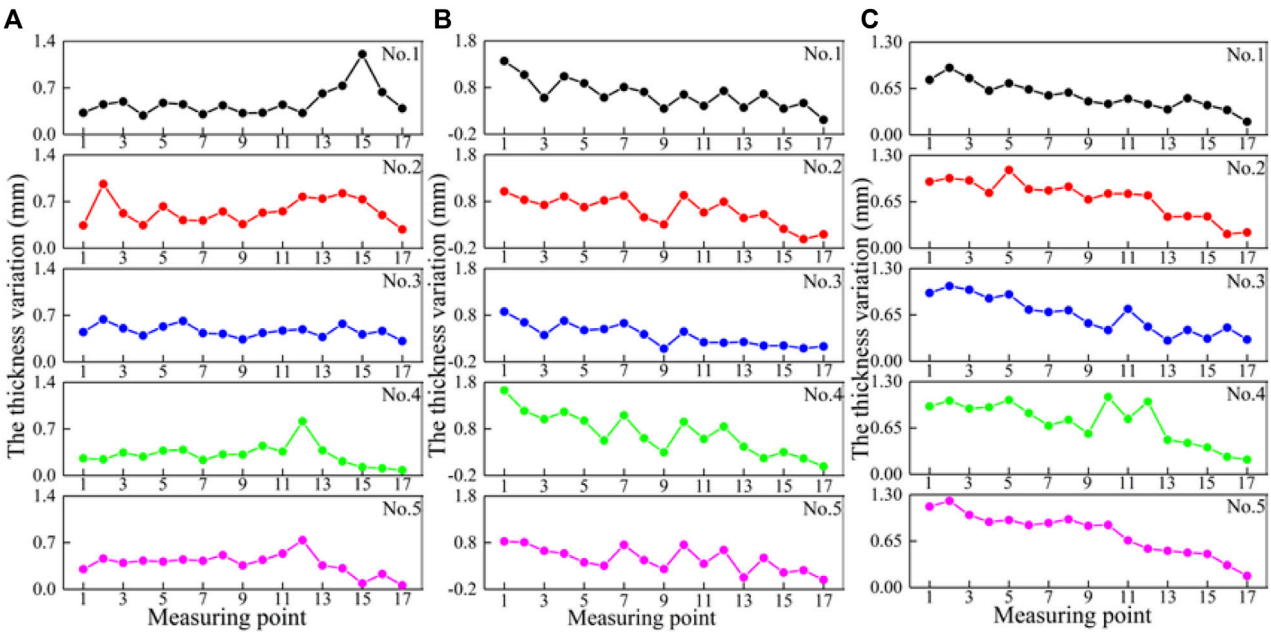

FIGURE 8 | Thickness variation of the blade at measuring points related with different mass concentrations **(A)** 15% mass concentrations, **(B)** 20% mass concentrations, and **(C)** 30% mass concentrations.

According to **Figure 8**, the thickness variation at the measuring point of each blade in the same impeller is very close. When the mass concentration is 20 and 30%, the thickness variation value from the head of the blade to the trailing edge of the blade tends to increase, which is due to the secondary flow generated near the trailing edge of the blade when the mass concentration is higher. The secondary flow causes solid particles to scour the blade surface repeatedly, which leads to increased wear. The secondary flow is relatively small when the mass concentration is 15%. This result is consistent with the numerical simulation results of Dong Xing (Xing et al., 2009).

Influence of Solid Particle Diameters on Impeller Erosion Wear

This section analyzes the influence of solid particle diameters on impeller erosion wear. The experiment was conducted under the

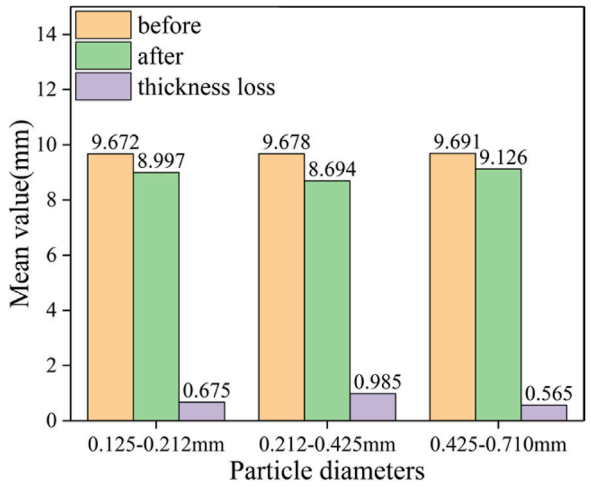

FIGURE 9 | Mean value of blade thickness at the measuring point related with different particle diameters.

solid particle diameter 0.125–0.212 mm, 0.212–0.425 mm, and 0.425–0.710 mm. The mass concentration of solid is 30%, and the material of impellers is Q235.

As can be seen from **Figure 9**, when the particle size is 0.212–0.425 mm, the variation of blade thickness is the largest. When the solid particle diameter is 0.425–0.710 mm, the variation of blade thickness is the minimum. As the particle diameters increase, the wear first increases and then decreases. The reason for this result is related to the "size effect" of particles. At the condition of higher mass concentration, the increase of particle diameters will lead to decrease in the number of particles in per unit volume, which causes the decrease of impact between particles and blade surface. The "size effect" of the particles can reduce the wear.

From **Figure 10**, with the increase of the solid particle size, the wear of the blade near the front cavity increases, and the wear of the hub surface increases. That is because the larger the particle size of the solid particles, the greater the momentum and inertial force of the solid particles. When the particles enter the cavity of the centrifugal pump, the velocity component of the particles in the circumferential direction is smaller, which will directly impact the hub.

According to **Figure 11**, the wear of the pressure surface of the blade is more serious, and it is concentrated at the tail and middle part of the pressure surface. The reason for this phenomenon is that the larger the particle size, the greater is the inertia that will cause the particles to move to the tail of the pressure surface, which will eventually cause more serious wear on the blade surface; as the particle size increases, the wear of the pressure surface of the blade has a tendency to spread to the head of the blade. The area where the pressure surface of the blade is close to the front cavity side is more severely worn. The reason is that the experimental prototype pump is an open impeller, and the internal flow channel will produce a split, which will cause serious wear on the edge of the blade. When the particle size is 0.212–0.425 mm, the wear of the pressure surface is more severe than when the particle size is 0.125–0.212 mm and 0.425–0.710 mm.

As shown in **Figure 12A**, when the solid particle diameter is 0.125–0.212 mm, the thickness variation of the head and tail of the five blades is relatively close, and there is no obvious regularity. The thickness variation at the position of point 15 on No. 1 blade, point 2 on No. 2 blade, point 12 on No. 4 blade, and point 12 on No. 5 blade is large, all exceeding 0.7 mm. The thickness variation at the position of each point on the No. 3 blade is relatively close, and there is no large fluctuation. The heads of the No. 4 blade and No. 5 blade (the position of points 13, 14, 15, 16, and 17) are more worn.

FIGURE 10 | Blade wear under different particle sizes. **(A)** 0.125–0.212 mm, **(B)** 0.212–0.425 mm, and **(C)** 0.425–0.710 mm.

FIGURE 11 | Pressure surface wear under different particle sizes. **(A)** 0.125–0.212 mm, **(B)** 0.212–0.425 mm, and **(C)** 0.425–0.710 mm.

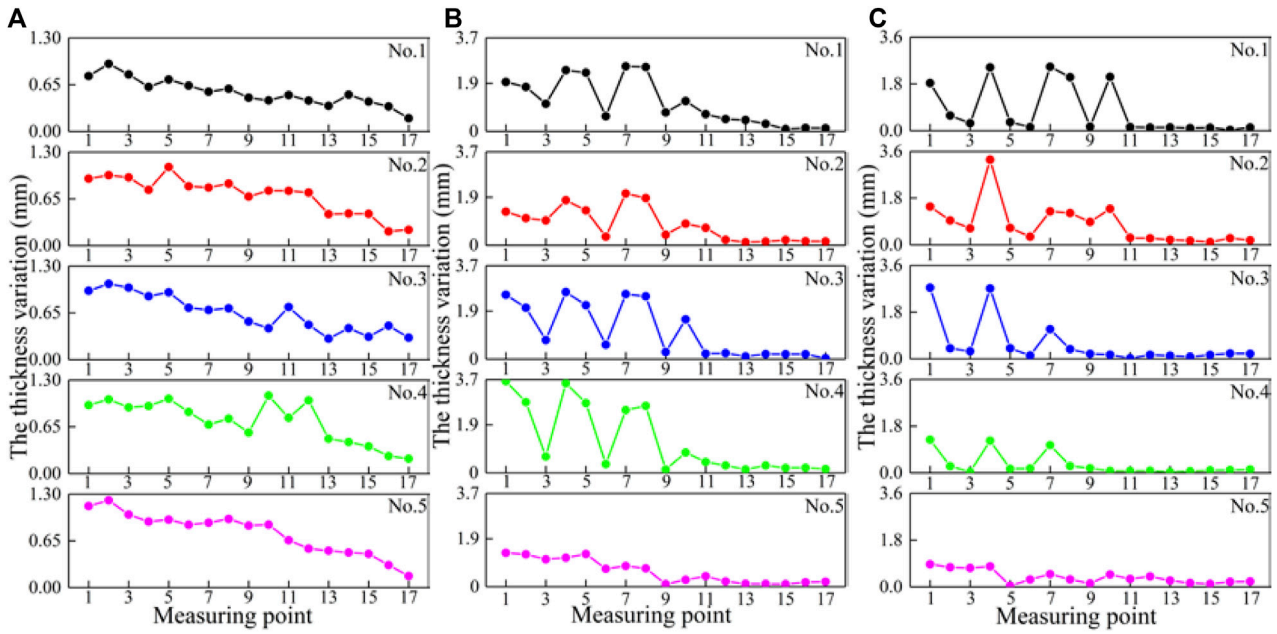

FIGURE 12 | Thickness variation of the impeller at measuring points related with different particle diameters **(A)** 0.125–0.212 mm, **(B)** 0.212–0.425 mm, and **(C)** 0.425–0.710 mm.

Figure 12A shows that the thickness variation at the measuring point when the solid particle diameter is 0.212–0.425 mm. Along the axial direction of the impeller, the upper edge of the blade (the position of points 1, 2, 4, 5, 7, 8, 10, 11, and 12) is more worn. The blades of impeller 5 are worn lighter than the blades of the other four impellers. At points 12, 13, 14, 15, 16, and 17, the wear loss is almost the same and fluctuates about 0.243 mm.

Figure 12B shows the thickness variation at the position of the measuring point when the solid particle diameter is 0.425–0.710 mm. The degree of wear in different areas of the blade surface has a great difference. At points 11, 12, 13, 14, 15, 16, and 17, the wear loss is almost the same and fluctuates about 0.125 mm. The wear loss at different positions of the No. 5 impeller fluctuates about 0.382 mm. This situation is very different from other impellers.

For different mass concentrations, the most severe position of blade wear is the trailing edge. The reason is related to the fluidity and movement state of solid particles in high mass concentration. When the particle diameter is small, the particle flow is more fluid. When the particles enter the impeller channel, the axial velocity increases faster. Therefore, the impact of the blade is less, which causes little difference in wear at each measuring point. When the particle diameter is large, the fluidity of the particles becomes worse, and the interaction between the particles suppresses the movement of the particles. When the particles enter the impeller channel, the axial velocity increases slowly, so it will impact the pressure surface at the middle and trailing edge of the blade strongly, which will cause more serious wear in these positions. This result is consistent with the numerical simulation result of Liu (Ojala et al., 2016).

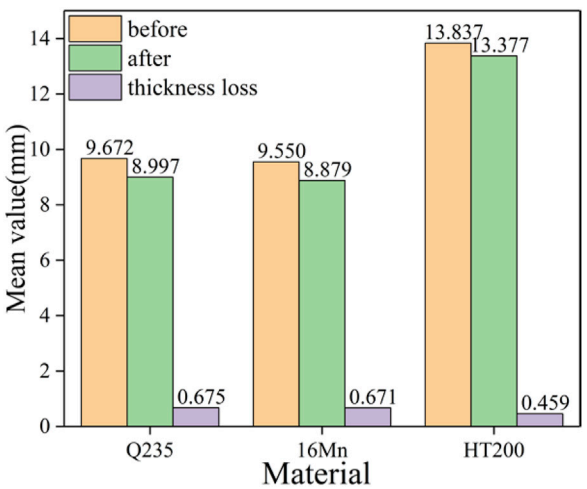

FIGURE 13 | Mean thickness value of different material blades at measuring points.

Influence of Impeller Material on Impeller Erosion Wear

This section analyzes the influence of impeller material on impeller erosion wear. The experiment was conducted under

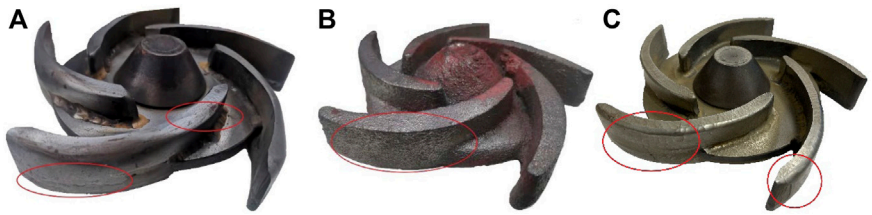

FIGURE 14 | Blade wear under different materials. **(A)** 16 Mn, **(B)** HT200, and **(C)** Q235.

FIGURE 15 | Pressure surface wear under different materials. **(A)** 16 Mn, **(B)** HT200, and **(C)** Q235.

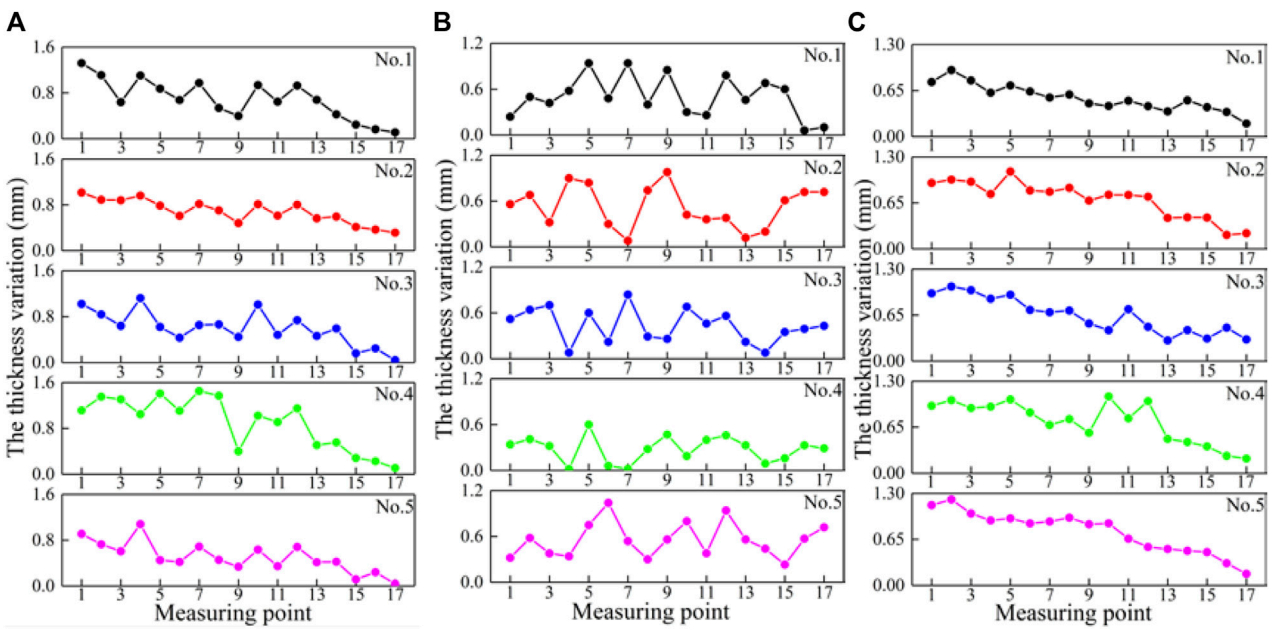

FIGURE 16 | Thickness variation of the blade at measuring points related with different materials **(A)** 16 Mn, **(B)** HT200, and **(C)** Q235.

the material of impellers 16Mn, HT200, and Q235. The mass concentration of the solid is 30%, and the solid particle diameter is 0.125–0.212 mm.

As can be seen from **Figure 13**, the material with the largest thickness variation is Q235, followed by 16 Mn, and the smallest is HT200. Moreover, the variation values of blade thickness of Q235 and 16 Mn are similar but are quite different from those of HT200. The reason may be that Q235 and 16 Mn have similar mechanical properties. The hardness of HT200 is greater than that of the other two materials, so its loss of wear is less when compared to the other two materials. The result is consistent with that of Niko (Marshall, 2009).

Figures 14, **15** show the surface wear of impellers of different materials. The impellers made of 16 Mn and Q235 have similar wear shapes on the pressure surface. There are small erosion pits in the middle of the pressure surface and larger wear shapes at the end edge and lower end of the pressure surface, which may be because the crystal structures of the two materials are relatively similar. The wear performance of the impeller made of HT200 is slightly different, and because red paint is applied, it can be seen

FIGURE 17 | Surface micrographs of the trailing edge of the blade wear different material.

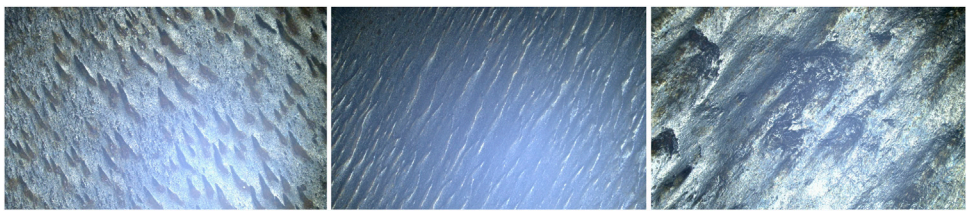

FIGURE 18 | Surface micrographs of the head of the blade of different material after erosion wear.

that the middle part of the pressure surface is obviously darker, and when the red paint is basically obliterated, it indicates that the middle part of the pressure surface is severely worn. This should be determined by the material structure. The roughness of the Q235 material surface is relatively large, which affects the flow characteristics of solid–liquid two-phase flow on the impeller surface.

Figure 16A shows the thickness variation at the measuring point when the material is 16 Mn. It can be found that from point 1 to point 14, the wear loss is larger, while from point 14 to point 17, the wear loss begins to decrease. Along the axial direction of the impeller, the position of points 1, 2, 4, 5, 7, 8, 10, 11, 12, and 14 are more worn. **Figure 16B** shows the thickness variation at the measuring point when the material is HT200. The amount of wear has fluctuated greatly; this is because the HT200 material brittleness is higher; therefore, when damaged by impact, there will be pieces that fall off.

Erosion Mechanism Analysis

Figures 17, **18** show the wear morphology of the three kinds of materials of blade (Q235, 16 Mn, and HT200) under the same test conditions. From the pictures, it can be seen that the wear morphology of the three kinds of materials was different. **Figure 17** shows the wear of the trailing edge of the blade. **Figure 17A,B** show that the wear morphology is corrugated. This is because the plasticity and toughness of Q235 and 16 Mn are relatively large, and the corrugated morphology will be generated when the mass concentration is large. Compared with **Figure 17B**, there is an impact pit in **Figure 17A**;the reason is that the matrix structure of Q235 is ferrite–pearlite. When the solid particles impact the blade surface, the ferrite with greater brittleness is more likely to fracture and break to form the pit. The matrix of 16Mn is also ferrite–pearlite, but due to the addition of alloying elements, it has a role in fine-grain strengthening, and it is not easy to produce erosion pits.

Figure 18 shows the wear of the head of the blade. **Figure 18A,B** show an erosion pit at the position of the blade head. This is because at the blade head, the wear of the solid particles on the blade is impact wear. The impact pit is a groove mark in a certain direction. Since ferrite and pearlite structures are directionally distributed, directional plough marks are generated. **Figure 17C**, **Figure 18C** show a large area of erosion grooves and peeling off, which attribute to the fact that the matrix of HT200 is pearlite, its graphite content is large, and the distribution is a medium flake. The presence of flake graphite splits the continuity of the pearlite matrix, and the graphite tip will also cause stress concentration, so its mechanical properties are relatively poor. When solid particles impact the blade surface, erosion pits and brittle flaking will occur.

The presence of a large amount of graphite in gray cast iron improves its wear resistance. Moreover, the hardness of HT200 is much greater than that of Q235 and 16Mn. Therefore, the wear loss of HT200 is far less than that of the other two materials.

CONCLUSION

In this study, the erosion wear of centrifugal pump blades was studied by experiment and the following conclusions were obtained:

(1) The wear of solid particles on the blade is mainly concentrated in the middle and trailing edge of the blade. In the axial direction of the impeller, the wear on the top of the pressure surface is more serious.
(2) Under the conditions of the experiment, the increase of the mass concentration will aggravate the wear loss of the impeller. The change of particle size also has an important effect on wear.
(3) The matrix structure of carbon structural steel (Q235), gray cast iron (HT200), and low-alloy high-strength steel (16 Mn) determines their erosion wear characteristics. HT200 has high hardness and brittleness, and its erosion wear characteristics are mainly fractured and spalling. However, Q235 and 16 Mn have stronger plasticity and toughness, so their wear characteristics are mainly cutting erosion wear. Among them, the material with high hardness and a large amount of graphite has good erosion resistance. Under the same test conditions, the order of wear loss from large to small is Q235 > 16 Mn > HT200.
(4) In this study, the influence of three parameters on blade wear is studied. By comparing the thickness changes, it is found that the influence of particle size on blade wear is greater than that of the other two parameters (material and concentration).

DATA AVAILABILITY STATEMENT

The raw data supporting the conclusions of this article will be made available by the authors, without undue reservation.

AUTHOR CONTRIBUTIONS

Conceptualization: YW, ZZ, and HL; formal analysis: TH, WL, and CH; investigation: YW and TH; writing—original draft preparation: TH and WL; writing—review and editing, YW, TH, and WL; supervision: ZZ and HL. All authors have read and agreed to the published version of the manuscript.

FUNDING

Top-notch Talent Support Program of Zhejiang Province (2019R51002). The authors thanks for the financial support of National Natural Science foundation of China (Grant No. 51676174), the National Natural Science Foundation of China (Grant No. U1709209) and the Open Research Subject of Key Laboratory (Research Base) of szjj 2016-073.

REFERENCES

Amaro, A. M., Loureiro, A. J. R., Neto, M. A., and Reis, P. N. B. (2020). Residual Impact Strength of Glass/epoxy Composite Laminates after Solid Particle Erosion. *Compos. Struct.* 238, 112026. doi:10.1016/j.compstruct.2020.112026

Arabnejad, H., Shirazi, S. A., McLaury, B. S., Subramani, H. J., and Rhyne, L. D. (2015). The Effect of Erodent Particle Hardness on the Erosion of Stainless Steel. *Wear* 332-333, 1098–1103. doi:10.1016/j.wear.2015.01.017

Aslfattahi, N., Samylingam, L., Abdelrazik, A. S., Arifutzzaman, A., and Saidur, R. (2020). MXene Based New Class of Silicone Oil Nanofluids for the Performance Improvement of Concentrated Photovoltaic Thermal Collector. *Sol. Energy Mater. Sol. Cells* 211, 110526. doi:10.1016/j.solmat.2020.110526

Azimian, M., and Bart, H.-J. (2015). Erosion Investigations by Means of a Centrifugal Accelerator Erosion Tester. *Wear* 328-329, 249–256. doi:10.1016/j.wear.2015.02.002

Bansal, A., Singh, J., and Singh, H. (2020). Erosion Behavior of Hydrophobic Polytetrafluoroethylene (PTFE) Coatings with Different Thicknesses. *Wear* 456-457, 456203340–456203457. doi:10.1016/j.wear.2020.203340

Bozzini, B., Ricotti, M. E., Boniardi, M., and Mele, C. (2003). Evaluation of Erosion-Corrosion in Multiphase Flow via CFD and Experimental Analysis. *Wear* 255, 237–245. doi:10.1016/S0043-1648(03)00181-9

Das, L., Rubbi, F., Habib, K., Aslfattahi, N., Saidur, R., Baran Saha, B., et al. (2021). State-of-the-art Ionic Liquid & Ionanofluids Incorporated with Advanced Nanomaterials for Solar Energy Applications. *J. Mol. Liq.* 336, 116563. doi:10.1016/j.molliq.2021.116563

Feng, C., Chen, D., Xu, M., Shen, C., Yang, L., and Jiang, J. (2020). Study of Solid Particle Erosion Wear Resistance of WC-Co Cemented Carbide. *J Fail. Anal. Preven.* 20, 543–554. doi:10.1007/s11668-020-00861-6

Grant, G., and Tabakoff, W. (1975). Erosion Prediction in Turbomachinery Resulting from Environmental Solid Particles. *J. Aircr.* 12, 471–478. doi:10.2514/3.59826

Guangjie, P., Zhengwei, W., Yexiang, X., and Yongyao, L. (2013). Abrasion Predictions for Francis Turbines Based on Liquid-Solid Two-phase Fluid Simulations. *Eng. Fail. Anal.* 33, 327–335. doi:10.1016/j.engfailanal.2013.06.002

Islam, M. A., and Farhat, Z. N. (2014). Effect of Impact Angle and Velocity on Erosion of API X42 Pipeline Steel under High Abrasive Feed Rate. *Wear* 311, 180–190. doi:10.1016/j.wear.2014.01.005

Iwai, Y., and Nambu, K. (1997). Slurry Wear Properties of Pump Lining Materials. *Wear* 210, 211–219. doi:10.1016/S0043-1648(97)00055-0

Kadirgama, K., Samylingam, L., Aslfattahi, N., Mahendran, S., Ramasamy, D., and Saidur, R. (2021). Experimental Investigation on the Optical and Stability of Aqueous Ethylene Glycol/Mxene as a Promising Nanofluid for Solar Energy Harvesting. *IOP Conf. Ser. Mat. Sci. Eng.* 1062 (1), 012022. (9pp). doi:10.1088/1757-899X/1062/1/012022

Lai, F., Wang, Y., Ei-Shahat, S. A., Li, G., and Zhu, X. (2019). Numerical Study of Solid Particle Erosion in a Centrifugal Pump for Liquid-Solid Flow. *J. Fluids Eng.* 141, 121302. doi:10.1115/1.4043580

Liu, J. H., and Zhu, M. Y. (2011). Simulation Study on Attrition to Centrifugal Sewerage Pump. *Kem* 474-476, 1107–1110. doi:10.4028/www.scientific.net/kem.474-476.1107

Liu, J., Xu, H., Qi, L., and Li, H. (2004). Study on Erosive Wear and Novel Wear-Resistant Materials for Centrifugal Slurry Pumps. Proceedings of the ASME 2004 Heat Transfer/Fluids Engineering Summer Conference 3, Charlotte, North Carolina, USA: ASME, 101–104. doi:10.1115/HT-FED2004-56248

Marshall, J. S. (2009). Discrete-element Modeling of Particulate Aerosol Flows. *J. Comput. Phys.* 228 (5), 1541–1561. doi:10.1016/j.jcp.2008.10.035

Medvedovski, E., and Antonov, M. (2020). Erosion Studies of the Iron Boride Coatings for Protection of Tubing Components in Oil Production, Mineral Processing and Engineering Applications. *Wear* 452-453, 452203277–452203453. doi:10.1016/j.wear.2020.203277

Ng, B. H., Ding, Y., and Ghadiri, M. (2008). Assessment of the Kinetic-Frictional Model for Dense Granular Flow. *Particuology* 6 (1), 50–58. doi:10.1016/j.cpart.2007.10.002

Nguyen, Q. B., Lim, C. Y. H., Nguyen, V. B., Wan, Y. M., Nai, B., Zhang, Y. W., et al. (2014). Slurry Erosion Characteristics and Erosion Mechanisms of Stainless Steel. *Tribol. Int.* 79, 1–7. doi:10.1016/j.triboint.2014.05.014

Ojala, N., Valtonen, K., Antikainen, A., Kemppainen, A., Minkkinen, J., Oja, O., et al. (2016). Wear Performance of Quenched Wear Resistant Steels in Abrasive Slurry Erosion. *Wear* 354-355, 21–31. doi:10.1016/j.wear.2016.02.019

Oka, Y. I., Okamura, K., and Yoshida, T. (2005). Practical Estimation of Erosion Damage Caused by Solid Particle Impact. *Wear* 259, 95–101. doi:10.1016/j.wear.2005.01.039

Ovchinnikov, N. P., Vikulov, M. A., and Portnyagina, V. V. (2019). Calculation of the Maximum Metal Consumption Loss for a Single-Stage Centrifugal Pump Impeller. *IOP Conf. Ser. Earth Environ. Sci.* 229, 012012. doi:10.1088/1755-1315/229/1/012012

Prasanna, N. D., Siddaraju, C., Shetty, G., Ramesh, M. R., and Reddy, M. (2018). Studies on the Role of HVOF Coatings to Combat Erosion in Turbine Alloys. *Mater. Today Proc.* 5, 3130–3136. doi:10.1016/j.matpr.2018.01.119

Rubbi, F., Das, L., Habib, K., Aslfattahi, N., Saidur, R., and Alam, S. U. (2021). A Comprehensive Review on Advances of Oil-Based Nanofluids for Concentrating Solar Thermal Collector Application. *J. Mol. Liq.* 338 (4), 116771. doi:10.1016/j.molliq.2021.116771

Samylingam, L., Aslfattahi, N., Saidur, R., Yahya, S. M., Afzal, A., Arifutzzaman, A., et al. (2020). Thermal and Energy Performance Improvement of Hybrid PV/T System by Using Olein Palm Oil with MXene as a New Class of Heat Transfer Fluid. *Sol. Energy Mater. Sol. Cells* 218 (C), 110754. doi:10.1016/j.solmat.2020.110754

Shah, S. N., and Jain, S. (2008). Coiled Tubing Erosion during Hydraulic Fracturing Slurry Flow. *Wear* 264, 279–290. doi:10.1016/j.wear.2007.03.016

Shen, Z. J., Li, R. N., Han, W., Zhao, W. G., and Wang, X. H. (2016). The Research on Particle Trajectory of Solid-Liquid Two-phase Flow and Erosion Predicting in Screw Centrifugal Pump. *IOP Conf. Ser. Mat. Sci. Eng.* 129, 012052–012059. doi:10.1088/1757-899X/129/1/012052

Singh, J., Kumar, S., and Mohapatra, S. K. (2019). Tribological Performance of Yttrium (III) and Zirconium (IV) Ceramics Reinforced WC-10Co4Cr Cermet Powder HVOF Thermally Sprayed on X2CrNiMo-17-12-2 Steel. *Ceram. Int.* 45, 23126–23142. doi:10.1016/j.ceramint.2019.08.007

Tarodiya, R., and Gandhi, B. K. (2019). Experimental Investigation of Centrifugal Slurry Pump Casing Wear Handling Solid-Liquid Mixtures[J]. *Wear* 434, 202972. doi:10.1016/j.wear.2019.202972

Walker, C. I., and Bodkin, G. C. (2000). Empirical Wear Relationships for Centrifugal Slurry Pumps. *Wear* 242, 140–146. doi:10.1016/s0043-1648(00)00413-0

Walker, C. I., and Robbie, P. (2013). Comparison of Some Laboratory Wear Tests and Field Wear in Slurry Pumps. *Wear* 302, 1026–1034. doi:10.1016/j.wear.2012.11.053

Xing, D., Hai-lu, Z., and Xin-yong, W. (2009). Finite Element Analysis of Wear for Centrifugal Slurry Pump. *Procedia Earth Planet. Sci.* 1, 1532–1538. doi:10.1016/j.proeps.2009.09.236

Xiong, J., Guo, Z., Yang, M., Dong, G., and Wan, W. (2013). Erosion Behavior of Ti(C,N)-based Cermet in Solid-Liquid Two Phase Flow. *Int. J. Refract. Metals Hard Mater.* 41, 224–228. doi:10.1016/j.ijrmhm.2013.04.004

Conflict of Interest: The authors declare that the research was conducted in the absence of any commercial or financial relationships that could be construed as a potential conflict of interest.

Publisher's Note: All claims expressed in this article are solely those of the authors and do not necessarily represent those of their affiliated organizations, or those of the publisher, the editors, and the reviewers. Any product that may be evaluated in this article, or claim that may be made by its manufacturer, is not guaranteed or endorsed by the publisher.

frontiers | Frontiers in Energy Research

ORIGINAL RESEARCH
published: 28 June 2022
doi: 10.3389/fenrg.2022.937299

Analysis of Surface Pressure Pulsation Characteristics of Centrifugal Pump Magnetic Liquid Sealing Film

Zhenggui Li[1], Kun Wang[1], Wangxu Li[1], Shengnan Yan[1], Fang Chen[1] and Shengyang Peng[2]*

[1]Key Laboratory of Fluid and Power Machinery, Ministry of Education, Xihua University, Chengdu, China, [2]Huaneng Mingtai Electric Power Co. Ltd., Mianyang, China

In order to discuss the surface pressure pulsation characteristics of the magnetic-fluid sealing membrane of centrifugal pump, this paper studies the surface pressure pulsation characteristics of the shaft end sealing membrane under different flow operating conditions of centrifugal pump based on the combination of numerical calculation and experimental verification. The results show that the pressure value on the surface of the magnetic-fluid sealing film decreases with the increase of the flow rate of the centrifugal pump, and the pressure on the surface of the magnetic-fluid sealing film has periodic pulsation, and the period is the time required for a single blade to sweep the volute separating tongue. In one rotation cycle of the runner, the number of reciprocating movements of the magnetic-hydraulic sealing film is the same as the number of blades of the runner. The main reason for the pressure pulsation is that the impeller periodically sweeps the fixed surface of the centrifugal pump.

Keywords: centrifugal pump, magnetic liquid, seal, pressure pulsation, numerical calculations

OPEN ACCESS

Edited by:
Kan Kan,
College of Energy and Electrical Engineering, China

Reviewed by:
Qiang Gao,
University of Minnesota Twin Cities, United States
Xianbei Huang,
Yangzhou University, China

****Correspondence:***
Zhenggui Li
lzhgui@mail.xhu.edu.cn

Specialty section:
This article was submitted to Process and Energy Systems Engineering, a section of the journal Frontiers in Energy Research

Received: *06 May 2022*
Accepted: *09 June 2022*
Published: *28 June 2022*

Citation:
Li Z, Wang K, Li W, Yan S, Chen F and Peng S (2022) Analysis of Surface Pressure Pulsation Characteristics of Centrifugal Pump Magnetic Liquid Sealing Film. Front. Energy Res. 10:937299. doi: 10.3389/fenrg.2022.937299

INTRODUCTION

As an important strategic machine for the national economy, people's livelihood and national security, the development of industry and science and technology, the demand for energy and the environment, and the construction of the national economy all promote the development of pumps in the direction of high speed, high efficiency and high stability Lu (2017). However, the high-speed operation of the centrifugal pump also causes the unreliability of the shaft end seal of the centrifugal pump. In order to prevent seal failure, leakage of liquid in the pump or impurities outside the pump from entering the pump cavity, the shaft seal must be considered when designing and applying centrifugal pumps Peng (2021); Xu (2004); Zhao et al. (2001). Magnetic liquid seal is a new type of non-contact seal, which shows good advantages in dynamic sealing Li W. et al. (2021); Li et al. (2022). It has been widely used in dry Roots vacuum pump Li et al. (2002), reactor Xu. (2013) and other equipment. However, there has not been a major breakthrough in the magnetic liquid sealing technology of the centrifugal pump shaft end using liquid as the transport medium. The fundamental reason is that the surface of the magnetic liquid sealing film is unstable. Therefore, scholars at home and abroad have explored the principle of magnetic liquid sealing.

Jianfeng Zhou and Haoliang Fan (Zhou et al., 2016) studied the influence of magnetic field strength and rotational speed on film thickness, friction torque, characteristic temperature and magnetohydrodynamic loss, revealing the influence of magnetic field on magnetohydrodynamic effect; Zhang Haina (Zhang et al., 2013) studied the influence of sealing progression, magnetic liquid injection amount and standing time at room temperature on the tripping torque, and at the same

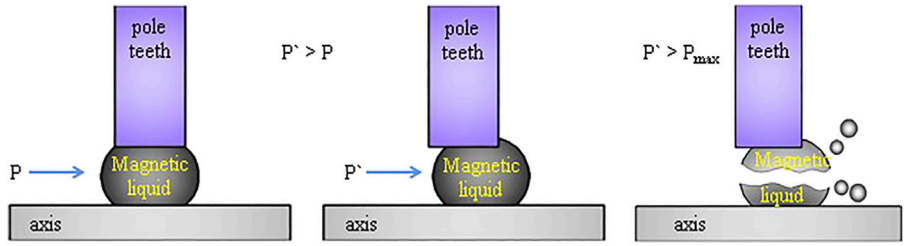

FIGURE 1 | The sealing film fluctuates and breaks.

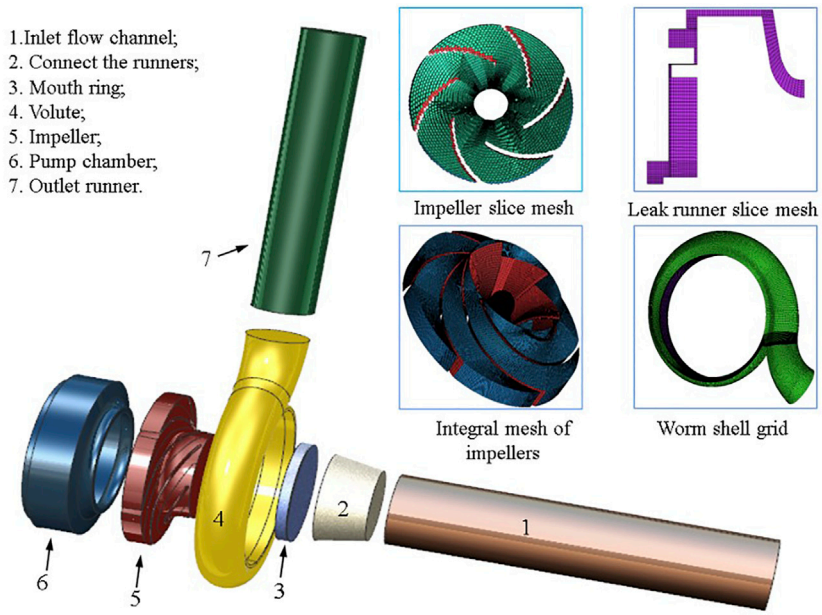

FIGURE 2 | Centrifugal pump model and partial grid diagram.

time, based on the magnetic liquid rotary sealing model, the torque formula of magnetic liquid rotary sealing at low temperature was derived from the Navier-Stokes equation; Jibin Zou (Zou et al., 2003) discovered that multi-pole multi-stage magnetic fluid sealing is an effective way to obtain higher sealing capacity, and studied the method of magnetic fluid filling and differential pressure application; Yibiao Chen (Chen et al., 2020) et al. studied the variation of magnetic fluid temperature and its influence on sealing performance; In order to establish a stable interface in the sealing process, Tonggang Liu (Liu et al., 2005) optimized the structural parameters by using the simulation device, and developed a new type of magnetic fluid seal, which has good sealing performance and long service life according to the optimization parameters; Marcin, Szczech (Szczech M. 2020) introduced the leakage mechanism between multi-stage magnetic fluid seals when magnetic fluids were applied to magnetic fluid seals in rotational motion, and Marcin, Szczech (Szczech M. 2018) proposed a critical pressure calculation method for magnetic fluid seals based on numerical simulation of magnetic fields, which had better calculation effect than previous methods; Qian Jiguo et al. (Qian and Yang, 2008) elaborated on the interfacial stability analysis method of the magnetic liquid sealed liquid, and obtained the stability criterion and the critical value of the parameters of the interface between the magnetic liquid and the sealed liquid according to the Kelvin-Helmholtz interface stability analysis model of the moving fluid, and discussed the main factors affecting the stability of the liquid-liquid interface of the magnetic liquid dynamic seal. The above scholars analyzed the influence of magnetic fluid temperature and sealing series on sealing performance, and optimized the magnetic liquid sealing performance in combination with numerical calculations, and studied the stability of the magnetic liquid sealing interface and improved its related theory, but at present, there is a lack of research on the stability of the surface of the magnetic liquid sealing film at the shaft end when the centrifugal pump operates at high speed under different flow conditions.

However, the surface pressure ripple of the magnetic seal film is an important cause of the emulsification, dilution, dissolution

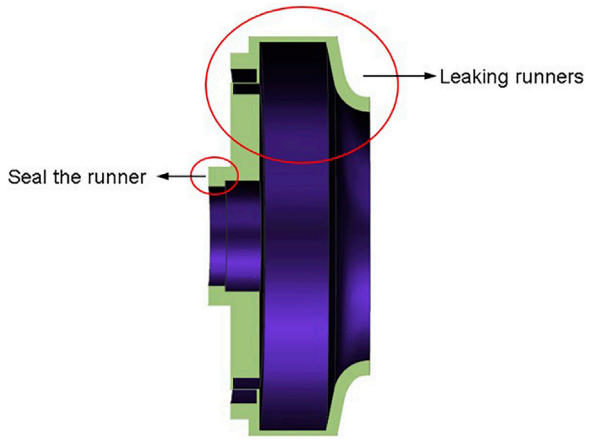

FIGURE 3 | Schematic diagram of the interior of the pump chamber.

and sealing failure of the magnetic liquid (He et al., 2014). In rotating machinery with impeller, due to its special structure, the periodic sweeping of the fixed surface of the impeller, the reflection of the pressure fluctuations on the wall surface of the volute, the complex three-dimensional transient flow during the normal operation of the centrifugal pump, the extrusion of the high-pressure fluid in the sealing channel to the surrounding low-pressure fluid, the fluid return flow, and the fluid vortex movement will all produce pressure pulsations on the surface of the magnetic liquid sealing film (Li Z. et al., 2021). Magnetic liquid seal is the use of magnetic liquid where the magnetic pressure difference (Xu et al., 2010) to achieve the sealing effect, so the position of the magnetic liquid at the bottom of the polar tooth corresponds to the pressure bearing capacity: when the pressure of the sealing interface changes, the axial position of the magnetic liquid will change accordingly, when the pressure is pulsating, the surface state of the magnetic liquid sealing film is unstable, if the maximum pulsation amplitude is higher than the maximum pressure of the seal, the sealing film will rupture, as shown in **Figure 1**.

Therefore, it has certain research significance to study the pressure pulsation law on the surface of the magnetic fluid sealing membrane at the shaft end and its causes under various flow conditions of the centrifugal pump.

NUMERICAL MODEL AND CALCULATION SETUP

Division of 3D Model and Mesh Model

The centrifugal pump selected in this article is a single-stage single-suction model pump, and its overcurrent components are composed of inlet runner, connecting runner, mouth ring, volute, impeller, pump chamber, and outlet runner, and the pump chamber contains a leaking runner and a sealed runner inside the pump chamber. **Figure 2** shows a model of the pump and a partial mesh of the pump, and **Figure 3** is a Schematic diagram of the interior of the pump chamber, with a full-flow channel model of the pump plotted with NX.10. The computational stability, calculation accuracy and calculation speed reflected in the structural grid are better than those of non-structural grids, so the structural grid drawn by ICEM CFD is used for numerical calculation. Winslow P. et al. (2010); Guo et al. (2019); Cheng et al. (2021); Zeng, (2022); Cheng et al. (2022).

The main parameters of the model pump are shown in **Table 1**. In order to eliminate the influence of the number of grids on the calculation results, before the analysis of the results, the external characteristics of the centrifugal pump's rated operating conditions—the head are taken as the criterion, and the grid independence is verified, as shown in **Table 2**, when the overall number of grids is greater than 2317541, the head change of the centrifugal pump is less than 0.3%, so it can be considered that the number of grids is greater than this value to meet the calculation requirements.

Boundary Condition Settings

The centrifugal pump test bench used in the experiment is equipped with a pressure sensor at the pump inlet to collect the pressure value of the centrifugal pump inlet; at the same time, a turbine flowmeter is set at the outlet of the pump, so the mass flow of the pump outlet is known, so the pressure inlet is used as the inlet boundary condition, and the flow outlet is used as the outlet boundary condition.

Because the internal structure of the centrifugal pump is known, and the rotor area is different from other overcurrent components, which carries out independent rotational motion, the single reference frame (SRF) model is selected for the steady-state calculation of the flow field in the centrifugal pump, the sliding mesh model is selected for transient

TABLE 1 | Main parameters of centrifugal pump.

parameter	symbol	Value (units)
Centrifugal pump inlet/outlet diameter	D_s/D_d	63/48 mm
Impeller inlet/outlet diameter	D_j/D_2	80/140 mm
Rated head	H_d	20.0 m
Rated flow rate	Q_d	50.6 m^3/h
Rated speed	n	2,910 r/min
Number of blades	Z	6
Specific speed of the pump at the rated working point	n_s	132.2
Shaft diameter	D_l	36 mm
Seal the outside diameter of the runner	D_k	50 mm

TABLE 2 | Grid model parameters of centrifugal pump.

scheme	Number of meshes	Head(m)
A	1013514	19.98
B	1537624	21.33
C	2317541	22.01
D	2841908	22.04
E	3174019	22.02

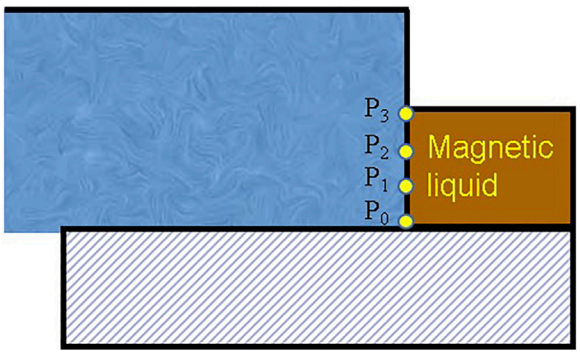

FIGURE 4 | Position of monitoring point.

calculation, and the impeller surface is set to relatively static to the rotation domain, and the rest of the wall surface is set to absolute stationary.

For the flow state of the flow field in the centrifugal pump, due to the boundary conditions and the complexity of the structure in the pump, the internal rotation area and strong swirl, the RNG k-ε model has corrected the turbulence viscosity, which is suitable for the numerical calculation of strong flow line bending and vortex, so the turbulence model selected in this paper is the RNG k-ε model. Zhou et al. (2007); Ren et al. (2009).

Transient Calculation Parameter Setting

Taking the calculation result of the stable flow field as the initial value of the transient calculation can accelerate convergence and ensure the stability of the calculation, therefore, the constant result of each flow condition is used as the initial condition for the transient calculation of each flow condition of the centrifugal pump. At the same time, in order to better capture the pressure pulsation signal, the transient time step is set to 0.00017182 s, that is, the pressure value is recorded every 3° rotation of the rotor.

In the initial process of transient calculations, the results are often unstable, deviating from the exact solution (Cao et al., 2019). In order to avoid the difference in results caused by these problems, the centrifugal pump wheel is set to rotate a total of 12 turns, the calculation time is 3.77 s, and the results of the last four turns are taken for analysis.

Pressure pulsation monitoring point is set on the surface of the magnetic liquid sealing film, starting from the shaft surface, every 0.1 mm to take a monitoring point, because the sealing gap is 0.3 mm, so the monitoring point is a total of 4, **Figure 4** is the monitoring point setting diagram.

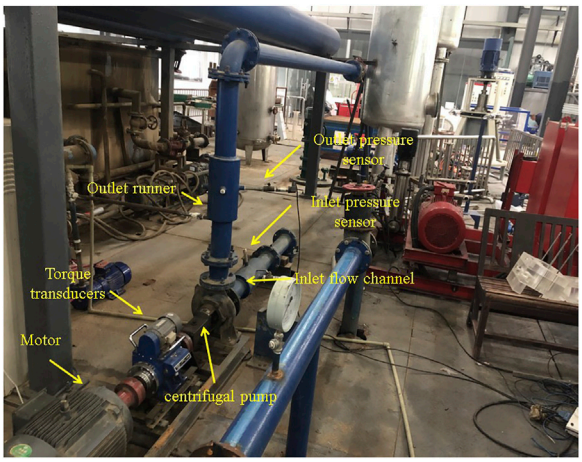

FIGURE 5 | Field experimentation.

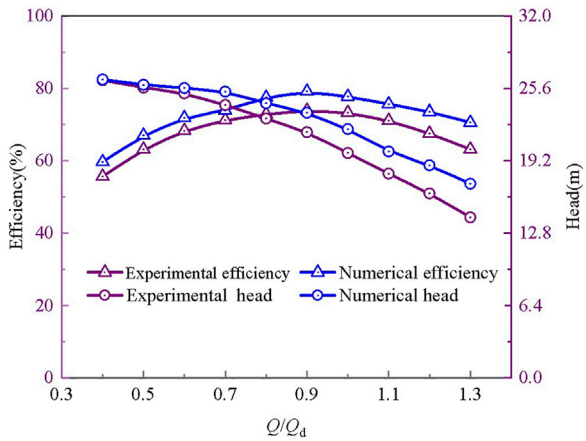

FIGURE 6 | Comparison of simulation results with experiments.

EXPERIMENTAL VERIFICATION OF NUMERICAL CALCULATION OF FLOW FIELD IN CENTRIFUGAL PUMP

In order to verify the accuracy of turbulence model selection, boundary condition setting and calculation results, the external characteristics of the model pump were tested in the Key Laboratory of Fluid and Power Machinery of the Ministry of Education of Xihua University, and the experimental apparatus is shown in **Figure 5**:

The experimental bench is an open experimental bench, centrifugal pump inlet and outlet with pressure sensor, and turbine flowmeter, prime mover for the motor, through the torque sensor to drive the centrifugal pump rotation, under the deck of the experimental device, with a water tank, to give the pump body water source, and accept the liquid flowing out of the pump, forming a closed loop.

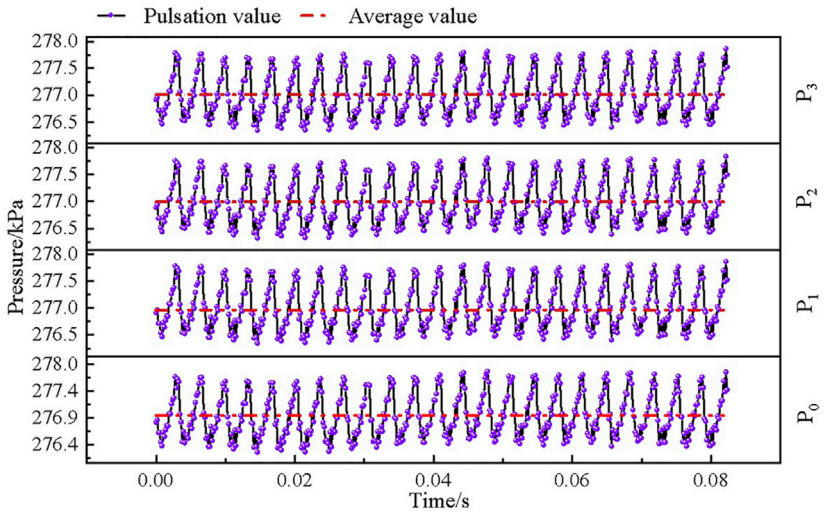

FIGURE 7 | Time domain diagram of pressure pulsation under rated operating conditions.

During the experiment, the centrifugal pump 0.4–1.3Q_d working conditions, when the working conditions are adjusted, the data is temporarily not recorded, and the data is collected after the flow is stable. **Figure 6** shows the external characteristic data (head, efficiency) collected by the experiment compared with the numerically calculated data.

The head H of the pump is the energy appreciation of the liquid pumped by the pump per unit weight from the inlet of the pump to the outlet of the pump, and its calculation formula is:

$$H = \frac{p_d - p_s}{\rho g} + \frac{V_d - V_s}{2g} + (Z_d - Z_s) \tag{1}$$

Wherein, the p_d indicates the pump outlet pressure; the p_s indicates the pump inlet pressure; the V_d indicates the pump outlet liquid speed; the V_s indicates the pump inlet liquid velocity; the Z_d indicates the distance between the pump outlet and the datum; the Z_s indicates the distance between the pump inlet and the datum; ρ is the liquid density; and g represents the gravitational acceleration.

The efficiency η of the pump is the ratio between the effective power of the pump P_e and the shaft power P of the pump. Head H, in turn, represents an increase in the amount of energy obtained by the liquid per unit weight from the pump, so there is:

$$P_e = HQ_m g \tag{2}$$

wherein, the Q_m represents the mass flow of the pump. The shaft power expression for the pump is:

$$P = T\omega \tag{3}$$

where T is the torque and ω is the angular velocity. Therefore, the efficiency of the pump can be expressed as:

$$\eta = \frac{HQ_m g}{T\omega} \tag{4}$$

TABLE 3 | Pressure pulsation at each monitoring point.

	P_0	P_1	P_2	P_3
Negative peaks	276274	276346	276322	276346
average value	276975	276963	276996	277013
Positive peak	277812	277866	277842	277865

It can also be concluded from **Figure 6** that the head and efficiency of the numerical calculation are higher than the experimental values, and the main reason for this phenomenon is that the obstruction and wear effect of the solid surface on the liquid is not considered in the numerical calculation process (Hu 2004). However, the numerically calculated head and centrifugal pump efficiency values are the same as the experimental values, and the maximum deviation value of the head is less than 3 m, so it can be considered that the results of the numerical calculation have a certain degree of credibility.

PRESSURE PULSATION ANALYSIS OF SEALING FILM AT THE SHAFT END OF CENTRIFUGAL PUMP

Time Domain Characteristics of Surface Pressure Pulsation of Magnetic Liquid Sealing Film Under Rated Working Conditions

Figure 7 is a time domain diagram of the surface pressure ripple of the magnetic liquid sealing film under rated operating conditions. It can be seen from the figure that the time difference between the adjacent two positive peaks is about 0.0034 s, that is, 20 time steps, and in each time step, the wheel can be rotated by 3°, and the number of blades of the

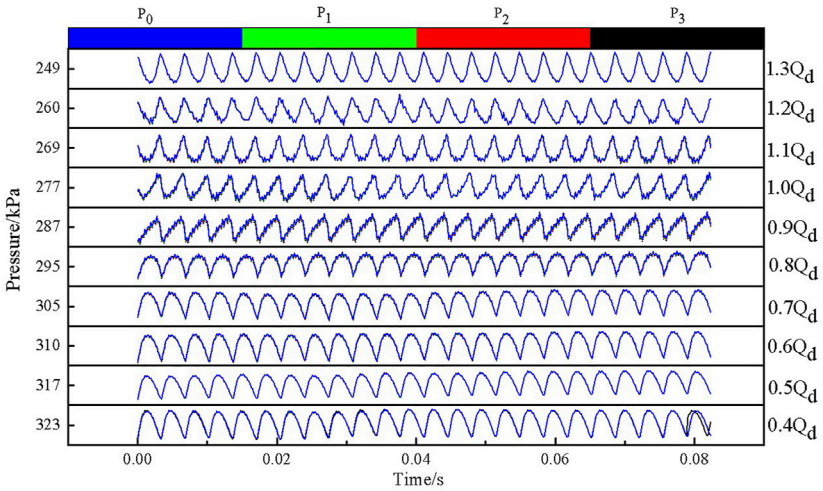

FIGURE 8 | Time domain diagram of pressure pulsation under partial conditions.

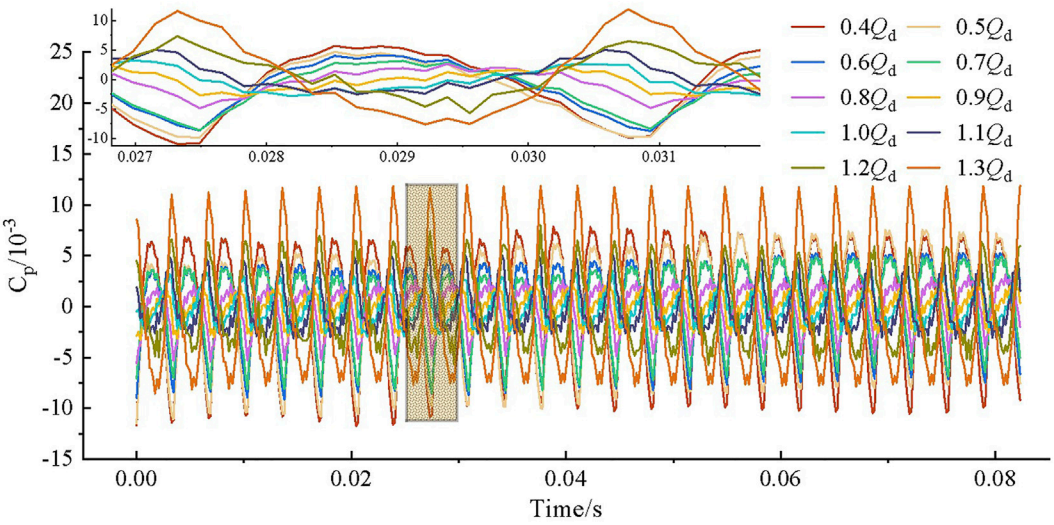

FIGURE 9 | Time domain diagram of pressure pulsation under dimensionless partial conditions.

centrifugal pump applied herein is 6, therefore, the time difference between the adjacent two positive peaks is similar to the time required for the wheel to rotate 60°, so the time difference between the adjacent two positive peaks is equal to the time required for one blade to sweep through the septum of the centrifugal pump. Therefore, the pressure pulsation cycle on the surface of the magnetic-liquid seal film is equal to the time required for a single leaf to sweep through the septum.

Table 3 shows the negative peak, average and positive peak data of pressure pulsation at each monitoring point on the surface of the magnetic liquid sealing film. From **Table 3**, it can be seen that under the rated working conditions, the difference between the negative peaks, average values and positive peaks between the monitoring points at the same time point is less than 100 Pa, and the pressure pulsation law of the monitoring points on the surface of the magnetic liquid sealing film can be considered to be consistent under the rated working conditions. And under the rated working conditions, the peak-to-peak difference between the surface of the magnetic liquid sealing film is about 1,500 Pa.

From the above analysis, it can be seen that the time interval and pressure pulsation cycle between the adjacent two pressure peaks are the time required for a single blade to sweep through the septum, and during the magnetic liquid sealing process, the position of the sealing film corresponds to the external pressure one-to-one, so the pressure pulsation cycle on the surface of the sealing film is the displacement movement cycle of the sealing film. Therefore, in a rotary rotation cycle, the magnetic liquid sealing film reciprocates 6 times, and the number of reciprocating movements is the same as the number of blades. At the same time, the pressure amplitude change on the surface of

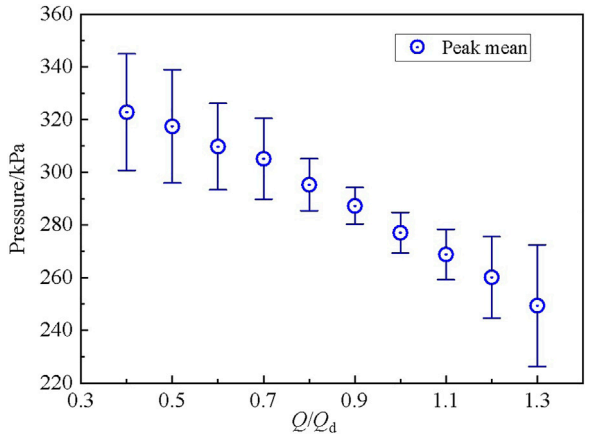

FIGURE 10 | Peak difference diagram of pressure pulsation.

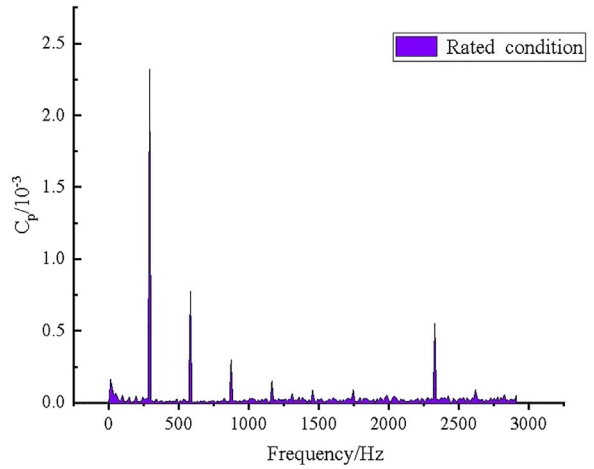

FIGURE 11 | Pulsation frequency domain diagram of rated working conditions.

the magnetic liquid sealing film is about 1,500 Pa, while the single-stage sealing capacity of the magnetic liquid is about 120 kPa (Wang, 2004), so the pressure fluctuation on the surface of the magnetic liquid sealing film in the centrifugal pump is less likely to cause a breakdown pressure, and the available pressure average is used as the benchmark when the magnetic liquid sealing device is designed. However, when the centrifugal pump speed is high, the frequency of pressure pulsation fluctuations on the surface of the sealing film is accelerated, which will promote the emulsification, dilution and dissolution of the magnetic liquid.

Time Domain Characteristics of Surface Pressure Pulsation of Magnetic Liquid Sealing Film Under Partial Working Conditions

Figure 8 is a time domain diagram of the surface pressure ripple of the magnetic liquid sealing film of the centrifugal pump under partial working conditions. It can be seen from the figure that under various working conditions, due to the narrow sealing gap, the pressure pulsation time domain curves of each monitoring point on the surface of the magnetic liquid sealing film overlap together. That is, when the centrifugal pump is running under the working conditions of $0.4–1.3Q_d$ flow, the pressure fluctuation law of each monitoring point is consistent. In the subsequent analysis, the pressure value of any point in P_0, P_1, P_2, P_3 can be applied instead of the surface pressure value of the magnetic liquid sealing film, and the P_2 point is used as the representative point.

And from **Figure 8**, it can also be learned that when the centrifugal pump is running under the working conditions of 0.4–1.3 Q_d flow, the fluctuation cycle of the pressure pulsation on the surface of the magnetic liquid sealing film is consistent, which is the length of time required for a single blade to sweep the septum, which shows that when the centrifugal pump is running under different flow conditions, the impact on the periodicity of the pressure pulsation of the magnetic liquid sealing film surface is weak, and it can be inferred from this result that the pressure pulsation on the surface of the magnetic liquid sealing film is mainly generated by the periodic sweeping fixed surface of the blade. Although the periodic sweeping of the fixed surface of the blade dominates the pressure ripple of the magnetic liquid sealing film, the reflection of the pressure fluctuation of the volute wall surface, the complex three-dimensional transient flow during the normal operation of the centrifugal pump, the extrusion of the high-pressure fluid in the sealing channel on the surrounding low-pressure fluid, the fluid return flow, and the fluid vortex movement will have a certain impact on the pressure ripple on the surface of the magnetic-liquid sealing film, so there are differences in the waveform of the pressure ripple under each flow condition.

In order to better compare the law of the surface pressure pulsation characteristics of the magnetic liquid sealing film under various flow conditions, the pressure pulsation value is dimensionlessly treated, and the pressure pulsation coefficient is used as the standard for measuring the size of the pressure fluctuation, and its definition is as follows (Jin, 2020):

$$c_p = \frac{p - \bar{p}}{0.5\rho\mu_2^2} \tag{5}$$

$$\mu_2 = \frac{\pi n D_2}{60} \tag{6}$$

where p is the measured pressure pulsation value, $\bar{p}$ is the average value of the pressure pulsation, ρ is the fluid density, μ_2 is the circumferential velocity of the liquid at the outlet of the impeller, n is the speed, and D_2 is the diameter of the rotor outlet.

Figure 9 is a pressure ripple pattern of each flow condition after the dimensionless treatment of the pressure amplitude, it can be seen from the figure that there is a phase difference in the pressure fluctuation law under each flow condition, but its pulsation period is similar. And it can be seen that under the condition of $1.3Q_d$, the positive peak of the surface pressure pulsation of the magnetic liquid sealing film is the largest, and the negative peak of the pressure pulsation under the condition of $0.4Q_d$ is the largest, but only from the positive peak or negative peak size can not judge the

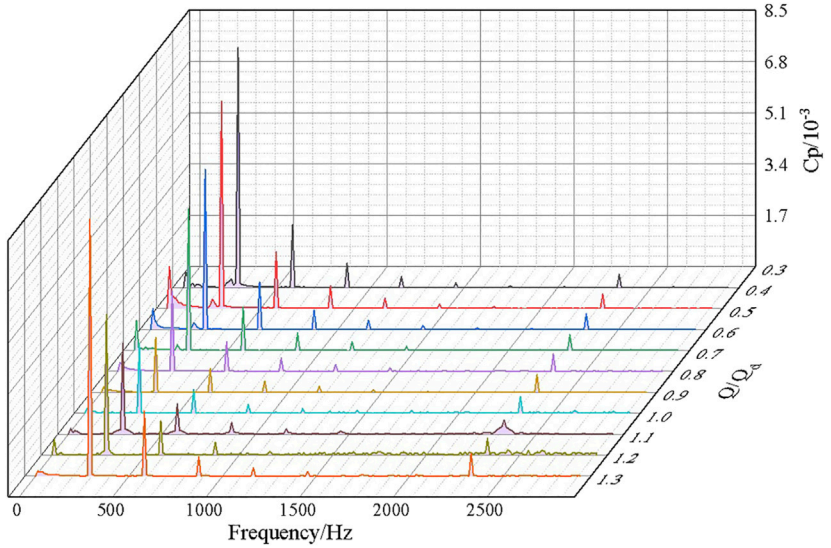

FIGURE 12 | Off-mode pulsation frequency domain diagram.

stability of the magnetic seal film under each working condition, because in the process of magnetic sealing, in a pulsation cycle, the magnetic liquid displacement distance is determined by the difference between the positive peak and the negative peak. Therefore, the fluctuation of the magnetic liquid sealing film must be judged by the difference between peak and peak.

Figure 10 shows the difference between the pressure pulsation peak and peak of the P_2 point under different working conditions, the midpoint position represents the average value of the positive peak and the negative peak, and the upper and lower error bars represent the positive peak and negative peak respectively. It can be seen from the figure that the peak-to-peak difference is the smallest in the 0.9 and $1.0Q_d$ working conditions, and the peak-to-peak difference gradually increases when the working conditions deviate from the 0.9 and $1.0Q_d$ working conditions, and the peak-to-peak difference in the 0.4 and $1.3Q_d$ working conditions is twice that of the 0.9 and $1.0Q_d$ working conditions. Therefore, when the centrifugal pump works at the rated working point or its nearby working point, the displacement path of the magnetic liquid sealing film is shorter, and the displacement length of the magnetic liquid sealing film is twice that of the working condition of 0.4 and $1.3Q_d$ when it is operating under partial working conditions such as 0.4 and $1.3Q_d$. Therefore, when the centrifugal pump works at the rated working point or the working point near it, the surface stability of the magnetic liquid sealing film is better than that of the partial working condition.

Surface Pressure Pulsation Frequency Domain Characteristics of Magnetic Liquid Sealing Film Under Rated Working Conditions

The relationship between the signal amplitude and the frequency change is called the frequency domain. Time domain analysis is an applied mathematical method to study the characteristics of pressure change over time, which mainly studies the amplitude, periodicity and other issues, and cannot well describe the causes of pressure pulsation. However, frequency domain analysis is to obtain the spectral characteristics of pressure pulsation in each working condition by fast Fourier transform, and apply mathematical methods to express the causes of pressure pulsation (Zhang et al., 2020).

Figure 11 is the pressure pulsation frequency domain diagram under the rated working conditions of the centrifugal pump, the abscissa indicates the frequency, and the ordinate coordinate is the pressure pulsation coefficient C_p. As shown in **Figure 11**, the first main frequency of the surface pressure ripple of the magnetic liquid sealing film under rated conditions is 291 Hz, the second frequency is 582 Hz, and the third main frequency is 2,328 Hz. The centrifugal pump selected for this article has a rotational speed of 2,910 rpm, which can be known according to the axial frequency calculation **Eq. 7**, and its axis frequency f_n is 48.5 Hz, and according to the leaf frequency calculation **Eq. 8**, the leaf frequency is 291 Hz. It can be seen that the first main frequency of the surface pressure ripple of the magnetic liquid sealing film is the leaf frequency, the second main frequency is two times the leaf frequency, and the third main frequency is eight times the leaf frequency. Therefore, the main reason for the pressure ripple on the surface of the magnetic liquid sealing film is that the impeller periodically sweeps over the fixed surface of the centrifugal pump.

$$f_n = n/60 \tag{7}$$

$$f_r = Zf_n \tag{8}$$

Characteristics of the Surface Pressure Pulsation Frequency Domain of the Magnetic Liquid Sealing Film Under Partial Working Conditions

Figure 12 shows the surface pressure ripple frequency domain diagram of the magnetic liquid sealing film under partial working conditions. It can be seen from the figure that under the working

conditions of each flow of the centrifugal pump, the frequency values of the first main frequency, the second main frequency and the third main frequency are the same, so under each flow condition, the main reason for inducing pressure pulsation on the surface of the magnetic liquid sealing film is the periodic sweeping of the fixed surface of the centrifugal pump by the impeller.

When the centrifugal pump is running at $0.4Q_d$, there is a broadband frequency at 0–291 Hz, and as the flow rate increases, the broadband phenomenon gradually weakens, reaching a minimum at $1.0Q_d$, increasing again at $1.1Q_d$, and then weakening. The reason for this phenomenon is that the centrifugal pump is not fully developed under the operation of small flow conditions, and the internal structure of the centrifugal pump is extremely complex, so its three-dimensional transient flow will cause slight fluctuations in the surface pressure of the magnetic liquid sealing film, and with the increase of the flow rate, the internal fluid flow of the centrifugal pump is fully developed, so the effect on the magnetic liquid sealing film is reduced and the broadband phenomenon is weakened. When the flow rate continues to increase from the rated flow rate, the operating conditions of the centrifugal pump deviate from the design conditions, the fluid in the pump has a more complex non-linear flow, and the phenomenon of liquid return at the outlet of the impeller and the reflection of the liquid at the volute is intensified, and the effect on the surface pressure of the magnetic liquid sealing film increases, so the broadband increases again. When the flow rate is further increased, the fluid development state in the pump is more sufficient than that of the low flow state, and the pressure fluctuation of the magnetic liquid sealing film caused by the non-linear turbulence movement of the fluid in the centrifugal pump has a good inhibitory effect, and the inhibition effect is stronger than the surface pressure of the magnetic liquid sealing film caused by the return of the liquid at the outlet of the impeller and the reflection wave on the wall surface of the volute, so the broadband is reduced again.

When the centrifugal pump is operating at $1.1Q_d$, there is a broadband at the third main frequency at 2328 Hz. Under the remaining flow conditions, the broadband phenomenon at the third main frequency is not obvious. The broadband at this location is mainly caused by the vortex generated by the return of liquid inside the sealed runner. While the liquid in the pump is transported outward after the impeller is periodically pressurized, the high-pressure fluid is periodically transported to the sealed runner, so there is a return flow and vortex liquid generated by the periodic input of the high-pressure fluid in the sealed runner. Under the action of the vortex, the surface of the magnetic liquid sealing film produces high-frequency pulsation, and the cause of the vortex at this place is related to the periodic rotation of the impeller, so the high frequency at this place is an integer multiple of the leaf frequency, that is, 8 times the leaf frequency.

CONCLUSION

(1) There is a good periodicity of pressure pulsation on the surface of the magnetic fluid sealing film, which is the time required for a single blade to sweep through the worm tongue. During a rotary cycle of the rotor, the number of reciprocating movements of the magnetic liquid sealing film is the same as the number of rotor blades.
(2) The pressure fluctuation law at different positions on the surface of the magnetic liquid sealing film is very similar under the same flow condition, and the pressure ripple waveform under different flow conditions is different. When working in the rated working condition of the centrifugal pump and its nearby working condition point, the difference between the peak and peak of the surface pressure pulsation of the magnetic liquid sealing film is less than 2000 Pa, and when it deviates from the rated working condition point, the peak-to-peak difference increases by nearly two times.
(3) Under different flow conditions, the surface pressure pulsation frequency domain diagram of the magnetic liquid sealing film is similar, and the first main frequency is the leaf frequency, the second main frequency is two times the leaf frequency, and the third main frequency is eight times the leaf frequency. The surface pressure ripple of the magnetic liquid sealing film has a broadband phenomenon under the working conditions of 0.4–1.0Qd, and the broadband frequency occurs near 0–291 and 2,328 Hz. The broadband phenomenon obtained at 0–291 Hz decreases by increasing the flow rate, increases again when the flow rate is 1.1Qd, and then decreases with the further increase of the flow rate. The third main frequency of the surface pressure pulsation of the magnetic liquid sealing film is mainly caused by the vortex movement caused by the periodic delivery of high-pressure liquid at the outlet of the impeller in the sealing runner.

DATA AVAILABILITY STATEMENT

The original contributions presented in the study are included in the article/Supplementary Material, further inquiries can be directed to the corresponding author.

AUTHOR CONTRIBUTIONS

KW completed the main writing of the paper, ZL revised the paper, WL and FC provided writing opinions, SY provided experimental guidance, and SP provided software guidance.

FUNDING

This work was supported by the National Natural Science Foundation of China (Grant No. 52079118), Central leading local (scientific and technological innovation base construction) project XZ202201YD0017C.

REFERENCES

Cao, W., Liu, Y., Dong, J., Niu, Z., and Shi, Y. (2019). Research on Pressure Pulsation Characteristics of Gerotor Pump for Active Vibration Damping System. *IEEE Access* 7, 116567–116577. doi:10.1109/access.2019.2936489

Chen, Y., Li, D., Zhang, Y., Li, Z., and Zhou, H. (2020). The Influence of the Temperature Rise on the Sealing Performance of the Rotating Magnetic Fluid Seal. *IEEE Trans. Magn.* 56 (11), 1–10. doi:10.1109/tmag.2020.3023018

Cheng, C., Li, Z., He, F., Wu, S., Zeng, C., Zhang, K., et al. (2022). Influence of Solid–Liquid Two-Phase Flow on Cavitation of Tubular 399 Turbine Blades Under Combined Conditions. *Front. Energy Res.*, 509. doi:10.3389/fenrg.2022.904201

Cheng, C., Li, Z., Peng, S., and Ma, B. (2021). Theoretical Analysis of Entropy Generation at the Blade Interface of a Tubular Turbine under Cooperative Conditions. *Front. Energy Res.*, 763. [J]. doi:10.3389/fenrg.2021.788416

Guo, Z., Xiao, J., Liu, J., and Hu, X. (2019). Comparison of Structured and Unstructured Grids in Marine Controlled Source Electromagnetic Inversions for Offshore Hydrocarbon Exploration. *Mar. Petroleum Geol.* 100, 204–211. doi:10.1016/j.marpetgeo.2018.11.008

He, Xinzhi., Li, Decai., and Wang, Hujun. (2014). The Effect of Gravity on the Sealing Performance of Magnetic Liquids [J]. *J. Vac. Sci. Technol.* 34 (11), 1160–1163. doi:10.13922/j.cnki.cjovst.2014.11.05

Hu, Yuxian (2004). *Research on Flow Simulation of Pumping Station Inflow and Outflow Channel Based on FLUENT Software*. Wuhan, China: Wuhan University. [D].

Jibin Zou, J., Jiming Zou, J., and Jianhui Hu, J. (2003). Design and Pressure Control of High-Pressure Differential Magnetic Fluid Seals. *IEEE Trans. Magn.* 39 (5), 2651–2653. doi:10.1109/tmag.2003.815543

Jin, En (2020). *Research on the Influence of Elbow Inflow on the Internal Flow of Centrifugal Pump*. Xi'an, China: Xi'an University of Technology. [D].

Li, Decai., Hong, Jianping., and Yang, Qingxin. (2002). Research on Magnetic Fluid Sealing of Dry Roots Vacuum Pump. *Vac. Sci. Technol.* 2002 (04), 78–81. [J]. doi:10.13922/j.cnki.cjovst.2002.04.019

Li, W., Li, Z., Qin, Z., Yan, S., Wang, Z., Peng, S., et al. (2022). Influence of the Solution pH on the Design of a Hydro-Mechanical Magneto-Hydraulic Sealing Device. *Eng. Fail. Anal.* 135, 106091. [J]. doi:10.1016/j.engfailanal.2022.106091

Li, W., Li, Z., Wang, Z., Wu, F., Xu, L., and Peng, S. (2021a). Turbulence Intensity Characteristics of a Magnetoliquid Seal Interface in a Liquid Environment. *Coatings* 11 (11), 1333. doi:10.3390/coatings11111333

Li, Z., Li, W., Li, W., Wang, Q., Xiang, R., Cheng, J., et al. (2021b). Effects of Medium Fluid Cavitation on Fluctuation Characteristics of Magnetic Fluid Seal Interface in Agricultural Centrifugal Pump. *Int. J. Agric. Biol. Eng.* 14 (6), 85–92. doi:10.25165/j.ijabe.20211406.6718

Liu, T., Cheng, Y., and Yang, Z. (2005). Design Optimization of Seal Structure for Sealing Liquid by Magnetic Fluids. *J. Magnetism Magnetic Mater.* 289, 411–414. doi:10.1016/j.jmmm.2004.11.116

Lu, Jiaxing (2017). *Study on Cavitation-Induced Unsteady Dynamic Characteristics and Mechanism of Centrifugal Pump*. Zhenjiang, China: Jiangsu University. [D].

Peng, Tao (2021). Centrifugal Pump Mechanical Seal Leakage Phenomenon and Maintenance Countermeasures Research. *Mod. Manu. Tech. and Equi.* 57, 158–159. doi:10.16107/j.cnki.mmte.2021.0480

Qian, Jiguo., and Yang, Zhiyi. (2008). Stability Analysis of Liquid-Liquid Interface of Magnetic Hydraulic Seals. *Fluid Mach.* 36 (12), 21–23. doi:10.3969/j.issn.1005-0329.2008.12.005

Ren, Z. A., Hao, D., and Xie, H. J. (2009). Several Turbulence Models and Their Applications in FLUENT. *Chem. Equi. Tech.* 30, 38–40+44. doi:10.16759/j.cnki.issn.1007-7251.2009.02.005

Szczęch, M. (2020). Magnetic Fluid Seal Critical Pressure Calculation Based on Numerical Simulations. *Simulation* 96 (4), 403–413. doi:10.1177/0037549719885168

Szczech, M. (2018). Experimental Study on the Pressure Distribution Mechanism Among Stages of the Magnetic Fluid Seal. *IEEE Trans. Magn.* 54 (6), 1–7. doi:10.1109/tmag.2018.2816567

Wang, Yaohua (2004). *Numerical Simulation Design of High Temperature Magnetic Fluid Seal and its Application Research*. Wuhan, China: Wuhan University of Technology. [D].

Winslow, P., Pellegrino, S., and Sharma, S. B. (2010). Multi-objective Optimization of Free-form Grid Structures[J]. *Struct. Multidiscip. Optim.* 40 (1), 257–269. doi:10.1007/s00158-009-0358-4

Xu, Bing. (2013). Rui Yannian. Research on Mechanical and Magnetic Fluid Composite Dynamic Sealing Technology of Pressure Reactor Stirring Shaft. *Mech. Des.* 30 (04), 6–10. [J]. doi:10.13841/j.cnki.jxsj.2013.04.012

Xu, Zhaohui (2004). *Study on Three-Dimensional Flow of Full Flow Channel in High-Speed Centrifugal Pump and its Fluid-Induced Pressure Pulsation*. Beijing, China: Tsinghua University. [D].

Xu, Zhenshi., Fan, Jun., and Xie, Yuanjian. (2010). Introduction to Modern Sealing Technology. *Mod. Manuf. Technol. Equip.* 2010 (01), 7–9. doi:10.16107/j.cnki.mmte.2010.01.008

Zeng, H., Li, Z., Li, D., Chen, H., and Li, Z. (2022). Vortex Distribution and Energy Loss in S-Shaped Region of Pump Turbine. *Front. Energy Res.* 10, 904202.

Zhang, Chenghua., You, Jianfeng., Tai, Rong., Wang, Xi., Liu, Ying., and Cheng, Yongguang. (2020). CFD Simulation of Pressure Pulsation during Runaway Process of Water Pump, Turbine, Water Pump and Runaway. *J. Hydroelectr. Power Generation* 39 (04), 62–72. doi:10.11660/slfdxb.20200407

Zhang, H., Li, D., Wang, Q., and Zhang, Z. (2013). Theoretical Analysis and Experimental Study on Breakaway Torque of Large-Diameter Magnetic Liquid Seal at Low Temperature. *Chin. J. Mech. Eng.* 26 (4), 695–700. doi:10.3901/cjme.2013.04.695

Zhao, Guowei., Chi, Changqing., Wang, Zhishan., and Wang, Guangzhen. (2001). Flow Field Analysis of Magnetic Fluid Seal on High-Speed Shaft. *J. Beihang Univ.* 27 (06), 628–631. [J]. doi:10.13700/j.1001-5965.2001.06.003

Zhou, J., Fan, H., and Shao, C. (2016). Experimental Study on the Hydrodynamic Lubrication Characteristics of Magnetofluid Film in a Spiral Groove Mechanical Seal. *Tribol. Int.* 95, 192–198. doi:10.1016/j.triboint.2015.11.018

Zhou, Zhijun., Lin, Zhen., Zhou, Junhu., Liu, Jianzhong., and Cen, Kefa. (2007). Application and Comparison of Different Turbulence Models in the Calculation of Pipeline Flow Resistance. *Therm. Power Gener.* 2007 (01), 18–23. [J]. doi:10.19666/j.rlfd.2007.01.006

Conflict of Interest: Author SP was employed by Huaneng Mingtai Electric Power Co. Ltd.

The remaining authors declare that the research was conducted in the absence of any commercial or financial relationships that could be construed as a potential conflict of interest.

frontiers | Frontiers in Energy Research

ORIGINAL RESEARCH
published: 01 July 2022
doi: 10.3389/fenrg.2022.911874

Experimental and Computational Fluid Dynamics Study of the Flow Field of a Model Pump Turbine

Yuxuan Deng, Jing Xu, Yanna Li, Yanli Zhang and Chunyan Kuang*

Bailie School of Petroleum Engineering, Lanzhou City University, Lanzhou, China

The pumped storage unit has a hump area and S characteristics during operation. The operating conditions of the unit are complex, and it is necessary to switch between working conditions. The unit frequently crosses the hump area and the S characteristic area, thus hindering the unit to connect to the grid. Severe vibration affects the safe and stable operation of a power station. With the joint efforts of the industry, the impact of the hump and S-shaped problems on project commissioning has been fundamentally resolved, but the mechanism of inducing hump and S-shaped problems has not yet been well established. Therefore, in this study, the particle image velocity measurement method based on a full-characteristic test was adopted. According to the operating characteristics of the unit, 32 operating points with four guide-vane opening degrees were selected to test the flow pattern in the vaneless space. After subtracting the average flow velocity, the vortex image of the leafless area was obtained, which provided a reference for the design of the runner of the water pump turbine.

Keywords: pump turbine, pump mode, turbine mode, particle imaging velocimetry, fluid

OPEN ACCESS

Edited by:
Daqing Zhou,
Hohai University, China

Reviewed by:
An Yu,
Hohai University, China
Jintao Liu,
China Academy of Space Technology, China

****Correspondence:***
Yuxuan Deng
lzcsdengyx@163.com

Specialty section:
This article was submitted to Process and Energy Systems Engineering, a section of the journal Frontiers in Energy Research

Received: *03 April 2022*
Accepted: *14 June 2022*
Published: *01 July 2022*

Citation:
Deng Y, Xu J, Li Y, Zhang Y and Kuang C (2022) Experimental and Computational Fluid Dynamics Study of the Flow Field of a Model Pump Turbine. Front. Energy Res. 10:911874. doi: 10.3389/fenrg.2022.911874

INTRODUCTION

Currently, pumped storage power stations are globally used as energy storage devices with huge capacities. As of 2020, the total installed capacity of China's pumped-storage power plants was 40 million kilowatts. A pump turbine is the core component of a pumped storage power station, and its operational stability directly affects the benefit of the power station and the stability of the power grid; thus, it has high research significance.

In the pump mode of a Francis pump turbine, the hump characteristic is a typical feature that may affect the starting stability of the pump mode of the unit (Lu, 2018). Several studies have been conducted on the causes of hump area formation. Gülich (2008) proposed that a sudden change in the flow regime caused the appearance of a hump. The flow regime changes in the hump area have also been studied extensively. Braun et al. (Braun 2009; Eisele et al., 1998; Pacot 2014; Zuo and Liu, 2017; Yin 2011) proposed that the separation of the rotating flow and the pre-swirl of the runner's outflow are the causes of the hump phenomenon. Furthermore, Ciocan et al. (Ciocan and Kueny, 2006; Ubaldi and Zunino, 1990) pointed out that the transfer of the separation zone causes the hump phenomenon. Braun et al. (Braun et al., 2005; Wang 2009; Yao 2015) also proposed that the flow separation at the runner outlet and the flow loss caused by the backflow phenomenon causes the hump phenomenon. Li et al. (2015). (Guedes et al., 2002) proposed that the separation vortex of the guide vane area plays an important role in the formation of hump characteristics. The change in the

TABLE 1 | Table of basic geometric parameters of model.

Parameter	Value
Rated hydraulic head H_r (m)	59.8
Runner inlet diameter D_1 (mm)	556
Runner outlet diameter D_2 (mm)	250
Guide vane height b (mm)	38.258
Number of runner blades Z_r	9
Number of guide vanes Z_g	22
Optimal GVO	14°

flow pattern inside the unit is critical in the formation of the hump area; therefore, it is important to visualize the flow pattern inside the unit.

The vortex motion inside the turbine induces pressure pulsations, such as vortex rope of drafttube (Ji et al., 2022) and channel vortices. The Large eddy simulation is also increasingly being used in the calculation of vortex motion inside turbines (Hu and Zhang, 2020). For internal turbine flow, entropy production theory becomes a new analytical tool. By means of entropy production analysis, the vortex characteristics of the hump and S characteristic area of the pump turbine are correlated with the energy loss phenomenon (Li et al., 2017; Chen 2018). Therefore it is important to study the swirl flow inside the turbine.

Under the working conditions of the Francis pump turbine, the S characteristic is also a phenomenon that hinders the safe and stable operation of the unit. It is affected by the vortex generated by the flow separation development at the inlet of the runner (Li et al., 2013). To verify this assertion, the flow pattern in the vaneless space must be observed.

Particle image velocimetry (PIV), as a transient, multi-point, non-contact hydrodynamic velocity measurement method, has been widely used in researching the internal flow of fluid machinery in recent years. Compared with other non-contact measurement means (such as LDV, ultrasonic measurement, etc.), PIV has the advantages of high accuracy, large imaging area, easy installation, and strong anti-interference ability (Li et al., 2021a)

Yan et al., (2019) used the PIV test method to study the flow pattern inside the runner of a Francis pump turbine, and determined the influence of the impingement angle of the runner blade and the GVO on the flow pattern. Tang et al. (2020), Xu et al. (2021) used the PIV test method to study the inter-blade vortex of a Francis turbine and obtained the initiation and development of the inter-blade vortex. The author also used the PIV test method to test the pump turbine under four-quadrant working conditions. The flow pattern in the vaneless space of the pump turbine was observed, and the vortex change and development laws were obtained (Tang 2020). Liu et al., 2021 studied the vortex structure of the vaneless space of two different runners in–the turbine multiple working conditions under different working conditions through the PIV test. Moreover, they studied the working characteristics of the unit under unstable conditions.

With the rapid development of computer technology, CFD (Computational fluid dynamics) technology has become an important method to study fluid (Li et al., 2021b; Li et al., 2021c). In this study, we employed numerical calculation and PIV test method study the vaneless space of a Francis pump-turbine under pump and turbine modes. The generation and evolution processes of the vortex structure in the vaneless space under different operating conditions were conducted to study the effect of the vortex structure in the vaneless space in the hump zone and the S characteristic zone.

COMPUTATIONAL FLUID DYNAMICS SIMULATION

The typical parameters of the model pump turbine are listed in **Table 1**. The model diagram of the pump turbine is shown in **Figure 1**.

Using ICEM and Turbogrid, the model pump turbine is divided into hexahedral mesh. At the same time, Since the number of grids affects the calculation results, the grid independence is verified (Li et al., 2021a). When the number of grids reached 4.9 million, the efficiency and head fluctuation were less than 0.05%, which met the accuracy required by the numerical simulation. The grid diagram and grid independence diagram are shown in **Figure 2** (Since this article focuses on the flow characteristics of the vaneless space, only the grid of the runner and the guide vane area is shown). The number of grids in each part is shown in **Table 2**.

SST k-ω turbulence model (Menter, 1992; Menter 1994; Menter 1997; Deng et al., 2022) is used in CFD simulation. The SST k-ω model can accurately predict the onset of flow and flow separation at negative pressure gradients, and the SST k-ω model is widely used in the calculation of S-characteristic area and hump area (Xia et al., 2019). In the CFD simulation, only the pump turbine with Optimal GVO is calculated. The operating point parameters are shown in **Table 3**. (Positive and negative flow rates indicate the direction of flow, with positive values in the table when the water flows in the direction of the pump and negative values in the table when the water flows in the direction of the turbine) In the pump condition, the opening inlet and the flow outlet are adopted; in the hydraulic turbine condition, the flow inlet and the opening outlet are adopted.

The unit flow and unit speed are defined as follows:

$$n_{11} = \frac{nD_2}{\sqrt{H}} \tag{1}$$

$$Q_{11} = \frac{Q}{D_2^2\sqrt{H}} \tag{2}$$

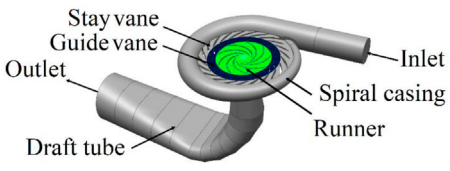

FIGURE 1 | Model pump turbine.

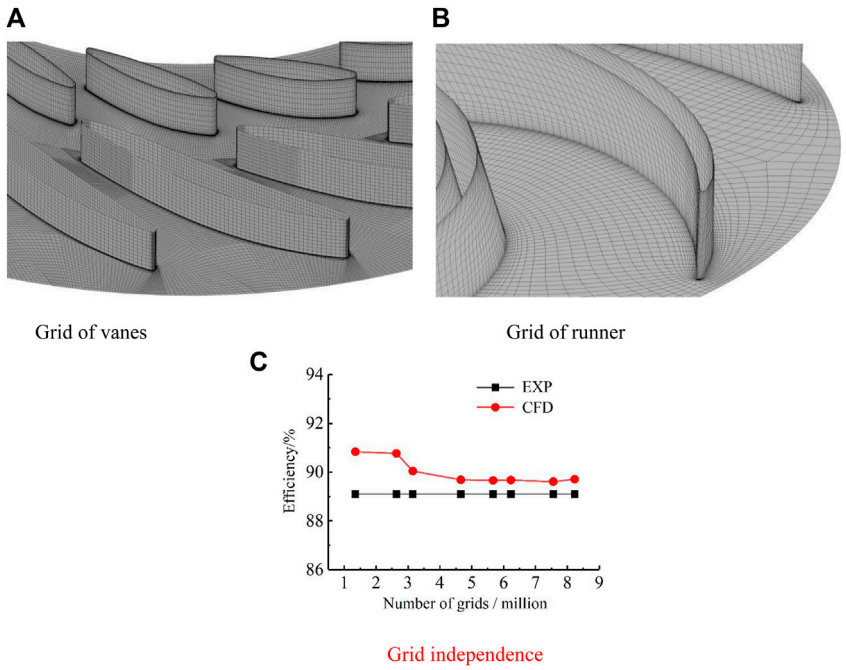

FIGURE 2 | Grids and grid independence. **(A)** Grid of vanes **(B)** Grid of runner **(C)** Grid independence.

TABLE 2 | Number of grids and nodes.

Part	Grid cells	Nodes
Spiral casing	1 052 685	1 005 387
Stay vane	1 072 038	987 630
Guide vane	1 384 504	1 282 424
Runner	1 579 356	1 486 674
Draft tube	547 189	529 856
Total	5 635 772	5 291 971

where n_{11} is the unit speed (rpm), Q_{11} is the unit flow (L/s), n is the speed (rev/min), Q is the flow (L/s), H is the working head (m), and D_2 is the nominal diameter of the runner (m).

This is shown in **Figure 3**, OP14-1 has the best flow pattern, and only one guide vane channel has a vortex. As the unit flow rate (absolute value) decreases, vortices begin to appear in the runner area and continue to increase. At OP14-4, the flow pattern was the worst.In the turbine mode, the flow pattern is the best when OP14-5, and the flow line in the flow channel is smooth at this time, and there is no vortex at all. As the unit flow rate decreases, vortices begin to appear in the guide vane area and runner area, and the number of vortices increases as the unit flow rate decreases.

Although we have obtained the flow characteristics of the flow field inside the unit through CFD simulation, it is very difficult to obtain the flow characteristics of the vaneless space through CFD simulation. Therefore, it is very important to obtain the flow field in the vaneless space through experimental methods.

METHODS

PIV Technology Principle

Particle image velocimetry is a method that uses multiple shots to record the position of particles in the flow field and analyze the captured images to measure the flow velocity. Tracer particles were added to the flow field, and then irradiated by high-frequency pulsed lasers. Using the light reflectivity and followability of the tracer particles to visualize the transient changes in the flow field, the velocity measurement principle is shown in **Figure 4A**.

TABLE 3 | Table of operating point in CFD Simulation. (A positive value represents the direction of the turbine, and a negative value represents the direction of the pump).

Operating Point	Q_{11}/(L/s)	n_{11}/(r/min)	n/(r/min)	Operating Point	Q_{11}/(L/s)	n_{11}/(r/min)	n/(r/min)
OP14-1	−76.6	−36.2	−599.92	OP14-5	−287.05	48.08	599.92
OP14-2	−211.07	−36.25	−599.95	OP14-6	2.99	42.46	599.89
OP14-3	−336.93	−36.03	−599.91	OP14-7	187.02	44.93	599.86
OP14-4	−504.33	−37.78	−599.85	OP14-8	524.09	33.53	599.86

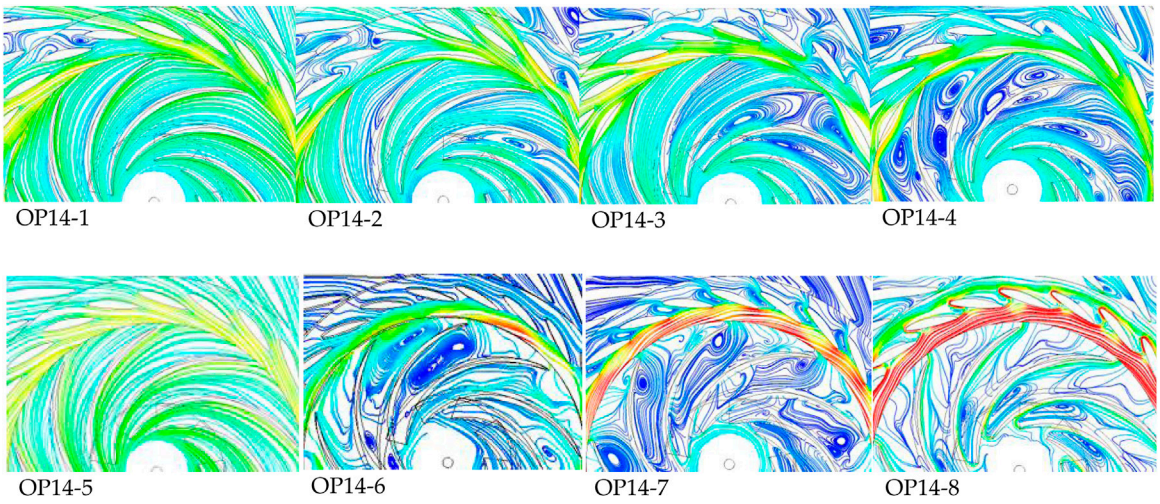

FIGURE 3 | Streamlines of runner and vanes at Span = 0.50.

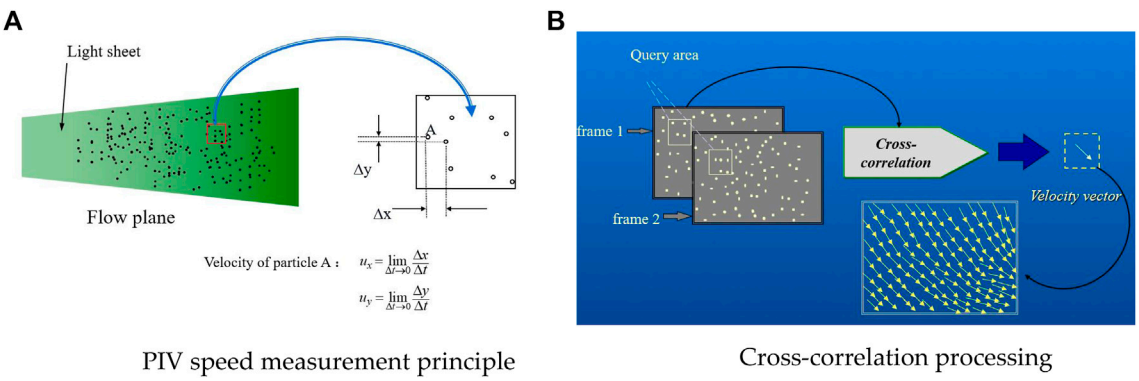

FIGURE 4 | PIV principle. **(A)** PIV speed measurement principle **(B)** Cross-correlation processing.

TABLE 4 | Technical index of PIV test system.

Parameter	Value
Speed measurement range/m/s	0~1,000
Speed measurement accuracy/%	≤1
Measured area/mm2	≥900*1,000
Overall operating frequency/Hz	≤15
Bits	16

In the figure, Vt is the time interval between two exposures, and u_x and u_y are the velocity components of particle A in the x and y directions, respectively. The PIV test images obtained from the test were processed using PIV view3C image analysis software. The software obtains the velocity vector of the flow field through the cross-correlation algorithm, as shown in **Figure 4B**. Except for the tracer particles, the test components used in the PIV test technology were all located outside the flow field to be measured. It is a non-contact indirect fluid velocity measurement technology. Because the density of the tracer particle is comparable to that of the fluid medium, and the light reflectivity and followability were good, the velocity of the tracer particle was considered to be the fluid velocity of the flow field where the particle was located.

PIV System and Model Pump Turbine Parameters

The PIV test system is composed of tracer particles, pulsed laser and sheet light source lens group, CCD camera, synchronizer, and special workstation. The main technical indicators of the PIV test system are listed in **Table 4**. The parameters of the model pump turbine used in the test are consistent with the CFD model.

PIV Test System Transparency Solution

To realize the shooting of the flow pattern in the vaneless space of the model pump turbine, the spiral casing and top cover of the vaneless space of the model pump turbine were opened to set up

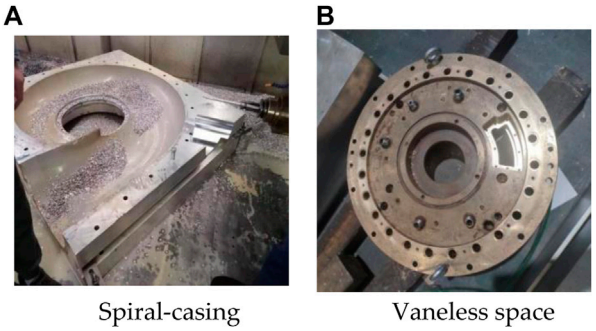

FIGURE 5 | Observation window. **(A)** Spiral-casing **(B)** Vaneless space.

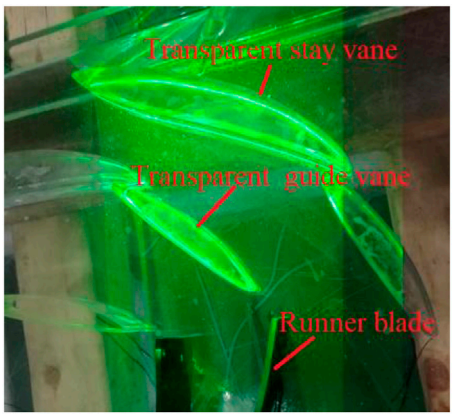

FIGURE 6 | Transparent stay vane and guide vane.

transparent windows. The window material used was plexiglass (polymethyl methacrylate). A physical picture of the observation window of the spiral casing opening and the top cover of the vaneless space is shown in **Figure 5**. Meanwhile, to realize the shooting of the vaneless space, some stay vanes and guide vanes were transparently processed. A picture of the transparent vane is shown in **Figure 6**. A schematic of the laser incident light path and test location are shown in **Figure 7**.

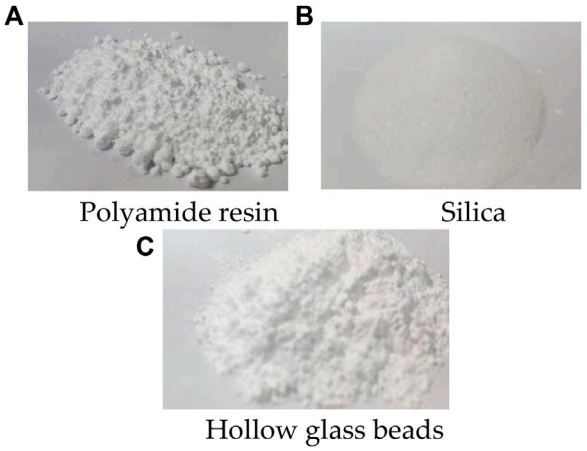

FIGURE 8 | Tracer particles. **(A)** Polyamide resin **(B)** Silica **(C)** Hollow glass beads.

Tracer Particle Selection

Tracer particles are the key test material in the PIV test, and their performance can have a greater impact on the test effect. The tracking particles must meet the requirements of followability and reflectivity. Followability reflects the error of the velocity of the particles and the fluid medium, while the reflectivity has a greater impact on the camera imaging and calculations in the post-processing software. The influence of the particle size, density, and optical properties of the tracer particles on the test should be considered during the preliminary preparation of the test. In the PIV test of this subject, three types of tracer particles were compared through comparative tests, namely polyamide resin particles, silica, and hollow glass beads, as shown in **Figure 8**.

By integrating the test of light reflectivity and followability (Mainly the imaging effect and the deviation from the theoretical flow velocity were velocimetrically measured in a circular tube

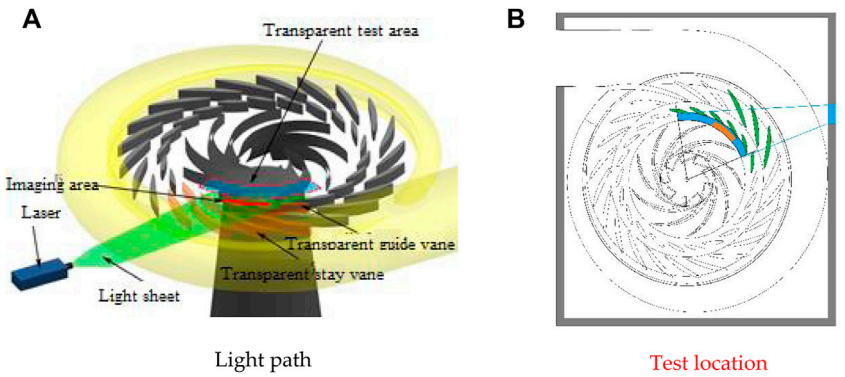

FIGURE 7 | Diagram of laser incident light path. **(A)** Polyamide resin **(B)** Silica.

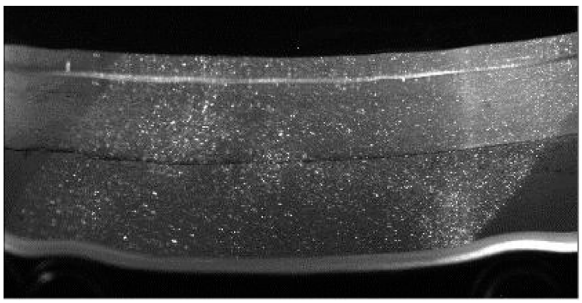

FIGURE 9 | Display effect of hollow glass beads.

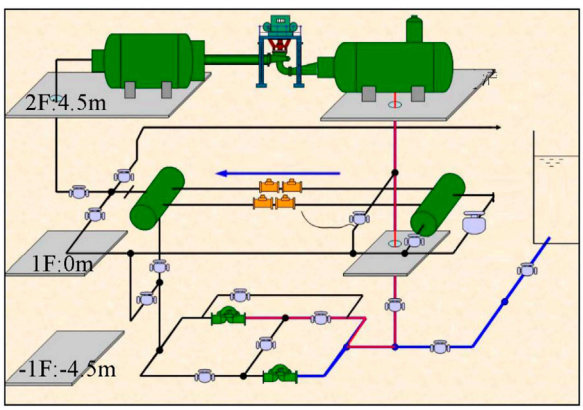

FIGURE 10 | Hydraulic machinery general test bench system.

test to compare the followability.), the tracer particles used in the PIV test observation in this vaneless space are hollow glass beads. The hollow glass beads have a diameter between 10 and 14 μm, and the density (1.0081 g/cm3) is close to that of water. The performance of the tracer particles in the PIV vaneless space test is shown in **Figure 9**.

Test Bench

The structural system of the test bench includes a high-pressure water tank, a model water pump turbine test section (including a dynamometer), a low-pressure water tank, and a vacuum pump system, which is a closed-loop test system. The system was supplied by two 24SA-10 single-stage double-suction centrifugal water pumps. The pumps were connected to two 850 kW bidirectionally rotating DC motors. The DC motors were powered by two sets of fully digital DC speed-regulating devices. The pump unit can realize stable operation within a range of 400 ~ 1,000 r/min. The maximum lift of the single pump was 85 m. The maximum flow rate was 1.0 m^3/s, and the maximum speed was 1,000 r/min. The maximum water head of the test bench was 170 m, and the speed stabilization accuracy was 0.1%. The diameter of the high-pressure pipeline of the system was 500 mm, and that of the low-pressure pipeline was 700 mm. A bidirectional electromagnetic flowmeter was used for flow calibration. The diameter of the high-pressure water tank and the low-pressure water tank of the test bench was 2.4 m. These large containers stabilize the water flow before and after the model unit, and the water flows through the electromagnetic flowmeter. A schematic diagram of the hydraulic test bench is shown in **Figure 10**. The parameters of the test bench are listed in **Table 5**.

TABLE 5 | Table of test bed parameters.

Parameter	Value
Test bench number	DF-150
Maximum test flow/m^3	1.5
Maximum test head/m	150
Maximum test speed/(r/min)	2500
Diameter of model runner/mm	250–500
Maximum power of dynamometer/kW	500
Rated power of pump motor/kW	2×850
Tail water pressure/kPa	−85~ + 250
Uncertainty of efficiency measurement	≤ ± 0.25%
Test bed model type	Counterattack hydraulic machinery

Experiment Procedure

1.Turn on the power and debug the test bench and PIV system.
2.Add tracer particles individually to the draft tube until the display effect meets the requirements.
3.Run the pump turbine according to the test conditions, and then take pictures after the standby group runs stably.
4.After the test is completed in all working conditions, shut down the system, and transfer the original images taken by the CCD camera to the computer for data processing.

A total of 32 operating points under four GVO of 6°, 14°, 18°, and 20° were tested for PIV.

RESULTS AND ANALYSIS

Pump Mode

In the pump mode, a total of 16 operating points was selected for testing, and the test working condition points are listed in **Table 6**.

Flow coefficient φ and head coefficient ψ are defined as follows:

$$\varphi = \frac{4Q}{\pi D^2 u} \tag{3}$$

$$\psi = \frac{2gH}{u^2} \tag{4}$$

where Q is the flow rate, u is the average velocity of the exit section, H is the head, and g is the gravitational acceleration.

The flow pattern in the vaneless space at each operating point is displayed on the flow–pressure coefficient curve of each GVO, as shown in **Figure 11** (The test curve is drawn through the full-characteristic test, and the test points are only part of the full-characteristic operating conditions).

TABLE 6 | Table of operating point in pump mode. (A negative value indicates that the running direction of the unit in the test is the pump direction).

Operating point	Q_{11}/(L/s)	n_{11}/(r/min)	n/(r/min)	Operating point	Q_{11}/(L/s)	n_{11}/(r/min)	n/(r/min)
OP6-1	−32.86	−35.46	−639.84	OP18-1	−115.21	−36.51	−599.93
OP6-2	−70.84	−35.7	−639.9	OP18-2	−192.84	−36.42	−599.89
OP6-3	−206.66	−35.58	−639.88	OP18-3	−322.74	−36.26	−599.89
OP6-4	−348.46	−38.01	−639.87	OP18-4	−540.4	−38.32	−599.84
OP14-1	−76.6	−36.2	−599.92	OP20-1	−96.4	−37.04	−599.92
OP14-2	−211.07	−36.25	−599.95	OP20-2	−240.96	−36.62	−599.86
OP14-3	−336.93	−36.03	−599.91	OP20-3	−467.41	−37.14	−599.86
OP14-4	−504.33	−37.78	−599.85	OP20-4	−704.83	−40.17	−599.92

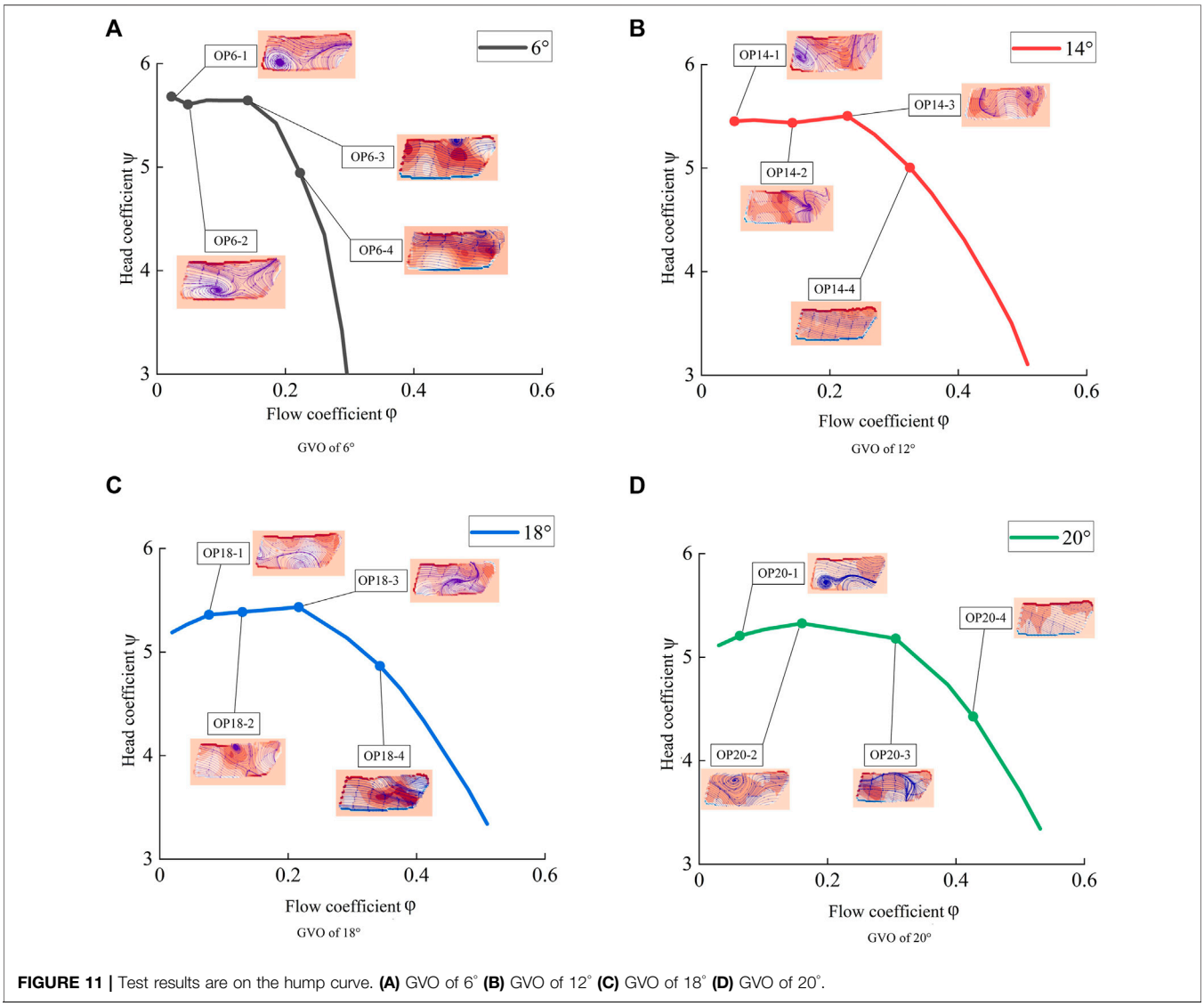

FIGURE 11 | Test results are on the hump curve. **(A)** GVO of 6° **(B)** GVO of 12° **(C)** GVO of 18° **(D)** GVO of 20°.

In the figure, a negative value of vorticity indicates counterclockwise rotation, while a positive value indicates clockwise rotation. In **Figure 8**, as the flow coefficient decreases, the flow state gradually deteriorates. At OP6-3, OP14-3, OP18-3, and OP20-2, the main points of the hump and vortices began to appear. With a decrease in the discharge coefficient, the vortex begins to develop fully, and the existence of the vortex reduces the water flow in the guide vane area. With a further decrease in the discharge coefficient, the vortex begins to separate and develop fully, and the hump phenomenon gradually

TABLE 7 | Table of operating point in turbine mode. (A positive value represents the direction of the turbine, and a negative value represents the direction of the pump).

Operating point	Q11/(L/s)	n11/(r/min)	n/(r/min)	Operating point	Q11/(L/s)	n11/(r/min)	n/(r/min)
OP6-5	−238.71	46.81	599.86	OP18-5	−196.72	45.2	599.91
OP6-6	4.33	39.33	599.88	OP18-6	46.34	44.24	599.95
OP6-7	107.8	40.55	599.92	OP18-7	213.63	45.96	599.82
OP6-8	237.28	31.6	599.91	OP18-8	636.4	34.3	599.95
OP14-5	−287.05	48.08	599.92	OP20-5	−221.64	46.11	599.95
OP14-6	2.99	42.46	599.89	OP20-6	4.78	43.94	599.98
OP14-7	187.02	44.93	599.86	OP20-7	241.42	46.8	599.84
OP14-8	524.09	33.53	599.86	OP20-8	667.8	36.27	599.92

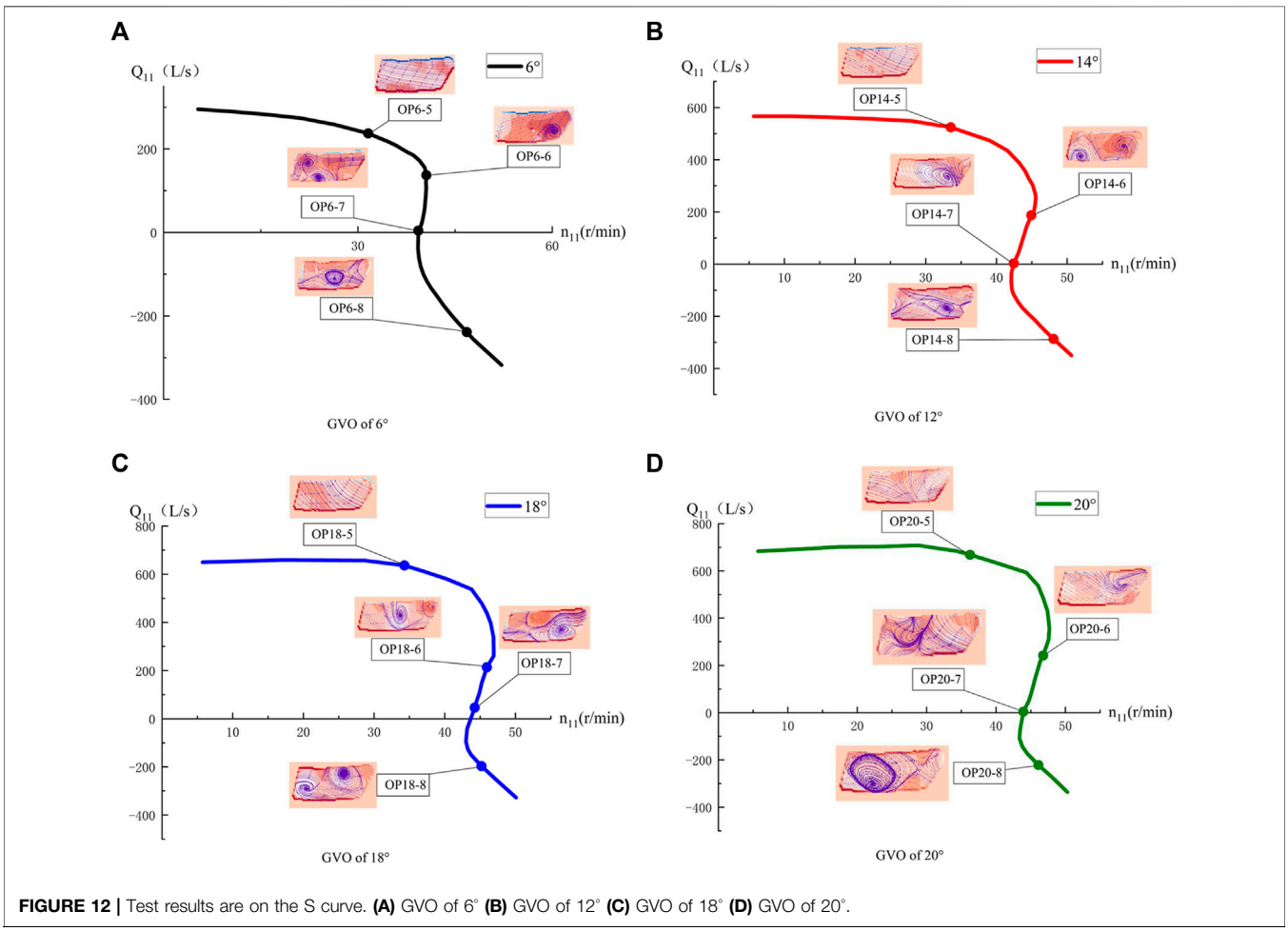

FIGURE 12 | Test results are on the S curve. **(A)** GVO of 6° **(B)** GVO of 12° **(C)** GVO of 18° **(D)** GVO of 20°.

disappears at this time. Water can smoothly pass through the guide vane area, and the pumping capacity is restored. The stall vortex in the vaneless space is an important cause of the hump phenomenon. The vortex structure in the vaneless space under the pump mode is a counterclockwise rotating flow separation phenomenon that starts to occur at the entrance of the rotating wheel flow channel, and the separated flow spreads in the vaneless space and forms a vortex. The vortex structure moves in the vaneless space with water flow in the guide vane area. During the movement, the vortex structure changes the flow field around it, and the streamlines are twisted to form a new vortex structure. At this time, a part of the vortex structure showed a clockwise rotation trend. The blocking effect of these vortices on the water flow hinders water from passing through the guide vane channel, causing a large hydraulic loss. The increase in hydraulic loss causes the effective head of the pump turbine to deviate further from the Euler head, leading to the emergence of the hump phenomenon.

Turbine Mode

In the turbine mode, a total of 16 operating points were selected for testing, and the test working condition points are listed in **Table 7**. The flow pattern in the vaneless space at each operating point is shown in the S characteristic curve of each GVO, as shown in **Figure 9** (The test curve is drawn through the full-characteristic test, and the test points are only part of the operating conditions).

In **Figure 12**, as the unit flow decreases, the flow regime in the vaneless space gradually deteriorates. In high-efficiency zones OP6-5, OP14-5, OP18-5, and OP20-5 of the turbine mode, it can be observed that the internal flow of the vaneless space is even, and the water flow cannot be effectively hindered from entering the interior of the runner. When the unit flow is reduced, the pump turbine deviates from the optimal operating point, and at this time, a flow vortex occurs at the inlet of the runner blade. When entering the no-load condition, a large number of vortices begin to appear in the vaneless space, and the vortices at this time are generated from the de-flow of the fixed guide vane and the wake of the guide vane. Meanwhile, it was observed that vortices with different rotation directions appeared in the leafless area of OP14-6, which may be derived from the Karman vortices generated by the guide vanes. As the unit flow continues to decrease, when entering a small flow condition, the extremely low flow distorts the internal streamline of the vaneless space, generating large-scale vortices, which almost block the vaneless space. In the working condition of the reverse-pump mode, the vortex scale in the vaneless space is large, and a free vortex rotating clockwise appears. In most working conditions, there is a double vortex structure in the visible area, which is derived from the backflow of the pressure surface of the runner blade. The existence of the vortex hinders the normal movement of the water flow in the vaneless space and produces a backflow toward the inlet of the runner. After the recirculation vortex flows out of the runner channel, it moves along the guide vane area of the vaneless space. Because each runner channel has a recirculation vortex, a continuous vortex distribution appears in the vaneless space. The local low pressure caused by these continuous high-speed vortices causes high-frequency characteristics of the pressure pulsation in the vaneless space. Similar to the pump mode, the rotation direction of the vortex rotates clockwise in the turbine mode.

The vortex motion in the S-characteristic zone is an important factor in the unstable operation of the unit. These swirls originate from the strong FSI effects and the violent changes in the speed triangle at the exit of the runner. The strong pressure pulsation phenomenon induced by vortex motion can seriously affect the operational safety of the unit, so the vortex structure in the vane free zone due to different runner configurations can be compared by means of PIV tests to optimize the runner design.

CONCLUSION

The PIV test of the vaneless space was conducted on the model pump turbine under four GVOs of the pump and turbine modes, and the following conclusions were drawn:

1.In the stable operation section of the pump-turbine mode, the water flow in the vaneless space is smooth, and vortices begin to appear after entering the hump zone. The vortices show the characteristics of separation and development as the discharge coefficient decreases.

2.In the pump-turbine mode, the vortices in the vaneless space mostly exist in the form of clockwise rotation, and only a small part of the vortices rotate counterclockwise owing to the influence of the water flow. The size of the vortex in the vaneless space of the hump area is related to the GVO, and the vortex scale is larger when the GVO is small. The hydraulic loss caused by the vortex in the vaneless space is an important cause of the hump phenomenon of the pump turbine.

3.The pump turbine flows steadily in the vaneless space of the high-efficiency zone of the turbine. After the unit flow decreases and enters the low-load zone, large-scale vortices begin to appear. The vortex size gradually increased with a decrease in the unit flow until the vaneless space was blocked. The vortices in the hydraulic turbine operating conditions mostly rotate in a clockwise direction. The continuous distribution of vortices in the vaneless space affects the pressure pulsation in the vaneless space under turbine conditions.

4 The vortex motion in the S-characteristic zone is an important factor in the unstable operation of the unit. These swirls originate from the strong FSI effects and the violent changes in the speed triangle at the exit of the runner.

The limitation of the PIV test for the vaneless space in this paper is due to the fact that we used a 2D PIV device, which is defective for the accurate description of the 3D flow, and we will use a more advanced 3D PIV device to test the vaneless space flow in the next step of our work.

DATA AVAILABILITY STATEMENT

The raw data supporting the conclusion of this article will be made available by the authors, without undue reservation.

AUTHOR CONTRIBUTIONS

The YD wrote and improved the paper; JX provided guidance and advice on writing the paper; YL provided guidance on the analysis of the study, YZ provided guidance on the test apparatus, and CK provided guidance on the tests.

FUNDING

Doctoral Research Foundation of Lanzhou City University (LZCU-BS2019-07), Open Fund of Key Laboratory of Fluid Machinery, Ministry of Education (LTDL 2020-005).

REFERENCES

Braun, O., Kueny, J., and Avellan, F. (2005). "Numerical Analysis of Flow Phenomena Related to the Unstable Energy-Discharge Characteristic of a Pump-Turbine in Pump Mode[C]," in *ASME 2005 Fluids Engineering Division Summer Meeting* (American Society of Mechanical Engineers (ASME)). 2005.

Braun, O. (2009). *Part Load Flow in Radial Centrifugal Pumps*. Zurich: École Polytechnique Fédérale de Lausanne. 2009. doi:10.5075/epfl-thesis-4422

Chen, Q. (2018). *Entropy Production Rate Analysis in S Zone for a Pump-Turbine*. Beijing: Tsinghua University. PhD Thesis.

Ciocan, G., and Kueny, J. (2006). "Experimental Analysis of Rotor Stator Interaction in a Pump-Turbine[C]," in *Proc. XXIII IAHR Symposium on Hydraulic Machinery and Systems* Yokohama, Japan.

Deng, W., Xu, L., Li, Z., Tang, W., Wang, X., Shang, L., et al. (2022). Stability Analysis of Vaneless Space in High-Head Pump-Turbine under Turbine Mode: Computational Fluid Dynamics Simulation and Particle Imaging Velocimetry Measurement. *Machines* 10, 143. doi:10.3390/machines10020143

Eisele, K., Muggli, F., Zhang, Z., Casey, M., and Sallaberger, M. (1998). "Experimental and Numerical Studies of Flow Instabilities in Pump -turbine Stages[C]," in *XIX IAHR Symposium* Singapore. 1998.

Guedes, A., Kueny, J., and Ciocan, G. (2002). "Unsteady Rotor-Stator Analysis of Hydraulic Pump-Turbine: CFD and Experimental Approach[C]," in *21st IAHR Symposium* (Switzerland: Lausaunne). 2002.

Gülich, J. (2008). *Centrifugal Pumps[M]*, 5. Berlin: Springer, 495–505. 2008.

Hu, X., and Zhang, L. (2020). F Numerical Simulation of Unsteady Flow for a Pump-Turbine in Transition Cases with Large-Eddy Simulation. *J. Hydraulic Eng.* 49 (04), 492–500. doi:10.13243/j.cnki.slxb.20170340

Ji, L., Xu, L., and Peng, Y. (2022). Experimental and Numerical Simulation Study on the Flow Characteristics of the Draft Tube in Francis Turbine. *Machines* 10 (4). 2022. doi:10.3390/machines10040230

Li, D., Wang, H., and Xiang, G. (2015). Unsteady Simulation and Analysis for Hump Characteristics of a Pump Turbine Model. *Renew. Energy* 77, 32–42. doi:10.1016/j.renene.2014.12.004

Li, D., Wang, H., Qin, Y., Han, L., Wei, X., and Qin, D. (2017). Entropy Production Analysis of Hysteresis Characteristic of a Pump-Turbine Model. *Energy Convers. Manag.* 149, 175–191. doi:10.1016/j.enconman.2017.07.024

Li, R., Liu, D., and Dong, Z. (2013). Numerical Simulation Analysis of the Whole Flow Passage of Pump Turbine in S-Shaped Area. *J. Drainage Irrigation Mach. Eng.* 31 (05), 401–405. (in Chinese). doi:10.3969/j.issn.1674-8530.2013.05.007

Li, W., Li, Z., and Qin, Z. (2021c). Influence of the Solution pH on the Design of a Hydro-Mechanical Magneto-Hydraulic Sealing Device[J]. *Eng. Fail. Anal.* 135, 106091. doi:10.1016/j.engfailanal.2022.106091

Li, W., Zhenggui, L., Wanquan, D., Lei, J., Yilong, Q., and Huiyu, C. (2021a). Particle Image Velocimetry Flowmeter for Natural Gas Applications. *Flow Meas. Instrum.* 82, 102072. doi:10.1016/j.flowmeasinst.2021.102072

Li, Z., Li, W., Li, W., Wang, Q., Xiang, R., Cheng, J., et al. (2021b). Effects of Medium Fluid Cavitation on Fluctuation Characteristics of Magnetic Fluid Seal Interface in Agricultural Centrifugal Pump. *Int. J. Agric. Biol. Eng.* 14 (6), 85–92. doi:10.25165/j.ijabe.20211406.6718

Liu, D., Ma, L., and Li, N. (2021). Experimental Research on Flow Field of High Head Pump Turbine Based on PIV Test. *IOP Conf. Ser. Earth Environ. Sci.* 627, 012016. doi:10.1088/1755-1315/627/1/012016

Lu, G. (2018). *Investigations on the Influence of the Flow Separation in Guide Vane Channels on the Positive Slope on the Pump Performance Curve in a Pump-Turbine*. Beijing: Tsinghua university. 2018. (in Chinese).

Menter, F. (1992). *Improved Two-Equation K-W Turbulence Models for Aerodynamic Flows*. NASA Ames, CA: NASA Technical Memorandum TM 103975. 1992.

Menter, F. R. (1997). Eddy Viscosity Transport Equations and Their Relation to the K-ε Model. *J. Fluid Eng.* 119, 876–884. doi:10.1115/1.2819511

Menter, F. R. (1994). Two-equation Eddy-Viscosity Turbulence Models for Engineering Applications. *AIAA J.* 32 (8), 1598–1605. doi:10.2514/3.12149

Pacot, O. (2014). *Large Scale Computation of the Rotating Stall in a Pump -turbine Using an Overset Finite Element Large Eddy Simulation Numerical Code [D]*. Zurich: École Polytechnique Fédérale de Lausanne. 2014.

Tang, Z., Liu, X., and Wang, X. (2020). PIV Test Study on the Vaneless Space of Pump Turbine in Four Quadrants Working Condition. *Water Resour. Power* 38 (07), 154–156. (in Chinese).

Tang, Z. (2020). *Experimental and Numerical Study on Channel Vortex of Francis Turbine*. Chengdu: Xihua university. 2020. (in Chinese). doi:10.27411/d.cnki.gscgc.2020.000213

Ubaldi, M., and Zunino, P. (1990). "Experimental Investigation of the Stalled Flow in a Centrifugal Pump-Turbine with Varied Diffuser[C]," in *ASME 1990 International Gas Turbine and Aeroengine Congress and Exposition* (American Society of Mechanical Engineers (ASME)), V001T01A069. 1990.

Wang, H. (2009). *Numerical Simulation and Experimental Research on the Hump Region of Francis Pump Turbine*. Wuhan: Huazhong University of Science and Technology. 2009. (in Chinese).

Xia, L.-S., Cheng, Y.-G., Yang, J.-D., and Cai, F. (2019). Evolution of Flow Structures and Pressure Fluctuations in the S-Shaped Region of a Pump-Turbine. *J. Hydraulic Res.* 57 (1), 107–121. doi:10.1080/00221686.2018.1459893

Xu, L., Jin, X., Li, Z., Deng, W., Liu, D., and Liu, X. (2021). Particle Image Velocimetry Test for the Inter-blade Vortex in a Francis Turbine. *Processes* 9, 1968. doi:10.3390/pr9111968

Yan, R., Bi, Y., and Wu, R. (2019). Study on Flow Characteristics in the Runner of Francis Pump-Turbine Based on Piv Technology. *Chin. J. Hydrodynamics* 34 (06), 720–725. (in Chinese). doi:10.16076/j.cnki.cjhd.2019.06.003

Yao, Y. (2015). *Numerical Study on the Flow Mechanism of the Hump Characteristics of Pump Turbines under Pump Mode*. Beijing: Tsinghua university. (in Chinese).

Yin, L. (2011). Prediction of Pressure Fluctuations of Pump -turbine under Ff-Design Condition in Pump Mode. *J. Eng. Thermophys.* 32 (7), 1141–1144.

Zuo, Z., and Liu, S. (2017). Flow-Induced Instabilities in Pump-Turbines in China. *Engineering* 3 (4), 504–511. doi:10.1016/j.eng.2017.04.010

Conflict of Interest: The authors declare that the research was conducted in the absence of any commercial or financial relationships that could be construed as a potential conflict of interest.

frontiers | Frontiers in Energy Research

METHODS
published: 05 July 2022
doi: 10.3389/fenrg.2022.949639

Influence of Inlet Groove on Flow Characteristics in Stall Condition of Full-Tubular Pump

Lijian Shi[1,2], Yuhang Jiang[1], Yiping Cai[3], Beishuai Chen[4], Fangping Tang[1,2], Tian Xu[1], Jun Zhu[1] and Yao Chai[1]*

[1]College of Hydraulic Science and Engineering, Yangzhou University, Yangzhou, China, [2]Hydrodynamic Engineering Laboratory of Jiangsu Province, Yangzhou, China, [3]Jiangsu Hydraulic Research Institute, Nanjing, China, [4]Jiangsu Pumping Station Technology Co.,Ltd., of South-to-North Water Diverslon Project, Yangzhou, China

The full-tubular pump is a new type of pump with a narrow range of stable operation. In order to improve the internal flow characteristics of the full-tubular pump under small flow conditions and improve the safe and stable operating range of the pump, this paper conducts numerical simulation of the full-tubular pump model based on the Reynolds time-averaged N-S equation and the SST k-ω turbulence model. The improvement mechanism of the parameters of the inlet grooves on the stall area of the full-tubular pump is studied, and the reliability of the numerical simulation of the full-tubular pump is verified by model tests. The research results show that the inlet groove can improve the head and efficiency of the full-tubular pump in the small flow area, and the head at the deep stall condition is increased by nearly 1.61 m. The inlet groove increases the pressure difference of the impeller, which increases the head and improves the hump. At the same time, the increase in the pressure difference of the impeller increases the backflow flow in the gap between the stator and the rotor. The groove can reduce the vortex strength and backflow range at the inlet pipe wall near the stall operating, and also improve the flow field at the impeller inlet. In terms of pressure pulsation, the groove can effectively suppress the low-frequency pressure pulsation at the inlet of the impeller of the full-tubular pump under stall conditions, and effectively reduce the amplitude of the main frequency pressure pulsation and improve the internal flow. The research in this paper can provide a reference for improving the flow characteristics in the stall condition of the full-tubular pump.

Keywords: stall condition, numerical simulation, gap backflow, hydraulic performance, model test, full-tubular pump

OPEN ACCESS

Edited by:
Kan Kan,
College of Energy and Electrical Engineering, China

Reviewed by:
Tianyi Li,
University of Minnesota Twin Cities, United States
Wenjie Wang,
Jiangsu University, China

****Correspondence:***
Lijian Shi
shilijian@yzu.edu.cn

Specialty section:
This article was submitted to Process and Energy Systems Engineering, a section of the journal Frontiers in Energy Research

Received: *21 May 2022*
Accepted: *13 June 2022*
Published: *05 July 2022*

Citation:
Shi L, Jiang Y, Cai Y, Chen B, Tang F, Xu T, Zhu J and Chai Y (2022) Influence of Inlet Groove on Flow Characteristics in Stall Condition of Full-Tubular Pump. Front. Energy Res. 10:949639. doi: 10.3389/fenrg.2022.949639

INTRODUCTION

Every pump has an optimal working condition area. Once it deviates from this area, it will affect the performance of the pump. Especially in the area of small flow conditions, it is easy to generate a saddle zone. The flow state at this working conditions is unstable, which seriously affects the performance and service life of the pump. It is not conducive to the safe and stable operation of the pump. As a new type of mechatronics pump, the full-tubular pump (Tang et al., 2012; Yang et al., 2012; Liu, 2015) has the advantages of compact structure, convenient installation and stable operation, but it has a more obvious saddle zone (Li et al., 2018; Gs et al., 2020; Zhang et al., 2021; Zhang and Tang, 2022) than the axial-flow pump in the area of small flow conditions. Shi et al. (Shi et al., 2020; Shi et al., 2021a; Shi et al., 2021b) analyzed the backflow clearance of the full-tubular pump and found that when the clearance is constant,

as the flow rate of the impeller decreases, the backflow of the clearance increases and the closer it is to the rim, the greater the influence of backflow. In terms of pressure pulsation, Zhang et al. (2017a); and Zhang et al. (2017b) found that under different working conditions, the main frequency of the pressure pulsation at the inlet and outlet of the impeller is the blade frequency, and the main frequency of the guide vane changes with the flow.Kan et al. (2018); Kan et al. (2021a) studied the internal flow of the axial-flow pump under the stall condition, and used the Q-criterion to study the evolution law of the guide vane vortex structure core under the deep stall condition. It is found that the evolution law of the vortex core area is basically the same as the streamline diagram of the guide vane and the low frequency pressure pulsation is caused by the vortex in the guide vane.Zheng et al. (2011); Zheng et al. (2017) analyzed the flow characteristics of the axial-flow pump under small flow conditions, and found that there is backflow at the front edge of the back of the blade near the rim and the trailing edge near the hub under stall conditions.Chen et al. (2012) analyzed the impeller inlet flow field of an axial-flow pump under small flow conditions, and found that the secondary backflow in the pump would lead to inlet pre-swirl, which is reflected in the saddle zone in the performance curve. At present, the improvement methods (Zhang et al., 2013; Wang et al., 2020a; Kan et al., 2021b; Wang et al., 2022) in the area of small flow conditions include slitting the impeller blades, adding front guide vanes, and applying grooves in the wall of inlet pipe. Wang et al. (2016) studied the slit at the impeller inlet of a centrifugal pump and found that the slit at the blade inlet can improve the cavitation performance of the centrifugal pump, and the energy distribution in the impeller channel is more uniform after slitting. Qu et al. (2021) added a bracket at the inlet water guide cone of the axial-flow pump, and found that the inlet water guide cone bracket effectively suppressed the range and intensity of the backflow vortex, and reduced the low-frequency pressure fluctuation, improving the stability of the overall pump device. As for the groove (Saha et al., 2000; Zhang and Chen, 2014; Feng et al., 2018; Wang et al., 2020b; Mu et al., 2020) of the inlet pipe, many scholars at home and abroad have made grooves on the inlet pipe wall of the axial flow pump and mixed flow pump. They found that the axial groove can reduce the back flow of the blade, improve the hump of the pump, and improve the head and efficiency of small flow conditions.

In this paper, according to the flow instability characteristics of the full-tubular pump under small flow conditions, the internal flow mechanism is revealed and the influence of the grooves on the inlet pipe wall on the performance of the full-tubular pump will be explored. The influence of the geometrical parameters of the grooves on the head and efficiency of the full-tubular pump was explored, and the optimal scheme was selected to compare with the original scheme, and the improvement effect of the grooves on the stall condition of the full-tubular pump was explored.

1 NUMERICAL CALCULATION

1.1 Calculation Model

The full-tubular pump model used in this paper does not consider the coil arrangement. The impeller diameter (D_1) is 350mm, the number of blades is 4, the backflow gap between the stator and rotor of the full-tubular pump is 0.65mm, the speed (n_s) is 950r/min, and the hub ratio (d_{h1}) is 0.4. The diameter (D_2) of the guide vane is 350mm, the number of blades is 7, and the hub ratio (d_{h2}) is 0.4. The three-dimensional calculation model of the full-tubular pump is shown in **Figure 1**, including the inlet pipe, impeller, motor rotor, guide vane and the outlet pipe. Axial grooves are uniformly distributed at the outlet of the inlet pipe near the impeller. The number of axial grooves is 40, the groove length is L (L/D_1 = 0.67), that is, the groove length is 230 mm.

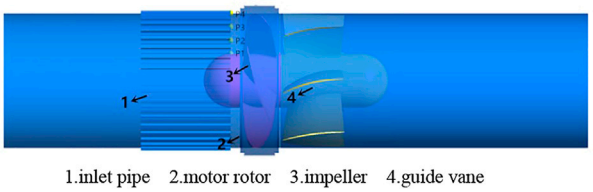

FIGURE 1 | 3D model of numerical calculation of full-tubular pump.

1.2 Meshing and Mesh Independence Verification

The model grid of the computational domain adopts the block drawing method. The impeller and guide vane are imported into Turbo-Grid for modeling and dividing the structured grid. The number of impeller grids is about 600,000, and the number of guide vane grids is about 800,000. The grooved inlet pipe and the motor rotor are modeled by UG, and the unstructured grid is divided by ICEM and the grid of the pipe wall is refined. The number of grids is about 700,000 and 1,700,000 respectively, the grid quality is above 0.5, and the y + value of each part of this paper is controlled within 100 to meet the calculation requirements. The grid diagram of the main components of the calculation model of the full-tubular pump is shown in **Figure 2**.

In order to avoid the influence of the number of grids on the calculation results, the grid-independent analysis of the calculation domain was carried out in the design condition (Q_d = 390L/s). As shown in **Figure 3**, it can be found that when the total number of grids is from 4.2 million to 8 million, the increase in the number of grids has little effect on the efficiency of the full-tubular pump. In order to save computing resources and reduce the total calculation time, the total number of grids was finally selected as 4.2 million for further numerical calculation of the full-tubular pump.

1.3 Governing Equations and Boundary Conditions

In this paper, ANSYS CFX is used to carry out the numerical calculation of the full-tubular pump. The control equation adopts the time-averaged Navier-Stokes equation, and the turbulence model adopts the SST k-ω turbulence model. The turbulence model has high predictability in terms of internal flow and external energy characteristics. Especially for the flow separation under the adverse pressure gradient, it has high prediction accuracy.

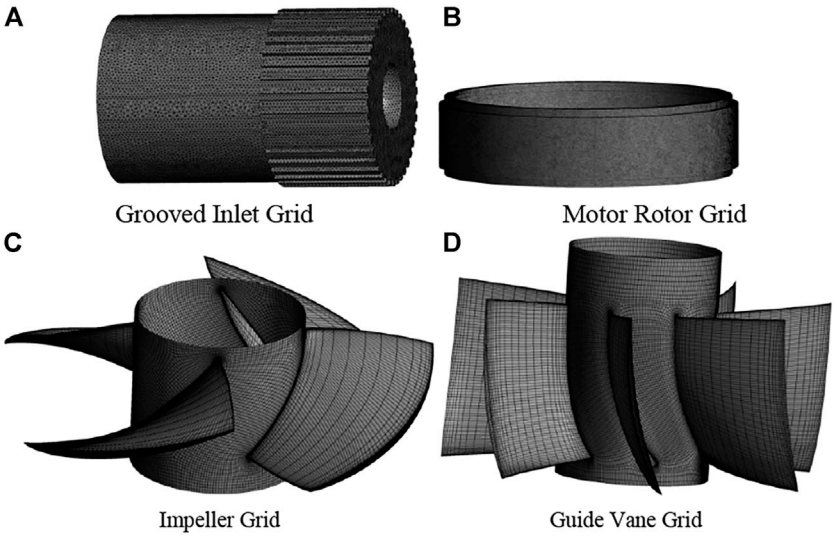

FIGURE 2 | Meshing of the main components of the computational domain. **(A)** grooved inlet grid, **(B)** motor rotor grid, **(C)** impeller grid, **(D)** guide vane grid.

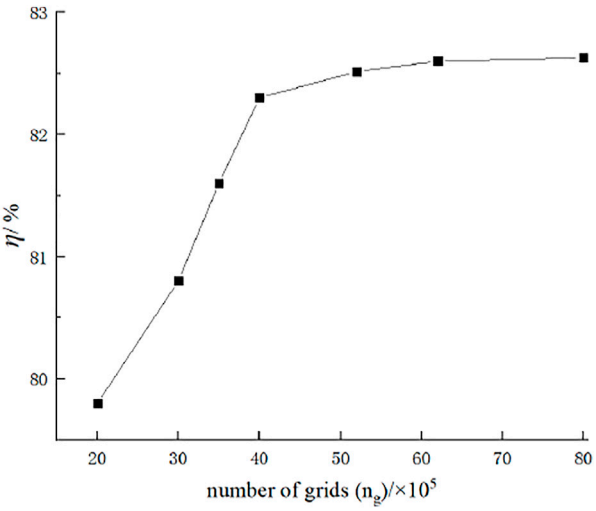

FIGURE 3 | Grid-independent analysis of computational domain of the full-tubular pump.

The continuity equation is:

$$\frac{\partial u_i}{\partial x_i} = 0 \tag{1}$$

The Navier-Stokes equation is:

$$\rho\frac{\partial u_i}{\partial t} + \rho u_j\frac{\partial u_i}{\partial x_j} = \rho f_i - \frac{\partial p}{\partial x_i} + \mu\frac{\partial^2 u_i}{\partial x_j \partial x_j} \tag{2}$$

Where u_i is fluid the velocity, ρ is the fluid density, f_i is mass force, p is pressure intensity, u is dynamic viscosity, and x_i and x_j are position vectors.

The turbulent eddy viscosity u_t, the turbulent energy k equation and the turbulent eddy frequency ω equation are as follows:

$$\mu_t = \rho\frac{k}{w} \tag{3}$$

$$\frac{\partial(\rho k)}{\partial t} + \frac{\partial}{\partial x_j}\left(\rho U_j k\right) = \frac{\partial}{\partial x_j}\left[\left(\mu + \frac{\mu_t}{\sigma_{k1}}\right)\frac{\partial k}{\partial x_j}\right] - \beta_1\rho k\omega + P_k \tag{4}$$

$$\frac{\partial(\rho\omega)}{\partial t} + \frac{\partial}{\partial x_j}\left(\rho U_j \omega\right) = \frac{\partial}{\partial x_j}\left[\left(\mu + \frac{\mu_t}{\sigma_{\omega 1}}\right)\frac{\partial \omega}{\partial x_j}\right] + \alpha_1\frac{\omega}{\mathrm{k}}P_k - \beta\rho\omega^2 \tag{5}$$

Where k is the turbulent kinetic energy, ω is the turbulent frequency, ρ is the fluid density, U_j is the velocity vector, P_k is the production rate of turbulence, x_j is position vectors, The model constants are given by: $\beta_1 = 0.09$, $\alpha_1 = 5/9$, $\beta = 0.075$, $\sigma_{k1} = 2$, $\sigma_{\omega 1} = 2$.

The boundary conditions are: the inlet is set to total pressure and the pressure is 1 atm; the outlet is set to mass-flow, and the design flow is 390L/s; the flow is incompressible and the density is constant everywhere; the flow-passing part adopts a smooth non-slip wall. Set the impeller and rotor as rotating domains and the other computational domains as stationary domains. At the same time, for the unstable stall condition, this paper conducts an unsteady calculation of the flow field inside the full-tubular pump. The dynamic and static interface is set to Transient Rotor Stator, the time step is set to 5.2632×10^{-4}s, each time step the impeller rotates 3°.

2 MODEL TEST AND SCHEME SELECTION

2.1 Numerical Reliability Verification

Numerical simulation is carried out on the calculation model of the initial full-tubular pump without the grooved inlet pipe in

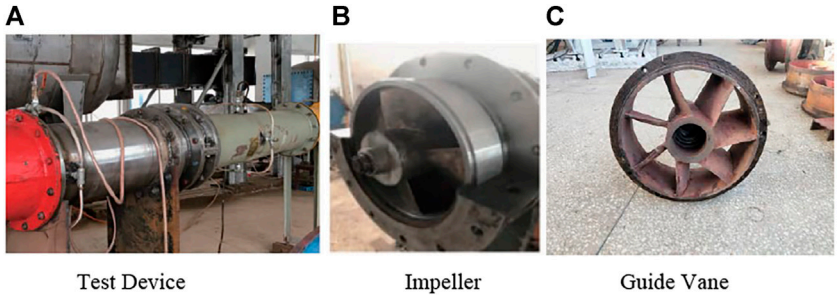

FIGURE 4 | Model pump device. **(A)** test device, **(B)** impeller, **(C)** guide vane.

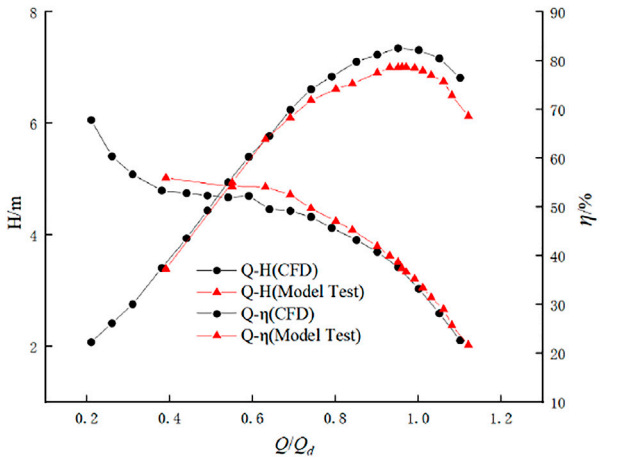

FIGURE 5 | Model test and numerical simulation comparison.

Figure 1, and compared with the existing model experiments. In this paper, the model test of the full-tubular pump is carried out on the high-precision vertical closed-cycle hydraulic mechanical test bench. The actual test picture is shown in **Figure 4**.

The test refers to the relevant model test procedures, and the external characteristics experiment of six blade placement angles is carried out on a full-tubular pump with a clearance of 0.65 mm. Each placement angle has at least 18 test points. In this paper, the blade placement angle is 0°for comparative research.

According to the comparison in **Figure 5**, it can be seen that the flow-head curve of the test and numerical simulation of the full-tubular pump is in good agreement near the design condition, and the maximum head error value is 0.23 m under the small flow condition ($Q/Q_d = 0.62$); The flow-efficiency curve has a high degree of agreement near the small flow condition. The experimental efficiency under the design condition is 78.83%, the numerical simulation efficiency is 82.24%, and the error value is 3.41%. The head and efficiency errors are within the allowable range and meet the calculation accuracy requirements. Through the comparison between the test and the numerical simulation of the full-tubular pump, it shows that the numerical simulation (Kan et al., 2020) of the full-tubular pump in this paper is accurate and credible.

2.2 Influence of Inlet Groove Parameters on Hydraulic Performance of Full-Tubular Pump

In this paper, the number of grooves n, the groove length L and the groove depth h are respectively studied to explore the degree of improvement of the saddle zone of the full-tubular pump with different groove parameters, and select the optimal solution for analysis. Take the number of grooves $n = 40, 60$, the groove length $L/D_1 = 0.33$ and 0.67, and the groove depth $h/D_1 = 0.01, 0.02, 0.03$ for comparison. The specific parameter corresponding scheme is shown in **Tab.1**.

According to **Figure 6**, it can be found that the flow-head curve of scheme Ⅰ has a long flat section with the decrease of the flow rate in the small flow condition, indicating that the pump has entered the stall area operation at this time. After the inlet pipe is grooved, it is found that the saddle zone is significantly improved in this working condition, the flat head section basically disappears, and the efficiency is improved under the small flow conditions. Compared with other groove parameters, the length of the groove has the greatest influence on the head of the full-tubular pump, and when the number of grooves and the groove length are constant, the groove depth of 0.02 is better. Among all the schemes, scheme Ⅲ is the best, which is embodied in: in terms of head, the head near the deep stall condition ($Q/Q_d = 0.40$) is about 1.61 m higher than scheme one; In terms of efficiency, it is about 1.5% smaller than that of scheme Ⅰ near the design flow, but the efficiency is improved by about 2.2% under small flow conditions. By comparison, this paper selects the original scheme, scheme Ⅰ, and the optimal scheme, scheme Ⅲ, to analyze the internal flow field.

COMPUTATIONAL RESULTS AND ANALYSIS

Variation of Static Pressure of Full-Tubular Pump

In order to analyze the influence of grooves on the working performance of each component of the full-tubular pump, **Figure 7B** describes the pressure difference changes of the

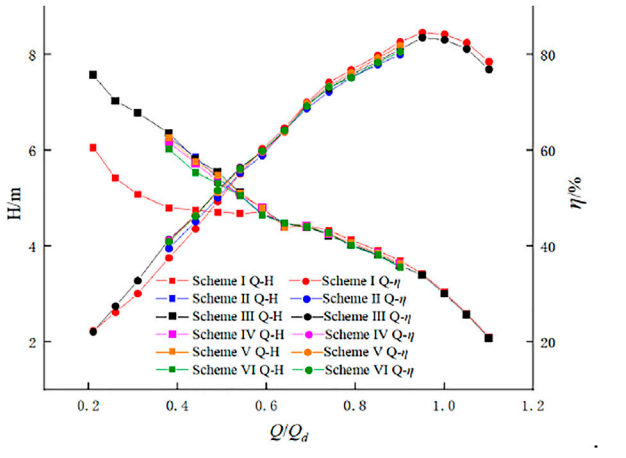

FIGURE 6 | Performance curves under different groove parameters.

full-tubular pump under the conditions of $Q/Q_d = 0.40$ and $Q/Q_d = 0.62$. The central cross section of the impeller blade is taken as the reference plane, and the direction of the water flow is positive, D_1 is the diameter of the impeller, and X/D_1 represents the relative position to the reference plane, as shown in **Figure 7A**. ΔH represents the static pressures between the cross section of the corresponding relative position and the inlet, and the specific formula is as follows:

$$\Delta H = \frac{P_{X_i} - P_{inlet}}{\rho g} \tag{6}$$

It can be seen from the **Figure 7B** that when $Q/Q_d = 0.62$, the changes of the pressures between the two schemes are almost the same, indicating that the groove has no effect on the performance of the full-tubular pump before entering the saddle zone, that is, when the stall does not occur. When the full-tubular pump is in deep stall $Q/Q_d = 0.40$, it can be found that the pressure difference value of scheme III in the impeller area is 1.32 times that of scheme I, indicating that the groove greatly improves the pressure difference in the impeller area. This can also explain why the head of the groove schemes in **Figure 6** has a significant increase in the saddle zone. The negative pressure area of scheme I in the inlet pipe area is significantly higher than that of scheme III, indicating that scheme I has a longer backflow. In the guide vane area, the variation law of the pressure difference between the two schemes is almost the same.

Analysis of Inlet Pipe Flow Field

In order to analyze how grooving affects the hydraulic characteristics of the full-tubular pump, the axial velocity cloud diagrams and streamline diagrams of the inlet pipe and impeller under two different working conditions ($Q/Q_d = 0.62$, 0.40) in the saddle zone are taken in this paper, as shown in **Figure 8**. Through comparison, it can be found that when $Q/Q_d = 0.62$, there is no obvious difference in the flow state of the inlet pipe of the two schemes, indicating that the

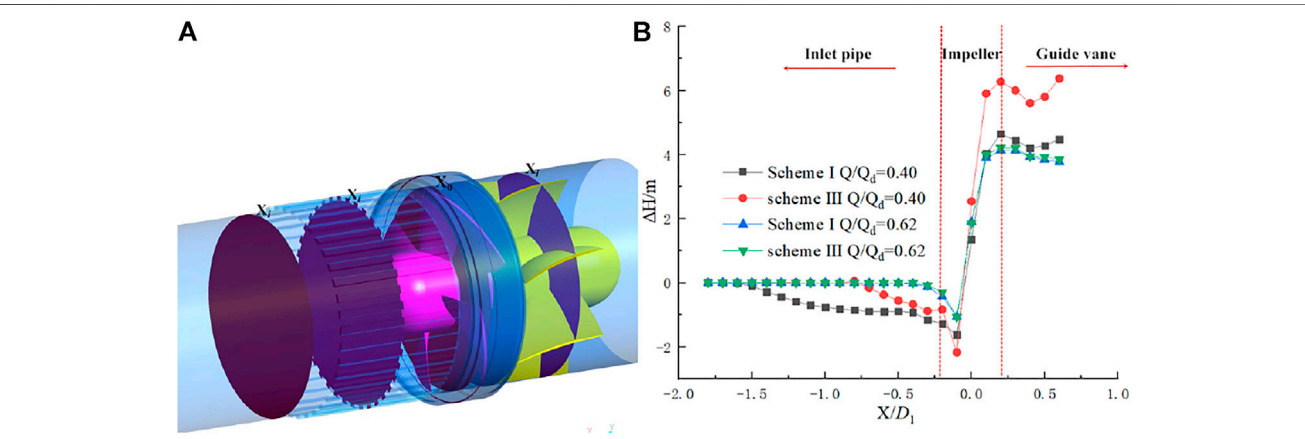

FIGURE 7 | Variation of hydraulic performance in different computational domains.

TABLE 1 | Schemes of inlet grooves of different full-tubular pumps.

	Number of grooves *n*	Groove length L/D_1	Groove Depth h/D_1
Scheme I	0	0	0
Scheme II	60	0.67	0.02
Scheme III	40	0.67	0.02
Scheme IV	40	0.67	0.03
Scheme V	40	0.67	0.01
Scheme VI	40	0.33	0.02

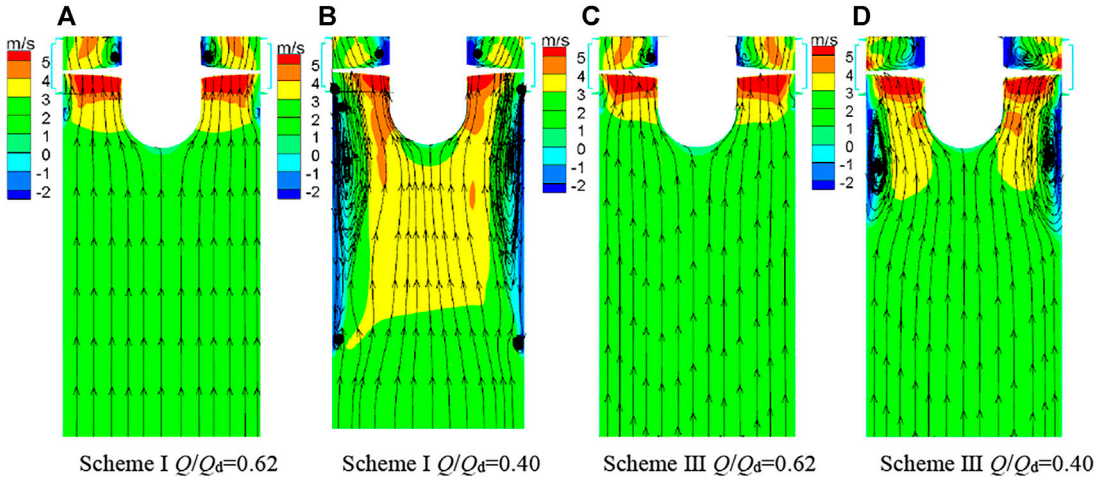

FIGURE 8 | Internal flow characteristics of the inlet pipe and impeller of the full-tubular pump. **(A)** Scheme I Q/Qd=0.62, **(B)** Scheme I Q/Qd=0.40, **(C)** Scheme III Q/Qd=0.62, **(D)** Scheme III Q/Qd=0.40.

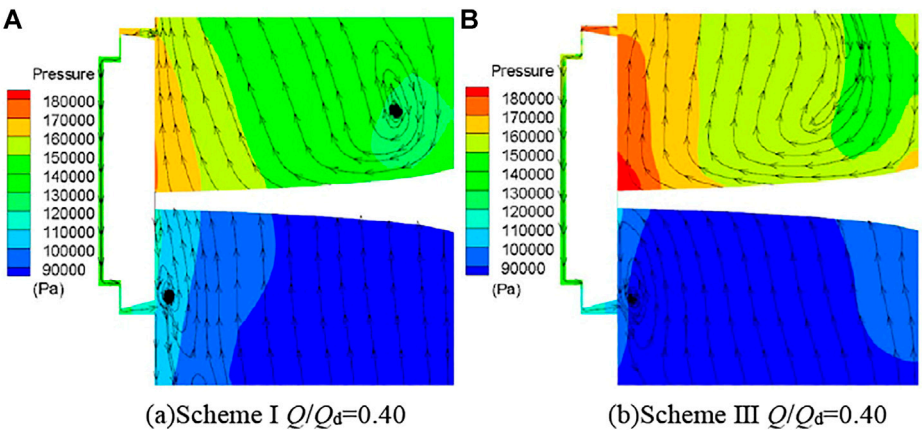

FIGURE 9 | Characteristics of internal flow in the gap of the full-tubular pump. **(A)** Scheme I Q/Q_d = 0.40 **(B)** Scheme III Q/Q_d = 0.40.

groove does not affect the flow state of the design condition. In the deep stall condition, the velocity distribution of the inlet pipe of scheme I is uneven, and the velocity gradient changes greatly at the impeller inlet. In scheme III, it is obvious that the velocity distribution of the inlet pipe is uniform, and the velocity gradient of the impeller inlet is slowed down, which also explains why the groove can increase the head and efficiency of the full-tubular pump under small flow conditions. It can also be found that in the case of deep stall conditions (Q/Q_d = 0.40) in scheme I, there are obvious vortices and backflows at the impeller inlet near the wheel rim, which seriously squeeze the flow state of the inlet pipe, especially at the side wall of the inlet pipe. From **Figure 8D**, we can see that the groove effectively reduces the vortex strength and backflow range of the full-tubular pump under stall conditions, and the flow pattern of the inlet pipe is significantly improved compared with the scheme I.

Since the backflow gap in the full-tubular pump has a great influence on the hydraulic characteristics of the impeller, for the vortex and backflow changes when Q/Q_d = 0.40, this paper analyzes the effect of grooves on the gap flow characteristics under this working condition. It can be seen from **Figure 9** that since the backflow flow in the gap flows from the rim of the impeller outlet to the rim of the inlet of the impeller, there is an obvious bias flow from the outlet of the impeller to the rim of the impeller in scheme I. In the scheme III, the pressure at the backflow inlet of the gap increases due to the groove, so that the bias flow phenomenon at the outlet of the impeller is improved.

As shown in **Figure 10**, the gap backflow of scheme I increases gradually as the flow rate decreases, and the pressure difference between the inlet and outlet of the impeller also gradually increases. However, when Q/Q_d = 0.62, the backflow begins to decrease, and the growth of the inlet and outlet pressure difference begins to slow down. However, the backflow in the

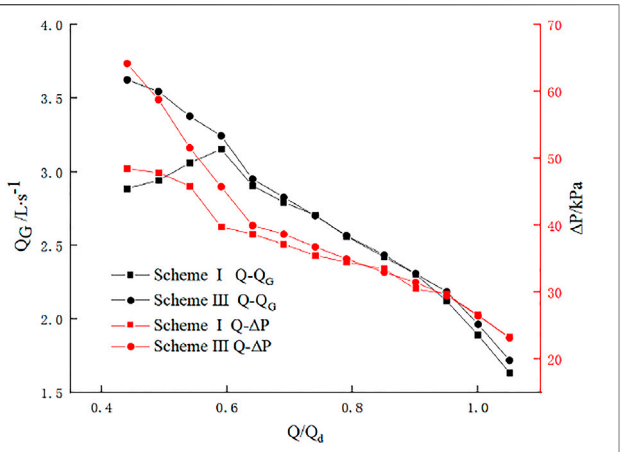

FIGURE 10 | Gap backflow and pressure difference between impeller inlet and outlet under all working conditions.

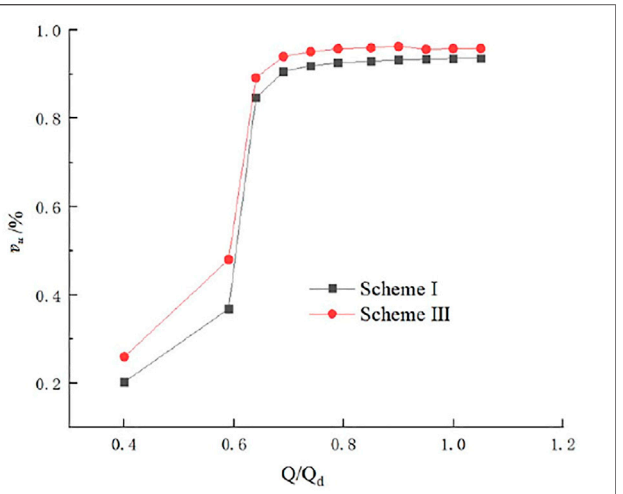

FIGURE 11 | Impeller inlet axial velocity uniformity under all working conditions.

gap of scheme III keeps increasing as the flow rate decreases, and the pressure difference between the inlet and outlet of the impeller still increases rapidly when Q/Q_d = 0.62 due to the groove. The increase in the pressure difference between the inlet and outlet of the impeller increases the head of the full-tubular pump behind the groove in the stall condition, and at the same time, the gap backflow at the stator and rotor also increases.

Axial Velocity Uniformity of the Impeller Inlet

In order to further illustrate the degree of turbulence of the impeller inlet flow field of the two, this paper uses the axial velocity distribution uniformity to describe the quality of the impeller inlet flow state. The calculation formula is:

$$\bar{v}_u = \left\{ 1 - \frac{1}{\bar{v}_a} \sqrt{\left[\sum_{i=1}^{n} (v_{ai} - \bar{v}_a)^2 \right] / n} \right\} \times 100\% \qquad (7)$$

Where $\bar{v}_u$ is the uniformity of the axial velocity distribution of the impeller inlet section, %; $\bar{v}_a$ is the average axial velocity of the impeller inlet section,m/s; v_{ai} is the axial velocity of each calculation unit of the impeller inlet section, m/s; n is the number of units divided in the calculation of the impeller inlet section.

Figure 11 shows the axial velocity uniformity of the impeller inlet under all working conditions. It can be seen that the values of scheme III are higher than those of scheme I. Under the design conditions (Q/Q_d = 1.0), the axial velocity uniformity values of the two schemes are both higher than 92%, indicating that the grooves have no influence on the impeller inlet flow state under the design conditions and large flow conditions. When the flow rate decreases, the uniformity values of the two schemes both decrease and the decreasing trend of scheme I is higher than that of scheme III. When in the deep stall condition (Q/Q_d = 0.40), we can see that the axial velocity uniformity value of scheme III is increased by nearly 10%, indicating that the groove improves the flow state of the impeller inlet. This also proves the reliability of the velocity cloud diagrams and streamline diagram of the inlet pipe and impeller in **Figure 8** and **Figure 9**.

Analysis of Impeller Inlet Pressure Pulsation

The above analysis of the inlet flow field of the full-tubular pump shows that under the stall condition, there are complex flows such as vortex and secondary backflow at the impeller inlet, which may cause hydraulic excitation, and the pressure pulsation is the main manifestation of hydraulic excitation. In this paper, four monitoring points are set along the radial direction at the impeller inlet section (as shown in **Figure 1** P1-4), to study the effect of grooves on the pressure pulsation of the impeller inlet of the full-tubular pump. The rotational frequency f_n of the blade and the pressure pulsation coefficient C_p are cited as indicators for evaluating the internal pressure pulsation characteristics. The formula is as follows:

$$f_n = \frac{60F}{n} \qquad (8)$$

$$C_p = \frac{\Delta P}{0.5\rho u^2} \qquad (9)$$

Where F is the actual frequency after taking the Fourier transform; n is the impeller speed; ΔP is the difference between the instantaneous pressure and the time-averaged pressure; ρ is the liquid density; u is the peripheral speed of the blade tip.

Figure 12 shows the time domain diagram of the impeller inlet pressure pulsation under the deep stall condition. The periodicity of the pressure pulsation changes in the two schemes is good. There are four obvious peaks and troughs in one rotation cycle of the impeller, which are consistent with the number of blades, which indicates that the impeller is the main factor for inducing hydraulic vibration. The pressure pulsation amplitude of scheme I changes drastically, while the change of the pressure pulsation amplitude of scheme III after slotting is much smaller than that of

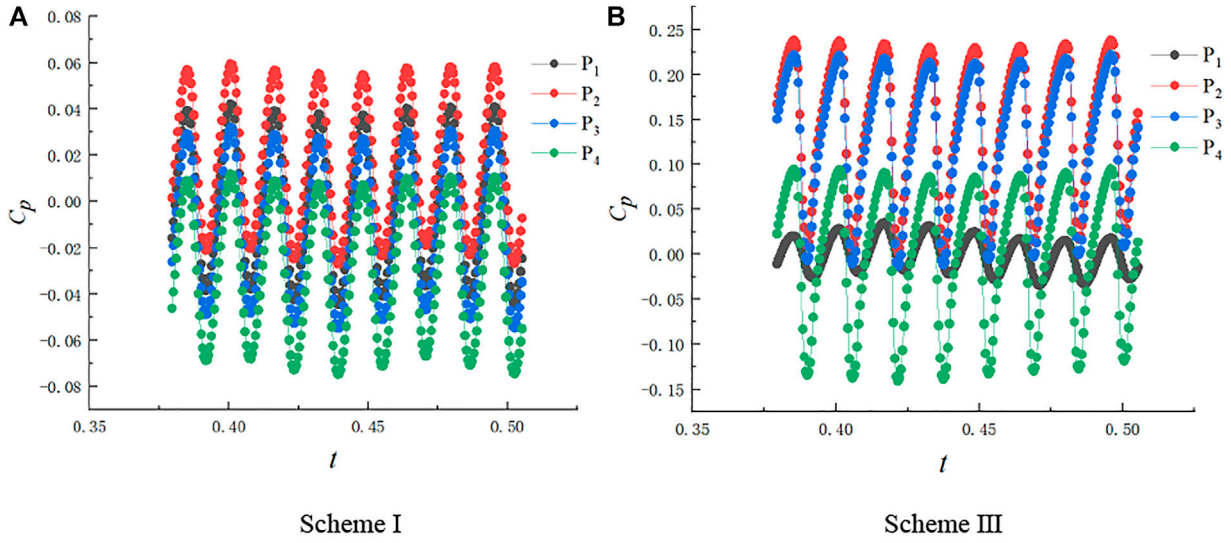

FIGURE 12 | Time domain diagram of impeller inlet pressure pulsation(Q/Q_d = 0.40). **(A)** Scheme I, **(B)** Scheme III.

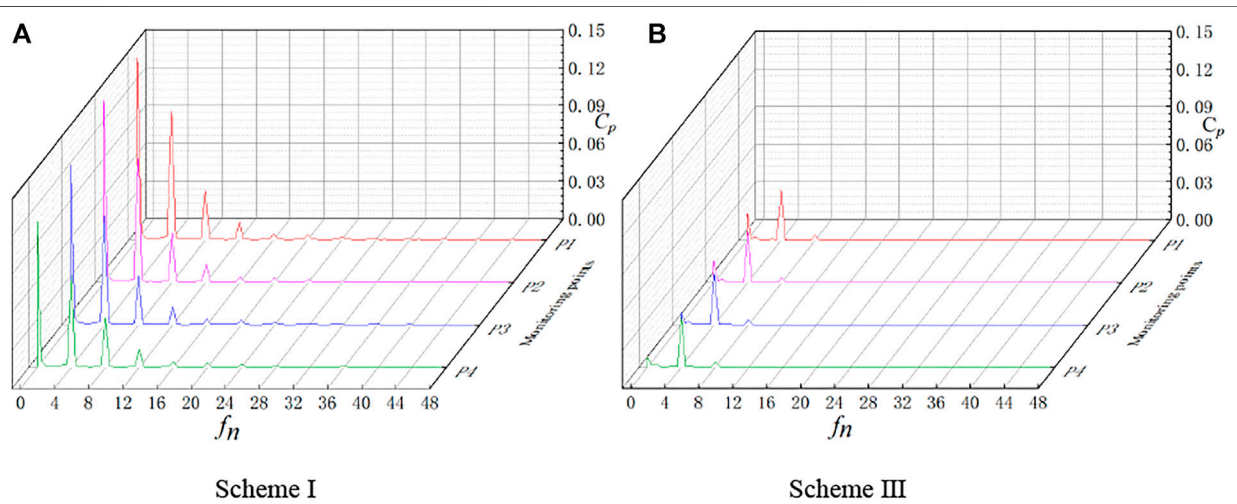

FIGURE 13 | Frequency domain diagram of impeller inlet pressure pulsation(Q/Q_d = 0.40).**(A)** scheme I, **(B)** scheme III.

scheme I. **Figure 13** shows the frequency domain diagram of the impeller inlet pressure pulsation under deep stall conditions. It can be seen that since the circumferential speed of the impeller increases with the increase of the radius, the pressure pulsation amplitude decreases from the rim to the hub. The internal flow field of scheme I is extremely unstable, and there is obvious low-frequency pulsation at the inlet. The main frequency of the pressure pulsation is 0.45 times the frequency and 4 times the frequency, and the amplitudes are 0.1439, 0.1324, 0.1272, 0.1154 and 0.102, 0.0984, 0.0865, 0.0732. In scheme III, it is found that the low-frequency pressure pulsation at the impeller inlet is significantly improved, and the amplitude is nearly 6.6 times lower than that of the scheme I. The high-frequency pulsation almost disappears, the main frequency of the pressure pulsation is 4 times the rotational frequency, and the amplitude of the blade frequency is about 3 times smaller than that of the scheme I. The impeller inlet pressure pulsation can be obviously improved by grooving in stall condition, which proves that grooving can reduce the hydraulic excitation of the full-tubular pump in small flow condition and improve the internal flow.

CONCLUSION

This paper uses numerical simulation to study the improvement of the inlet groove on the saddle area of the full-tubular pump and its influence on the impeller inlet flow field. The specific conclusions are as follows:

1) When the flow gradually decreases, the full-tubular pump has a longer saddle zone, and the inlet groove improves the saddle zone and lifts the maximum head by 1.61 m. The groove mainly increases the pressure difference of the impeller under the condition of small flow, thereby increasing the head of the full-tubular pump.
2) When in the deep stall condition, the flow state of the full-tubular pump is extremely poor, and there are serious backflow and vortex on the pipe wall. The groove obviously reduces the backflow length and vortex range of the inlet pipe wall and improves the velocity gradient distribution at the impeller inlet. Due to the increase in head, the groove will increase gap backflow at the stator and rotor.
3) By comparing the time domain characteristics and frequency domain characteristics of the pressure pulsation between the original model and the groove model under the stall condition, the impeller inlet pressure pulsation is affected by the impeller. The groove can effectively improve the impeller inlet pressure pulsation characteristics under stall conditions, and reduce the pressure pulsation amplitude and low frequency components.

DATA AVAILABILITY STATEMENT

The original contributions presented in the study are included in the article/Supplementary Material, further inquiries can be directed to the corresponding author.

AUTHOR CONTRIBUTIONS

Conceptualization, LS and FT; methodology, YJ and YGC; software, TX and JZ; validation, LS and BC; data curation, BC and YAC; writing original draft preparation, LS, YJ and FT; writing review and editing, LS, YJ and YGC; visualization, BC and JZ; supervision, LS, YGC, and FT; funding acquisition, LS and FT; All authors have read and agreed to the published version of the manuscript.

FUNDING

This article was supported by the Natural Science Foundation of the Jiangsu Province of China (No. BK20190914); the China Postdoctoral Science Foundation Project (No.2019M661946); the Natural Science Foundation of Jiangsu Higher Education Institutions of China (No. 19KJB570002); the Jiangsu Water Conservancy Science and Technology project (No. 2021012); the Postdoctoral Research Fund project of the Jiangsu Province (No. 2021K360C); the Postgraduate Research Innovation Program of the Jiangsu Province (No. KYCX21_3227); the Postgraduate Practice Innovation Program of the Jiangsu Province (No. SJCX21_1585); the Priority Academic Program Development of Jiangsu Higher Education Institutions (No. PAPD).

REFERENCES

Chen, W., Lu, L., Wang, G., and Dong, L. (2012). Influence of Axial-Flow Pump Operating Condition on the Pre-swirl at Impeller Chamber Inlet[J]. *J. Hydroelectr. Eng.* 31 (01), 213.

Feng, J., Yang, K., Zhu, G., Luo, X., and Li, W. (2018). Elimination of Hump in Axial Pump Characteristic Curve by Adopting Axial Grooves on Wall of Inlet Pipe[J]. *Trans. Chin. Soc. Agric. Eng.* 34 (13), 105. doi:10.11975/j.issn.1002-6819.2018.13.013

Gs, A., Zl, A., Yx, B., Hl, A., and Xl, A. (2020). Tip Leakage Vortex Trajectory and Dynamics in a Multiphase Pump at Off-Design Condition. *Renew. Energy* 150, 703. doi:10.1016/j.renene.2020.01.024

Kan, K., Chen, H., Zheng, Y., Zhou, D., Binama, M., and Dai, J. (2021). Transient Characteristics during Power-Off Process in a Shaft Extension Tubular Pump by Using a Suitable Numerical Model. *Renew. Energy* 164, 109–121. doi:10.1016/j.renene.2020.09.001

Kan, K., Yang, Z., Lyu, P., Zheng, Y., and Shen, L. (2021). Numerical Study of Turbulent Flow Past a Rotating Axial-Flow Pump Based on a Level-Set Immersed Boundary Method. *Renew. Energy* 168, 960–971. doi:10.1016/j.renene.2020.12.103

Kan, K., Zheng, Y., Chen, H., Zhou, D., Dai, J., Binama., M., et al. (2020). Numerical Simulation of Transient Flow in a Shaft Extension Tubular Pump Unit during Runaway Process Caused by Power Failure. *Renew. Energy* 154, 1153–1164. doi:10.1016/j.renene.2020.03.057

Kan, K., Zheng, Y., Chen, Y., Xie, Z., Yang, G., and Yang, C. (2018). Numerical Study on the Internal Flow Characteristics of an Axial-Flow Pump under Stall Conditions. *J. Mech. Sci. Technol.* 32 (10), 4683–4695. doi:10.1007/s12206-018-0916-z

Li, D., Wang, H., Qin, Y., Wei, X., and Qin, D. (2018). Numerical Simulation of Hysteresis Characteristic in the Hump Region of a Pump-Turbine Model. *Renew. Energy* 115, 433–447. doi:10.1016/j.renene.2017.08.081

Liu, C. (2015). Researches and Developments of Axial-Flow Pump System[J]. *Trans. Chin. Soc. Agric. Mach.* 46 (06), 49. doi:10.6041/j.issn.1000-1298.2015.06.008

Mu, T., Zhang, R., Xu, H., Zheng, Y., and Li, J. (2020). *Study on Improvement of Hydraulic Performance and Internal Flow Pattern of the Axial Flow Pump by Groove Flow Control technology[J]*. Renewable Energy.

Qu, H., Chen, Y., Tang, F., Zhang, W., Liu, H., Bai, Z., et al. (2021). The Impact of the Inlet Water Guide Cone Bracket on Function of the Saddle Zone in Vertical Axial-Flow Pump[J]. *J. Irrigation Drainage* 40 (7), 97. doi:10.13522/j.cnki.ggps.2020694

Saha, S. L., Kurokawa, J., Matsui, J., and Imamura, H. (2000). Suppression of Performance Curve Instability of a Mixed Flow Pump by Use of J-Groove. *J. Fluids Eng.* 122 (3), 592–597. doi:10.1115/1.1287855

Shi, L., Jiao, H., Gou, J., Yuan, Y., Tang, F., and Yang, F. (2020). Influence of Backflow Gap Size on Hydraulic Performance of Full-Flow Pump[J]. *Trans. Chin. Soc. Agric. Mach.* 51 (04), 139. doi:10.6041/j.issn.1000-1298.2020.04.016.

Shi, L., Zhu, J., Wang, L., Chu, S., Tang, F., Jiang, Y., et al. (2021). Analysis of Strength and Modal Characteristics of a Full Tubular Pump Impeller Based on Fluid-Structure Interaction[J]. *Energies*, 14. doi:10.21203/rs.3.rs-627588/v1

Shi, L., Zhu, J., Yuan, Y., Tang, F., Huang, P., Zhang, W., et al. (2021). Numerical Simulation and Experiment of the Effects of Blade Angle Deviation on the Hydraulic Characteristics and Pressure Pulsation of an Axial-Flow Pump. *Shock Vib.* 2021 (6), 1–14. doi:10.1155/2021/6673002

Tang, F., Liu, C., Xie, W., Yuan, J., and Cheng, L. (2012). Experimental Studies on Hydraulic Models for a Reversible, Tubular, and Submersible Axial-Flow Pump Installation[J]. *Trans. Chin. Soc. Agric. Mach.*, 74–77.

Wang, W., Tai, G., Pei, J., Pavesi, G., and Yuan, S. (2022). Numerical Investigation of the Effect of the Closure Law of Wicket Gates on the Transient Characteristics of Pump-Turbine in Pump Mode. *Renew. Energy* 194, 719–733. doi:10.1016/j.renene.2022.05.129

Wang, W., Wang, W., Zhang, L., Zhao, L., Lu, J., Feng, J., et al. (2020). X Mechanism for End-Wall Slots to Improve Hump in an Axial Flow Pump [J]. *Trans. Chin. Soc. Agric. Eng.* 36 (23), 12–20.

Wang, W., Zhang, X., Lu, J., Luo, X., and Chu, W. (2020). Coupling Method and Mechanism of Stability Enhancement for Endwall Stall in Axial-Flow Compressor[J]. *J. Propuls. Technol.* 41 (03), 544. doi:10.11975/j.issn.1002-6819.2020.23.002.

Wang, Y., Xie, S., and Wang, W. (2016). Numerical Simulation of Cavitation Performance of Low Specific Speed Centrifugal Pump with Slotted Blades[J]. *J. Drainage Irrigation Mach. Eng.* 34 (03), 210. doi:10.3969/j.issn.1674-8530.15.0009.

Yang, F., Jin, Y., Liu, C., Tang, F., and Yang, H. (2012). Numerical Analysis and Performance Test on Diving Tubular Pumping System with Symmetric Aerofoil Blade[J]. *Trans. Chin. Soc. Agric. Eng.* 28 (16), 60. doi:10.3969/j.issn.1002-6819.2012.16.010.

Zhang, D., Liu, J., Geng, L., Shi, L., and Zhang, J. (2017). Numerical Simulation and Experiment of Pressure Fluctuation in Mixed-Flow Pumps under Low Flow Conditions[J]. *Trans. Chin. Soc. Agric. Mach.* 48 (02), 117. doi:10.6041/j.issn.1000-1298.2017.02.016.

Zhang, D., Shi, L., Zhao, R., Shi, W., Pan, Q., and Van Esch, B. P. (2017). Study on Unsteady Tip Leakage Vortex Cavitation in an Axial-Flow Pump Using an Improved Filter-Based Model[J]. *J. Mech. Sci. Technol.* 31, 659–667. doi:10.1007/s12206-017-0118-0

Zhang, H., Wu, J., Chu, W., Wu, Y., and Wang, W. (2013). Full-annulus Numerical Investigation of Influence on Flow-Field in an Axial Flow Compressor with Inlet Distortion[J]. *J. Propuls. Technol.* 34 (08), 1056.

Zhang, R., and Chen, H. (2014). Study on the Improvement of Hydrodynamic Performance of Axial-Flow Pump at Stall Condition[J]. *J. Hydroelectr. Eng.* 33 (03), 292. doi:10.4321/S0004-05922009000400017.

Zhang, X., and Tang, F. (2022). Investigation of the Hydrodynamic Characteristics of an Axial Flow Pump System under Special Utilization Conditions[J]. *Sci. Rep.* 12 (1), 9157. doi:10.1038/s41598-022-09157-1

Zhang, X., Tang, F., Liu, C., Shi, L., Liu, H., Sun, Z., et al. (2021). Numerical Simulation of Transient Characteristics of Start-Up Transition Process of Large Vertical Siphon Axial Flow Pump Station. *Front. Energy Res.* 9, 706975. doi:10.3389/fenrg.2021.706975

Zheng, Y., Chen, Y., Zhang, R., Ge, X., and Sun, A. (2017). Analysis on Unsteady Stall Flow Characteristics of Axial-Flow Pump[J]. *Trans. Chin. Soc. Agric. Mach.* 48 (07), 127. doi:10.6041/j.issn.1000-1298.2017.07.016.

Zheng, Y., Mao, Y., Zhou, D., and Zhang, D. (2011). Flow Characteristics of Low-Lift and Large Flow Rate Pump Installation in Saddle Zone[J]. *J. Drainage Irrigation Mach. Eng.* 29 (05), 369. doi:10.3969/j.issn.1674-8530.2011.05.001.

Conflict of Interest: Author BC was employed by the company Jiangsu Pumping Station Technology Co.Ltd. of South-to-North Water Diverslon Project

The authors declare that the research was conducted in the absence of any commercial or financial relationships that could be construed as a potential conflict of interest.

NOMENCLATURE

D_1 the diameter of the impeller:mm.

D_2 the diameter of the guide vane:mm.

N_s the rotation speed, r/min.

d_{h1} the impeller hub ratio.

d_{h2} the guide vane hub ratio.

Lgroove length: groove length:mm.

Q_d the design flow of the pump, L/s.

ρ fluid density.

hgroove depth: groove depth:mm.

n number of grooves.

k the turbulent kinetic energy.

ω the turbulent frequency.

x_i a cross section.

ΔH the pressure difference between a cross section and the inlet pipe.

P_{xi} static pressure of a cross section, kPa.

P_{inlet} static pressure of the inlet pipe, kPa.

Q_G gap backflow, L/s.

ΔP the pressure difference between the inlet and outlet of the impeller, kPa.

$\bar{v}_u$ the uniformity of the axial velocity distribution of the impeller inlet section, %.

f_n the rotational frequency of the blade.

C_p the pressure pulsation coefficient.

frontiers | Frontiers in Energy Research

ORIGINAL RESEARCH
published: 13 July 2022
doi: 10.3389/fenrg.2022.935888

Numerical Analysis of Unsteady Internal Flow Characteristics of Impeller-Guide Vane in a Vertical Axial Flow Pump Device

Fan Yang[1,2], Pengcheng Chang[1], Hongfu Jian[2], Yuting Lv[1], Fangping Tang[1] and Yan Jin[3]*

[1]College of Hydraulic Science and Engineering, Yangzhou University, Yangzhou, China, [2]Jiangxi Research Center on Hydraulic Structures, Jiangxi Academy of Water Science and Engineering, Nanchang, China, [3]Hydrodynamic Engineering Laboratory of Jiangsu Province, Yangzhou University, Yangzhou, China

A vertical axial flow pump device has the characteristics of low head and large flow and has various forms, simple structure, and flexible installation. It is widely used in low-head pumping stations in plain areas. In order to explore the transient characteristics of the internal flow in the impeller and guide vane of the vertical axial flow pump at different flow rates, this article analyzes the internal flow field distribution on the surface of the impeller blade, the velocity and pressure distribution of the impeller inlet and outlet, and the pressure pulsation characteristics of the impeller. The flow field characteristics of the guide vane section, the entropy production loss, and the main frequency change of the pressure pulsation inside the guide vane are analyzed at different radii. The results show that under 0.8 Q_{bep} condition, the streamline distortion area of the blade working face accounts for the largest part of the blade area, and the streamline distortion area of the blade surface decreases significantly at 1.2 Q_{bep}. The circumferential pressure distribution at the impeller inlet presents four high-pressure regions and four low-pressure regions, and the number of regions is consistent with the number of impeller blades. The ratio of axial force to flow rate of 0.8Q_{bep}, 1.0Q_{bep}, and 1.2Q_{bep} is approximately 11:10:9. The radial force on the impeller is the largest under the condition of 0.8 Q_{bep}, and the radial force on the impeller is not significantly different between 1.0 Q_{bep} and 1.2 Q_{bep}. The pressure pulsation amplitude gradually decreases from the inlet to the outlet of the guide vane.

Keywords: vertical axial flow pump device, internal flow field, pressure pulsation, unsteady, numerical simulation

OPEN ACCESS

Edited by:
Kan Kan,
College of Energy and Electrical Engineering, China

Reviewed by:
Tianyi Li,
University of Minnesota Twin Cities, United States
Yin Pengbo,
Fuzhou University, China

****Correspondence:***
Fan Yang
fanyang@yzu.edu.cn

Specialty section:
This article was submitted to Process and Energy Systems Engineering, a section of the journal Frontiers in Energy Research

Received: *04 May 2022*
Accepted: *13 June 2022*
Published: *13 July 2022*

Citation:
Yang F, Chang P, Jian H, Lv Y, Tang F and Jin Y (2022) Numerical Analysis of Unsteady Internal Flow Characteristics of Impeller-Guide Vane in a Vertical Axial Flow Pump Device. Front. Energy Res. 10:935888. doi: 10.3389/fenrg.2022.935888

1 INTRODUCTION

An axial flow pump has the characteristics of low head and large flow, which is widely used in inter-basin water transfer projects, plain municipal engineering, shipbuilding industry, military industry, and other important fields in China. With the development of social economy and the change in global climate and situation, China's demand for efficient axial flow pumps is very urgent in the fields of military industry, nuclear energy development, municipal engineering, large-scale water diversion projects, and marine resources development (Shen et al., 2020).

A vertical axial flow pump device has the characteristics of various forms, simple structure, and flexible installation. In the first phase of the East Route Project of the South-to-North Water Diversion in China, 57% of the pumping stations are vertical axial flow pump stations (Yang et al.,

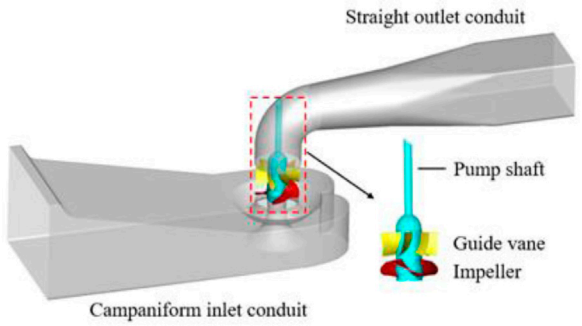

FIGURE 1 | 3D model of the vertical axial flow pump device.

TABLE 1 | Main parameters of the pump device.

Parameters	Value
Design flow rate Q_{bep}	338L/s
Design head	7.75 m
Rotational speed	1433r/min
Impeller diameter D	300 mm
Number of impeller blades	4
Tip clearance	0.2 mm
Hub ratio	0.483
Blade angle of impeller	0°
Axial distance between impeller and guide vane	0.089D
Number of guide vane blades	7

2022a). During the operation of the vertical axial flow pump device, the internal flow is a complex three-dimensional unsteady turbulent flow, and the flow obtains energy through the impeller domain. In the process of flow out of the outlet channel through the guide vane rectifier, it is easy to produce unstable flow leading to flow separation due to the limitation and influence of boundary conditions such as tip clearance, blade root clearance, and hub rotation (Zhang et al., 2012). The complex flow phenomena such as vortex, impact, secondary flow, and tip clearance leakage lead to a significant reduction in the operation efficiency of the axial flow pump device and affect the efficient and stable operation of the pumping station. So far, many scholars have carried out a lot of research on axial flow pump devices. Zhang et al. (2022) used a physical model test to study the hydrodynamic characteristics and pressure fluctuation of bidirectional axial flow pump under forward and reverse conditions and revealed the energy characteristics and pressure fluctuation propagation law of a bidirectional axial flow pump under forward and reverse conditions. Kan et al. (2021a) used the SST k-ω turbulence model to simulate the stall condition of bidirectional axial flow pump and compared and analyzed the difference of torque and pressure pulsation of bidirectional axial flow pump under forward stall condition and reverse stall condition. Zhao et al. (2021) studied the dominant vortex structure in a diagonally separated flow in an axial flow pump impeller and obtained the average vortex intensity change, turbulent vortex dissipation change, and the evolution process of vortex in a life cycle under various working conditions. Meng et al. (2021) used entropy production theory as the evaluation criterion of energy dissipation, based on numerical simulation technology, to study the influence of backflow clearance on the energy characteristics of axial flow pump. It was found that the loss of impeller decreased first and then increased with the increase of clearance radius, and the other flow components decreased with the increase of clearance radius. Mu et al. (2020) proposed a flow control technology to improve the hydraulic performance of the axial flow pump when a rotating stall occurs in the saddle area. Shi et al. (2021) compared the structural mechanical properties of the full tubular pump and the axial flow pump. The results show that the maximum equivalent stress of the full tubular pump occurs at the outer edge of the blade, and the maximum equivalent stress of the axial flow pump occurs at the hub center of the blade. Yang et al. (2021a) revealed the phenomenon of flow deviation in the outlet channel of an axial flow pump and the influence of flow deviation on the pressure fluctuation distribution in the outlet channel by experimental research combined with CFD technology. Song and Liu (2021) studied the change process of FAV at the inlet of an axial flow pump and analyzed the energy change and velocity change of FAV combined with V3V. Yang W et al. (2022) used different flange load distribution types of axial flow pump impeller model based on CFD technology to study the influence of these three types of flange load distribution on the tip clearance leakage flow and leakage eddy current of axial flow pump. Zhou et al. (2022) designed a double-layer conduit structure to study the influence of different geometric parameters of the double-layer conduit structure on the external characteristics and internal flow field of the axial flow pump. Xie et al. (2022) studied the double hump characteristics of an axial flow pump under small flow conditions and explored the relationship between the head-flow curve of the axial flow pump and the characteristics of the internal flow field through an internal flow field test. Lin et al. (2021) simulated the influence of sediment concentration, particle size, and cavitation on the internal flow pressure fluctuation of axial flow pump under the combined action of clear water, sediment water, clear water cavitation, and cavitation and sediment wear based on CFD technology. Xu et al. (2021) studied the difference between the forward and reverse runaway transition process of axial flow pump, and calculated and analyzed the loss position and cause of loss in forward and reverse runaway transition process of axial flow pump based on entropy production theory.

The vertical axial flow pump device includes the pump and inlet and outlet conduits with good hydraulic performance. The impeller and guide vane are the core of the axial flow pump device, and their efficient and stable operation determines the operation state of the whole pump device. In actual operation, the internal flow field of the pump device is instantaneous change, and due to the influence of boundary conditions such as blade tip clearance, blade root clearance, and hub rotation, unstable flow is easily generated in the impeller domain. The internal flow of the guide vane becomes very complicated by the influence of the flow velocity loop at the outlet of the impeller, which is easy to induce the vibration of the axial flow pump device and affect the safe and stable operation of the

TABLE 2 | Boundary condition settings.

Location	Boundary Condition
Inlet of pump device	Flow
Outlet of pump device	Pressure
Solid wall	No-slip wall
Interfaces on both sides of impeller in steady calculation	Stage
Interfaces on both sides of impeller in unsteady calculation	Transient Rotor Stator (Jin et al., 2019)
Other computing domain interfaces	None
Convergence accuracy	10^{-5}

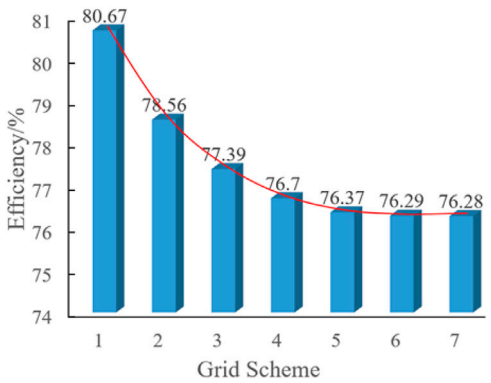

FIGURE 2 | Efficiency comparison of pump devices under different grid schemes.

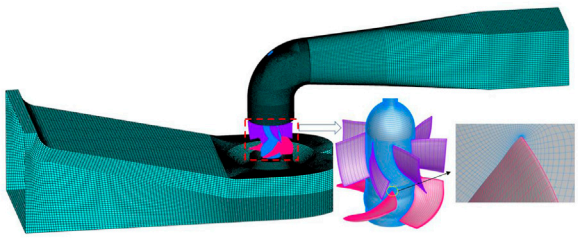

FIGURE 3 | Structured grid diagram of pump device.

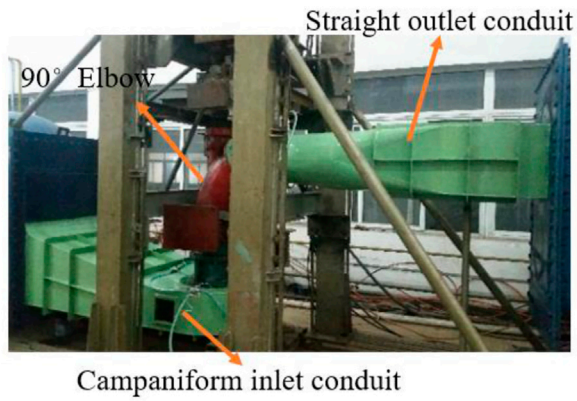

FIGURE 4 | Pump device test bench.

pump station. In order to study the transient internal flow characteristics of the impeller and guide vane in vertical axial flow pump device, based on the theoretical basis and methods of previous research on axial flow pump devices, CFD technology is used to simulate the transient flow characteristics of vertical axial flow pump device under different flow conditions, and the distribution law and development mechanism of the transient flow of impeller and guide vane are clarified.

2 SIMULATION MODEL

The vertical axial flow pump device consists of five flow passage components: campaniform inlet conduit, impeller, guide vane, 90°elbow, and straight outlet conduit. The three-dimensional model of the vertical axial flow pump device is shown in **Figure 1**. The geometric dimensions of the vertical axial flow pump device can be seen in the study by Yang et al. (2021b). The main parameters of the vertical axial flow pump device are shown in **Table 1**.

3 NUMERICAL METHOD

3.1 Calculation Method and Boundary Conditions

The internal flow medium of the vertical axial flow pump device studied in this research work is an incompressible viscous fluid, and the water flow obtains energy through the rotation of the pump impeller. There are some situations in which the swirling flow and some streamlines have a large bending degree. The RNG k-ε turbulence model considers this kind of rotation and swirling flow and can deal well with the flow with a high strain rate and large streamline bending degree. Based on the works of Mompean (1998), Fu et al. (2020), Wang et al. (2020), and Zhang et al. (2021), this study used the Reynolds time-averaged N-S (Navier-Stokes) equation and the RNG k-ε turbulence model to simulate and predict the flow field and hydraulic performance of the vertical axial flow pump device.

Commercial software ANSYS CFX was used to simulate the steady and unsteady numerical simulation of the vertical axial flow pump device under three working conditions of $0.8Q_{bep}$, $1.0Q_{bep}$, and $1.2Q_{bep}$. In order to avoid the influence of initial

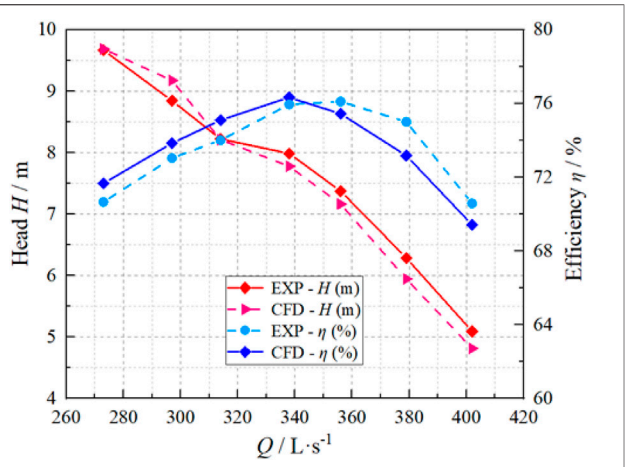

FIGURE 5 | Comparison of model test and numerical simulation results.

velocity distribution on the flow pattern of inlet and outlet channels, the inlet extension section and outlet extension section were added before the campaniform inlet conduit and after the straight outlet conduit. The boundary conditions in the calculation domain are set as shown in **Table 2**. The time parameter setting of unsteady numerical simulation of the vertical axial flow pump device can be used for the transient calculation of the axial flow pump device (Yang et al., 2021b).

3.2 The Independent Analysis and Convergence Analysis of Grids

ICEM CFD software was used to carry out the hexahedral structured grid for the pump device, and the grid quality was greater than 0.4. The grid number independence of the vertical axial flow pump device was analyzed when the rotational speed was 1433 r/min and the flow rate was 338 L/s. The seven groups of grids were numbered 1–7, and the corresponding number of grids were 2.84 million, 3.33 million, 3.6 million, 3.87 million, 4.1 million, 4.26 million, and 4.8 million, respectively. The efficiency comparison of different grid schemes is shown in **Figure 2**. The device efficiency of grid schemes 6 and 7 tended to be stable, and the absolute error of efficiency was controlled within 0.2%, which met the accuracy requirement of numerical simulation (Chalghoum et al., 2018).

Based on the works by Roache (1997), Celik et al. (2008), and Nandan Kumar and Govardhan (2014), we obtained grid error using the grid convergence index (GCI) criterion as the evaluation criteria, compared seven groups of different number of grids to solve the simulation value and extrapolation value, and selected a suitable number of grids, so that the solution of numerical simulation could achieve pseudo-steady-state conditions.

Based on the GCI calculation formula used by Celik et al. (2008), after calculation, GCI_{21} = 5.91%, GCI_{32} = 4.56%, GCI_{43} = 4.01%, GCI_{54} = 3.22%, GCI_{65} = 1.99%, and GCI_{76} = 1.14% and GCI_{65} and GCI_{76} were less than 3%, indicating that the discrete

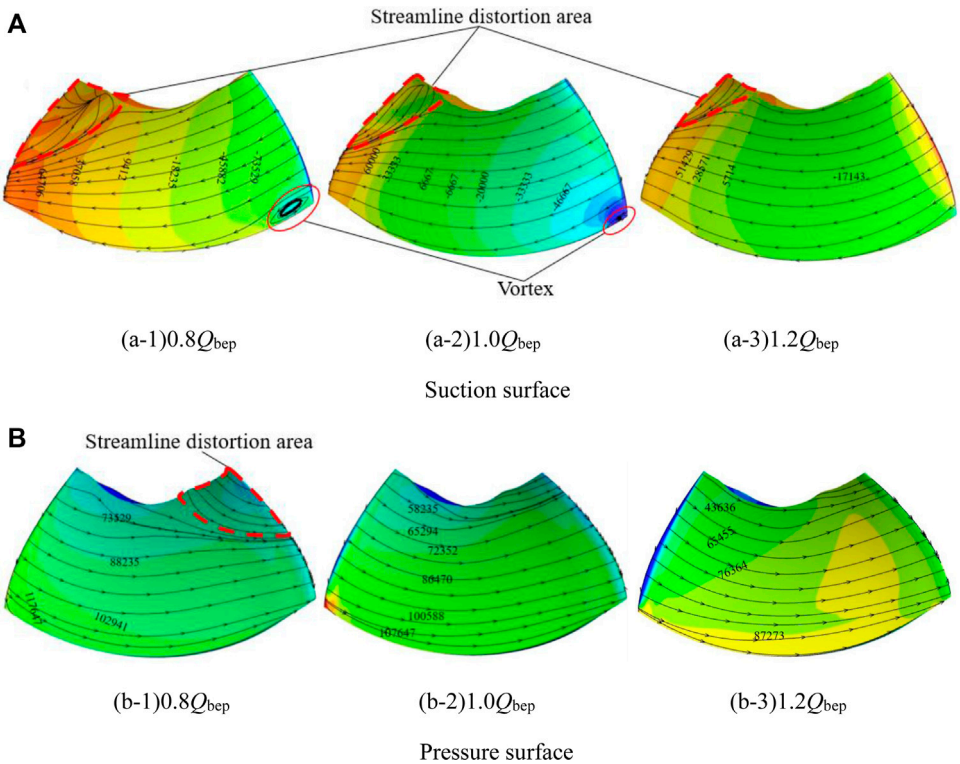

FIGURE 6 | Pressure distribution and streamline distribution of blade surface (Unit: Pa).

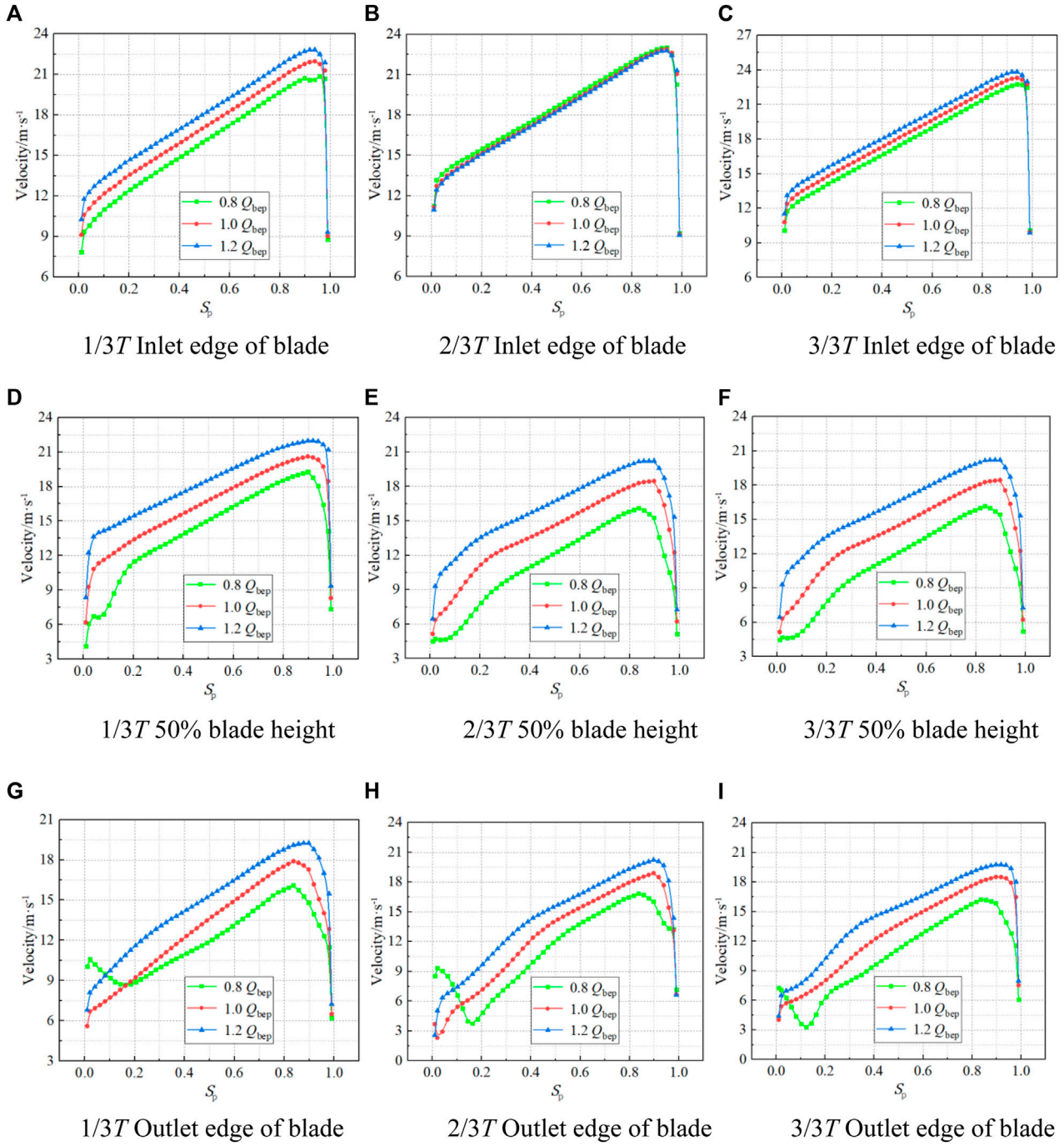

FIGURE 7 | Velocity distribution of the impeller blade inlet and outlet edge and 50% blade height under different flow conditions at different times.

error was small (Liu et al., 2014; Kan et al., 2021b). Combined with the analysis of grid number independence, 4.26 million grids were finally used as the final number of grids. The structured grid of the vertical axial flow pump device is shown in **Figure 3**.

In order to ensure the influence of the grid on the calculation accuracy, the dimensionless parameter y + was introduced as the dimensionless number of the distance from the nearest grid node to the wall. At $1.0Q_{bep}$ condition, the y^+ value of the impeller was about 36, and the y^+ value of the guide vane was about 78, which met the requirements of Wang (2020), Yang (2020), and Kan et al. (2021c).

3.3 Physical Model Test Verification

The physical model test of the vertical axial flow pump device was carried out on the high-precision hydraulic mechanical test bench of the Hydrodynamic Engineering Laboratory of Jiangsu

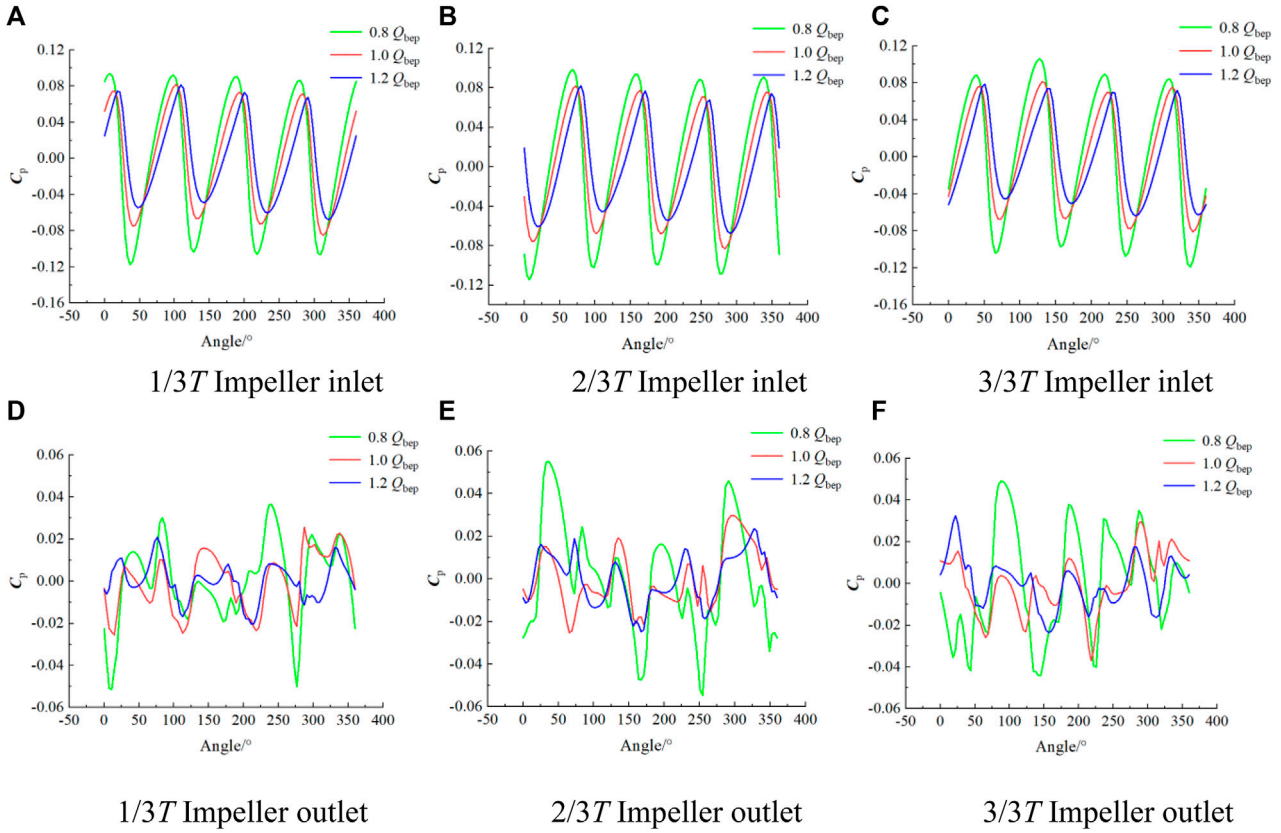

FIGURE 8 | Distribution of circumferential pressure coefficient of the impeller inlet and outlet at different time.

Province, China. The uncertainty of the test bench system was ±0.261%. The physical model test bench is shown in **Figure 4**. The parameters of the impeller and guide vane used in the physical model test can be referred to in **Table 1**. The pump device data from the physical model test are compared with the energy performance data from the numerical simulation, as shown in **Figure 5**. The maximum relative error between the predicted head by numerical simulation and the experimental value was 5.5%, and the minimum relative error was 0.2%. The maximum difference between the efficiency of the pump device by numerical simulation and the experimental value was 1.83%, and the minimum difference was 0.379%. The small error indicated that the numerical simulation of the vertical axial flow pump device had high accuracy.

4 RESULTS AND ANALYSIS

4.1 Unsteady Flow Characteristics in the Impeller

The pressure and streamline distribution of the impeller blade surface are shown in **Figure 6**. Under the condition of 0.8 Q_{bep}, streamline distortion occurred at the blade suction surface hub and pressure surface hub, and there was a small range of vortex at the blade suction surface inlet edge. The streamline distortion area of the suction surface accounted for 11.5% of the blade area, and the streamline distortion area of the pressure surface accounted for 14.4% of the blade area, which indicated that secondary flow occurred near the hub under small flow conditions. Under 1.0 Q_{bep} and 1.2 Q_{bep} conditions, the streamline allocation on the impeller blade pressure surface was uniform, and there was no reverse flow phenomenon. The local streamline distortion existed in the suction surface, and the streamline distortion area was reduced by 40 % and 73% compared with the 0.8 Q_{bep} condition. The vortex at the rim disappeared at 1.2 Q_{bep} condition, which indicated that the streamline allocation on the blade surface was straight, and the flow pattern was better in large flow. Under 0.8 Q_{bep} and 1.0 Q_{bep}, the blade inlet flow angle was negative, the local high-pressure area was formed at the pressure surface inlet edge, and the local low-pressure area was formed at the suction surface edge. Under 1.2 Q_{bep}, the blade inlet flow angle was positive, forming a local low-pressure area at the pressure surface inlet of the blade and a small range of high-pressure area at the suction surface inlet. Under different flow conditions, the impeller head of the axial flow pump was also different, and the hydraulic work of the blade pressure surface and the suction surface of the impeller was also different, so the surface flow field of the blade pressure surface and suction surface were also different. When the flow changed from 0.8Q_{bep} to 1.0Q_{bep}, the flow increased by 25%, and when the

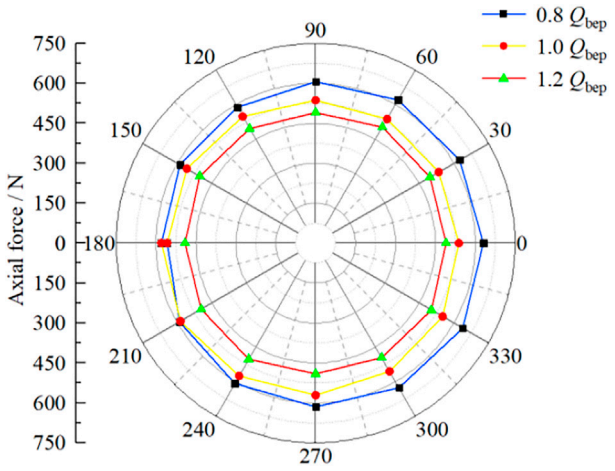

FIGURE 9 | Transient changes of axial force on the impeller in a rotating cycle.

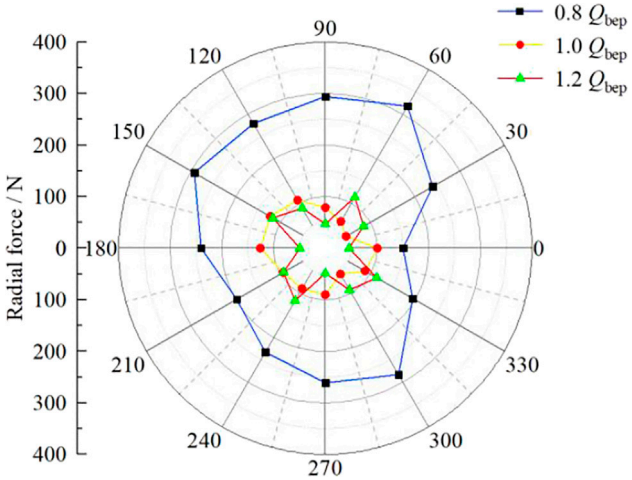

FIGURE 10 | Transient changes of radial force on the impeller at different times.

flow changed from $1.0Q_{bep}$ to $1.2Q_{bep}$, the flow increased by 20%. When the flow rate changed by more than 20%, there were obvious differences in the flow rate. The velocity distribution at the outlet edge of impeller blades with different flow rates (**Figure 7**) was different near the hub, especially $0.8Q_{bep}$, and the flow pattern had a significant impact on the velocity distribution.

In this article, the blade radial coefficient S_p is defined to represent the dimensionless distance from the blade root to the blade tip of the pump device impeller. The expression of blade radial coefficient is as follows:

$$S_p = \frac{r - R_m}{R - R_m}. \quad (1)$$

FIGURE 11 | Distribution of monitoring points of the impeller.

Figure 7 shows the velocity distribution at the inlet and outlet edges of impeller blades and at 50% of blade height. The flow velocity distribution at the impeller inlet increases gradually from the blade root to the blade tip. The flow is affected by the impeller hub wall and liquid viscous resistance, resulting in the decrease of flow velocity near the impeller hub. The sudden drop in the flow velocity near the tip of the blade is mainly due to the leakage of the tip clearance. In a rotating cycle, the velocity of the blade inlet side will change, and the maximum average velocity at the inlet edge of the blade is 17.68 m/s under $1.2Q_{bep}$ at $1/3T$. At the time of $2/3T$, the inlet velocity of the blade at three working conditions decreases with the increase of flow rate, and the inlet velocity at each flow condition has little difference. At the time of $3/3T$, the inlet velocity of the blade increases with the increase in flow rate, and the average inlet velocity of the blade is 17.47 m/s, 18.09 m/s, and 18.76 m/s, respectively. The velocity at 50% of blade height and at the outlet edge of the blade fluctuates to some extent near the blade root (S_p is 0–0.2), and the velocity at the outlet edge of the blade first decreases and then increases under $0.8Q_{bep}$. This is because the secondary flow and other adverse flow patterns near the hub are affected by the impeller blade root clearance, and the distortion of the airfoil blade at the hub position is large, resulting in local reverse flow and flow velocity fluctuation. The speed at the blade height of 50% and the outlet edge of the blade increases from the hub to the rim and reaches the maximum near $S_p = 0.9$, and the speed at the rim decreases sharply. The velocity at the blade height 50% and the outlet edge of the blade increases with the increase of flow rate. As the impeller rotates, the velocity changes at 50% of the blade height in a rotating cycle are not significant, and the velocity changes at the impeller outlet are mainly concentrated near the hub (S_p is 0–0.2). This is because the changes in adverse flow patterns, such as secondary flow near the hub in the rotating cycle, lead to the most obvious change, and the change regularity is not strong under the flow condition.

For the convenience of analysis, the pressure is dimensionless in this study. According to Zhang et al. (2019), the pressure is transformed into the pressure coefficient C_p. The formula is as follows:

$$C_p = \frac{P - \bar{P}}{0.5\rho V^2}. \quad (2)$$

Figure 8 shows the C_p distribution on the impeller inlet and outlet diameter of $0.725D$ at different times. The distribution of the C_p is relatively regular at the impeller inlet. The C_p distribution range of the impeller inlet is the largest at

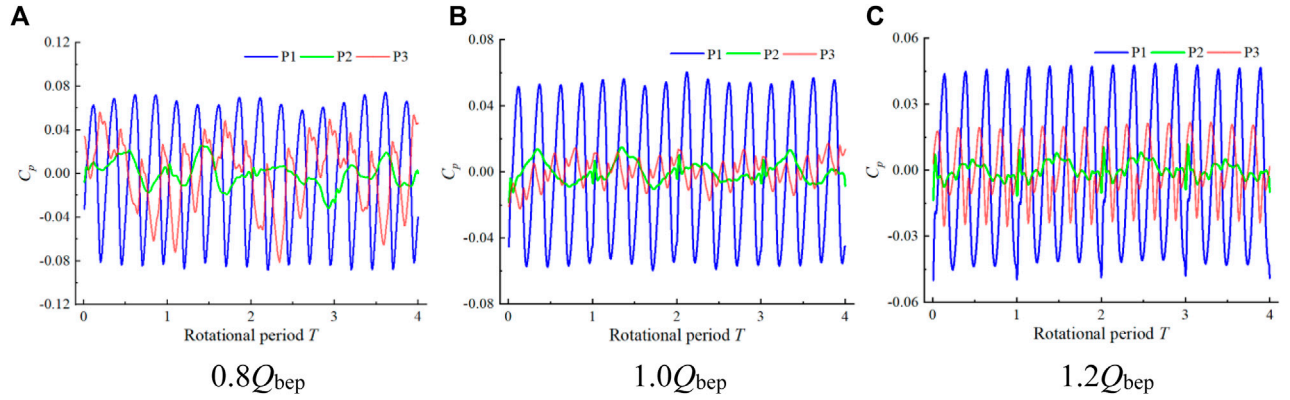

FIGURE 12 | Time domain diagram of pressure pulsation at each monitoring point of the impeller.

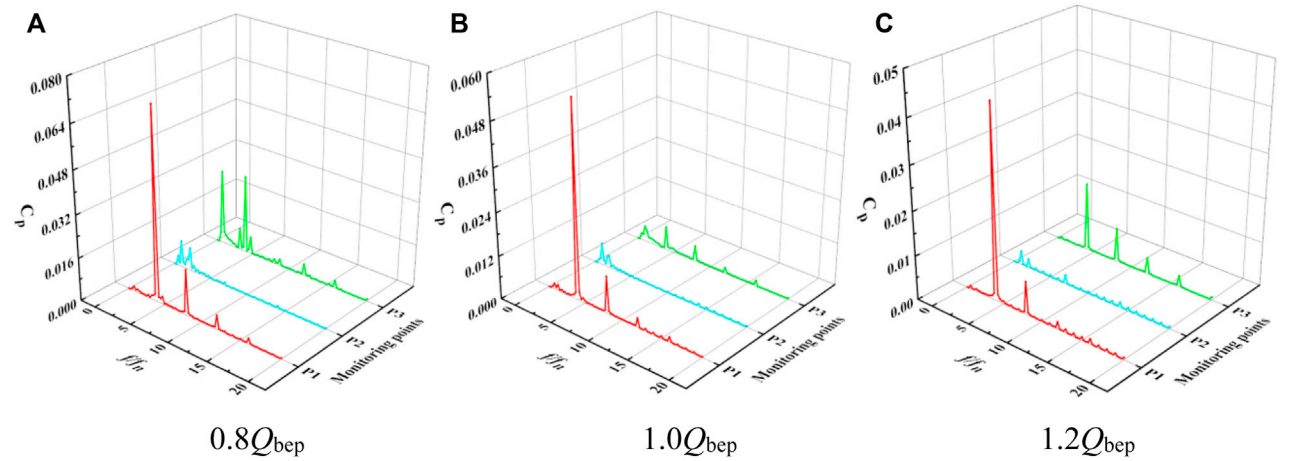

FIGURE 13 | Frequency domain diagram of pressure pulsation at each monitoring point of the impeller.

0.8 Q_{bep}, and the C_p allocation range of the impeller inlet is the smallest at 1.2 Q_{bep}, showing four high-pressure regions and four low-pressure regions, the number of which corresponds to the number of blades. The water flows through the impeller, forming a low-pressure area at the head of the suction side of the impeller, and a high-pressure region at the head of the pressure side. As the position of the impeller blades changes, the angles corresponding to these high-pressure and low-pressure regions will change. Compared with the impeller inlet, the C_p allocation at the impeller outlet is less regular, indicating that the flow state of the impeller outlet is poor. The flow obtains energy through the rotation of the impeller, and the flow has a large circumferential speed at the impeller outlet. The moving flow is restrained by the solid wall of the guide vane itself, and the low-speed water flow on the pressure surface of the impeller blade and the high-speed water flow on the suction surface converge. This leads to the turbulence of the flow state of the impeller outlet, resulting in a significant change in the distribution of the C_p. At $0.8Q_{bep}$, the maximum C_p at the impeller outlet is 0.0546, and the angle distribution is around 250°at 2/3T. At $1.0Q_{bep}$ and $1.2Q_{bep}$, the distribution of C_p fluctuates slightly, and the distribution trend at each time is similar.

In order to clarify the force variation of the impeller in the calculation condition, the axial force (F_Z) and radial force (F_R) of the impeller are calculated (Yang et al., 2022b). The calculation formulas of axial force and radial force are as follows:

$$F_z = P_z + P_{zh} = \pi\rho g H_y \left(R^2 - R_m^2\right), \tag{3}$$

$$F_i = P_i\left(\frac{2\pi R D_2}{N}\right), \tag{4}$$

$$F_x = \sum_{i=1}^{N} - F_i\left(\frac{x_i}{R}\right), \tag{5}$$

$$F_y = \sum_{i=1}^{N} - F_i\left(\frac{y_i}{R}\right), \tag{6}$$

$$F_r = \sqrt{F_x^2 + F_y^2}. \tag{7}$$

The transient changes of axial force at various moments are shown in **Figure 9**. The axial force on the impeller of the pump device changes slightly at each time under three flow conditions of

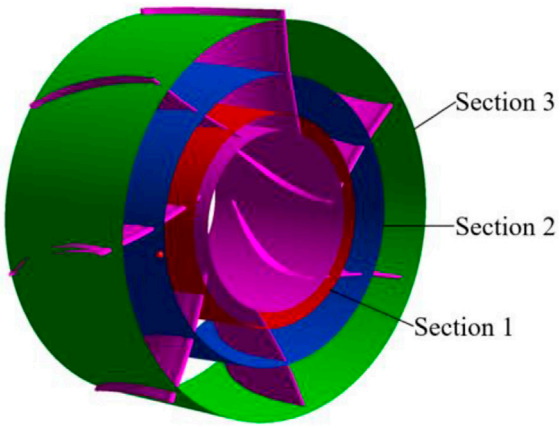

FIGURE 14 | Section diagram of guide vane with different radii.

0.8 Q_{bep}, 1.0 Q_{bep}, and 1.2 Q_{bep}. The axial force on the impeller is greatly affected by the change of the flow rate. The larger the flow rate, the axial force get smaller. The ratio of the average F_Z on the impeller in the calculation conditions of 0.8 Q_{bep}, 1.0Q_{bep}, and 1.2Q_{bep} is about 11:10:9.

Figure 10 shows the radial force in the calculation condition. The F_R is not significantly affected by the change in flow rate, and the F_R is greatly affected by the change in the internal flow field of the pump device. Under 0.8 Q_{bep} flow conditions, the large F_R is the largest. The average F_R is 249 N, and the fluctuation range of the F_R is 60.2 %—127.7% of the average F_R. The average F_R under the calculation conditions of 1.0Q_{bep}, and 1.2Q_{bep} is similar. The average F_R at 1.0Q_{bep} is 89 N, respectively, and the average F_R at 1.2Q_{bep} is about 95.5% of that at 1.0Q_{bep}. The fluctuation range of F_R at each time under 1.0Q_{bep} flow condition is 51.7 %–141.6% of the average F_R, and the F_R fluctuation range at each time under 1.2Q_{bep} flow condition is 55.3 %—138.8% of the average F_R. The F_R on the impeller changes with no obvious regularity at each moment.

The impeller is the core component of the axial flow pump device, and its efficient and stable operation determines the operation stability of the whole pump device. The impeller produces obvious pressure pulsation when rotating. Three pressure pulsation monitoring points are set in the impeller domain to monitor the pressure pulsation in the impeller domain. Three monitoring points are P1, P2, and P3, respectively. Along the axial direction of the pump, P1 is set at the impeller domain inlet, P2 is set at the tip clearance at 50% of the blade height, and P3 is set at the impeller domain outlet. The location of monitoring points is shown in **Figure 11**.

Figure 12 shows the time-domain diagram of pressure pulsation at each monitoring point of the impeller. The C_p allocation at P1 is relatively regular and has obvious periodicity. In four cycles, there are 16 peaks and 16 valleys in total. The number of peaks and valleys in each cycle is equal, and the time of occurrence is roughly the same. The number of peaks and valleys in the interior corresponds to the number of blades, which is due to the periodic pressure fluctuations caused by the interaction between the two working surfaces of the impeller rotating. The C_p allocation in the tip clearance is not regular,

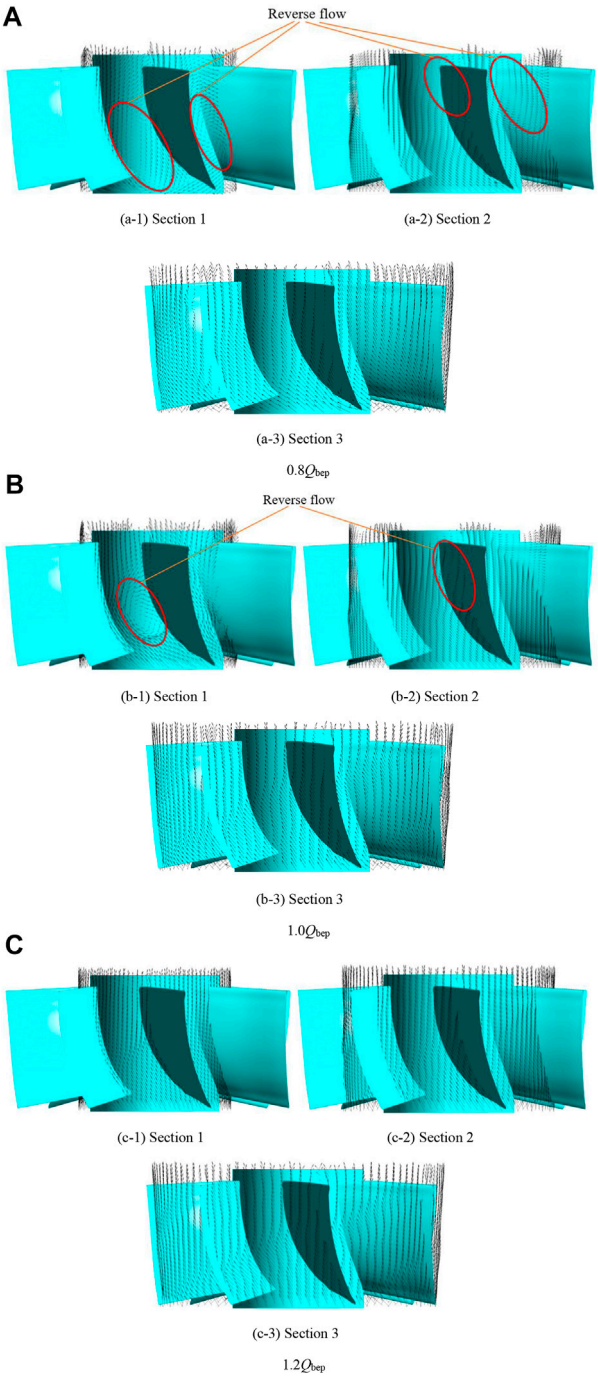

FIGURE 15 | Flow field diagram of guide vane with different radii.

and the C_p allocation in the tip clearance is unstable mainly due to the leakage of the tip clearance. The tip clearance leakage is mainly caused by the pressure difference between the pressure surface and the suction surface of the axial flow pump blade, and the tip clearance leakage becomes more serious in small flow. Therefore, the fluctuation of the pressure fluctuation coefficient of the tip clearance at 1.2Q_{bep} is smaller than that at 0.8Q_{bep}. The C_p allocation at P3 presents four peaks and four troughs, but the fluctuation law is unstable. The

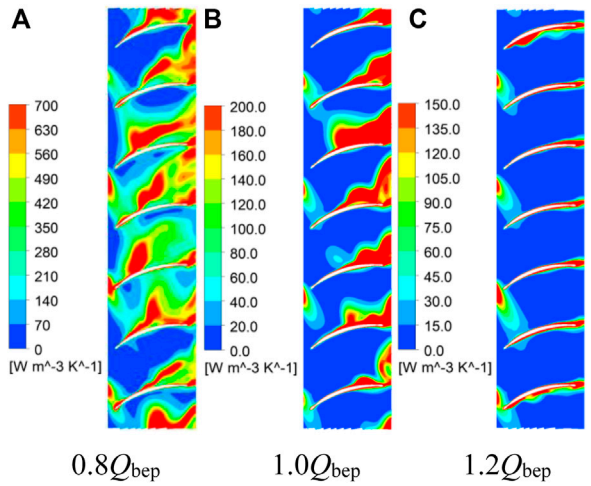

FIGURE 16 | Distribution of entropy production loss in guide vane.

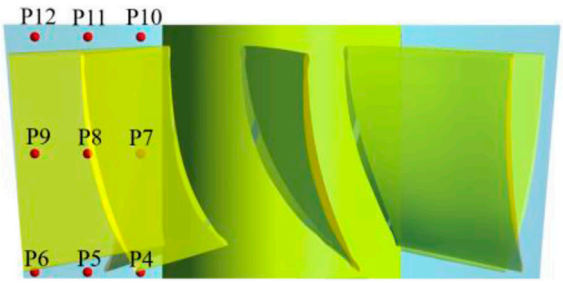

FIGURE 17 | Location of monitoring points of guide vane.

change of C_p is sometimes large and sometimes small, which is caused by static and dynamic interference. However, when the flow rate is 1.2 Q_{bep}, the pressure pulsation at the impeller outlet has good regularity, and the fluctuation tends to be stable.

In this study, the time-domain signal of pressure pulsation was converted into the frequency-domain signal based on FFT (Fast Fourier Transform). As shown in **Figure 13**, the main frequency of P1 was 1 times the blade passing frequency (BPF), and the secondary main frequency was 2 times the BPF. The C_p amplitude of $1.0Q_{bep}$ and $1.2Q_{bep}$ was lower than that of $0.8Q_{bep}$, and the maximum C_p amplitude was 0.07113 at $0.8Q_{bep}$. The amplitude of C_p at $1.0Q_{bep}$ was about 23.5% lower than that at $0.8Q_{bep}$, and the amplitude of C_p at $1.2Q_{bep}$ was about 38.4% lower than that at $0.8Q_{bep}$. The pressure pulsation in the tip clearance was affected by the tip clearance leakage, and the main frequency distribution of pressure pulsation was irregular. The main frequency amplitude of C_p in $0.8Q_{bep}$ blade tip clearance was 0.00869, and the main frequency amplitude of C_p in $1.2Q_{bep}$ blade tip clearance was reduced by 63.1%, mainly because the pressure difference between the pressure surface and the suction surface of the impeller blade was reduced under the condition of large flow rate, which led to the decrease of tip clearance leakage. The pressure pulsation of P3 was still affected by the number of impeller blades, and the main frequency was the BPF. The C_p amplitude of the P3 was significantly lower than that of the P1, which was mainly due to the suction effect of the blade at the impeller inlet. There was a local impact between the flow and the blade, and a large pressure gradient was formed at the impeller inlet. There was dynamic and static interference at the impeller outlet, the flow at the impeller outlet was more complex, and the spectrum distribution area was more extensive than the P1.

4.2 Unsteady Flow Characteristics Inside Guide Vane

In order to better analyze the internal flow field in the guide vane of the vertical axial flow pump device, three typical sections with different radii were selected from the hub to the rim to analyze the internal flow features of the pump. The radii of each section were 0.205*D*, 0.375*D*, and 0.495*D*, and they were numbered as 1–3, respectively. The selected sections are shown in **Figure 14**.

Figure 15 shows the flow field of the guide vane section. The entropy production loss calculation formula in the references (Li et al., 2017; Li et al., 2019; Li et al., 2020; Yang et al., 2022c) was used to calculate the entropy production loss of **section 2** inside the guide vane, as shown in **Figure 16**. It can be seen from **Figure 15** that there was a large range of reverse flow area on the guide vane back at $0.8Q_{bep}$ condition. The reverse flow area of **section 1** was the largest and was mainly located in the guide vane middle and lower section. The reverse flow area of **section 2** was located in the guide vane middle and upper section, and the area of the reverse flow region decreased. The reverse flow area of **section 3** was further reduced, mainly distributed near the guide vane trailing edge. Under $1.0Q_{bep}$ condition, the reverse flow area in the guide vane was significantly reduced compared with $0.8Q_{bep}$ condition. There was an obvious reverse flow area on the guide vane back of **section 1**, and the flow pattern in the guide vane of **section 2** was better. Only a small range of reverse flow area existed on the back of the guide vane. Under 1.2 Q_{bep} condition, the flow pattern in the guide vane was the best without obvious vortex and reverse flow. Under small flow condition, there was a wide range of recirculation zone and vortex motion in the guide vane, which led to the poor recovery effect of the guide vane on the flow velocity circulation and increased the hydraulic loss of the guide vane. When the flow increased, the flow pattern in the guide vane became better under the $1.0Q_{bep}$ condition, and the decrease of the entropy production loss area was mainly concentrated in the guide vane back and the guide vane outlet. When the flow increased, the entropy production loss was further reduced in the guide vane, and the entropy production loss area was mainly concentrated on the trailing edge of the guide vane.

The design purpose of the guide vane is to recover the velocity circulation of the flow, correct the flow pattern of the flow, reduce the hydraulic loss of the flow in the radial direction, and enable the flow to enter the outlet conduit smoothly. This article studied the influence of the flow pattern inside the guide vane on the internal pressure pulsation. Therefore, nine monitoring points were set along the flow direction in the guide vane to explore the

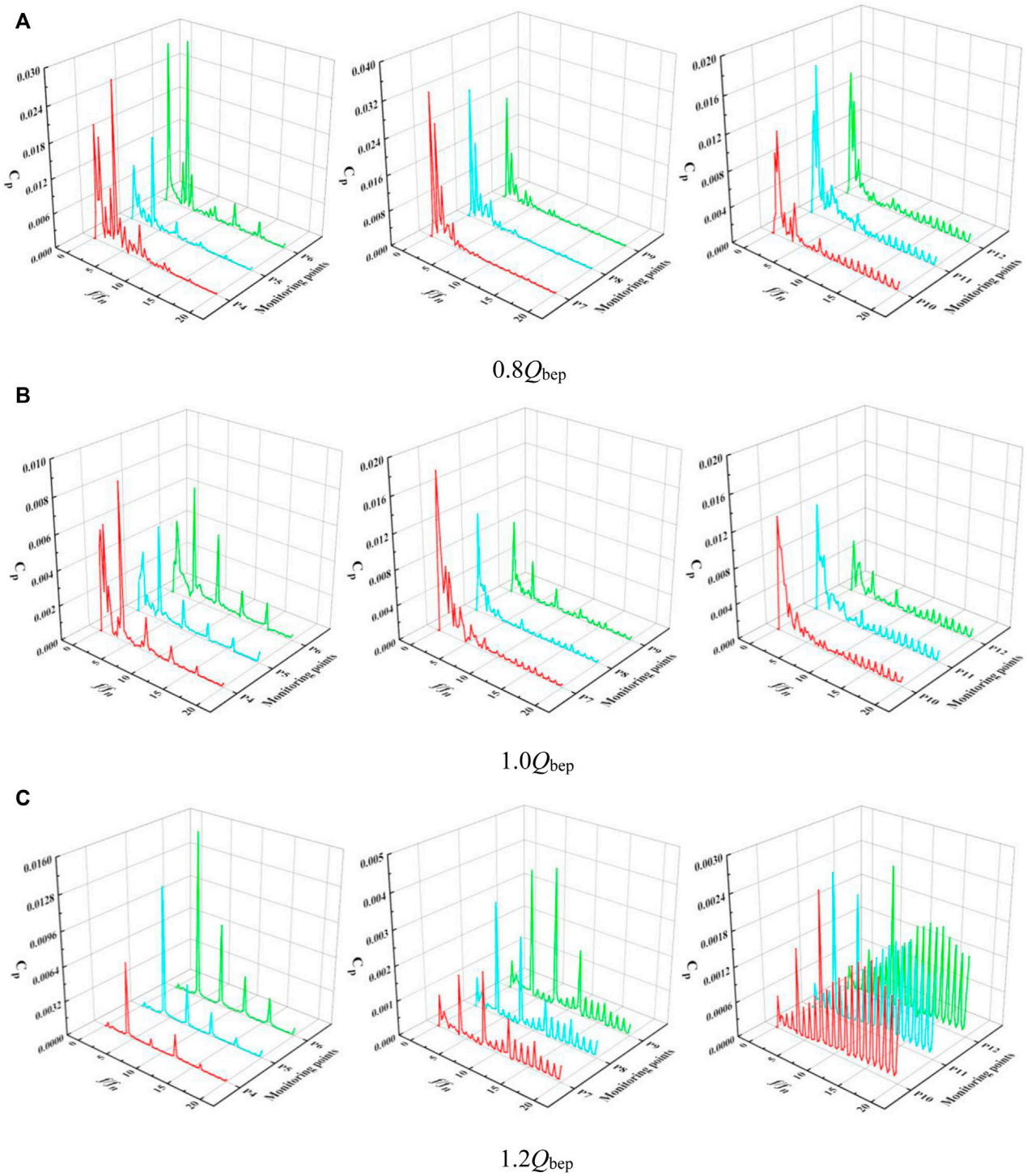

FIGURE 18 | Frequency domain diagram of pressure pulsation in guide vane.

variation of pressure pulsation in the guide vane. Monitoring points P4, P5, and P6 were set at the guide vane inlet, P7, P8, and P9 were set at the guide vane middle, and P10, P11, and P12 were set at the guide vane outlet. The position of monitoring points is shown in **Figure 17**.

Figure 18 shows the frequency domain diagram of pressure pulsation in the guide vane. The pressure pulsation at the guide vane inlet was mainly affected by impeller rotation, and the main frequency was BPF. The flow at the guide vane inlet was affected by dynamic and static interference. It had a large velocity circulation,

and with a large circumferential velocity was limited by the wall of the guide vane, which made the flow field at the guide vane inlet complicated, resulting in the C_p at the guide vane inlet being more complex and intense than that at the impeller inlet. Therefore, the peak number of the C_p amplitude at the guide vane inlet was more than that at the impeller inlet. When the flow increased, the C_p amplitude of the guide vane inlet decreased gradually. The main frequency of C_p in the middle and the guide vane outlet was not the BPF, indicating that the C_p amplitude at each monitoring point was less affected by the impeller rotation. At this time, the main excitation source of pressure pulsation was the velocity circulation of water flow. At small flow rate condition, the internal and outlet monitoring points of the guide vane were also affected by the local reverse flow. At 1.2 Q_{bep}, the reverse flow area gradually disappeared, and the C_p in the guide vane decreased. The C_p amplitudes of P7, P8, and P9 were higher than those at each monitoring point at the guide vane outlet. At 0.8Q_{bep}, the average C_p amplitude at the guide vane inlet was 1.33 times that at the guide vane middle, and the average C_p amplitude at the guide vane middle was 28.2% higher than that at the guide vane outlet. At 1.0Q_{bep}, the average C_p amplitude at the guide vane inlet was 0.553 times that at the guide vane intermediate, and the average C_p amplitude at the guide vane intermediate was 17.5% higher than that at the guide vane outlet. At 1.2Q_{bep}, the average C_p amplitude at the guide vane inlet was 6.46 times that at the guide vane intermediate, and the average C_p amplitude at the guide vane intermediate was 20.2% higher than that at the guide vane outlet.

5 CONCLUSION

In this article, the reliability of numerical simulation was verified by comparing the energy performance test of the pump device with the energy performance test of the numerical calculation of the pump device. The transient hydraulic characteristics of the impeller and the guide vane of the vertical axial flow pump device were studied, and the following three conclusions were obtained:

1) When the flow increases, the area of streamline distortion at the hub of the blade working face decreases. The velocity distribution on the impeller blade increases gradually from the blade root to the tip. The flow is affected by the viscous resistance of the impeller hub wall to the liquid and the leakage of the tip clearance, resulting in the decrease of the flow velocity near the impeller hub and the rim.
2) The ratio of the average F_Z on the impeller under the three flow conditions of 0.8 Q_{bep}, 1.0Q_{bep}, and 1.2Q_{bep} is about 11:10:9. Under 0.8 Q_{bep} condition, the F_R on the impeller is the largest, and the average F_R is 249 N. The fluctuation range of F_R is 60.2 %—127.7% of the average F_R. Under different flow conditions, the main frequency of C_p at the impeller inlet and outlet is 1 times the BPF. When the flow increases, the C_p amplitude decreases. The pressure pulsation in the tip clearance is affected by the tip clearance leakage, and there is no obvious regularity.
3) The internal flow pattern of the guide vane is the worst at 0.8 Q_{bep}, and the internal hydraulic loss is large. At 1.2 Q_{bep}, the flow pattern is good, and the hydraulic loss caused by flow disorder is decreased. The pressure pulsation amplitude gradually decreases from the inlet to the outlet of the guide vane, and the main frequency of the pressure pulsation at the guide vane inlet is 1 times the BPF, while the guide vane outlet is not the BPF.

DATA AVAILABILITY STATEMENT

The original contributions presented in the study are included in the article/Supplementary Material; further inquiries can be directed to the corresponding author.

AUTHOR CONTRIBUTIONS

Conceptualization, FY; software and writing—original draft, PC; formal analysis, FY and PC; methodology, FY and PC; funding, FY and HJ; investigation, HJ and FT; resources, YJ and FT; supervision, FY and FT; visualization, PC and FY; and writing—review and editing, YL and YJ. All authors have read and agreed to the published version of the manuscript.

FUNDING

This research was funded by the National Natural Science Foundation of China (Grant No. 51609210), Major Projects of the Natural Science Foundation of the Jiangsu Higher Education Institutions of China (Grant No. 20KJA570001), the Technology Project of the Water Resources Department of the Jiangsu Province (Grant No. 2020029), Open Project of Jiangxi Research Center on Hydraulic Structures (Grant No.2021SKSG06), the Scientific Research Program of Jiangsu Hydraulic Research Institute (Grant No. 2021), the Priority Academic Program Development of the Jiangsu Higher Education Institutions (Grant No. PAPD), and Postgraduate Research & Practice Innovation Program of Jiangsu Province-Yangzhou University (Grant No. SJCX21_1590).

REFERENCES

Celik, I. B., Ghia, U., Roache, P. J., and Freitas, C. J. (2008). Procedure for Estimation and Reporting of Uncertainty Due to Discretization in CFD Applications. *J. Fluids Eng.* 130, 078001. doi:10.1115/1.2960953

Chalghoum, I., Elaoud, S., Kanfoudi, H., and Akrout, M. (2018). The Effects of the Rotor-Stator Interaction on Unsteady Pressure Pulsation and Radial Force in a Centrifugal Pump. *J. Hydrodyn.* 30 (4), 672–681. doi:10.1007/s42241-018-0073-y

Fu, S., Zheng, Y., Kan, K., Chen, H., Han, X., Liang, X., et al. (2020). Numerical Simulation and Experimental Study of Transient Characteristics in an Axial Flow Pump during Start-Up. *Renew. Energy* 146, 1879–1887. doi:10.1016/j.renene.2019.07.123

Jin, Y., He, X., Zhang, Y., Zhou, S., Chen, H., and Liu, C. (2019). Numerical and Experimental Investigation of External Characteristics and Pressure Fluctuation of a Submersible Tubular Pumping System. *Processes* 7 (12), 949. doi:10.3390/pr7120949

Kan, K., Zhang, Q., Xu, Z., Chen, H., Zheng, Y., Zhou, D., et al. (2021). Study on a Horizontal Axial Flow Pump during Runaway Process with Bidirectional Operating Conditions. *Sci. Rep.* 11 (1), 21834. doi:10.1038/s41598-021-01250-1

Kan, K., Chen, H., Zheng, Y., Zhou, D., Binama, M., and Dai, J. (2021b). Transient Characteristics during Power-Off Process in a Shaft Extension Tubular Pump by Using a Suitable Numerical Model. *Renew. Energy* 164, 109–121. doi:10.1016/j.renene.2020.09.001

Kan, K., Yang, Z., Lyu, P., Zheng, Y., and Shen, L. (2021). Numerical Study of Turbulent Flow Past a Rotating Axial-Flow Pump Based on a Level-Set Immersed Boundary Method. *Renew. Energy* 168, 960–971. doi:10.1016/j.renene.2020.12.103

Li, D., Wang, H., Qin, Y., Han, L., Wei, X., and Qin, D. (2017). Entropy Production Analysis of Hysteresis Characteristic of a Pump-Turbine Model. *Energy Convers. Manag.* 149, 175–191. doi:10.1016/j.enconman.2017.07.024

Li, D., Zuo, Z., Wang, H., Liu, S., Wei, X., and Qin, D. (2019). Review of Positive Slopes on Pump Performance Characteristics of Pump-Turbines. *Renew. Sustain. Energy Rev.* 112, 901–916. doi:10.1016/j.rser.2019.06.036

Li, Y., Zheng, Y., Meng, F., and Osman, M. K. (2020). The Effect of Root Clearance on Mechanical Energy Dissipation for Axial Flow Pump Device Based on Entropy Production. *Processes* 8 (11), 1506. doi:10.3390/pr8111506

Lin, P., Xiang, L., Hu, D., Zhai, S., Guo, P., and Wang, S. (2021). Effect of Cavitation on Pressure Pulsation Characteristics of an Axial-Flow Pump under Sand Conditions. *J. Vib. Shock* 40 (18), 140–147. doi:10.13465/j.cnki.jvs.2021.18.019

Liu, H., Liu, M., Bai, Yu., Du, H., and Dong, L. (2014). Grid Convergence Based on GCI for Centrifugal Pump. *J. Jiangsu Univ. Nat. Sci. Ed.* 35 (03), 279–283. doi:10.3969/j.issn1671-7775.2014.03.006

Meng, F., Li, Y., and Pei, J. (2021). Energy Characteristics of Full Tubular Pump Device with Different Backflow Clearances Based on Entropy Production. *Appl. Sci.* 11 (8), 3376. doi:10.3390/app11083376

Mompean, G. (1998). Numerical Simulation of a Turbulent Flow Near a Right-Angled Corner Using the Speziale Non-linear Model with RNG $K–\varepsilon$ Equations. *Comput. Fluids* 27 (7), 847–859. doi:10.1016/s0045-7930(98)00004-8

Mu, T., Zhang, R., Xu, H., Zheng, Y., Fei, Z., and Li, J. (2020). Study on Improvement of Hydraulic Performance and Internal Flow Pattern of the Axial Flow Pump by Groove Flow Control Technology. *Renew. Energy* 160, 756–769. doi:10.1016/j.renene.2020.06.145

Nandan Kumar, K., and Govardhan, M. (2014). On Topology of Flow in a Turbine Cascade. *J. Fluids Eng.* 136 (8), 081201. doi:10.1115/1.4026056

Roache, P. J. (1997). Quantification of Uncertainty in Computational Fluid Dynamics. *Annu. Rev. Fluid Mech.* 29, 123–160. doi:10.1146/annurev.fluid.29.1.123

Shen, X., Zhang, D., Xu, B., Jin, Y., and Shi, W. (2020). Experimental Investigation of the Transient Patterns and Pressure Evolution of Tip Leakage Vortex and Induced-Vortices Cavitation in an Axial Flow Pump. *J. Fluids Eng.* 142 (10), 101206. doi:10.1115/1.4047529

Shi, L., Zhu, J., Wang, L., Chu, S., Tang, F., and Jin, Y. (2021). Comparative Analysis of Strength and Modal Characteristics of a Full Tubular Pump and an Axial Flow Pump Impellers Based on Fluid-Structure Interaction. *Energies* 14 (19), 6395. doi:10.3390/en14196395

Song, X., and Liu, C. (2021). Experimental Study of the Floor-Attached Vortices in Pump Sump Using V3V. *Renew. Energy* 164, 752–766. doi:10.1016/j.renene.2020.09.088

Wang, Y., Yu, H., Guo, Y., Yan, M., Sui, H., Zhang, Y., et al. (2020). Numerical Study on Pressure Pulsation Characteristics of Liquid LBE Medium Axial-Flow Pump. *Nucl. Power Eng.* 41 (03), 202–207. doi:10.13832/j.jnpe.2020.03.0202

Wang, F. J. (2020). *Analysis Method of Flow in Pumps and Pumping Stations*. Beijing, China: China Water & Power Press.

Xie, R., Hua, E., Xu, G., Guo, X., Yang, F., and Tang, F. (2022). Research on Double Hump Phenomenon of Axial Flow Pump. *Trans. Chin. Soc. Agric. Mach.* 53 (01), 178–185. doi:10.6041/j.issn1000-1298.2022.01.019

Xu, Z., Zheng, Y., Kan, K., and Huang, J. (2021). Runaway Characteristics of Bidirectional Horizontal Axial Flow Pump with Super Low Head Based on Entropy Production Theory. *Trans. Chin. Soc. Agric. Eng.* 37 (17), 49–57. doi:10.11975/j.issn1002-6819.2021.17.006

Yang, F., Jiang, D., Wang, T., Chang, P., Liu, C., and Liu, D. (2021). Investigation into the Influence of Division Pier on the Internal Flow and Pulsation in the Outlet Conduit of an Axial-Flow Pump. *Appl. Sci.* 11 (15), 6774. doi:10.3390/app11156774

Yang, F., Chang, P., Yuan, Y., Li, N., Xie, R., Zhang, X., et al. (2021b). Analysis of Timing Effect on Flow Field and Pulsation in Vertical Axial Flow Pump. *J. Marine Sci. Eng.* 9 (12), 1429. doi:10.3390/jmse9121429

Yang, F., Li, Z., Fu, J., Lv, Y., Ji, Q., and Jian, H. (2022a). Numerical and Experimental Analysis of Transient Flow Field and Pressure Pulsations of an Axial-Flow Pump Considering the Pump-Pipeline Interaction. *J. Marine Sci. Eng.* 10 (2), 258. doi:10.3390/jmse10020258

Yang, F., Chang, P., Li, C., Shen, Q., Qian, J., and Li, J. (2022b). Numerical Analysis of Pressure Pulsation in Vertical Submersible Axial Flow Pump Device under Bidirectional Operation. *AIP Adv.* 12 (2), 025107. doi:10.1063/5.0063797

Yang, F., Li, Z., Hu, W., Liu, C., Jiang, D., Liu, D., et al. (2022). Analysis of Flow Loss Characteristics of Slanted Axial-Flow Pump Device Based on Entropy Production Theory. *R. Soc. open Sci.* 9 (1), 211208. doi:10.1098/rsos.211208

Yang, W., Yang, K., Fu, Z., and Wu, J. (2022). Numerical Study of Blade Loading Effects on Tip Leakage Flow in Axial Flow Pump. *Trans. Chin. Soc. Agric. Mach.* 1-12. [2022-03-23].

Yang, F. (2020). *Internal Flow Characteristics and Hydraulic Stability of Low-Head Pump Device*. Beijing, China: China Water & Power Press.

Zhang, D., Shi, W., Zhang, H., Yao, J., and Guan, X. (2012). Application of Different Turbulence Models for Predicting Performance of Axial Flow Pump. *Trans. Chin. Soc. Agric. Eng.* 28 (1), 6671+296. doi:10.3969/j.issn.1002-6819.2012.01.013

Zhang, Y., Xu, Y., Zheng, Y., Fernandez-Rodriguez, E., Sun, A., Yang, C., et al. (2019). Multiobjective Optimization Design and Experimental Investigation on the Axial Flow Pump with Orthogonal Test Approach. *Complexity* 2019, 1–14. doi:10.1155/2019/1467565

Zhang, X., Tang, F., Liu, C., Shi, L., Liu, H., Sun, Z., et al. (2021). Numerical Simulation of Transient Characteristics of Start-Up Transition Process of Large Vertical Siphon Axial Flow Pump Station. *Front. Energy Res.* 9, 382. doi:10.3389/fenrg.2021.706975

Zhang, X., Tang, F., Chen, Y., Huang, C., Chen, Y., Wang, L., et al. (2022). Experimental Study on the Internal Pressure Pulsation Characteristics of a Bidirectional Axial Flow Pump Operating in Forward and Reverse Directions. *Machines* 10 (3), 167. doi:10.3390/machines10030167

Zhao, H., Wang, F., Wang, C., Chen, W., Yao, Z., Shi, X., et al. (2021). Study on the Characteristics of Horn-like Vortices in an Axial Flow Pump Impeller under Off-Design Conditions. *Eng. Appl. Comput. Fluid Mech.* 15 (1), 1613–1628. doi:10.1080/19942060.2021.1985615

Zhou, Y., Chen, B., Zhang, D., Zhang, H., and Yang, C. (2022). Influence of Double-Layer Flow Passage Structure after Impeller on External Characteristics of Axial-Flow Pump. *Trans. Chin. Soc. Agric. Mach.* 53 (02), 149–157+176. doi:10.6041/j.issn.1000-1298.2022.02.15

Conflict of Interest: The authors declare that the research was conducted in the absence of any commercial or financial relationships that could be construed as a potential conflict of interest.

NOMENCLATURE

List of symbols

C_p Pressure coefficient

D_2 Exit diameter of shroud

D Impeller diameter

F_R Radial force

F_x The radial force component on x axis

F_y The radial force component on y axis

F_Z Axial force

GCI_{21} Grid convergence index of grid scheme 2 and grid scheme 1

GCI_{32} Grid convergence index of grid scheme 3 and grid scheme 2

GCI_{43} Grid convergence index of grid scheme 4 and grid scheme 3

GCI_{54} Grid convergence index of grid scheme 5 and grid scheme 4

GCI_{65} Grid convergence index of grid scheme 6 and grid scheme 5

GCI_{76} Grid convergence index of grid scheme 7 and grid scheme 6

H_y Working head of impeller

N The number of grid nodes on the coupling surface

$\bar{P}$ Average pressure

P Instantaneous pressure

P_i The pressure at the ith grid node

P_{zh} The axial force generated by water flow on the hub

P_z The axial force on the blade

Q_{bep} Design flow rate

R The radius of the impeller

r The radius from the measuring point to the hub

R_m Hub radius

S_p Blade radial coefficient

T Rotation cycle

ρ The density of water

V Circular velocity

Abbreviations

CFD Computational fluid dynamics

FAV Floor-attached vortex

N-S Navier–Stokes

RNG Renormalization group

GCI Grid convergence index

FFT Fast Fourier transform

BPF Blade passing frequency

frontiers | Frontiers in Energy Research

ORIGINAL RESEARCH
published: 22 July 2022
doi: 10.3389/fenrg.2022.955492

Investigation on the Effect of the Shaft Transition Form on the Inflow Pattern and Hydrodynamic Characteristics of the Pre-Shaft Tubular Pump Device

Can Luo[1], Kang Du[1], Weijun Qi[2], Li Cheng[1], Xianbei Huang[3] and Jiaxing Lu[4,5]*

[1]College of Hydraulic Science and Engineering, Yangzhou University, Yangzhou, China, [2]Huaian Water Conservancy Survey Design and Research Institute Co., Ltd., Huaian, China, [3]College of Electrical, Energy and Power Engineering, Yangzhou University, Yangzhou, China, [4]Key Laboratory of Fluid and Power Machinery, Ministry of Education, Xihua University, Chengdu, China, [5]School of Energy and Power Engineering, Xihua University, Chengdu, China

OPEN ACCESS

Edited by:
Kan Kan,
College of Energy and Electrical Engineering, China

Reviewed by:
Qiang Gao,
University of Minnesota Twin Cities, United States
Shibiao Fang,
Shenzhen University, China

***Correspondence:**
Can Luo
luocan@yzu.edu.cn

Specialty section:
This article was submitted to Process and Energy Systems Engineering, a section of the journal Frontiers in Energy Research

Received: *28 May 2022*
Accepted: *20 June 2022*
Published: *22 July 2022*

Citation:
Luo C, Du K, Qi W, Cheng L, Huang X and Lu J (2022) Investigation on the Effect of the Shaft Transition Form on the Inflow Pattern and Hydrodynamic Characteristics of the Pre-Shaft Tubular Pump Device. Front. Energy Res. 10:955492. doi: 10.3389/fenrg.2022.955492

The shaft tubular pump device is widely used in low head pumping stations in plain areas. The N-S equation and the SST *k*-*ω* turbulence model are adopted. Then, the investigation on the influence of the shaft transition form on the inflow pattern and hydrodynamic characteristics of the pre-shaft tubular pump device is carried out. By designing three transition forms of shafts, different inflow patterns are provided for the tubular pump device. The characteristic parameters of the shafts and external and internal flow characteristics of the pumping device under different inflow patterns are compared and analyzed. Finally, the optimal transition form is selected for model tests, and unsteady pressure pulsation characteristics are studied. The results show that the flow pattern in the inlet passage of each case is relatively uniform and smooth, and the range of the high-efficiency zone of the pump device is roughly within $0.9Q_d$–$1.2Q_d$. The energy loss and the weighted average angle on the outlet of each case are similar. The axial velocity distribution uniformity on the impeller inlet of case 1 is better than that of the other cases. The numerical simulation results are consistent with the experimental results, and the numerical simulation method is reliable. Under the design condition, the pressure pulsation amplitude at the impeller inlet is the largest. It gradually increases from the hub to the shroud. The main frequency of pressure pulsation is the blade frequency. The pressure pulsation amplitude at the impeller outlet decreases from the hub to the shroud. The main frequency is not constant due to the rotor–stator interaction between the impeller and the guide vane. The outcome will be beneficial to the design and optimization of the shaft tubular pump device, which is helpful for broadening the corresponding theory and applying it to the actual project.

Keywords: shaft tubular pump device, shaft transition, hydraulic performance, pressure pulsation, numerical simulation, model test

1 INTRODUCTION

Shaft tubular pump devices are widely used in extra-low head pumping stations (0–2 m) with low head and large discharge (Liu, 2015; Kan, 2021). The motor operates in the shaft for the shaft tubular pump device, which has a simple structure, small flat size, straight inlet and outlet passages, convenient maintenance, and low construction cost (Jin et al., 2021). According to the location of the shaft, the shaft tubular pump device can be divided into the pre-shaft type and the post-shaft type. The overall flow pattern and hydraulic performance of the pre-shaft tubular pump device are better than those of the post-shaft tubular pump device. Therefore, the pre-shaft tubular pump device is more commonly applied in the pumping station (Chen et al., 2014).

With the development of CFD (computational fluid dynamics), numerical simulation has become a mature research tool and has been widely used in hydraulic engineering. On the one hand, some researchers have paid attention to the shaft tubular pump device by using the CFD method in recent years (Gonza´lez et al., 2002; Landvogt et al., 2014; Lucius and Brenner, 2011; Kan et al., 2021a; Kan et al., 2021b; Kan et al., 2020; Ansar et al., 2002). Liu et al. (2010) studied and analyzed the flow pattern of the pre-shaft and post-shaft tubular pumps. The results show that the guide vane and the shaft are the key factors affecting the flow pattern in the inlet passage and the efficiency of the device. Xu et al. (2011), (2012) conducted a comprehensive study on the shaft tubular pump device and pointed out the excellent hydraulic performance of the shaft tubular pump device. Lu and Zhang (2012) conducted a model test study on the shaft tubular pump device of an extra-low head pumping station and analyzed its hydraulic performance at different blade angles. Yang et al. (2014a) and (2014b) studied the evolution of the shaft profile and its effect on the internal flow characteristics of the tubular pump system, and the one-dimensional hydraulic design method is used to optimize the inlet passage. Shi et al. (2016) utilized the CFD method combined with a model test to finish the design optimization of the bidirectional shaft tubular pump device. The results showed that the inside and outside lines of the bifurcation segment type of the inlet passage had a large impact on the hydraulic loss of the inlet passage and directly affected the hydraulic loss of the following part after the bifurcation segment of the inlet passage. Meng et al. (2017) investigated the guide vane position affecting the hydraulic performance and flow pattern of the bidirectional tubular pump device. In addition, Xie et al. (2015), Zhou et al. (2021), and Qian et al. (2022) also optimized the shaft tubular pump device. The results showed that the optimization of the shaft tail profile is more beneficial to reducing hydraulic loss than the optimization of the shaft head profile and length, while optimizing the bifurcation segment profile of the shaft can significantly improve the hydraulic performance of the pump device. On the other hand, lots of previous research work about the pressure pulsation in hydraulic machinery had also been carried out. Zhu et al. (2010) pointed out that pressure pulsation has an important effect on the stable operation of the pump device. Wang et al. (2007) used a large eddy simulation method to conduct a more comprehensive and in-depth study and analysis of the pressure pulsation characteristics in the axial flow pump. The main frequency of the pressure pulsation in the axial flow pump is the blade frequency, and the pulsation at the outlet of the guide vane is dominated by low frequency. Dai et al. (2013) analyzed the effect of the turbulent flow model on pressure pulsation and pointed out that the SST k-ω model is suitable for studying the pressure pulsation of circulating pumps. Zhen et al. (2010) studied the pressure pulsation characteristics of the axial flow pump under different blade angles of the impeller and heads by using the model test method. Zhang et al. (2014) measured the pressure pulsation of the axial flow pump under different conditions. The experimental results revealed the pressure pulsation law at different locations inside the axial flow pump. Shi et al. (2014) tested the pressure pulsation of the key points at different speeds for the axial-flow pump. Shen et al. (2018) utilized the computational fluid dynamics method to study the hydrodynamic characteristics of the axial flow pump with different tip clearance distances. Wei et al. (2019) studied the propagation of pressure pulsation in a two-stage double suction centrifugal pump using an unsteady method. Al-Obaidi (2020) studied the hydrodynamic characteristics of axial flow pumps with different impeller blade numbers. Ji et al. (2022) compared

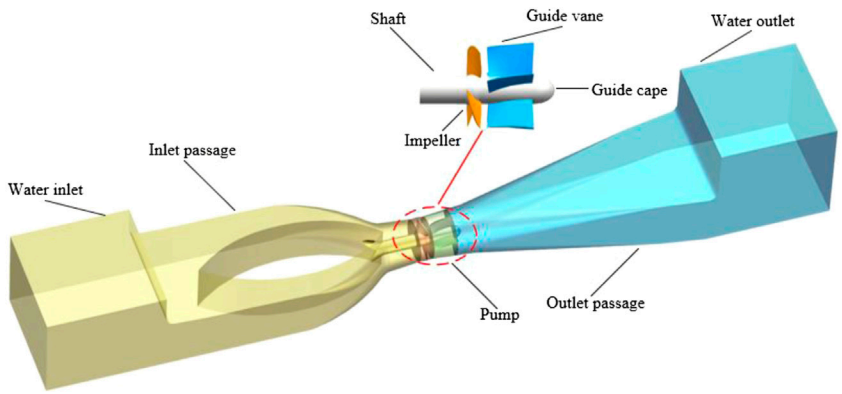

FIGURE 1 | Computational domain.

TABLE 1 | Main design parameters.

Parameter	Impeller diameter *D* (mm)	Rotation speed *n* (rev/min)	Design flow rate Q_d (L/s)	Blade number	Guide vane number
Value	300	981	210	3	5

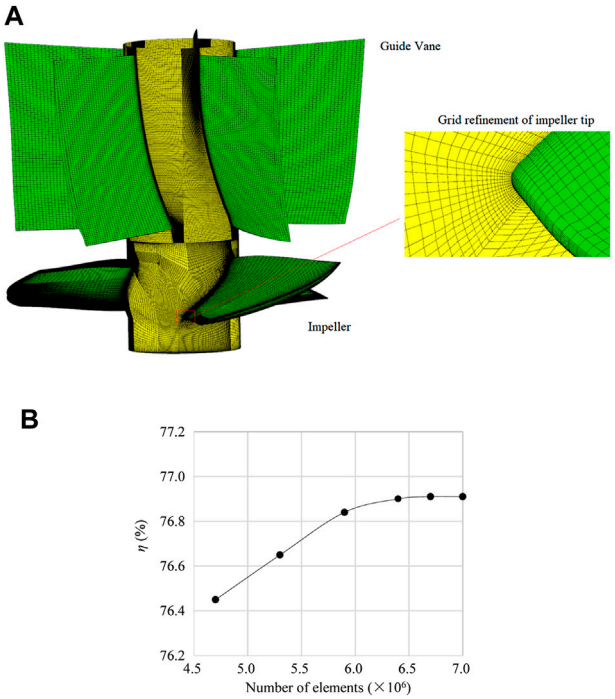

FIGURE 2 | (A) Mesh generation. **(B)** Grid independence analysis.

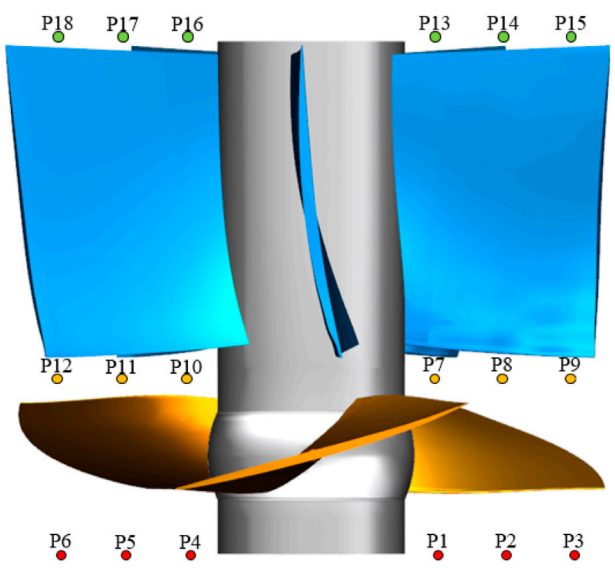

FIGURE 3 | Layout of monitoring points.

the hydraulic performance and pressure pulsation characteristics of the pre-shaft tubular pump and the post-shaft tubular pump by applying the numerical simulation and model test method. Shi et al. (2021) investigated the pressure pulsation characteristics between a full tubular pump and an axial flow pump based on the CFD method.

In this study, a pre-shaft tubular pumping station is used as the research object. By using the CFD method, the inflow pattern of the tubular pump with different shaft transition types and its influence on its hydraulic performance are analyzed. Then, the optimal shaft transition form is confirmed to promote the model experiment and unsteady pressure pulsation characteristics in the following. The results will benefit the optimization of the inlet passage design for the shaft tubular pump.

2 NUMERICAL SIMULATION

2.1 Governing Equations

The flow in the shaft tubular pump device follows the mass conservation equation and the momentum conservation equation. In this study, the Reynolds time-averaged N-S equation is selected to describe the flow in the shaft tubular pump device, and its governing equation (Kan et al., 2020) is as follows:

The continuity equation is as follows:

$$\frac{\partial \rho}{\partial t} + \frac{\partial}{\partial x_j}\left(\rho \overline{u_j}\right) = 0. \tag{1}$$

The momentum equation is expressed as follows:

$$\frac{\partial \rho \overline{u_i}}{\partial t} + \frac{\partial}{\partial x_j}\left(\rho \overline{u_i u_j}\right) = -\frac{\partial \bar{p}}{\partial x_i} + \frac{\partial}{\partial x_i}\left(\mu \frac{\partial \overline{u_i}}{\partial x_j} - \rho \overline{u_i{}' u_j{}'}\right) + f_i, \tag{2}$$

where $\overline{u_i}$ and $\overline{u_j}$ denote the components of the Reynolds time mean velocity in the i and j directions, respectively, m/s. x_i and x_j denote the components of the Cartesian coordinates in the i and j directions, respectively, m. t denotes time, s. ρ denotes the fluid density, kg/m^3. $\bar{p}$ denotes the time-averaged pressure, Pa. μ denotes the dynamic viscosity, Pa·s. $-\rho \overline{u_i{}' u_j{}'}$ denotes the Reynolds stress, Pa. f_i denotes the mass force component, N.

The shear–stress transport (SST) k-ω (Zhao et al., 2021) turbulence model can modify the turbulent viscosity equation. Thus, the shear stress on the wall and the flow in the near-wall region are better transferred and predicted. Moreover, the over-prediction of the turbulent viscosity can be avoided. Therefore, the SST k-ω turbulence model is chosen to close the governing equations, where the turbulent kinetic energy k equation is as follows:

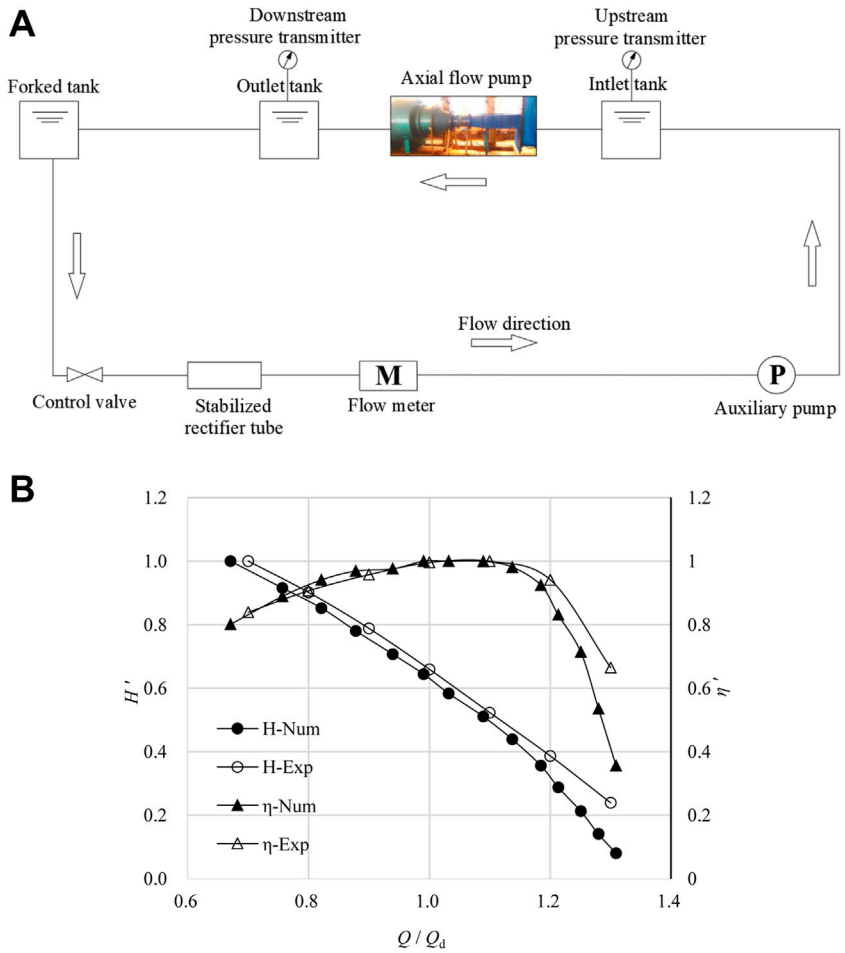

FIGURE 4 | (A) Schematic diagram of the test system. **(B)** Experimental and numerical simulation results.

$$\rho\frac{\partial(k)}{\partial t}+\rho\frac{\partial}{\partial x_j}\left(U_j k\right)=\frac{\partial}{\partial x_j}\left[\left(\mu+\frac{\mu_t}{\sigma_k}\right)\frac{\partial k}{\partial x_j}\right]+P_k-\beta'\rho k\omega. \quad (3)$$

The turbulent dissipation rate ω equation is given by the following:

$$\frac{\partial(\rho\omega)}{\partial t}+\frac{\partial}{\partial x_j}\left(\rho U_j\omega\right)=\frac{\partial}{\partial x_j}\left[\left(\mu+\frac{\mu_t}{\sigma_\omega}\right)\frac{\partial\omega}{\partial x_j}\right]+\alpha\frac{\omega}{k}P_k-\beta\rho\omega^2+2\left(1-F_1\right)\rho\frac{1}{\sigma_{\omega 2}\omega}\frac{\partial k}{\partial x_j}\frac{\partial\omega}{\partial x_j}, \quad (4)$$

where U_j is the vector velocity, m/s. μ_t is the turbulent viscosity, m^2/s. P_k is the turbulent generation rate. F_1 is the mixing function. β' is the empirical coefficient, usually taken as 0.09. α, β, and σ are correlation constants.

2.2 Computational Domain

To ensure the incoming and outgoing flow patterns of the inlet and outlet passages, the extension parts named as the water inlet and water outlet are provided before the inlet passage and after the outlet passage, respectively. In other words, the computational domain includes the water inlet, inlet passage, impeller, guide vane, outlet passage, and water outlet, as shown in **Figure 1**. Its main design parameters are listed in **Table 1** below.

2.3 Mesh Generation

Based on the ANSYS ICEM platform, the pre-shaft tubular pump is divided into blocks, and the structured meshes are generated, as shown in **Figure 2A**. The inlet passage is spatially discretized with a more adaptive unstructured mesh. To obtain the reliable mesh, the grid-independence analysis is performed. The efficiency is selected as the characteristic parameter. **Figure 2B** shows the efficiency growth trend of six different meshes under the design condition. When the number of grids exceeds 6.74 million, the error of the efficiency is less than 0.04%, so the number of meshes is confirmed as 6.74 million.

2.4 Boundary Condition

For steady simulation, the inlet of the water inlet is set as the mass flow. The outlet of the water outlet is set as the pressure. The impeller is set as the rotational domain with a speed of −981 rev/

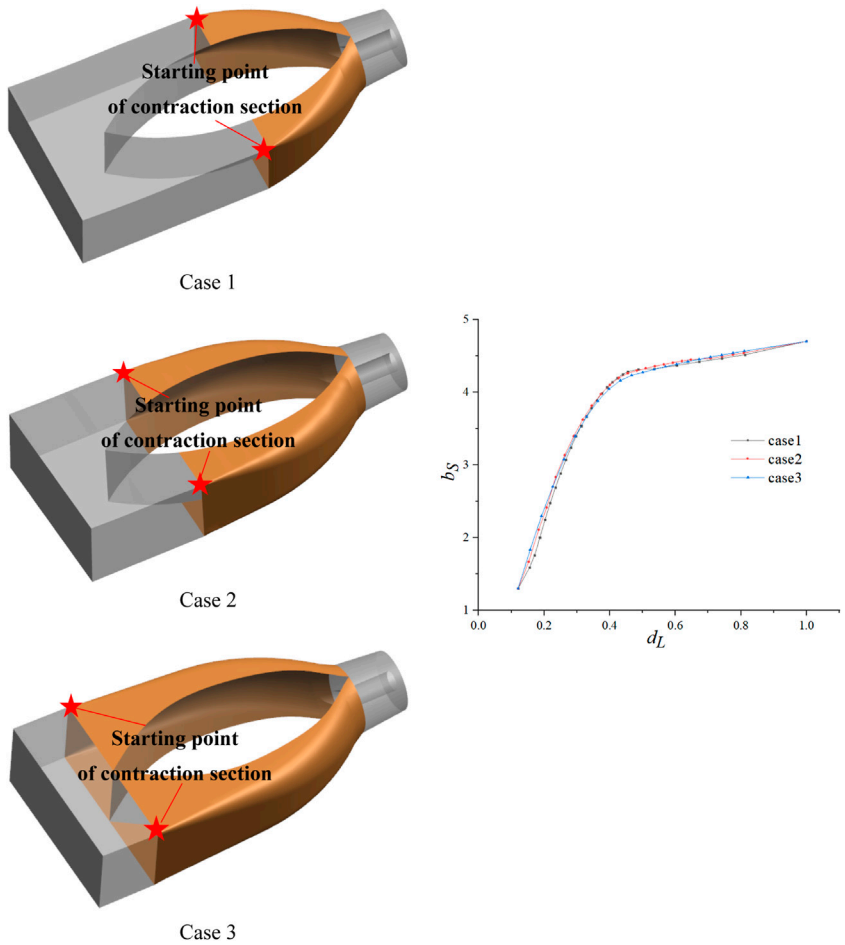

FIGURE 5 | Cross-sectional area of the variation curve of the inlet passage for each case.

min. The "Stage" model is applied for the interfaces between the rotating domain and the non-rotating domain, such as the "inlet passage outlet—impeller inlet" interface and the "impeller outlet—guide vane inlet" interface. All other interfaces are static interfaces. No slip boundary is adopted for the wall, and the near-wall region is treated as a standard wall function. The convergence accuracy is set to 1.0×10^{-4}. Under unsteady simulation, the time step is set to 1.02×10^{-4} s, the impeller rotates 6° per time step, and the total calculation time is 0.489 s. The monitoring probes are shown in **Figure 3**. Two groups of monitoring probes are arranged from the hub to the shroud on the outlet of the impeller, which are P1–P3 and P4–P6. Another two groups of monitoring probes are arranged along the radial direction on the inlet of the impeller, which are P7–P9 and P10–P12. In addition, two groups of monitoring probes are arranged from the hub to the shroud on the outlet of the guide vane, which are P13–P15 and P16–P18.

2.5 Model Test

Figure 4A shows the high-precision hydraulic cycle test system. The system has a comprehensive error of ±0.39%. The random error of this experiment is ±0.1321%. Meanwhile, based on the pump head and efficiency of the best efficiency point, the head and efficiency of the other conditions are normalized. **Figure 4B** shows the numerical simulation results and the experiment results. The external characteristic curves obtained from the numerical simulation and the experiment are basically consistent. The errors of the efficiency and the head under the design condition are not more than 5%. It shows that the numerical simulation method is reliable.

3 RESEARCH CASES

In order to obtain the influence on the hydrodynamic characteristics of the shaft tubular pump device under different inflow patterns, three different transition forms of the shaft are designed. As shown in **Figure 5**, the sections are sliced and numbered from the outlet to the inlet of the inlet passage, according to the location of the beginning of the contraction section. The b_S is the relative area, which is obtained by b_i/S, where b_i is the area of the ith section, and S is the impeller inlet area. d_L is the relative spacing, which is calculated by d_i/L, where d_i is the distance of the inlet section of the inlet passage of the ith section, and L is the total length of the inlet passage.

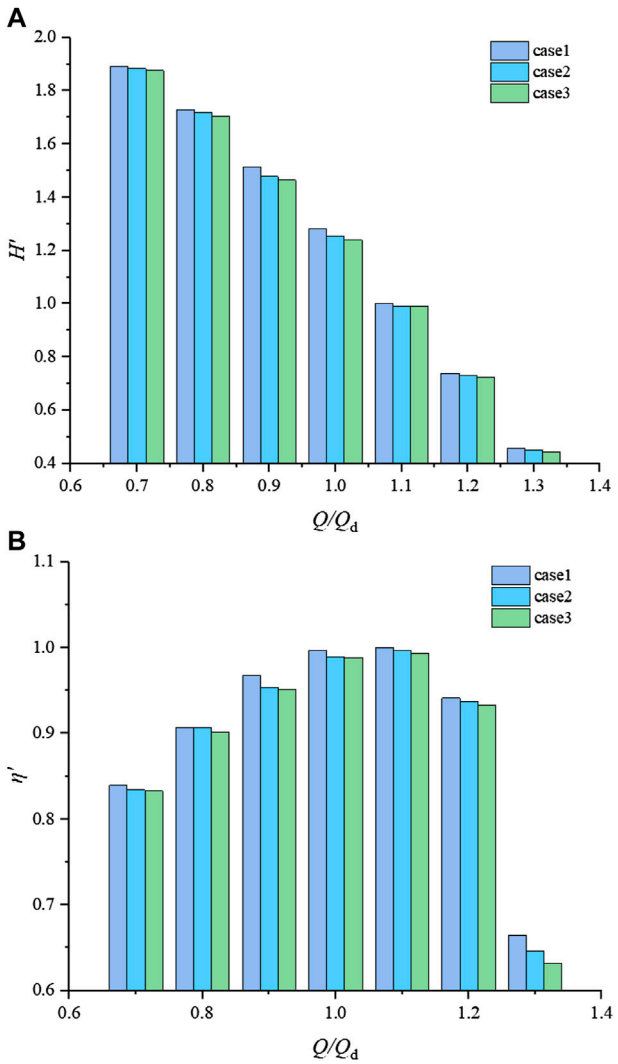

FIGURE 6 | Hydraulic performance of each case. **(A)** *Q-H′* curve. **(B)** *Q-η′* curve.

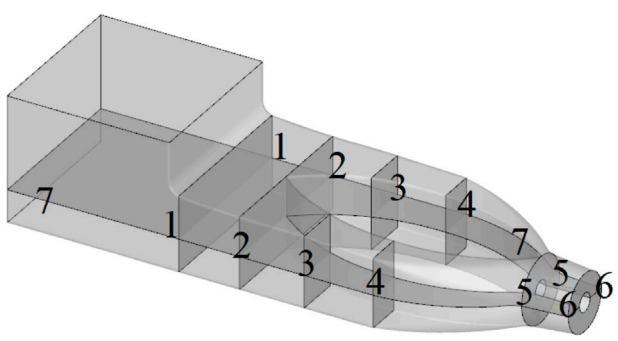

FIGURE 7 | Location of the analysis cross section.

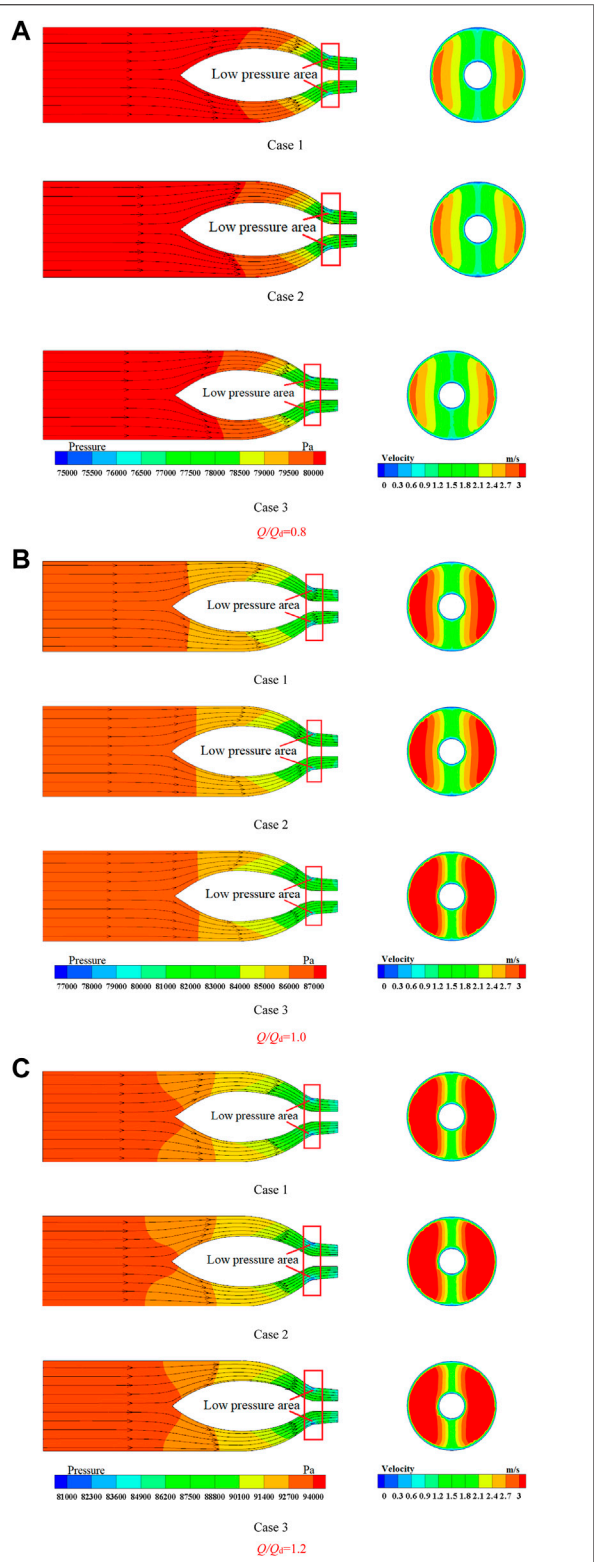

FIGURE 8 | Streamlines and the pressure distribution on the center section (left) and the velocity distribution on section 5-5 (right) of different cases under each condition. **(A)** $Q/Q_d = 0.8$ **(B)** $Q/Q_d = 1.0$ **(C)** $Q/Q_d = 1.2$.

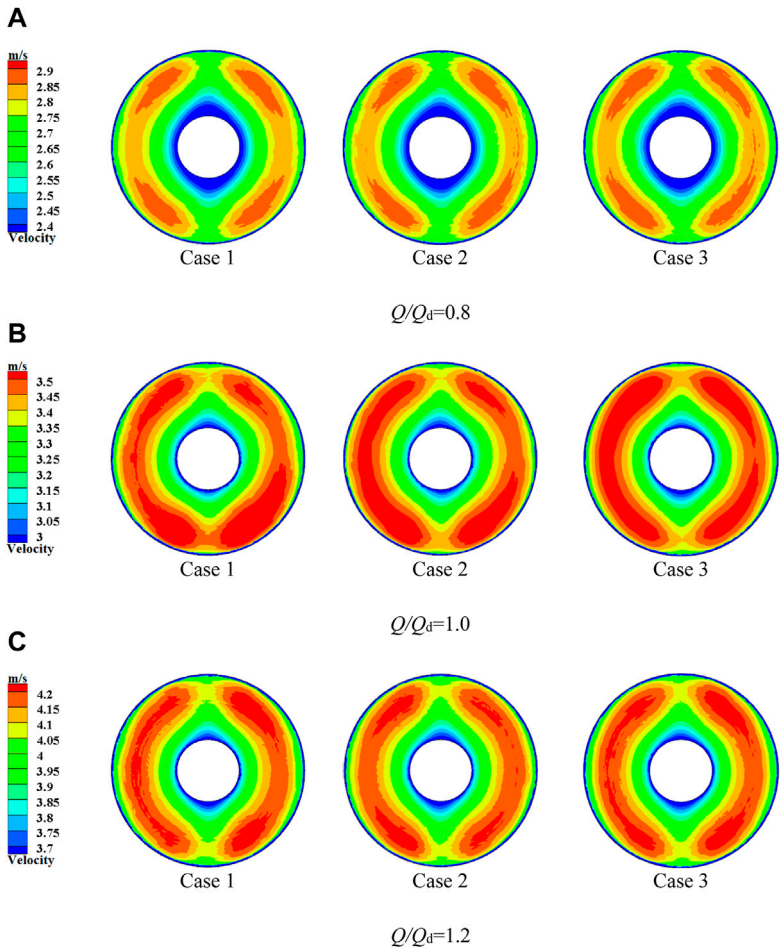

FIGURE 9 | Velocity contours on the outlet of the inlet passage. **(A)** Q/Q_d = 0.8 **(B)** Q/Q_d = 1.0 **(C)** Q/Q_d = 1.2.

4 RESULT ANALYSIS

4.1 External Characteristics

The head and efficiency reflect the external characteristic performance of the pump unit. Based on the head and efficiency of the best efficiency point of case 1, the head and efficiency of the other conditions are normalized. The dimensionless head and efficiency of each case are shown in **Figure 6A,B**.

4.2 Analysis Sections and Parameters

4.2.1 Analysis Sections

To capture the energy characteristics and flow features of the inlet passage in detail, seven characteristic sections are sliced along the flow direction, which is noted as *n-n* sections (*n* takes 1–7). As shown in **Figure 7**, the seven characteristic sections are the inlet section of the inlet passage, the starting transition section of each case, the outlet section of the inlet passage, and the center section of the inlet passage, which are intercepted sequentially.

4.2.2 Analysis Parameters

An evaluation index should be introduced to quantitatively analyze the hydraulic performance of the inlet passage of each case. Therefore, energy loss ratio ζ, axial velocity distribution uniformity V_u, and velocity-weighted average angle θ are defined. The energy loss ratio ζ represents the ratio of the energy loss ΔC_i of each adjacent section at different conditions to the total energy loss ΔC_t of the intake passage of case 1 under the optimal condition. Axial velocity distribution uniformity V_u indicates the uniformity of axial velocity distribution on the outlet section of the inlet passage. The velocity-weighted average angle θ indicates the angle between the velocity at the outlet of the inlet passage and the outlet cross section. Generally speaking, when the axial velocity distribution uniformity V_u is closer to 100%, the velocity distribution is more uniform. When the velocity-weighted average angle θ is closer to 90°, the flow goes smoothly. Similarly, the smaller the inlet passage energy loss ratio ζ, the higher the efficiency is.

$$H_i + \frac{P_i}{\rho g} + \frac{\gamma_i^2}{2g} = C, \tag{5}$$

where H_i denotes the elevation of the section, m. P_i denotes the total pressure of the section, Pa. v_i denotes the average velocity of the section, m.

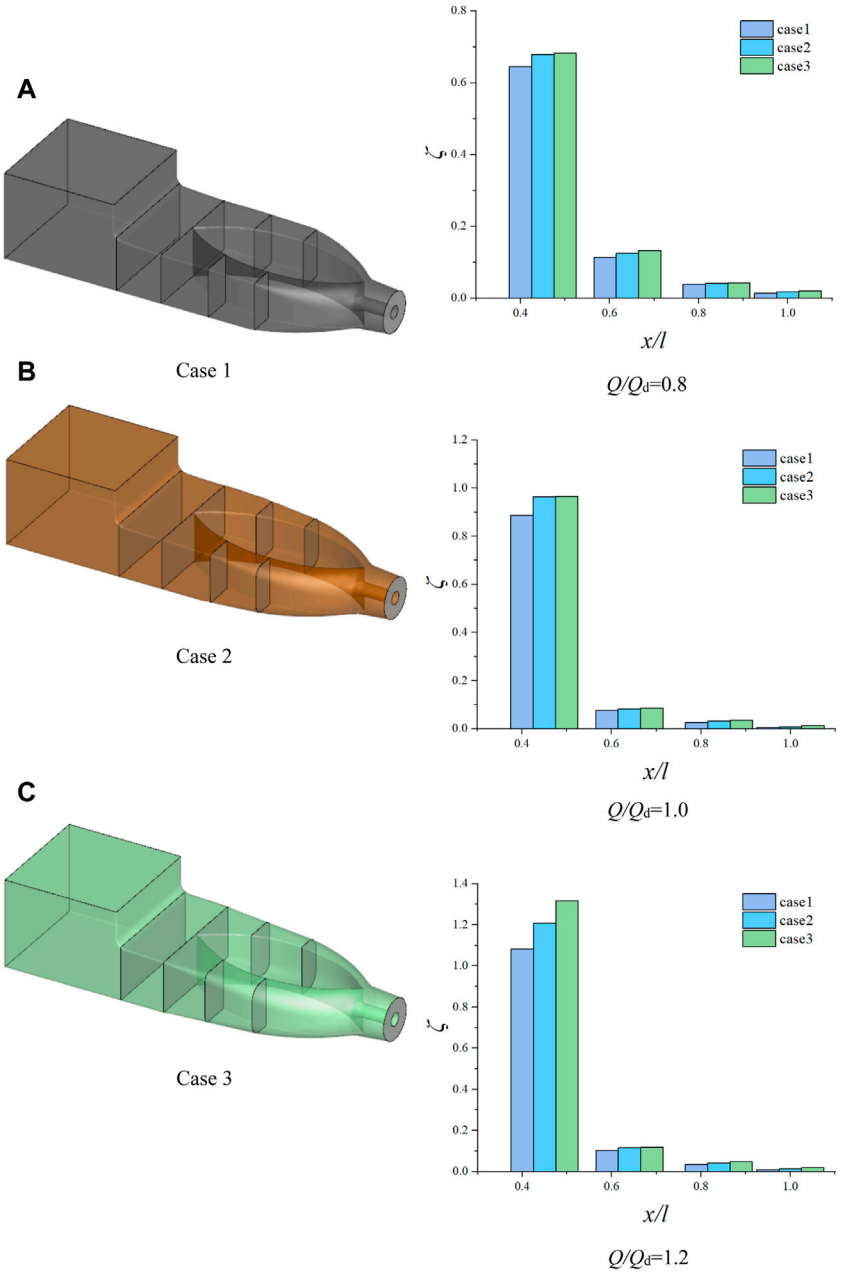

FIGURE 10 | Energy characteristics in the inlet passage for each case. **(A)** Q/Q_d = 0.8 **(B)** Q/Q_d = 1.0 **(C)** Q/Q_d = 1.2.

$$V_u = \left[1 - \frac{1}{\bar{u}_a}\sqrt{\frac{\sum (u_{ai} - \bar{u}_a)^2}{m}}\right] \times 100\%, \quad (6)$$

$$\theta = \frac{\sum_{i=1}^{n}\left[u_{ai}\left(90 - \arctan\frac{u_{ti}}{u_{ai}}\right)\right]}{\sum_{i=1}^{n} u_{ai}}, \quad (7)$$

where u_{ai} and $\bar{u}_a$, respectively, are the axial velocity of the node on the outlet of the inlet passage and the average axial velocity on the outlet of the inlet passage, m/s. u_{ti} indicates the normal velocity of the node on the outlet of the inlet passage, m/s.

4.3 Internal Flow Characteristics

Figure 8 shows the static pressure distribution and streamlines on section 7-7 and the velocity contours on section 5-5 with different transition forms under various conditions. As shown in **Figure 10**, the overall flow patterns in the inlet passage for all three cases are smooth, and there is no separation flow. At the head of the shaft, the flow is evenly divided into two streams. The velocity on both sides of the shaft increases, and the pressure decreases when the sections tend to contract. The streamline and pressure distribution are symmetrical on both sides of the shaft. At the end of the shaft, the flow merges into one stream smoothly. There is a small low

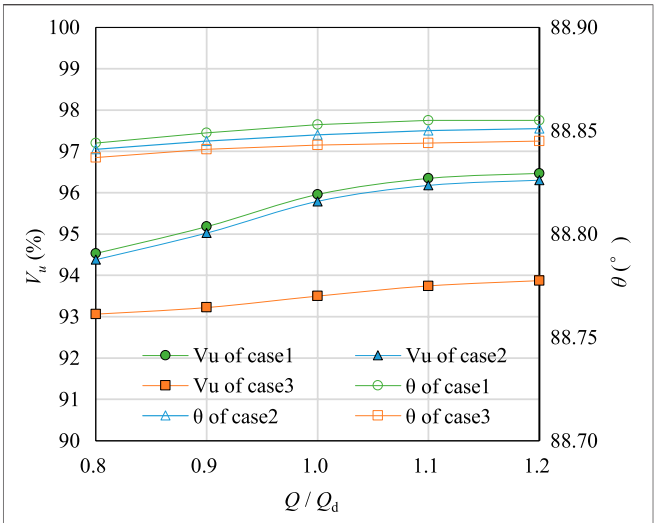

FIGURE 11 | Axial velocity distribution uniformity V_u and the velocity-weighted average angle θ on the outlet of the inlet passage for each case.

pressure area on both sides of the end in the contraction segment of the shaft. The low pressure area of cases 2 and 3 is approximately the same, which are slightly larger than that of case 1. Thus, section 5-5 is sliced, and there is a symmetrically distributed high velocity area which is corresponding to the low pressure area. The velocity at the outside of the shaft is larger than at the inside, and such a trend appears more obvious when the flow rate enlarges.

The inlet passage is mainly installed to provide a uniform flow pattern for the impeller. Therefore, it should ensure and give priority to the uniformity of the velocity on the outlet of the inlet passage. As shown in **Figure 9**, the velocity contours on the outlet of the inlet passage of each case under different conditions are given. As shown in **Figure 9**, the velocity on the outlet of each case is symmetrically distributed bilaterally and vertically under different conditions. The low velocity near the wall is observed. The velocity growth rate near the shaft is significantly greater than that which is far away from the shaft on the outlet.

Under the same condition, the velocity distribution on the outlet of each case shares the same trend. The velocity magnitude is basically similar. The symmetrical contraction on the left and right is much larger than that on the top and bottom. The mainstream is concentrated on the left and right near the outside, and the velocity on the top and bottom near the inside tends to be small. Moreover, the velocity distribution on the outlet is positively correlated with the flow rate. The maximum velocity under the condition of $1.0Q_d$ is about 1.20 times the maximum velocity under the condition of $0.8Q_d$. However, the maximum velocity under the condition of $1.2Q_d$ is also about 1.20 times the maximum velocity under the condition of $1.0Q_d$.

4.4 Energy Characteristics

Figure 10 shows the energy characteristics' trend of each section for each case under different conditions. The horizontal coordinate is the relative distance of each section from the outlet of the inlet passage, which is defined as x/l. The vertical coordinate is the energy loss ratio ζ of the section. For the inlet passage, the energy loss in the inlet passage is hydraulic loss, and there is no leakage loss. As shown in **Figure 10**, the energy from the inlet to the outlet in the inlet passage decreases with the increasing flow rates. In other words, the hydraulic losses keep increasing. The largest energy loss of each case happens in the shaft tail, which is from section 4-4 to section 6-6 under different conditions. Another major energy loss is located from section 3-3 to section 4-4. The energy loss originates from the severe transition of the shaft. The energy loss of case 1 is significantly smaller than that of the other two cases.

4.5 Velocity Uniformity Characteristics

Figure 11 shows the axial velocity distribution uniformity V_u and the velocity-weighted average angle θ on the outlet of the inlet passage for each case under different conditions. It can be seen that V_u and θ increase rapidly in the flow rate range of $0.8Q_d$ to $1.1Q_d$, and then, the increment is small. The V_u of case 1 is the highest. The axial velocity distribution uniformity is the best under the condition of $1.2Q_d$, whose value is 96.47%. The V_u and θ of case 3 are the worst, and its axial velocity distribution uniformity is the worst under the condition of $0.8Q_d$, whose value is 93.06%. Under the same flow rate condition, the axial velocity distribution uniformity on the outlet of the inlet passage for case 1 and case 2 is nearly the same, which is higher than that of case 3. The velocity-weighted average angle on the outlet of the inlet passage for case 1 is the largest, reaching 88.86°.

4.6 Pressure Pulsation Characteristics

The complex flow in the axial flow pump can lead to rapid pressure pulsation, which causes vibration and noise that reduces the efficiency and the life cycle of the pump. The flow is not stable in the early periods; therefore, the data on the last four periods are selected to analyze the pressure pulsation.

To establish the relationship between the pressure pulsation and the flow rate, the pressure pulsation of monitoring points P1-P3, P7-P9, and P13-P15 under the flow rate conditions of $0.8Q_d$, $1.0Q_d$, and $1.2Q_d$ is compared.

The pressure pulsation coefficient C_p and the multiplier of the shaft frequency f_n are introduced and calculated as follows：

$$f_n = \frac{60F}{n}, \tag{8}$$

$$C_p = \frac{2(p - \bar{p})}{\rho u^2}, \tag{9}$$

where F is the frequency by utilizing fast Fourier transform, Hz. p is the pressure at the monitoring point, Pa. $\bar{p}$ is the average pressure at the monitoring point during a period of the impeller, Pa. ρ is the fluid density, kg/m^3. u is the circumferential speed of the impeller, m/s.

Figure 12 shows the time domain chart (subfigures on the left) and frequency domain chart (subfigures on the right) of the pressure pulsation on the impeller inlet at monitoring points P1-P3 under different conditions. In the time domain chart of **Figure 12**, it can be seen that the pressure pulsation under each condition is sinusoidally distributed with obvious periodic fluctuations. When the rotator runs per round, three peaks and troughs appear. The number of

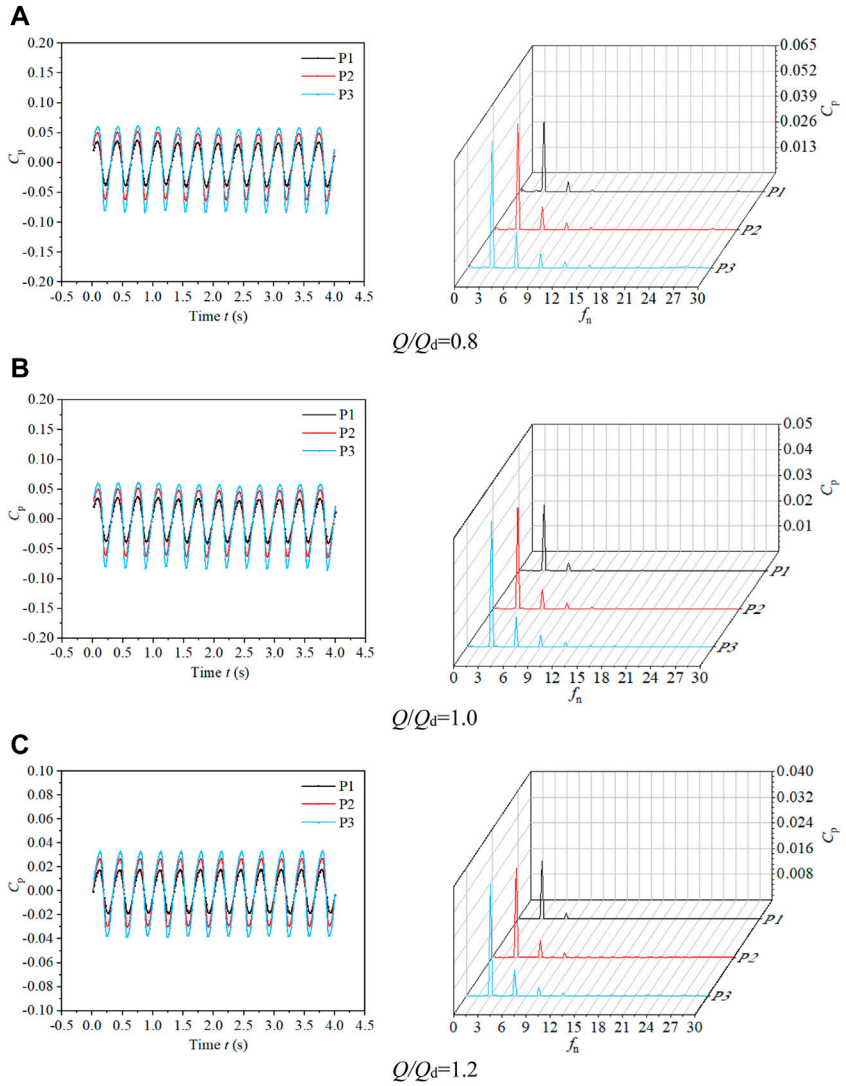

FIGURE 12 | Time domain chart and frequency domain chart of pressure pulsation on the impeller inlet at monitoring points P1-P3 under different conditions. **(A)** Q/Q_d = 0.8 **(B)** Q/Q_d = 1.0 **(C)** Q/Q_d = 1.2.

peaks and troughs is consistent with the blade number. The farther the monitoring point is from the hub, the larger the pressure pulsation amplitude is. The pressure pulsation amplitude of P3 is about 1.83 times that of P1 under the conditions of $0.8Q_d$, $1.0Q_d$, and $1.2Q_d$. The pressure pulsation of the impeller inlet is obviously periodic under each condition.

In the frequency domain chart of **Figure 12**, the amplitude of monitoring points P1, P2, and P3 increases gradually from the hub to the shroud along the radial direction at the impeller inlet under each condition. The pressure pulsation amplitude of P2 under the condition of $0.8Q_d$ is 1.36 times than that under the condition of $1.0Q_d$ and 1.94 times than that under the condition of $1.2Q_d$, respectively. Meanwhile, the main frequency of each monitoring point is 3 times the shaft frequency, and the secondary frequency is 6 times the shaft frequency. Therefore, the pressure pulsation at the impeller inlet is greatly influenced by the blade number.

Figure 13 shows the time domain chart (subfigures on the left) and frequency domain chart (subfigures on the right) of the pressure pulsation on the impeller outlet at monitoring points P7-P9 under different conditions. In the time domain chart of **Figure 13**, it is shown that the general trend of pressure pulsation of each condition is consistent. There are three peaks and troughs in a period for P7 and P8. However, there are five peaks and troughs for P9. The result shows that the pressure pulsation at the impeller outlet is still mainly influenced by the blade number of the impeller. For the monitoring point P9, the guide vane number dominates the growth low of the pressure pulsation on it. The reason is its location, which is close to the shroud of the impeller outlet and the guide vane.

In the frequency domain chart of **Figure 13**, the main frequencies of P7 and P8 at the impeller outlet are 3 times the shaft frequency under each condition. The main frequency of P9 is 5 times the shaft

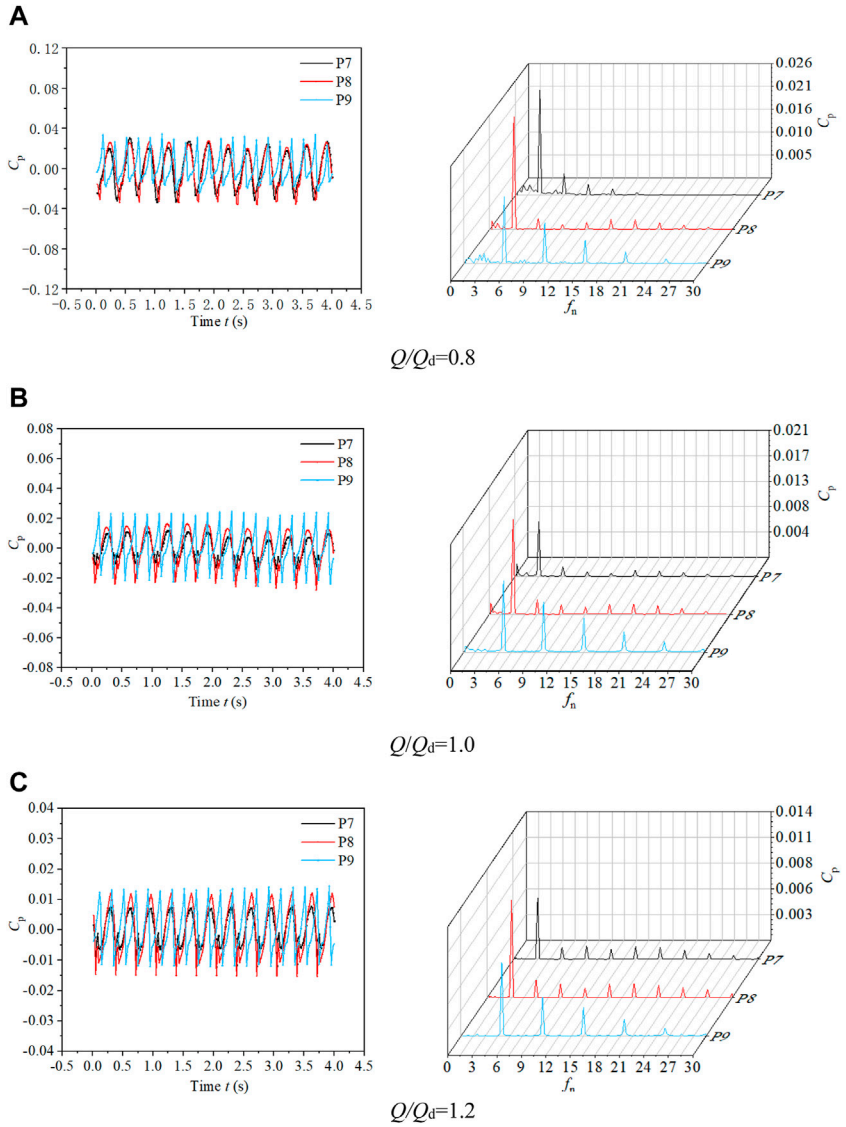

FIGURE 13 | Time domain chart and frequency domain chart of pressure pulsation on the impeller outlet at monitoring points P7-P9 under different conditions. **(A)** Q/Q_d = 0.8 **(B)** Q/Q_d = 1.0 **((C)** Q/Q_d = 1.2.

frequency. The pressure pulsation amplitude grows higher from the shroud to the hub. Due to the rotor–stator interaction between the impeller and the guide vane existing in the pump, the frequency spectrum is varied. Considering that the strength of the circulation caused by the pre-rotation of the impeller exceeds the circulation recovery caused by the guide vane, the absolute value of the pressure pulsation on the inlet of the impeller is larger than that on the outlet of the impeller for each case.

Figure 14 shows the time domain chart (subfigures on the left) and frequency domain chart (subfigures on the right) of the pressure pulsation on the guide vane outlet at monitoring points P13-P15 under different conditions. In the time domain chart of **Figure 14**, there is no obvious regular pattern and periodicity of the pressure pulsation for each condition, and random pulsation is observed. Under the conditions of $0.8Q_d$ and $1.0Q_d$, the wave of the pressure pulsation is relatively disordered. Under the condition of $1.2Q_d$, there are three peaks and troughs in a period. It shows that the pressure pulsation at the outlet of the guide vane is still influenced by the blade number of the impeller.

In the frequency domain chart of **Figure 14**, it is found that the frequency spectrum of the pressure pulsation at each monitoring point at the outlet of the guide vane under each condition is more complex due to the hydraulic conductivity and energy recovery of the guide vane, which is obviously different from the pressure pulsation characteristics of the impeller inlet and outlet. Under the conditions of $0.8Q_d$ and $1.0Q_d$, the pressure pulsation in the low frequency band is more complex, and the major frequency at each monitoring point is not obvious, and the amplitude is similar. Under the condition of $1.2Q_d$, the major frequency of the pressure pulsation at each monitoring point is the shaft

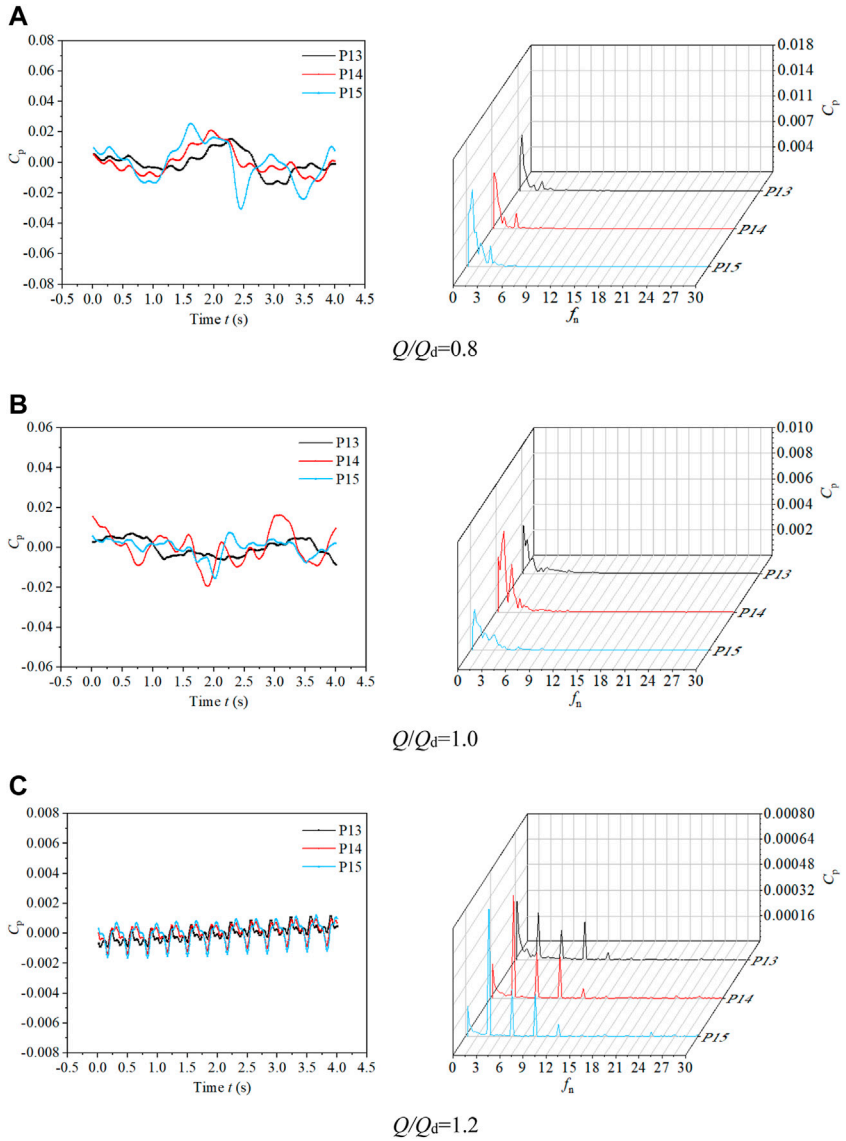

FIGURE 14 | Time domain chart and frequency domain chart of pressure pulsation on the guide vane outlet at monitoring points P13-P15 under different conditions. **(A)** Q/Q_d = 0.8 **(B)** Q/Q_d = 1.0 **(C)** Q/Q_d = 1.2.

frequency. But there are multiple secondary frequencies near it, which are multiples of the shaft frequency of the impeller.

5 CONCLUSION

In this study, the investigation on the influence of the shaft transition form on the inflow pattern and hydrodynamic characteristics of the pre-shaft tubular pump device is carried out by using the CFD method. The pump device with the optimal transition form of the shaft is experimented upon, and unsteady pressure pulsation characteristics are studied. The conclusions are as follows:

1) The numerical simulation results are verified with model tests. The numerical simulation prediction results and experimental results are compared under different flow rate conditions. The errors are less than 5%, and the hydraulic performance curves match well. The numerical method is reliable, and the result is correct.
2) The hydraulic performance of case 1 is better than that of case 2 and case 3. The flow rate of the high-efficiency region is roughly in the range of $0.9Q_d$–$1.2Q_d$.
3) The flow in the inlet passage of three cases is smooth, and no obvious separation flow is observed. The velocity contours on the outlet of the shaft are symmetrically distributed bilaterally and vertically, providing the outstanding flow pattern for the impeller.
4) The transition form of the shaft has a limited effect on the energy characteristics and the weighted average angle of the inlet passage. The smoother the inlet passage transits, the lower the energy loss is. The axial velocity uniformity on the

outlet of the inlet passage for case 1 is better than that of the other cases.

5) The periodic pressure pulsation at the impeller inlet is obvious, and the amplitude is the largest compared with the impeller outlet and the guide vane outlet. The pressure pulsation increases from the hub to the shroud. However, the pressure pulsation at the guide vane outlet is aperiodic, and the amplitude is the smallest. The pressure pulsation near the hub is larger than that near the shroud.
6) The pressure pulsation at the impeller inlet is mainly related to the blade number of the impeller. Thus, the main frequency at the impeller inlet is the blade frequency. The main frequency near the hub at the impeller outlet also follows the regular pattern as mentioned previously. On the contrary, the main frequency near the shroud at the impeller outlet is related to the guide vane, and its value is not the blade frequency. In addition, the pressure pulsation at the guide vane outlet is also affected by the impeller under large flow rate conditions.

DATA AVAILABILITY STATEMENT

The raw data supporting the conclusion of this article will be made available by the authors, without undue reservation.

AUTHOR CONTRIBUTIONS

LC, data curation; WQ, formal analysis; JL and CL, methodology; CL and KD, writing—original draft; CL, KD, and WQ, writing—review and editing; XH, supervision.

FUNDING

This research was funded by the Jiangsu Province Science Foundation for Youths (Grant no. BK20170507), the Natural Science Foundation of the Jiangsu Higher Education Institutions (Grant no. 17KJD580003), the Jiangsu Planned Projects for Postdoctoral Research Funds (Grant no. 1701189B), the Open Research Subject of Key Laboratory of Fluid and Power Machinery (Xihua University), the Ministry of Education (Grant nos. szjj2019-018), the National Natural Science Foundation of China (Grant Nos. 51779214 and 51909231), the Open Research Subject of Key Laboratory of Fluid and Power Machinery (Xihua University), the Ministry of Education (Grant number LTDL2021-009), and the Priority Academic Program Development of Jiangsu Higher Education Institutions (PAPD).

REFERENCES

Al-Obaidi, A. R. (2020). Investigation of the Influence of Various Numbers of Impeller Blades on Internal Flow Field Analysis and the Pressure Pulsation of an Axial Pump Based on Transient Flow Behavior. *Heat. Transf.* 49 (4), 2000–2024. doi:10.1002/htj.21704

Ansar, M., Nakato, T., and Constantinescu, G. (2002). Numerical Simulations of Inviscid Three-Dimensional Flows at Single- and Dual-Pump Intakes. *J. Hydraulic Res.* 40 (4), 461–470. doi:10.1080/00221680209499888

Chen, S., Yan, H., Zhou, Z., He, Z., and Wang, L. (2014). Three-dimensional Turbulent Numerical Simulation and Model Test of Fro Shaft Tubular Inlet Conduit of the Pumping Station. *Trans. Chin. Soc. Agric. Eng.* 30 (02), 63–71. doi:10.3969/j.issn.1002-6819.2014.02.009

Dai, C., Kong, F.-y., and Dong, L. (2013). Pressure Fluctuation and its Influencing Factors in Circulating Water Pump. *J. Cent. South Univ.* 20 (1), 149–155. doi:10.1007/s11771-013-1470-6

Gonza´lez, J., Ferna´ndez, J. n., Blanco, E., and Santolaria, C. (2002). Numerical Simulation of the Dynamic Effects Due to Impeller-Volute Interaction in a Centrifugal Pump. *J. Fluids Eng.* 124 (2), 348–355. doi:10.1115/1.1457452

Ji, D., Lu, W., Lu, L., Xu, L., Liu, J., Shi, W., et al. (2022). Study on the Comparison of the Hydraulic Performance and Pressure Pulsation Characteristics of a Shaft Front-Positioned and a Shaft Rear-Positioned Tubular Pump Devices. *Jmse* 10, 8. doi:10.3390/jmse10010008

Jin, K., Chen, Y., Tang, F., Shi, L., Liu, H., and Zhang, W. (2021). Influence of Shaft Location on Hydraulic Characteristics of Bidirectional Tubular Pump Systems. *J. Hydroelectr. Eng.* 40 (09), 67–77. doi:10.11660/slfdxb.20210907

Kan, K. (2021). Hydrodynamic and Structural Stability Analysis for Shaft Tubular Pump Unit. *IOP Conf. Ser. Earth Environ. Sci.* 647 (1), 012038. doi:10.1088/1755-1315/647/1/012038

Kan, K., Chen, H., Zheng, Y., Zhou, D., Binama, M., and Dai, J. (2021). Transient Characteristics during Power-Off Process in a Shaft Extension Tubular Pump by Using a Suitable Numerical Model. *Renew. Energy* 164, 109–121. doi:10.1016/j.renene.2020.09.001

Kan, K., Yang, Z., Lyu, P., Zheng, Y., and Shen, L. (2021). Numerical Study of Turbulent Flow Past a Rotating Axial-Flow Pump Based on a Level-Set Immersed Boundary Method. *Renew. Energy* 168, 960–971. doi:10.1016/j.renene.2020.12.103

Kan, K., Zheng, Y., Chen, H., Zhou, D., Dai, J., Binama, M., et al. (2020). Numerical Simulation of Transient Flow in a Shaft Extension Tubular Pump Unit during Runaway Process Caused by Power Failure. *Renew. Energy* 154, 1153–1164. doi:10.1016/j.renene.2020.03.057

Landvogt, B., Osiecki, L., Patrosz, P., Zawistowski, T., and Zylinski, B. (2014). Numerical Simulation of Fluid-Structure Interaction in the Design Process for a New Axial Hydraulic Pump. *Prog. Comput. Fluid Dyn.* 14 (1), 31–37. doi:10.1504/PCFD.2014.059198

Liu, C. (2015). Researches and Developments of Axial-Flow Pump System. *Trans. Chin. Soc. Agric. Mach.* 46 (06), 49–59. doi:10.6041/j.issn.1000-1298.2015.06.008

Liu, J., Zhen, Y., Zhou, D., Mao, Y., and Zhang, L. (2010). Analysis of Basic Flow Pattern in Shaft Front-Positioned and Shaft Rea Positioned Tubular Pump Systems. *Trans. Chin. Soc. Agric. Mach.* 41 (S1), 32–38. doi:10.3969/j.issn.1000-1298

Lu, W., and Zhang, X. (2012). Research on the Model Test of Hydraulic Characteristics for Super-low Hea Shaft-Well Tubular Pump Unit. *J. Irrigation Drainage* 31 (06), 103–106+125. doi:10.13522/j.cnki.ggps.2012.06.009

Lucius, A., and Brenner, G. (2011). Numerical Simulation and Evaluation of Velocity Fluctuations During Rotating Stall of a Centrifugal Pump. *J. Fluids Eng.* 133 (8), 081102. doi:10.1115/1.4004636

Meng, F., Pei, J., Li, Y., Yuan, S., and Chen, J. (2017). Effect of Guide Vane Position on the Hydraulic Performance of Two-Direction Tubular Pump Device. *Trans. Chin. Soc. Agric. Mach.* 48 (02), 135–140. doi:10.6041/j.issn.1000-1298.2017.02.018

Qian, Z., Zhou, X., Jiao, H., Xia, Z., and Chen, S. (2022). *Research on the Passage and Front Guide Vane of Shaft Tubular Pump Unit Based on CFD. J. China Rural Water Hydropower* (05), 101–106+112.

Shen, S., Qian, Z., Ji, B., and Agarwal, R. K. (2018). Numerical Investigation of Tip Flow Dynamics and Main Flow Characteristics with Varying Tip Clearance Widths for an Axial-Flow Pump. *Proc. Institution Mech. Eng. Part A J. Power Energy* 233, 476–488. doi:10.1177/0957650918812541

Shi, D., Yao, J., Zhang, S., Wu, Q., and Wang, Y. (2014). Test Comparative Study on the Impact of Different Revolving Speeds on Pressure Fluctuation in Axial Flow

Pumps. *Trans. Chin. Soc. Agric. Mach.* 45 (03), 66–71. doi:10.6041/j.issn.1000-1298.2014.03.012

Shi, L., Liu, X., Tang, F., Yao, Y., Xie, S., and Zhang, W. (2016). Design Optimization and Experimental Analysis of Bidirectional Shaft Tubular Pump Device. *Trans. Chin. Soc. Agric. Mach.* 47 (12), 85–91. doi:10.6041/j.issn.1000-1298.2016.12.012

Shi, L., Yuan, Y., Jiao, H., Tang, F., Cheng, L., Yang, F., et al. (2021). Numerical Investigation and Experiment on Pressure Pulsation Characteristics in a Full Tubular Pump. *Renew. Energy* 163, 987–1000. doi:10.1016/j.renene.2020.09.003

Wang, J., Zhang, L., and Zhang, M. (2007). Analysis of Pressure Fluctuation of Non-constant Flow in Axial-Flow Pump. *J. Hydraulic Eng.* 38 (08), 1003–1009. doi:10.3321/j.issn:0559-9350.2007.08.019

Wei, Z., Yang, W., and Xiao, R. (2019). Pressure Fluctuation and Flow Characteristics in a Two-Stage Double-Suction Centrifugal Pump. *Symmetry* 11 (1), 65. doi:10.3390/sym11010065

Xie, R., Wu, Z., He, Y., Tang, F., Xie, C., and Tu, L. (2015). Optimization Research on Passage of Bidirectional Shaft Tubular Pump. *Trans. Chin. Soc. Agric. Mach.* 46 (10), 68–74. doi:10.6041/j.issn.1000-1298.2015.10.011

Xu, L., Lu, L. G., Chen, W., and Wang, G. (2012). Flow Pattern Analysis on Inlet and Outlet Conduit of Shaft Tubular Pump System of Pizhou Pumping Station in South-To-North Water Diversion Project. *Trans. Chin. Soc. Agric. Eng.* 28 (06), 50–56. doi:10.3969/j.issn.1002-6819.2012.06.009

Xu, L., Lu, L. G., Chen, W., and Wang, G. (2011). Study on Comparison of Hydraulic Design Cases for Shaft Tubular Pump System. *J. Hydroelectr. Eng.* 30 (05), 207–215. CNKI:SUN:SFXB.0.2011-05-036.

Yang, F., Liu, C., Tang, F., and Zhou, J. (2014). Shaft Shape Evolution and Analysis of its Effect on the Pumping System Hydraulic Performance. *J. Basic Sci. Eng.* 22 (01), 129–138. doi:10.3969/j.issn.1005-0930.2014.01.013

Yang, F., Liu, C., Tang, P., Cheng, L., and Lv, D. (2014). Numerical Simulation of 3D Internal Flow and Performance Analysis of the Shaft Tubular Pump System. *J. Hydroelectr. Eng.* 33 (01), 178–184. CNKI:SUN:SFXB.0.2014-01-028.

Zhang, S., Wang, Y., Shi, D., and Shao, P. (2014). Analysis of Pressure Fluctuation of Non-constant Flow in Axial-Flow Pump. *J. Hydraulic Eng.* 45 (11), 139–145. doi:10.6041/j.issn.1000-1298.2014.11.022

Zhao, W., Zhang, J., Yu, X., Zhou, D., and Calamak, M. (2021). Multiobjective Optimization of a Tubular Pump to Improve the Applicable Operating Head and Hydraulic Performance. *Proc. Institution Mech. Eng. Part C J. Mech. Eng. Sci.* 235 (9), 1555–1566. doi:10.1177/0954406220947116

Zhen, Y., Liu, J., Zhou, Q., Mao, T., and Liu, Q. (2010). Pressure Pulsation of Model Test in Large-Size Axial-Flow Pump. *J. Drainage Irrigation Mach. Eng.* 28 (01), 51–55. JournalArticle/5af5957cc095d718d826de01.

Zhou, C., Zhang, J., Jiao, W., Cheng, L., and Jiang, Y. (2021). Numerical Simulation of the Influence of Shaft on the Performance of Low Heat Tubular Pumping System. *J. Drainage Irrigation Mach. Eng.* 39 (03), 231–237. doi:10.3969/j.issn.1674-8530.20.0148

Zhu, R., Su, B., Yang, A., Fu, Q., and Wang, L. (2010). Numerical Investigation of Non-constant Pressure Fluctuations in a Centrifugal Pump. *Trans. Chin. Soc. Agric. Mach.* 41 (11), 43–47. doi:10.3969/j.issn.1000-1298.2010.11,008

Conflict of Interest: WQ was employed by Huaian Water Conservancy Survey Design and Research Institute Co., Ltd.

The remaining authors declare that the research was conducted in the absence of any commercial or financial relationships that could be construed as a potential conflict of interest.

Publisher's Note: All claims expressed in this article are solely those of the authors and do not necessarily represent those of their affiliated organizations, or those of the publisher, the editors, and the reviewers. Any product that may be evaluated in this article, or claim that may be made by its manufacturer, is not guaranteed or endorsed by the publisher.

frontiers | Frontiers in Energy Research

ORIGINAL RESEARCH
published: 22 July 2022
doi: 10.3389/fenrg.2022.943339

Analysis of Runner Dynamics of Reversible Hydraulic Turbine by Alternating Fluid–Solid Action

Lu Xin[1], *Qifei Li*[1,2]*, *Zhenggui Li*[3], *Gengda Xie*[1] and *Qifan Wang*[4]

[1]School of Energy and Power Engineering, Lanzhou University of Technology, Lanzhou, China, [2]State Key Laboratory of Fluid Machinery and Systems, Lanzhou, China, [3]Key Laboratory of Fluid and Power Machinery, Ministry of Education, Xihua University, Chengdu, China, [4]Huaneng Gansu Hydropower Development Co., Ltd, Lanzhou, China

In order to study the effect of alternating fluid–solid action on the dynamic characteristics of the runner of a reversible hydraulic turbine, a reversible hydraulic turbine model is used as the research object, and the two-way fluid–solid coupling method is used to iteratively calculate and analyze the fluid and structural equations to obtain the effect of the reversible hydraulic turbine on the runner under the two-way fluid–solid coupling action of the runner of the reversible hydraulic turbine under typical operating conditions. The results showed that under the influence of a high-speed water ring area under a certain working condition, the incoming flow direction forms a certain impulse angle with the blade, and under the joint action of the runner rotating at high speed, the vortex structure is generated in the blade area, and the speed change in the inlet area has a large random fluctuation, which is not conducive to the stability of the runner area and causes a strong pressure pulsation at the inlet. Under different working conditions, the runner stress area phenomenon is obvious, concentrated in the runner blade inlet side and the upper crown, lower ring connection. The maximum deformation region appears in the lower region of the middle of the blade inlet. The comparison of the modal analysis shows that the dynamic stress frequency caused by the dynamic interference is very unlikely to trigger the resonance of the runner.

Keywords: water pump turbines, bidirectional fluid–structure interaction, modal analysis, eddy, vibration

OPEN ACCESS

Edited by:
Kan Kan,
College of Energy and Electrical Engineering, China

Reviewed by:
Xiuli Mao,
Northwest A&F University, China
Yandong Gu,
Yangzhou University, China
Fan Yang,
Yangzhou University, China

***Correspondence:**
Qifei Li
lqfy@lut.cnmailto:lqfy@lut.cn

Specialty section:
This article was submitted to Process and Energy Systems Engineering, a section of the journal Frontiers in Energy Research

Received: *13 May 2022*
Accepted: *15 June 2022*
Published: *22 July 2022*

Citation:
Xin L, Li Q, Li Z, Xie G and Wang Q (2022) Analysis of Runner Dynamics of Reversible Hydraulic Turbine by Alternating Fluid–Solid Action. Front. Energy Res. 10:943339. doi: 10.3389/fenrg.2022.943339

INTRODUCTION

With the proposal of the goal of "a carbon peak" in 2030 and the vision of "carbon neutralization" in 2060, green and low carbon has become synonymous with current industrial development (Li et al., 2021; Li et al., 2022). Hydraulic machinery with clean and efficient characteristics is attracting much attention. Reversible hydraulic turbine high head, ultra-high head, and other performance indicators become the need of industrial development. However, there is a complex coupling vibration problem of solid blades submerged in fluid. The internal turbulence excitation of the unit operation is intense, and the instability is very prominent. The runner is prone to fatigue fracture, which affects the safe and stable operation of the unit (Zhu et al., 2012; Wang et al., 2012) . Therefore, it is important to reveal the dynamics of hydraulic turbine rotor blades and establish a sound theoretical system (Zheng et al., 2016; Zhang et al., 2021; Yue et al., 2017).

Fluid–solid coupling mainly studies the fluid–solid interaction and the interference phenomenon of interaction. Researching so far, for different theoretical problems, many solutions have been developed. Some scholars use Newton's method to study the overall solution of strong coupling with large displacement, which is expensive and time-consuming and not suitable for solving complex

FIGURE 1 | Model reversible turbine calculation area.

TABLE 1 | Model reversible turbine geometry parameters.

Parameter name	Numerical value
Number of blades/pc	9
Active guide leaf/pc	20
Rotor high-pressure side diameter/mm	473.6
Worm shell inlet diameter/mm	315
Height of guide lobe b_0/mm	66.72
Number of fixed guide vane/pc	20
Height of guide leaf/mm	66.72
Rotor low-pressure side diameter/mm	300
Tailpipe outlet diameter/mm	660

practical engineering problems (Heil, 2003; Wood et al., 2010). For example, using the boundary element-based method and considering the damping effect of the surrounding water flow, the deformation problem is studied using the time-domain FSI analysis method (Lee et al., 2014).

The high reliability of experimental studies in the research method is also essential to test the results of theoretical and numerical analysis. Many experts and scholars use advanced measurement techniques and equipment to observe deformation problems in fluid–solid coupling tests (Kalmbach and Breuer, 2013), and the remote sensing device composed of different damping caused by the vibration aspects are taken into account for in-depth exploration and research (Seidel et al., 2012). However, due to the diversity of water flow and the complexity of the internal structure of hydraulic machinery, direct observation of the internal coupling of hydraulic machinery seems impractical (Li et al., 2021), which hinders the research on the fluid–solid mechanism of hydraulic machinery by scientific researchers. With the development of computer technology and image processing technology, a new independent discipline computational fluid dynamics (CFD) is gradually derived on the basis of classical fluid dynamics and numerical calculation methods (Li et al., 2021). It replaces the continuous physical quantities in the time domain and space domain of the original physical field with the set of physical quantities of finite discrete points and applies certain principles and methods to establish algebraic equations about the relationship between physical quantities of discrete points. The approximate solution of the flow field is obtained by solving the algebraic equations. Due to its small investment, short time-consuming, and visualization of the internal flow characteristics of fluid machinery, CFD has quickly become an important means to study the cavitation characteristics of hydraulic machinery (Liang et al. 2020). Zheng et al. (2016). In order to study the influence of runner dynamic characteristics and internal flow field of cross-flow hydraulic turbine under fluid–solid coupling, the coupling solution of its solid domain and fluid domain is performed by using CFX and ANSYSAPDL, and compared with the measured values, and it is found that the coupling effect will reduce the hydraulic performance of the runner to some extent, which provides a reference for the blade transient response and runner hydraulic performance prediction in practical engineering. Hu et al. (2016) used the finite volume method for the fluid domain and the finite element method for the solid domain to study the fluid–solid coupling of the flexible airfoil under the action of water flow. It is found that the blade deformation caused by the fluid–solid coupling will lead to the change of the dynamic pressure frequency of the blade, and its airfoil impulse angle and water flow velocity will have some influence on the blade deformation. Zhu et al. (2012) took a mixed-flow hydraulic turbine as an example and carried out process simulation to calculate the blade stress distribution, based on which fatigue analysis was performed and optimized to reduce the maximum stress to improve the fatigue life. Wang et al. (2012) predicted the fatigue life of a hydraulic turbine runner during start-up, steady operation, and stopping and optimized the leaf root area where the stress is concentrated to improve the fatigue life.

Therefore, this study takes a reversible hydraulic turbine runner as the research object and analyzes the influence of alternating fluid–solid coupling on the dynamic characteristics of the runner blade under the variable operating conditions of the reversible hydraulic turbine and obtains the conclusions related to the stress, strain, and vibration of the runner area. This study provides a theoretical reference for the design of reversible hydraulic turbine blades.

MODEL ESTABLISHMENT AND MESHING

The object of this study is a reversible hydraulic turbine model, and the overflow components consist of a worm shell, fixed guide vane, movable guide vane, runner, and tailpipe, and the schematic diagram is shown in **Figure 1**, and the specific parameters are shown in **Table 1**.

In order to ensure that the numerical calculation results are feasible and reliable, this meshing is performed using the sub-function ICEM of commercial software ANSYS for full flow channel hexahedral meshing. In order to eliminate the errors arising from the number of meshes, mesh-independence verification is required. Seven different sets of meshes are generated by choosing different mesh scales. The calculation conditions (a0 = 33 mm, Q11 = 0.66 m^3/s, and n11 = 70.8 r/

TABLE 2 | Mesh division of each component.

Project	Worm housing and fixed guide vane	Active guide leaf	Rotating wheel	Tailpipe
Number of grid cells	1894316	1218511	1605320	1556111
Number of nodes	316,841	1028423	1217820	1432144
Minimum angle/(°)	18	29	30	36
Minimum grid mass	0.45	0.5	0.50	0.65

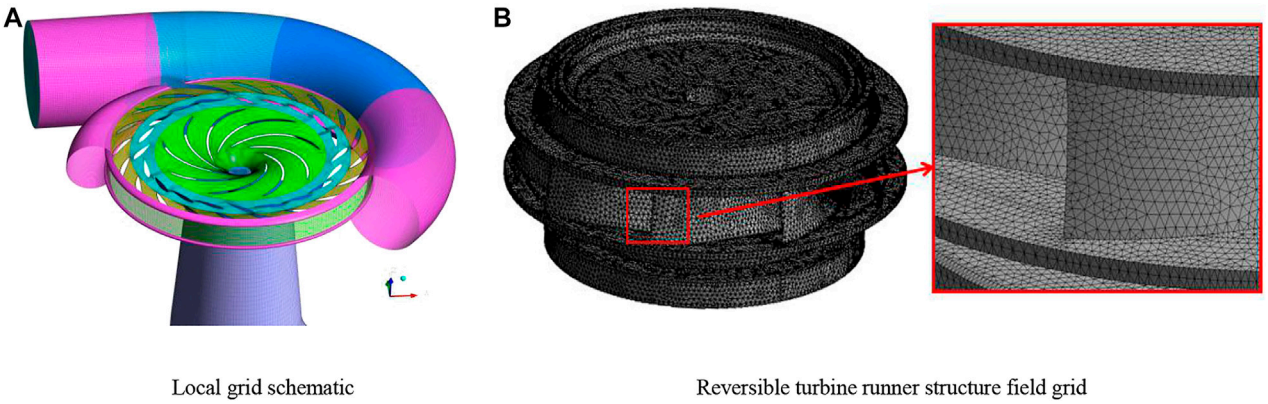

FIGURE 2 | Schematic diagram of the partial grid of the flow field and structural field of the reversible turbine. [**(A)** Local grid schematic **(B)** Reversible turbine runner structure field grid].

TABLE 3 | Model reversible turbine geometry parameters.

Working condition point	Q1	Q2	Q3	Q4	Q5
Flow rate Q_{11} (m^3/s)	0.83	0.76	0.66	0.54	0.3
Rotational speed n_{11} (r/min)	56.8	65.6	70.8	72.3	67.4

min) are taken, and the constant calculation is performed. By comparing the efficiency characteristics, it is found that the efficiency basically does not change with the increase of grid number, and the runner blade y + under this working condition meets the turbulence model requirements, and finally the grid quality of minimum 0.4 or more is adopted, and the total number of grids is about 6.1 million for calculation. The mesh quality is shown in **Table 2** the finite element mesh of the solid region is generated in transient structure, and the number of mesh cells is 289,230. The mesh division results are shown in **Figure 2**.

METHODS

Test Device and Reliability Verification

In this study, the model reversible hydraulic turbine with movable guide vane a_0 = 33 mm was selected for numerical calculation reliability verification. Five operating points are selected as shown in **Table 3**, for which constant numerical calculations are performed. **Figure 3** shows the reversible hydraulic turbine experimental setup. The results of the numerical calculations

FIGURE 3 | Reversible hydraulic turbine experimental setup.

are converted to unit speed and unit flow rate with the following equations:

$$n_{11} = \frac{nD_2}{\sqrt{H}}, \tag{1}$$

$$Q_{11} = \frac{Q}{D_2^2\sqrt{H}}, \tag{2}$$

where n_{11} is the unit speed (rpm), Q_{11} is the unit flow rate (L/s), n is the speed (rev/min), Q is the flow rate (L/s), H is the working head (m), and D_2 is the nominal diameter of the runner (m).

Q_{11} and n_{11} were obtained by conversion, and then the n_{11}–Q_{11} characteristic curve was plotted. The n_{11}–Q_{11} characteristic curve obtained by the conversion is compared

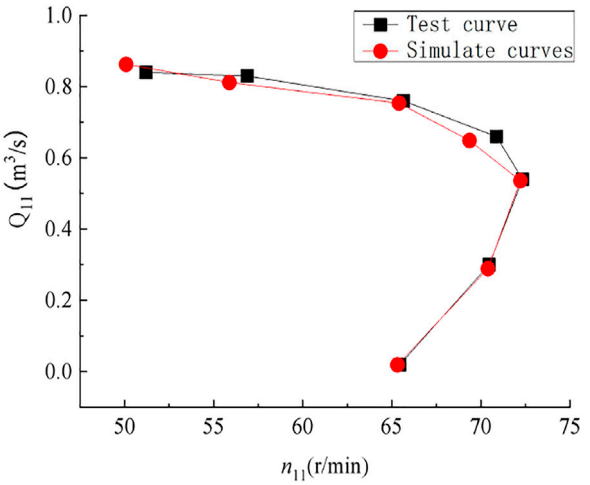

FIGURE 4 | Comparison of experimental and simulation results of "S" characteristics.

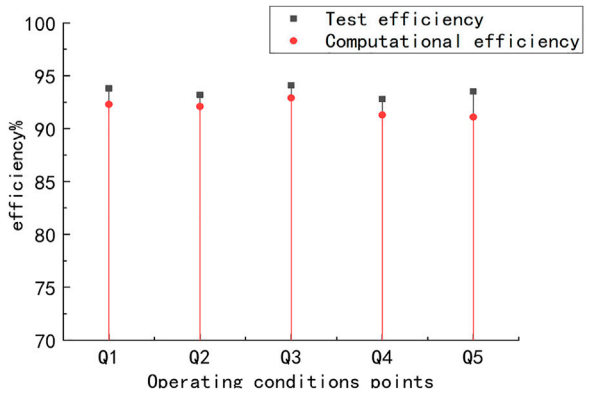

FIGURE 5 | Efficiency diagram under different working conditions.

with the test curve, and the results are shown in **Figure 4**. Through comparison, the two have a high degree of agreement and the error value is kept near 4%, which meets the requirements of engineering research. **Figure 5** shows the comparison of efficiency for different working conditions, and the difference between the experimental and calculated efficiency is around 1.4%. Therefore, the model selected for this numerical calculation has high reliability.

Reliability Analysis of Pressure Pulsation

The pressure pulsations are measured over all operating ranges of turbine operating conditions and at the cavitation factor of the power plant unit. It is necessary to measure the amplitude and frequency of pressure pulsations between the worm shell, runner, and guide vane as well as between the top cover and the upper crown of the runner. The sensor arrangement should be located where the maximum pressure pulsation amplitude can be measured. The pressure pulsations are recorded and analyzed. Spectrum analysis of the collected data should be performed to determine the main frequency and amplitude of the pressure pulsation. ΔH is used to represent the degree of pressure pulsation in the turbine/pump, and H is the amplitude of the turbine/pump, and H is the turbine head/pump head, which is the characteristic amplitude. According to the IEC60193-1999 "hydraulic turbine, storage pump, and pump turbine model acceptance test," 18 characteristic amplitude values using statistics were recorded, and given probability range (for example, 97%) values beyond this probability range will be ignored, so the pressure pulsation peak is derived by the confidence method, and the confidence level is consistent with the model test as far as possible. Since the turbine pressure pulsation test is performed in the full range of operating conditions, the corresponding pressure pulsation amplitude is 97% of the peak confidence level. Each operating point and each measurement signal were analyzed, and the test results are shown in **Table 4**.

Turbulence Model and Boundary Conditions

Reversible turbines have frequent changes under operating conditions and complex and variable flow conditions. The application of SST k-*w* in ANSYS can accurately capture surface vortices and near-wall flow, which is applicable to a wide range of applications (Liang et al., 2020). Therefore, this turbulence model is selected for numerical calculation. The inlet and outlet pressures are 404300 pa and 101325 pa, respectively. Interface coupling and SIMPLEC velocity pressure coupling algorithm are used to solve the time-averaged N-S equation. The residual value is set to 10^{-6}, and the iteration time step is set to 10^{-4}s. The steady-state numerical calculation of the whole flow field of pump turbine is carried out first, and the convergent steady-state result is taken as the initial value of transient calculation. During transient numerical calculation, the time step is set to 3.867×10^{-4} s, and 120 steps are required for one rotation, and each time step is rotated by 3°. In terms of a solid domain, normal temperature clean water is used as the medium, the density is 1 g/cm^3, and the viscosity is 1c$_p$; the model material of pump turbine runner is structural steel, the density is 7850kg/m^3, and the elastic modulus is 166.67 Gpa. Poisson's ratio is 0.3. Fixed constraints are imposed on the central part of the runner, the centrifugal force is applied through the angular velocity counterclockwise around the *z*-axis, the gravity direction is the negative direction of the *z*-axis, and the fluid domain acts on the water pressure of the structure by increasing the fluid–structure coupling surface.

Dynamic Mesh Solving Method

For the bi-directional fluid–solid coupling study of hydraulic turbine conditions of reversible hydraulic turbine, dynamic treatment of the runner basin is required, so the dynamic mesh update method of spring smoothing and local reconstruction is needed for the runner area mesh. The fluid domain and the solid domain are iterated several times, and the node non-boundary in the computational domain undergoes relative displacement changes and reaches a new equilibrium. The spring smooth method is based on the principle given in **Eqn. 3**. The original is replaced by the newly generated mesh, backward to the newly generated mesh difference.

TABLE 4 | Hydraulic turbine working condition pressure pulsation test.

Location of measurement point	Operating condition	Test result (ΔH/H)	Guaranteed value (ΔH/H)
Worm shell import	At rated operating conditions	2.02	<3%
	Partial working condition operation	2.14	<3%
Movable guide vane—between runners	At rated operating conditions	2.64	<7%
	Partial working condition operation	5.76	<7%
Between the top cover and runner	At rated operating conditions	3.45	<7%
	Partial load or no-load operation	5.22	<7%
Tailpipe	Optimum operating conditions	1.10	<2%
	Part-load or no-load operation	6.39	<7%

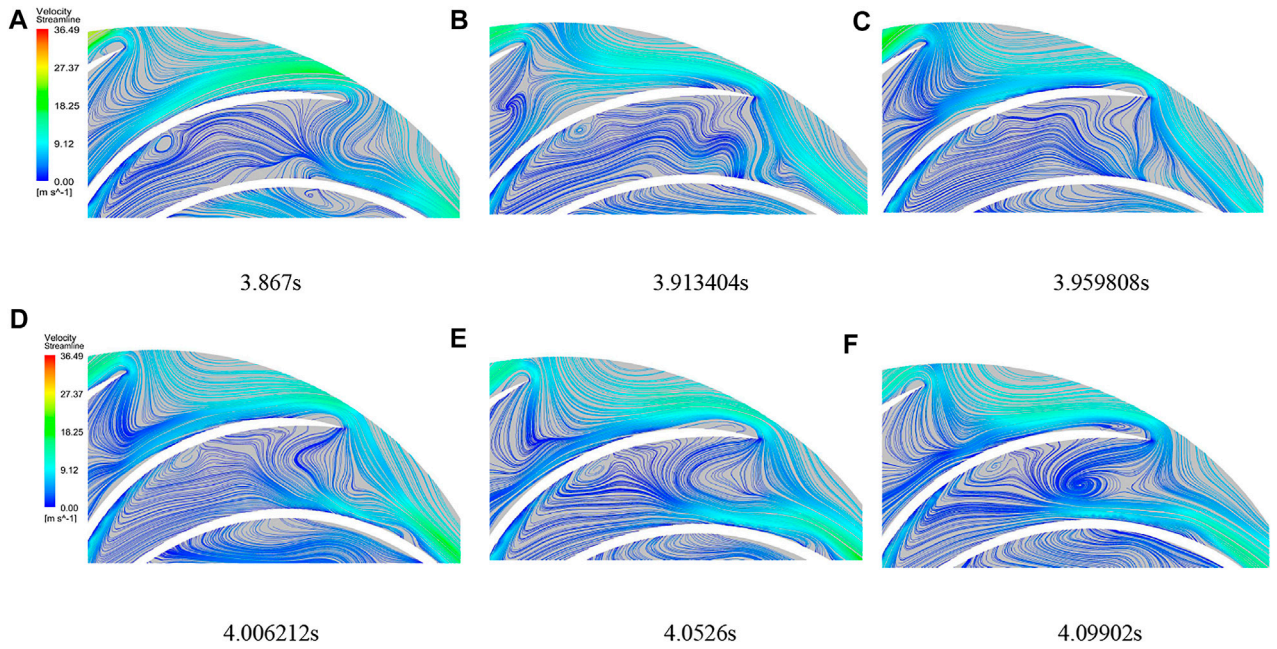

FIGURE 6 | Blade inlet section position flow line diagram. [**(A–F)** are the flow diagrams of the inlet area of the runner at different times].

$$\vec{F} = \sum_{j}^{n} k_{ij}\left(\Delta\vec{x}_j - \Delta\vec{x}_i\right), \tag{3}$$

$$k_{ij} = \frac{k_f}{\sqrt{\left|\vec{x}_i - \vec{x}_j\right|}}, \tag{4}$$

where $\vec{F}$ is the resistance on the node, k_{ij} is the elastic constant between two nodes, ΔX_i is the move distance for the node, X_i is the node location, and X_f is the elastic factor.

CALCULATION RESULTS AND ANALYSIS

Effect of Water Flow in the Leaf-Free Zone on the Leaf Area

When the reversible turbine is operating under the optimal working condition, the direction of water flow at the inlet of the runner is close to its inlet angle, and the relative resistance of water flow becomes smaller. But in the case of partial working condition Q5 (larger unit speed and smaller flow rate), the water flow state is relatively complex, and the water flow and blade placement angle will produce a rush angle, which will cause the effective flow rate to be reduced, forming a more obvious high-speed water ring phenomenon. Not only the phenomenon, but it will also cause this chaotic water flow state wave to the rotor blade. From the blade inlet section, vortex development can be seen in **Figure 6**, in the impulse angle, stronger centrifugal force and blade coupling under the composite effect, blade working surface, and blade between the formation of unstable vortex structure. The existence of the vortex causes the instability of the water flow, making the blade by the water repeatedly hit the intensity of the increase; cavitation performance due to the vortex generation also produces a certain degree of decline. There is a separation flow–complex flow where chaotic water flow filled in the leafless area and between the rotor blades.

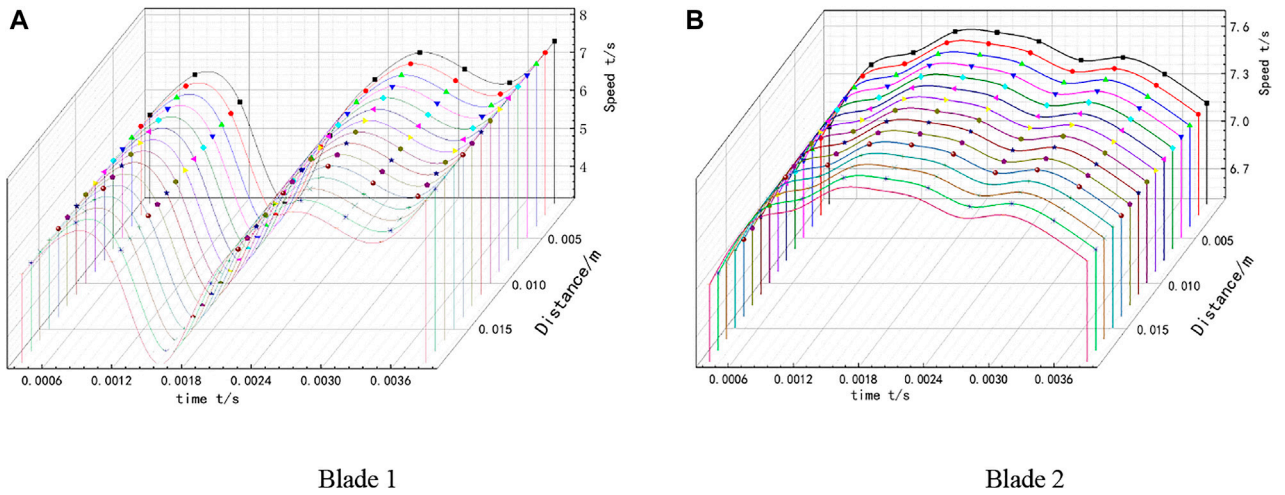

FIGURE 7 | Variation of blade inlet speed with time. [**(A,B)** are the velocity variation curves of different guide vane inlet areas].

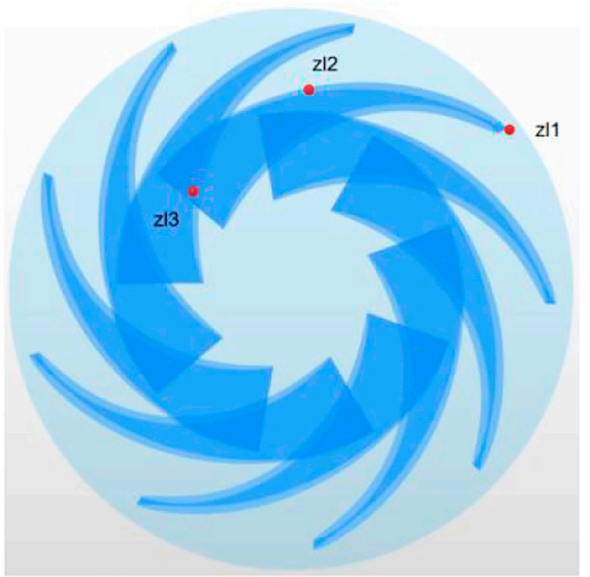

FIGURE 8 | Rotor blade monitoring point distribution map.

As the velocity distribution of the blade inlet section is extremely uneven, in order to study the impact of the velocity of the incoming impulse angle on the rotor blade inlet, the velocity extraction line is established in the vertical direction of the blade profile tangent line, and the incoming impulse angle is triangulated according to the fluid flow velocity. Two runner blade inlet velocities are selected for calculation and analysis, as shown in **Figure 7**. There is a certain impulse angle in the blade under this condition; at the same time, the blade inlet velocity change law analysis found: when a regional velocity fluctuation of the blade is larger, there is an obvious trough; when two regional velocity fluctuations are smaller, in this region, there is no more obvious peak and trough. Not only that but also both did not appear at the same time point to increase or decrease the same or common peak and valley values, that in the runner high-speed rotation, no leaf area and blade between the existence of a large speed difference and strong static and dynamic interference make the blade inlet area speed and direction change fluctuations, and there is strong randomness. This effect on the blade inlet area of the blade will not only produce a relatively larger force and ensure the safety of the runner from producing harm but also have the possibility of partial resonance.

Analysis of Transient Flow Field Pressure Pulsation in the Rotor Blade Area

The Q2 and Q5 working conditions were selected for the non-constant pressure pulsation analysis. In order to obtain the pressure changes in the flow field, three fluid domain measurement points are set for the bi-directional fluid–solid coupling rotor blade area, and the monitoring points are shown in **Figure 8**.

Figure 9 shows the frequency domain waterfall plots of pressure pulsations at each monitoring point on the blade area of the runner area under the two operating conditions of the turbine under bi-directional fluid–solid coupling calculation. The pressure pulsations are mostly dominated by low frequencies, as shown in **Figure 9A**. The first main frequency reaches 78.7 at $5f_n$, and the second main frequency reaches 51.4 at $13f_n$, which is 34.6% lower than the first main frequency amplitude. Near the inlet of the rotor, i.e., near the bladeless area, there is a strong dynamic interference, and the branch water flow coming out through the movable guide vane gathers in this part and then diverges again after the rotor blades. Therefore, the flow pattern here is complex, with a large number of vortices and more violent pressure pulsation. When the two-way fluid–solid coupling is considered, the slight deformation of the runner blade area also produces a certain degree of disturbance to the flow field, which intensifies the pressure pulsation of the reversible turbine and has a certain influence on the fundamental frequency of the pressure

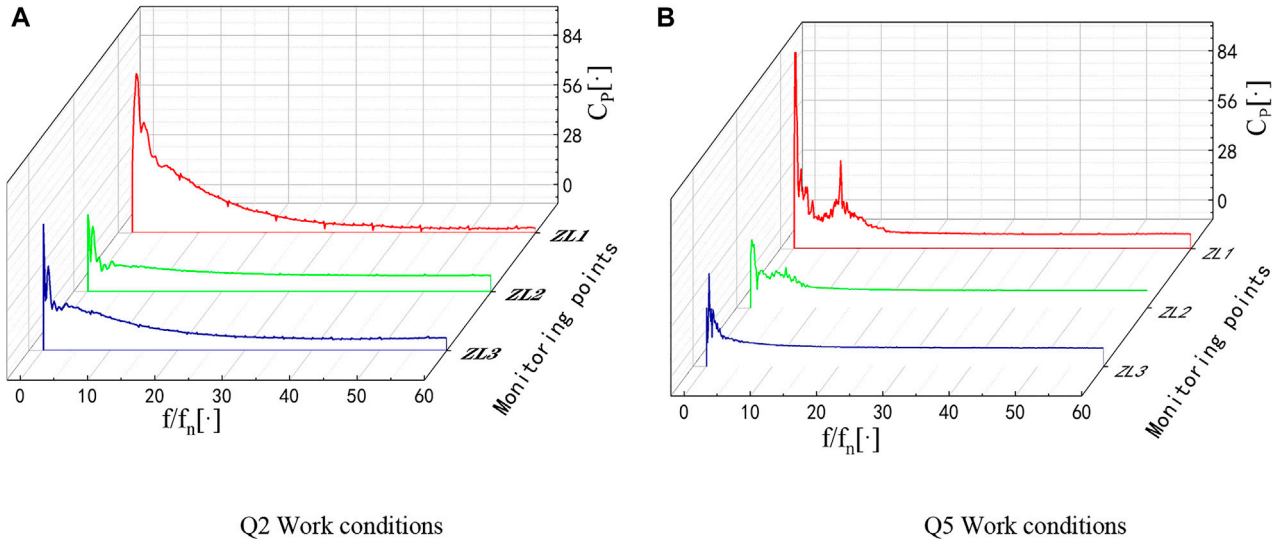

FIGURE 9 | Reversible turbine runner area pressure pulsation frequency domain waterfall diagram. [**(A,B)** are Q2 and Q5 working conditions respectively].

pulsation, so the pressure pulsation amplitude in this part of $25f_n$–$60f_n$ produces some fluctuation phenomenon, as shown in **Figure 9B**. Under Q5 working condition, compared with Q2 working condition, the pressure pulsation in the first $15f_n$ is much intense, the first main frequency reaches 99.4 at $3f_n$, the second main frequency is 38.6 at $7f_n$, and the main frequency increases by 26.3%. Compared with Q2 working condition, the flow rate in this working condition is reduced but the speed is relatively high, the water flow into the rotor is much complicated, and the velocity flow line distribution is extremely uneven, which increases the flow field. The random and instability of the flow field, which will make the runner blade under this working condition by the water pressure to become larger, are not conducive to the safe operation of the runner blade. ZL1 monitoring point in the two working conditions of the pressure pulsation amplitude is significantly greater than the other two monitoring points and there are strong fluctuations. ZL2 is in the middle of the blade position, the water flow channel is reduced, the effective overflow is less, there is a structural steel blade before and after the restraint of water movement, and the water in the front blade and after the reaction force of the blade there is a certain amount of mutual resistance to the filling situation. ZL3 resistance to the filling effect exists and is in the connection with the tailpipe, and the pressure difference between the front and rear is larger, so the pressure pulsation of the monitoring point will be less than that of ZL1. Pressure pulsation will also be less than that of the ZL1 situation.

Analysis of Transient Stress and Its Deformation in the Rotor Area

Influenced by many secondary flows, different moments under the blade stress distribution have changed, there is an uneven stress distribution in the blade inlet, the stress area is concentrated in the blade inlet in the front of the high-pressure area, and the maximum stress in the blade is near the lower ring connection place, as shown in **Figure 10**. **Figure 11** shows the stress and deformation diagram of the runner under Q2 working condition. **Figure 12** shows the maximum stress and deformation fluctuation curve under this condition. So, in the upper ring under the crown of the T-shaped connection, a part of the stress exists leading to abrupt change of the situation. Due to the periodically repeated action of the water in the runner blade, the blade formed a different degree of stress distribution and selected different moments under the fluid on the blade surface as maximum stress, taken as the deformation situation for analysis. The 1 S results were selected to perform the analysis. **Figure 11** shows the two working conditions of the runner blade stress; the blade working surface stress distribution trend from the inlet side to the middle of the blade gradually reduced, and this pressure distribution trend is in line with the hydraulic machinery blade pressure law. In the Q2 working condition, the runner blade stress presents “a C”-type distribution, the stress is concentrated in the upper and lower side of the blade inlet, the middle stress is small, and the blade tail end stress tends to zero. The maximum stress in 0.1–0.3 s changes drastically and then appears as slight up and down fluctuations. For the blade deformation, the inlet position directly impact gravity, centrifugal force, and high-pressure high-speed fluid on the thin blade, and there is a big stress difference in the middle and the two ends; the middle of the blade inlet has no restraint, making deformation maximum parts concentrated in the middle of the blade; because of the model structure material reasons, the overall deformation variable is small. The maximum deformation is only about 0.01 mm, and the trend of change and the maximum stress changes are roughly the same but there is a certain hysteresis. The deformation in the middle is the largest and gradually spreads to the surrounding area and gradually decreases.

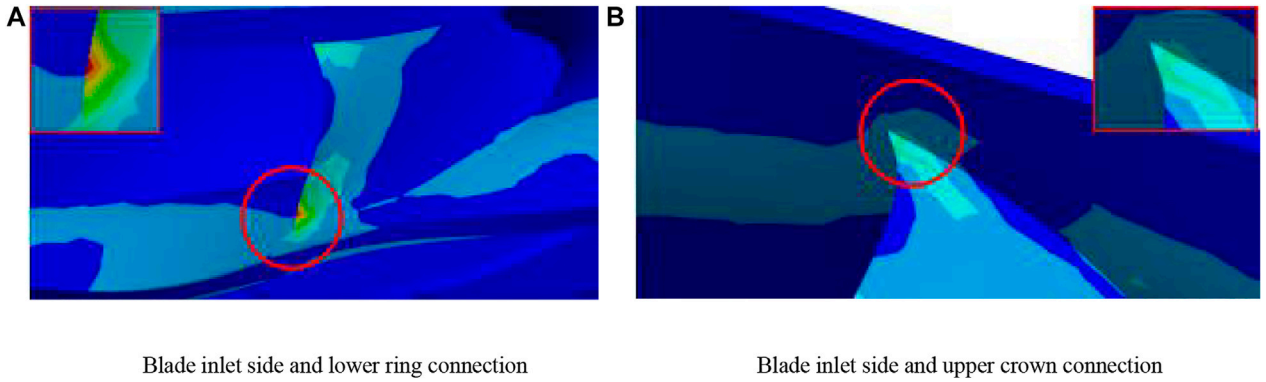

FIGURE 10 | Local enlargement of stress concentration area. [**(A,B)** are local enlargements of stress concentration areas at different locations].

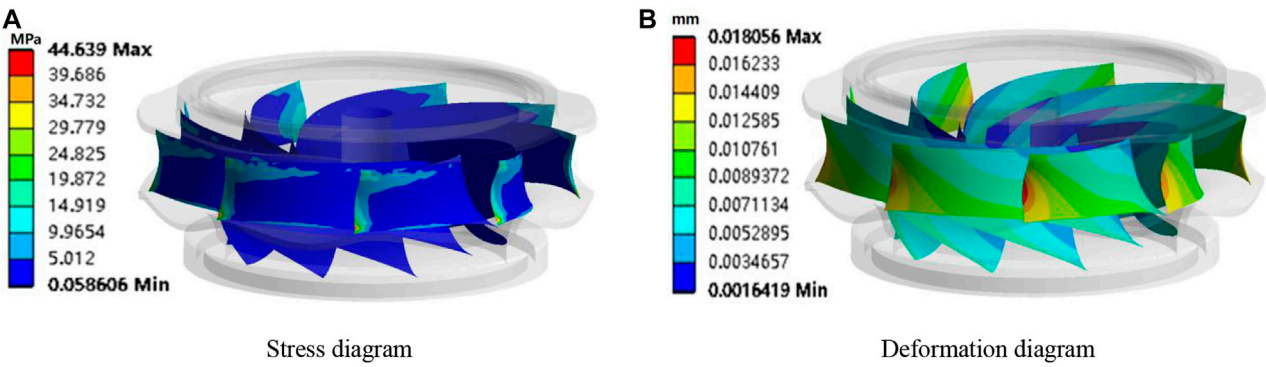

FIGURE 11 | Stress and deformation diagram under the Q2 working condition. [**(A,B)** are the stress and deformation diagrams for this working condition].

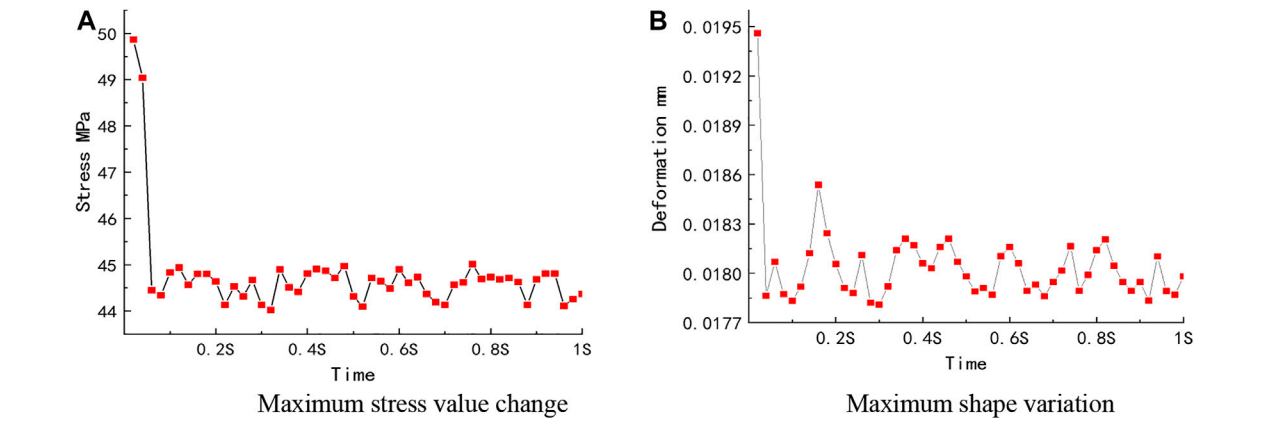

FIGURE 12 | Maximum stress and deformation change curve under Q2 working condition. [**(A,B)** are the maximum stress and deformation value fluctuation curves under this working condition].

Figure 13 shows the stress and deformation diagram of the runner under Q5 working condition. **Figure 14** shows the maximum stress and deformation fluctuation curve under this condition. Under the Q5 working condition, the runner blade stress is a "D"-type distribution, that is, the stress is concentrated in the middle of the blade inlet and the upper and lower side of the stress is small, but the maximum stress part is still in the lower side of the blade and the same will undergo sudden change of

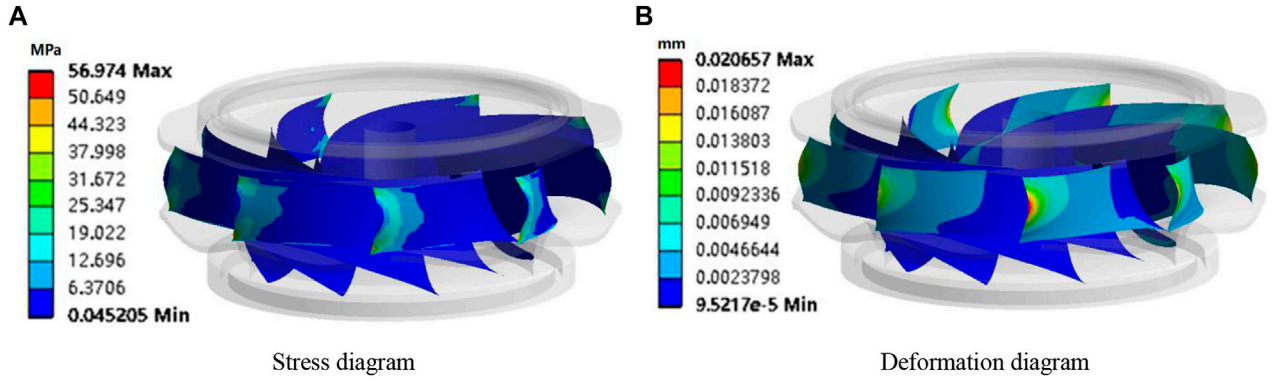

FIGURE 13 | Stress and deformation diagram under the Q5 working condition. [**(A,B)** are the stress and deformation diagrams for this working condition].

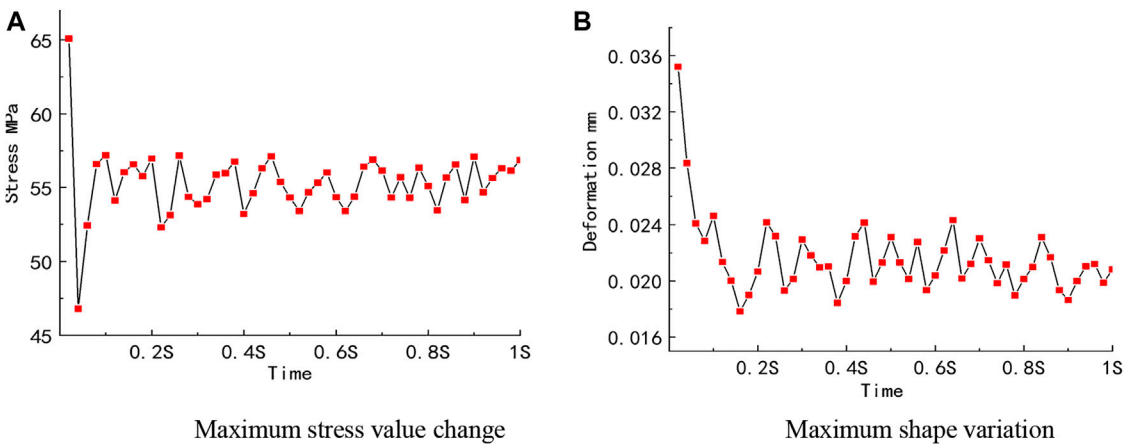

FIGURE 14 | Maximum stress and deformation change curve under Q5 working conditions. [**(A,B)** are the maximum stress and deformation value fluctuation curves under this working condition].

stress situation. The stress distribution with the time change is not big, but this condition stresses maximum value change more strongly, changes amplitude more than 15%, and in the subsequent time the maximum stress value in 55 MPa fluctuates up and down; the stress value is greater than that of Q2 condition. The deformation position is concentrated in the middle of the blade inlet, but the overall variation is larger than that of the Q2 condition, and the maximum value of deformation shows a large and small phenomenon, which is not conducive to the safe operation of the reversible hydraulic turbine.

Comparison of Rotor Area Modal Analysis

In order to obtain the inherent frequencies of the reversible turbine runner, the existing models were analyzed in dry mode, prestressed mode, and wet mode for the sixth-order nodal modal analysis, respectively. In **Figure 15**, it can be seen that the difference between the dry mode and the dry mode vibration frequency under pre-stress in the rotor blade area is very small, and to some extent, the rotor blade is not affected by the pre-stress on its fixed frequency. The overall vibration trend increases with the increase of the order. The first- and second-order and the fifth- and sixth-order vibration frequencies have similar regular changes. Due to the additional mass force of the water medium in the wet mode and the damping diffusion effect, the vibration frequency of the wet mode starts to differ from the dry mode in the fourth order, and the increasing rate of frequency in the wet mode becomes smaller by about 5.1%. Because the influence of water on the vibration becomes larger in the higher-order cases, the frequency difference is about 11% at the sixth order, which has a tendency to increase gradually.

Since the study involves the submerged reversible turbine runner, the wet mode analysis is more suitable for the actual operating environment of the reversible turbine runner so that the numerical calculation results are closer to the actual situation. Therefore, it is necessary to further analyze the modal vibration pattern of the reversible hydraulic turbine runner under wet mode. **Figure 16** shows the first six orders of the wet mode vibration pattern of the reversible hydraulic turbine runner. The first- and second-order formations are left–right and front–back oscillations, respectively. The deformation is symmetrically

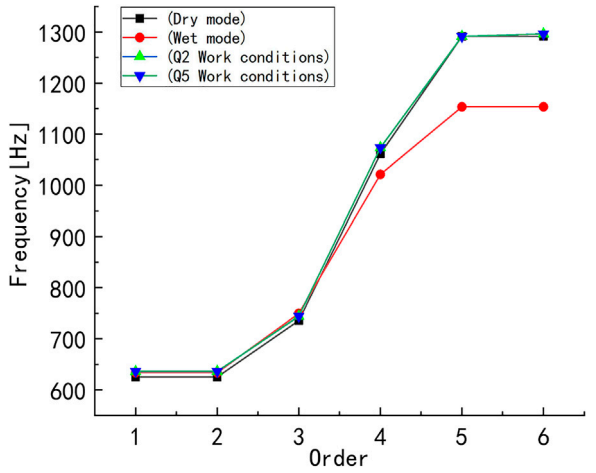

FIGURE 15 | Comparison of the first six orders of vibration frequency of the runner.

distributed, and the maximum deformation is at the farthest point of the runner oscillation. The third-order vibration pattern is rotation around the axis left up, and the largest variable is located at the lower ring. The fourth-order model is up-and-down vibration along the central axis, the deformation is centrally symmetric at the main axis, and the largest deformation is at the upper crown of the runner. The fifth- and sixth-order mode vibration pattern is more similar, producing larger bending deformation at the center, with smaller deformation at the upper part, and the larger deformation is concentrated at the upper and lower crown and lower ring areas. The first-, second-, third-, and fourth-order modal vibration patterns are all vibration phenomena of the whole structural part of the runner, while the fifth- and sixth-order modal vibration patterns are bending deformation at a certain position. Since the connection between the upper crown and the main shaft is specified as a fixed constraint, the deformation in the area near it is low. The larger deformation area is concentrated at the edge of the upper crown and lower ring. The deformation of the runner blade is

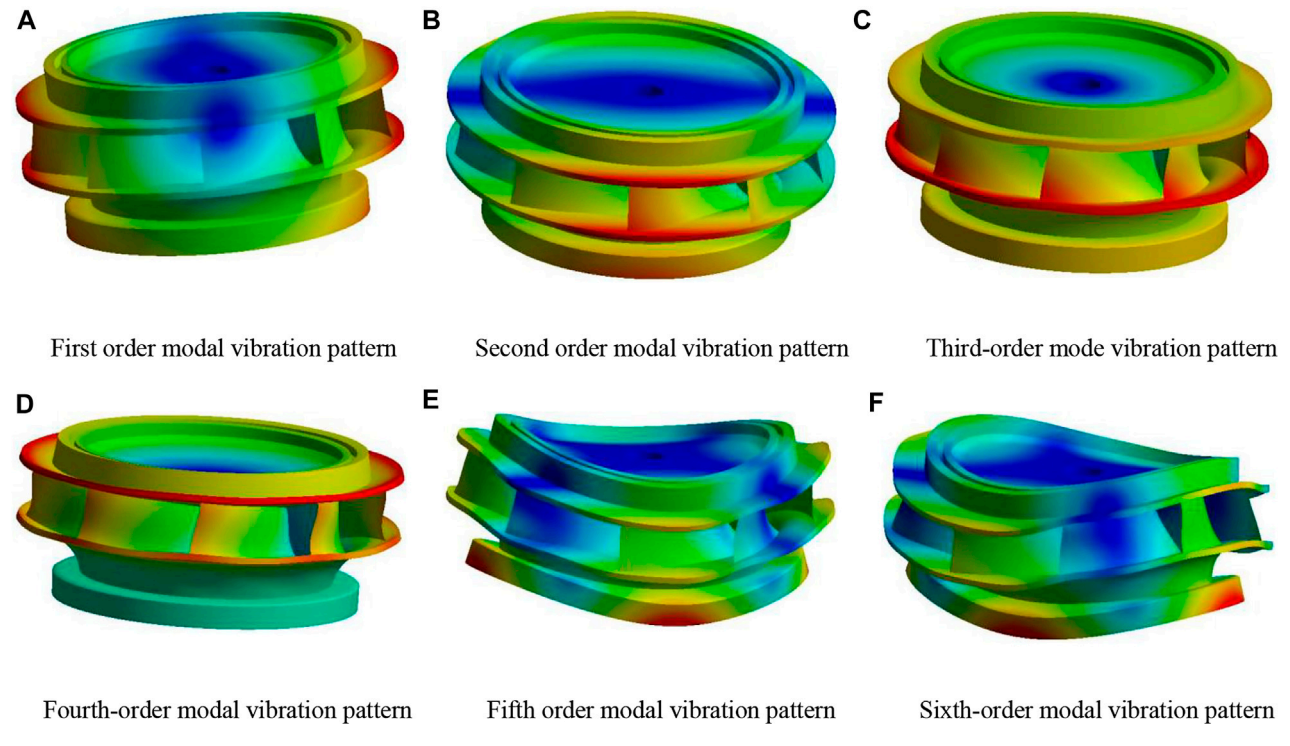

FIGURE 16 | Sixth-order modal vibration pattern of the runner of a reversible hydraulic turbine. [**(A–F)** are the first, second, third, fourth, fifth and sixth order mode vibration patterns respectively].

TABLE 5 | Comparison of the first six orders of vibration frequency of the runner of reversible hydraulic turbine.

Modal order	First	Second	Third	Fourth	Fifth	Sixth
Dry mode (Hz)	625.32	625.34	735.8	1,061.6	1,291.6	1,291.8
Wet mode (Hz)	633.98	633.98	749.69	1,021.33	1,153.6	1,153.6
Q2 work conditions (Hz)	636.13	636.14	744.26	1,073.6	1,291.6	1,296.62
Q5 work conditions (Hz)	636.46	636.46	744.28	1,073.6	1,291.6	1,296.29

relatively uniform and decreases gradually along the runner from the inlet. The stress concentration area is distributed near the connection of the runner blade with the upper crown and lower ring, which is easy to produce fatigue damage and creates a hidden danger to the safety of the reversible hydraulic turbine.

Table 5 shows reversible hydraulic turbine runner's first six orders of vibration frequency comparison and hydraulic excitation force–frequency comparison. The hydraulic turbine speeds to get the runner rotational frequency f_n were 17.2 Hz and 21.4 Hz, while the blade passing frequencies $9f_n$ were 154.8 Hz and 192.648 Hz. The guide vane passing frequencies $20f_n$ were 344 Hz and 428 Hz. The main frequencies of pressure pulsation at the internal flow field monitoring points are $3f_n$, $5f_n$, $7f_n$, and $13f_n$. Compared with the inherent frequency of the runner, there is a big difference. The minimum residual (guide vane passing frequency $20f_n$) is also at 46.03%, far exceeding the safety residual threshold of 20%, so the possibility of a resonance phenomenon of dynamic stress is very small.

CONCLUSION

1 Under high-speed and small flow conditions by the influence of high-speed water ring region, there is a large random fluctuation of speed change in the inlet region. The vortex structure is generated in the blade area, which is not conducive to the stability of the runner area, and the gradual development of the vortex also reduces the blade cavitation performance, and there is a certain safety risk.

2 In the case of considering the two-way fluid–solid coupling, the pressure pulsation in the fundamental frequency region exacerbates the pressure pulsation fluctuations. The blade inlet is influenced by the pressure pulsation of the static and dynamic interference in the bladeless area, which gradually decreases along the flow path direction. The water flow state is more complex under Q5 conditions, and the pressure pulsation is high and unstable, which increases the risk of runner blade fatigue.

3 Through the two-way fluid–solid coupling analysis of the runner area, it can be seen that the hydraulic turbine stress is concentrated at the inlet of the runner blade and distributed in the area near the connection between the runner blade and the upper crown and lower ring; the maximum deformation is concentrated in the middle of the blade, which is prone to fatigue damage.

4 Using the acoustic-solid coupling technique, the inherent frequencies of the runner in the three cases were obtained and compared with the pulsation frequencies in the main frequency region of the blade passage frequency, guide vane passage frequency, and its pressure pulsation analysis, and it was found that the difference was large and the possibility of resonance was small.

DATA AVAILABILITY STATEMENT

The original contributions presented in the study are included in the article/Supplementary Material; further inquiries can be directed to the corresponding author.

AUTHOR CONTRIBUTIONS

LX wrote and improved the manuscript. QL provided guidance and advice on writing the manuscript. ZL provided guidance on the analysis of the study. ZL provided guidance on handling the test apparatus, and GX provided guidance on the tests.

FUNDING

This study was supported by the National Natural Resources Foundation of China (52066011) under the project name "Study on the effect of the change of movable guide vane wing shape on the internal flow characteristics of water pump turbine."

REFERENCES

Heil, M. (2003). An Efficient Solver for the Fully-Coupled Solution of Large-Displacement Fluid-Structure Interaction Problems in Print in: Computer Methods in Applied Mechanics and Engineering (January 2003) [J]. (Preprint submitted to elsevier sciencecomputer methods in applied mechanicsandengineering).

Hu, S., Lu, C., and He, Y. (2016). Fluid-structure Interaction Simulation of Three-Dimensional Flexible Hydrofoil in Water Tunnel. *Appl. Math. Mech.-Engl. Ed.* 37 (1), 15–26. doi:10.1007/s10483-016-2011-9

Kalmbach, A., and Breuer, M. (2013). Experimental PIV/V3V Measurements of Vortex-Induced Fluid-Structure Interaction in Turbulent Flow-A New Benchmark FSI-PfS-2a. *J. fluids Struct.* 42 (42), 369–387. doi:10.1016/j.jfluidstructs.2013.07.004

Lee, H., Song, M-C., Suh, J-C., and Chaung, B. J. (2014). Hydro-elastic Analysis of Marine Propellers Based on a BEM-FEM Coupled FSI Algorithm [J]. *Int. Nav. Archit. Ocean Eng.* 6 (3), 562-577. doi:10.2478/ijnaoe-2013-0198

Li, Q., Chen, X., Cai, T., Guo, Y., and Wei, M. (2021). Study on the Influence of Non-synchronous Guide Vanes on Unit Characteristics under Different Arrangements[J]. *J. Sol. Energy* 42 (08), 23–31. doi:10.19912/j.0254-0096.tynxb.2019-0769

Li, W., Li, Z., Qin, Z., Yan, S., Wang, Z., and Peng, S. (2022). Influence of the Solution pH on the Design of a Hydro-Mechanical Magneto-Hydraulic Sealing Device. *Eng. Fail. Anal.* 135, 106091. doi:10.1016/j.engfailanal.2022.106091

Li, Z., Cheng, C., Peng, S., and Ma, B. (2021a). Theoretical Analysis of Entropy Generation at the Blade Interface of a Tubular Turbine under Cooperative Conditions [J]. *Front. Energy Res.* 9. doi:10.3389/fenrg.2021.788416

Li, Z., Li, W., Li, W., Wang, Q., Xiang, R., Cheng, J., et al. (2021b). Effects of Medium Fluid Cavitation on Fluctuation Characteristics of Magnetic Fluid Seal Interface in Agricultural Centrifugal Pump. *Int. J. Agric. Biol. Eng.* 14 (6), 85–92. doi:10.25165/j.ijabe.20211406.6718

Liang, W., Huang, H., Wu, Z., Dong, W., Yan, X., and Liu, Y. (2020). Analysis of Internal Flow Field and Unidirectional Fluid-Structure of Crown Cavity

Structure on Mixed-Flow Turbine [J]. *J. Hydraulic Eng.* 51 (11), 1383–1392+1400.

Seidel, U., Hübner, B., Löfflad, J., and Faigle, P. (2012). Evaluation ofRSI-Induced Stressesin Francis Runners [J]. *Iop Conf. Ser. Earthandenvironmental Sci.* 15 (5), 52010. doi:10.1088/1755-1315/15/5/052010

Wang, X. F., Li, H. L., and Zhu, F. W. (2012). The Calculation of Fluid-Structure Interaction and Fatigue Analysis for Francis Turbine Runner [J]. *Iop Conf. Ser. earth Environ. Sci.* 15 (5), 52014. doi:10.1088/1755-1315/15/5/052014

Wood, C., Gil, A. J., Hassan, O., and Bonet, J. (2010). Partitioned Block-Gauss-Seidelcoupling for Dynamic Fluid-Structure Interaction [J]. *Comput. Struct.* 88 (23-24), 1367–1382. doi:10.1016/j.compstruc.2008.08.005

Yue, Z., Zheng, Y., Kan, K., Chen, Y., Li, D., and Zang, W. (2017). Turbine Strength and Modal Analysis of Reversible Hydraulic Turbine in a Pumped Storage Power Station Based on Fluid-Structure Interaction [J]. *Hydropower Energy Sci.* 35 (02), 181–184+152.

Zhang, J., Song, H., Zhang, F., Cai, H., Lai, L., and Hong, Q. (2021). Rotor Strength and Modal Analysis of Water Turbine with Shunt Vane [J]. *J. Drainage Irrigation Mach. Eng.* 39 (10), 981–986.

Zheng, X., Wang, L., and Weng, K. (2016). Dynamic Characteristics Analysis of Cross-Flow Turbine Based on Bidirectional Fluid-Structure Interaction [J]. *Trans. Chin. Soc. Agric. Eng.* 32 (04), 78–83.

Zhu, W. R., Xiao, R. F., Yang, W., and Liu, J. (2012). Study on Stress Characteristics of Francis Hydraulic Turbine Runner Based on Two-Way FSI [J]. *Iop Conf. Ser. Earth Environ. Sci.* 15 (5), 52016. doi:10.1088/1755-1315/15/5/052016

Conflict of Interest: The authors declare that the research was conducted in the absence of any commercial or financial relationships that could be construed as a potential conflict of interest.

Publisher's Note: All claims expressed in this article are solely those of the authors and do not necessarily represent those of their affiliated organizations, or those of the publisher, the editors, and the reviewers. Any product that may be evaluated in this article, or claim that may be made by its manufacturer, is not guaranteed or endorsed by the publisher.

frontiers | Frontiers in Energy Research

ORIGINAL RESEARCH
published: 22 July 2022
doi: 10.3389/fenrg.2022.956209

Fluid-Structure Interaction in a Pipeline Embedded in Concrete During Water Hammer

Yu Chen[1,2], Caihu Zhao[1], Qiang Guo[3], Jianxu Zhou[3], Yong Feng[1] and Kunbo Xu[1]*

[1]School of Mechanical Engineering, Nanjing Institute of Technology, Nanjing, China, [2]Haitian Plastics Machinery Group Co., Ltd., Ningbo, China, [3]College of Water Conservancy and Hydropower Engineering, Hohai University, Nanjing, China

Pipe vibration induced by water hammer frequently emerges in water conveyance system, especially in the hydropower plant or pumped storage power station with long diversion pipelines. This vibration in turn affects the hydraulic pulsation so that undesired fluid-structure interaction (FSI) arises. In this research, attention is given to a pipeline embedded in concrete. A six-equation model was derived to describe the fluid-pipe-concrete interaction considering Poisson coupling and junction coupling. With the elastic and homogeneous hypotheses, an iterative approach was proposed to solve this model, and the results were validated by experiment and classical water-hammer theory. Then dynamic FSI responses to water hammer were studied in a reservoir-pipe-valve physical system. Hydraulic pressure, pipe wall stress and axial motion were discussed with respect to different parameters of concrete. Results obtained by the two-equation model, four-equation model and six-equation model show characteristics of pressure wave and stress wave separately with and without FSI.

Keywords: water hammer, pipe vibration, fluid-structure interaction, iterative method, concrete

OPEN ACCESS

Edited by:
Kan Kan,
College of Energy and Electrical Engineering, China

Reviewed by:
Lei Xu,
Yangzhou University, China
Qiang Gao,
University of Minnesota Twin Cities, United States
Tianyi Li,
University of Minnesota Twin Cities, United States

****Correspondence:***
Yu Chen
yuchen@njit.edu.cn

Specialty section:
This article was submitted to Process and Energy Systems Engineering, a section of the journal Frontiers in Energy Research

Received: *30 May 2022*
Accepted: *15 June 2022*
Published: *22 July 2022*

Citation:
Chen Y, Zhao C, Guo Q, Zhou J, Feng Y and Xu K (2022) Fluid-Structure Interaction in a Pipeline Embedded in Concrete During Water Hammer. Front. Energy Res. 10:956209. doi: 10.3389/fenrg.2022.956209

1 INTRODUCTION

Water conveyance pipeline has been widely used in marine engineering, petrochemical engineering, energy and power engineering, spacecraft power system and also daily life. Repeated stimuli inside and outside the pipeline have been proven to excite pulsations in the pressurized fluid. Water hammer is a typical trigger frequently inducing structural vibration and new pressure fluctuations. This fluctuation further causes pipe expansion or contraction, which in turn affects the hydraulic pressure inside the pipe. This phenomenon is the typical fluid-structure interaction (FSI). However, FSI responses closely depend on the operating condition of the pipe system. Hence, FSI analysis should be carried out according to various constraints and boundary conditions (Mahmoodi, et al., 2019; Tijsseling, 2019; Rajbamshi, et al., 2020).

Friction coupling, Poisson coupling and Junction coupling are three main types when pipeline interacts with fluid. The first two emerge throughout the whole pipeline, whereas Junction coupling only happens in local positions including the elbows, branches, valves, boundaries, and variable cross-sections (Zanganeh, et al., 2015). System coupling in these locations becomes stronger (Alaei, et al., 2019). Furthermore, response to friction coupling is the weakest and has a long duration of oscillation (Huang and Alben, 2016). As the most important coupling form, Junction coupling depends on the robustness of the system and usually causes a pressure head larger than the classical water hammer (Karakouzian, et al., 2019). Poisson coupling and friction coupling can greatly

influence Junction coupling. And in turn, Junction coupling has a greater impact on the pipeline system compared with Poisson coupling.

Regarding the constraints of pipeline, Li, et al. (2012) and Liu and Li. (2011) analyzed the elastic support and found the complex boundary conditions can be successfully simulated by the six-equation elastic spring model. Then, Li, et al. (2014) expanded the application of this elastic model. The FSI is continuously induced and transmitted in fluids and pipelines. This interaction becomes much stronger in pipes with few or no support (Liu and Li. 2011). Meanwhile, FSI has a crucial effect on fluid pressure and pipe stress when the pipe axial stiffness is greater than the rigidity of the supports (Li, et al., 2012). In a typical case study, Riedelmeier (Riedelmeier, et al., 2014) analyzed FSI phenomenon under four kinds of axial support and determined proper support to mitigate the displacement and stress in pipes.

The preceding achievements mainly focused on the FSI response of water conveyance systems with various pipeline layouts. Notably, the external constraints of pipes were generally discrete and their effects on FSI response were simplified as boundary conditions. For example, a pipe with continuity constraints degenerates into a multi-span pipeline model (Wu and Shih, 2001; Yang, et al., 2004). This simplification omits the global restriction of the constraint as well as its vibration. So the current model available in the literature is yet to be completely suitable. Herein, this paper investigates the constraints and dynamic responses in a water conveyance pipeline surrounded by concrete, focusing on fluid-pipe-concrete interaction. Pipe and concrete are integrated as a composite structure in this research, similar to that in a pre-stressed concrete cylinder pipe (PCCP) (Lee, et al., 2012; Hu, et al., 2019; Sun, et al., 2020). Compared to the typical FSI, FSI arising in such a system contains an extra pipe-concrete interaction. However, this extra effect is yet to be included in the current PCCP model.

A typical reservoir-pipe-valve system is used in this paper to produce water hammer. With the simplified elastic model of concrete, as well as continuity and motion equations of fluid, pipe and concrete, the fluid-pipe-concrete six-equation model is derived. Then an iterative approach is proposed to solve this model and the results get validated by experiment. Dynamic responses concerning the fluid-pipe-concrete interaction of the reservoir-pipe-valve system are subsequently scrutinized, including hydraulic pressure, pipe wall stress and vibration.

2 NUMERICAL MODEL

When water conveyance system with a straight pipe suffers from water hammer, the axial structural vibration becomes obvious. In the fluid-pipe-concrete model, system characteristics can be described by solid constitutive equations and fluid governing equations. Then the FSI in such a composite structure is mathematically deduced. Two global hypotheses should be followed.

- The axial component of parameters in the control volume is equivalent to the average value in the corresponding section (Ting, et al., 2017).
- Axial stress, strain and displacement are separately assumed to be constant at the radial direction on a certain cross-section.

2.1 Stress at Inner Interface and Outer Interface

As for a piping system embedded in concrete, the pipe concrete coupling is taken into account. A sketch of stress from concrete imposing on pipe wall is shown in **Figure 1**. **Figure 1A** illustrates the external forces applied on an element of pipe wall. In this work, section of the concrete segment is considered to be annular. Then the inner interface is defined by the fluid and pipe wall, while outer interface by the pipe wall and ambient concrete, as seen in **Figure 1B**.

Since the pipeline is symmetric, the stress of concrete uniformly distributes around the pipe ring and can be assumed as a function of the radial coordinate (Wu, 2017; Mirjavadi, et al., 2020). By extension, Lame solutions of the radial stress of pipe wall σ_r, hoop stress of pipe wall σ_θ, radial stress of concrete σ_{rs} and hoop stress of concrete $\sigma_{\theta s}$ in this encased system are separately presented as follows (Daoxiang and Weinlin, 2006):

$$\sigma_r = \frac{\frac{(R+e)^2}{r^2} - 1}{\frac{(R+e)^2}{R^2} - 1} p|_{r=R} - \frac{1 - \frac{R^2}{r^2}}{1 - \frac{R^2}{(R+e)^2}} P_b \tag{1}$$

$$\sigma_\theta = \frac{\frac{(R+e)^2}{r^2} + 1}{\frac{(R+e)^2}{R^2} - 1} p|_{r=R} - \frac{1 + \frac{R^2}{r^2}}{1 - \frac{R^2}{(R+e)^2}} P_b \tag{2}$$

$$\sigma_{rs} = \frac{\frac{R_s^2}{r^2} - 1}{\frac{R_s^2}{(R+e)^2} - 1} P_b, \sigma_{\theta s} = \frac{\frac{R_s^2}{r^2} + 1}{\frac{R_s^2}{(R+e)^2} - 1} P_b \tag{3}$$

where R is the internal diameter of pipe, e is the thickness of pipe wall, P_b and $p|_{r=R}$ are external and internal pressure of pipe wall, separately.

Pipe wall and concrete have the identical radial strain $\varepsilon_r|_{r=R+e}$ on their interface. Due to the assumption of linear radial displacement, $\varepsilon_r|_{r=R+e} = \varepsilon_r|_{r=R}$. According to Hooke law, $\varepsilon_r|_{r=R+e}$ is defined as:

$$\varepsilon_r|_{r=R+e} = \frac{1}{E}\left[\sigma_r|_{r=R+e} - \nu(\sigma_\theta|_{r=R+e} + \sigma_z|_{r=R+e})\right] \tag{4}$$

where σ_z is the axial stress of pipe wall, E is the elastic modulus of pipe wall, and ν is the Poisson's ratio of pipe wall.

According to the reference (Sinha, et al., 2001) in a concrete-encased piping system, the concrete strain is small enough so that the stress-strain relation degenerates into an elastic model, shown as:

$$P_b = \sigma_{rs}|_{r=R+e} = E_s\varepsilon_{rs}|_{r=R+e} + \nu_s(\sigma_{\theta s}|_{r=R+e} + \sigma_{zs}|_{r=R+e}) \tag{5}$$

where σ_{zs} is the concrete axial stress because of expansion or contraction of the outer pipe wall. P_b is the constant pressure imposed on the outer pipe wall by ambient concrete, thus, $P_b = \sigma_{rs}|_{r=R+e}$. ν_s and E_s are the Poisson's ratio and elastic modulus of concrete, separately.

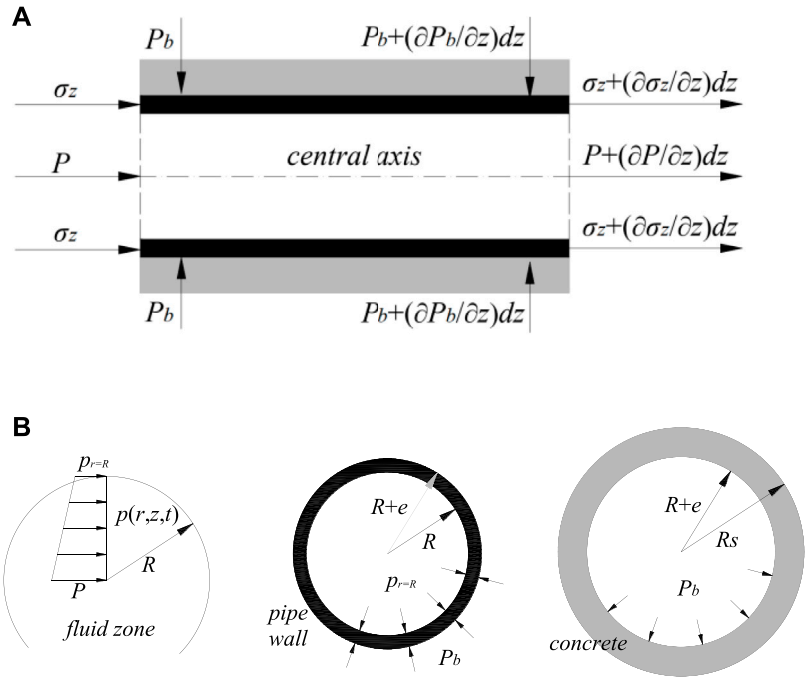

FIGURE 1 | Sketch of stress acting on pipe wall. **(A)** Side view. **(B)** Cross-sectional view.

Recalling linear displacement at the radial direction and substituting **Eqs 1**–**4** into **Eq. 5**, yields the radial stress on the outer interface:

$$P_b = \frac{E_s}{E}\left[- P_b - \nu\left(\frac{2R^2 p|_{r=R}}{(R+e)^2 - R^2} - \frac{(R+e)^2 + R^2}{(R+e)^2 - R^2}P_b + \sigma_z\right)\right] + \nu_s\sigma_{zs} + \frac{R_s^2 + (R+e)^2}{R_s^2 - (R+e)^2}\nu_s P_b \tag{6}$$

The fluid radial velocity component V_r is assumed to be constant at a certain section. So V_r is equal to the radial velocity of pipe u_r on the inner interface (Lai, et al., 2020). Then pressure relationship with respect to pipe center-line and inner interface is established:

$$P - p|_{r=R} = \frac{1}{2}\rho_f R\frac{\partial u_r|_{r=R}}{\partial t} \tag{7}$$

where P is the pressure at the pipe center line. ρ_f is the fluid density. And radial motion equation of pipeline is defined as:

$$\rho_t\frac{\partial u_r}{\partial t} = \frac{Rp|_{r=R}}{(R+e/2)e} - \frac{(R+e)P_b}{(R+e/2)e} - \frac{\int_R^{R+e}\sigma_r dr}{(R+e/2)e} \tag{8}$$

where ρ_t is the density of pipe wall material. Substitute **Eq. 1** into **Eq. 8**:

$$\rho_t\frac{\partial u_r}{\partial t} = \frac{R^2 p|_{r=R}}{(R+e/2)^2 e} - \frac{(R+e)^2 P_b}{(R+e/2)^2 e} \tag{9}$$

The following can be obtained by solving **Eqs 6**, **7**, **Eq. 9**.

$$P_b = aP + b\sigma_z + c\sigma_{zs} \tag{10}$$

$$p|_{r=R} = dP + f\sigma_z + h\sigma_{zs} \tag{11}$$

The definition of coefficients *a, b, c, d, f* and *h* can be seen in the Appendix.

2.2 Governing Equations for Fluid

2.2.1 Axial Motion Equation of Incompressible Flow

The equation of axial motion of fluid at pipe centerline is:

$$\rho_f A_f dz\frac{DV}{Dt} + A_f\left(P + \frac{\partial P}{\partial z} - P\right)dz = 0 \tag{12}$$

where t and z are time and axial direction respectively. V is the fluid velocity at pipe centerline. A_f is the area of the flow section. The total acceleration of fluid is composed of the convective acceleration and the local one. So **Eq. 12** can be converted to:

$$\rho_f A_f dz\left(\frac{\partial V}{\partial t} + V\frac{\partial V}{\partial z}\right) + A_f\left(P + \frac{\partial P}{\partial z} - P\right)dz = 0 \tag{13}$$

The one-dimensional axial motion equation of fluid at pipe centerline is obtained.

$$\frac{\partial V}{\partial t} + V\frac{\partial V}{\partial z} + \frac{1}{\rho_f}\frac{\partial P}{\partial z} = 0 \tag{14}$$

2.2.2 Continuity Equation of Incompressible Flow

Ignoring the hoop velocity of the pipe, continuity equation of the symmetric flow can be expressed in cylindrical coordinate:

$$\frac{\partial \rho_f}{\partial t} + \frac{1}{r}\frac{\partial}{\partial r}\left(\rho_f r V_r\right) + \frac{\partial}{\partial z}\left(\rho_f V\right) = 0 \tag{15}$$

Recalling the definition of fluid bulk modulus K, $\partial P/\partial \rho_f = K/\rho_f$, **Eq. 15** is converted to:

$$\frac{1}{K}\frac{\partial P}{\partial t} + \frac{1}{r}\frac{\partial (rV_r)}{\partial r} + \frac{\partial V}{\partial z} = 0 \tag{16}$$

Averaging over the cross-section, a continuity equation of one-dimensional flow is derived as (Tijsseling, 2007):

$$\frac{1}{\pi R^2}\int_0^R 2\pi r\left(\frac{1}{K}\frac{\partial P}{\partial t} + \frac{1}{r}\frac{\partial (rV_r)}{\partial r} + \frac{\partial V}{\partial z}\right)dr = 0 \tag{17}$$

The Resultant Equation Is:

$$\frac{1}{K}\frac{\partial P}{\partial t} + \frac{2V_r}{R} + \frac{\partial V}{\partial z} = 0 \tag{18}$$

$$\frac{V_r}{R} = \frac{u_r}{R} = \frac{1}{E}\frac{\partial [\sigma_\theta|_{r=R} - \nu(\sigma_z|_{r=R} + \sigma_r|_{r=R})]}{\partial t} \tag{19}$$

Substituting **Eqs 1**, **2** into **Eq. 19**:

$$\frac{V_r}{R} = \frac{1}{E}\left[\frac{(R+e)^2 + R^2}{(R+e)^2 - R^2}\frac{\partial p|_{r=R}}{\partial t} - \frac{2(R+e)^2}{(R+e)^2 - R^2}\frac{\partial P_b}{\partial t} - \nu\left(\frac{\partial p|_{r=R}}{\partial t} + \frac{\partial \sigma_z}{\partial t}\right)\right] \tag{20}$$

Substituting **Eqs 10**, **11**, into **Eq. 20**:

$$\frac{V_r}{R} = \alpha\frac{\partial P}{\partial t} + \beta\frac{\partial \sigma_z}{\partial t} + \gamma\frac{\partial \sigma_{zs}}{\partial t} \tag{21}$$

in which

$$\begin{pmatrix}\alpha\\ \beta\\ \gamma\end{pmatrix} = -\frac{1}{E}\frac{2(R+e)^2}{(R+e)^2 - R^2}\begin{pmatrix}a\\ b\\ c\end{pmatrix} + \frac{1}{E}\left[\frac{(R+e)^2 + R^2}{(R+e)^2 - R^2} - \nu\right]\begin{pmatrix}d\\ f\\ h\end{pmatrix} + \frac{\nu}{E}\begin{pmatrix}0\\ 1\\ 0\end{pmatrix}$$

Substituting **Eq. 21** Into **Eq. 18**:

$$\frac{\partial V}{\partial z} + \left(\frac{1}{K} + 2\alpha\right)\frac{\partial P}{\partial t} + 2\beta\frac{\partial \sigma_z}{\partial t} + 2\gamma\frac{\partial \sigma_{zs}}{\partial t} = 0 \tag{22}$$

2.3 Governing Equations for Pipe

2.3.1 Axial Motion Equation of Structures

For pipe walls, the axial external force is the shear force. Considering pipe-concrete coupling, the motion equation of the pipe is:

$$\rho_t A_t dz\frac{\partial u_z}{\partial t} + A_t\left[\left(\sigma_z + \frac{\partial \sigma_z}{\partial z}dz\right) - \sigma_z\right] = -G\varepsilon_s 2\pi(R+e)dz \tag{23}$$

where u_z and σ_z are axial velocity and axial stress of pipe, A_t is the cross-sectional area of the pipe wall. $G = E/2(1+\nu_s)$ is the shear modulus of elasticity of concrete. The axial strain of concrete $\varepsilon_s = \partial w_s/\partial z$. w_s is the axial displacement of concrete.

Eq. 23 is then Simplified:

$$\rho_t\frac{\partial u_z}{\partial t} + \frac{\partial \sigma_z}{\partial z} = -\frac{R+e}{(R+e/2)e}\frac{E_s}{2(1+\nu_s)}\frac{\partial W_s}{\partial z} \tag{24}$$

Due to the concrete axial velocity $u_s = \partial w_s/\partial t$, **Eq. 24** is updated.

$$\rho_t\frac{\partial u_z}{\partial t} + \frac{\partial \sigma_z}{\partial z} + \frac{R+e}{(R+e/2)e}\frac{E_s}{2(1+\nu_s)}\frac{\partial\left(\int_t u_s dt\right)}{\partial z} = 0 \tag{25}$$

2.3.2 Pipeline Continuity Equation

According to the Hooke law, the strain-stress relation applied to pipe axial direction is:

$$\varepsilon_z = \frac{\partial W_z}{\partial z} = \frac{1}{E}\left[\sigma_z - \nu\left(\overline{\sigma_r} + \overline{\sigma_\theta}\right)\right] \tag{26}$$

where w_z is the axial displacement of pipe wall and $u_z = \partial w_z/\partial t$. According to **Eqs 1**, **2**, the sum of radial and hoop mean stresses is:

$$\begin{aligned}\overline{\sigma_r} + \overline{\sigma_\theta} &= \frac{1}{2\pi(R+e/2)e}\int_R^{R+e} 2\pi(\sigma_r + \sigma_\theta)dr \\ &= \frac{R^2(R+e)^2}{2(R+e/2)^2e^2}\ln\left(1 + \frac{e}{R}\right)p|_{r=R} - \frac{R^2}{2(R+e/2)e}P_b\end{aligned} \tag{27}$$

For convenience, **Eq. 27** is written as:

$$\overline{\sigma_r} + \overline{\sigma_\theta} = kP + l\sigma_z + m\sigma_{zs} \tag{28}$$

in which

$$\begin{pmatrix}k\\ l\\ m\end{pmatrix} = \frac{R^2}{2(R+e/2)e}\begin{pmatrix}a\\ b\\ c\end{pmatrix} + \frac{R^2(R+e)^2}{2(R+e/2)^2e^2}\ln\left(1 + \frac{e}{R}\right)\begin{pmatrix}d\\ f\\ h\end{pmatrix}$$

Substituting **Eq. 28** into **Eq. 26**:

$$\frac{\partial u_z}{\partial z} - \left(\frac{1}{E} - \frac{\nu l}{E}\right)\frac{\partial \sigma_z}{\partial t} + \frac{\nu k}{E}\frac{\partial P}{\partial t} + \frac{\nu m}{E}\frac{\partial \sigma_{zs}}{\partial t} = 0 \tag{29}$$

2.4 Governing Equations for Concrete

Considering structural vibration caused by FSI, the axial motion equation of concrete is:

$$\rho_s A_s dz\frac{\partial u_s}{\partial t} + A_s\frac{\partial \sigma_s}{\partial z}dz = \frac{E_s\varepsilon_s}{2(1+\nu_s)}2\pi(R+e)dz \tag{30}$$

where ρ_s and A_s are density and sectional area of concrete, respectively. **Eq. 30** can be simplified.

$$\rho_s\frac{\partial u_s}{\partial t} + \frac{\partial \sigma_s}{\partial z} = \frac{\pi(R+e)E_s\varepsilon_s}{(1+\nu_s)A_s} \tag{31}$$

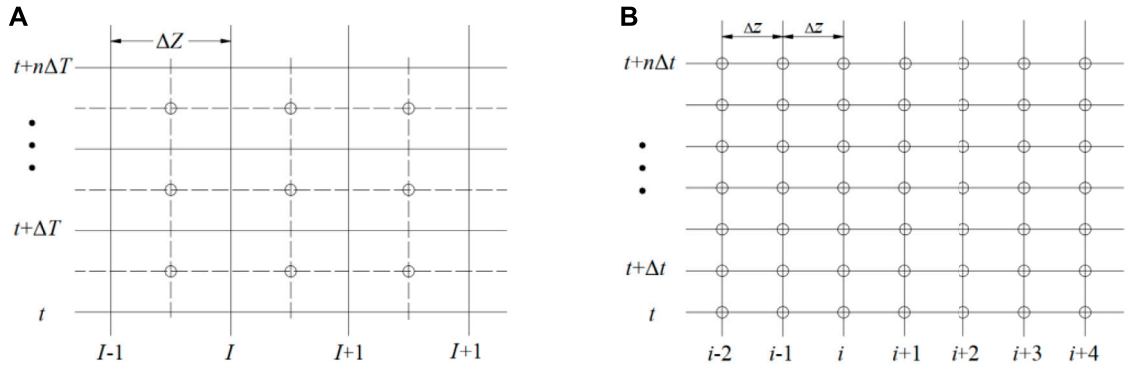

FIGURE 2 | Discretization grids system **(A)** Cell-centered form of FVM. **(B)** An equivalent grid system of A.

According to Hooke law, the strain-stress relation of concrete is:

$$\varepsilon_s = \frac{\partial w_s}{\partial z} = \frac{1}{E}\left[\sigma_s - \nu(\bar{\sigma}_{sr} + \bar{\sigma}_{s\theta})\right] \tag{32}$$

Taking time derivative of **Eq. 32**:

$$\frac{\partial u_s}{\partial z} = \frac{1}{E}\left[\frac{\partial \sigma_s}{\partial t} - \nu\frac{\partial(\bar{\sigma}_{sr} + \bar{\sigma}_{s\theta})}{\partial t}\right] \tag{33}$$

Based on **Eq. 3**, the sum of radial and hoop mean stresses can be expanded as:

$$\begin{aligned}\bar{\sigma}_{sr} + \bar{\sigma}_{s\theta} &= \frac{1}{2\pi(R_s + e_s/2)e_s}\int_{R_s}^{R_s+e_s} 2\pi r(\sigma_{sr} + \sigma_{s\theta})dr \\ &= \frac{R_s^2}{(R_s + e_s/2)e_s}P_b = \frac{R_s^2}{(R_s + e_s/2)e_s}(aP + b\sigma_z + c\sigma_{zs})\end{aligned} \tag{34}$$

Then substituting **Eq. 34** into **Eq. 33**:

$$\frac{\partial u_s}{\partial z} = \frac{1}{E}\frac{\partial \sigma_s}{\partial t} - \frac{\nu_s}{E}\frac{R_s^2}{(R_s + e_s/2)e_s}\left(a\frac{\partial P}{\partial t} + b\frac{\partial \sigma_z}{\partial t} + c\frac{\partial \sigma_{zs}}{\partial t}\right) \tag{35}$$

Till now, a six-equation model describing the fluid-pipe-concrete system is derived. This model consists of continuity and motion equations of fluid and pipe, and constitutive equations of concrete. And these equations are coupled by the boundary conditions on their interfaces, at $r = R$ and $r = R + e$.

3 SOLUTION METHODOLOGY

3.1 Finite Volume Discretization

The finite volume method (FVM) can provide satisfactory predictions to flow transients by solving equations in each control volume (Ferras, et al., 2017) and by presenting each physical term in integral form (Cardiff, et al., 2016). Based on cell-centered FV discretization, an iterative approach is proposed in this paper to calculate the FSI responses. As shown in **Figure 2A**, the control volume includes two dimensions, namely the time step ΔT and the control volume length ΔZ. The model is solved at the center of each cell. In order to numerically keep higher accuracy, the discretization grids system is shown in **Figure 2B**, where $\Delta Z = 2\Delta z$ and $\Delta T = 2\Delta t$.

This method discretizes **Eq. 14** and **Eq. 22**, **Eq. 25**, **Eq. 29**, **Eq. 31** and **Eq. 35** using the control volume and integrates differential equations from t to $t + \Delta t$ in each control volume. The generalized differential equation can be expressed as:

$$\boldsymbol{A}\frac{\partial \boldsymbol{Q}}{\partial t} + \boldsymbol{B}\frac{\partial \boldsymbol{Q}}{\partial z} = \boldsymbol{S} \tag{36}$$

The Crank-Nicolson implicit form of time-centered difference provides a second-order accuracy to predict the partial differential terms. And unconditional stability is guaranteed with respect to the solution process (Ramírez, et al., 2018).

$$\iint_{\Delta t\Delta z}\left(\boldsymbol{A}\frac{\partial \boldsymbol{Q}}{\partial t} + \boldsymbol{B}\frac{\partial \boldsymbol{Q}}{\partial z} - \boldsymbol{S}\right)dtdz = 0 \tag{37}$$

$$\boldsymbol{A}\int_{\Delta z}\partial \boldsymbol{Q}dz + \boldsymbol{B}\int_{\Delta t}\partial \boldsymbol{Q}dt - \boldsymbol{S}\iint_{\Delta t\Delta z}dtdz = 0 \tag{38}$$

$$\boldsymbol{A}(\boldsymbol{Q}_i^{n+1} - \boldsymbol{Q}_i^n)\Delta z + \frac{\boldsymbol{B}}{2}\left[(\boldsymbol{Q}_{i+1}^{n+1} - \boldsymbol{Q}_i^{n+1}) + (\boldsymbol{Q}_{i+1}^n - \boldsymbol{Q}_i^n)\right]\Delta t = \boldsymbol{S}\Delta z\Delta t \tag{39}$$

$$\boldsymbol{A}\boldsymbol{Q}_i^{n+1}\Delta z + \frac{\boldsymbol{B}}{2}(\boldsymbol{Q}_{i+1}^{n+1} - \boldsymbol{Q}_i^{n+1})\Delta t = \boldsymbol{A}\boldsymbol{Q}_i^n\Delta z - \frac{\boldsymbol{B}}{2}(\boldsymbol{Q}_{i+1}^n - \boldsymbol{Q}_i^n)\Delta t + \boldsymbol{S}\Delta z\Delta t \tag{40}$$

where $\boldsymbol{Q}$ denotes the state matrix in each control volume at each time step.

$$\boldsymbol{Q} = \begin{bmatrix} V & u_z & u_s & P & \sigma_z & \sigma_s \end{bmatrix}^{\mathrm{T}}$$

$\boldsymbol{A}$, $\boldsymbol{B}$ and $\boldsymbol{S}$ are shown in the Appendix. n denotes the nth time step. i is the ith calculation nodes. Δt denotes the time step. Δz denotes the axial interval of each node.

According to **Eqs 37–40**, the iterative matrix between adjacent time steps for the water conveyance system is built as follows:

$$\begin{pmatrix} \boldsymbol{A}_1 & \boldsymbol{D}_1 & & & & & \\ \boldsymbol{B}_2 & \boldsymbol{A}_2 & \boldsymbol{D}_2 & & & & \\ & \boldsymbol{B}_3 & \boldsymbol{A}_3 & \boldsymbol{D}_3 & & & \\ & & \ddots & \ddots & \ddots & & \\ & & & \boldsymbol{B}_{N-1} & \boldsymbol{A}_{N-1} & \boldsymbol{D}_{N-1} & \\ & & & & \boldsymbol{B}_N & \boldsymbol{A}_N & \end{pmatrix}_{8N\times 8N} \begin{pmatrix} \boldsymbol{Q}_1 \\ \boldsymbol{Q}_2 \\ \boldsymbol{Q}_3 \\ \vdots \\ \boldsymbol{Q}_{N-1} \\ \boldsymbol{Q}_N \end{pmatrix}_{8N\times 1} = \begin{pmatrix} \boldsymbol{C}_1 \\ \boldsymbol{C}_2 \\ \boldsymbol{C}_3 \\ \vdots \\ \boldsymbol{C}_{N-1} \\ \boldsymbol{C}_N \end{pmatrix}_{8N\times 1} \tag{41}$$

in which

$$\boldsymbol{B}_i = \frac{1}{2}\boldsymbol{B}\begin{pmatrix} \boldsymbol{I}_{4\times 4} & \\ & 0_{4\times 4} \end{pmatrix}$$

$$\boldsymbol{D}_i = \frac{1}{2}\boldsymbol{B}\begin{pmatrix} 0_{4\times 4} & \\ & \boldsymbol{I}_{4\times 4} \end{pmatrix}$$

$$\boldsymbol{C}_i = \boldsymbol{A}\boldsymbol{Q}_i^n\Delta z - \frac{\boldsymbol{B}}{2}\left(\boldsymbol{Q}_{i+1}^n - \boldsymbol{Q}_i^n\right)\Delta t + \boldsymbol{S}\Delta z\Delta t$$

Vector $\boldsymbol{C}_i$ and $\boldsymbol{Q}_i$ separately denote the state vector in the ith node at the nth and $(n+1)^{\text{th}}$ time step. $i = 1$ to N, where 1 and N refer to the inlet and outlet of the pipeline, respectively. When discontinuity happens between adjacent pipelines or fluid, this discontinuous section will be modeled as an interior boundary condition. $\boldsymbol{A}_i$ and $\boldsymbol{C}_i$ are included in the following equations of boundary conditions.

3.2 Boundary Conditions

Given that the cross-sectional area of the reservoir is much larger than that of the pipeline, the water level in the tank can be treated as a constant (Vardy et al., 1996):

$$P = P_0 \tag{42}$$

where P_0 denotes the pressure provided by the water level in the reservoir. The pipe inlet and outlet are rigidly connected to the system respectively, so the corresponding continuity equations of axial direction are as follows (De Santis and Shams, 2019):

$$u_z = 0,\ u_s = 0 \tag{43}$$

When the outlet valve is closed, fluid flow velocity, axial velocity of the pipe wall and discharge satisfy:

$$A_f\left(V - u_z\right) = \tau Q_0 \tag{44}$$

where $\tau = (1—t/T_c)^{1.5}$, τ is the closing coefficient which gradually changes from 1 to 0 when the valve is closed. T_c is the total shutdown time. Subscript 0 denotes the initial value.

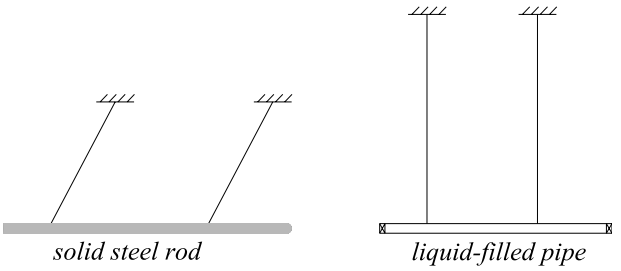

FIGURE 3 | Experimental apparatus (Vardy et al., 1996).

4 METHOD VALIDATION

4.1 Experimental Data Comparison

A more general apparatus proposed by Vardy and Fan is used for benchmark purposes, as seen in **Figure 3** (Vardy et al., 1996). This system consists of a single pipe of 4.5 m and a rod of 5.006 m. The pipe is suspended and kept horizontal by long wires. Both ends of it are sealed by steel caps. And the pipe contains pressurized water to prevent cavitation. Then the steel rod axially impacts the stationary pipe to generate waves in the fluid and in the pipe.

This system during transients is solved by the six-equation model and the iterative methodology. Herein, the pipe is regarded as a thin-wall pipe encased in the same material ($\rho_t = \rho_s$, $\nu = \nu_s$, $E = E_s$). The corresponding cross-section is similar to the sketch in **Figure 1B**.

Results from the experiment and numerical iteration are presented in **Figure 4**, including pressure fluctuations at the impact end (**Figure 4A**) and at the remote end (**Figure 4B**) of the pipe. The time step in the numerical calculation is 10^{-4} s to ensure this algorithm can capture the high-frequency fluctuation. While in the test, the max sampling frequency is 80 Hz. So the black curve in **Figure 4** is relatively smooth compared to the red line. The latter one contains more fluctuating features. In **Figure 4A**, pressure values at the first peak are 2.82 MPa for experiment and 2.74 MPa for simulation. The relative error is 2.84%. Moreover, this six-equation model mainly takes axial coupling and radial coupling into account, while failing to include torsion coupling. Due to experimental error, the discrepancy between the two curves is acceptable. Generally, numerical results are in good agreement with the experimental data. This reveals this numerical model is suitable to investigate the dynamics and kinematics of the piping system embedded in concrete. And the FV discretization method is feasible to solve this system.

4.2 Classical Model Comparison

A typical reservoir-pipe-valve system is built up with pipe length L = 10 m, R = 0.1 m, e = 0.01 m. **Figure 5** sketches this system encased in concrete.

In this system, the water hammer induced by closing the valve was separately calculated by the classical two-equation model and the six-equation model established in this paper. As seen in **Figure 6**, little deviation arises between these two models

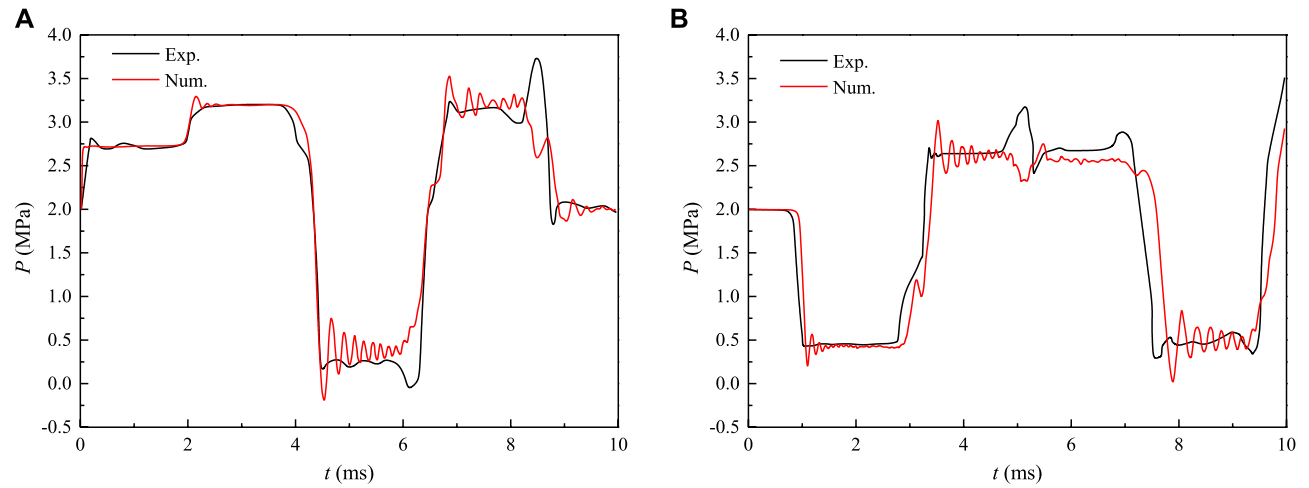

FIGURE 4 | Time history of pressure **(A)** Impact end. **(B)** Remote end.

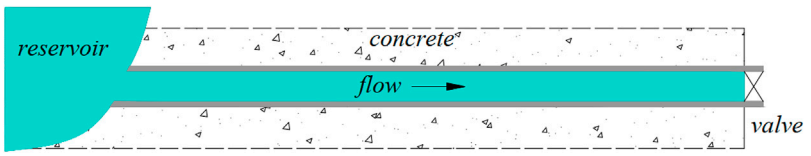

FIGURE 5 | Side view of water conveyance system encased in concrete.

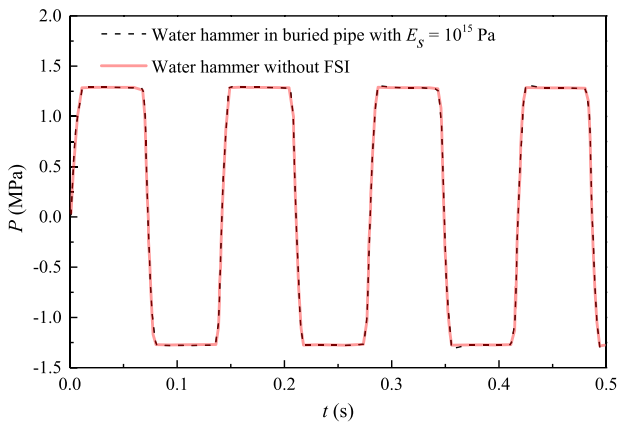

FIGURE 6 | Dynamic pressure with and without FSI.

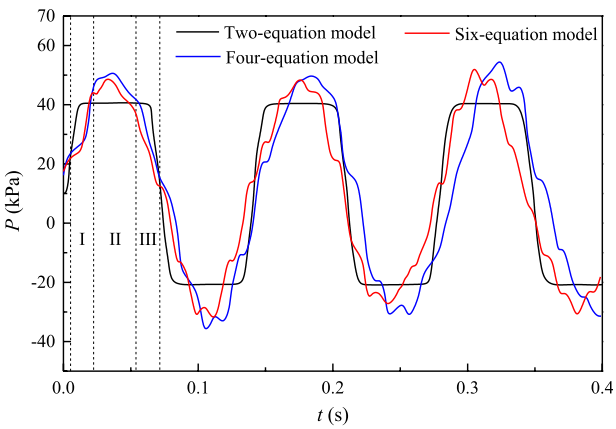

FIGURE 7 | Hydraulic pressure by different models.

when $E_S = 10^{15}$ Pa. The two-equation model neglects fluid-pipe interaction based on the classical water hammer theory. With respect to the six-equation model, the elastic modulus of concrete is large enough so that the pipe vibration is negligible and the FSI response is weak. In such a case, the six-equation model degenerates to the classical model and their results are almost identical.

To further justify the derived six-equation model, comparisons to the two-equation model, and four-equation model are discussed with respect to the water hammer in a typical reservoir-pipe-valve system. The pressure fluctuations upstream the valve by these models are illustrated in **Figure 7**. The two-equation model omits the FSI, so the pressure curve is trapezoidal waveform in shape. The four-equation model involves fluid-pipe interaction but neglects constraints on the pipe's outer surface. This is equivalent to an exposed pipe system.

The peak segment of the black line in **Figure 7** can be split into three parts. In region I, the red and blue lines are lower than the black

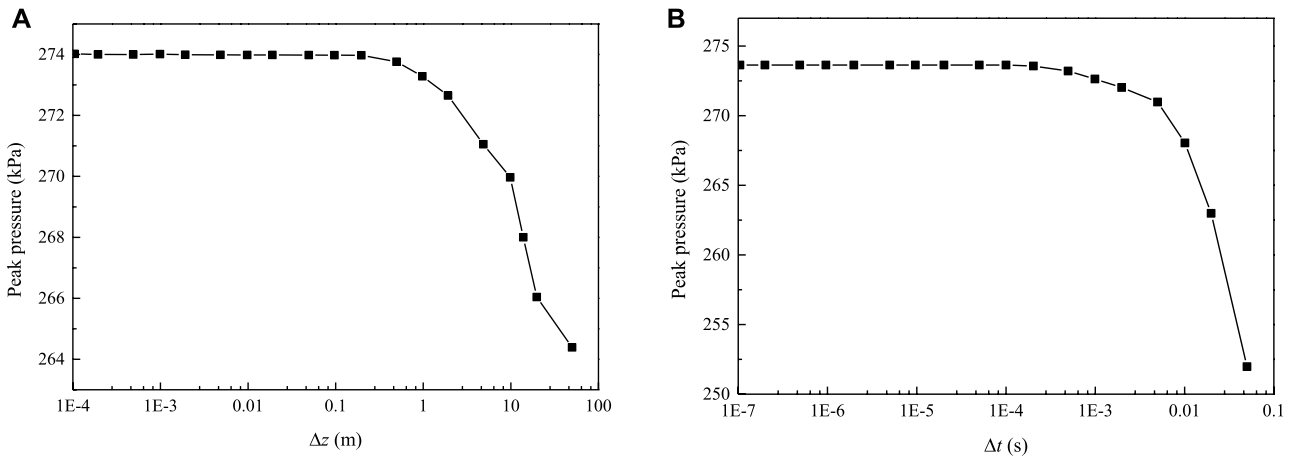

FIGURE 8 | Validation of independence **(A)** grid size. **(B)** time step.

line due to pipe expansion at the valve. In region II, red and blue lines climb over the black line. Because in FSI-involved models, contraction of the pipe wall plays pumping effects on fluid, triggering a larger pressure than the classical result. In region III, the axial stress wave bounces back, expands again the pipe and results in the last pressure drop over the pressure surge. Moreover, an exposed pipe (four-equation model) has a smaller pressure wave speed, but stronger FSI responses due to less support. When the pipe is embedded into concrete, constraints weaken the contributions of the pumping effect. Peak pressure is suppressed, shown as the red line lower than the blue one. When the stiffness of the concrete is large enough, peak pressure and pressure wave speed are similar to those in the classical model, as shown in **Figure 6**.

5 RESULTS AND DISCUSSIONS

This section deals with the kinematic and dynamic characteristics based on the layout in **Figure 5** when the fluid-pipe-concrete interaction is taken into account. Hydraulic transients is triggered by closing the valve in 0.01 s. And the closing law depends on the coefficient τ in **Eq. 44**.

Sensitive analysis of grid size and time step is first discussed, which determines the result precision. In this process, the Courant number is well controlled to ensure a stable iteration and reliable results. Numerical results of peak pressure vary with these two parameters are given in **Figure 8**. When $\Delta z > 0.1$ m in **Figure 8A**, the peak pressure drops dramatically with the increase of grid interval. On the contrary, if $\Delta z < 0.1$ m, the numerical result is not sensitive to grid size. **Figure 8B** shows a similar manner when the threshold value of the time step is 10^{-4} s. Consequently, the node interval and time step are separately set to be 0.1 m and 10^{-4} s in the iterative algorithm.

5.1 Influence of Concrete on Hydraulic Pressure

As known from **Eq. 22** and **Eq. 31**, FSI responses to water hammer greatly depend on parameters of concrete, including its Poisson's ratio, thickness-radius ratio, elastic modulus and density. Hydraulic pressure upstream the valve fluctuates with these parameters are shown in **Figures 9A–D**, respectively.

It is clear that the Poisson's ratio and concrete density hardly affect the hydraulic pressure as the two curves are almost overlapped, as seen in **Figures 9A,D**. Firstly, coefficients in **Eqs 10**, **11** are the function of ν_s from their definitions in the Appendix. But the difference of $R{\cdot}p|_{r=R}$ - $(R + e){\cdot}P_b$ can be ignorable. Moreover, ν_s mainly contributes to the axial shear force between concrete and pipe, while little affects the pressure. With respect to the concrete density, ρ_s only dominates the inertia of concrete, then affects the frictional force on the outer interface. However, hydraulic pressure hardly changes when ρ_s becomes ten times larger. This reveals that the axial vibration of concrete plays a negligible role in FSI responses.

In contrast, the thickness-radius ratio and elastic modulus play an important role in the FSI response. By extension, larger E_s alleviates the pumping effect on fluid and further weakens the FSI response. Hydraulic pressure fluctuates more moderately in this case and decays faster, as seen in **Figure 9C**. Besides, E_s and e_s/R_s both influences the pressure wave speed, then change the fluid inner pressure. **Figure 10** shows the wave speed changing with the product of E_s and e_s/R_s.

In the graph when $E_s e_s/R_s < 10^6$ Pa, pressure wave speed is almost constant and the pumping effect can be ignored. So the pipe encased in concrete is approximate to an exposed one, and the four-equation model is suitable in this case. When $E_s e_s/R_s > 10^{11}$ Pa, influences of wave speed and pumping effect are also negligible. In this case, the FSI response is weak, so the two-equation model is suitable. When $E_s e_s/R_s$ increases from 10^6 Pa to 10^{11} Pa, the wave speed changes dramatically as well as the FSI responses. Notably, the $E_s e_s/R_s$ of concrete is within this range. Thus, studying the FSI in a piping system embedded in concrete is of great importance.

5.2 Pipe-Wall Stress

In this study, pressure gradients applied to the interface cause pipe wall expansion or contraction, and further compress or relax

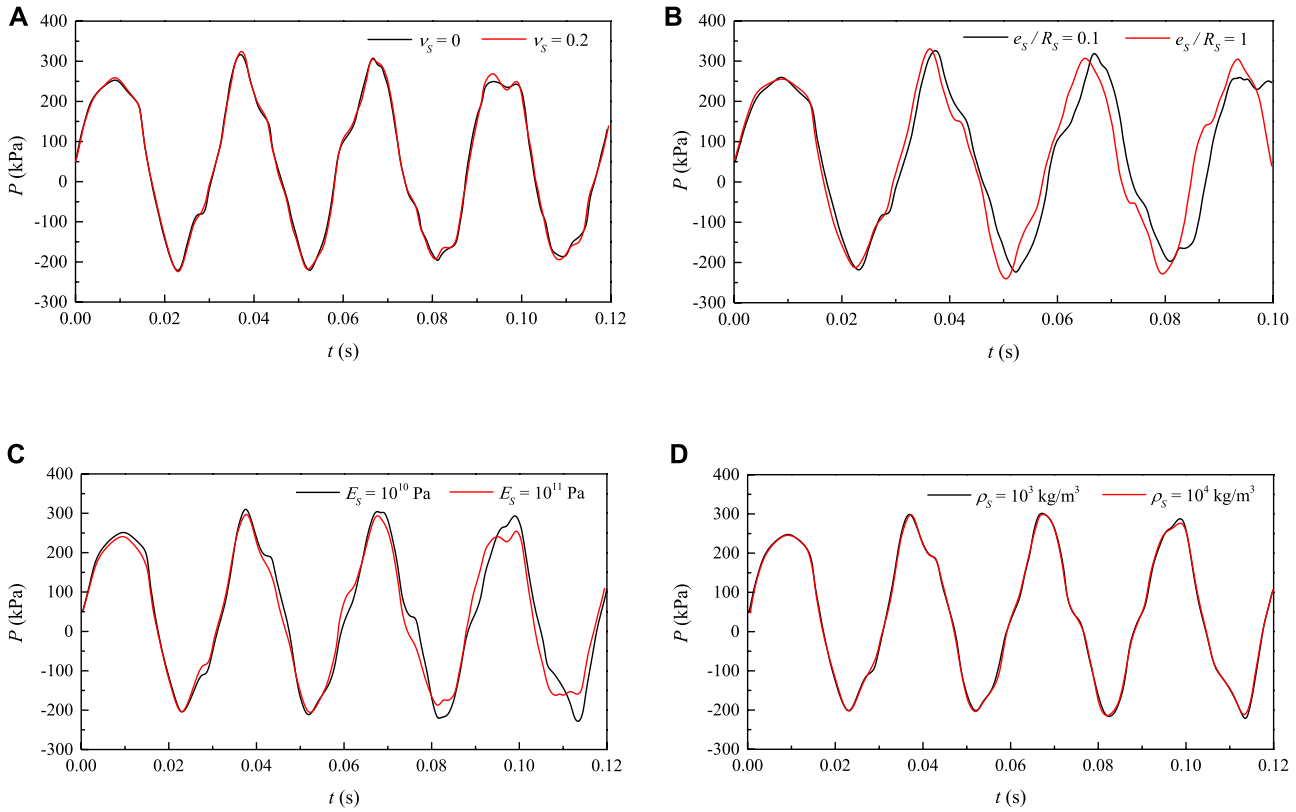

FIGURE 9 | Dynamic pressure varies with the parameters of concrete **(A)** Poisson's ratio. **(B)** Thickness-radius ratio. **(C)** Elastic modulus. **(D)** Density.

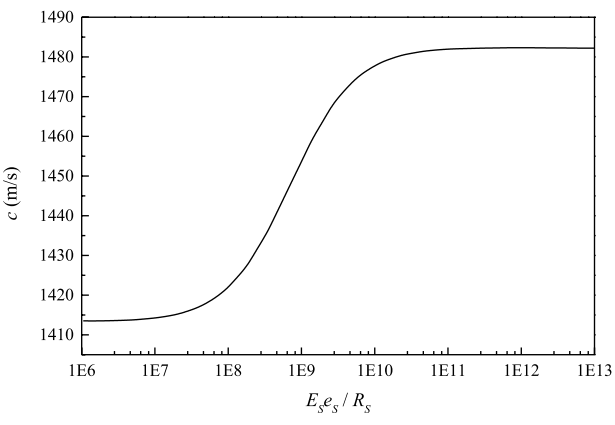

FIGURE 10 | Pressure wave speed varies with $E_S e_S / R_S$.

the ambient concrete. Thus, P_b is produced and subsequently weakens the FSI responses. The dynamic pressure on the inner and the outer interfaces are separately shown in **Figures 11A,B**.

Stronger pulsations are caused by larger $E_S e_S / R_S$ on both inner and outer interfaces. With larger P_b, a weaker pumping effect is obtained. Hoop stress and radial stress of pipe wall become smaller due to restrictions by concrete from **Eqs 1**, **2**. The result is the piping system gets safer. Moreover, the difference between $R \cdot p|_{r=R}$ and $(R + e) \cdot P_b$ is smaller in the case of larger $E_S e_S / R_S$, which can further lead to weaker axial stress pulsation in the pipe wall, as shown in **Figure 12**.

The six-equation model derived in this paper aims to investigate FSI subject to water hammer. Due to the deformation of structures, FSI response to some extent weakens the stress pulsation in the pipe wall. As shown in **Figure 13**, both the hoop and radial stress are larger using the classical model without FSI.

5.3 Pipe-Wall Motion

In this segment, the axial vibration of the system is analyzed. Axial displacement of the pipe wall relates to the fluid and concrete, while the concrete plays the damping role. Signals of axial displacement in the time domain and frequency domain are shown in **Figures 14A,B**, separately. When FSI is taken into account, the pipe-wall motion is found to relate to the pressure wave in fluid and stress wave in solid. These two waves propagate throughout the pipeline system in the axial direction, contributing to the vibration amplitude in **Figure 14A**. In radial direction, pipe expansion or contraction is confined by the ambient concrete, so the radial vibration of the pipe wall is weak.

Pipe vibration is mainly caused by hydraulic pressure fluctuation, especially when FSI is included. All vibration modes in this case are system modes. However, pipe deformation mode can be identified by data processing. The first eight modes of pipe

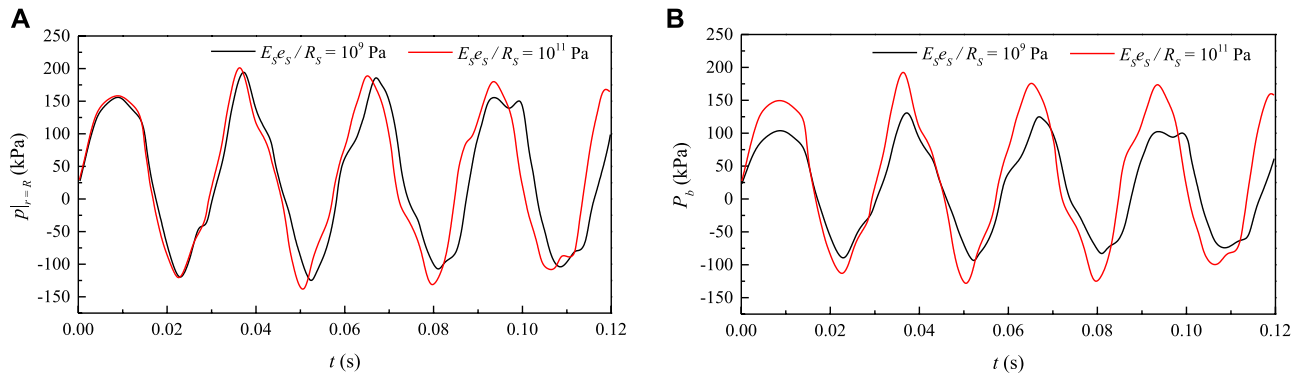

FIGURE 11 | Pressure fluctuates with $E_s e_s/R_s$ **(A)** On the inner interface. **(B)** On the outer interface.

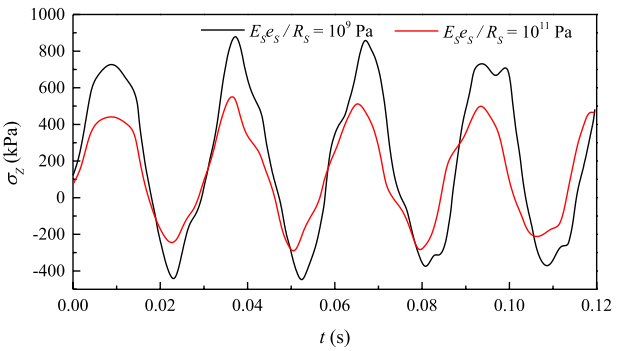

FIGURE 12 | Axial stress of pipe wall fluctuates with $E_s e_s/R_s$.

with respect to different models are shown in **Table 1**. Data in the right column correspond to the local peaks in **Figure 14B**. According to calculation results, the frequency of pressure wave is 35.2 Hz, the frequency of stress wave in pipe wall is 129.3 Hz, and the frequency of stress wave in concrete is 99.6 Hz.

The two-equation model predicts the highest frequency value at each mode without FSI. Compared with the four-equation model, constraints by concrete enlarges the frequency value in the six-equation model. Wave speed in this model is faster, in accord with the curve tendency in **Figure 10**. Additionally, Pipe and concrete absorb more energy from water hammers so that FSI responses are alleviated. Similar results are obtained in **Figure 7**. Comparison of the three models shows that inherent frequency of the piping system is changed when different factors are taken into account, like the concrete. On the other, the pressure surge acts as an unstable source during FSI responses. When parameters of the concrete change, nature frequency of the pressure pulsation is changed accordingly. This situation may lead to undesirable resonance, especially in a more complex pipeline layout.

6 CONCLUSION

This work studies the FSI responses of a piping system embedded in concrete during water hammers. Based on area average treatment on a cross-section, a six-equation model is derived

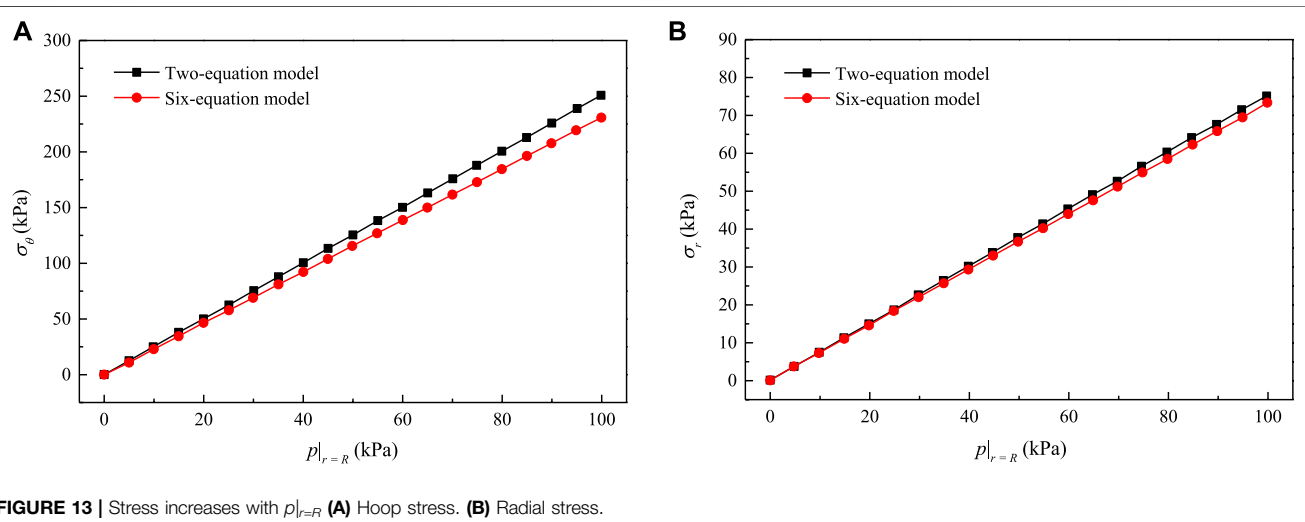

FIGURE 13 | Stress increases with $p|_{r=R}$ **(A)** Hoop stress. **(B)** Radial stress.

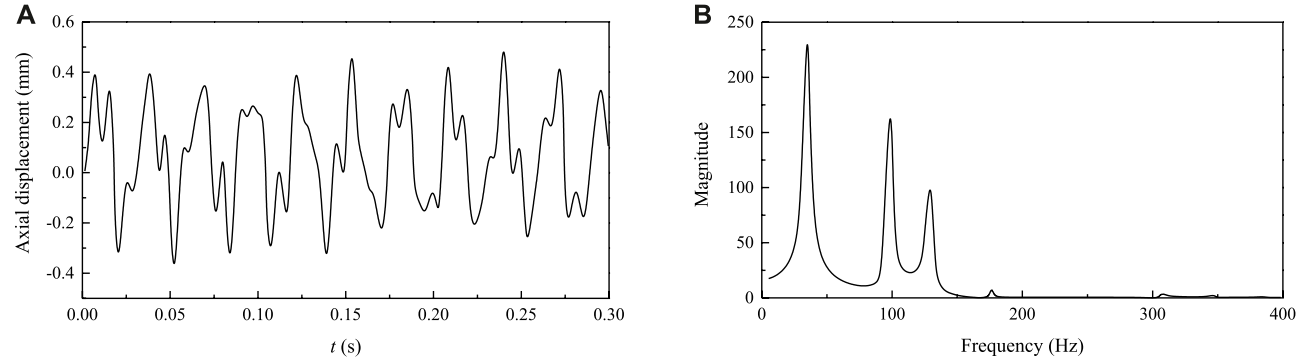

FIGURE 14 | Dynamic axial displacement **(A)** Time domain. **(B)** Frequency domain.

TABLE 1 | First eight modes of pipe with respect to three models.

Mode	Two-Equation Model (Hz)	Four-Equation Model (Hz)	Six-Equation Model (Hz)
1	36.7	33.4	35.2
2	103.1	97.2	99.6
3	134.0	126.6	129.3
4	184.8	176.3	179.0
5	321.1	305.3	310.1
6	362.3	343.7	348.3
7	412.7	387.7	393.7
8	465.3	443.3	450.3

to describe the fluid-pipe-concrete interaction. This model is subsequently solved by numerical iteration and results are compared with experimental data and classical models, showing good agreements.

In a reservoir-pipe-valve system, hydraulic pressure with respect to concrete parameters is discussed. Numerical results reveal that Poisson's ratio and density of concrete hardly contribute to FSI responses, while elastic modulus and thickness-radius ratio play crucial roles. More specifically, E_s mainly weakens the pipe pumping effect and e_s/R_s determines pressure wave speed. Larger E_s and smaller e_s/R_s result in more mild pressure fluctuations. When $E_s e_s/R_s < 10^6$ Pa, this six-equation model is approximate to the four-equation model, namely an exposed pipeline system. When $E_s e_s/R_s > 10^{11}$ Pa, constraints from concrete are large enough so that the classical two-equation model is suitable.

Structural vibration caused by FSI mitigates stress pulsations separately in circumferential, radial and axial directions of the pipe wall. These pulsations are more moderate in the case of weaker FSI responses. Without FSI, the classical water-hammer theory may lead to an unintended large safety margin and uneconomic design. It should be noted that weaker FSI responses cause higher structural frequency in a water conveyance system, which justifies more explorations in the design and operation stage of the piping system.

DATA AVAILABILITY STATEMENT

The original contributions presented in the study are included in the article/Supplementary Material, further inquiries can be directed to the corresponding author.

AUTHOR CONTRIBUTIONS

YC: conceptualization, computation, visualization, writing–original draft; CZ: data analysis, writing–original draft and editing; QG: methodology, formal analysis, validation, writing–review and editing; JZ: methodology, resources, supervision; YF: supervision, writing–review and editing; KX: funding acquisition, assistance with analysis.

FUNDING

This work was supported by the National Natural Science Foundation of China (Grant No. 12002150), the Natural Science Foundation of Jiangsu Province (BK20201041), the High–education Natural Science Foundation of Jiangsu Province (21KJB570001), and the Research Foundation for High–level Talents of Nanjing Institute of Technology (YKJ202131).

REFERENCES

Alaei, D., Kwon, Y. W., and Ramezani, A. (2019). Fluid-structure Interaction on Concentric Composite Cylinders Containing Fluids in the Annulus. *Multiscale Multidiscip. Model. Exp. Des.* 2 (3), 185–197. doi:10.1007/s41939-019-00044-3

Cardiff, P., Tuković, Ž., Jasak, H., and Ivanković, A. (2016). A Block-Coupled Finite Volume Methodology for Linear Elasticity and Unstructured Meshes. *Comput. Struct.* 175, 100–122. doi:10.1016/j.compstruc.2016.07.004

Daoxiang, Z., and Weinlin, Z. (2006). *Foundation of Engineering Elasticity*. Hefei, China: Hefei University of Technology Press.

De Santis, D., and Shams, A. (2019). Scaling of Added Mass and Added Damping of Cylindrical Rods by Means of Fsi Simulations. *J. Fluids Struct.* 88, 241–256. doi:10.1016/j.jfluidstructs.2019.05.011

Ferras, D., Manso, P. A., Schleiss, A. J., and Covas, D. I. C. (2017). Fluid-Structure Interaction in Straight Pipelines with Different Anchoring Conditions. *J. Sound Vib.* 394, 348–365. doi:10.1016/j.jsv.2017.01.047

Hu, S., Sun, Y., Xue, X., and Huang, Y. (2019). Calculation Model for Bar-Wrapping during Prestressing of an Embedded Bar-Wrapped Cylinder Concrete Pressure Pipe. *Thin-Walled Struct.* 139, 39–45. doi:10.1016/j.tws.2019.02.036

Huang, W.-X., and Alben, S. (2016). Fluid-structure Interactions with Applications to Biology. *Acta Mech. Sin.* 32 (6), 977–979. doi:10.1007/s10409-016-0608-9

Karakouzian, M., Karami, M., Nazari-Sharabian, M., and Ahmad, S. (2019). Flow-Induced Stresses and Displacements in Jointed Concrete Pipes Installed by Pipe Jacking Method. *Fluids* 4 (1), 34. doi:10.3390/fluids4010034

Lai, M. H., Liang, Y. W., Wang, Q., Ren, F. M., Chen, M. T., and Ho, J. C. M. (2020). A Stress-Path Dependent Stress-Strain Model for Frp-Confined Concrete. *Eng. Struct.* 203, 109824. doi:10.1016/j.engstruct.2019.109824

Lee, C. K., Chiew, S. P., and Jiang, J. (2012). Residual Stress Study of Welded High Strength Steel Thin-Walled Plate-To-Plate Joints, Part 1: Experimental Study. *Thin-Walled Struct.* 56, 103–112. doi:10.1016/j.tws.2012.03.015

Li, S.-J., Liu, G.-M., and Chen, H. (2012). Pressure Wave Propagation Characteristics in Fluid-Filled Pipes with Fluid-Structure Interaction. *J. Vib. Shock* 31 (24), 177–182. doi:10.13465/j.cnki.jvs.2012.24.029

Li, S.-j., Liu, G.-m., and Kong, W.-t. (2014). Vibration Analysis of Pipes Conveying Fluid by Transfer Matrix Method. *Nucl. Eng. Des.* 266, 78–88. doi:10.1016/j.nucengdes.2013.10.028

Liu, G., and Li, Y. (2011). Vibration Analysis of Liquid-Filled Pipelines with Elastic Constraints. *J. Sound Vib.* 330 (13), 3166–3181. doi:10.1016/j.jsv.2011.01.022

Mahmoodi, R., Zolfaghari, A., and Minuchehr, A. (2019). Laplace Transform Finite Volume Modeling of Water Hammer along Fluid-Structure Interaction. *Comput. Math. Appl.* 77 (10), 2821–2832. doi:10.1016/j.camwa.2019.01.014

Mirjavadi, S. S., Forsat, M., and Badnava, S. (2020). Nonlinear Modeling and Dynamic Analysis of Bioengineering Hyper-Elastic Tubes Based on Different Material Models. *Biomech. Model. Mechanobiol.* 19 (3), 971–983. doi:10.1007/s10237-019-01265-8

Rajbamshi, S., Guo, Q., and Zhan, M. (2020). Model Updating of Fluid-Structure Interaction Effects on Piping System. *Dyn. Substruct.* 4, 133–139. doi:10.1007/978-3-030-12184-6_12

Ramírez, L., Nogueira, X., Ouro, P., Navarrina, F., Khelladi, S., and Colominas, I. (2018). A Higher-Order Chimera Method for Finite Volume Schemes. *Arch. Comput. Methods Eng.* 25 (3), 691–706. doi:10.1007/s11831-017-9213-8

Riedelmeier, S., Becker, S., and Schlücker, E. (2014). Measurements of Junction Coupling during Water Hammer in Piping Systems. *J. Fluids Struct.* 48, 156–168. doi:10.1016/j.jfluidstructs.2014.03.001

Sinha, J. K., Singh, S., and Rama Rao, A. (2001). Finite Element Simulation of Dynamic Behaviour of Open-Ended Cantilever Pipe Conveying Fluid. *J. Sound Vib.* 240 (1), 189–194. doi:10.1006/jsvi.2000.3113

Sun, Y., Hu, S., Huang, Y., and Xue, X. (2020). Analytical Stress Model for Embedded Bar-Wrapped Cylinder Concrete Pressure Pipe under Internal Load. *Thin-Walled Struct.* 149, 106540. doi:10.1016/j.tws.2019.106540

Tijsseling, A. S. (2019). An Overview of Fluid-Structure Interaction Experiments in Single-Elbow Pipe Systems. *J. Zhejiang Univ. Sci. A* 20 (4), 233–242. doi:10.1631/jzus.A1800564

Tijsseling, A. S. (2007). Water Hammer with Fluid-Structure Interaction in Thick-Walled Pipes. *Comput. Struct.* 85 (11-14), 844–851. doi:10.1016/j.compstruc.2007.01.008

Ting, Z., Yongzhen, L., Zhiqiang, Y., Chiaming, F., and Tsunghan, L. (2017). Axial Vibration Response of Viscoelastic Pipe Conveying Fluid Induced by Water Hammer. *J. Vib. Eng.* 30 (2), 241–248. doi:10.16385/j.cnki.issn.1004-4523.2017.02.009

Vardy, A. E., Fan, D., and Tijsseling, A. S. (1996). Fluid-Structure Interaction in a T-Piece Pipe. *J. Fluids Struct.* 10 (7), 763–786. doi:10.1006/jfls.1996.0052

Wu, J.-S., and Shih, P.-Y. (2001). The Dynamic Analysis of a Multispan Fluid-Conveying Pipe Subjected to External Load. *J. Sound Vib.* 239 (2), 201–215. doi:10.1006/jsvi.2000.3119

Wu, Z. (20172017). *Elasticity*. Beijing: Beijing Institute of Technology.

Yang, K., Li, Q., and Zhang, L. (2004). Longitudinal Vibration Analysis of Multi-Span Liquid-Filled Pipelines with Rigid Constraints. *J. Sound. Vib.* 273 (1-2), 125–147. doi:10.1016/S0022-460X(03)00422-X

Zanganeh, R., Ahmadi, A., and Keramat, A. (2015). Fluid-structure Interaction with Viscoelastic Supports during Waterhammer in a Pipeline. *J. Fluids Struct.* 54, 215–234. doi:10.1016/j.jfluidstructs.2014.10.016

Conflict of Interest: YC is employed by the Company Haitian Plastics Machinery Group Co., Ltd.

The remaining authors declare that the research was conducted in the absence of any commercial or financial relationships that could be construed as a potential conflict of interest.

APPENDIX

$$a = \frac{-\frac{E_s}{E}\nu\frac{2R^2}{(R+e)^2-R^2}\frac{2\rho_t(R+e/2)^2e\rho_t}{\rho_f R^2+2\rho_t(R+e/2)e}}{1+\frac{E_s}{E}+\frac{E_s}{E}\nu\frac{2R^2}{(R+e)^2-R^2}-\nu_s\frac{R_s^2+(R+e)^2}{R_s^2-(R+e)^2}-\frac{2\rho_t(R+e/2)^2e\rho_t}{\rho_f R^2+2\rho_t(R+e/2)e}}$$

$$b = \frac{-\frac{E_s}{E}\nu}{1+\frac{E_s}{E}+\frac{E_s}{E}\nu\frac{2R^2}{(R+e)^2-R^2}-\nu_s\frac{R_s^2+(R+e)^2}{R_s^2-(R+e)^2}-\frac{2\rho_t(R+e/2)^2e\rho_t}{\rho_f R^2+2\rho_t(R+e/2)e}}$$

$$c = \frac{\nu_s}{1+\frac{E_s}{E}+\frac{E_s}{E}\nu\frac{2R^2}{(R+e)^2-R^2}-\nu_s\frac{R_s^2+(R+e)^2}{R_s^2-(R+e)^2}-\frac{2\rho_t(R+e/2)^2e\rho_t}{\rho_f R^2+2\rho_t(R+e/2)e}}$$

$$d = \frac{2\rho_t(R+e/2)^2e+2(R+e)^2a}{\rho_f R^2+2\rho_t(R+e/2)^2e}$$

$$f = \frac{2(R+e)^2b}{\rho_f R^2+2\rho_t(R+e/2)^2e}$$

$$h = \frac{2(R+e)^2c}{\rho_f R^2+2\rho_t(R+e/2)^2e}$$

$$\boldsymbol{A} = \begin{pmatrix} \rho_f & & & & \\ & & 1/K+2\alpha & 2\beta & 2\gamma \\ & \rho_t & & & \\ & & \nu k & \nu l-1 & \nu m \\ & \rho_s & & & \\ & & \frac{\nu_s R_s^2 a}{(R_s+e_s/2)e_s} & \frac{\nu_s R_s^2 b}{(R_s+e_s/2)e_s} & \frac{\nu_s R_s^2 c}{(R_s+e_s/2)e_s}-1 \end{pmatrix}$$

$$\boldsymbol{B} = \begin{pmatrix} \rho_f\left|V_i^n\right| & & & 1 & \\ 1 & & & & \\ & & \frac{E_s(R+e)\Delta t}{2(1+\nu_s)(R+e/2)e} & & 1 \\ & 1 & & & \\ & & -\frac{E_s\pi(R+e)\Delta t}{2(1+\nu_s)A_s} & & 1 \\ & & 1 & & \end{pmatrix}$$

$$\boldsymbol{S} = \begin{pmatrix} 0 \\ 0 \\ \frac{E_s(R+e)\Delta t}{2(1+\nu)(R+e/2)e}\frac{\partial\sum_{n=0}^{(n-1)\Delta t}(u_s)_n}{\partial z} \\ 0 \\ -\frac{E_s\pi(R+e)\Delta t}{2(1+\nu)A_s}\frac{\partial\sum_{n=0}^{(n-1)\Delta t}(u_s)_n}{\partial z} \\ 0 \end{pmatrix}$$

frontiers | Frontiers in Energy Research

TYPE Original Research
PUBLISHED 04 August 2022
DOI 10.3389/fenrg.2022.943289

OPEN ACCESS

EDITED BY
Yongguang Cheng,
Wuhan University, China

REVIEWED BY
Qiang Gao,
University of Minnesota Twin Cities, United States
Wenjie Wang,
Jiangsu University, China

*CORRESPONDENCE
Huixiang Chen,
chenhuixiang@hhu.edu.cn

SPECIALTY SECTION
This article was submitted to Process and Energy Systems Engineering, a section of the journal Frontiers in Energy Research

RECEIVED 13 May 2022
ACCEPTED 05 July 2022
PUBLISHED 04 August 2022

CITATION
Chen Y, Sun Q, Li Z, Gong Y, Zhai J and Chen H (2022), Numerical study on the energy performance of an axial-flow pump with different wall roughness. *Front. Energy Res.* 10:943289. doi: 10.3389/fenrg.2022.943289

Numerical study on the energy performance of an axial-flow pump with different wall roughness

Yuling Chen[1], Qing Sun[1], Zhixiang Li[2], Yan Gong[1], Jianwei Zhai[3] and Huixiang Chen[1]*

[1]College of Agricultural Science and Engineering, Hohai University, Nanjing, China, [2]College of Water Conservancy and Hydropower Engineering, Hohai University, Nanjing, China, [3]College of Energy and Electrical Engineering, Hohai University, Nanjing, China

Pumping stations play an important role in China's South-to-North Water Diversion, agricultural irrigation, and municipal drainage. Some pumping station units have been put into operation for long periods with improper operation and require maintenance. Moreover, the surfaces of the flow components have been worn and corroded, leading to an increase in the relative roughness and a decrease in the hydraulic performance efficiencies of pumping station units. In this work, we performed field measurements and numerical simulations to study the influence of the wall roughness on the hydraulic performance of slanted axial-flow pump devices under multiple working conditions. The effects of the wall roughness of the impeller chamber on the hydraulic performance of the pump, the guide vane chamber, and the inlet and outlet flow channel were investigated. Wall roughness had the largest influence on the hydraulic performance of the pump and the smallest influence on the inlet and outlet flow channels. For devices with different roughness values on the impeller chamber wall under different flow rate conditions, the performance of the pump device worsened under the large-flow-rate condition, and the device performance was better under the small-flow-rate and designed flow conditions. The efficiency of the slanted axial-flow pump device decreased significantly as the flow rate increased. Under the same flow rate condition, the performance of the device with Ra = 5 μm was similar to that with a smooth wall, where Ra is the roughness of the wall. With the increase in the roughness, the uniformity of the axial velocity distribution coefficient decreased, and the velocity-weighted average drift angle increased. External characteristic parameters, such as the torque and the static pressure, on the blade pressure surface gradually decreased with the increase in the wall roughness. A large roughness could induce instability of the wall flow and enhance the turbulent kinetic energy near the blade surface.

KEYWORDS

axial flow pump, wall roughness, hydraulic performance, external characteristic, turbulent kinetic energy

1 Introduction

Axial-flow pumps are commonly used in water diversion, municipal drainage, water source protection, and other fields. Based on the installation position of the pump shaft, they can be divided into vertical, horizontal, and slanted axial-flow pumps (Shi et al., 2020; Kan et al., 2021b). Unlike the vertical axial-flow pump, the installation angle between the slanted axial-flow pump and the inlet does not need to turn at a right angle, leading to a small hydraulic loss (Wang et al., 2020; Fei et al., 2022a). Furthermore, the slanted axial-flow pump has better-operating conditions than the tubular pump, and the pump section can be placed between the inlet and outlet channels. In the processing of an axial-flow pump, the absolute smoothness of the wall cannot be guaranteed. The flow pattern in the pump device is always affected by the wall roughness, which causes a performance difference between the design and practical application of the axial-flow pump (Wang et al., 2010; Hu et al., 2021). In particular, the internal space curvature structure of the slanted axial-flow pump, because of the limited machining accuracy, can only ensure that the walls of the flow components are relatively smooth. After being put into use for a long time, the slanted axial-flow pump is affected by sediment, oxidation, and corrosion, and its operational performance changes significantly (Wang et al., 2010; Fei et al., 2022b).

Research on the effect of surface roughness on the performances of blades and airfoils has been carried out extensively. Walker et al. (2013) and Walker et al. (2014) verified numerical models of smooth and rough blades by experiments, and they studied the lift and drag coefficients of blade airfoils with different roughness values. The results showed that blade roughness reduced the turbine performance (19% reduction in maximum C_P and shift of the entire C_P performance curve downward). Tao et al. (2014) studied the effects of the surface roughness on the boundary development and loss behavior of turbine blades at different Reynolds numbers. The result showed that the velocity profile in the boundary layer was plumper on a rough surface than on a smooth blade. The aerodynamic loss was lower at low Reynolds numbers, but it became significantly larger at high Reynolds numbers. Echouchene et al. (2011) studied the influence of the wall roughness on the performance of an injector and its internal cavitation flow characteristics, and they found that a certain degree of roughness improved the performance of the cavitation nozzle. Deng et al. (2016) studied the influence of the inner surface roughness of a jet nozzle on the characteristics of a submerged cavitation jet through experiments, and they found that too rough of a surface would cause a large amount of energy dissipation, resulting in jet divergence and reducing the cavitation intensity. The study of Soltani and Birjandi (2013) showed that the performance of a fan was also significantly affected by the surface roughness of the blade. Kang et al. (2006) used numerical simulations to predict the influence of the roughness on the performance of a single-stage axial turbine. The results showed that the change of the surface roughness directly affected the efficiency of an axial turbine. Moreover, Marzabadi and Soltani (2013) used a hot film sensor to find that the roughness caused the boundary layer transition point to move to the inlet, leading to a boundary separation phenomenon occurring earlier and weakening the effect of the airfoil. With the deepening of research, some scholars have begun to study the local surface roughness. Ren and Ou (2009) set the roughness at different positions on the airfoil surface, and it was found that the leading edge was more affected by roughness than the trailing edge. Long and Wang. (2004), Zhu et al. (2006) used a computational fluid dynamics numerical simulation method to analyze the influence of different roughness values on the performance of an axial-flow pump in detail.

The influence of wall roughness on the pump performance remains elusive. Most investigations were based on pumps with small flow rates and powers, and the influence of the wall roughness on the working condition of large, slanted axial-flow pumps has been less studied. Therefore, in this work, the hydraulic performance of the slanted axial-flow pump device was studied. To ensure the safety and stability of the unit and improve the intact rate and operating life of the equipment, the influence of the wall roughness on the hydraulic performance of a slanted axial-flow pump device under different flow rates was analyzed. Corresponding research results can provide a reference for the optimal operation of pumping stations.

The rest of this article is organized as follows. The calculation model, numerical method, computation setup, and an equivalent sand grain model are introduced in Section 2. The experimental test validation, characteristics, and hydraulic performance are presented and analyzed in Section 3. Finally, an overall summary is provided in Section 4.

2 Numerical methodology

2.1 Governing equations

In this study, the Reynolds time-averaged Navier–Stokes equation was employed to simulate the internal flow field of the slanted axial-flow pump. The correlative continuity and momentum conservation equations are given as follows (Qin et al., 2021; Wang et al., 2022):

$$\frac{\partial \rho}{\partial t} + \frac{\partial (\rho u_i)}{\partial x_i} = 0 \tag{1}$$

$$\frac{\partial (\rho u_i)}{\partial t} + \frac{\partial (\rho u_i u_j)}{\partial x_j} = -\frac{\partial p}{\partial x_j} + \frac{\partial}{\partial x_j}\left[\mu\left(\frac{\partial u_i}{\partial x_j} + \frac{\partial u_j}{\partial x_i}\right)\right] + \frac{\partial \tau_{ij}}{\partial x_j} \tag{2}$$

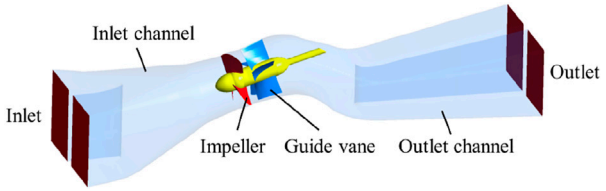

FIGURE 1
Three-dimensional model of slanted axial-flow pump.

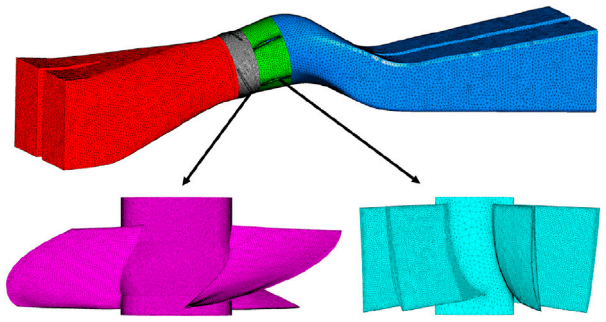

FIGURE 2
Grid diagram of the computational domain.

where ρ is the fluid density, t is the time, p is the pressure, μ is the dynamic viscosity, x_i and x_j (i, j = 1, 2, 3) denote the Cartesian coordinate components, u_i and u_j represent the components of the velocity, τ_{ij} represents the Reynolds stress. In addition, we apply the renormalization group (RNG) k-ε model, which can model a wide range of flow profiles with increased accuracy. The equations for the turbulent kinetic energy k and the turbulent kinetic energy dissipation rate ε are as follows (Pang et al., 2016; Kan et al., 2021a):

$$\frac{\partial(\rho k)}{\partial t}+\frac{\partial(\rho k u_i)}{\partial x_i}=\frac{\partial}{x_j}\left(\alpha_k\mu_{eff}\frac{\partial k}{\partial x_j}\right)+G_k-\rho\varepsilon \tag{3}$$

$$\frac{\partial(\rho k)}{\partial t}+\frac{\partial(\rho k u_i)}{\partial x_i}=\frac{\partial}{x_j}\left(\alpha_k\mu_{eff}\frac{\partial k}{\partial x_j}\right)+\mu_t\left(\frac{\partial u_i}{\partial x_j}+\frac{\partial u_j}{\partial x_i}\right)\frac{\partial u_i}{\partial x_j}-\rho\varepsilon \tag{4}$$

$$\frac{\partial(\rho\varepsilon)}{\partial t}+\frac{\partial(\rho\varepsilon u_i)}{\partial x_i}=\frac{\partial}{\partial x_j}\left(\alpha_k\mu_{eff}\frac{\partial k}{\partial x_j}\right)+\frac{C^*_{\varepsilon1}}{k}G_k-C_{\varepsilon2}\rho\frac{\varepsilon}{k} \tag{5}$$

where

$$\mu_{eff}=\mu+\mu_t, C^*_{\varepsilon1}=C_{\varepsilon1}-\frac{\eta(1-\eta/\eta_0)}{1+\beta\eta^3}, \eta=\frac{k}{\varepsilon}\sqrt{\left(\frac{\partial u_i}{\partial x_j}+\frac{\partial u_j}{\partial x_i}\right)}$$

Here, $C_{\varepsilon2}$, α_k, and α_ε are constants, and G_k is the generation of turbulent kinetic energy due to the average velocity gradient.

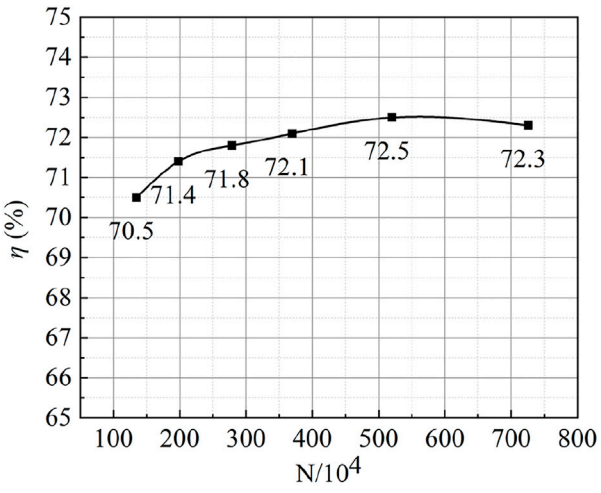

FIGURE 3
Efficiency of axial-flow pump system with different numbers of grid elements.

2.2 Geometry and grid

We numerically studied the flow physics in a slanted axial-flow pump prototype in a pumping station. Figure 1 shows a three-dimensional (3D) model of the slanted axial-flow pump, which consisted of an inlet channel section, an impeller section, a guide vane section, and an outlet channel section. The basic parameters of the prototype pump are the impeller diameter D = 3,250 mm, rotation speed n = 122 r/min, and designed flow rate Q_0 = 45.5 m^3/s.

All the simulations were performed using the commercial software ANSYS Fluent 18.0. ICEM was used to generate the unstructured grid (Chen et al., 2016; 2021) to match the axial-flow pump. The schematic diagram of the grid is presented in Figure 2.

To ensure the reliability of the numerical simulation, six sets of grids from coarse to fine were selected and relevant data are shown in Figure 3. Once the number of the grid elements reached a certain order of magnitude (i.e., N > 2 million), there would be no significant influence on the numerical simulation result of the efficiency. The number of grid points used in the simulation was 2.9 million. The numbers of grid elements of the inlet channel, outlet channel, guide vane section, and impeller section were determined to be 0.68, 0.75, 0.7, and 0.8 million, respectively.

2.3 Computational set-up

A mass flow inlet was applied to the inlet of the domain, and the outlet boundary condition was set to zero pressure. No-slip boundary conditions were applied at the channel walls. A standard wall

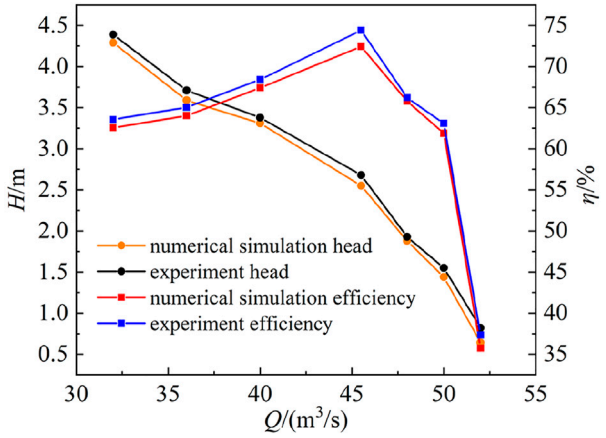

FIGURE 4
Comparison of the head and efficiency of the slanted axial-flow pump.

function was selected to model the turbulent boundary layers. The interface was used to transfer information between each computing area. To guarantee reliability and accuracy, the convergence residual was set to 10^{-5} (Kan et al., 2022).

2.4 Equivalent sand grain model

The roughness constant *Cs* and equivalent sand height Ks can be achieved in Fluent. The roughness constant *Cs* had little effect on the hydraulic performance of the pump with a high specific speed. The specific speed of the axial-flow pump in this work was very high, with a value of 1,450. Therefore, we neglected the roughness constant *Cs* in the numerical simulations and focused on the influence of the equivalent sand height *Ks* on the hydraulic performance of the axial-flow pump device. In engineering, the roughness *Ra* describes the surface roughness of the material during processing. The equivalent sand particle height *Ks* is based on an arranged row of uniform small balls. The formula relating the equivalent sand height *Ks* and the surface roughness *Ra* is as follows (Feng et al., 2016):

$$Ks = 11.0293Ra \tag{6}$$

The effect of roughness on the flow pattern inside the pump unit was incorporated *via* a wall function, where a term ΔB was added. Different roughness values would produce different ΔB values, which would affect the flow near the wall. The wall function considering the wall roughness is shown as follows:

$$u^{+} = \frac{1}{\kappa} In(Ey^{+}) - \Delta B \tag{7}$$

where u^{+} *is* the dimensionless velocity, κ and E are empirical constants, which were 0.4187 and 9.793, respectively, and $y+$ is the dimensionless wall normal distance.

3 Results and analysis

3.1 Model test and validation

To verify the reliability of the numerical simulation model, experiments were performed under the same operating conditions. As shown in Figure 4, the head and efficiency of the simulation results were in great agreement with those of the experiment. The maximum relative errors of the head and efficiency between the simulation and the experimental result were 4.4% and 4.1%, respectively. The error between them may have been related to the high experimental error, due to the smooth wall adopted in the simulation. Overall, the comparison proved that the numerical simulation method utilized in this work could accurately predict the external characteristics of the slanted axial-flow pump and the simulation results were reliable.

3.2 Hydraulic performance of flow components with different *Ra* values

In this work, we set three roughness *Ra* values for different flow components of the axial-flow pump (channel, guide vane, and impeller). Figure 5 shows the variation in the head and efficiency of the slanted axial-flow pump devices with different roughness values and flow rates. For example, for *Ra* = 100 μm (Figure 5B), compared with the pump device with smooth walls, when $Q = 0.7Q_0$, the efficiencies of the devices with different rough sections (channel, guide vane, and impeller) decreased by 0.86%, 1.44%, and 1.98%, respectively, and the corresponding heads decreased by 0.04, 0.05, and 0.08 m. Under the designed condition, the efficiencies of the device with different rough sections decreased by 0.52%, 0.89%, and 1.31%, and the corresponding heads decreased by 0.15, 0.17, and 0.2 m respectively. When the flow rate increased, the efficiencies and heads of the devices further decreased. Under different flow conditions, the addition of roughness to the wall of the impeller chamber caused the largest reduction of the efficiencies and heads, followed by the guide vane chamber, and the inlet and outlet channel had the least impact.

The hydraulic losses of the slanted axial-flow pump devices with different roughness values of the flow components are plotted in Figure 6. Under the small-flow-rate condition (Q = 32 m^3/s), the hydraulic losses of the pump devices with *Ra* = 100 μm at the inlet and outlet channel walls, guide vane chamber wall, and impeller chamber wall were 0.29, 0.42, and 0.71 m, respectively. Under the designed flow condition (Q = 45.5 m^3/s), the hydraulic losses of the three pump devices with roughness

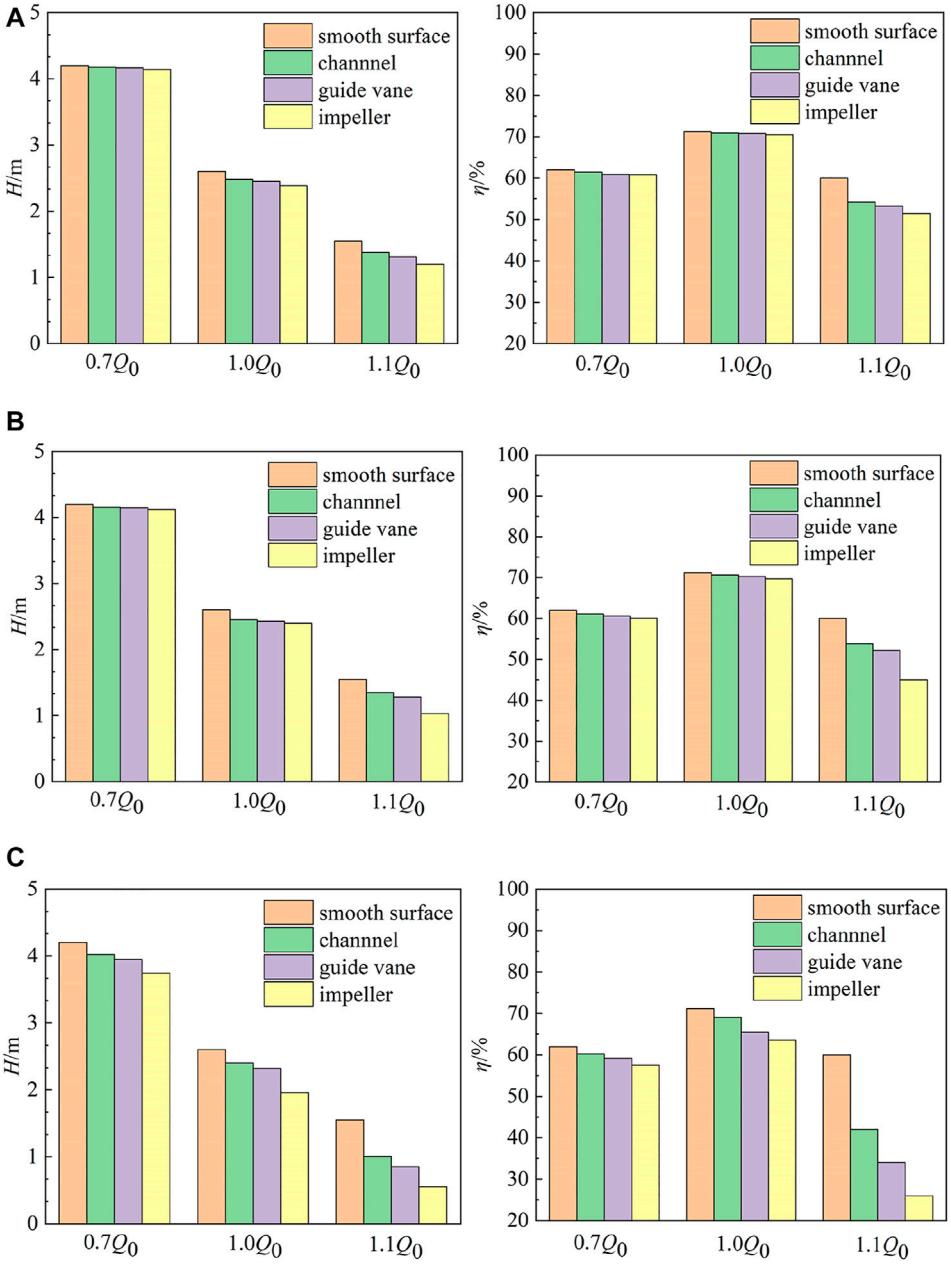

FIGURE 5
Variations in the heads and efficiencies of axial-flow pump devices: **(A)** *Ra* = 10 μm, **(B)** *Ra* = 100 μm, and **(C)** *Ra* = 1,000 μm.

values set for different flow components were 0.15, 0.3, and 0.62 m, respectively. Under the condition of a large flow rate (Q = 50 m^3/s), the hydraulic losses of the three changed to 0.38, 0.62, and 1 m, respectively. Under the large-flow-rate condition, the hydraulic loss increased faster by adding roughness to the impeller chamber wall. The influence of the impeller chamber wall roughness on the hydraulic loss of the pump device was the largest.

For the convenience of discussion, the slanted axial-flow pump device with inlet and outlet flow channel roughness is named the CR pump, the slanted axial-flow pump device with guide vane chamber roughness is named the GVR pump, and the slanted axial-flow pump with impeller chamber roughness is named the IR pump. Figure 7 shows the 3D streamlines in the outlet channel of the axial-flow pump devices with different roughness values of the flow components. The roughness was

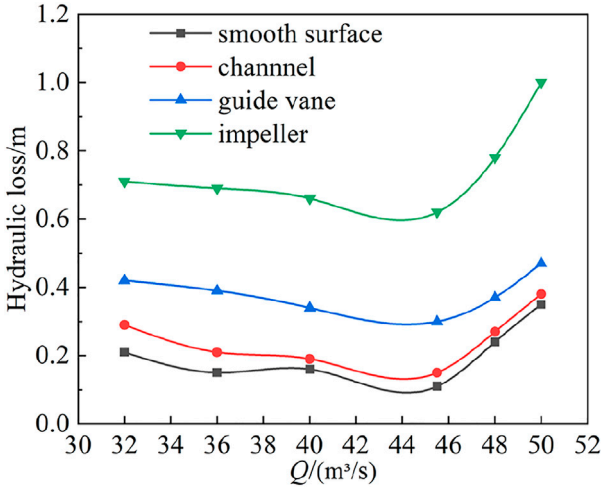

FIGURE 6
Hydraulic losses of different flow components with wall roughness.

specified as Ra = 100 μm. Under the condition of a small flow rate, the streamlines of the GVR, and CR pump devices were relatively smooth, and the flow was deflected from the left side. Partial reflux occurred in the right flow channel of the IR pump. Under the specified flow rate, the streamlines of the IR pump were smooth, and the flow pattern was relatively good. Under the condition of a large flow rate, the streamlines in the outlet channel were disordered, and a significant reflux phenomenon occurred in the right outlet channel, which affected the performance of the IR pump device. Compared with the IR pump device, the flow patterns of the GVR, and CR pump devices were better. The 3D streamlines of the outlet channel showed that the wall roughness had a greater impact on the flow pattern of the IR pump than those of the GVR and CR pumps.

Under the condition of a large flow rate, the hydraulic performances of the pumps were significantly different, so this condition was selected to analyze the difference after adding roughness to the flow components. Figure 8 shows the distributions of the pressure, vorticity, and turbulent kinetic energy (TKE) near the tip region (R^* = 0.95). There were no significant differences in the pressure and vorticity, and the differences between the pump devices with rough flow components were reflected in the TKE distribution. The TKE of the IR pump naturally increased significantly due to the roughness being set directly in the runner chamber. In addition, the pressure on the suction surface of the IR pump increased, and the negative pressure decreased. The vorticity also increased compared to those of

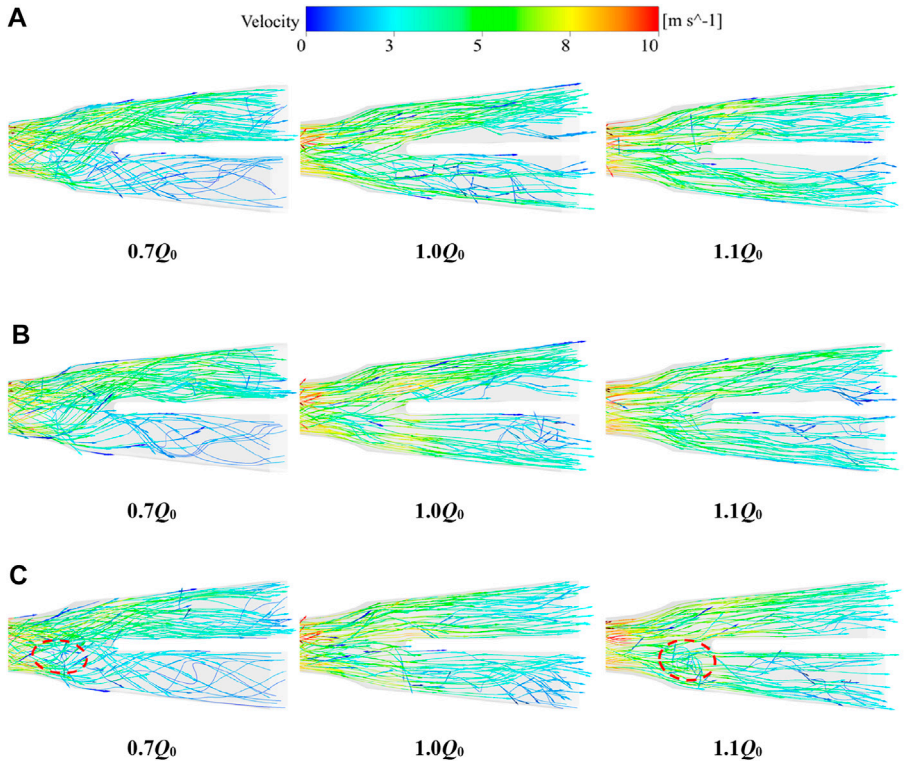

FIGURE 7
Three-dimensional Streamlines in the outlet channel: **(A)** IR pump, **(B)** GVR pump, and **(C)** CR pump.

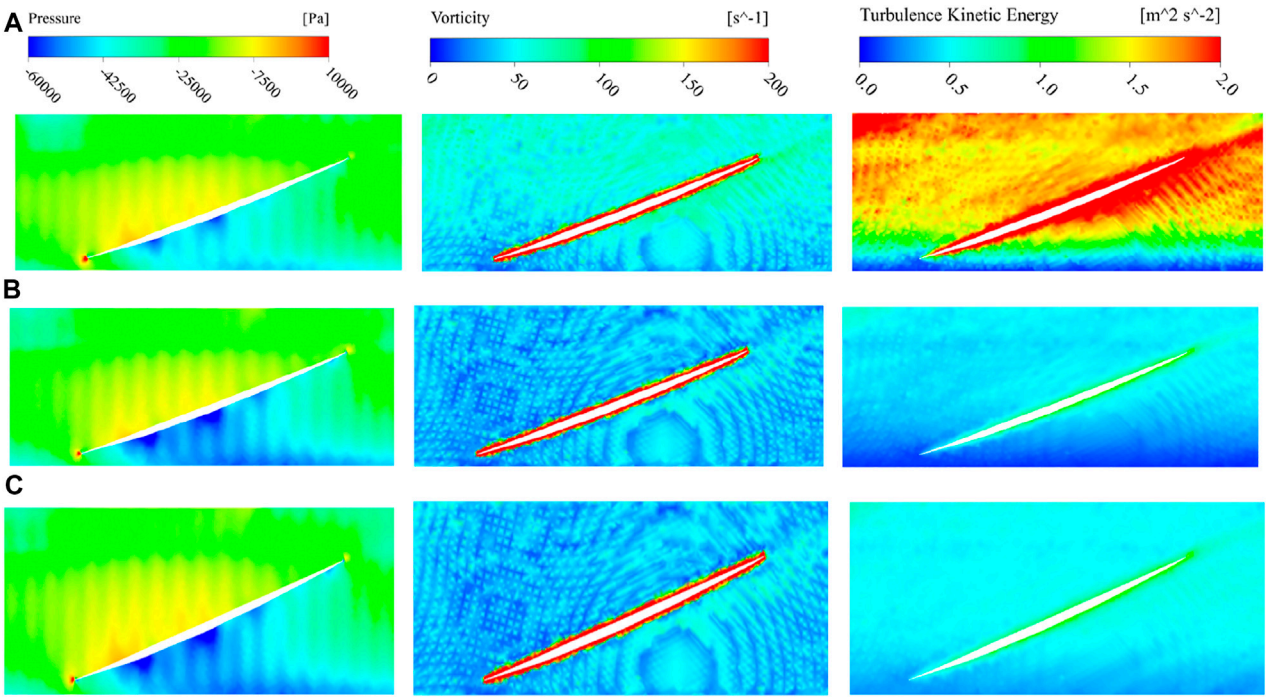

FIGURE 8
Distributions of pressure, vorticity, and turbulent kinetic energy (TKE) near the tip region (R^* = 0.95): **(A)** IR pump, **(B)** GVR pump, and **(C)** CR pump.

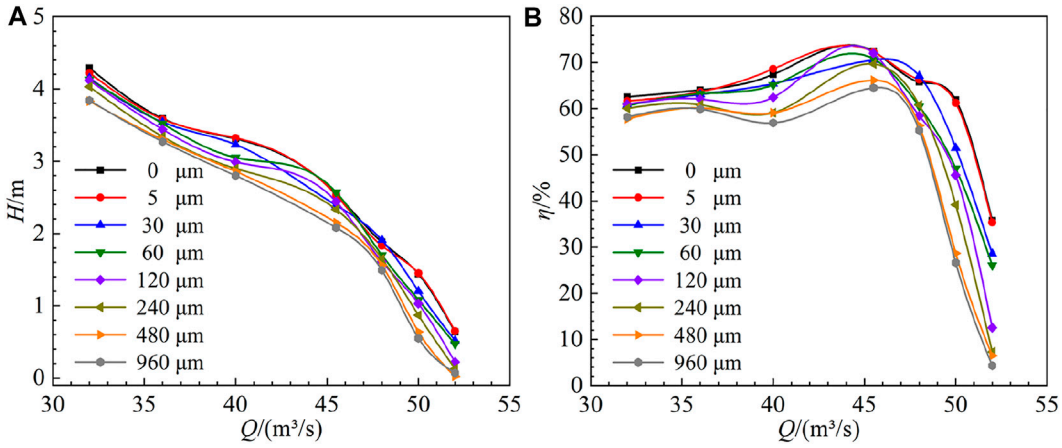

FIGURE 9
Head and efficiency of IR pumps with different roughness values: **(A)** H versus Q and **(B)** η versus Q.

the other two pump devices. The TKE of the CR pump was larger than that of the GVR pump at the runner inlet because the TKE increased after the roughness of the inlet flow channel was set. The GVR pump only had increased roughness in the guide vane chamber, which hardly affected the TKE of the runner inlet.

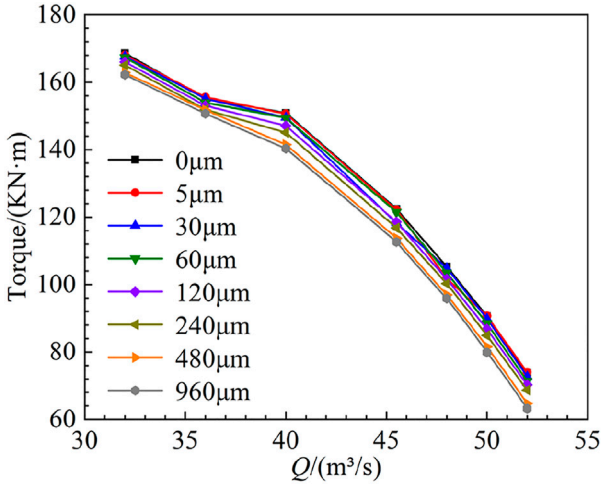

FIGURE 10
Impeller torque of IR pumps with different *Ra* values.

3.3 Analysis of IR pump performance with different *Ra* values

Figure 9 shows the external characteristic curves of IR pumps with different *Ra* values. From Figure 9A, it can be seen that the smaller the roughness the IR pumps had, the closer the head values were to those calculated by the smooth wall condition. At the same time, the head curves showed a gradual downward trend with the increase in the flow rate. Under the same flow rate condition, the head gradually decreased with the increase in the roughness. It is worth noting that under the condition with a large flow rate (Q = 52 m^3/s) when the roughness of the IR pump increased from 0 to 960 μm, the pump device changed from pump conditions to turbine conditions. When *Ra* was in the range of (0 μm, 60 μm), the increase in the roughness had little effect on the head of the device. When *Ra* was in the range of (60 μm, 960 μm), the effect of the roughness on the head of the device was significant. This indicated that the head of an inclined axial-flow pump device is greatly affected by roughness when it is running under the large-flow-rate condition.

From Figure 9B, it can be seen that the efficiencies of the IR pumps with smaller roughness values were closer to those with smooth wall conditions. With the increase in the flow rate, the efficiency of the device increased gently first and then decreased rapidly after the optimal operating point. The flow rate of the optimal operating point was Q = 45.5 m^3/s. When the flow rate was fixed, the device efficiency decreased significantly with the increase in the roughness. With the increase in the roughness, the friction loss caused by the fluid flowing through the wall boundary layer increased, which was significant under the condition with a large flow rate. When the roughness increased from 0 to 960 μm, the pump device changed from pump conditions to turbine conditions. Under the condition of a small flow rate, the influence of the wall roughness on the device efficiency was relatively small, followed by the designed flow rate condition, and the largest influence was under the large-flow-rate condition.

Figure 10 shows the impeller torques of the IR pumps with different *Ra* values. Under the condition of a small flow rate, the impeller torques were 1,68,054.09, 1,67,631.29, 1,67,379.05, 1,66,039.27, 1,65,088.09, 1,62,854.3, and 1,62,253.33 Nm for *Ra* = 5, 30, 60, 120, 240, 480, and 960 μm. Compared to the pump with a smooth wall, the impeller torques of the IR pumps decreased by 0.31%, 0.56%, 0.71%, 1.5%, 2.7%, 3.4%, and 3.8%, respectively. Under the designed flow condition, when *Ra* = 5, 30, 60, 120, 240, 480, and 960 μm, the impeller torque was 1,22,183, 1,18,244, 1,21,493, 1,18,553, 1,16,786, 1,13,763, and 1,12,622 Nm, respectively. Compared with the pump with smooth walls, impeller torques of the IR pumps decreased by 0.19%, 3.4%, 0.75%, 3.16%, 4.6%, 7.6%, and 8%, respectively. The impeller torques were 73,989, 72,688, 71,367, 70,293, 68,682, 64,728, and 63,232 N when *Ra* = 5, 30, 60, 120, 240, 480, and 960 μm at a large flow rate.

The outlet flow field of the guide vane can be evaluated by the axial velocity distribution uniformity coefficient ω and velocity-weighted average drift angle of water flow θ. The closer ω is to 100%, a smaller θ represents a better flow pattern of the outlet flow field, and the hydraulic loss is relatively small. The formulas for ω and θ are as follows (Zhu et al., 2007; Yang et al., 2012):

$$\omega = \left[1 - \frac{1}{V_a}\sqrt{\sum_{i=1}^{n}[(V_{ai} - V_a)]}\right] \times 100\% \quad (8)$$

$$\theta = \sum_{i=1}^{n} V_{ai}\left\{90° - \mathrm{tg}^{-1}\frac{V_{ti}}{V_{ai}}\right\} \Big/ \sum_{i=1}^{n} V_{ai} \quad (9)$$

where V_a is the arithmetic mean value of the axial velocity at the section of the guide vane outlet, V_{ai} is the axial velocity of each calculation unit of the section, V_{ti} is the transverse velocity of each calculation unit of the section, and n is the number of calculation units on the section. In this work, n was equal to 200.

Figure 11 shows the influence of the roughness on ω and θ under different flow rate conditions. From Figure 11A, we see that the axial velocity distribution uniformity coefficient ω was the highest at the optimal condition point. With the increase in the roughness from 0 to 960 μm, the axial velocity uniformity decreased from 81.2% to 75.5%. Under the small-flow-rate condition, the axial distribution uniformity coefficient curve trend was similar to that of the designed flow condition, and the overall downward migration was about 3 percentage points. Under the condition of a high flow rate, the uniformity of the axial velocity distribution was the lowest. As the roughness increased from 0 to 960 μm, the uniformity of axial velocity distribution decreased from 72% to 56.5%. Under the pump conditions, the increase in the wall roughness led to a decrease in the axial velocity distribution uniformity, especially when the flow rate was large. From Figure 11B, it can be seen that at the optimal condition point, the velocity weighted average flow angle was the smallest. With the increase in the roughness from

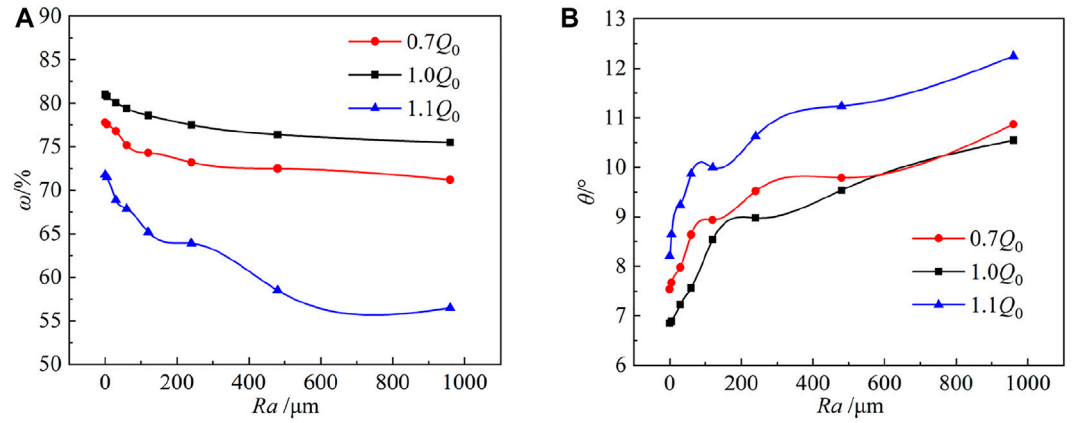

FIGURE 11
Effect of roughness on ω and θ under different flow rate conditions: **(A)** ω versus *Ra* and **(B)** θ versus *Ra*.

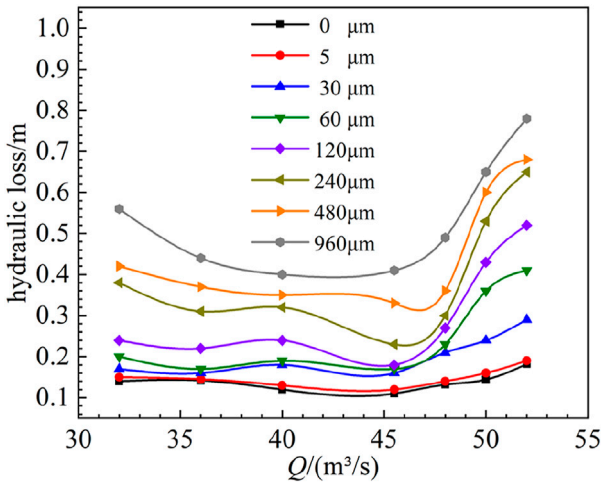

FIGURE 12
Effect of roughness on the hydraulic loss.

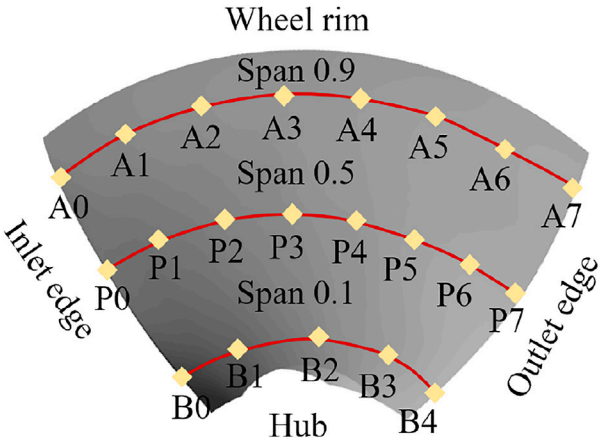

FIGURE 13
Monitoring point layout in blade working face.

0 to 960 μm, the velocity-weighted average drift angle increased from 6.85° to 10.55°. Under the condition of a small flow rate ($Q = 0.7Q_0$), the velocity-weighted average drift angle curve was similar to that under the designed condition, with an overall increase of 1°–2°. Under the condition of a large flow rate ($Q = 1.1Q_0$), the velocity-weighted average drift angle was the largest. With the increase in the roughness from 0 to 960 μm, the velocity-weighted average drift angle increased from 8.21° to 12.55°. We can infer that the increase in the wall roughness leads to increases in the velocity weighted average deviation angle and the axial velocity distribution uniformity coefficient, and the increases are more significant under the large-flow-rate condition.

Figure 12 shows the effect of roughness on the hydraulic losses of the IR pumps under different flow rate conditions. With the increase in the roughness, the hydraulic loss increased. The hydraulic loss of the IR pump with *Ra* = 5 μm was close to that with smooth walls. With the increase in the roughness, the hydraulic loss increased. When *Ra* = 960 μm, the hydraulic loss was the largest under all flow rate conditions relative to that of the smooth wall condition. Under the condition with a small flow rate, the hydraulic loss was 0.58 m. Under the designed flow conditions, the hydraulic loss was 0.42 m. Under the condition with a large flow rate, the hydraulic loss was 0.78 m. Regardless of what the roughness was, the loss of the designed flow condition was the smallest compared with the other groups. When the flow rate was large, the increase in

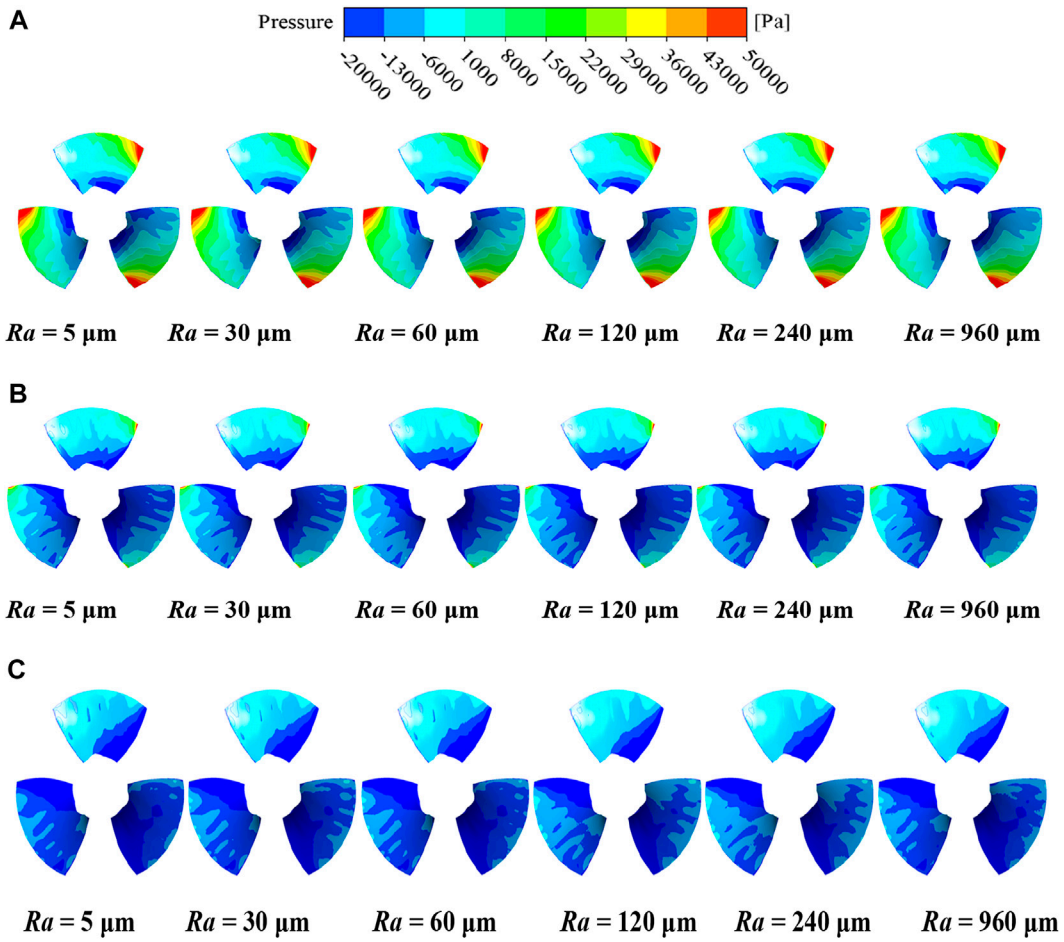

FIGURE 14
Static pressure distribution of blade working face: **(A)** $0.7Q_0$, **(B)** $1.0Q_0$, and **(C)** $1.1Q_0$.

hydraulic loss was slower in the *Ra* range of (5 μm, 60 μm) and faster in the *Ra* range of (60 μm, 960 μm).

To study the effect of wall roughness on the internal flow field, a total of 21 monitoring points were arranged on the surface of the blade, as shown in Figure 13. A0–A7 were arranged on span 0.9 near the outer edge of the blade, P0–P7 were arranged on span 0.5 along the flow direction center of the impeller, and B0–B4 were arranged on span 0.1 near the root of the blade.

Figure 14 shows the static pressure distributions of the blade pressure surface under three different flow rate conditions. The static pressure value of the blade surface layer was large, and the static pressure value of the blade root near the hub was small. Under the condition of a small flow rate, the static pressure value increased gradually along the flow direction, and the pressure value near the outlet of the blade near the rim reached the highest value. Under the designed flow condition and the large-flow-rate condition, the radial static pressure value increased hierarchically along the pressure surface. There was a negative pressure near the hub because the fluid flowed through the runner blade from the inlet channel, and only a small part of the separated fluid passed through the impeller near the hub. The energy obtained by the impeller near the hub was lower, so there was a local negative pressure on the surface of the blade near the hub, which greatly increased the possibility of cavitation.

Under the same flow rate condition, with the increase in the roughness, the range of the negative pressure zone increased significantly. When the IR pumps had the same roughness, with the increase in the flow rate, the static pressure value of the pressure surface decreased. Under the condition of a small flow rate, the static pressure value of the pressure surface was larger than that of the designed flow rate and the large flow rate. This was because, under the condition of a small flow rate, the flow velocity near the pressure surface of the blade was larger, and the flow pattern disorder near the blade caused an increase in energy loss. The increase in the roughness may account for the cavitation. Near the pressure surface of the impeller outlet,

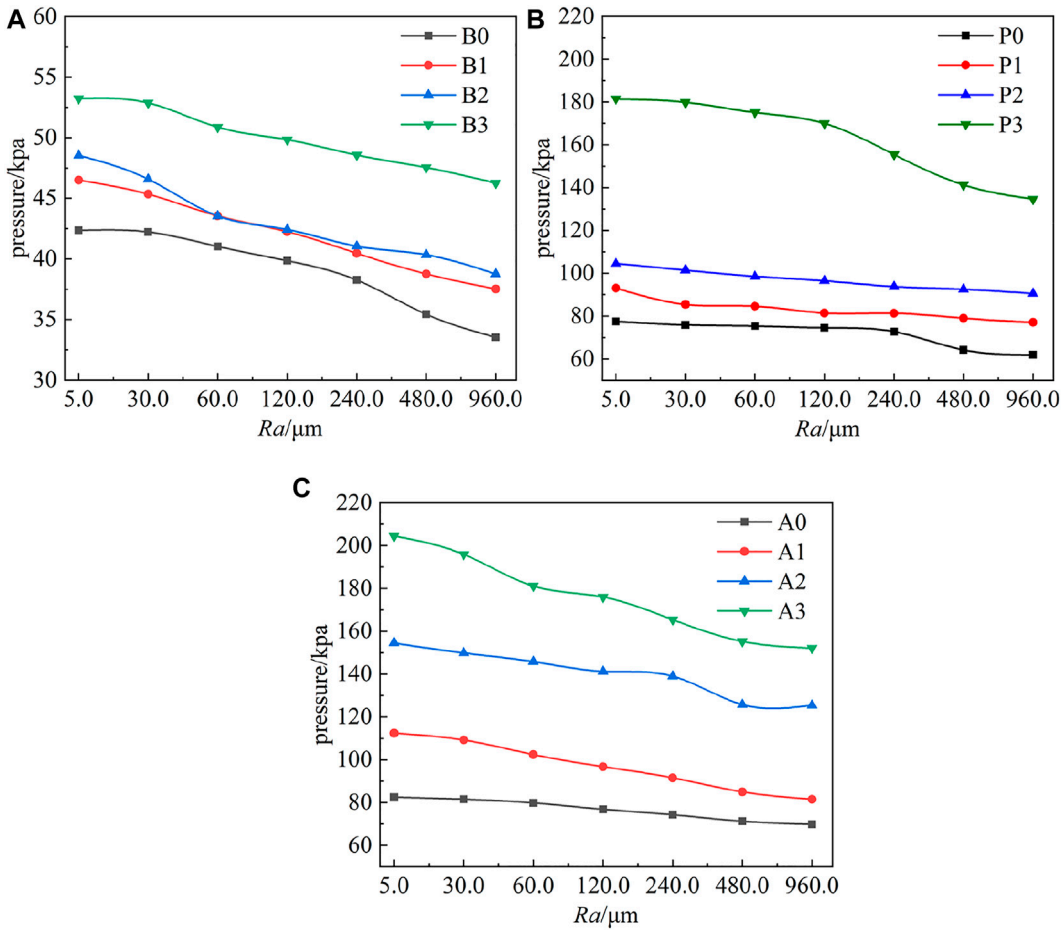

FIGURE 15
Static pressure variations with roughness at different monitoring point: **(A)** span 0.1, **(B)** span 0.5, and **(C)** span 0.9.

under the same pressure level, the range of the high-pressure zone was the largest under the condition of a small flow rate, followed by the designed flow rate high, while the pressure zone was not evident under the large-flow-rate condition. This also verified that the *H* versus *Q* curve (Figure 9A) decreased with the increase in the flow rate.

Figure 15 shows the variations in the histogram of the monitoring points on the blade working surface with the roughness in the designed flow rate condition. With the increase in the wall roughness, the energy loss near the boundary layer increased, resulting in a decrease in the static pressure value at the monitoring point. Figure 15A indicates that the static pressure values at span 0.1 near the blade root were generally smaller than those at span 0.5 and span 0.9. When *Ra* = 960 μm, the static pressure values of points B0–B4 ranged from 33,544 to 46,254 Pa. Compared with their static pressure values at *Ra* = 5 μm, they decreased by 20.8%, 19%, 20.16%, and 13%. Figure 15B shows that the static pressure value of the monitoring point P0 in the smooth wall condition was 75,887 Pa, and the static pressure value of the impeller pressure surface under the wall with different *Ra* values was lower than that under the smooth wall condition. Thus, at the P0 monitoring point, when the roughness was greater than 240 μm, the roughness had a significant influence on the wall static pressure value. The variation trend of the static pressure value of the pressure surface at monitoring points P2 and P5 with the roughness was similar to that at P0. At monitoring point P7, the static pressure value of the pressure surface in the smooth wall condition was 1,81,423 Pa. With the increase in the roughness, the static pressure value of the pressure surface under each roughness condition decreased by 0.08%, 0.12%, 3.5%, 7%, 13.4%, 20.2%, and 30.1%, respectively. We infer that when the roughness was less than 30 μm, the roughness had little effect on the static pressure value of monitoring point P7, which was set at the impeller outlet. It can be seen from Figure 15C that the static pressure value of span 0.9 near the blade's outer edge was larger than that of span 0.5 overall, and the static pressure value decreased with the increase in the roughness. When *Ra* =

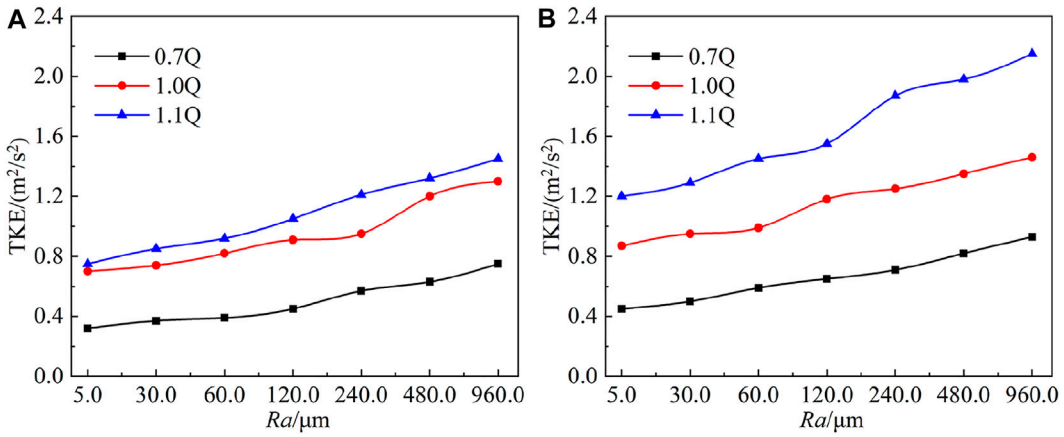

FIGURE 16
Variations of turbulent kinetic energy with different *Ra* values: **(A)** pressure surface and **(B)** suction surface.

960 μm, the static pressure values of A0, A2, A5, and A7 were 69,875, 81,544, 1,25,424, and 1,52,125 Pa, respectively. Compared with those at *Ra* = 5 μm, the static pressure values decreased by 15.3%, 27.4%, 18.8%, and 25.6%, respectively. When *Ra* was in the range of (5 μm, 120 μm), the decrease in the static pressure of the blade was larger. When *Ra* was in the range of (120 μm, 960 μm), the decrease in the static pressure of the blade was smaller.

The influence of the roughness on the TKE of the blade pressure surface and the suction surface under the three flow rate conditions is shown in Figure 16. The turbulent kinetic energy increased with the increase in the roughness, which indicated that the energy loss near the boundary layer increased, and it is also an important reason for the decrease in the pump efficiency. Figure 16A shows that with different *Ra* values, the turbulent kinetic energy of the pressure surface was about 0.46 m^2/s^2. The turbulent kinetic energy on the pressure surface was about 48% smaller than that under the designed flow condition, and it was about 52.8% smaller than that under the large-flow-rate condition. With the same roughness, the turbulent kinetic energy of the pressure surface was the largest under the large-flow-rate condition, followed by the designed flow condition, and the turbulent kinetic energy of the pressure surface was the smallest under the small-flow-rate condition.

It can be seen from Figure 16B that when *Ra* was in the range of (5 μm, 60 μm), the corresponding turbulent kinetic energy ranged from 0.45 to 0.59 m^2/s^2, with values that were 48.2%, 47.3%, and 40.4% smaller than that under the designed flow condition, and 2.5%, 61.2%, and 59.3% smaller than that under the large-flow-rate condition. When *Ra* was in the range of (120 μm, 960 μm), the turbulent kinetic energy ranged from 0.65 to 0.93 m^2/s^2 at a small flow rate, which was about 40.9% lower than that of the designed flow rate and about 58.8% lower than that at the large flow rate. Under different flow rate conditions, with the increase in the roughness, the turbulent kinetic energy of the pressure surface increased gradually.

The comparison of the turbulent kinetic energy of the pressure surface in Figure 16A and the suction surface in Figure 16B showed that when the flow rate was small, the turbulent kinetic energy of the blade suction surface was generally greater than that of the blade pressure surface. Due to the small-flow-rate condition, the impeller inlet water had adverse flow patterns, such as vortices and backflow, which caused high turbulent kinetic energy to be created at the blade suction surface. Under the designed flow condition, when the wall roughness values were 5, 30, 60, 120, 240, 480, and 960 μm, the corresponding turbulent kinetic energies on the pressure surface were 0.7, 0.74, 0.82, 0.91, 0.95, 1.2, and 1.3 m^2/s^2, respectively. The turbulent kinetic energy of the suction surface ranged from 0.87 to 1.46 m^2/s^2. The turbulent kinetic energy of the suction surface was higher than that of the pressure surface by 24.2%, 28.4%, 15.9%, 29.7%, 31.5%, 11.1%, and 12.3% respectively. When the flow rate increased to 1.1Q, the corresponding turbulent kinetic energies on the pressure surface were 0.75, 0.85, 0.92, 1.05, 1.21, 1.32, and 1.45 m^2/s^2, respectively.

4 Conclusion

In this study, simulations were performed, and the performance of the slanted axial-flow pump under the effects of wall roughness and flow rates was analyzed. The specific conclusions are as follows:

1) Model tests of slanted axial-flow pump devices were carried out, and the consistency between the model test results and

the numerical simulation results showed that the numerical method used in this article was credible.

2) The influence of the roughness of the different flow components on the hydraulic performance of the pump devices under different flow rate conditions was studied. From the perspective of external characteristics, the device efficiency and head of the IR pump devices were the lowest, and the hydraulic loss was the highest. From the perspective of the internal flow characteristics, the roughness of the impeller chamber wall had a slight influence on the flow pattern of the device, and backflow and vortices appeared in the device under the large-flow-rate condition. The roughness of the impeller chamber wall had the greatest impact on the hydraulic performance of the pump device, followed by the roughness of the guide vane chamber, and the roughness of the inlet and outlet flow channel had the smallest impact.
3) The influence of different roughness values on the hydraulic performance of the IR pump device was studied. The optimal working condition of the pump was obtained, which was a flow rate of 45.5 m^3/s. The flow-head curve of the pump device showed a downward trend with the increase in the flow rate. The flow efficiency characteristic curve showed a trend of first increasing and then decreasing. Under the condition of a large flow rate, the curve dropped faster. Under the same flow rate condition, the increase in the roughness caused a decrease in the head, efficiency, torque, and surface static pressure of the blade pressure surface. When *Ra* was in the range of (0 μm, 60 μm), the roughness had little effect on the performance parameters. While a roughness *Ra* beyond 60 μm had a significant effect on the performance parameters. With the increase in the roughness, the hydraulic loss and turbulent kinetic energy of the device increased since the energy loss on the boundary layer in the device increased, which was more significant under the large-flow-rate condition. With the increase in the roughness, the uniformity of the axial-flow velocity distribution coefficient decreased, and the velocity-weighted average bias angle increased, which was responsible for the decrease in the device performance.

Data availability statement

The raw data supporting the conclusion of this article will be made available by the authors, without undue reservation.

Author contributions

Conceptualization: YC and HC; methodology: ZL, YG, and JZ; software: QS, ZL, and JZ; validation: YC and HC; formal analysis: YC, QS, ZL, and HC; resources: YC and HC; writing and original draft preparation, YC, QS, ZL, YG, and JZ; writing-review and editing: YC and HC; funding acquisition: HC.

Funding

This research was funded by the National Natural Science Foundation of China (52006053), Natural Science Foundation of Jiangsu Province (BK20200508), China Postdoctoral Science Foundation (2021M690876), and Postdoctoral Research Fund of Jiangsu Province (2021K498C). The computational work was supported by the High Performance Computing Platform, Hohai University. The support of Hohai University, China, is also gratefully acknowledged.

Conflict of interest

The authors declare that the research was conducted in the absence of any commercial or financial relationships that could be construed as a potential conflict of interest.

Publisher's note

All claims expressed in this article are solely those of the authors and do not necessarily represent those of their affiliated organizations, or those of the publisher, the editors, and the reviewers. Any product that may be evaluated in this article, or claim that may be made by its manufacturer, is not guaranteed or endorsed by the publisher.

References

Chen, E. Y., Ma, Z. L., Zhao, G. P., Li, G. P., Yang, A. L., Nan, G. F., et al. (2016). Numerical investigation on vibration and noise induced by unsteady flow in an axial-flow pump. *J. Mech. Sci. Technol.* 30 (12), 5397–5404. doi:10.1007/s12206-016-1107-4

Chen, H., Zhou, D., Kan, K., Guo, J., Zheng, Y., Binama, M., et al. (2021). Transient characteristics during the co-closing guide vanes and runner blades of a bulb turbine in load rejection process. *Renew. Energy* 165, 28–41. doi:10.1016/j.renene.2020.11.064

Deng, L., Yong, K., Wang, X., Ding, X., and Fang, Z. (2016). Effects of nozzle inner surface roughness on the cavitation erosion characteristics of high speed submerged jets. *Exp. Therm. Fluid Sci.* 74, 444–452. doi:10.1016/j.expthermflusci.2016.01.009

Echouchene, F., Belmabrouk, H., Penven, L. L., and Buffat, M. (2011). Numerical simulation of wall roughness effects in cavitating flow. *Int. J. Heat Fluid Flow* 32 (5), 1068–1075. doi:10.1016/j.ijheatfluidflow.2011.05.010

Fei, Z., Xu, H., Zhang, R., Zheng, Y., Mu, T., Chen, Y., et al. (2022a). Numerical simulation on hydraulic performance and tip leakage vortex of a slanted axial-flow pump with different blade angles. *Proc. Institution Mech. Eng. Part C J. Mech. Eng. Sci.* 236 (6), 2775–2790. doi:10.1177/09544062211032989

Fei, Z., Zhang, R., Xu, H., Feng, J., Mu, T., Chen, Y., et al. (2022b). Energy performance and flow characteristics of a slanted axial-flow pump under cavitation conditions. *Phys. Fluids* 34 (3), 035121. doi:10.1063/5.0085388

Feng, J., Zhu, G., He, R., Luo, X., and Lu, J. (2016). Influence of wall roughness on performance of axial-flow pumps. *J. Northwest A F Univ. Nat. Sci. Ed.* 44 (3), 196–202. doi:10.13207/j.cnki.jnwafu.2016.03.027

Hu, W., Tong, D., Li, Z., Wang, R., and Yang, F. (2021). Numerical analysis of internal flow in a slanted axial-flow pump. *J. Irrigation Drainage* 40 (11), 66–72. doi:10.13522/j.cnki.ggps.2021247

Kan, K., Chen, H., Zheng, Y., Zhou, D., Binama, M., Dai, J., et al. (2021a). Transient characteristics during power-off process in a shaft extension tubular pump by using a suitable numerical model. *Renew. Energy* 164, 109–121. doi:10.1016/j.renene.2020.09.001

Kan, K., Zhang, Q., Xu, Z., Chen, H., Zheng, Y., Zhou, D., et al. (2021b). Study on a horizontal axial-flow pump during runaway process with bidirectional operating conditions. *Sci. Rep.* 11 (1), 21834. doi:10.1038/s41598-021-01250-1

Kan, K., Zhang, Q., Xu, Z., Zheng, Y., Gao, Q., Shen, L., et al. (2022). Energy loss mechanism due to tip leakage flow of axial flow pump as turbine under various operating conditions. *Energy* 255, 124532. doi:10.1016/j.energy.2022.124532

Kang, Y. S., Yoo, J. C., and Kang, S. H. (2006). Numerical predictions of roughness effects on the performance degradation of an axial-turbine stage. *J. Mech. Sci. Technol.* 20 (7), 1077–1088. doi:10.1007/bf02916007

Long, L., and Wang, Z. (2004). Simulation of the influence of wall roughness on the performance of axial-flow pumps. *Trans. Chin. Soc. Agric. Eng.* 1, 132–135. doi:10.1300/J064v24n01_09

Marzabadi, F. R., and Soltani, M. R. (2013). Effect of leading-edge roughness on boundary layer transition of an oscillating airfoil. *Sci. Iran.* 20 (3), 508–515. doi:10.1016/j.scient.2012.12.035

Pang, A., Skote, M., and Lim, S. Y. (2016). Modelling high Re flow around a 2D cylindrical bluff body using the k-ω (SST) turbulence model. *Prog. Comput. Fluid Dyn. Int. J.* 16 (1), 48. doi:10.1504/pcfd.2016.074225

Qin, D., Huang, Q., Pan, G., Han, P., Luo, Y., Dong, X., et al. (2021). Numerical simulation of vortex instabilities in the wake of a preswirl pumpjet propulsor. *Phys. Fluids* 33 (5), 055119. doi:10.1063/5.0039935

Ren, N. X., and Ou, J. P. (2009). Dust effect on the performance of wind turbine airfoils. *J. Electromagn. Analysis Appl.* 1 (2), 102–107. doi:10.4236/jemaa.2009.12016

Shi, L., Zhang, W., Jiao, H., Tang, F., Wang, L., Sun, D., et al. (2020). Numerical simulation and experimental study on the comparison of the hydraulic characteristics of an axial-flow pump and a full tubular pump. *Renew. Energy* 153, 1455–1464. doi:10.1016/j.renene.2020.02.082

Soltani, M. R., and Birjandi, A. H. (2013). Effect of surface contamination on the performance of a section of a wind turbine blade. Paper presented at the Aiaa Aerospace Sciences Meeting & Exhibit.

Tao, B., Liu, J., Zhang, W., and Zou, Z. (2014). Effect of surface roughness on the aerodynamic performance of turbine blade cascade. *Propuls. Power Res.* 3 (2), 82–89. doi:10.1016/j.jppr.2014.05.001

Walker, J., Flack, K., Lust, E., Schultz, M., and Luznik, L. (2013). The effects of blade roughness and fouling on marine current turbine performance. Paper presented at the European Wave & Tidal Energy Conference.

Walker, J. M., Flack, K. A., Lust, E. E., Schultz, M. P., and Luznik, L. (2014). Experimental and numerical studies of blade roughness and fouling on marine current turbine performance. *Renew. Energy* 66, 257–267. doi:10.1016/j.renene.2013.12.012

Wang, Z. W., Peng, G. J., Zhou, L. J., and Hu, D. Y. (2010). Hydraulic performance of a large slanted axial-flow pump. *Eng. Comput. Swans.* 27 (1-2), 243–256. doi:10.1108/02644401011022391

Wang, C., Wang, F., Tang, Y., Zi, D., Xie, L., He, C., et al. (2020). Investigation into the phenomenon of flow deviation in the S-shaped discharge passage of a slanted axial-flow pumping system. *J. Fluids Eng.* 142 (4). doi:10.1115/1.4045438

Wang, W., Tai, G., Pei, J., Pavesi, G., and Yuan, S. (2022). Numerical investigation of the effect of the closure law of wicket gates on the transient characteristics of pump-turbine in pump mode. *Renew. Energy* 194, 719–733. doi:10.1016/j.renene.2022.05.129

Yang, F., Tang, F., and Liu, C. (2012). Numerical analysis on hydrodynamics of large-scale mixed-flow pump system. *J. Hydroelectr. Eng.* 31 (3), 217–222.

Zhu, H. G., Yan, B. P., and Zhou, J. R. (2006). Study on the influence of wall roughness on the hydraulic performance of axial-flow pumps. *J. Irrigation Drainage* 1, 81–88. doi:10.13522/j.cnki.ggps.2006.01.020

Zhu, H., Yuan, S., Liu, H., and Shi, W. (2007). Numerical simulation of the 3-D flow of a volute-type discharge passage in large pumping stations. *Trans. Chin. Soc. Agric. Mach.* 10, 49–53. doi:10.3969/j.issn.1000-1298.2007.10.012

frontiers | Frontiers in Energy Research

TYPE Original Research
PUBLISHED 25 August 2022
DOI 10.3389/fenrg.2022.910834

OPEN ACCESS

EDITED BY
Muhammad Wakil Shahzad,
Northumbria University,
United Kingdom

REVIEWED BY
Muhammad Ahmad Jamil,
Northumbria University,
United Kingdom
Swarnendu Sen,
Jadavpur University, India

*CORRESPONDENCE
Yongguang Cheng,
ygcheng@whu.edu.cn

SPECIALTY SECTION
This article was submitted to Process and Energy Systems Engineering, a section of the journal Frontiers in Energy Research

RECEIVED 01 April 2022
ACCEPTED 25 July 2022
PUBLISHED 25 August 2022

CITATION
Hou X, Liu H, Cheng Y, Liu K, Liu D and Chen H (2022), Clearance flow patterns and pressure distribution of a pump-turbine: Measurement and simulation of a rotating disk flow.
Front. Energy Res. 10:910834.
doi: 10.3389/fenrg.2022.910834

Clearance flow patterns and pressure distribution of a pump-turbine: Measurement and simulation of a rotating disk flow

Xiaoxia Hou[1], Herui Liu[1], Yongguang Cheng[1]*, Ke Liu[1], Demin Liu[2] and Hongyu Chen[3]

[1]State Key Laboratory of Water Resources and Hydropower Engineering Science, Wuhan University, Wuhan, China, [2]Dongfang Electric Machinery Co., Ltd, Deyang, China, [3]CSG Power Generation Co., Ltd., Guangzhou, China

The clearance flow patterns and pressure distribution determine the clearance axial hydraulic thrust of a pump turbine, which has a substantial impact on the unit axial imbalance. However, due to the tiny size and complex shape of the clearance flow channel, there is no detailed description of the flow patterns and pressure characteristics. In this study, we conducted a model test with particle image velocimetry (PIV) measurements and CFD simulation of a rotating disk flow that was a simplified model of the pump-turbine clearance flow. It is shown that a typical Batchelor flow is formed in the clearance region, demonstrating a "core region + double-boundary layers" distribution for the circumferential velocity along the clearance height direction; the core region rotates at a speed of only around 41–42% of the rotating disk speed and is independent of the clearance inlet pressure and clearance height. Driven by centrifugal force, the flow is radially outward around the rotating disk, while inward around the stationary disk in the meridian section, showing secondary flow vortices. The pressure in the clearance region has a circumferentially symmetric and radially quadratic distribution. Based on the liquid differential equilibrium equation and core region circumferential velocity, the pressure and clearance axial hydraulic thrust in the clearance region can be expressed as a function of the clearance inlet pressure and the square of the runner rotating speed. These findings can be used to investigate axial force imbalance issues of the pump-turbine unit.

KEYWORDS

pump turbine, clearance axial hydraulic force, clearance pressure distribution, clearance flow patterns, circumferential velocity core region, rotating disk flow

1 Introduction

To achieve the goal of "carbon neutrality and emission peak," the power system must be dominated by clean energy, such as wind power, photovoltaic power, and solar energy, which faces a new challenge to energy storage. As the main way to store energy on a large scale, a pumped-storage plant plays an important role in ensuring grid safety and enhancing performance, known as the "stabilizer" and "regulator" of the power

system. In the power grid, pumped-storage power undertakes functions such as peak and valley load regulation, frequency modulation, phase modulation, spinning reserve, and black-start with the advantages of quick start-up and fast regulation. To match the time-varying demand of the power grid, pump-turbine units frequently operate in various off-design conditions and fast and frequent transitions of operating modes, which easily lead to runner dynamic instabilities (Goyal and Gandhi, 2018). One of the most concerning issues is the axial force imbalance of pump-turbine units, which has been frequently reported, such as at the Kazunogawa Pumped Storage Plant in Japan (Kurokawa et al., 2002) and Tianhuangping Pumped Storage Plant in China (Le and Kong, 2005; Mao et al., 2021). The unit axial instability can be attributed to the imbalanced axial hydraulic thrust acting on the runner (Zhang, 2017), which can be divided into the axial hydraulic thrust in the main flow channel (MFC) and that in the clearance flow channel (CFC) for the pump turbine. Many studies showed that the axial hydraulic thrust in the CFC is huge enough to affect the runner's stability (Zhang, 2017; Fu et al., 2018). For example, a small variation in clearance leakage could cause huge fluctuations of the clearance axial hydraulic force, resulting in accidents of bearing burning and unit lifting (Wu et al., 2004; Wu et al., 2005). During the runaway transient process, the axial hydraulic thrust in the CFC fluctuates violently and is as important to runner stability as the axial hydraulic thrust in the MFC (Hou et al., 2021b). However, because the clearance flow patterns and pressure distribution and the relationship between them are not clear, the axial thrust in the CFC cannot be described quantitatively and accurately at present. Moreover, the CFC design is largely dependent on engineering experience because of a lack of relevant specifications and references. In research methods, due to the small size and complicated structure of the CFC, the model test is constrained by geometric scale, while prototype observation is difficult to perform. When taking the clearance flow as a part of the CFD model, the calculation cost of multi-scale grid coupling between the large grid in the MFC and the small grid in the CFC is extremely high, and the results are not necessarily completely accurate. All of the aforementioned limitations make the clearance flow research stagnant, despite the fact that it is critical to uncover the unit axial imbalance mechanism. Fortunately, the clearance flow channel of the Francis pump turbine is similar to a thin-layer cavity composed of two parallel disks, in which one disk is rotating and the other is stationary. Therefore, the clearance flow patterns and pressure distribution of the pump turbine can be studied using a rotating–stationary disk model, which is a simplified model of the clearance flow channel of a pump turbine.

For studies of the disk flow, Von Kármán (1921) found a boundary layer around the rotating disk by self-similarly solving a single rotating disk in infinite stationary fluid as early as 1921. Bödewadt (1940) studied the rotating flow on a stationary disk and found a boundary layer around the stationary disk in the same way as Kármán. Combining the research from Kármán and Bödewadt, Batchelor (1951) proposed the flow between a rotating and stationary disk with infinite boundary. It was found that there were two separated boundary layers around the rotating disk and the stationary disk, but the fluid between the two boundary layers rotated at a fixed circumferential speed, called the Batchelor flow. Different from Batchelor, Stewartson (1952) pointed out that the fluid between the two boundary layers was stationary, and only the boundary layer around the rotating disk was rotating, called the Stewartson flow. The two flow patterns represented different solutions to the flow equation, which were verified by many studies (Mellor et al., 1968; Kreiss and Parter, 1983; Zandbergen and Dijkstra, 1987). In recent years, van Eeten et al. (2013) found that the Stewartson flow was an intermediate flow pattern that would eventually develop into the Batchelor flow. The research on the rotating–stationary disk flow described previously was conducted with an infinite boundary condition.

Under the finite boundary, most studies focused on the qualitative flow pattern. Daily and Nece (1960) summarized four kinds of flow patterns for a rotating–stationary disk flow, which were the laminar flow and turbulence flow with combined and separated boundary layers, respectively. Brady and Durlofsky (1987) discovered that the flow patterns showed Batchelor flow characteristics, even if the flow did not quantitatively conform to the self-similarity solution for the two coaxial rotating disk models. During the transient process, axisymmetric propagating waves and helical flow were observed around the stationary disk when the rotating disk was spinning to stop (Savaş, 1983; Lopez and Weidman, 1996; Lopez, 1996). With the increase in the rotating disk speed, the flow patterns showed circular flow, spiral flow, and corrugated turbulence, successively (Gauthier et al., 2002; Poncet et al., 2009; Hendriks, 2010; Watanabe et al., 2016). Singh (2014) found that the circumferential velocity of the rotating–stationary disk increased gradually from zero on the stationary wall to the maximum on the rotating wall for laminar flow. For the turbulence with large flow leakage, Poncet et al. (2005) observed a core region of circumferential velocity, which increased with the increase of the flow coefficient. Gauthier et al. (1999) and Serre et al. (2001) claimed that the circumferential velocity of the core region was closely related to the radius. For the pressure distribution in the rotating–stationary disk cavity, Singh (2017) pointed out that the pressure drop in the cavity increased with the rotating disk speed. In summary, the possible flow patterns of disk flow systems have been widely investigated, ranging from single rotating disk flow to flow between two disks with infinite boundary, then to rotating–stationary disk flow with finite boundary. However, the quantitative descriptions of flow patterns, cavity pressure distribution, and the relationship between flow patterns and pressure are not clearly clarified at present.

To explore the clearance flow patterns and pressure distribution in the clearance region of the pump turbine, we

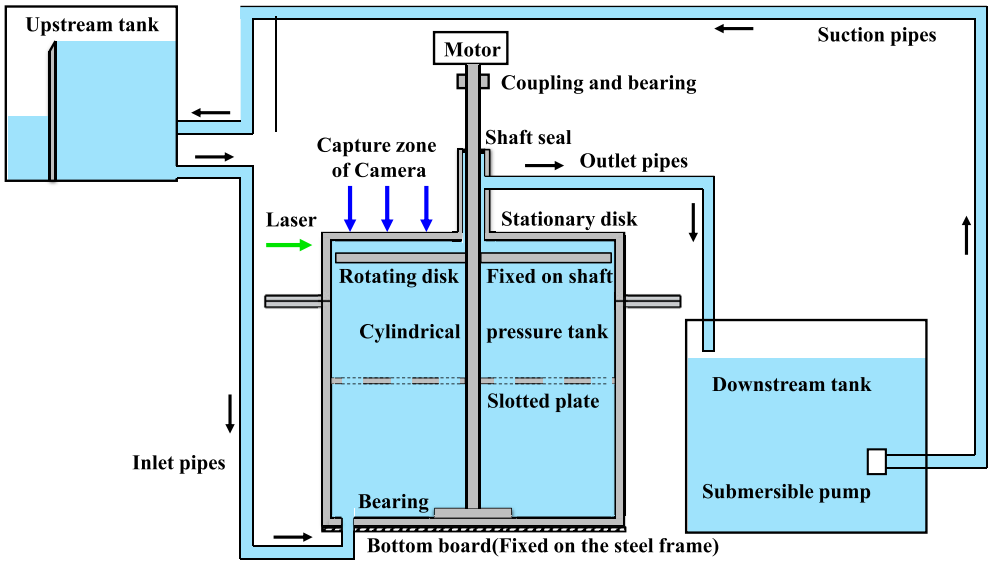

FIGURE 1
Testing setup of the rotating–stationary disk model test.

conducted a model test with PIV measurements and CFD simulations of a rotating–stationary disk flow that was a simplified model of the pump turbine clearance flow. Based on the model test and numerical simulation, some sensitive factors that could affect the clearance flow patterns and clearance axial thrust were analyzed. Finally, the calculation formulas of clearance pressure and axial hydraulic thrust were obtained by combining the theoretical analysis and model test, providing a foundation for the axial force imbalance problems of pump turbine units.

2 Testing setup and the numerical simulation method

2.1 Testing setup for particle image velocimetry measurement

The testing setup of the rotating–stationary disk model test is shown in Figure 1. It was composed of a rotating disk, cylindrical pressure tank, shaft, motor, upstream and downstream tanks, small submersible pump, and pipes. The rotating disk was fixed on the shaft in the center of the cylindrical pressure tank and driven to rotate by the motor. In this way, a clearance cavity was formed between the rotating disk and the head cover of the stationary cylindrical pressure tank. In shape, it was similar to the clearance flow channel that was composed of the hub upper surface and the cover lower surface of the pump turbine. The rotating disk and tank were made of plexiglass. The water flows into the tank from the bottom plate and flows out of the tank at the middle of the head cover, and is then pumped from the downstream tank to the upstream tank, forming the water recirculation. The velocity distributions in different height cross-sections of the rotating–stationary disk cavity were measured by PIV. The laser light was shot horizontally, while the images were captured from the top of the cylinder pressure tank. The laser exposure plane was adjusted to be perpendicular to the camera capture plane.

The geometrical characteristics of the rotating–stationary disk cavity are shown in Figure 2A. The radii of the rotating disk and the cylindrical pressure tank were 280 and 290 mm, respectively. There was a 10 mm gap between the rotating disk and the pressure tank to fill water in the clearance cavity. The cylindrical pressure tank was divided into two parts along the height direction to adjust the clearance height and a flange was used to connect them. The adjustment range of the clearance cavity height was from 40–130 mm, which was consistent with the clearance heights of most pump turbines at present. To simulate the shape of the seal ring of the pump turbine, the shaft at the outlet was slotted with a depth and height of 10 and 8 mm, respectively. The outlet pipe was sleeved on the shaft with a 10 mm gap between them. In addition, a speed sensor was set to monitor the rotation angular velocity of the rotating disk, and seven piezometer tubes were arranged on the head cover of the cylindrical pressure tank to detect the radial pressure distribution. The photo of the model test is shown in Figure 2B.

2.2 Numerical simulation method

As the main way to study the clearance flow of a pump turbine, CFD numerical simulation was also used to calculate the

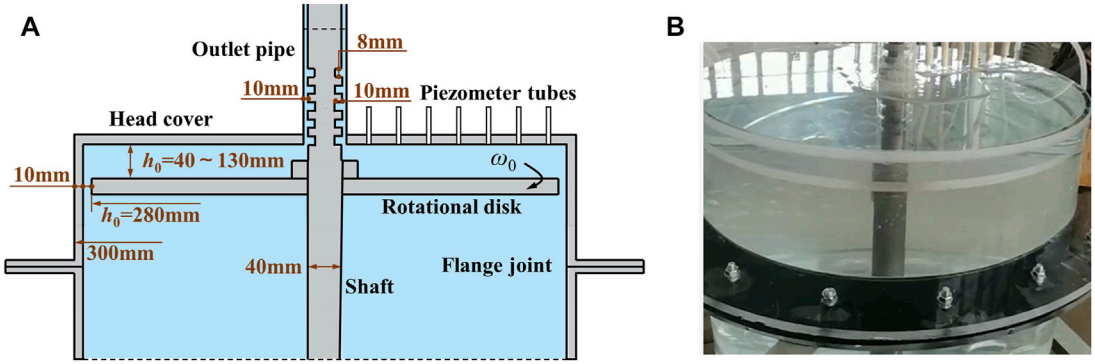

FIGURE 2
Schematic of the experimental setup with adjustable parameters. **(A)** Geometrical characteristics of the model. **(B)** Photo of the rotating–stationary disk model.

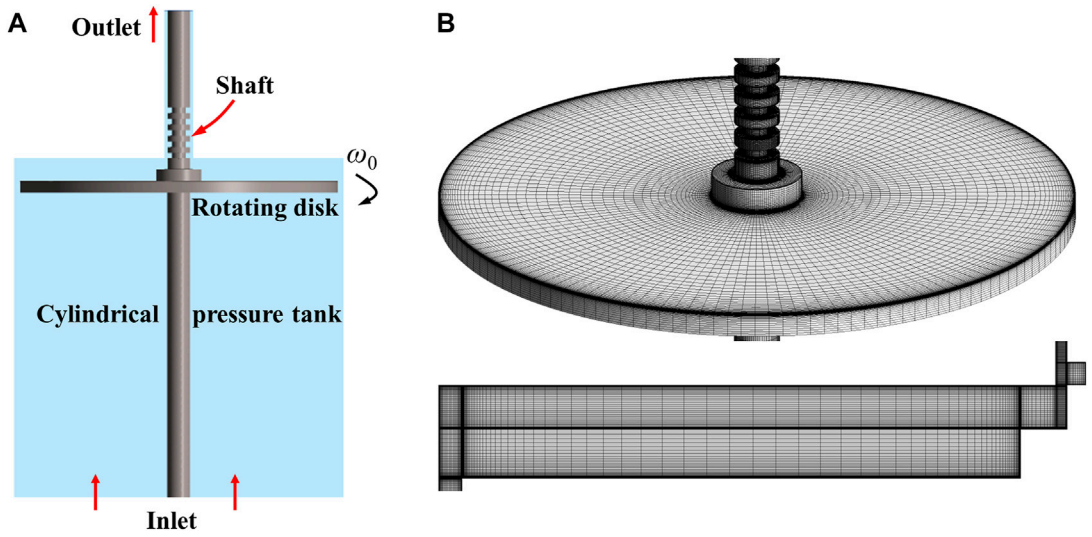

FIGURE 3
Simulation model and grid discretization. **(A)** Simulation model. **(B)** Grid discretization and boundary layer treatments.

rotating–stationary disk model in this study for two reasons. The first is to find out the suitable numerical method for clearance flow by comparing it with the test, and the second is to offer data that are difficult to measure in the model test.

2.2.1 Simulation domain and grid discretization

As shown in Figure 3A, the numerical calculation domain was completely consistent with the model test. Structural hexahedral grids were used in the whole domain and all of the walls were treated with boundary layers (Figure 3B). The grid size for the first layer was set as 0.005 mm, and the grid growth was controlled within 1.2. Grid independence verification adopted five stepwise levels, from 2.12 to 3.10, 4.21, 5.14, and 6.00 million. According to the results, the circumferential velocity of the simulation was in good agreement with the model test when the grid number was more than 6 million and treated with boundary layers. Therefore, the 6.38 million grid level was used for the simulations. For the boundary conditions, the bottom of the cylinder pressure tank was set as the pressure inlet boundary, while the outlet of the cylinder pressure tank was set as the zero mass outlet boundary because of extremely small clearance flow leakage of the pump turbine. The rotating disk and shaft were specified as the rotating wall, while the rest surfaces were set as the stationary wall.

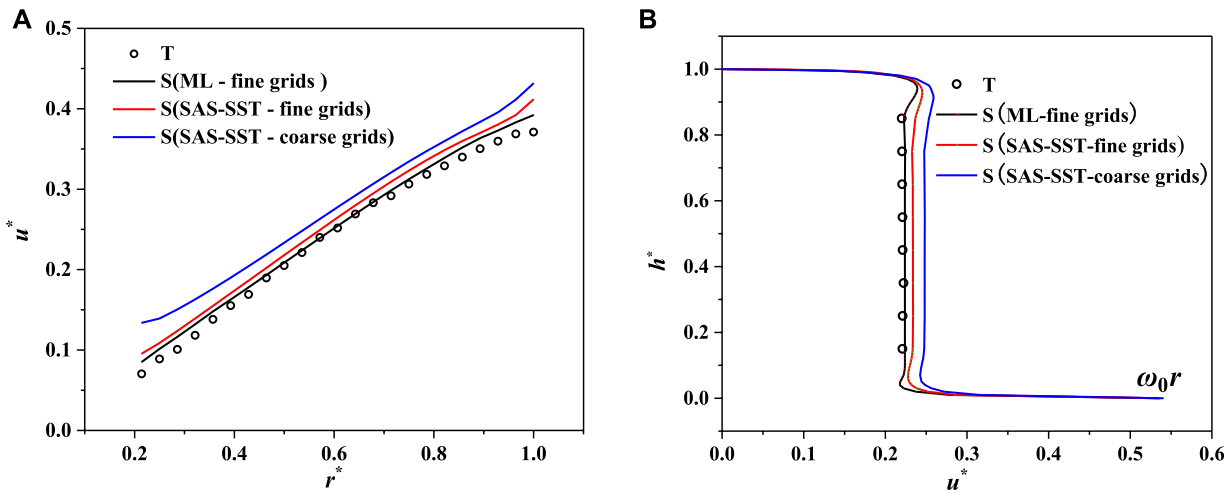

FIGURE 4
Circumferential velocity distribution with different simulation methods (ω_0=200rpm, h_0= 40 mm). **(A)** Distribution in radial direction (0.45 h_0). **(B)** Distribution in height direction (r^* =0.536).

2.2.2 Numerical simulation method

The finite volume method of commercial software Fluent was used for the simulations and the SIMPLEC pressure velocity coupling algorithm was selected. The second-order scheme was adopted both in space and time discretization. The time step size was set as 0.001 s. Due to the driving action of the rotating disk, the near-wall treatments and turbulence models are very important for accurate CFD simulations.

2.2.2.1 Near-wall treatments and the turbulence model

There are two approaches for near-wall treatments at present. One is the near-wall modeling approach, which can accurately solve the viscous boundary layer but requires extremely fine grids; the other is the wall function approach, which uses semi-empirical wall functions to bridge the viscosity-affected region between the wall and the fully-turbulence region. Even if the viscosity-affected region is not resolved, the wall function approach is ideal for calculations that do not pay much attention to walls due to lower grid requirements. For the advanced turbulence model SST and SAS–SST that are often applied to the simulation of the pump turbine, the wall treatments revert to near-wall modeling if the grid is fine enough, while reverting to the wall function approach if the grid is coarse enough. In theory, the near-wall modeling method has some deficiencies, such as the regions with very low values of turbulence kinetic energy might be treated with a near-wall formulation, even if they are far away from the wall. However, the Menter–Lechner (ML) near-wall treatment is designed to avoid these defects.

2.2.2.2 Calculation method selection

To select a suitable simulation model, we compared the wall function method and the near-wall modeling method of the SAS–SST turbulence model, and the ML method of the $k-\varepsilon$ turbulence model in this model. Consistent with the analysis in Section 2.2.2.1, the velocity distribution of the clearance cavity obtained by the ML boundary treatment method matches best with the test results, as shown in Figure 4A (T and S in this study represent the results of the model test and numerical simulation, respectively). In terms of velocity value, the velocity obtained by the wall function method (the SAS–SST turbulence model with coarse grids) is 15% larger than the test results, but their distribution laws are similar (Figure 4B). In addition, the velocity difference obtained by the ML boundary treatment and near-wall modeling of SAS-SST with a fine grid is only 4.5%. Due to the advantages of the ML boundary treatment, the ML wall treatment method of the $k-\varepsilon$ turbulence model was selected for the numerical simulation in this study.

It is worth noting that it is indispensable to reconcile the contradiction between calculation accuracy and resources when applying the CFD method to simulate the clearance flow of a prototype pump turbine. Due to the large size of the prototype pump turbine, the semi-empirical wall function method is often used because it is very difficult to meet the fine grid requirements. According to the aforementioned analysis, the circumferential velocity obtained by the wall function method is 15% larger than the model test in value, but their flow patterns are similar. Therefore, the wall function approach can still be used to analyze the clearance flow of the prototype pump turbine.

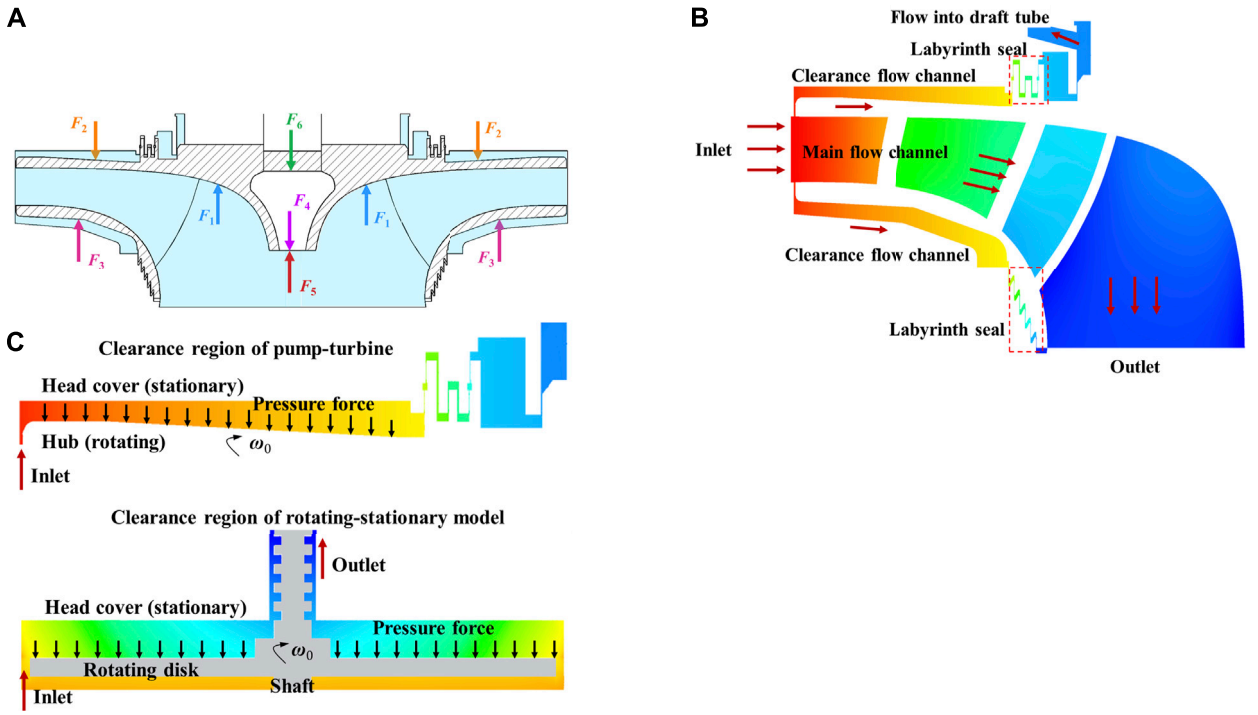

FIGURE 5
Pressure and axial hydraulic thrust in the clearance cavity. **(A)** Schematic of axial forces of the pump turbine. **(B)** Clearance pressure distributions of the pump turbine. **(C)** Axial hydraulic thrust in the clearance cavity of the pumpturbine and rotating–stationary model.

3 Results and discussions

To generally describe the results, the radial size, circumferential velocity, and pressure are expressed as the following dimensionless parameters:

$$r^* = \frac{r}{r_0},\ u^* = \frac{u}{\omega_0 r_0},\ p^* = \frac{p}{p_0}, \tag{1}$$

where r, u, and p and r^*, u^*, and p^* are the radius, circumferential velocity, and pressure before and after the normalization, respectively; r_0 is the radius of the rotating disk, with a value of 280 mm; and ω_0 and p_0 are the rotating disk speed and the inlet pressure of the model, respectively. They were set as 200 rpm and 2.12 m because most calculation conditions in this study were analyzed in this condition.

3.1 Clearance axial hydraulic thrust of the pump turbine

For the pump turbine, the clearance flow channels are the small gaps between the rotating and stationary parts. It can be divided into the clearance region between the hub upper surface (rotating surface) and the head cover lower surface (stationary surface), and the clearance region between the shroud lower surface (rotating surface) and the bottom ring upper surface (stationary surface). The schematic of the runner axial forces is shown in Figure 5A, where F_1 is the axial hydraulic force in the main flow channel in the upward or downward direction; F_2 is that in the hub clearance in the downward direction; F_3 is that in the shroud clearance in the upward direction; F_4 is the self-weight of the runner in the downward direction; F_5 is the buoyancy force in the upward direction; and F_6 is the axial force acting on the shaft end in the downward direction. The total axial force on the runner is the summation of these six forces. Compared with other axial forces, the summation of F_4 and F_5 is small enough to be neglected. Since the value of F_6 is fixed, it will not be discussed in this study. The sum of F_1, F_2, and F_3 is the total axial hydraulic thrust of the runner.

Because the clearance regions are directly connected with the vaneless space of the main flow channel, the inlet pressure of the clearance flow channel is equal to the pressure in the vaneless space and is extremely high (Figure 5B) (Hou et al., 2021b). After entering the clearance flow channel, the pressure in the clearance flow channel drops inward along the radial direction due to the pressure consumption caused by a strong rotating shear flow. Different from the main flow channel, the hydraulic pressure in the clearance flow channel cannot be converted into kinetic energy; therefore, the pressure drop is relatively low. Radially inward, the pressure in the clearance channel decreases slower

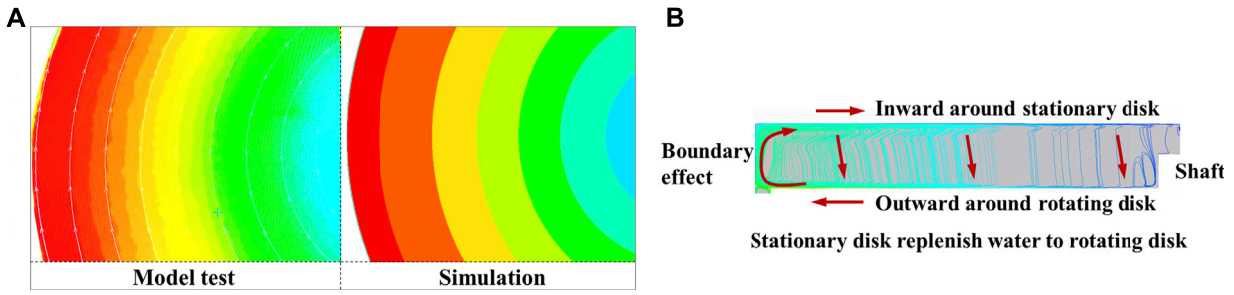

FIGURE 6
Qualitative velocity distributions (ω_0=200 rpm, h_0= 40 mm). **(A)** Circumferential velocity contours (0.45h_0). **(B)** Velocity distribution in the meridian section.

than that in the main flow channel; therefore, the axial thrust of the clearance flow channel is greater than that of the main flow channel on the hub or shroud of the runner. The enormous pressure in the clearance region generates a huge axial hydraulic thrust on the runner, which can be calculated by integrating the pressure acting on the hub and shroud (Figure 5C). Similarly, for the rotating–stationary disk model, the pressure in the clearance cavity acts on the rotating disk and produces an axial hydraulic thrust. To calculate the clearance axial hydraulic thrust, it is essential to clarify the flow pattern and clearance pressure distribution laws and the relationship between them.

3.2 Clearance flow patterns and pressure distribution

The clearance basic flow patterns and pressure distribution were investigated with a disk rotating speed ω_0 of 200 rpm and a clearance height h_0 of 40 mm. PIV was used to measure the velocity distributions in eight horizontal cross-sections of the clearance cavity (0.15 h_0 to 0.85 h_0 with an interval of 0.1 h_0).

3.2.1 Clearance flow patterns

The velocity contours in the 0.45h_0 section of the rotating–stationary disk cavity obtained by the model test and numerical simulation are shown in Figure 6A. Qualitatively, the main flow patterns show a strong rotating shear flow under the driving action of the rotating disk. The circumferential velocity is circumferentially uniform but increases outward along the radial direction. Driven by the centrifugal force, the water flows outward around the rotating disk in the meridian section, then flows inward around the stationary wall because of the boundary effect (Figure 6B), forming secondary flow vortices. To maintain continuity, the water body near the stationary wall continues to supply water to the rotating wall. In terms of velocity magnitude, the circumferential rotating shear flow dominates the flow patterns in the clearance cavity, and the radial and axial velocities are very small.

Quantitatively, the circumferential velocity follows linear distribution laws along the radial direction (Figure 7A), except for the outer edge position of the rotating disk, which is impacted by boundary effects. Along the height direction, a “core region + double boundary layers” distribution is presented for the circumferential velocity (Figure 7B). The circumferential velocity in the core region is constant along the height direction, suggesting that the water body in the clearance cavity rotates like a rigid body. The circumferential velocity is the largest on the rotating disk surface, while it is zero on the stationary wall due to the non-slipping wall, and the core region velocity is between them. Around the rotating wall and the stationary wall, two boundary layers are formed with thicknesses of δ_d and δ_s, respectively. In terms of the value, δ_s is larger than δ_d, and both of them increase with the radius, which is consistent with the conclusion of Singh (2014).

In the laminar flow condition, Singh and Zosimovych (2016) found that the circumferential velocity continuously decreased from the maximum on the rotating disk to zero on the stationary disk, and no velocity core region exists by linearizing the N-S equation. According to the flow pattern classification from Daily and Nece (1960), the flow patterns in the rotating–stationary disk cavity belong to the turbulent flow. Moreover, because the distance between the two disks is substantially greater than the thickness sum of the two boundary layers, the boundary layers around the rotating and stationary walls are separated, called Kármán and Bödewadt boundary layers, respectively. In short, the flow patterns in this model test show a “core region + double boundary layers” distribution and belong to typical Batchelor flow. The flow in the clearance cavity is dominated by the circumferential velocity of the core region, in which the inertial force is considerably larger than the viscous force, and there is no velocity gradient along the height direction.

Despite the fact that the circumferential velocity in the core region increases as the radius grows, the rotating coefficient k

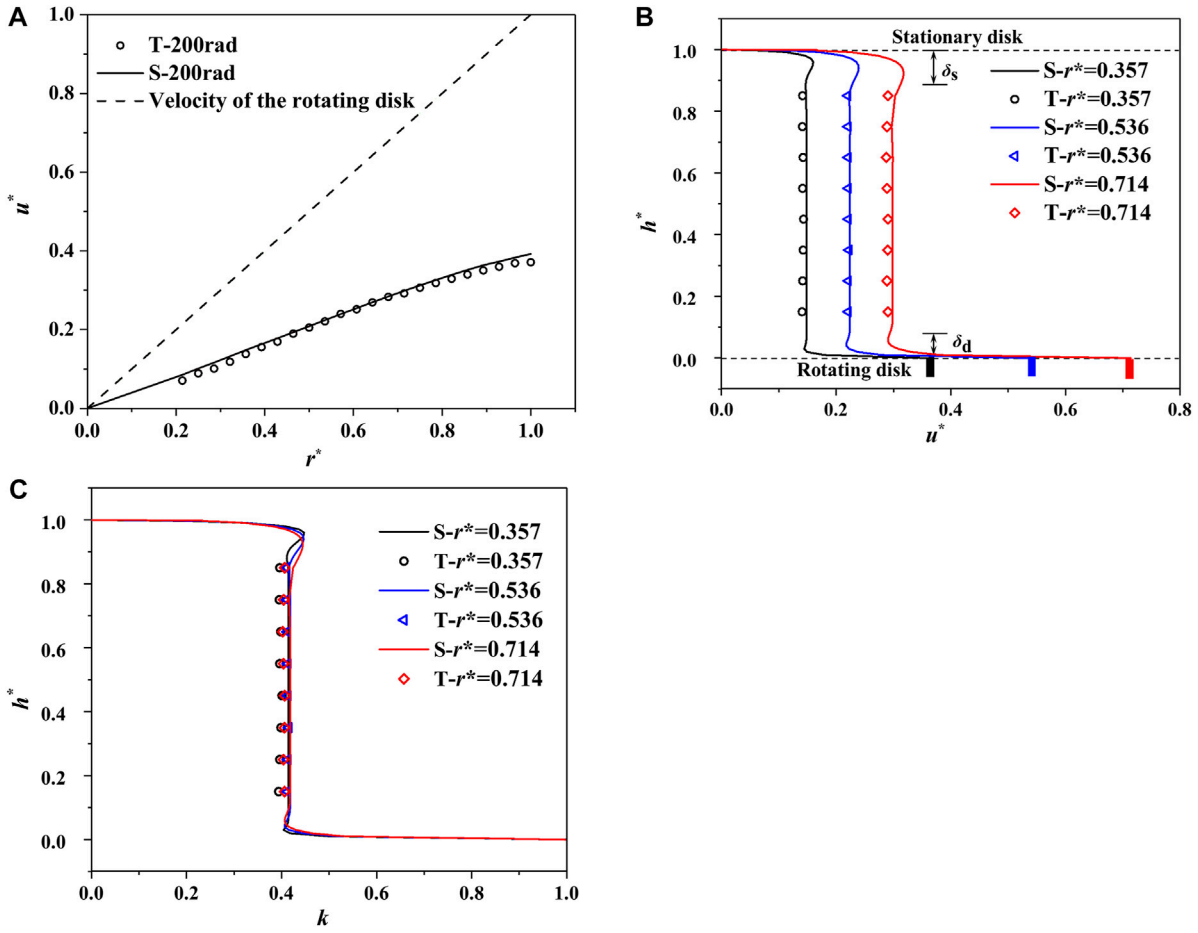

FIGURE 7
Quantitative circumferential velocity distributions (ω_0=200 rpm, h_0= 40 mm). **(A)** Velocity along the radial direction (0.45h_0). **(B)** Velocity along the height direction. **(C)** Rotating coefficient k along the height direction.

(rotating velocity radio of the core region to the rotating disk) remains constant and does not change with the radius (Figure 7C). When ω_0 and h_0 are set as 200 rpm and 40 mm, respectively, k is about 0.413 for the model test, while it is around 0.42 for numerical simulation. Elena and Roland (1996) and Cheah et al. (1994) investigated the rotating coefficient k at a fixed radius and found that k is also around 0.41. Therefore, the model test and numerical simulation results in this study are reliable.

For the turbulent plane Couette flow, it is composed of two plates, in which one plate translates with constant velocity in a direction and the other is stationary. Similar to the rotating–stationary disk flow, the velocity core region was also formed for Couette flow, and it flowed at 0.5 times the moving plate velocity (Bech et al., 2006; Pirozzoli et al., 2014). However, the rotating coefficient of the core region for the rotating–stationary disk is less than 0.5 for two reasons. The first is that the circular shear deformation rate in the core region is not equal to zero due to the rotating effect; therefore, the driving action of the rotating disk needs to provide more energy consumption to keep up with the shear deformation rate. In addition, the radial secondary flow in the radial direction weakens the circumferential velocity in the core region due to the centrifugal force and the boundary effect.

3.2.2 Pressure distributions and the axial hydraulic thrust

In the model test and numerical simulation, the cavity pressure shows a circumferentially symmetric distribution. Due to the energy consumption caused by the strong rotating shear flow, the pressure gradually drops inward in the radial direction (Figures 8A,C). For the water body in the clearance cavity, the core region circumferential velocity of the strong rotating shear flow dominates the major flow patterns in the clearance cavity due to the driving action of the rotating disk,

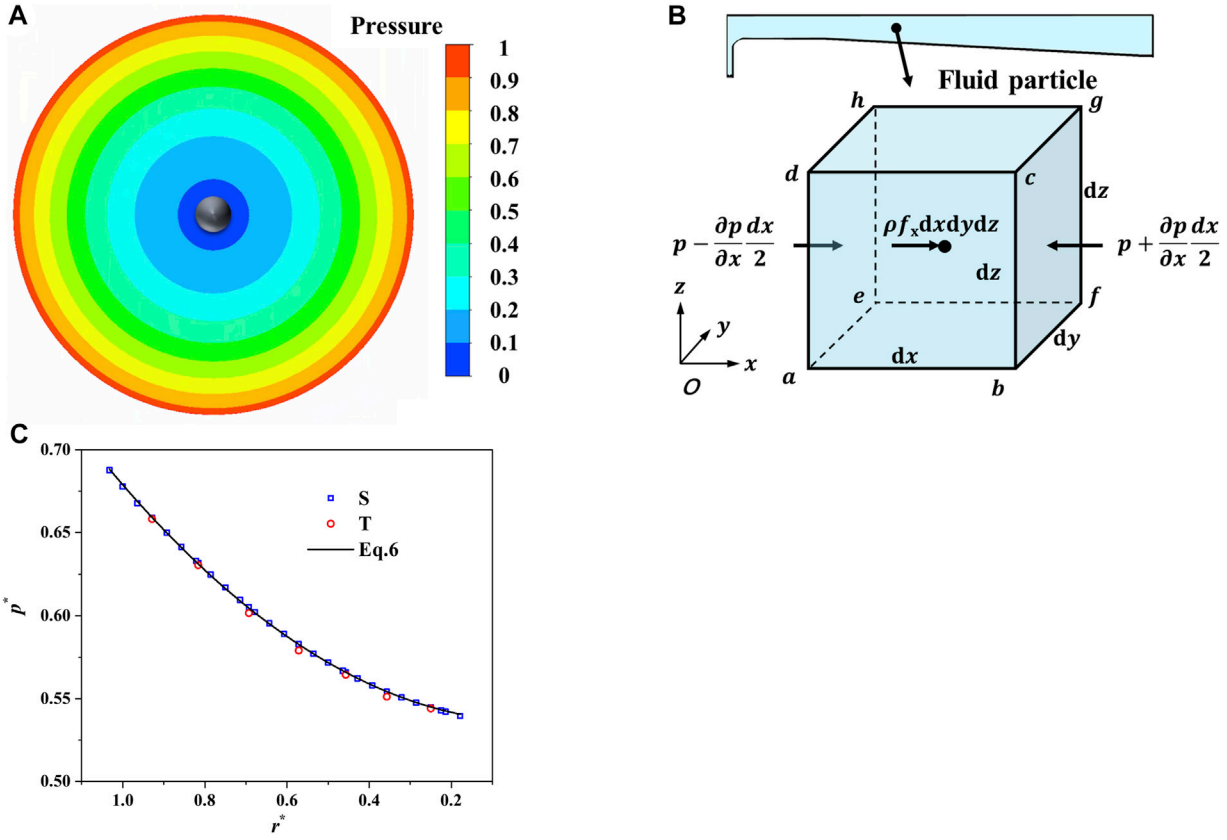

FIGURE 8
Pressure distributions (ω_0=200 rpm and h_0 = 40 mm). **(A)** Pressure contours in the 0.45h_0 cross-section. **(B)** Fluid force diagram (Hou et al., 2021b). **(C)** Pressure distribution along the radial direction.

while the radial velocity is extremely small. Therefore, Eq. 2 can be obtained by applying the liquid equilibrium differential equation in the radial direction. Due to the extremely small radial velocity, the surface forces are equal to the mass forces on any fluid mass in the radial direction (Figure 8B), and Eq. 2 can be simplified as Eq. 3:

$$\left(p-\frac{\partial p}{\partial x}\right)\mathrm{d}y\mathrm{d}z-\left(p+\frac{\partial p}{\partial x}\right)\mathrm{d}y\mathrm{d}z+\rho f_x\mathrm{d}x\mathrm{d}y\mathrm{d}z=0, \quad (2)$$

$$\frac{\partial p}{\partial x}=\rho f_x, \quad (3)$$

where ρ is the density; p is the pressure; and f_x is the mass force, which is the centrifugal force for the flow in the cavity. Assuming that the core region rotational velocity is $k\omega_0$, we can modify Eq. 3 to

$$\mathrm{d}p=\rho(k\omega_0)^2 r. \quad (4)$$

By integrating Eq. 4 from the outer edge of the rotating disk, we can obtain the radial pressure drop Δp and the pressure distribution p in the clearance cavity as Eq. 5 and Eq. 6:

$$\Delta p=\frac{\rho(k\omega_0)^2}{2}\left(R_1^2-r^2\right), \quad (5)$$

$$p=p_1-\frac{\rho(k\omega_0)^2}{2}\left(R_1^2-r^2\right), \quad (6)$$

where R_1 and p_1 are the radius and pressure, respectively, at the outer edge of the rotating disk. According to Eq. 6, the pressure distribution along the radial direction can be expressed as a function of the clearance inlet pressure p_1 and the circumferential velocity of core region $k\omega_0$.

As shown in Figure 8C, the pressure distribution estimated by Eq. 6 matches well with the model test and numerical simulation when the rotating coefficient k is set as 0.413 according to Section 3.2.1, and the maximum error is only 1.2%. Therefore, Eq. 6, which is based on the premise of the accurate circumferential velocity of the core region, can be used to calculate the clearance pressure distribution. Even though the pressure distribution calculated by Eq. 6 neglects the flow losses caused by the radial secondary flow and wall friction, and only takes the losses caused by the strong rotating shear flow into account, it is still relatively accurate because the strong rotational

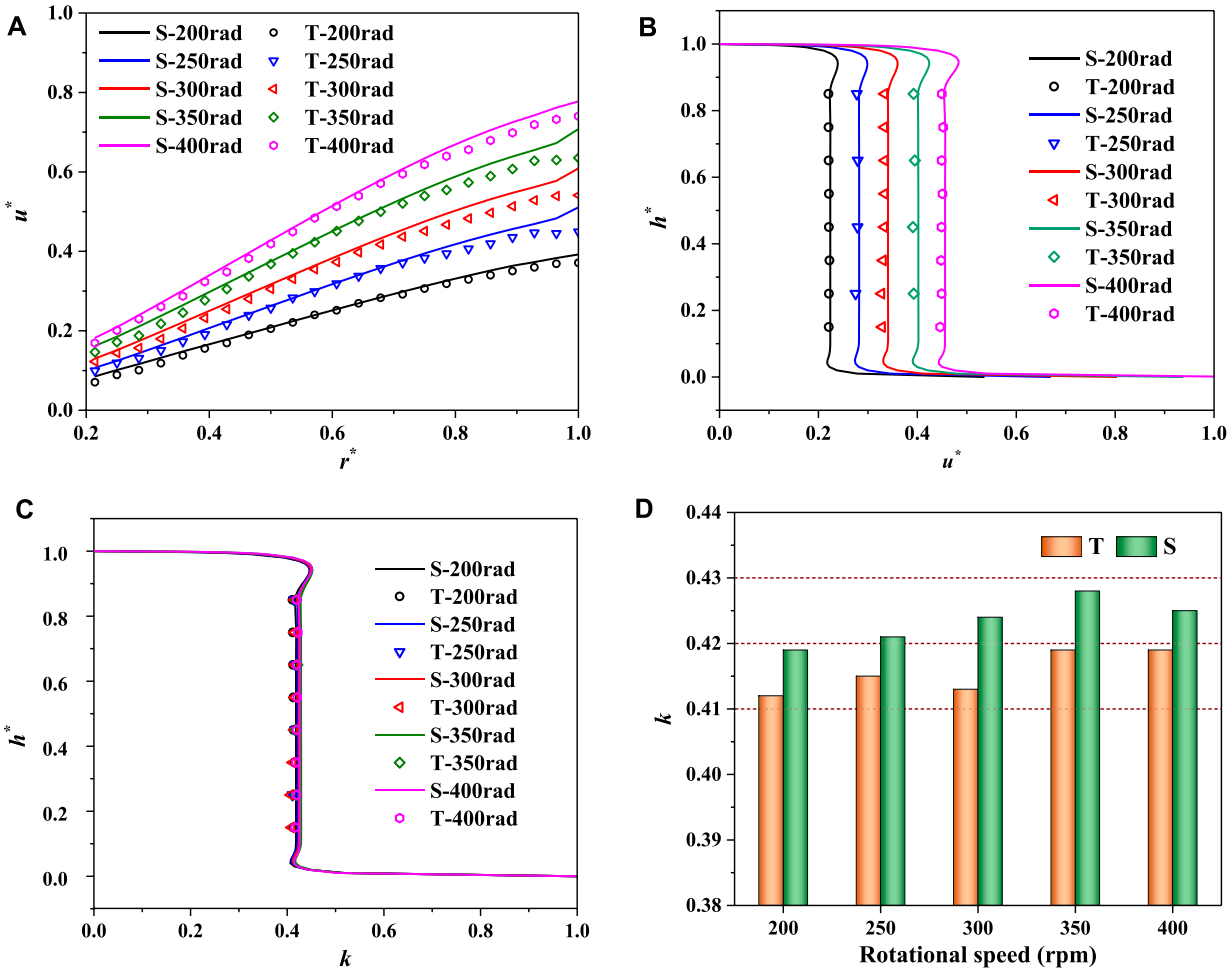

FIGURE 9
Circumferential velocity distributions under different disk rotating speeds. **(A)** Radial distribution ($0.45h_0$). **(B)** Height distribution (r^*=0.536 m). **(C)** Rotating coefficient k distribution. **(D)** Rotating coefficient k in the core region.

shear flow is the primary source for the energy consumption in the clearance cavity.

3.3 Sensitive factors of clearance flow patterns and pressure distributions

According to the aforementioned analysis, the flow patterns present a typical Batchelor turbulence in the rotating–stationary disk cavity, which means the circumferential velocity has a "core region + double boundary layers" distribution. However, the pump turbine is frequently subjected to a variety of off-design operations and frequent and quick transition processes. Under these operating conditions, the change of the runner rotational speed and the clearance inlet pressure change in real-time. Moreover, for the clearance flow channel sizes of the pump turbine, the radial size is determined by the runner diameter, while the height size (clearance height) is variable and largely dependent on the engineering experience. At present, the clearance height of the Francis pump turbine ranges from a few centimeters to tens of centimeters. Under these different conditions, how do the flow patterns evolve in the clearance cavity? Are the Batchelor flow characteristics still maintained? How does the rotating coefficient change in the core region? What is the relationship between flow patterns and pressure distribution? These questions need to be further investigated. Therefore, the effects of the disk rotating speed, clearance inlet pressure, and clearance height on the flow patterns and pressure distribution in the clearance cavity were studied in this study.

3.3.1 Effects of the disk rotating speed

The disk rotating speed was set as 200–400 rpm with a gradient of 50 rpm to analyze the influence of the disk

rotating speed on the velocity and pressure distribution in the clearance cavity.

3.3.1.1 Flow patterns

Under different disk rotating speeds, the circumferential velocity in the cavity still presents a linear distribution in the radial direction, but it increases with the increase in the disk rotating speed (Figure 9A). Along the cavity height direction, the core regions of the circumferential speed are formed under all the disk rotating speeds (Figure 9B). However, the circumferential velocity of the core region increases with the rise of the disk rotating speed. The thickness of the boundary layer on the rotating and stationary disks decreases with the increase in the rotating speed, which is consistent with the law that the boundary layer thickness decreases with the increase of velocity (Cao and Qiu, 1998). Although the circumferential speed in the core region increases with the rise of the disk rotating speed, the rotating coefficient k in the core region remains constant under different disk rotating speeds (Figure 9C). The rotating coefficient k of numerical simulation is slightly larger than that of the model test, around 0.42 to 0.43 and 0.41 to 0.42, respectively (Figure 9D). We simulated the clearance flow patterns during the runaway transient process of a prototype pump turbine and discovered that the circumferential velocity in the core region had a positive correlation change with the rotating disk speed, while the rotating coefficient in the core region did not dramatically change with the disk rotating speed (Hou et al., 2021b).

For the rotating–stationary disk cavity, the rotational Reynolds number, defined by Eq. 7, varies with the radius and rotating speed. When the rotating speed decreases to only 200 rpm, the average Reynolds number is 9.2×10^5. Although the Reynolds number in the clearance cavity is not high enough, it is difficult to maintain laminar flow. For the clearance flow of the prototype pump turbine, it is more difficult to maintain laminar flow because of the larger radius and higher rotating speed. Therefore, Batchelor turbulence is the main flow pattern in the clearance flow channel of the pump turbine, and the core region rotates at a speed of around 41–42% of the rotating disk speed.

$$Re = \omega_0 r^2 / \nu, \tag{7}$$

where ν is the kinematic viscosity.

3.3.1.2 Pressure distributions

According to the clearance flow patterns, the energy dissipation in the disk cavity is mostly caused by strong rotating shear flow. The stronger the rotating intensity, the greater the energy dissipation. Consistent with the aforementioned analysis, the cavity pressure decreases gradually inward radially, and the higher the disk rotating speed is, the greater will be the pressure drop (Figure 10A). The pressure drop Δp increases in a parabolic law with the disk rotating speed, which matches well with Eq. 5 (Figure 10B). Δp of numerical simulation is slightly larger than that of the model test, which can be attributed to the slightly higher rotating speed of the core region for the numerical simulation. However, the two are in good agreement with a difference of less than 5%.

Eq. 5 can be used to fit Δp acquired from the model test and numerical simulation, as shown by the black and red curves, respectively, in Figure 10B. The fitted k value of the model test and numerical simulation values are 0.413 and 0.423, respectively, which are in good agreement with the aforementioned flow pattern analysis (0.41–0.42 for the model test and 0.42–0.43 for the numerical simulation). Therefore, the core region rotates at a speed of around 41–42% of the rotating disk speed, which can accurately predict the pressure distribution in the clearance cavity based on Eq. 6 and the axial hydraulic thrust by integrating the cavity pressure.

3.3.2 Effects of the clearance inlet pressure

For the pump turbine, because the clearance regions are directly connected with the vaneless space of the main flow channel, the clearance pressure is closely related to the clearance inlet pressure (pressure in the main flow channel), which violently fluctuates during various transient processes. However, it is still unknown whether the inlet pressure affects the velocity and pressure distribution of the clearance cavity. With the help of the rotating–stationary disk test, the velocity and pressure distributions for the clearance inlet pressure ranging from 1.22–2.42 m with a gradient of 0.3 m were studied. Due to the limited inlet pressure in the model test, the inlet pressure of 30 m was increased for the numerical simulation to analyze the influences of the clearance inlet pressure on the velocity and pressure distributions.

3.3.2.1 Flow patterns

As shown in Figure 11A and Figure 11B, the clearance inlet pressure does not affect the circumferential velocity distribution in the rotating–stationary disk cavity. Because of the increased boundary impact, the circumferential velocity exhibits a little reduction at the disk boundary position when the clearance inlet pressure reaches 30 m. In the radial direction, the water flows outward near the rotating disk and inward near the stationary disk due to the imbalance between the pressure force and centrifugal force. When the centrifugal force remains constant, the larger the pressure force, the greater will be the radial force imbalance and the boundary effect, resulting in a slight decrease in the circumferential velocity at the boundary location. However, if the location is far from the boundary effect, the circumferential velocity in the core region is unaffected by the clearance inlet pressure, and still presents a “core region + double boundary layers” distribution.

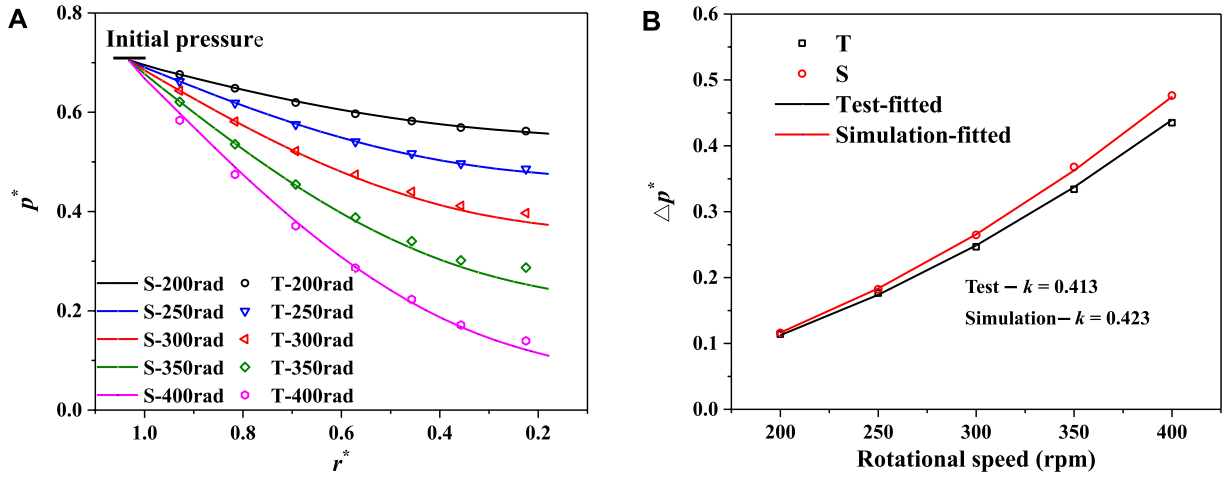

FIGURE 10
Pressure distributions under different disk rotating speeds. **(A)** Pressure distributions along the radial direction. **(B)** Variation laws of pressure drop Δp.

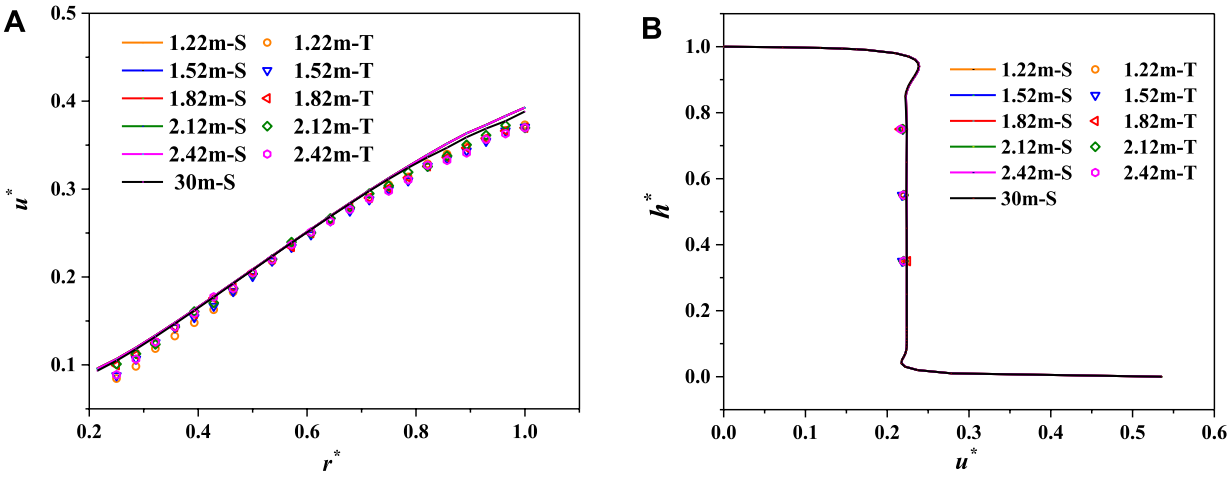

FIGURE 11
Circumferential velocity distribution under different clearance inlet pressures. **(A)** Radial distribution ($0.45h_0$). **(B)** Height distribution (r^*=0.536 m).

3.3.2.2 Pressure distributions

The pressure in the clearance cavity increases with the increases of the clearance inlet pressure, though it shows similar distributions and radially decreases inward the clearance cavity under different clearance inlet pressure conditions (Figure 12A). Although the pressure in the cavity is closely related to the clearance inlet pressure, the total pressure drop Δp in the cavity is unaffected (Figure 12B), which is consistent with the conclusions of Eq. 5 and Eq. 6. The pressure in the cavity can be expressed as the inlet pressure and the square of the circumferential velocity of the core region, while the pressure drop is only related to the latter. According to the circumferential velocity distribution in the core region, when the inlet pressure increases to 30 m, the circumferential velocity decreases slightly at the boundary position, resulting in a small decrease in the pressure drop due to the influence of the boundary effect.

3.3.3 Effects of the clearance height

The clearance flow channel of the pump turbine is a thin-layer cavity composed of the runner and the cover lower surface

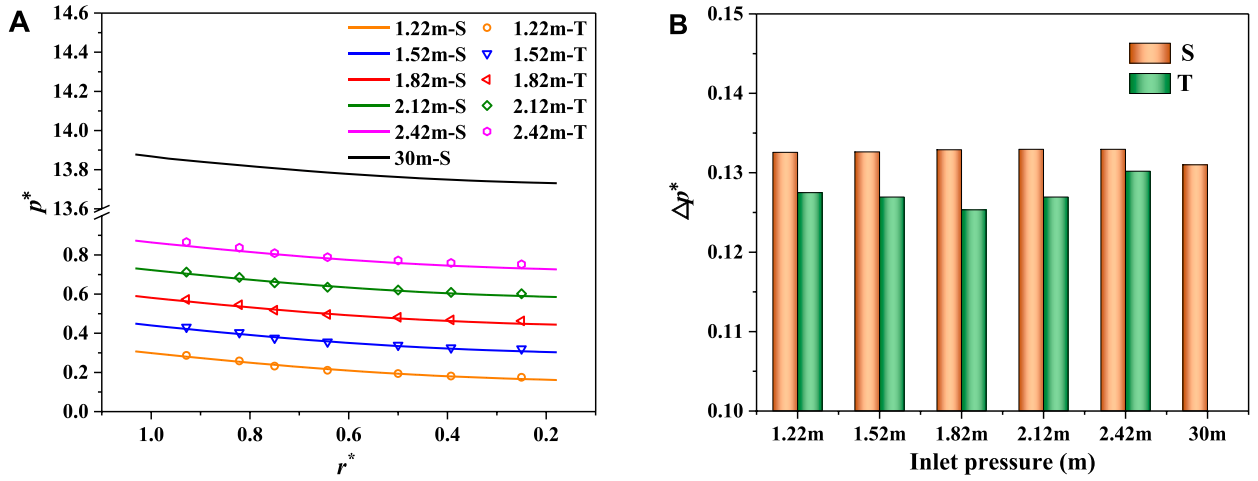

FIGURE 12
Pressure distributions under different clearance inlet pressures. **(A)** Pressure distributions along the radial direction. **(B)** Pressure drop Δp.

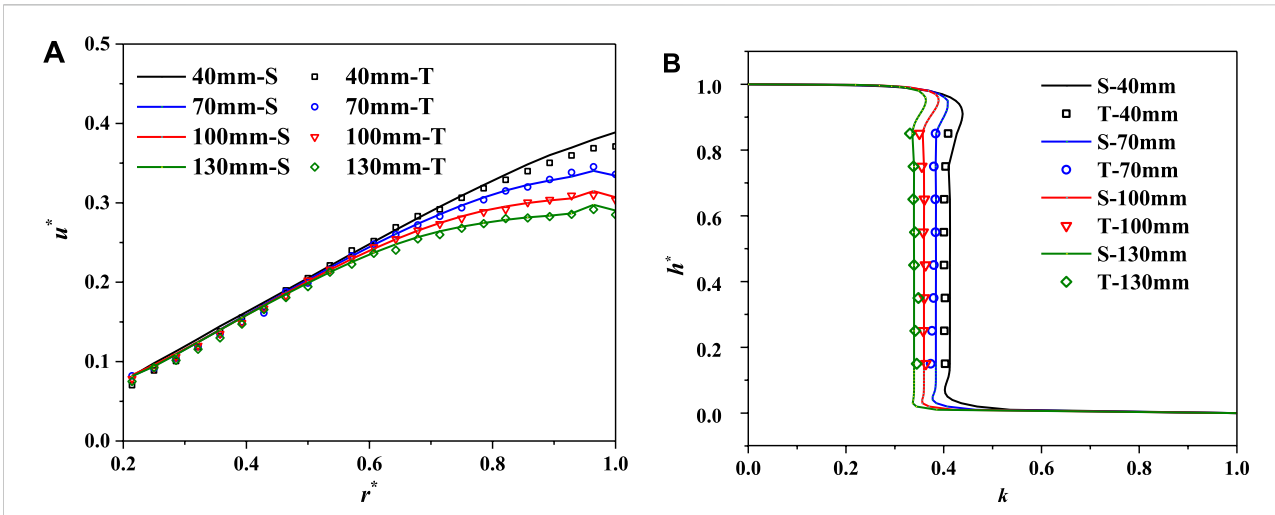

FIGURE 13
Circumferential velocity distribution under different clearance heights. **(A)** Radial distribution ($0.45h_0$). **(B)** Height distribution (r^*=0.821).

or bottom ring upper surface. Due to the lack of design specification, the clearance cavity height is largely dependent on experience. At present, most clearance heights range from a few centimeters to more than 10 cm, and even the cavity height changes along the radial direction. To investigate the effects of the clearance height on the flow patterns and pressure distribution in the cavity, the clearance height h_0 was set as 40–130 mm with a gradient of 30 mm.

3.3.3.1 Flow patterns

As shown in Figure 13A, the circumferential velocity gradually decreases with the increase of the clearance height at the outer edge of the rotating disk but remains invariable at the inner edge and middle position. Due to the strong centrifugal force near the rotating disk, the water flows outward in the radial direction and crashes against the boundary. After the collision, the water flows inward near the stationary wall. The larger the cavity height, the broader the collision interaction range, in which the circumferential speed was weakened to a great extent. Although it is greatly weakened, the circumferential velocity remains Batchelor turbulent flow (Figure 13B). However, the rotating coefficient k in the core region gradually decreases with the increase of the clearance height near the outer edge. Therefore, the clearance height has little

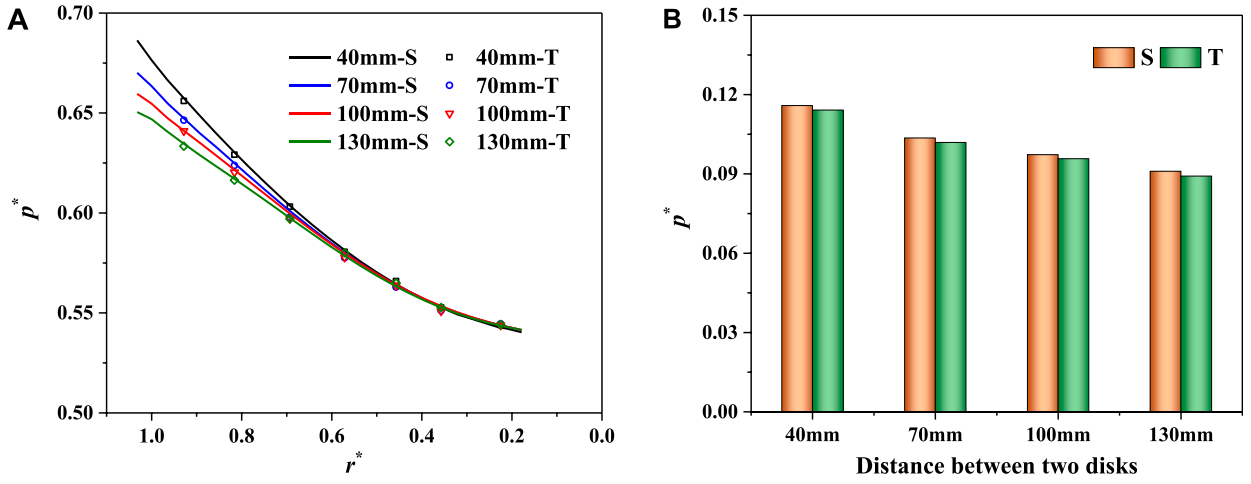

FIGURE 14
Pressure distributions under different clearance heights. **(A)** Pressure distributions along the radial direction. **(B)** Pressure drop Δp.

effect on the circumferential velocity if the location is far from the influence range of boundary effects.

For the clearance flow channel of the pump turbine, the clearance cavity height is nearly equal to the height of this rotating–stationary disk model, while the clearance radial size is much larger than the influence range of the boundary effect. Therefore, we can assume that the clearance height has little effect on the clearance flow patterns of the pump turbine.

For the laminar flow in the rotating–stationary disk cavity, Singh (2014) demonstrated that the average circumferential velocity decreases with the increase of the clearance height. For the turbulence with large leakage flow, Poncet et al. (2005) discovered that the flow patterns in the rotating–stationary disk are not sensitive to the clearance height, which is consistent with our conclusion. Therefore, once the Batchelor turbulence flow with boundary layer separation is formed in the clearance cavity, the circumferential velocity of the core region is unaffected by the clearance height when the location is far away from the boundary. However, when the clearance height increases to a certain extent that the stationary disk no longer affects the flow near the rotating disk or the influence weakens, the Batchelor flow and the core region of circumferential velocity will no longer be formed. The flow patterns will eventually transform into a single free rotating disk flow. It cannot happen to the clearance flow of the pump turbine because of the limited space in the height direction. Therefore, once the Batchelor flow is formed in the clearance cavity, the clearance height has little effect on the circumferential velocity in the core region if the location is far from the boundary effect.

3.3.3.2 Pressure distributions

Under different clearance heights, the pressure distribution along the radial direction shows a substantial variation near the outer edge of the disk but remains unchanged at the inner edge and the middle position of the rotating disk (Figure 14A). Near the outer edge of the disk, the larger the clearance height, the smaller the circumferential velocity and the smaller the energy dissipation, resulting in a smaller pressure drop. Therefore, the total pressure drop Δp decreases with the increase of the clearance height (Figure 14B).

We numerically simulated the pressure distributions of the clearance channel with different clearance heights for a pump turbine and found that the clearance height is not sensitive to the clearance pressure distribution (Hou et al., 2021a). Therefore, the clearance height has little effect on the pressure distribution in the clearance cavity of the pump turbine if the location is far from the boundary effect.

3.4 Clearance axial hydraulic thrust of the pump turbine

3.4.1 Clearance flow patterns

Compared with the rotating–stationary disk model test in this study, the clearance flow of the prototype pump turbine has a higher Reynolds number and larger radial size, which leads to Batchelor turbulence in the clearance flow channel. The circumferential velocity shows the “core region + double boundary layers” distribution. Though the fact that the circumferential velocity in the core region increases with the increased rotating disk speed, the core region rotates at a speed of around 41–42% of the rotating disk speed. In the meridian

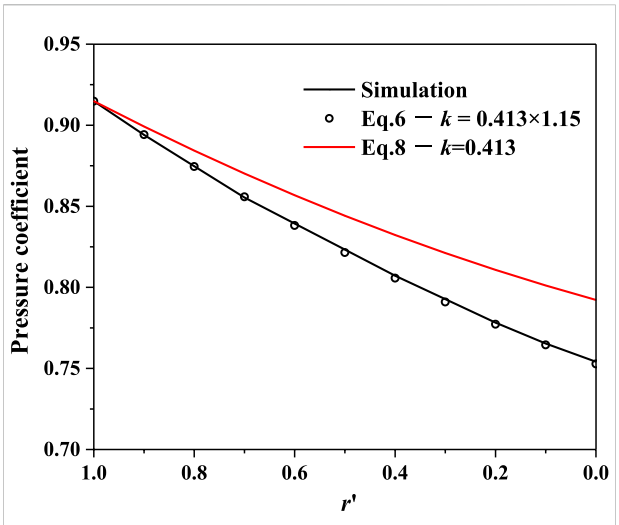

FIGURE 15
Clearance pressure distributions of a prototype pump turbine.

section, the water flows outward around the rotating disk, while flowing inward around the stationary wall, forming the secondary flow vortices.

3.4.2 Clearance axial hydraulic thrust

It is difficult to estimate the pressure distribution in the clearance cavity of the pump turbine by Eq. 6 before we recognize the clearance flow patterns and the rotating coefficient k. According to the analysis in this study, the k value of the core region can be quadratically fitted to 0.413 and does not dramatically change with relevant factors. Therefore, Eq. 6 can be modified as follows:

$$p = p_1 - 0.085\rho\omega_0^2\left(R_1^2 - r^2\right). \tag{8}$$

To verify the correctness of Eq. 8, we did a numerical simulation of a prototype pump turbine containing the clearance flow channel and obtained the pressure distributions in the clearance cavity (the related parameters were shown in reference (Hou et al., 2021b)). Due to the contradiction between calculation accuracy and calculation resources, the wall function method was used to solve the clearance flow channel of the pump turbine. As shown in Figure 15, the simulated pressure drops faster than that calculated by Eq. 8. However, the numerically simulated pressure matches well with that calculated by Eq. 6 when the circumferential velocity of the core region increases by 15% (k is equal to 0.413 × 1.15). The main reason is that the simulated circumferential velocity of the core region solved by the wall function method is 15% larger than the model test. The larger velocity consumes more energy and leads to a larger pressure drop in the clearance region. Therefore, Eq. 6 and Eq. 8 can be used to predict accurately the clearance pressure distributions of the pump turbine. Actually, k is about 0.413 in the clearance region both for the model test and fine numerical simulation, and the modified pressure distribution of Eq. 8 tends to be smaller, as shown in the red curve in Figure 15.

According to the pressure distribution law in Eq. 8, the clearance axial thrust acting on the runner can be expressed as a function of the clearance inlet pressure and the square of the runner rotating speed by integrating the pressure on the rotating wall.

$$F_c = \pi\left(R_{1r}^2 - R_{2r}^2\right)\left[p_{1r} - 0.043\rho\omega_{0r}^2\left(R_{1r}^2 - R_{2r}^2\right)\right], \tag{9}$$

where F_c is the clearance axial hydraulic thrust; R_{1r} and R_{2r} are the outside and inside radius, respectively, of the clearance flow channel; p_{1r} is the clearance inlet pressure; and ω_{0r} is the rotating speed of the runner.

4 Conclusion

In this study, a rotating–stationary disk model that was a simplified model of the pump turbine clearance flow was measured by PIV measurements and simulated by CFD simulation to study the clearance flow patterns and pressure distributions and the relationship between them. The results show that the circumferential velocity in the clearance region presents a distribution of "core region + double boundary layers." The pressure in the clearance region has a circumferentially symmetric and radially quadratic distribution. Quantitatively, the clearance pressure and axial thrust can be expressed as a function of the clearance inlet pressure and the square of the runner rotating speed, which provides a basis for the axial force imbalance problems of pump turbine units.

(1) Driven by the rotating disk, the flow patterns in the clearance flow channel present a typical Batchelor turbulence flow with separated boundary layers. The circumferential velocity core region is formed in the middle region along the height direction, while Kármán and Bödewadt boundary layers are formed on the rotating and stationary disks. Due to the centrifugal force and boundary effects, the flow is radially outward around the rotating wall, while inward around the stationary wall in the meridian section, showing secondary flow vortices. Numerically, the strong rotating shear flow in the core region dominates the clearance flow patterns.
(2) The core region rotates at a speed of around 41–42% of the rotating disk speed for all conditions. The circumferential velocity in the core region is dominated by the rotating disk speed, while being unaffected by the clearance inlet pressure and the clearance height if the location is far from the boundary effect.
(3) Based on the liquid differential equilibrium equation and circumferential velocity in the core region, the clearance

pressure and axial hydraulic thrust can be expressed as a function of the clearance inlet pressure and the square of the runner rotating speed, which provides a basis for the axial force imbalance problems of the pump turbine unit.

(4) In terms of CFD numerical calculation for clearance flow, although the circumferential velocity obtained by the empirical wall function method is 15% larger than the model test in value, their velocity distribution laws are similar. Therefore, it is still feasible to calculate the clearance flow of the prototype pump turbine by using the wall function method to reconcile the contradiction between calculation accuracy and resources.

For the theoretical analysis of the findings in the study, the accurate calculation of the two viscous boundary layers serves as the foundation for the core region. In fact, despite extensive research on the turbulent boundary layer, the relative theory is extremely immature, and most theories applied in engineering are summarized from experiments and calculations. In recent years, many numerical simulations based on the Reynolds-average method were used to numerically calculate the boundary layer. However, the turbulence boundary layer equation for the Reynolds-average approach has a pulsation item that is difficult to solve theoretically. Therefore, intensive studies in conjunction with numerical calculation techniques and tests will be required to calculate the turbulent boundary layer of the rotating disk in the future.

Data availability statement

The original contributions presented in the study are included in the article/Supplementary Material; further inquiries can be directed to the corresponding author.

Author contributions

XH and YC contributed to the conception and design of the study. XH and HL carried out the model test and CFD simulation. YC and KL contributed to the interpretation of the results. YC, HC, and DL contributed to the manuscript revision. All authors have read and agreed to the published version of the manuscript.

Funding

This work was supported by the National Natural Science Foundation of China (NSFC) (Grant Nos. 51839008 and 51909226), the China Postdoctoral Science Foundation (Grant No. 2020M673568XB), and the Seed Fund Program for Sino-Foreign Joint Scientific Research Platform of Wuhan University.

Acknowledgments

The numerical simulations were conducted on the supercomputing system in the Supercomputing Center of Wuhan University.

Conflict of interest

Author DL was employed by Dongfang Electric Machinery Co., Ltd., and author HC was employed by CSG Power Generation Co., Ltd.

The remaining authors declare that the research was conducted in the absence of any commercial or financial relationships that could be construed as a potential conflict of interest.

Publisher's note

References

Batchelor, G. K. (1951). Note on a class of solutions of the navier-stokes equations representing steady rotationally symmetric flow. *Q. J. Mech. Appl. Math.* 4, 29–41. doi:10.1093/qjmam/4.1.29

Bech, K. H., Tillmark, N., Alfredsson, P. H., and Andersson, H. I. (2006). An investigation of turbulent plane Couette flow at low Reynolds numbers. *J. Fluid Mech.* 286, 291–325. doi:10.1017/s0022112095000747

Bödewadt, U. T. (1940). Die drehstrmung bber festem grund. *Z. Angew. Math. Mech.* 20, 241–253. doi:10.1002/zamm.19400200502

Brady, J., and Durlofsky, L. (1987). On rotating disk flow. *J. Fluid Mech.* 175, 363–394. doi:10.1017/s0022112087000430

Cao, Y., and Qiu, X. (1998). *Experimental heat transfer*. Beijing: National Defense Industry Press.

Cheah, S. C., Iacovides, H., Jackson, D. C., Ji, H., and Launder, B. E. (1994). Experimental investigation of enclosed rotor-Stator disk flows. *Exp. Therm. Fluid Sci.* 9, 445–455. doi:10.1016/0894-1777(94)90022-1

Daily, J. W., and Nece, R. E. (1960). Chamber dimension effects on induced flow and frictional resistance of enclosed rotating disks. *J. Basic Eng.* 82, 217–230. doi:10.1115/1.3662532

Elena, L., and Roland, S. (1996). Turbulence modeling of rotating confined flows. *Int. J. Heat Fluid Flow* 17, 283–289. doi:10.1016/0142-727x(96)00032-x

Fu, X., Li, D., Wang, H., Zhang, G., Li, Z., and Wei, X. (2018). Influence of the clearance flow on the load rejection process in a pump-turbine. *Renew. Energy* 127, 310–321. doi:10.1016/j.renene.2018.04.054

Gauthier, G., Gondret, P., Moisy, F., and Rabaud, M. (2002). Instabilities in the flow between co- and counter-rotating disks. *J. Fluid Mech.* 473, 1–21. doi:10.1017/s0022112002002525

Gauthier, G., Gondret, P., and Rabaud, M. (1999). Axisymmetric propagating vortices inthe flow between a stationary and a rotating diskenclosed by a cylinder. *J. Fluid Mech.* 386, 105–126. doi:10.1017/s0022112099004346

Goyal, R., and Gandhi, B. K. (2018). Review of hydrodynamics instabilities in Francis turbine during off-design and transient operations. *Renew. Energy* 116, 697–709. doi:10.1016/j.renene.2017.10.012

Hendriks, F. (2010). On Taylor vortices and Ekman layers in flow-induced vibration of hard disk drives. *Microsyst. Technol.* 16 (1-2), 93–101. doi:10.1007/s00542-008-0765-2

Hou, X., Cheng, Y., Hu, D., Xue, S., Wang, B., Zhang, X., et al. (2021a). Influence factors of clearance leakage flowrate and clearance hydraulic axial force of pump-turbine. *IOP Conf. Ser.* 1037, 012035. doi:10.1088/1755-1315/1037/1/012035

Hou, X., Cheng, Y., Yang, Z., Liu, K., Zhang, X., and Liu, D. (2021b). Influence of clearance flow on dynamic hydraulic forces of pump-turbine during runaway transient process. *Energies* 14 (10), 2830. doi:10.3390/en14102830

Kreiss, H., and Parter, S. (1983). On the swirling flow between rotating coaxial disks: existence and nonuniqueness. *Commun. Pure Appl. Math.* 36, 55–84. doi:10.1002/cpa.3160360104

Kurokawa, J., Inagaki, M., Imamura, H., Taguchi, T., and Niikura, K. (2002). "Transient axial thrust of high-head pump-turbine at load rejection," in 21st IAHR symposium, Lausanne, September 9-12, 2002, 361–371.

Le, Z., and Kong, L. (2005). Cause analysis on rotating part lifting of unit 2 in tianhuangping pumped storage plant. *Mech. Electr. Tech. Hydropower Stn.* 28 (5), 11–14.

Lopez, J. M. (1996). Flow between a stationary and a rotating disk shrouded by a co-rotating cylinder. *Phys. Fluids* 8 (10), 2605–2613. doi:10.1063/1.869047

Lopez, J. M., and Weidman, P. D. (1996). Stability of stationary endwall boundary layers during spin-down. *J. Fluid Mech.* 326, 373–398. doi:10.1017/s0022112096008361

Mao, Z., Tao, R., Chen, F., Bi, H., Cao, J., Luo, Y., et al. (2021). Investigation of the starting-up axial hydraulic force and structure characteristics of pump turbine in pump mode. *J. Mar. Sci. Eng.* 9 (2), 158. doi:10.3390/jmse9020158

Mellor, G. L., Chapple, P. J., and Stokes, V. K. (1968). On the flow between a rotating and a stationary disk. *J. Fluid Mech.* 31 (01), 95. doi:10.1017/s0022112068000054

Pirozzoli, S., Bernardini, M., and Orlandi, P. (2014). Turbulence statistics in Couette flow at high Reynolds number. *J. Fluid Mech.* 758, 327–343. doi:10.1017/jfm.2014.529

Poncet, S., Chauve, M. P., and Le Gal, P. (2005). Turbulent rotating disk flow with inward throughflow. *J. Fluid Mech.* 522, 253–262. doi:10.1017/s0022112004002046

Poncet, S., Serre, É., and Le Gal, P. (2009). Revisiting the two first instabilities of the flow in an annular rotor-stator cavity. *Phys. Fluids* 21 (6), 064106. doi:10.1063/1.3156859

Savaş, O. (1983). Circular waves on a stationary disk in rotating flow. *Phys. Fluids (1994).* 26 (12), 3445. doi:10.1063/1.864124

Serre, E., Crespo Del Arco, E., and Bontoux, P. (2001). Annular and spiral patterns in flows between rotating and stationary discs. *J. Fluid Mech.* 434, 65–100. doi:10.1017/s0022112001003494

Singh, A. (2014). Inward flow between stationary and rotating disks. *J. Fluids Eng.* 136 (10), 101205. doi:10.1115/1.4027322

Singh, A. (2017). Theoretical investigation on inflow between two rotating disks. *J. Fluids Eng.* 139 (11), 111202. doi:10.1115/1.4037058

Singh, A., and Zosimovych, N. (2016). Laminar flow investigation between a stationary and a rotating disk with a source at centre. *Eng. Sci./Mech.* 1, 1–10.

Stewartson, K. (1952). On the flow between two rotating coaxial disks. *Math. Proc. Camb. Phil. Soc.* 49 (2), 333–341. doi:10.1017/s0305004100028437

van Eeten, K. M. P., van der Schaaf, J., van Heijst, G. J. F., and Schouten, J. C. (2013). Lyapunov-stability of solution branches of rotating disk flow. *Phys. Fluids* 25 (7), 073602. doi:10.1063/1.4812704

Von Kármán, T. (1921). Uber laminare and turbulente reibung. *Z. Angew. Math. Mech.* 1, 233–252. doi:10.1002/zamm.19210010401

Watanabe, T., Furukawa, H., Fujisawa, S., and Endo, S. (2016). Effect of axial clearance on the flow structure around a rotating disk enclosed in a cylindrical casing. *J. Flow Control, Meas. Vis.* 04 (01), 1–12. doi:10.4236/jfcmv.2016.41001

Wu, G., Zhang, K., and Dai, Y. (2005). Influence of the runner gap and seal construction on the safety in operation of Francis water power sets. *Large Electr. Mach. Hydraulic Turbine* 1 (1), 44–52.

Wu, G., Zhang, K., Dai, Y., and Sun, J. (2004). Influences of the leakage rate of low specific speed Francis runner on phenomenon of the lifting hydroelectric generator set. *J. Hydroelectr. Eng.* 23 (4), 106–111.

Zandbergen, P., and Dijkstra, D. (1987). Von karman swirling flows. *Annu. Rev. Fluid Mech.* 19, 465–491. doi:10.1146/annurev.fl.19.010187.002341

Zhang, J. (2017). *Numerical simulation of multi-scale flows in Francis turbine and research on hydraulic stability of transient processes*. Nanjing: Hohai University.

frontiers | Frontiers in Energy Research

TYPE Original Research
PUBLISHED 30 September 2022
DOI 10.3389/fenrg.2022.969706

OPEN ACCESS

EDITED BY
Daqing Zhou,
Hohai University, China

REVIEWED BY
Ye Changliang,
Hohai University, China
Huixiang Chen,
Hohai University, China

*CORRESPONDENCE
Jin-Hyuk Kim,
jinhyuk@kitech.re.kr

SPECIALTY SECTION
This article was submitted to Process and Energy Systems Engineering, a section of the journal Frontiers in Energy Research

RECEIVED 15 June 2022
ACCEPTED 15 September 2022
PUBLISHED 30 September 2022

CITATION
Shamsuddeen MM, Kim S, Shahzer MA, Ma S-B and Kim J-H (2022), Numerical investigation of losses in a double-suction multistage centrifugal pump and its mitigation using baffle plates. *Front. Energy Res.* 10:969706. doi: 10.3389/fenrg.2022.969706

Numerical investigation of losses in a double-suction multistage centrifugal pump and its mitigation using baffle plates

Mohamed Murshid Shamsuddeen[1,2], Sung Kim[2], Mohammad Abu Shahzer[1,2], Sang-Bum Ma[2] and Jin-Hyuk Kim[1,2]*

[1]Convergence Manufacturing System Engineering (Green Process and Energy System Engineering), Korea University of Science & Technology, Daejeon, South Korea, [2]Carbon Neutral Technology R&D Department (Fluid Machinery), Korea Institute of Industrial Technology, Cheonan, South Korea

The flow in a double-suction twin-volute five-stage centrifugal pump is studied numerically using Computational Fluid Dynamics (CFD) calculations. The pump performance at various flow rates obtained numerically are compared with the theoretically results. The deterioration in pump performance at various flow rates were investigated to find the losses associated with the design of the pump components. The stage-wise performance analysis revealed the hydraulic losses associated with the second-stage impeller due to highly swirled flow exiting from the first stage twin-volute. The fluid exiting the twin-volute have a high circumferential velocity than its radial component leading to a high pre-swirl at the inlet of stage 2 impeller. In order to regulate the high pre-swirl, baffle plates were installed at the exit of the twin-volute. Three baffle plate configurations were studied and their effects on the pump performances were compared. The vertical configuration improved the pump efficiency by 1.36% and head by 6.04% while the horizontal configuration improved them by 2.42% and 5.96% respectively. The 4-plate baffle configuration improved the pump performance by only a small margin. The installation of the baffle plates also improved the stage performances in both design and off-design conditions. The horizontally installed baffle plates were then tested at various angles. The plates installed at 300° clock-wise increased the pump head by 9.08% and efficiency by 3.87%. A comprehensive analysis of the flow physics inside the pump are also presented.

KEYWORDS

multistage centrifugal pump, double-suction impeller, twin-volute, computational fluid dynamics, baffle plates, head loss

1 Introduction

In the recent years, CFD calculations have been extensively used in the early stages of product development even before manufacturing particularly in turbomachinery. The pump designers, in order to respond to rapid fluctuations in market requirements and to reduce development costs, use CFD methods to test their designs for their hydraulic performances prior to manufacturing. This eliminates the need to manually test several designs at various flow conditions in a turbomachinery test facility in the design stage. The design faults occurring at this stage can be identified and corrected by this technique. The design faults of a multi-stage centrifugal pump is identified and corrected in this study using CFD tools.

A 5-stage centrifugal pump was designed for application in several industries where a high head and high flow rate was required to pump water or other chemicals over a long distance. The pump was specially developed for unique applications such as boiler feedwater, reactor charge service, water injection, power recovery, seawater injection, and other high-pressure services (McGuire, 2019). In our previous study, the pump's design feasibility study demonstrated its ability to handle different fluids at vast flow rates ranges (Shamsuddeen et al., 2021b). A stage-to-stage loss analysis revealed the areas of performance degradation between stage 1 and stage 2. Two design proposals were made to correct the losses and improve the pump performance. One of the solutions was to install an additional guide vane between the first and second stage to correct the flow angle. This has been investigated previously (Shamsuddeen et al., 2021a), which showed significant improvement in the pump performance. However, the installation of an additional guide vane increased the length of the pump which accounted for additional manufacturing costs. The second solution was to install baffle plates at the twin volute exit such that it can decrease the losses without altering the pump dimensions. The proposal to install baffle plates at the exit of the twin-volute is presented in this study.

Installation of baffle plates is a standard practice to regulate the swirling flow in pumps. (Sato et al., 2010, 2011; Tanaka et al., 2012) studied the cavitation characteristics of a single-stage double suction volute pump with baffle plates. (Li et al., 2014; Li et al., 2018) investigated the effect of baffle plate on a single-stage self-priming pump. The baffle plate was found to prevent the formation of swirling flow in the pump chamber and increase the self-priming performance of the pump. The head and efficiency of the pump were increased when the baffle plate was installed at 36° in the clock-wise direction. (Luo et al., 2019) studied three baffle plate configurations in a low specific speed centrifugal pump and found that baffle plates helped in decreasing the pressure pulsation amplitude in the volute. (Lin et al., 2020) studied the effect of an inlet guide vane installed at the inlet of a centrifugal pump and found to reduce the hydraulic losses and improve the hydraulic performance. (Lin et al., 2022) further studied the effect of installation angle of the inlet guide vane and found that the head and efficiency improved at 25° angle. (Wang et al., 2017; Koranteng Osman et al., 2019) installed baffle plates at the inlet channel between the suction chamber and impeller in a two-stage axially split centrifugal pump and found to improve the head by a great margin. (Shukla et al., 2017) improved the pump characteristics at off-design conditions after modifying the baffle plate geometry in a single-stage double-suction centrifugal pump. (Wei et al., 2021) added baffle plates at the centrifugal pump inlet to suppress the pump vibration and cavitation instabilities. (Zhao and Zhou, 2022) studied the effect of adding a small plate (tiny blade) in the impeller flow passage to obtain a stable pump operation. From these studies, it is evident that the installation of baffle plates not only regulates the swirling flow but also improve the pump performance.

Several researchers have installed baffle plates for various purposes especially in single-stage pumps. However, the effects of baffle plates in a 5-stage centrifugal pump at the twin-volute between two stages and the significance of the installation location and angle are not found in literatures. In this study, the effects of the baffle plate on the multistage pump performance and on individual stages are studied in depth to determine its role in mitigating hydraulic losses and improving pump efficiency. Moreover, the significance of the baffle plate installation location and angle are studied and design recommendations are provided based on the performance of the pump. The internal flow physics observed inside the pump with the installation of the baffle plates are presented in detail. This scientific study aids the pump designers to correct their design flaws prior to manufacturing the pump.

2 Description of the models

The first stage of the centrifugal pump comprise of a double-suction impeller inscribed in an inlet passage followed by a twin-volute. The twin-volute is staggered at 180° to offset the radial forces to each other. A single-suction impeller, a diffuser and a return vane are assembled in the second stage and is repeated for stages 3 and 4. The fifth stage has an impeller similar to the previous stages, but the diffuser is larger and is secured to the outlet volute. The impeller is engineered to reach a high head with maximum efficiency, while a diffuser is designed to increase pressure in its vanes while reducing pressure gradients in the return vanes. Figure 1 shows the centrifugal pump design. The proposed 5-stage pump is assembled in such a way that the number of stages may be adjusted to obtain the Net Positive Suction Head Required (NPSHr) and flow rate requirements. They are usually determined by the API BB5 pump standards (Api, 1995). The specification and the dimensions of the pump is given in Table 1.

Three baffle plate designs were studied for its effect to control the swirl components of the fluid exiting the volute. The selected design is further studied to find the optimal angle of installation such that the overall efficiency and head of the pump is further improved. Figure 2 shows the reference volute design along with the three baffle plate designs. The baffle plates were installed vertically, horizontally, and

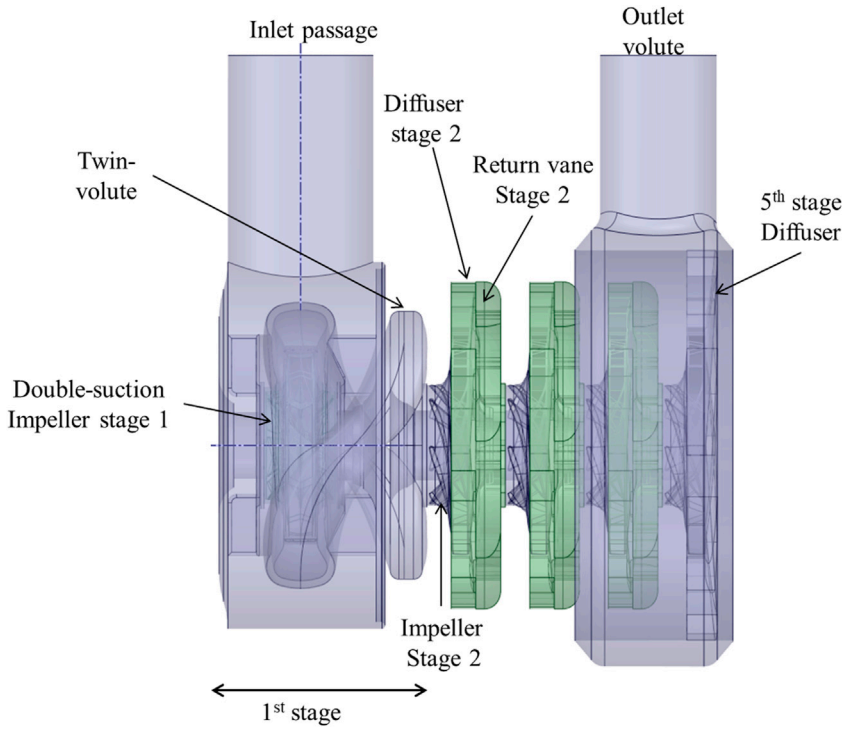

FIGURE 1
3D design of the five-stage centrifugal pump.

TABLE 1 Pump specification and dimensions.

Parameter	Value	Parameter	Value
Number of stages	5	Impeller diameter (Stage 2–5)	1.2D
Flow coefficient (∅)	0.01	Diffuser diameter (Stage 2–4)	1.78D
Head coefficient (ψ)	0.67	Diffuser diameter (Stage 5)	2.13D
Working fluid	Water	Return vane diameter (Stage 2–4)	1.5D
Specific speed	490	Overall pump length	3.94D
Rotational speed (rpm)	2,980	Casing diameter	3D
Impeller diameter (Stage 1)	D	Volute diameter	1.46D

combined horizontal and vertical design at the volute exit. Baffle plates are shaped according to the shape of the volute casing with 10 mm thickness, 46.5 mm height and 62.8 mm width.

3 Numerical model

3.1 Geometry and grid generation

The geometrical design process of the centrifugal pump structure was done using a CAD software, obtained from a geometrically similar scaled-down pump model used for low-flow rate applications provided by the manufacturer. ANSYS Bladegen tool was used to generate the impeller, diffuser and the return vane geometries. The fluid domains of all the components were extracted using ANSYS Space Claim. The baffle plates were added by modifying the geometry of the volute fluid domain. The fluid domains were then meshed using various meshing tools supplied by ANSYS. The suction chamber, the twin-volute, diffuser vanes, return vanes, and the outlet chamber were meshed using tetrahedral grids while the impellers were meshed using hexahedral grids. The generated grids are then

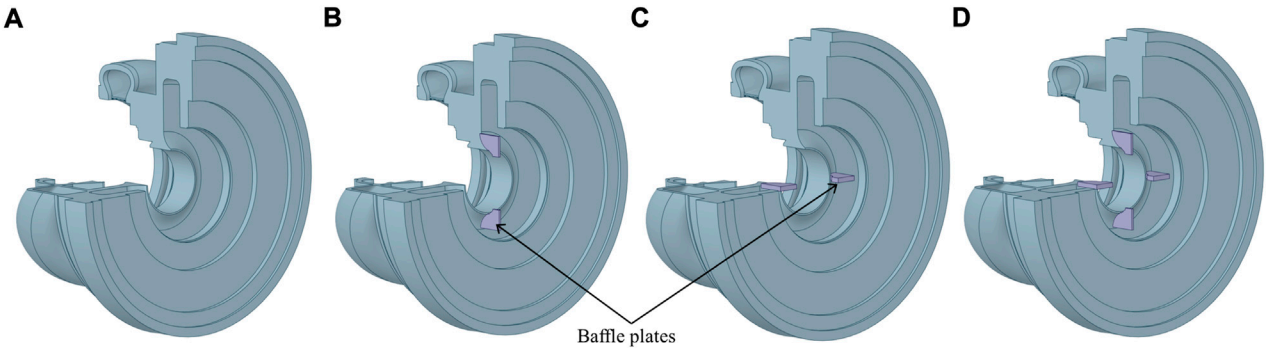

FIGURE 2
Volute configurations **(A)** Reference design **(B)** Baffle 1 **(C)** Baffle 2 **(D)** Baffle 3.

TABLE 2 Calculation of GCI values for the 2 stages.

Parameters	Stage 1	Stage 2
N1/N2/N3	1753943/1083687/670126	1385676/808556/480176
GCI_{fine} (η)	0.6	0.91
GCI_{fine} (H)	0.198	3.04

tested for grid independency so that the results do not show a discrepancy based on the grid size. To identify the most appropriate grid size for the study, the grids of first and second stages were studied independently instead of the entire pump since third, fourth and fifth stage grids are a repetition of the former stages. Multiple layers of boundary mesh were applied along the impeller suction and pressure side surfaces to resolve the boundary layers and keep the y+ value below 30. Diffuser and return channel grids were also given similar boundary layers. One passage of each component; impeller, diffuser and return vanes were modeled for reducing the computational costs.

The most accurate approach for a grid convergence research is the grid convergence index (GCI), which is obtained using the Richardson extrapolation method (Celik et al., 2008). For a key variable collected from three independent sets of grids with considerable resolutions, an estimated relative error (e_a) and fine grid convergence index (GCI_{fine}) are computed. The key variables studied are the efficiency (η) and the head (H) generated by the centrifugal pump. The GCI_{fine} can be calculated from the following formula:

$$GCI_{fine} = \frac{1.25\, e_a}{r - 1} \tag{1}$$

where r is the ratio between two grids in comparison.

The GCI values of the 2 stages are shown in Table 2.

The GCI values of both stages and for both variables are less than 4% for the fine mesh N1. Since the GCI values of both variables are reasonable, grid size N1 can be considered optimal, and additional grid refining is not required. Generating the grids for all pump stages using N1 grid size of stages 1 and 2 summed upto 6.25 million nodes. The optimum grids of the impeller, volute and the diffuser are shown in Figure 3.

The grids of all the components generated through the meshing software were assembled together in CFX-Pre module of the ANSYS CFX package. The initial and boundary conditions of the assembled fluid domains were defined for the inlet, outlet, boundary walls, periodic faces, and the interfaces between each component in this module. The pump inlet was defined at atmospheric pressure while the outlet was defined with mass flow rate. The boundary walls were defined as stationary walls and the periodic faces of the single passage domains were defined periodic with appropriate pitch ratios. All components where defined as stationary domains except for the impeller domains which rotates along the *z*-axis. The interfaces between the stationary and rotating domains were defined as mixing-plane (stage) interface due to a high pitch ratio between the components. A mesh connectivity is established at all interfaces to interconnect the non-conformal elements between the domains using a General Grid Interface (GGI). By means of an intersection algorithm, the GGI determines the connectedness between the grids on each side of the interface (ANSYS Inc, 2011). Water is used as the working fluid in the pump.

The governing equations for the fluid transportation were defined in a steady-state setting based on the Reynolds-averaged Navier-Stokes (RANS) formulas for incompressible fluids which are well-documented in a variety of sources (ANSYS, 2013; Siddique et al., 2017). In order to accurately model the turbulent behavior of the fluid inside the pump, the Shear Stress Transport (SST) turbulence model was used coupled with the standard wall function (Menter, 1994). The SST model is a widely used method for modeling turbulent flow in rotating fluid machinery

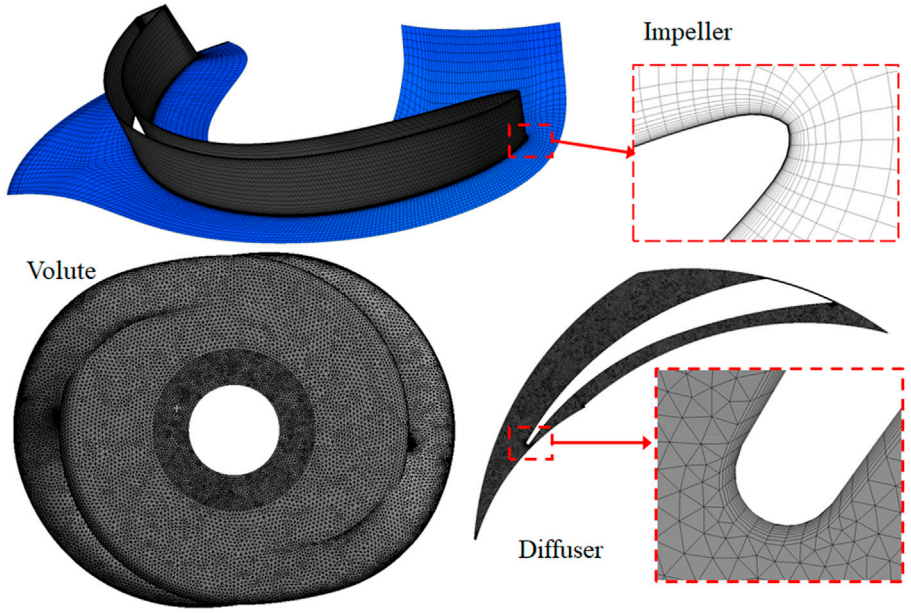

FIGURE 3
Optimal grid of the impeller, volute and diffuser.

and has been validated by several researchers from around the world (Kim et al., 2019a; Kim et al., 2019b). In the near-wall region and freestream area, the SST model uses the k–ω and k–ε equations, respectively, along with a blending function that guarantees seamless transitions between these models.

The computations are carried out using an Intel Xeon CPU with a clock speed of 2.4 GHz equipped with 56 cores and 128 GB RAM capacity. The computation time for each simulation was 18–20 h to achieve convergence.

4 Pump performance

The pump performances are expressed in terms of head coefficient (ψ), flow coefficient (φ), and efficiency which are calculated using the following formulas:

$$\psi = \frac{gH}{n^2D^2} \tag{2}$$

$$\varphi = \frac{Q}{nD^3} \tag{3}$$

$$\eta = \frac{\rho QgH}{P} \tag{4}$$

where D, g, n, P and ρ corresponds to the impeller diameter, acceleration due to gravity, rotational velocity, input power and fluid density, respectively.

A dynamically similar model pump design given by the supplier served as the basis for the proposed centrifugal pump's preliminary design. The model pump was a scaled-down model used for low flow rate industrial applications. The current pump prototype is the scaled-up design particularly to handle fluids at high flow rates and high head operations. The pump affinity rules are employed to extract the dynamically similar prototype design, as is seen below:

$$\frac{Q_1}{Q_2} = \left(\frac{n_1}{n_2}\right); \frac{H_1}{H_2} = \left(\frac{n_1}{n_2}\right)^2; \frac{P_1}{P_2} = \left(\frac{n_1}{n_2}\right)^3 \tag{5}$$

where the variables denoted by subscriptions 1 and 2 refer to the model and the prototype. The variables Q, n, H and P corresponds to the flow rate, rotational velocity, head and the input power, respectively.

The performance of the pump design derived from affinity laws is determined theoretically and then validated numerically using CFD tools. The theoretical prediction was confirmed by the projected trend of the head and efficiency curves at different flow rates. With an error margin of less than 8%, the graphs obtained from the CFD analysis are in satisfactory agreement with the theoretical results as shown in Figure 4. Due to the general constraints of the steady-state simulation with a simplified geometrical model, and the disregarding of losses in the numerical simulations, the computational accuracy does have a certain impact on the error margin. Therefore, the generated CFD results are suitable for further study since this is an initial design feasibility assessment prior to experimental testing without accounting for unexplained mechanical losses.

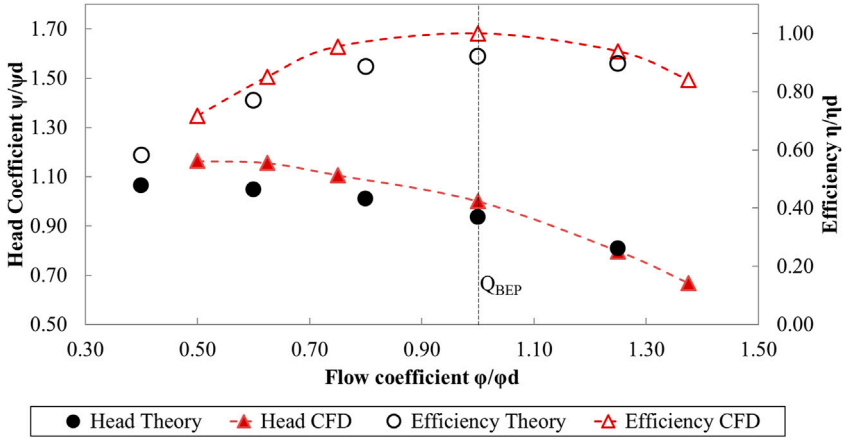

FIGURE 4
Comparison of theoretical calculations and numerical simulations.

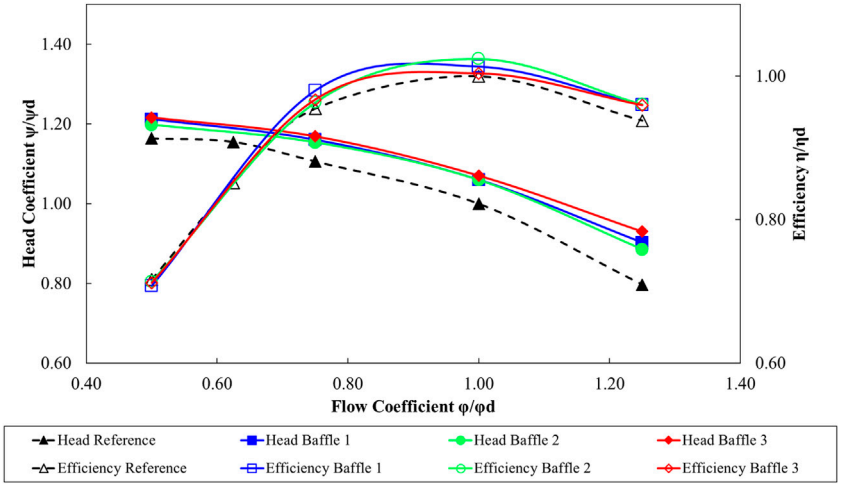

FIGURE 5
Performance comparison of different baffle designs with the reference pump.

Figure 5 compares the pump's performance comparison between different baffle plate designs. A significant increase in the head is witnessed at each flow rate for all cases with the baffle plates, with baffle 3 design having the highest head. The head at the Q_{BEP} increased by 6.04%, 5.97%, 7.07% for baffle 1, 2 and 3 designs, respectively compared to the reference pump. A fair increase in efficiency is also observed for the pump with baffle plates at large flow rates. The efficiency at the design point improved by 1.36%, 2.43%, and 0.37% respectively for baffle designs 1, 2, and 3 in comparison to the reference pump. The baffle 2 design shows the highest efficiency among the three designs. A similar increase in efficiency of 2.41% is observed at the high flow rate for baffle 2. However, the improved pump performance comes at the expense of slightly higher power consumption. With the installation of baffle plates, power consumption rose by 3.46 percent at the Q_{BEP} and by 8.46 percent at the highest flow rate condition for baffle 2 model. Even while power consumption increases at maximum flow rate, the gain in efficiency and head is sufficient to compensate for the difference. Therefore, with the installation of baffle plates, the pump's overall performance has considerably improved.

In a multistage centrifugal pump, individual stage performance is just as critical as the total pump performance.

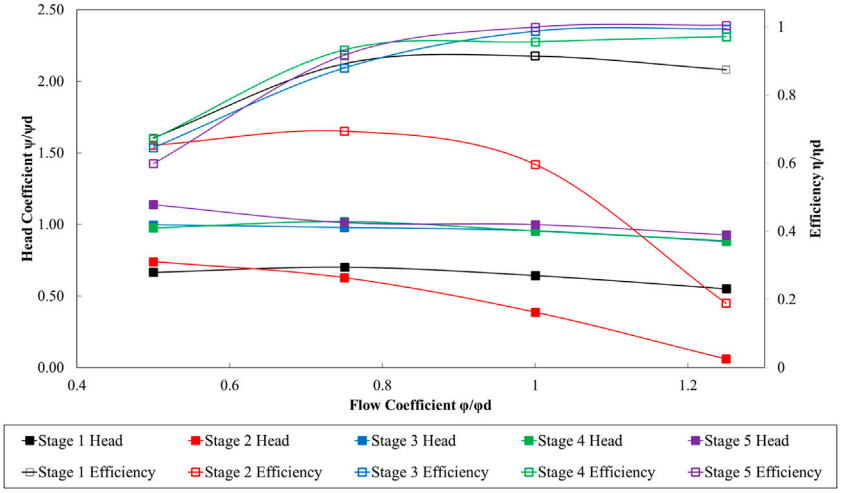

FIGURE 6
Stage-wise performance of the reference pump.

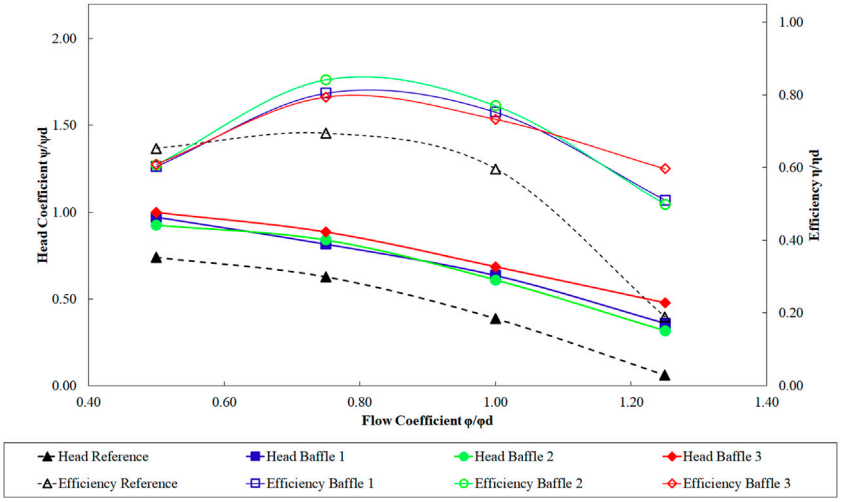

FIGURE 7
Performance comparison of stage 2.

Studying the efficiency and head of individual stages provides insight into the local characteristics of the pump and aids in identifying the losses associated with the pump. The stage-wise head is calculated by measuring the total pressure gradient at the entry and exit of each stage. The stage-wise efficiency is calculated from the input power measured by the torque on the impeller at that stage, the flow rate through the stage outlet and the stage-wise head put together in the efficiency equation. Figure 6 shows the stage-by-stage efficiency and head coefficient curves of the reference pump. At the low flow rate, the efficiency of the pump is nearly identical at all stages. Except for stage 2, all stages' hydraulic efficiency improves as the flow rate increases. Beyond Q_{BEP}, the efficiency and head at stage 2 plummets at a rapid pace. The reference pump's high decline in efficiency and head suggests a significant loss at the stage 2. The performance of the pumps with baffle plates are compared with the reference pump at the second stage in Figure 7. The installation of baffle plates has contributed to head loss recovery at the second stage at all flow rates. A difference of 63.7%, 57.3%, and 76.75% in head are observed for baffle designs 1, 2, and 3, respectively at the Q_{BEP}. Meanwhile, the efficiency increased substantially at high flow rates for all baffle plate models thereby decreasing the pump

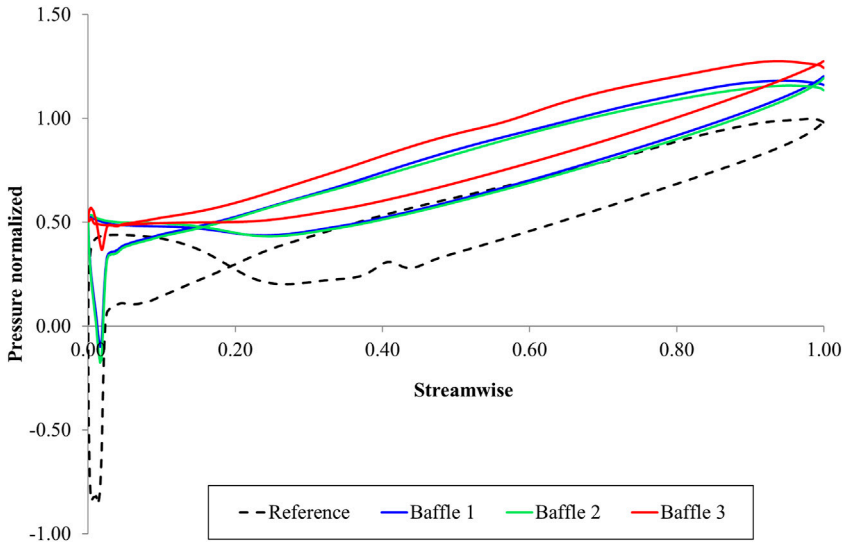

FIGURE 8
Blade loading comparison of the second stage impeller at Q_{BEP}.

stage losses. The baffle plate 2 model has the highest efficiency at stage 2 with an increase of 29.13% at the Q_{BEP}. A small improvement in performance can also be found in the subsequent stages as well. Installation of baffle plates has not only increased the stage 2 performance significantly, but it also enhanced the performance at all stages. The stage-to-stage improvement in performance has collectively reflected in the overall pump performance as seen in Figure 5.

To fully comprehend the flow dynamics at the volute-impeller interface, a thorough examination of the losses seen at stage 2 and the role of the baffle plates in reducing these losses is required. The pump running at the design point is chosen for the in-depth examination since it is operated at the design point more frequently than others. The impeller, diffuser, and return vanes make up the second stage. For the reason that the losses are most noticeable at the impeller's inlet, the loss analysis is limited to the flow through the volute to the second stage impeller. Unless otherwise noted, here onwards, the word 'impeller' refers to the second stage impeller.

Figure 8 displays the blade loading at the center-span of the impeller from leading edge to trailing edge for the 4 pump designs at Q_{BEP}. The maximum value of the pressure is used to normalize the parameter. The reference pump shows a significant drop in pressure along the leading edge, highlighting the location of the peak loss. Cavitation bubbles may form as a result of such rapid pressure drops, which can easily cause damage to the impeller. The baffle plates, installed at the exit of the volute, reduced the pressure loss at the impeller's leading edge by a great margin. The pressure drop at the leading edge has been curtailed by 88.37%, 79.49%, and 143.02% by the pump with baffle plates design 1, 2, and 3, respectively. The overall improvement in the blade loading curve is measured by calculating the weighted average of the pressure distribution which provides an accurate representation of the average change in percentage of the entire curve. The blade loading curves of baffle designs 1, 2, and 3 has improved by a weighted average of 39.4%, 37.62%, and 52.98%, respectively compared to the reference blade. The impact of the baffle plates on stage 2 impeller in improving the blade loading can also been seen in the subsequent stages as well.

4.1 Internal flow field analysis

The behavior of the fluid passing through the volute and the second stage impeller is investigated in order to discover the reasons of the losses and to study how baffle plates aid in the flow correction. The fluid exiting the impeller at stage 1, separates into the two arms of the symmetrical twin-volute, continues along the volute surface, and rejoins at the volute's outlet. The velocity vector and the pressure distribution at the exit of the twin-volute of the 4 pumps are shown in Figure 9. In the reference pump (Figure 9A), a low-pressure region is detected around the shaft due to a high circumferential velocity formed due to the rotating flow incoming from the two arms of the twin-volute. The rotating flow exits the volute after 2-3 revolutions. At the volute outlet, the fluid has a stronger circumferential velocity than the axial velocity, resulting in a pre-swirl at the leading edge of the stage two impeller. The circumferential velocity is found to be approximately 5 times higher than the axial velocity. This creates

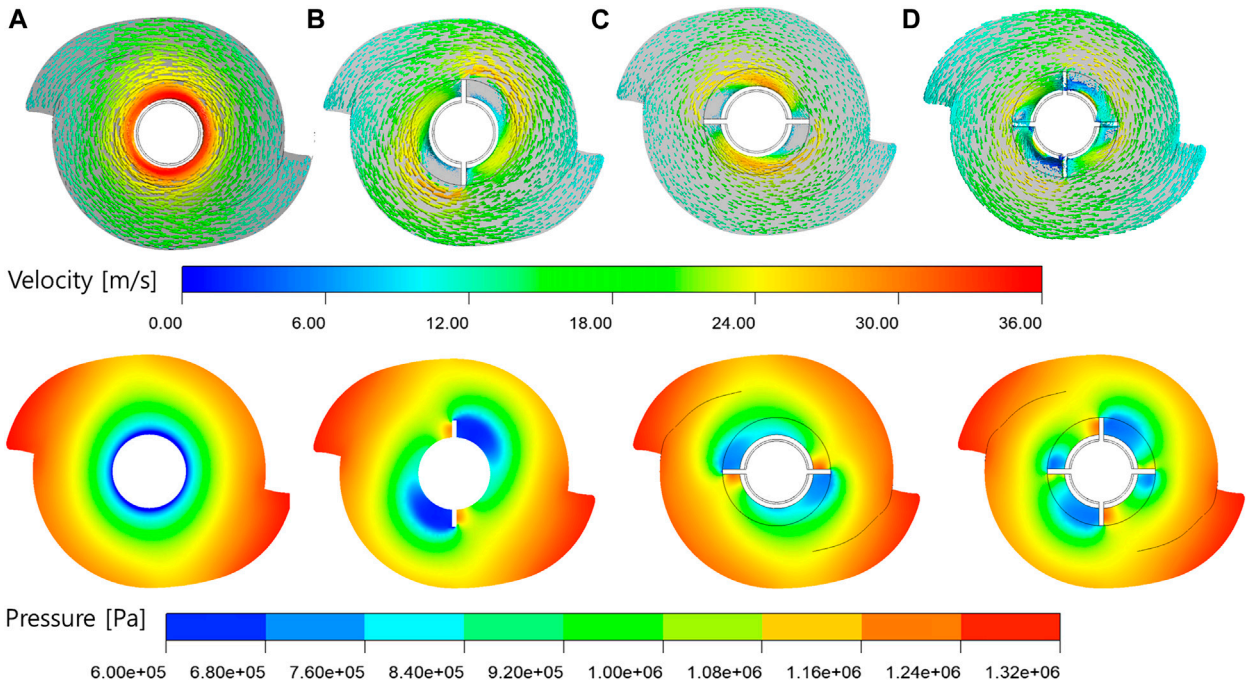

FIGURE 9
Velocity vector and pressure contour at the volute exit for **(A)** Reference pump **(B)** Baffle 1 **(C)** Baffle 2 **(D)** Baffle 3 designs.

recirculation zones between the impellers causing vertices to develop at the pressure side of the blade The vortices formed at the flow passage of the second stage impeller is shown in Figure 11A. These vortices create obstruction to the flow leading to the development of blockage effect on the flow through the impeller. These blockages have a direct impact on the stage-wise performance resulting in an overall performance loss of the pump.

With the introduction of the vertical baffle plates (baffle plate design 1) as shown in Figure 9B, the incoming flow from the two arms of the volute, strike on the baffle plate after a complete rotation. The fluid incoming from the top arm completes a revolution and strikes on the top baffle plate, while the fluid incoming from the bottom arm completes a revolution and strikes the bottom plate. The fluids striking the baffle plates loses its circumferential velocity and immediately changes its direction to exit the volute. The pre-swirl formation at the leading edge of the impeller is reduced thereby reducing the formation of vertices between the blades. The formation of vortices at the impeller flow passage has decreased considerably at the pressure side of the impeller as shown in Figure 11B. There are still few vortices observed at the leading edge and trailing edge of the runner. The reduction in vertex formations decrease the blockage to the flow through the impeller which directly contributes to decreasing head losses and improving the stage performance. The baffle plate design 1 however, has a drawback at the downstream of the plates. Low-pressure regions are formed behind the plates causing a cavity at the volute exit. This is due to the vertical orientation of the plates against the incoming flow direction. This low-pressure zone may cause cavitation of the plates and decrease the pump life rapidly.

Installing the baffle plates horizontally (baffle plate design 2) functions similarly to the design 1 by allowing the rotational flow to change its direction and exit the volute. The flow incoming from the top arm completes one revolution and strikes the left plate, while the flow from the bottom arm completes one revolution and strikes the right plate as shown in Figure 9C. The intensity of the low-pressure regions formed behind the plates have decreased by 16.53% compared to the vertical plates since the plates are installed parallel to the incoming flow. The change in flow direction of the fluid exiting the volute towards the impeller is shown in Figure 10. The fluid striking on the baffle plate, loses its momentum by half and turns towards the exit. The streamlines with high velocity, exit the volute without impact with the baffle plates. The fluid particles behind the plate due to the low-pressure zone loses all its momentum and recirculates at that region. However, the area of the recirculation zone has decreased compared to the vertical design. The effect of the change in installation location can be observed the behavior of the vortex formation in the impeller as seen in Figure 11C. The vortices formed at the leading edge and trailing have decreased while a small increase in vortex volume is observed at the pressure side.

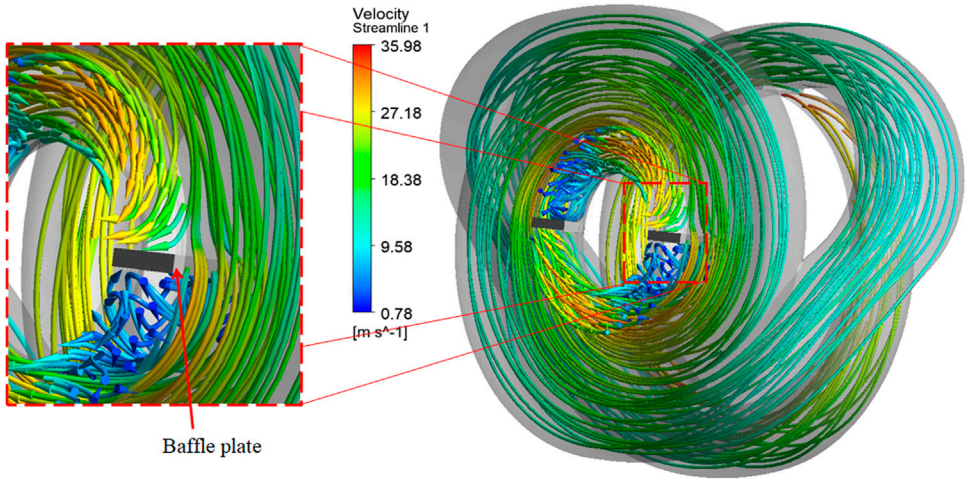

FIGURE 10
Velocity streamline at the volute exit of baffle 2 design.

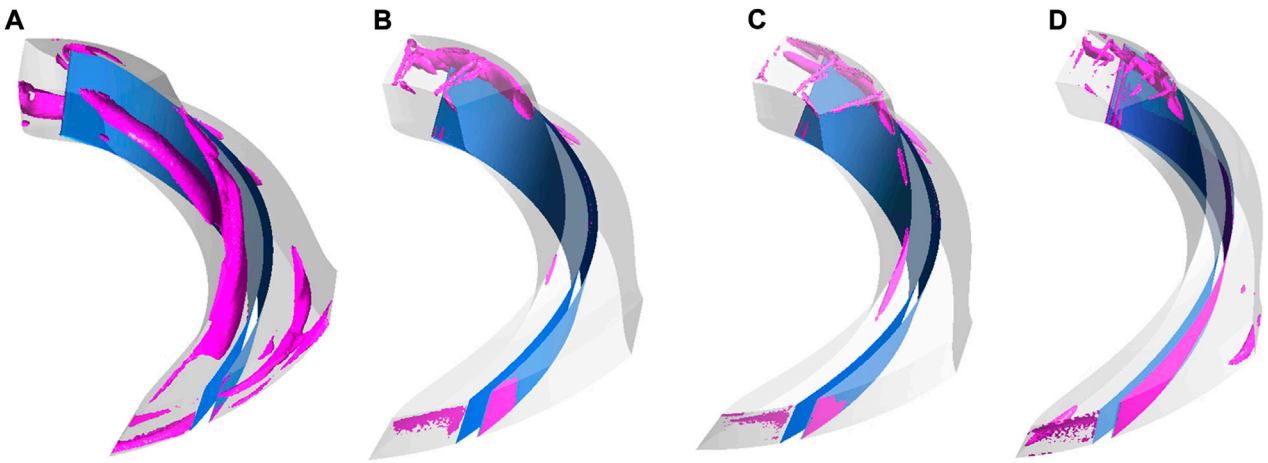

FIGURE 11
Comparison of vortex formation at the second stage impeller at Q_{BEP} (velocity swirling strength = 1,500 s^{-1}) for **(A)** Reference pump **(B)** Baffle 1 **(C)** Baffle 2 **(D)** Baffle 3 designs.

The baffle 3 design is a combination of vertical and horizontal plates. The flow incoming from the two arms of the volute, strike on the baffle plates before completing a full revolution as shown in Figure 9D. Several low-pressure recirculation zones are created at the downstream of the baffle plates causing more harm than good. However, the vortex formation at the impeller pressure side has been completely eliminated as seen in Figure 11D. This comes at a cost of small vortices forming at the suction side and at the trailing edge.

From Figure 11, it can be observed that the vortices formed between the impellers at stage two in the reference model has been diminished with the installation of baffle plates. The formation of these vortices at the impeller obstructs the incoming flow by creating a blockage effect thereby decreasing the pressure at the impeller pressure-side. This is further explained by drawing the velocity triangle at the impeller leading edge. The velocity triangles of the 4 models are shown in Figure 12. The angle β represents the relative flow angle, α represents the absolute flow angle, W is the relative velocity, C is the absolute velocity and U is the blade velocity. The velocity triangle of baffle 2 design shows a decrease in the relative angle from $\beta = 128.51^{\circ}$ to $\beta = 88.1^{\circ}$. The magnitude of

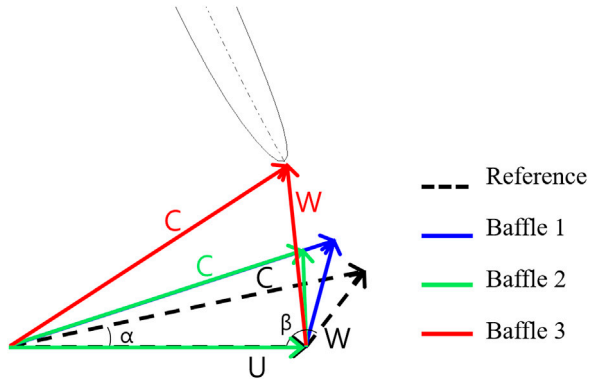

FIGURE 12
Velocity triangles at the impeller inlet of the pump models.

the relative velocity increased by 9.1% while the absolute velocity decreased by 36.26%. The significance of this flow angle correction can explain the decrease in the circumferential velocity at the leading edge of the impeller. The circumferential velocity decreased by 35.84% with horizontal installation of baffle plates.

The pump performance comparison and the internal flow field analysis showed that the baffle plate designs have succeeded in mitigating the losses associated with the twin-volute design. However, it is observed that there is still room for improvement in the baffle plate design as certain low-pressure stagnation zones are observed downstream of the plates. Among the three baffle designs, the baffle 2 pump is chosen for further analysis. The decision to choose the baffle 2 design over other designs for is based on the pump performance. The performance curve of different baffle designs (Figure 5) shows that the baffle 2 has the highest efficiency at the design point. Another important parameter in the decision making is the power consumption of the pump. The power consumption increased with the installation of the plates. At the Q_{BEP}, the baffle 3 pump consumed the highest power at 6.68% higher than the reference pump while baffle 1 and 2 designs consumed 4.62% and 3.45% higher power, respectively.

5 Study on baffle plate installation angle

The baffle plate installation angles are studied with an aim to reduce the low-pressure zones observed at the downstream of the plates and to improve the pump performance. The baffle plate design 2, being the most efficient design among others, is selected for this study. The baffle plates are installed at angles 45°, 315°, 300°, and 280° as shown in Figure 13. The angles 315°, 300°, and 280° correspond to −45°, −60°, and −80° in the anti-clockwise direction, respectively.

The angle of installation of the baffle plates has significant effect on the performance of the pump. The efficiency and head at the Q_{BEP} are plotted in Figure 14. The head and efficiency parameters are normalized with the head and efficiency of the baffle 2 design for ease of comparison. The subscript "B2" corresponds to the baffle 2 design installed horizontally at 0°. The baffle plate design 2 installed at 300° shows the highest efficiency and head with an increase of 1.41% and 2.94%, respectively compared to the baffle plate design 2 installed at 0°. This is because, the pressure behind the baffle plate as shown in Figure 15 has been increased by 27.29%, thereby eliminating any low-pressure zones at the volute exit. As a result, the velocity streamline plot shows low volute exit velocity for baffle plate at 300° than for other angles. The blade loading curve showed an increase in weighted average of 15.66%, 17.83%, and 8.17% for the 315°, 300°, and 280°, respectively compared to B2. Meanwhile, rotating the baffle plate to +45° showed negative impact since it is against the flow direction. The efficiency, head and weighted average of blade loading curve decreased by −0.97%, −1.41%, and −3.31%, respectively. Therefore, the baffle plate design 2 installed at an angle of 300° is selected for manufacturing.

In comparison with the initial reference pump (without baffle plates), the selected design (baffle plates installed at

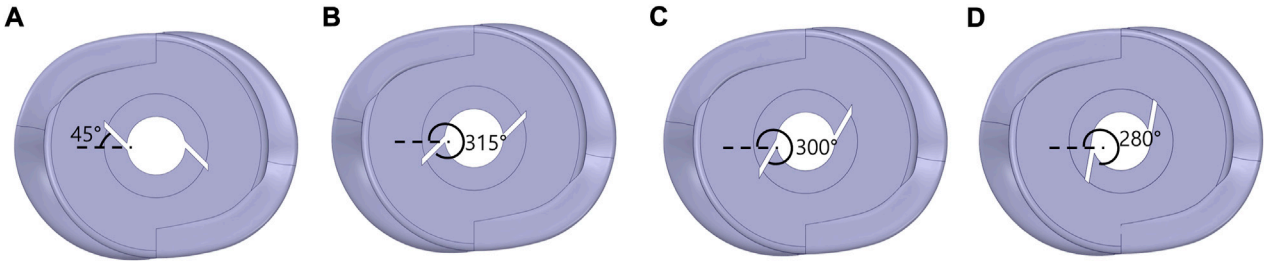

FIGURE 13
Baffle plate design 2 installed at various angles. **(A)** 45° **(B)** 315° **(C)** 300° **(D)** 280°.

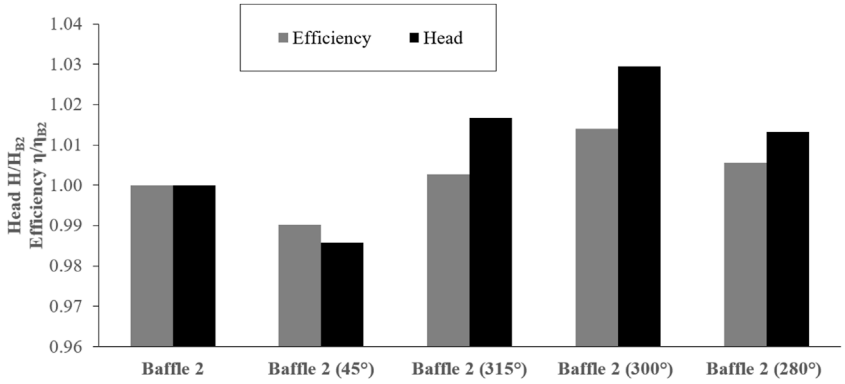

FIGURE 14
Efficiency and head comparison of baffle 2 design at various angles.

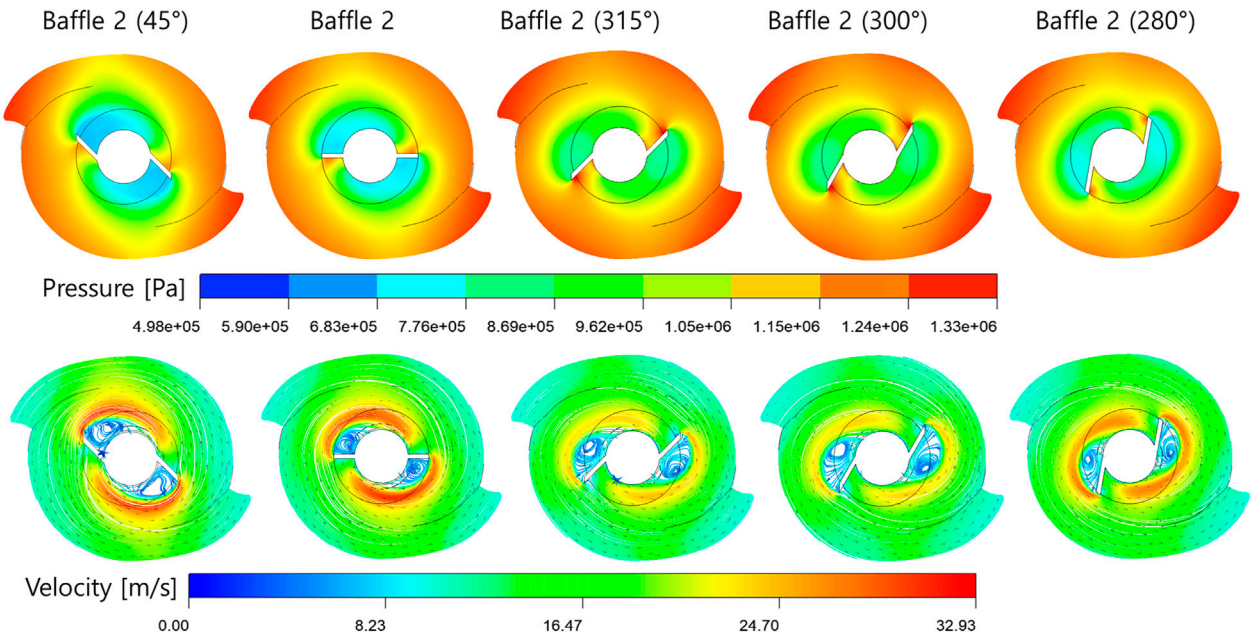

FIGURE 15
Pressure and velocity streamlines at volute exit for different baffle plate angles.

300°) exhibited substantial improvement in the overall pump performance. The efficiency of the pump at Q_{BEP} improved by 3.87% while the head increased by 9.1%. The overall blade loading distribution of the second stage impeller improved by a weighted average of 62.16%. The fluid pressure at the exit of the volute increased by 52.45% while the circumferential velocity weakened by −43.88%. Thereupon, the selected design is recommended for manufacturing and testing in a test facility.

6 Conclusion

A multistage centrifugal pump developed for high-head and high flow rate application in industrial flows, showed performance degradation due to faulty design. The 5-stage pump consisting of a double-suction impeller and a twin volute in the first stage; impeller, diffuser and return vanes in the consecutive stages exhibited head losses at the second stage. The in-depth flow analysis revealed that the flow exiting from

stage 1 to stage 2 had high radial forces than axial force, leading to formation of recirculation zones and vortices at the second stage impeller. The fluid exiting the twin-volute had a high circumferential velocity contributing to excessive pre-swirl formation at the impeller inlet. Installation of baffle plates at the volute exit weakened the circumferential velocity exiting the volute thereby regulating the pre-swirl formation at the second stage impeller inlet. Three baffle plate designs were tested for its loss mitigating capability and performance enhancement. A pair of vertical plates (baffle 1), horizontal plates (baffle 2) and a combination of both (baffle 3) were studied using computational fluid dynamic tools. The effects of the baffle plates on the pump performance compared with the initial pump model are:

1. An increase in head of the pump were observed for pump with baffle plates at all flow rates. At the design point, the pump with baffle plate showed a rise in pump head by 6.04%, 5.97%, 7.07% for baffle 1, 2, and 3 designs, respectively.
2. The efficiency of the pump had little change at low flow rates but at the high flow rates, the efficiency improved by 1.36%, 2.43%, and 0.37% respectively for baffle designs 1, 2, and 3.
3. The stage-to-stage analysis showed the loss mitigation at the second stage by the installation of the baffle plates in the first stage. The stage head loss decreased by 63.7%, 57.3%, and 76.75% while stage efficiency rose by 26.1%, 29.13%, and 22.84% for baffle plate designs 1, 2, and 3, respectively.
4. Plotting the blade loading chart over the blade mid-span revealed a low-pressure point at the leading edge which may cause cavitation of the pump impeller. The blade loading chart improved with a weighted average of 39.4%, 37.62% and 52.98% with the installation of baffle plates 1, 2, and 3 respectively.
5. Understanding the change in flow phenomena with the baffle plate installation was facilitated by a comprehensive flow field investigation at the volute-impeller interface. The baffle plates prevented the fluid from swirling within the volute before exiting towards the impeller. The fluid incoming from the volute arms strike at the baffle plate, thereby changing its course towards the second stage impeller.
6. Baffle plate design 2 being the most efficient design among the proposed designs were later tested at various installation angles to further enhance the effectiveness of the plates. The plates were studied at 45°, 315°, 300°, and 280° at the same flow conditions.
7. The baffle plate installed at 300° is found to be the most effective design with an increase in efficiency by 3.87% and head by 9.1% at the design point compared to the reference pump.

The installation of the baffle plates proved to be successful in mitigating losses associated with the second stage of the pump and thereby increasing the overall pump performance. The effect of the baffle plates would be tested experimentally prior to manufacturing the final prototype and is an ongoing research. The pump cavitation analysis and fatigue test of the twin-volute with the baffle plates using FSI techniques is the future work of this study. The baffle plate shape optimization can be carried out if necessary. The pump design and redesign technique using CFD in the design phase prior to manufacturing has indeed saved a certain amount of the testing cost before product commercialization. This study provides design recommendations to the pump designers to decrease the hydraulic losses and improve the pump performance in the design stage itself.

Data availability statement

The raw data supporting the conclusion of this article will be made available by the authors, without undue reservation.

Author contributions

Conceptualization: J-HK, SK, MMS, and S-BM, methodology: MMS; software: MMS; validation: J-HK and MMS; formal analysis: MMS investigation: MMS and SK; resources: J-HK; data curation: MMS and MAS; writing—original draft preparation: MMS; writing—review and editing: MMS, and MAS; visualization: MMS; supervision: J-HK; project administration: J-HK; funding acquisition: J-HK. All authors have read and agreed to the published version of the manuscript.

Funding

This work was supported by Korea Institute of Energy Technology Evaluation and Planning (KETEP) grant funded by the Korea government (MOTIE) (2021202080026A, Development of Variable Operating Technology for Medium and Large Size Pump) and partially supported by a grant (No. JB220011) from the Korean Institute of Industrial Technology (KITECH).

Conflict of interest

The authors declare that the research was conducted in the absence of any commercial or financial relationships that could be construed as a potential conflict of interest.

Publisher's note

References

ANSYS (2013). "ANSYS BladeModeler," in *ANSYS TurboSystem user's guide* (Fort Cannon, PA, USA: ANSYS, Inc).

ANSYS Inc (2011). "Domain interfaces," in *ANSYS CFX-pre user's guide* (Pennsylvania, USA: ANSYS, Inc.), 146–147.

API (1995). *API 610 - centrifugal pumps for petroleum, heavy duty chemical, and gas industry services*.

Celik, I. B., Ghia, U., Roache, P. J., Freitas, C. J., Coleman, H., and Raad, P. E. (2008). Procedure for estimation and reporting of uncertainty due to discretization in CFD applications. *J. Fluids Eng. Trans. ASME* 130, 0780011–0780014. doi:10.1115/1.2960953/444689

Kim, J. H., Cho, B. M., Kim, S., Lee, Y. K., and Choi, Y. S. (2019a). Detailed flow characteristic analysis of a three-stage centrifugal pump at design and off-design conditions. *IOP Conf. Ser. Earth Environ. Sci.* 240, 092004. doi:10.1088/1755-1315/240/9/092004

Kim, J. H., Cho, B. M., Kim, S., Lee, Y. K., and Choi, Y. S. (2019b). Steady and unsteady flow characteristics of a multi-stage centrifugal pump under design and off-design conditions. *Int. J. Fluid Mach. Syst.* 12, 64–70. doi:10.5293/IJFMS.2019.12.1.064

Koranteng Osman, M., Wang, W., Yuan, J., Zhao, J., Wang, Y., and Liu, J. (2019). Flow loss analysis of a two-stage axially split centrifugal pump with double inlet under different channel designs. *Proc. Institution Mech. Eng. Part C J. Mech. Eng. Sci.* 233, 5316–5328. doi:10.1177/0954406219843573

Li, G., Wang, Y., and Mao, J. (2018). Numerical investigation on the gas–liquid entraining and separating effects on self-priming performance in a flow-ejecting centrifugal pump. *Proc. Institution Mech. Eng. Part A J. Power Energy* 233, 232–248. doi:10.1177/0957650918784418

Li, G., Wang, Y., Yin, G., Cui, Y., and Liang, Q. (2014). "Investigation of the self-priming process of self-priming pump under gas-liquid two-phase condition," in *Volume 1B, symposia: Fluid machinery; fluid-structure interaction and flow-induced noise in industrial applications; flow applications in aerospace; flow manipulation and active control: Theory, experiments and implementation; multiscale methods for multi* (New York, United States: American Society of Mechanical Engineers ASME). doi:10.1115/FEDSM2014-21199

Lin, P., Li, Y., Xu, W., Chen, H., and Zhu, Z. (2020). Numerical study on the influence of inlet guide vanes on the internal flow characteristics of centrifugal pump. *Processes* 8, 122. doi:10.3390/pr8010122

Lin, P., Yang, T., Xu, W., and Zhu, Z. (2022). Influence of different offset angles of inlet guide vanes on flow characteristics of centrifugal pump. *Front. Energy Res.* 10, 2. doi:10.3389/fenrg.2022.818244

Luo, K., Wang, Y., Liu, H., Chen, J., Li, Y., and Yan, J. (2019). Effect of suction chamber baffles on pressure fluctuations in a low specific speed centrifugal pump. *J. Vibroengineering* 21, 1441–1455. doi:10.21595/jve.2018.18943

McGuire, J. T. (2019). "Centrifugal pumps," in *pumps for chemical processing* (Boca Raton, Florida, United States: CRC Press), 27–105.

Menter, F. R. (1994). Two-equation eddy-viscosity turbulence models for engineering applications. *AIAA Journal* 32 (8), 1598–1605. doi:10.2514/3.12149

Sato, T., Nagahara, T., Tanaka, K., Fuchiwaki, M., Shimizu, F., and Inoue, A. (2011). Vortex cavitation from baffle plate and pump vibration in a double-suction volute pump. *Int. J. Fluid Mach. Syst.* 4, 76–83. doi:10.5293/ijfms.2011.4.1.076

Sato, T., Nagahara, T., Tanaka, K., Fuchiwaki, M., and Shimizu, F. (2010). Vortex cavitation and oscillation in a double-suction volute pump. *IOP Conf. Ser. Earth Environ. Sci.* 12, 012019. doi:10.1088/1755-1315/12/1/012019

Shamsuddeen, M. M., Ma, S. B., Kim, S., Yoon, J. H., Lee, K. H., Jung, C., et al. (2021a). Effect of an inducer-type guide vane on hydraulic losses at the inter-stage flow passage of a multistage centrifugal pump. *Processes* 9, 526. doi:10.3390/pr9030526

Shamsuddeen, M. M., Ma, S., Kim, S., Yoon, J., Lee, K., Jung, C., et al. (2021b). Flow field analysis and feasibility study of a multistage centrifugal pump designed for low-viscous fluids. *Appl. Sci. (Basel).* 11, 1314. doi:10.3390/app11031314

Shukla, S. N., Khare, R., and Prasad, V. (2017). CFD approach for off-design efficiency improvement of double suction centrifugal pump. *Int. J. Mech. Prod. Eng. Res. Dev.* 7, 289–300. doi:10.24247/ijmperdoct201730

Siddique, M. H., Bellary, S. A. I., Samad, A., Kim, J. H., and Choi, Y. S. (2017). Experimental and numerical investigation of the performance of a centrifugal pump when pumping water and light crude oil. *Arab. J. Sci. Eng.* 42, 4605–4615. doi:10.1007/s13369-017-2592-1

Tanaka, K., Inoue, A., Sato, T., Nagahara, T., Fuchiwaki, M., and Shimizu, F. (2012). Oscillation caused by vortex cavitation in a double-suction volute pump. *ASME-JSME-KSME 2011 Jt. Fluids Eng. Conf. AJK 2011* 1, 2275–2284. doi:10.1115/AJK2011-08040

Wang, Y., Pei, J., Yuan, S., and Wang, W. (2017). "Effect of baffles in between stages on performance and flow characteristics of a two-stage split case centrifugal pump," in Am. Soc. Mech. Eng. Fluids Eng. Div. FEDSM 1A-2017, Waikoloa, Hawaii, USA, July 30–August 3, 2017. doi:10.1115/FEDSM2017-69121

Wei, Z., Tao, R., Xiao, R., and Hu, H. (2021). Hydrodynamic improvement by adding inlet baffles on centrifugal pump for reducing cavitation instabilities. *J. Vib. Control*, 1–12. doi:10.1177/10775463211047401

Zhao, W., and Zhou, Z. (2022). Influence of geometric parameters of tiny blades on the shroud of a centrifugal pump on the cavitation suppression effect. *Front. Energy Res.* 10, 289. doi:10.3389/fenrg.2022.865885

Frontiers in
Energy Research

Advances and innovation in sustainable, reliable and affordable energy

Explores sustainable and environmental developments in energy. It focuses on technological advances supporting Sustainable Development Goal 7: access to affordable, reliable, sustainable and modern energy for all.

Discover the latest Research Topics

See more →

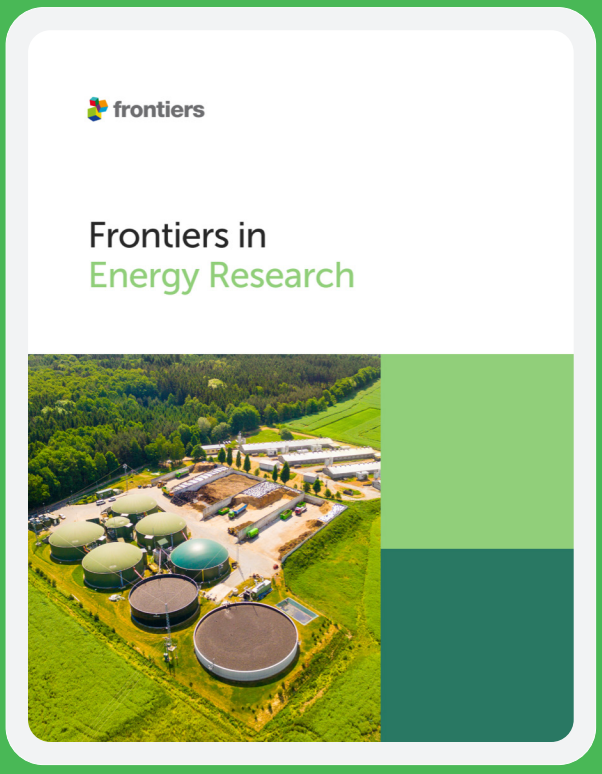

Frontiers

Avenue du Tribunal-Fédéral 34
1005 Lausanne, Switzerland
frontiersin.org

Contact us

+41 (0)21 510 17 00
frontiersin.org/about/contact